Transactions of the ASME®

Journal of Heat Transfer

Published Quarterly by The American Society of Mechanical Engineers

VOLUME 122 • NUMBER 4 • NOVEMBER 2000

Forced Convection

Jets, Wakes, and Impingements

Natural and Mixed Convection

Boiling and Condensation

Combustion

Phase Change and Multiphase Heat Transfer

(Contents continued on inside back cover)

This journal is printed on acid-free paper, which exceeds the ANSI Z39.48-1992 specification for permanence of paper and library materials. ♾™
♲ 85% recycled content, including 10% post-consumer fibers.

HEAT TRANSFER DIVISION
Chair, **L. C. WITTE**
Vice Chair, **J. H. KIM**
Past Chair, **R. A. NELSON**
Secretary, **Y. BAYAZITOGLU**
Treasurer, **R. D. SKOCYPEC**
Technical Editor, **V. DHIR** (2005)

Associate Technical Editors,
C. T. AVEDISIAN (2002)
H. H. BAU (2003)
C. BECKERMANN (2001)
A. BEJAN (2003)
V. P. CAREY (2003)
F. B. CHEUNG (2002)
T. Y. CHU (2002)
B. T. F. CHUNG (2001)
M. FAGHRI (2003)
J. G. GEORGIADIS (2003)
J. P. GORE (2002)
M. HUNT (2002)
D. A. KAMINSKI (2001)
R. L. MAHAJAN (2001)
A. MAJUMDAR (2001)
G. P. PETERSON (2003)
D. POULIKAKOS (2002)
S. S. SADHAL (2002)
R. D. SKOCYPEC (2003)
D. A. ZUMBRUNNEN (2001)

BOARD ON COMMUNICATIONS
Chairman and Vice President
R. K. SHAH

OFFICERS OF THE ASME
President, **J. R. PARKER**
Executive Director,
D. L. BELDEN
Treasurer,
J. A. MASON

PUBLISHING STAFF
Managing Director, Engineering
CHARLES W. BEARDSLEY

Director, Technical Publishing
PHILIP DI VIETRO

Managing Editor, Technical Publishing
CYNTHIA B. CLARK

Managing Editor, Transactions
CORNELIA MONAHAN

Production Coordinator
JUDITH SIERANT

Production Assistant
MARISOL ANDINO

Transactions of the ASME, Journal of Heat Transfer (ISSN 0022-1481) is published quarterly (Feb., May, Aug., Nov.) by The American Society of Mechanical Engineers, Three Park Avenue, New York, NY 10016. Periodicals postage paid at New York, NY and additional mailing offices. POSTMASTER: Send address changes to Transactions of the ASME, Journal of Heat Transfer, c/o THE AMERICAN SOCIETY OF MECHANICAL ENGINEERS, 22 Law Drive, Box 2300, Fairfield, NJ 07007-2300. **CHANGES OF ADDRESS** must be received at Society headquarters seven weeks before they are to be effective. Please send old label and new address. **STATEMENT from By-Laws.** The Society shall not be responsible for statements or opinions advanced in papers or ... printed in its publications (B7.1, Para. 3), **COPYRIGHT © 2000** by The American Society of Mechanical Engineers. For authorization to photocopy material for internal or personal use under those circumstances not falling within the fair use provisions of the Copyright Act, contact the Copyright Clearance Center (CCC), 222 Rosewood Drive, Danvers, MA 01923, tel: 978-750-8400, *www.copyright.com*. Request for special permission or bulk copying should be addressed to Reprints/Permission Department. **INDEXED** by Applied Mechanics Reviews and Engineering Information, Inc. Canadian Goods & Services Tax Registration #126148048.

Downloaded 04 Feb 2011 to 194.85.80.107. Redistribution subject to ASME license or copyright; see http://www.asme.org/terms/Terms_Use.cfm

(**Contents continued**)

Journal of Heat Transfer **Volume 122, Number 4** **NOVEMBER 2000**

Microscale Heat Transfer

Heat Transfer in Manufacturing

TECHNICAL NOTES

ANNOUNCEMENTS AND SPECIAL NOTES

Mass/Heat Transfer in a Ribbed Passage With Cylindrical Vortex Generators: The Effect of Generator-Rib Spacing

S. Acharya[1]
R. G. Hibbs
Y. Chen
D. E. Nikitopoulos

Mechanical Engineering Department,
Lousiana State University,
Baton Rouge, LA 70803

The effect of vortex generators on the heat transfer from internally ribbed passages is studied experimentally using a mass transfer technique. Cylindrical vortex generators placed directly above the ribs have been used in this study. Results are reported on the effect of the spacing between the vortex generator and the ribs. Detailed distributions of the Sherwood number contours and the centerline Sherwood number distributions are presented. Reynolds number values of 5000, 10,000, and 30,000 are studied and three generator-rib-spacing/rib-height (s/e) values of 0.55, 1, and 1.5 are considered. It is shown that at small generator-rib spacings (s/e=0.55), the two act as a single element, and lead to a retardation of the shear layer development past the reattachment point. This is generally associated with lower heat transfer. At a larger generator-rib spacing (s/e =1.5), the generator wake and the rib shear layer interact with each other to promote mixing and heat transfer. [S0022-1481(00)02103-4]

Keywords: Enhancement, Forced Convection, Heat Exchangers, Heat Transfer

Introduction

Ribbed heat-exchange passages are encountered in a variety of applications including process heat exchangers, turbine blade cooling, and electronic cooling. In these applications it is desired to enhance heat transfer from the surface to the flow stream through the passage. This paper deals with the heat/mass transfer in an internally ribbed channel and aims to examine heat transfer enhancement brought about by placing vortex generators above the ribs. This expected enhancement is based on observations made in flow past ribs ([1]) in which it was shown that the separated shear layer behind the rib was characterized by large-scale vortical structures, and that these structures could be manipulated by introducing an external perturbation into the flow in order to promote mixing behind the rib. Greater mixing and shear layer growth behind the ribs is expected to lead to enhancement in surface heat transfer. In this paper the vortex street behind a cylindrical vortex generator mounted above the rib will be used as the external perturbation, and the effect of placing the generator at different distances from the rib on the heat transfer from the ribbed surface will be examined.

Numerous experimental investigations reporting the local and average heat transfer behavior in ribbed channels are available in the literature (e.g., [2–8]). A number of studies have also reported flow measurements in ribbed channels in order to explain the observed heat transfer behavior. Humphrey and Whitelaw [9] have shown that the ribs induce a strong generation of turbulent kinetic energy as well as gradients in Reynolds stresses which result in a normal stress driven secondary flow. Developing flow characteristics in a ribbed duct show that the interaction of shear layers formed by consecutive ribs results in an increase in turbulent kinetic energy ([10]). Karniadakis, Mikic, and Patera [11] performed a numerical study, and using the Reynold's Analogy of momentum and heat transfer, showed that heat transfer rate increases with flow instability. Acharya et al. [12] have reported measurements of velocity and heat transfer past a surface mounted rib, and have shown the correlation between the surface heat transfer and near-wall turbulence levels.

In recent years, the use of vortex generators for more effective heat removal have been explored. A cylindrical vortex generator placed above and parallel to the ribs in a duct has been shown to significantly increase heat transfer at low Reynolds numbers ([13]). Further investigations with the cylindrical vortex generators have shown that the local streamwise distributions of heat transfer are more uniform, but are restricted to the inter-rib region immediately downstream of the generator ([14]). A later, more extensive study of the effects of cylindrical vortex generators has shown that heat transfer enhancement can be attributed to the enhancement of near-wall turbulence ([15]). It is believed that this increased turbulence is the result of the interaction of the wake downstream of the cylinder and the separated shear layer downstream of the rib ([16]).

The above studies of Acharya, Myrum and co-workers have, however, been performed in a two-dimensional rectangular geometry. In the applications of interest, such as internally ribbed heat exchangers, electronic cooling, and gas turbine blade cooling, the channel aspect ratio is not two-dimensional, and the flow is three-dimensional with secondary flows expected to have some effect on the flow structure. Thus in the present study, a square-cross-section ribbed geometry with three-dimensional secondary flows is considered and the effect of vortex generators on surface heat/mass transfer is investigated. In a recent study by Hibbs et al. [17], it was shown that the vortex generators were effective in increasing the heat transfer from the ribbed surfaces of a square-two-pass channel. However, the results were presented for a single generator-rib-spacing/rib-height (s/e) value of 0.55. This paper extends the study of Hibbs et al. [17] and focuses on the effect of vortex-generator-rib spacing on the heat transfer from the ribbed surface. The effect of this spacing is shown to be quite significant in this paper.

The Experiments

The experiments are performed in a test apparatus designed for the study of mass transfer (sublimation of naphthalene) in a two-

---

[1] To whom correspondence should be addressed.

Contributed by the Heat Transfer Division for publication in the JOURNAL OF HEAT TRANSFER. Manuscript received by the Heat Transfer Division, August 15, 1998; revision received, April 13, 1999. Associate Technical Editor: J. Han.

pass internally ribbed duct. Mass transfer measurements permit the acquisition of detailed local distributions of the Sherwood number which can then be converted to Nusselt numbers using the heat-mass transfer analogy.

Apparatus. Figure 1 shows a schematic of the test section. Compressed air is used as the working fluid for all experiments. The air is taken from large exterior reservoirs in order to minimize flow disturbances caused by the compressor. A concentric bore orifice plate is used to measure the mass flow rate in the meter run. A regulator is used to maintain a constant supply pressure in the meter run. Test section and meter run pressures are measured using mechanical pressure gauges that have a 17.2 kPa range, and are controlled independently with gate valves located downstream of both the meter run and test section. Naphthalene-laden exhaust air is directed through flexible tubing to a fume hood.

The aluminum alloy test section consists of a 69.85-mm tapered settling chamber, a frame that supports eight removable wall frames, and a removable 180-deg bend. These major components are secured in a flange-like manner, using O-rings between all parts to prevent air leakage. When assembled, the test section forms 25.4×25.4×304.8-mm long inlet and outlet sections 38.1 mm apart that are connected by the 180-deg, 25.4×25.4-mm square cross-section bend. The aluminum ribs are 2.54×2.54 ×25.4 mm long and have holes on either end for mounting (Fig. 2(*a*)). Steel, 0.635-mm-diameter music wire, is inserted into these holes to secure them to the side walls of the test section. The ribs are mounted only on opposite walls. All exposed surfaces except the ribs are coated with naphthalene. The vortex generators (rods) are made from 1.98-mm diameter steel music wire. The rods are positioned in the test section by means of small aluminum brackets that allow for variation of rib-rod spacing. Figure 2(*b*) shows a schematic of the longitudinal section of the channel together with geometrical notations used.

Detailed surface profiles of the cast surfaces are required for local mass transfer results. These profiles are obtained by moving the walls under a fixed linear variable differential transducer (LVDT) type profilometer. A bi-directional traversing table is securely mounted to the platform of a milling machine. The plates are secured to a 15.875-mm-thick tooling aluminum plate which is fixed to the traversing table. This mounting plate has been machined with an assortment of pin supports and machine screw taps to ensure the walls not only lie flat on the plate, but also are mounted in the same location for all scans. A custom written program run on a personal computer is used to control the motion of the traversing table through micro-step drive motors with a 0.00127-mm step size.

Procedure. Fresh 99 percent pure naphthalene crystals are melted in a heavy-walled glass beaker with an electric heating element. The clean test section walls are clamped to stainless steel plates which have been polished to a mirror-like finish. Molten naphthalene is quickly poured into the hollow cavity of the plate frame to fill completely the region between the walls. The cast plates stand for at least eight hours in a fume hood to attain thermal equilibrium with the laboratory.

Each wall is then separated from the casting plate and mounted to the mounting plate for scanning. After scanning, the plates are stored in an air-tight container, saturated with naphthalene vapor, to hinder natural sublimation until the test section is assembled.

Test section assembly is begun by first inserting the two inner side walls and then attaching the bend. Any ribs or vortex generators are then attached to these walls and the two outer side walls are mounted. The alignment of all ribs and vortex generators is checked before the four top and bottom walls are assembled. After placing the ribs it is ensured that there is no air gap below the rib; this is necessary to do only a single time since the casts are repeatable, and is done rib by rib. After placing each rib, the assembly is held up against a bright light. Silicone is added below the rib where any gaps are found. After the experiment is over, the test section is disassembled and the walls are placed in the storage container until they are scanned again.

Data Reduction. Mass flow rate in the meter run is calculated from measurements of temperature, pressure, and differential pressure using standard equations for concentric bore orifice meters ([18,19]).

Naphthalene sublimation depth is calculated from the two surface profiles for each wall. Each profile is normalized with respect to a reference plane computed from three points scanned on the aluminum surface of the walls. The difference between the normalized profiles gives the local sublimation depth.

The local mass flux $\dot{m}''$ at each location is calculated from the following expression:

$$\dot{m}'' = \rho_s\,, \delta/\Delta t \tag{1}$$

where ρ_s is the density of solid naphthalene, δ is the local subli-

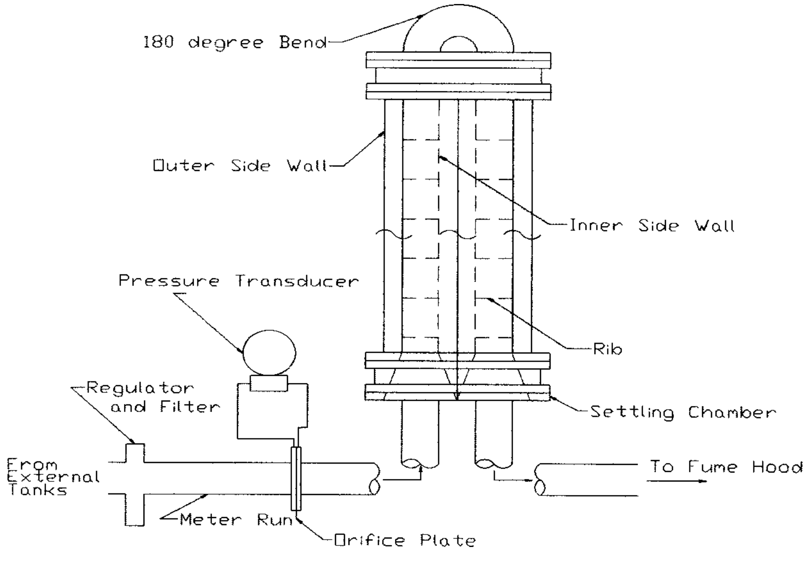

Fig. 1 Schematic of the test apparatus

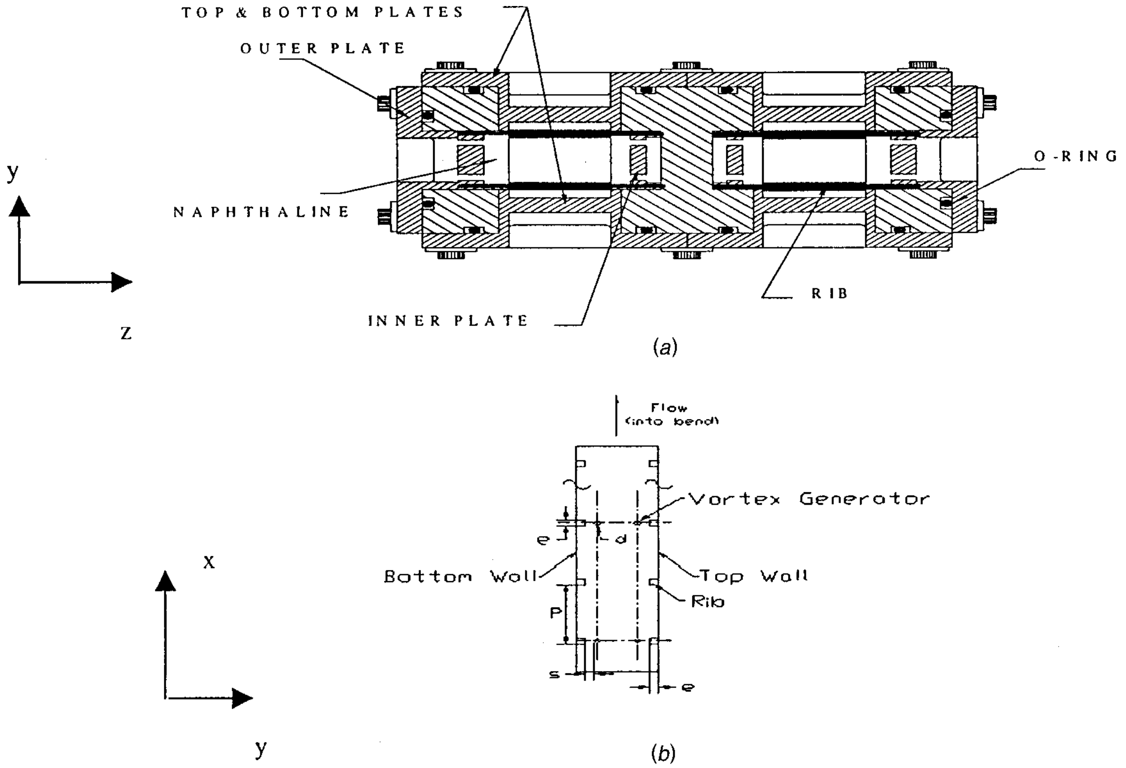

Fig. 2 Details of test section (*a*) cross-sectional plane, (*b*) schematic showing geometrical notation

mation depth, and Δt is the duration of the experiment. Vapor pressure at the wall p_w is calculated from the following equation ([20]):

$$\log_{10}(p_w) = A - B/T_w \tag{2}$$

where A and B are constants (11.884 and 6713, respectively) and T_w is the absolute wall temperature. Wall vapor density ρ_w is then calculated using the perfect gas law. Bulk vapor density of naphthalene $\rho_b(x)$ is obtained by mass conservation balances of naphthalene from the inlet $(x=0)$ to the streamwise location (x).

The local mass transfer convection coefficient h_m is then calculated as follows:

$$h_m = \dot{m}''/(\rho_w - \rho_b(x)). \tag{3}$$

The binary diffusion coefficient $D_{n\text{-}a}$ for naphthalene sublimation in air is taken as the ratio of the kinematic viscosity of air ν to the Schmidt number for naphthalene-air (Sc=2.5). The local Sherwood number Sh is then calculated by:

$$\mathrm{Sh} = h_m D / D_{n\text{-}a} = h_m D\,\mathrm{Sc}/\nu \tag{4}$$

where D is the hydraulic diameter of the test section. Sherwood number results presented in this study have been scaled with a correlation adapted from McAdams [21] for fully developed smooth wall pipe flow.

$$\mathrm{Sh}_o = 0.023\,\mathrm{Re}^{0.8}\mathrm{Sc}^{0.4} \tag{5}$$

where Re is the duct Reynolds number.

Comparison of heat transfer and mass transfer results is done through the use of the heat-mass transfer analogy ([20]):

$$\mathrm{Nu} = \mathrm{Sh}(\mathrm{Pr}/\mathrm{Sc})^{0.4} \tag{6}$$

where Nu is the Nusselt number and Pr is the Prandtl number of air. To facilitate comparison between mass and heat transfer results, a Sherwood number ratio, N_o, is defined as follows:

$$N_o = \mathrm{Sh}/\mathrm{Sh}_o = \mathrm{Nu}/\mathrm{Nu}_o \tag{7}$$

where Nu_o is the correlated fully developed Nusselt number, analogous to Sh_o. An augmentation number N is used to show mass transfer augmentation for tests involving vortex generators. It is defined as follows:

$$N = \mathrm{Sh}_{\text{rib-rod}}/\mathrm{Sh}_{\text{rib}} \tag{8}$$

where $\mathrm{Sh}_{\text{rib-rod}}$ is the Sherwood number with the vortex generators installed and Sh_{rib} is the Sherwood number for the baseline.

Both local (Sh, N) and area-averaged $(\overline{\mathrm{Sh}}, \overline{N})$ results are compared in this manner. Area averaging is performed as a simple arithmetic average of the 30×28 data points scanned over the region between consecutive ribs.

Uncertainty. Uncertainties for all computed values are estimated using the second-power equation method ([22]). The estimates for these experiments are comparable to previously reported values for both heat transfer and mass transfer studies, but are believed to be conservative.

Volume flow rate and duct Reynolds number (Re) uncertainties are estimated to be less than ten percent for Re>6000. The reported resolution of the LVDT is 0.00127 mm while the analog-to-digital (A/D) board is reported to have an accuracy of 0.002 mm in a 12-kHz acquisition rate, 16-bit resolution mode. Experimental tests of accuracy and repeatability for the entire acquisition system indicate a sublimation depth uncertainty of 0.0038 mm. Sublimation depths are maintained at about 0.152 mm by varying the duration of the experiment. This target depth was selected to minimize uncertainties in both depth measurement and changes in duct cross-section area. These uncertainties were found to be one and three percent, respectively. The resulting experimental duration was between 90 minutes for Re=30,000 and 180 minutes for Re=5000.

Vapor density uncertainty based on measured quantities is negligible for both wall and bulk values. Overall uncertainty in Sherwood number calculation is about eight percent and varies slightly with Reynolds number (<1 percent).

Comparisons With Published Data

As validation of the measurement technique, and the estimated uncertainties, centerline Sherwood number distributions along the ribbed top and bottom surfaces and smooth side surfaces are shown in Fig. 3(*a*) and compared with the corresponding mass transfer measurements of Han et al. [23]. The agreement of the present results with those of Han et al. is quite good. Further, measurements of the averaged Sherwood number are compared with the heat transfer measurements of Liou et al. [5] in a ribbed duct for a range of Reynolds number in Fig. 3(*b*), and again the agreement is very good. The excellent agreement obtained with the published data validates the measurement technique used in the present study.

Results and Discussion

As was stated earlier, the objective of this investigation is to report the effects of rib-vortex generator clearance (s/e) on both local and average heat transfer over a range of Reynolds numbers. In order to isolate these effects, the following experimental parameters have been fixed: rib height ratio ($e/D=0.1$), rib pitch ratio ($P/e=10.5$), vortex generator diameter ratio ($d/e=0.78$), and channel length ratio ($L/D=12$). Unlike earlier investigations of the authors, vortex generators have been placed only above alternate ribs, and only in the inlet portion of the duct, upstream of the 180-deg bend of the test section, and thus results are reported only for the portion of the test section containing rib-vortex generator pairs. The results obtained are presented in the form of local centerline mass transfer ratio profiles; local mass transfer distributions in a fully developed, inter-rib region downstream of a rib-vortex generator pair; and the corresponding augmentation ratio distributions in the same inter-rib region of the duct. A summary of the results is first presented in the form of regionally averaged mass transfer ratio over the range of clearances and Reynolds numbers investigated.

An overview of the effect of rib-vortex generator spacing on regionally averaged mass transfer ratio in the fully developed region of the channel is shown in Fig. 4 over the range of Reynolds numbers investigated. The interconnecting lines between the data points are somewhat arbitrary since results are available at only three Reynolds number. In particular, no effort is made to join the Re=10,000 and 30,000 data points, and arbitrary line extensions from these points are plotted as shown. The effect of vortex generator clearance on average mass transfer ratio along the ribbed top wall is shown in Figure 4(*a*). Since symmetry between the opposing ribbed top and bottom walls is within experimental uncertainty, only the top wall has been shown. A noteworthy feature of these averaged results is that the vortex generator induced enhancement is dependent on both the vortex generator clearance and Reynolds number. At the lowest Reynolds number investigated, Re=5000, enhancement can be seen to result from vortex generators with both the smallest and largest clearance. However, as the Reynolds number is increased, only the larger clearances

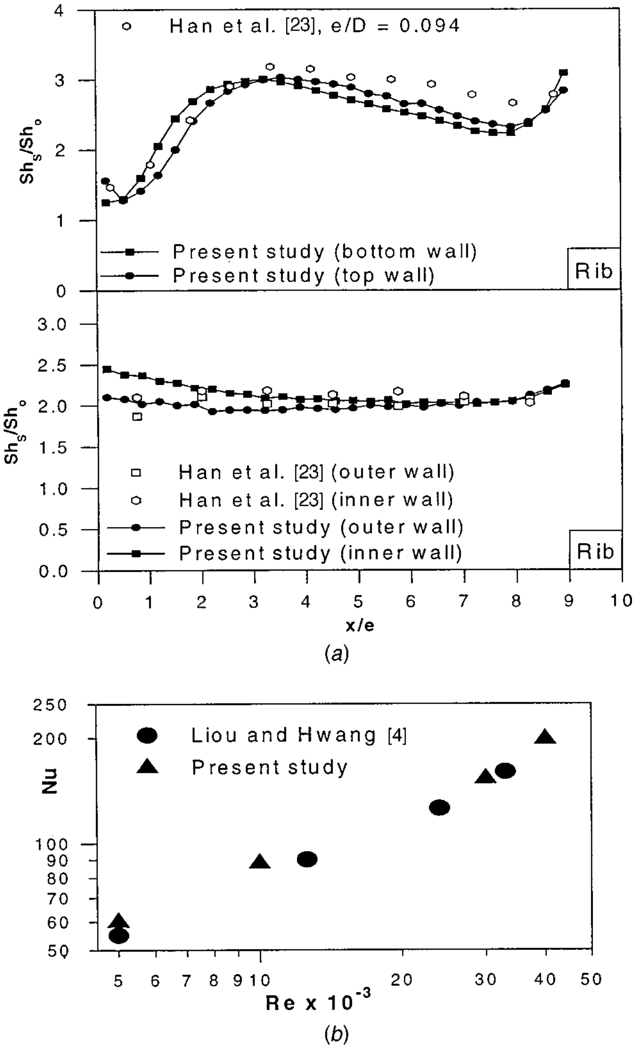

Fig. 3 Comparison with published data (*a*) centerline Sherwood number distributions in an inter-rib module (*b*) average Sherwood number in an inter-rib module

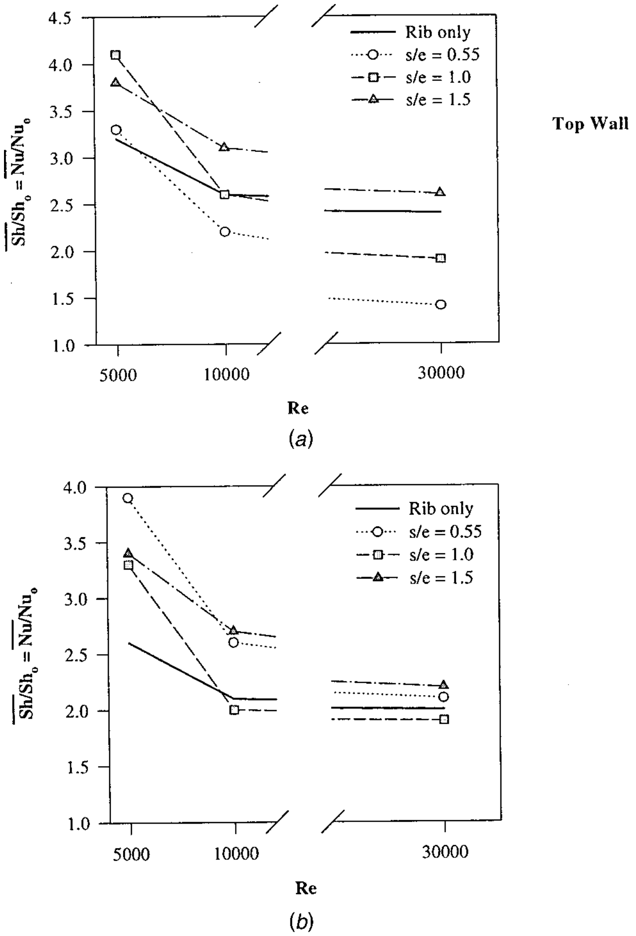

Fig. 4 Regionally averaged mass transfer ratio in the fully developed region of the (*a*) top ribbed wall and (*b*) outer smooth wall

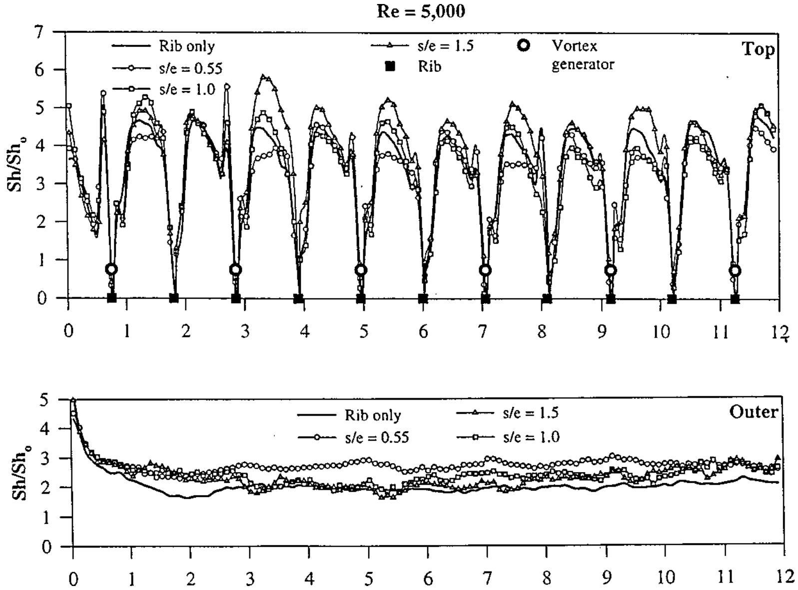

Fig. 5 Local centerline mass transfer profiles along all walls of the channel, Re=5000

result in enhancement, with only $s/e=1.5$ demonstrating enhancement at the highest Reynolds number, Re=30,000.

The effect of vortex generator clearance on averaged mass transfer ratio from the outer side wall is shown in Fig. 4(*b*). Again, because of symmetry between the opposing side walls, only the outer wall results have been presented. Unlike the ribbed top wall, nearly all clearance ratios result in an enhancement of averaged mass transfer ratio. The only exception occurs for $s/e=1.0$ at $\mathrm{Re}\geqslant 10{,}000$, in which an apparent reduction in mass transfer ratio can be seen. This reduction, as will be discussed, is only about ten percent and is within the nearly 15 percent uncertainty for this mass transfer ratio. Furthermore, at the high Re end, there is not as much of an effect of spacing on mass transfer enhancement along the side walls as is seen by the fact that results lie much closer together than for the top wall.

Local centerline mass transfer ratio profiles are shown in Fig. 5 along the top ribbed and outer smooth walls of the channel for Re=5000. The rib only baseline results are represented by the solid line while the vortex generator results are represented by the different symbols. The location of the ribs and vortex generators (located over alternate ribs) are shown along the abscissa. It is clear that the effect of vortex generators is stronger in the inter-rib region downstream of a rib-vortex generator pair since the differences among the mass transfer profiles in this region differ by as much as 50 percent while those downstream of a rib alone differ by less than 15–20 percent. On the top wall, the $s/e=1.5$ shows the highest enhancement. The results for the smallest clearance ($s/e=0.55$), represented by open circles, show a decline in mass transfer downstream of a rib-vortex generator pair. However, for the other clearances ($s/e=1$ and 1.5) the profiles indicate the same behavior as the rib-only case: low mass transfer in the separation region, a peak in mass transfer near the point of flow reattachment, declining mass transfer as the flow redevelops, followed by a sharp increase just upstream of the ribs in the separation region. The nearly constant mass transfer ratio observed for $s/e=0.55$ downstream of the vortex generators suggests that the flow does not begin to redevelop before the next rib is encountered. This behavior is believed to result from the fact that the rib vortex generator clearance is so small that the pair acts as a single large obstruction to the flow which lengthens the reattachment lengths.

The centerline profiles along the side walls indicate an overall enhancement in mass transfer ratio due to the vortex generators. Unlike the profiles for the top and bottom walls, the enhancements are nearly 50 percent greater for the smallest clearance, $s/e=0.55$. Profiles in the fully developed region indicate that the enhancement declines as clearance increases, with a small enhancement observed for the largest clearance, $s/e=1.5$. The most noteworthy effect of the vortex generators is that they act to shorten the development length by nearly one hydraulic diameter. This behavior can be seen in the first two diameters from the entrance in which the baseline results reach fully developed values after about 1–1.5 *D* while the vortex generator results reach fully developed values after only about 0.5 *D*. Upstream of the first rib (with vortex generator), all profiles coincide while afterward, only the baseline profile continues to decrease. Thus, along the side walls, the vortex generators result in both an elevation in mass transfer as well as a shorter development length.

Detailed mass transfer ratio contours are shown in Fig. 6 and the corresponding augmentation ratio contours are shown in Fig. 7 for an inter-rib module along the top and outer walls in the fully developed region of the channel. These regions correspond to the 840 equally spaced measurements taken on a uniform, 28×30 point grid. These graphs are presented for the rib-only baseline case as well as for each of the vortex generator clearances investigated for Re=5000. Above each is the regionally averaged mass transfer ratio that was presented in Fig. 4. The baseline contours along the top wall clearly indicate the expected regions of flow separation (reduced mass transfer), reattachment (near peak mass transfer), redevelopment (declining mass transfer), and separation (locally high mass transfer) upstream of the rib. The side wall distribution for the baseline case similarly indicates the expected high mass transfer ratios near the ends of the ribs which correspond to regions of elevated turbulence intensity ([12]). Peak mass transfer ratio ($\mathrm{Sh/Sh}_o=4.25$, shown by the dotted contour inside the contour labeled $\mathrm{Sh/Sh}_o=4.0$) near $x/D=9.6$ for the top wall of the baseline case is nearly 2.5 times the value observed ($\mathrm{Sh/Sh}_o=1.75$) in the separation region downstream of the rib. Similarly, the mass transfer ratios observed near the ribs of the outer wall ($\mathrm{Sh/Sh}_o=3.75$) are over 1.5 times the value near the centerline ($\mathrm{Sh/Sh}_o=2.25$) region.

As was suggested from the centerline profiles, the fully developed distributions for $s/e=0.55$ indicate a nearly uniform mass transfer distribution between $x/D=9.5$ and 10.1. Ratios in this region, however, are nearly 15 percent lower than the values observed for the baseline case. The nearly uniform distribution indicates the absence of or delayed flow reattachment and redevelop-

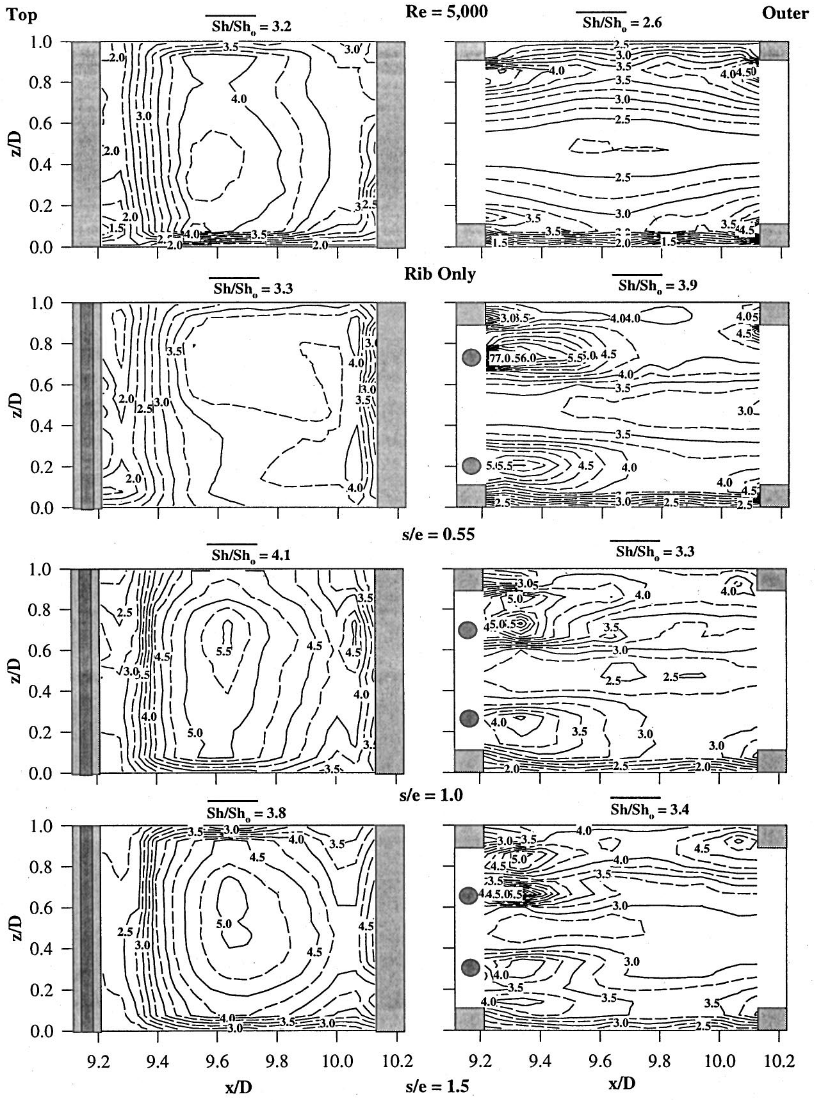

Fig. 6 Detailed mass transfer ratio distributions in selected regions of the top and other walls, Re=5000

ment of the flow. Mass transfer ratios immediately upstream of the next rib are, however, about 20 to 30 percent greater than the baseline case. The absence of redevelopment suggests that the rib-vortex generator pair may be acting as a single blockage of height 2.33*e*, and that this may be associated with a delayed reattachment. The outer wall distributions for this clearance indicate significantly enhanced mass transfer ratios (70 to 80 percent compared to the baseline) in the wake regions of the vortex generators. Furthermore, centerline mass transfer is 30 to 40 percent greater than the corresponding values from the baseline case. Only moderate enhancements (10 to 20 percent) are observed between the ribs and vortex generators which suggests that the vortex generators do not significantly alter the flow near the ends of the ribs along the outer wall. Additionally, mass transfer ratios near the downstream pair of ribs are not significantly different (less than ten percent) from those for the baseline.

When the rib-vortex generator clearance is increased to $s/e = 1.0$, the expected regions of separation, reattachment, and redevelopment are again present. Ratios in the separated region are 40 to 50 percent greater than those for the baseline case. Although the local peak in mass transfer ratio still occurs at $x/D = 9.6$, which indicates no significant change in reattachment length, this peak value ($\mathrm{Sh}/\mathrm{Sh}_o = 5.5$) is about 20 to 30 percent greater than was observed for the baseline case. Similarly, in the region of redevelopment the values are 20 to 30 percent greater. As was observed for the smaller clearance, mass transfer in the separation region upstream of the ribs is higher, and for $s/e = 1.0$ the mass transfer is about 40 percent greater than was observed for the baseline case.

Outer wall distributions also indicate substantial enhancements in mass transfer both in the wake regions of the vortex generators (40 to 50 percent) and near the centerline (15 to 20 percent). The major difference is that ratios in the wake regions are nearly 20 percent lower for this larger clearance and that the values near the centerline are also reduced (relative to $s/e = 0.55$). Overall, the larger clearance results in only a 20 percent enhancement in average mass transfer along the side walls while 40 percent was observed for the smaller clearance. The top wall, however, indicated a 30 percent increase in average mass transfer for $s/e = 1.0$ while the smaller clearance did not indicate any enhancement.

When the rib-vortex generator clearance is further increased to $s/e = 1.5$, mass transfer enhancement is attenuated somewhat with averaged mass transfer ratio decreasing about ten percent from the value for $s/e = 1.0$. The distribution along the top wall is not qualitatively different from that observed for the smaller clear-

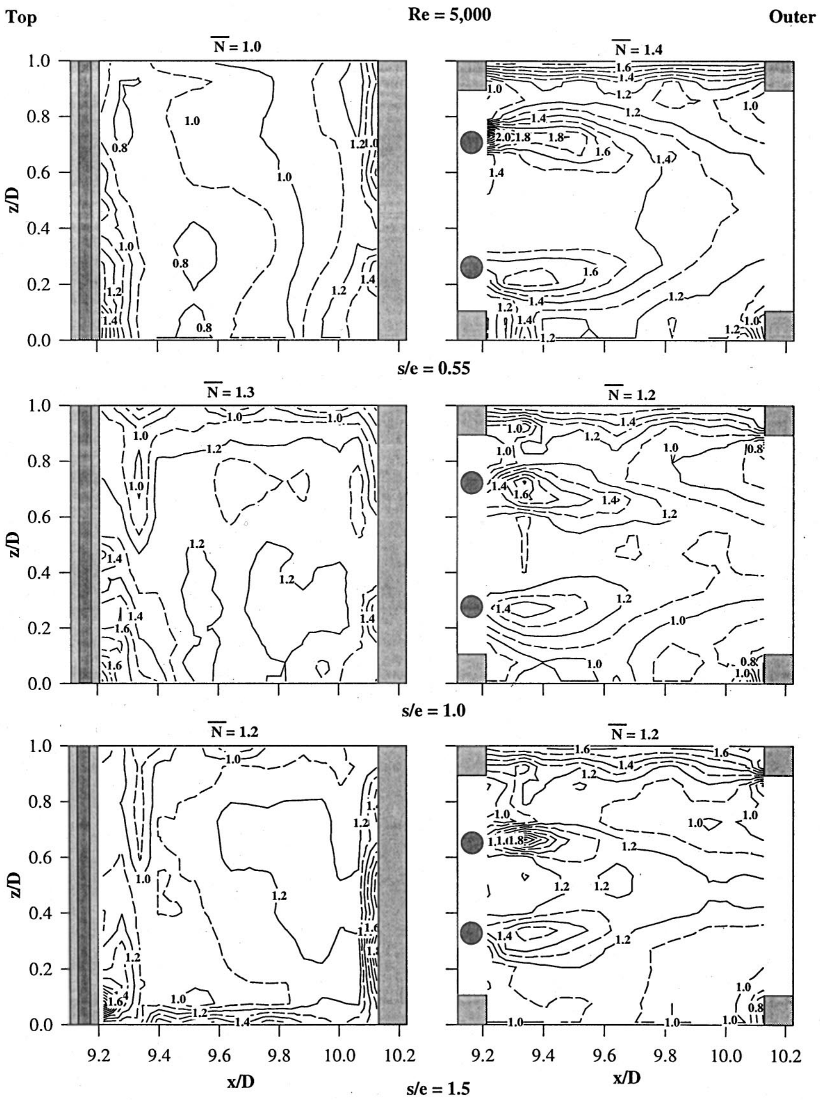

Fig. 7 Detailed mass transfer augmentation in selected regions of the top and other walls, Re=5000

ance, but quantitatively, peak mass transfer ratio is about ten percent lower than for $s/e=1.0$. Similarly, the distribution along the outer wall does not indicate a significant improvement in either local or average mass transfer over the smaller clearance.

Local centerline mass transfer ratio profiles along the walls of the channel are shown in Fig. 8 for Re=10,000. Local enhancements along the top walls are not as great as was observed for Re=5000 (Fig. 5) with values of only 10–15 percent occurring for $s/e=1.5$. Unlike the behavior seen for the lower Reynolds number, differences between the two smaller vortex generator clearances are typically within experimental uncertainty. However, the smallest clearance, $s/e=0.55$, continues to indicate a noticeable region of reduced mass transfer downstream of a rib-vortex generator pair that is indicative of longer flow separation. Furthermore, peak mass transfer ratios for Re=10,000 are about 20 percent lower than those for Re=5000, which implies that the ribbed ducts do not scale with Re in the same manner as the smooth duct correlation.

Mass transfer profiles along the smooth outer walls show an overall enhancement in mass transfer ratio resulting from the vortex generators. Unlike the lower Reynolds number case, at Re =10,000 there is a negligible overall effect of the vortex generator at $s/e=1.0$ along the outer wall. However, the largest clearance can be seen to result in 25–50 percent enhancement while the smallest clearance results in 0–50 percent enhancement.

Detailed mass transfer distributions in the fully developed regions of both top and outer walls are shown in Figs. 9 and 10 in the form of mass transfer ratios and augmentation numbers, respectively. Distributions for $s/e=0.55$ indicate a steady increase in mass transfer ratios over the first four rib heights past the upstream rib, followed by nearly constant mass transfer ratio over the next four rib heights. Augmentation ratios (Fig. 10) for this clearance indicate as much as a 40 percent reduction in local mass transfer and an overall (regionally averaged) reduction of ten percent. Distributions for the two larger clearances, on the other hand, indicate a distinct region of elevated mass transfer ratio about 4.5–5 rib heights downstream of the rib-vortex generator pair. This behavior suggests that the clearance is sufficient for the rib and vortex generator to act as separate obstructions, and that the flow is able to penetrate through the rib-rod gap. Furthermore, there is no discernible difference in the reattachment length, as indicated by a local peak in mass transfer, between the two larger clearances. The mass transfer ratios for $s/e=1.5$ are about 15 percent greater than those for $s/e=1.0$. This behavior suggests that the vortex-generator wake and the separated shear layer interaction is stronger at $s/e=1.5$ relative to $s/e=1.0$ or 0.55.

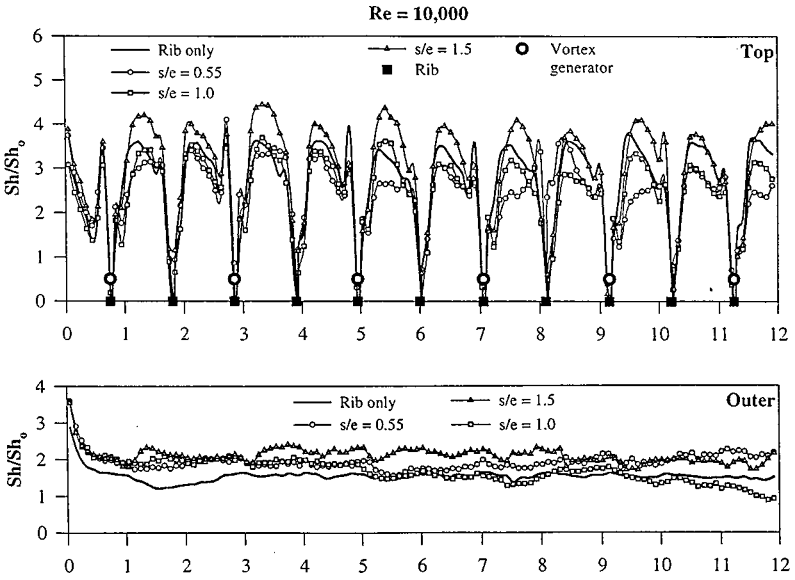

Fig. 8 Local centerline mass transfer profiles along all walls of the channel, Re=10,000

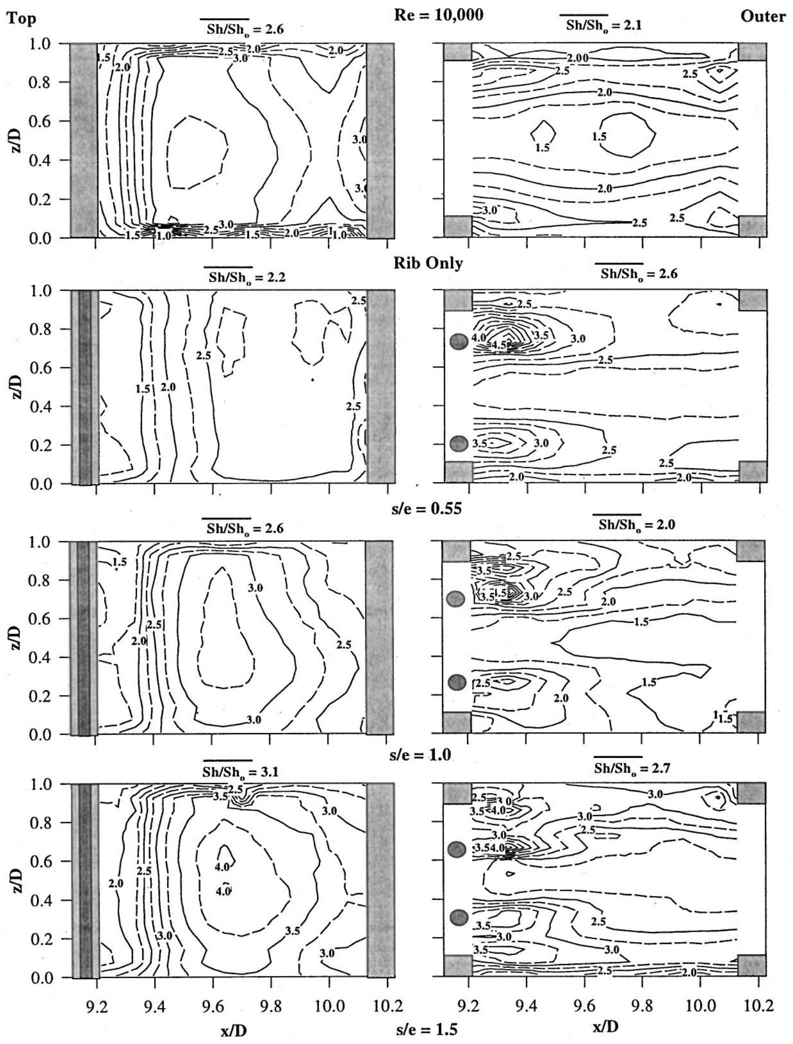

Fig. 9 Detailed mass transfer ratio distributions in selected regions of the top and other walls, Re=10,000

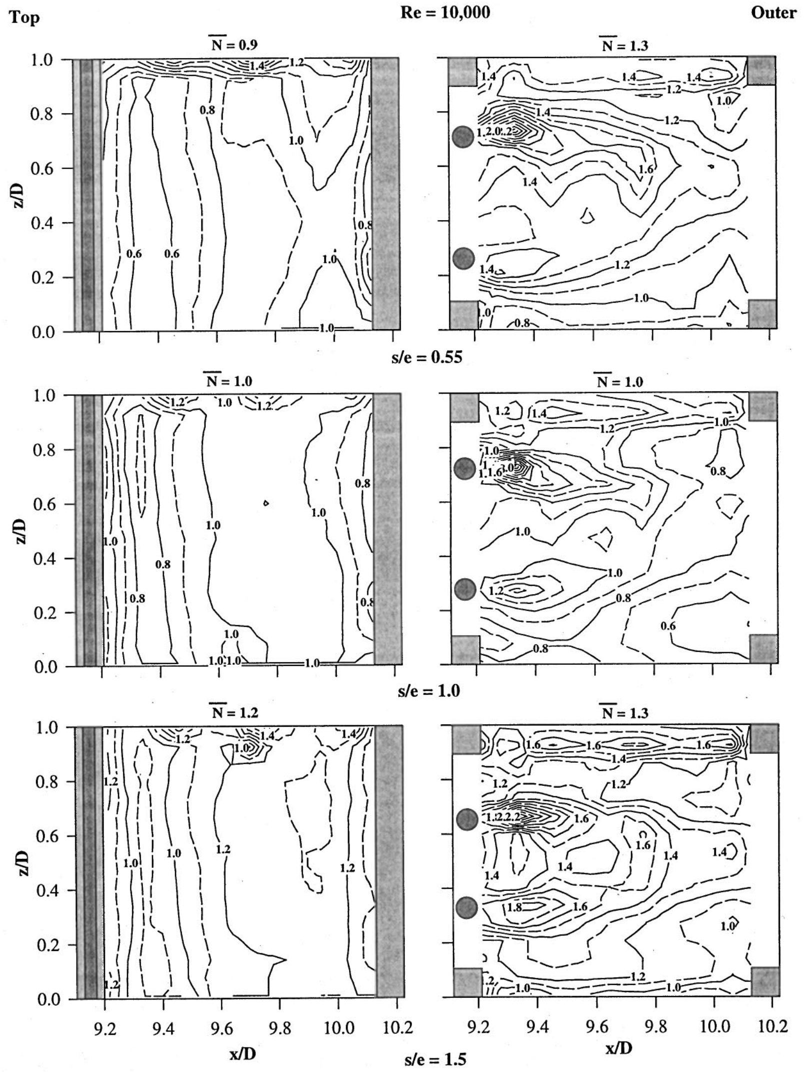

Fig. 10 Detailed mass transfer augmentation in selected regions of the top and other walls, Re=10,000

These observations are further supported by the augmentation number contours shown in Fig. 10. For $s/e=1.0$, a 20 percent reduction in mass transfer can be seen over the first four rib heights downstream of the rib-vortex generator pair, which corresponds to the separated region. For $s/e=1.5$, however, no reduction in mass transfer is observed in this region. Augmentation numbers near the reattachment point ($x/D=9.7$) are near unity for $s/e=1.0$, but are about 1.2 for $s/e=1.5$.

Local mass transfer ratio and augmentation number distributions along the smooth outer wall are also shown in Figs. 9 and 10, respectively. As was observed from the centerline profiles, mass transfer for $s/e=1.0$ is about 20–30 percent lower than that for the other clearances and five percent (within experimental uncertainty) lower than the baseline case. Further, as was noted in Fig. 4, at this Reynolds number, the highest enhancements were obtained for $s/e=1.5$. Augmentation numbers (Fig. 10) show local values as high as 2.0 in the wake region of the vortex generators and values as high as 1.6 near the midspan of the wall. A noteworthy feature is that the regions of elevated mass transfer downstream of the vortex generators appear to interact with each other for $s/e=1.5$, which results in 40–60 percent greater mass transfer.

Local centerline mass transfer ratio profiles are shown in Fig. 11 for all clearances investigated at Re=30,000. In general, the results for the smallest clearance, $s/e=0.55$ (shown as the open circles), indicate a nearly 50 percent reduction in local mass transfer downstream of a rib-vortex generator pair while those for the largest clearance, $s/e=1.5$, shown as the filled triangles, show as much as a 20 percent enhancement in mass transfer ratio, particularly near the expected reattachment point. Unlike the previous Reynolds numbers investigated, the effects of clearance on side wall mass transfer ratio is not as pronounced with enhancements typically less than 20 percent occurring. These enhancements near a rib-vortex generator pair suggest that turbulence intensity is increased as a result of the vortex generators. This conclusion is drawn in part from the fact that turbulence intensity has been shown ([12]) to increase near the ribs of a ribbed channel and that these regions correspond to regions of increased local mass transfer ([17]).

Local distributions of mass transfer ratio and augmentation number are shown in Fig. 12 and Fig. 13, respectively, for selected periodically fully developed regions of the channel. Regionally averaged results for the top wall indicate a 40 percent reduction in mass transfer for $s/e=0.55$ that improves to only a 20 percent reduction for $s/e=1.0$ and further improves to a 10 percent enhancement for $s/e=1.5$. The averages along the outer side wall, however, do not demonstrate such a strong dependence on vortex generator clearance, with enhancements between 0 and

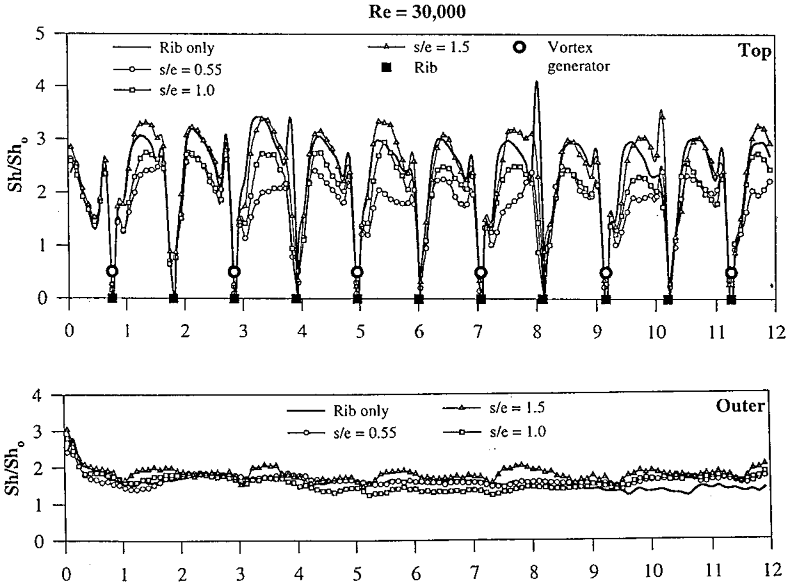

Fig. 11 Local centerline mass transfer profiles along all walls of the channel, Re=30,000

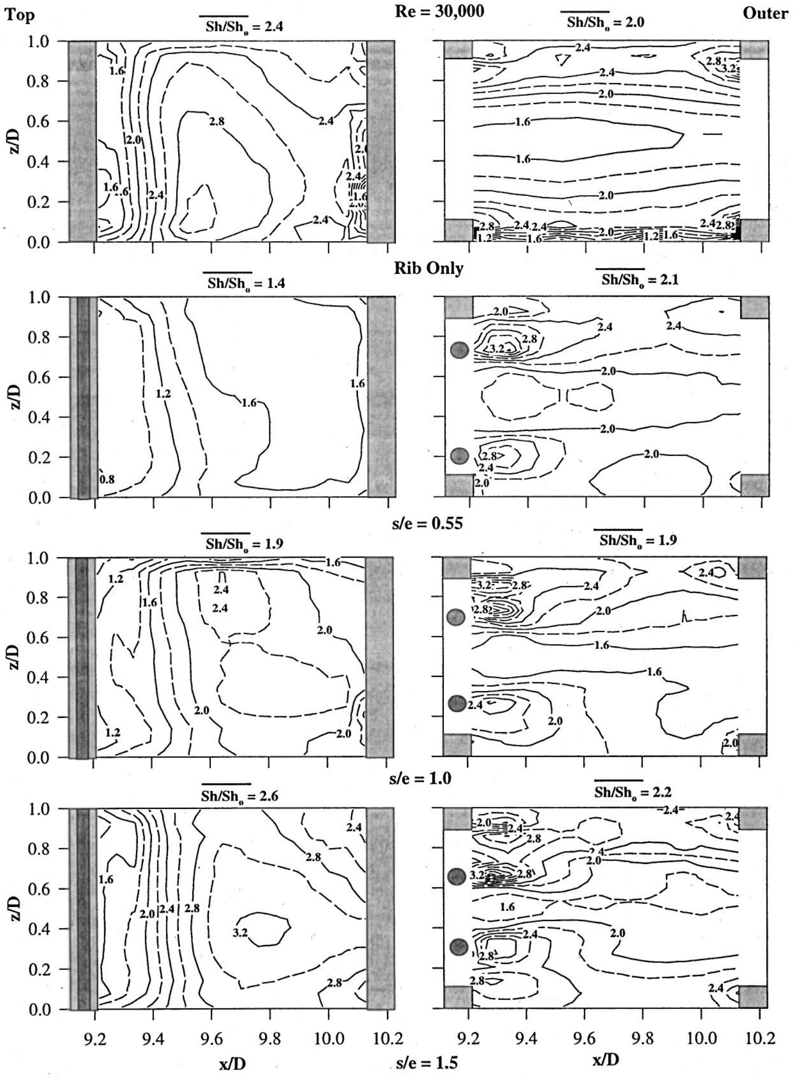

Fig. 12 Detailed mass transfer ratio distributions in selected regions of the top and other walls, Re=30,000

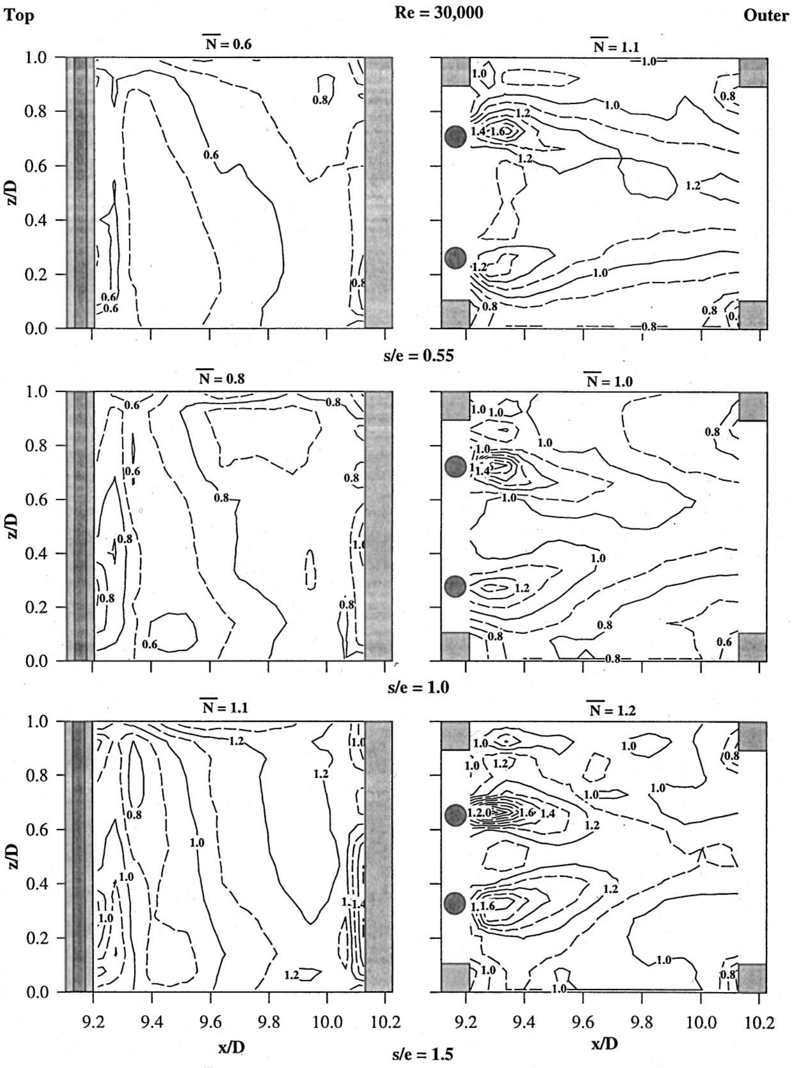

Fig. 13 Detailed mass transfer augmentation in selected regions of the top and other walls, Re=30,000

20 percent occurring for the three clearances investigated. Unlike the results from lower Reynolds numbers, results from both $s/e=0.55$ and $s/e=1.0$ along the top wall suggest that flow redevelopment is hindered in that local mass transfer ratios do not decrease after reaching a peak value near the reattachment point. Thus at this elevated Reynolds number, a larger rib-vortex generator clearance is required to achieve the desired effect of enhanced mass transfer. Results for $s/e=1.5$, however, indicate a distribution qualitatively resembling that of a ribbed channel. This combination of clearance and Reynolds number effect is clearly seen in the augmentation number distributions (Fig. 13).

Distributions for the outer side wall also demonstrate the combined effect of Reynolds number and clearance. For the two smaller clearances, a reduction (maximum of about 20 percent) in local mass transfer can be seen between the rib and vortex generator while for $s/e=1.5$, a 20 percent enhancement in mass transfer can be seen in this region. At these combinations of Reynolds number and vortex generator clearance ($s/e=0.55$ and 1.0), the rib-vortex generator pair act as a single obstruction to the flow. On the other hand, the enhancements along the side walls observed for $s/e=1.5$, together with the enhancements along the ribbed walls, suggests that the vortex generators are acting independently of the ribs at this s/e value. The deflection of the wakes behind the vortex generators and toward the centerline of the channel can be clearly seen in Fig. 13, and results in enhanced centerline and averaged mass transfer.

Concluding Remarks

An experimental study has been conducted to investigate the effect of placing cylindrical vortex generators at different vertical distances from the rib in a ribbed coolant channel. The goal is to delineate the importance of generator-rib-spacing (s), and results are presented for three s/e values of 0.55, 1, and 1.5. The following main conclusions are reached:

1 The heat/mass transfer from the ribbed surfaces depends both on the Re and s/e values. In general better overall enhancement is observed at lower Reynolds numbers.

2 At Re=5000, enhancement is generally obtained for all s/e values with the highest enhancements along the ribbed top and bottom walls at $s/e=1$ and along the smooth side walls at $s/e=0.55$. At Re=30,000 enhancement along the ribbed surfaces is only obtained at $s/e=1.5$ while along the smooth side walls enhancement is obtained for $s/e=1.0$ and 1.5.

3 In the $s/e=0.55$ case, the generator-rib gap is small, the flow is unable to penetrate this gap, and the generator-rib act as a

single element. This prevents the redevelopment of the shear layer, and generally leads to a reduction in heat transfer at higher Re numbers.

4 In the $s/e=1.5$ case, the flow is able to penetrate the rib-generator gap, and the generator wake and the rib shear layer interact with each other to promote mixing and heat/mass transfer. This is consistently observed for all Re values.

Acknowledgment

This research was performed under a subcontract from the South Carolina Energy Research and Development Center to Louisiana State University (93-01-SR015). The contract monitors were Dr. Daniel Fant and Dr. Larry Golan. Their help is gratefully acknowledged.

Nomenclature

d = vortex generator diameter, 0.00198 m
D = hydraulic diameter of test section, 0.0254 m
$D_{n\text{-}a}$ = binary diffusion coefficient for naphthalene-air, m^2/s
e = rib height, 0.00254 m
h_m = local mass transfer convection coefficient
$\dot{m}''$ = local mass flux, $\mathrm{kg/m^2/s}$
N = local augmentation number, Eq. (8)
N_o = local Sherwood number ratio, Eq. (7)
Nu = local Nusselt number
P = rib pitch, 0.0254 m
Pr = Prandtl number
p_w = wall vapor pressure of naphthalene, $\mathrm{kg/m^2}$
Re = test section Reynolds number
s = rod-rib clearance, 0.0014, 0.00254, 0.00381 m
Sc = Schmidt number of naphthalene-air
Sh = local Sherwood number
$\overline{\mathrm{Sh}}_{CL}$ = centerline average Sherwood number for entire duct
Sh_o = fully developed Sherwood number
T_w = wall temperature, °K
x = streamwise coordinate, m
y, z = cross stream coordinates, m
δ = local sublimation depth, m
Δt = time of experiment, s
ν = viscosity of air, $\mathrm{m^2/s}$
$\rho_b(x)$ = local bulk vapor density of naphthalene, $\mathrm{kg/m^3}$
ρ_s = density of solid naphthalene, $\mathrm{kg/m^3}$
ρ_w = wall vapor density of naphthalene, $\mathrm{kg/m^3}$

References

[1] Acharya, S., Myrum, T., and Inamdar, S., 1991, ''The Effect of Subharmonic Flow Pulsation in a Ribbed Pipe: Flow Visualization and Pressure Measurements,'' AIAA J., **29**, No. 9, pp. 1390–1400.
[2] Sparrow, E. M., and Tao, W. Q., 1983, ''Enhanced Heat Transfer in a Flat Rectangular Duct With Streamwise-Periodic Disturbances at One Principal Wall,'' ASME J. Heat Transfer, **105**, pp. 851–861.
[3] Han, J. C., and Zhang, P., 1991, ''Effect of Rib-Angle Orientation on Local Mass Transfer Distribution in a Three-Pass Rib-Roughened Channel,'' ASME J. Turbomach., **113**, pp. 123–130.
[4] Liou, T. M., and Hwang, J. J., 1992, ''Developing Heat Transfer and Friction in Periodic Fully Developed Channel Flows,'' ASME J. Heat Transfer, **114**, pp. 56–64.
[5] Liou, T. M., and Hwang, J. J., 1992, ''Turbulent Heat Transfer Augmentation and Friction in a Ribbed Rectangular Duct With Flow Separation at the Inlet,'' ASME J. Heat Transfer, **114**, pp. 565–573.
[6] Acharya, S., Dutta, S., Myrum, T., and Baker, R. S., 1993, ''Periodically Developed Flow and Heat Transfer in a Ribbed Duct,'' Int. J. Heat Mass Transf., **36**, No. 8, pp. 2069–2082.
[7] Acharya, S., Myrum, T., Sinha, S., and Qiu, X., 1995, ''Developing and Periodically Developed Flow, Temperature and Heat Transfer in a Ribbed Duct,'' *ASME/JSME Thermal Eng. Conf.*, Vol. 1, Mar. 1995, Maui, pp. 303–312; Int. J. Heat Mass Transf., **40**, No. 2, pp. 461–480.
[8] Acharya, S., Myrum, T. A., and Dutta, S., 1995, ''Heat Transfer in Turbulent Flow Past a Surface Mounted Two-dimensional Rib,'' ASME Int. Mech. Eng. Conf. and Expo., San Francisco, Nov.
[9] Humphrey, J. A. C., and Whitelaw, J. H., 1979, ''Turbulent Flow in a Duct With Roughness,'' *Turbulent Shear Flows 2*, Bradbury et al., eds., Berlin, Springer-Verlag, pp. 174–188.
[10] Liou, T. M., Chang, Y., and Hwang, D. W., 1990, ''Experimental and Computational Study of Turbulent Flows in a Channel With Two Pairs of Turbulence Promoters in Tandem,'' ASME J. Fluids Eng., **112**, pp. 302–310.
[11] Kamiadakis, George E., Mikic, Bora B., and Patera, A. T., 1988, ''Minimum-Dissipation Transport Enhancement by Flow Destabilization: Reynolds' Analogy Revisited,'' J. Fluid Mech., **192**, pp. 365–391.
[12] Acharya, S., Dutta, S., Myrum, T., and Baker, R. S., 1994, ''Turbulent Flow Past a Surface Mounted Rib,'' ASME J. Fluids Eng., **116**, No. 2, pp. 238–246.
[13] Myrum, T. A., Acharya, S., Inamdar, S., and Mehrotra, A., 1992, ''Vortex Generator Induced Heat Transfer Augmentation Past a Rib in a Heated Duct Air Flow,'' ASME J. Heat Transfer, **114**, pp. 280–284.
[14] Myrum, T. A., Qiu, X., and Acharya, S., 1993, ''Heat Transfer Enhancement in a Ribbed Duct Using Vortex Generators,'' Int. J. Heat Mass Transf., **36**, No. 14, pp. 3497–3508.
[15] Myrum, T. A., Acharya, S., Sinha, S., and Qiu, X., 1996, ''The Effect of Placing Vortex Generators Above Ribs in Ribbed Ducts on the Flow, Flow-Temperature and Heat Transfer Behavior,'' ASME J. Heat Transfer, **118**, pp. 294–300.
[16] Myrum, T. A., and Acharya, S., 1994, ''Enhanced Heat Transfer in Ribbed Ducts Using Vortex Generators,'' Final Report, GRI-94/0256.
[17] Hibbs, R., Acharya, S., Chen, Y., Nikitopoulos, D., and Myrum, T., 1996, ''Heat Transfer in a Two-Pass Internally Ribbed Turbine Blade Coolant Channel With Cylindrical Vortex Generators,'' *ASME-International Mechanical Engineering Congress and Exposition (IMECE)*, Atlanta, Nov.
[18] Stearns, R. F., Johnson, R. R., Jackson, R. M., and Larson, C. A., 1951, *Flow Measurement With Orifice Meters*, van Nostrand, Toronto.
[19] Miller, R. W., 1989, *Flow Measurement Engineering Handbook*, 2nd ed., McGraw-Hill, New York.
[20] Sogin, H. H., and Providence, R. I., 1958, ''Sublimation From Disks to Air Streams Flowing Normal to Their Surfaces,'' Trans. ASME, **80**, pp. 61–69.
[21] McAdams, W., 1954, *Heat Transmission*, 3rd ed., McGraw-Hill, New York.
[22] Kline, S. J., and McClintock, F. A., 1953, ''Describing Uncertainties in Single-Sample Experiments,'' Mech. Eng. (Am. Soc. Mech. Eng.), **75**, No. 1, pp. 3–8.
[23] Han, J. C., Chandra, P. R., and Lau, S. C., 1988, ''Local Heat/Mass Transfer Distributions Around 180° turns in Two-pass Smooth and Rib-Roughened Channel,'' ASME J. Heat Transfer, **110**, pp. 91–98.

M. Greiner
Associate Professor,
Assoc. Mem. ASME
e-mail: greiner@unr.edu

R. J. Faulkner
Research Assistant

V. T. Van
Research Assistant

Mechanical Engineering Department,
University of Nevada,
Reno, NV 89557

H. M. Tufo
Department of Computer Science,
University of Chicago,
Chicago, IL 60637

P. F. Fischer
Mathematics and Computer Science Division,
Argonne National Laboratory,
Argonne, IL 60439

Simulations of Three-Dimensional Flow and Augmented Heat Transfer in a Symmetrically Grooved Channel

Navier-Stokes simulations of three-dimensional flow and augmented convection in a channel with symmetric, transverse grooves on two opposite walls were performed for $180 \leqslant Re \leqslant 1600$ using the spectral element technique. A series of flow transitions was observed as the Reynolds number was increased, from steady two-dimensional flow, to traveling two and three-dimensional wave structures, and finally to three-dimensional mixing. Three-dimensional simulations exhibited good agreement with local and spatially averaged Nusselt number and friction factor measurements over the range $800 \leqslant Re \leqslant 1600$. [S0022-1481(00)00904-X]

Keywords: *Augmentation, Computational, Forced Convection, Heat Transfer, Unsteady*

Introduction

Engineering devices frequently employ enhanced heat transfer surfaces ([1]). Fins are typically used to extend surface areas and offset strips are often employed to promote thin boundary layers. In recent years a number of configurations that excite flow instabilities have been considered. Transversely grooved channels ([2–4]), passages with eddy promoters ([5,6]), and communicating channels ([7]) all contain fairly large features whose size is roughly half the channel wall-to-wall spacing. These features promote inflections in the passage velocity profile. Kelvin-Helmholtz instabilities of these inflected profiles project energy onto normally damped Tollmien-Schlichting waves, resulting in two-dimensional traveling waves at moderately low Reynolds numbers.

The current authors have presented a series of articles on rectangular cross-section passages with a contiguous set of transverse, V-shaped grooves cut into one wall. Experimental flow visualizations show that the grooves excite two-dimensional waves at Reynolds numbers as low as Re=350, followed by an early transition to three-dimensional mixing ([8]). Transport measurements using air show that both the Nusselt number and friction factor are greater than the corresponding values for a flat channel with the same minimum wall to wall spacing ([9]). A significant result is that fully developed heat transfer is enhanced relative to laminar flat channel flow by factors as large as 4.6 at equal Reynolds numbers and by a factor of 3.5 at equal pumping powers.

Navier-Stokes simulations of flow and heat transfer in the same grooved channel geometry were performed using the spectral element method ([10]). These simulations employed a computational domain that represents one periodicity cell of the grooved passage. A constant body force was applied uniformly to the fluid. This forcing is equivalent to driving the flow with a constant pressure drop across the computational domain. The unsteady flow field occasionally forces slow moving fluid from the groove into the fast external channel causing the volume flow rate to be very unsteady. At Re=2000 the amplitude of the flow rate unsteadiness was 30 percent of the mean value. The friction factor and Nusselt number versus Reynolds number relationships predicted by these simulations were within 20 percent of the earlier experiments. Moreover, two-dimensional simulations were shown to be incapable of capturing the transport processes in this channel for Reynolds numbers greater than Re=570.

The experiments by Greiner et al. [9] did not measure the time variations of the flow rate passing through the passage. However, two phenomena suggest that the experimental flow rate unsteadiness was smaller than the numerically predicted level. The first is that the experimental passage had 46 grooves and it is not likely that the flow in each groove was synchronized. Secondly, the experimental apparatus contained long flat sections whose inertia tends to reduce flow rate unsteadiness. Investigations of resonant heat transfer augmentation in grooved channels indicate that imposing unsteady flow rates at subcritical (normally steady) Reynolds numbers has the potential to more than double the heat transfer level compared to a constant flow rate ([3,11]). The good agreement between the numerical and experimental results suggests that flow rate unsteadiness has less effect on heat transfer at supercritical (normally unsteady) Reynolds numbers, but this effect has not been investigated.

Finally, all of our earlier heat transfer results employed a constant temperature on the grooved boundary and a uniform heat flux from the opposite flat surface. The heat transfer coefficients therefore quantify transport augmentation *from one surface to the other* and not the heat transfer to the bulk fluid.

In the current work, we consider a symmetrically grooved channel (with grooves on *both* surfaces) with constant temperature boundary conditions. The double-grooved geometry is more easily implemented in heat exchangers than the earlier configuration. The constant temperature wall conditions quantify the heat transfer from the passage to the fluid, and hence are more realistic for assessing the applicability of grooved channels to heat exchanger applications. Simulations are performed for both constant body

---

Contributed by the Heat Transfer Division for publication in the JOURNAL OF HEAT TRANSFER. Manuscript received by the Heat Transfer Division, Aug. 23, 1999; revision received, May 25, 2000. Associate Technical Editor: R. W. Douglass.

force and constant flow rate conditions to assess the effect of unsteady flow rate on transport at supercritical Reynolds numbers.

This work was performed in parallel with an experimental study ([12]). That work used a holographic interferometer to measure local heat transfer in the fully developed region of a passage with seven symmetric grooves. That measurement system was better suited for evaluating the fluid centerline temperature than it was for measuring bulk values, and hence the measured heat transfer coefficients are based on the centerline temperature. Analogous centerline Nusselt number and friction factor results are determined in the current numerical work and are directly compared to the experimental data.

Numerical Method

Computational Domain. Figure 1 shows the three-dimensional domain and spectral element mesh employed in this work. The upper and lower V-shaped boundaries are solid walls, and the fluid flows from left to right. The groove depth $a = 0.012$ m, groove length $b = 0.024$ m, and minimum wall-to-wall spacing $H = 0.01$ m are identical to the dimensions used in the companion experimental study ([12]). This domain is the same as our earlier studies of a channel with one grooved wall ([8–10]) except grooves are now placed on both the top and bottom surfaces. The groove dimensions were chosen to be compatible with the most slowly decaying Tollmien-Schlichting waves of the external channel flow.

Periodicity is imposed on the inflow and outflow boundaries at $x = 0$ and b. As a result these simulations model flows that are periodic from groove to groove. Periodicity is also imposed on the boundaries at $z = 0$ and W, where $W = 0.02$ m. The computational grid consists of four levels in the z-direction, each containing 160 hexahedral spectral elements ([13,14]), for a total of $K = 640$ elements. The mesh is more refined near the peaks of the grooves than in the rest of the domain. Within each element, the solution, data and geometric mapping are expressed as tensor-product polynomials of degree N in each spatial direction, corresponding to a total grid point count of roughly KN^3. Numerical convergence is achieved by increasing the spectral order N. Simulations in this work are performed with $N = 7$ and 9.

A shortcoming of the x and z-direction periodicity conditions is that they only admit modal wavelengths such that an integer number of waves exactly span the domain. That is x-direction and z-direction wavelengths equal to b/m and W/n, respectively, where m and n are integers. This limitation is most severe when the dominant flow field wavelengths are larger than or roughly the same as the domain dimensions. We will see that the eddy sizes generally decrease with increasing Reynolds number. As a result it is possible that the current simulations overpredict the Reynolds number where two and three-dimensional modes first appear. However, the periodicity limitation is less important to the prediction of transport quantities at higher Reynolds numbers.

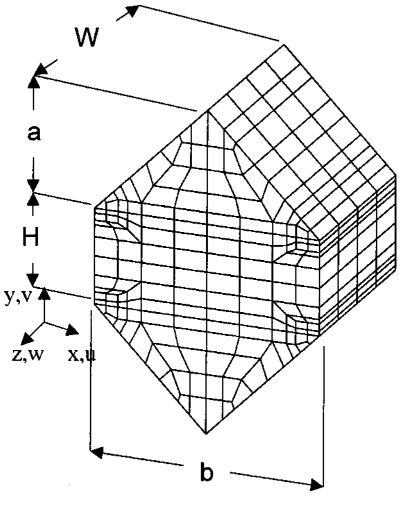

Fig. 1 Spectral element mesh

Two variations of the mesh are used to demonstrate grid independence. In mesh B, six z-levels are used instead of four to determine if a more refined grid affects the results. Mesh C has width $W = 0.03$ m and six z-levels. It is used to determine if a wider domain affects the results. Grid independence is also demonstrated by performing simulations with different spectral orders, N. Finally, two-dimensional simulations are performed using a planar grid equivalent to the face of the domain in Fig. 1.

Flow Field. The present simulations use a fractional step (or time splitting) approach ([15,16]). In this technique, the coupled momentum equations are advanced by first computing the convection term, followed by the projection of the velocity onto a divergence-free space, and finally a viscous update which incorporates the velocity boundary conditions.

The flow is driven from left to right by a uniform body force per unit mass f_x. This forcing is equivalent to a specified pressure drop across the domain, i.e., $f_x = \Delta p/(b\rho)$. At each time step, the velocity is integrated over the domain to determine the average speed through the minimum channel cross section, $U = (\int_\Omega u dV)/(bWH)$. This speed is used to calculate the Reynolds number $\mathrm{Re} = UD_h/\nu$, where $D_h = 2H$ is the hydraulic diameter of a flat passage with the same minimum wall to wall spacing as the grooved channel.

Simulations are performed beginning with an initial condition (zero velocity or a lower Reynolds number solution) and are run until ''steady state'' is observed for roughly one second of flow time. We will see that steady state at low Reynolds numbers is time-independent. However, as the Reynolds number increases, the flow field exhibits first time-periodic behavior and then random variations about a ''constant'' mean value.

Calculations are performed for both constant f_x (specified ''*cfx*'') and for constant flow rate (*cfr*) forcing conditions. For constant f_x calculations, the Reynolds number varies with time. For constant flow rate simulations the value of f_x is varied at each time step so that the Reynolds number remains constant ([16]).

For constant f_x simulations, the time-averaged speed U_a is computed after the flow field reaches steady state by averaging backwards from the final time over successively longer intervals until the result converged. This speed is used in the time-averaged Reynolds number $\mathrm{Re}_a = U_a D_h/\nu$ and time-averaged Fanning friction factor $f = (f_x D_h)/(2U_a^2)$. For constant flow rate simulations, the time average value of f_x is used in the calculation of the Fanning factor.

Constant Temperature Boundary Conditions. The solution technique for computing the fully developed temperature field for constant temperature boundary conditions follows the analysis of Patankar et al. [17]. The energy equation, and associated initial and boundary conditions are

$$\frac{\partial T}{\partial t} + \vec{U} \cdot \nabla T = \alpha \cdot \nabla^2 T \tag{1a}$$

$$T(x,y,z,t=0) = T_{\mathrm{init}}(x,y,z) \tag{1b}$$

$$T(x,y,z,t) = 0 \quad \text{on the walls} \tag{1c}$$

$$T(x=b,y,z,t) = e^{-cb} T(x=0,y,z,t). \tag{1d}$$

Equation (1*d*) corresponds to the fully developed and periodic condition where the temperature profile is self-similar from one cell to the next, i.e., $T(x+b,y,z,t) = e^{-cb} T(x,y,z,t)$ for all (x, y, z, t). The constant c is unknown and is a parameter to be determined as part of the computation. The fact that each cell independently satisfies the homogeneous Eq. (1) and that we are considering fully developed solutions that are independent of T_{init} implies that the solution to (1) for each cell would yield the same value of c. Hence, c cannot be a function of x. Moreover, it is readily demonstrated from energy arguments that under fully developed conditions c cannot be a function of time even when the flow is itself unsteady.

Any function satisfying the above self-similar condition has the unique decomposition $T(x,y,z,t)=e^{-cx}\theta(x,y,z,t)$ where $\theta(x+b,y,z,t)=\theta(x,y,z,t)$ is a periodic function. Thus, the computation of T is reduced to the computation of a periodic function θ, and the constant c. Substituting this decomposition into Eq. (1) yields

$$\frac{\partial\theta}{\partial t}+\vec{U}\cdot\nabla\theta-\alpha\cdot\nabla^2\theta=(\alpha\cdot c^2+uc)\theta-2\alpha\cdot c\,\frac{\partial\theta}{\partial x} \qquad (2a)$$

$$\theta(x,y,z,t=0)=\theta_{\mathrm{init}}(x,y,z) \qquad (2b)$$

$$\theta(x,y,z,t)=0 \quad \text{on the walls} \qquad (2c)$$

$$\theta(x=b,y,z,t)=\theta(x=0,y,z,t). \qquad (2d)$$

Since the fully developed solution is independent of the initial condition we may arbitrarily set $\theta_{\mathrm{init}}=1$. Equation (2*a*) is solved using a semi-implicit time-stepping procedure similar to that for our Navier-Stokes solver. The diffusive terms are treated implicitly while the convective terms are treated explicitly. In addition, all terms on the right of Eq. (2*a*) are treated explicitly using the latest available value for c.

In the steady-state case $(\partial/\partial t=0)$, Eq. (2) constitutes an eigenproblem for the eigenpair (c,θ). The constant c corresponds to the decay rate of the mean temperature in the *x*-direction. As such, a larger value of c implies more rapid decay and more effective heat transfer. In the convection-dominated limit where the Peclet number $U_a b/\alpha$ is large, Eq. (2*a*) becomes a linear eignvalue problem. In this case standard iterative methods for computing the lowest value of c (corresponding to the most slowly decaying mode in x) can be used even when the nonlinear (c^2) term in Eq. (2*a*) is not identically zero. We find that this method accurately computes the decay rate and Nusselt numbers for steady flows in square and round ducts ([18]).

For steady periodic flows with period τ, the temperature is periodic in time, implying $T(x,y,z,t+\tau)=T(x,y,z,t)$. Since c is independent of time, this implies that $\theta(x,y,z,t+\tau)=\theta(x,y,z,t)$. If the value of c is not chosen correctly, this condition will not be satisfied. Unfortunately, τ is not known a priori but is a result of the hydrodynamic part of the calculation. A robust approach to compute c and θ is obtained by multiplying Eq. (2*a*) by θ, integrating over a single cell Ω, and simplifying to yield

$$\frac{1}{2}\frac{d}{dt}\int_\Omega \theta^2 dV=\int_\Omega[(\alpha c^2+uc)\theta^2-\alpha\nabla\theta\cdot\nabla\theta]dV. \qquad (3)$$

While we do not expect the time derivative of the average temperature (represented by the left-hand side of Eq. (3)) to be identically zero, it will in general be less than the time derivative of θ at any one point in the domain. Moreover, if we integrate the right-hand side of Eq. (3) from time t to $t+\tau$, the resultant quantity must be zero due to the temporal periodicity.

This suggests a two-tier strategy for computing c in the unsteady case. Initially, we determine c such that the right-hand side of Eq. 3 is identically zero at each time step. This will permit a relatively coarse but quick determination of c and θ. Subsequently, once τ is well established, we use this value of c to advance θ for one or more periods, and monitor the decay or growth of $\int\theta^2 dV$. At the end of each trial period, we adjust c until convergence is attained.

The bulk fluid temperature in the domain $T_b=\int_\Omega uTdV/\int_\Omega udV$ and total heat transfer $q=\int_s(k\nabla T\hat{n})ds$ (where s includes both wall surfaces) are calculated at each time step. The time-dependent bulk and center-point Nusselt numbers are calculated using the expressions $\mathrm{Nu}_b(t)=qD_h/kT_bA_p$ and $\mathrm{Nu}_c(t)=qD_h/kT_cA_p$, respectively, where T_c is the center point fluid temperature at location $(x,y,z)=(b/2,H/2,W/2)$, and A_p is the total projected area of the surfaces $A_p=2Wb$. The time-average bulk and center-point Nusselt numbers $\mathrm{Nu}_{c,a}$ and $\mathrm{Nu}_{b,a}$, respectively, are calculated after transients decay and the time-dependent parameters reach steady state (exhibit constant window averaged values) for roughly one second. Then the time averages are calculated by averaging backwards from the final time over successively longer intervals until the results converge. Roughly 0.4 seconds of data are required at $\mathrm{Re}_a=1630$ for an accurate time average.

The three-dimensional simulations are performed in parallel, using 64-bit arithmetic, on 128 i860 processors on the Intel Paragon at Caltech ([19,20]). The two-dimensional simulations are performed on 32 processors. A typical three-dimensional simulation requires 15 seconds per time step $(\Delta t=0.0002\,\mathrm{sec})$ for a spectral order of $N=7$. This results in about 21 hours of computer time to calculate one second of real flow time. Some Reynolds numbers can require as much as ten seconds of flow time to reach steady-state conditions.

Results

Velocity and Temperature Fields. This section describes spatial and temporal variations of the flow and temperature fields for a range of forcing levels, $f_x=0.2$ to 12.5 N/kg. All the results in this section are for constant f_x (*cfx*) simulations. Results for constant flow rate (*cfr*) are presented in the next section. Figures 2(*a*) and 2(*b*) show streamlines from two-dimensional simulations at $f_x=0.2$ and 0.5 N/kg after steady-state conditions have been reached. For $f_x=0.2$ N/kg the flow field is time-independent. The grooves are filled with slowly turning vortices and fluid in the

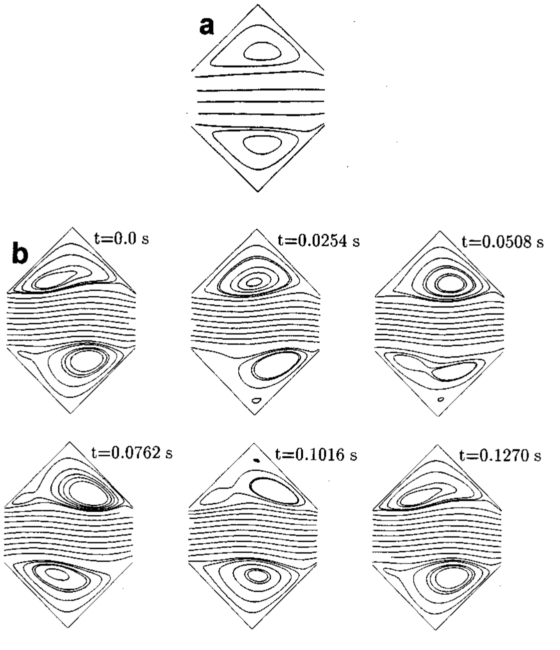

Fig. 2 Streamlines from two-dimensional simulations; (*a*) $f_x=0.2$ N/kg ($\mathrm{Re}_a=180$), (*b*) $f_x=0.5$ N/kg ($\mathrm{Re}_a=380$)

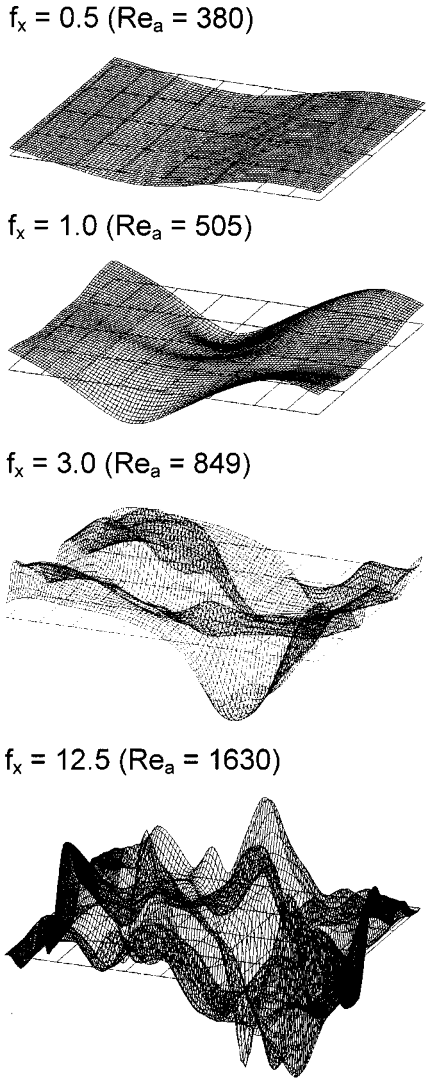

Fig. 3 Isometric views of *v*-velocity on the plane $y=H/2$

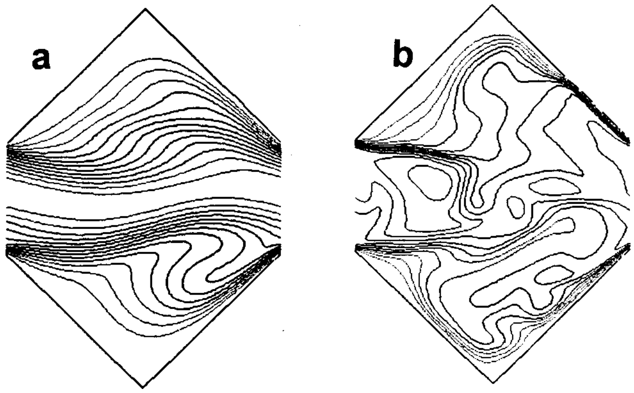

Fig. 5 Instantaneous isotherms at $z=0$; (*a*) $f_x=0.5$ N/kg ($Re_a=380$), (*b*) $f_x=3.0$ N/kg ($Re_a=849$)

open channel flows parallel to the *x*-direction. Integration of the velocity shows that the Reynolds number at this forcing level is $Re_a=180$.

Figure 2(*b*) shows streamlines at six equally spaced times for $f_x=0.5$ N/kg, corresponding to a time-averaged Reynolds number of $Re_a=380$. This flow exhibits a traveling wave structure with a wavelength equal to the channel periodicity length. We note that while this is the maximum wavelength that this computational domain can accommodate, the wavelength in a long grooved channel may actually be different. Moreover, the flow field repeats itself after a period of 0.1270 sec. The wave structure causes fluid to be alternately ejected from the top and bottom grooves. Similar traveling waves are observed in a single-grooved-wall channel at Re=350 ([8,10]).

Velocity data from two-dimensional simulation at $f_x=0.5$ N/kg were used as initial conditions for a three-dimensional simulation with the same forcing level. Figure 3 shows isometric views of the *y*-component of velocity (v) at the midplane $y=H/2$ at four different forcing levels, $f_x=0.5$, 1.0, 3.0, and 12.5 N/kg, corresponding to $Re_a=380$, 505, 849, and 1630, respectively. These surfaces are typical snapshots in time after steady-state conditions are reached. The velocity scale for each of these surfaces is the same.

The surface for $f_x=0.5$ N/kg shows that this flow field exhibits one wave in the *x*-direction and almost no variation in the *z*-direction. At $f_x=1.0$ N/kg the flow exhibits significant but regular variations in the *z*-direction. The variation in both the *x* and *z*-direction are much less regular at $f_x=3.0$ and 12.5 N/kg. The footprints of the peaks and valleys of these surfaces characterize the eddy length scales. We see that as the fluid forcing level and Reynolds number increase the flow structures become increasing irregular and their characteristic lengths decrease.

Figure 4 is a plot of the Reynolds number versus time for f_x

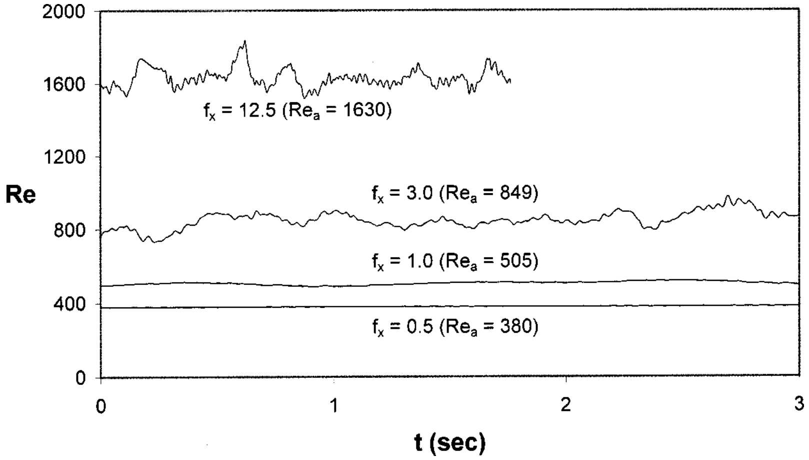

Fig. 4 Reynolds number versus time

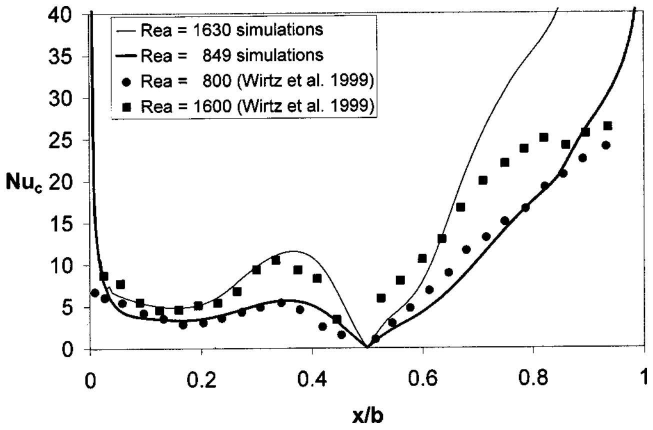

Fig. 6 Local center point Nusselt number versus location

$=0.5$, 1.0, 3.0, and 12.5 N/kg. These results are from three-dimensional simulations. Close examination of the $f_x=0.5$ N/kg data shows that the Reynolds number actually exhibits small oscillations with time. The period of this unsteadiness is 0.0635 sec, and its amplitude is only 0.14 percent of the mean value. These flow rate oscillations are caused by the periodic ejection of slow moving fluid from the grooves. The period of the Reynolds number oscillation is half the flow-field period since there are two fluid ejection events (from the top and bottom grooves) during each cycle. The Reynolds number versus time behavior from the three-dimensional simulation is essentially identical to that from two-dimensional calculations. This indicates that the small amount of three-dimensional behavior observed in Fig. 3 for $f_x=0.5$ N/kg does not significantly affect the flow rate.

The time-dependent Reynolds number for $f_x=1.0$ N/kg varies gently about a ''constant'' mean value of $\mathrm{Re}_a=505$. We note that *two*-dimensional simulations at this forcing level give a significantly greater time average Reynolds number of $\mathrm{Re}_a=640$. The lower flow rate predicted by three-dimensional simulations indicates that the structure exhibited in Fig. 3 for $f_x=1.0$ N/kg results in significantly higher levels of drag than two-dimensional waves.

As f_x increases to 3.0 and 12.5 N/kg ($\mathrm{Re}_a=849$ and 1630, respectively), the traces exhibit larger variations about their mean values and wider ranges of unsteady frequencies. The time step at $f_x=12.5$ N/kg is very small and so only 1.7 seconds of steady-state data was calculated at that forcing level.

Figures 5(*a*) and 5(*b*) show isotherms on planes of constant *z*-coordinate at $f_x=0.5$ and 3.0 N/kg ($\mathrm{Re}_a=380$ and 849). These snapshots are taken after steady-state conditions are reached. For $f_x=0.5$ N/kg, the isotherms in the outer channel exhibit a wave structure, and the effect of the vortices in transporting fluid within the grooves is evident. Snapshots at subsequent times show that this wave travels in the positive *x*-direction. Views at different *z*-locations are essentially identical, in agreement with the very small velocity variations observed in Fig. 3 for $\mathrm{Re}_a=380$.

For $f_x=1.0$ N/kg (not shown) the isotherms also exhibit smooth wave motion, similar to the pattern in Fig. 5(*a*). However, plots at different *z*-locations are not in phase. The isotherms for $f_x=3.0$ N/kg show that the temperature field is more irregular than it is at lower Reynolds numbers. Moreover, isotherms at different *z*-locations are substantially different from Fig. 5(*b*).

In Fig. 5 closely spaced isotherms near the walls indicate thin boundary layers. For both $f_x=0.5$ and 3.0 N/kg the boundary layers are significantly thinner on the downstream (right-hand) surface than they are on the upstream side. They are especially thin near the groove opening. This reversed boundary layer development is caused by the reversed flow in the groove, i.e., groove vortex. At $f_x=3.0$ N/kg, a very thin boundary layer also forms on the upstream (left-hand) wall near the groove trough. At this forcing level, the groove vortex is sufficiently strong to impinge fluid directly against that surface.

Figure 6 shows numerical and experimental center point Nusselt number versus location. The numerical results are for $f_x=3.0$ and 12.5 N/kg, corresponding to time average Reynolds numbers of $\mathrm{Re}_a=849$ and 1630, respectively. The experimental results are for $\mathrm{Re}=800$ and 1600 ([12]). While the simulations calculate heat transfer in the fully developed region of the channel, the measured results at $\mathrm{Re}=800$ are in the developing region.

The experimental and numerical data are in good quantitative agreement on the upstream portion of the groove. Both sets of data exhibit very similar plateaus near $x/b=0.35$ due to impingement of the groove vortex. Both data sets indicate that the Nusselt number on the downstream surface is greater than that on the upstream side. At $\mathrm{Re}_a=1630$, however, the numerical results are significantly higher than the experimental data, especially near the lip of the groove ($x/b=1$). The experimental result plateaus at roughly $\mathrm{Nu}_c=27$ while the numerical results reach considerably higher values. This difference may be due to differences in the thermal boundary conditions since the simulations do not account for conjugate heat transfer in the grooved walls. Alternately, the numerical grid may be slightly underresolved for high Reynolds

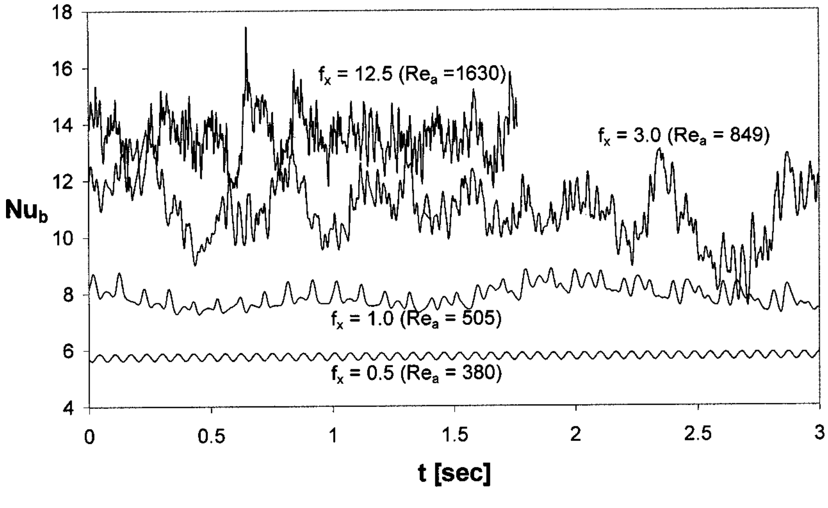

Fig. 7 Bulk Nusselt number versus time

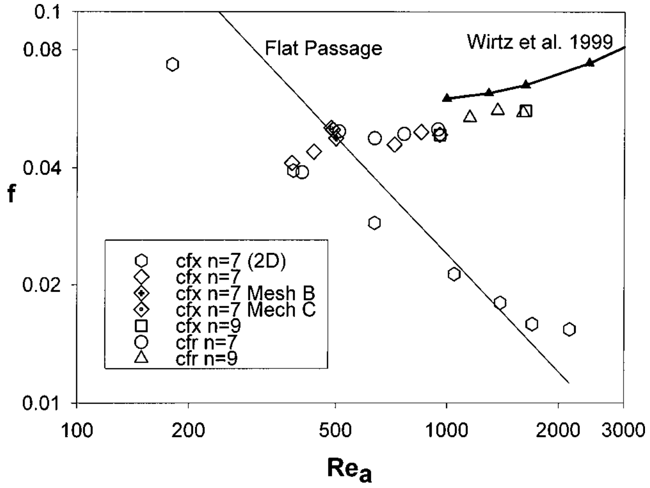

Fig. 8 Fanning friction factor versus Reynolds number

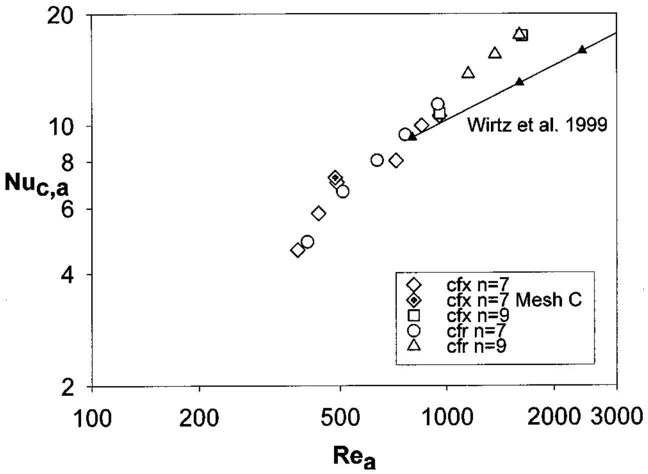

Fig. 10 Center point Nusselt number versus Reynolds number

numbers simulations (as discussed in the next section), or the experimental holographic technique may have been unable to accurately measure very large heat fluxes.

Figure 7 shows the time-dependent bulk Nusselt number, averaged over the entire computational domain, for the same four forcing levels as Fig. 4. For $f_x = 0.5\,\mathrm{N/kg}$ the two-dimensional wave motion exhibited in Fig. 2 causes regular Nusselt number variations with the same period as the Reynolds number oscillations. Furthermore, examination of the data shows that the time dependent Nusselt number from two-and three-dimensional simulation is the same. Generally speaking, the time scales of the Nusselt number variations exhibited in Fig. 7 are similar to those of the Reynolds number in Fig. 4. However, the amplitude of the Nusselt number unsteadiness is greater than that of the Reynolds number.

Transport Quantities. Figures 8–10 show time average transport quantities versus Reynolds numbers from both constant f_x (cfx) and constant flow rate (*cfr*) simulations. Fanning friction factor, bulk Nusselt number and center point Nusselt number are shown in Figs. 8, 9, and 10, respectively. All of these quantities are averaged over time and the computational domain. Experimental results from [12] for friction factor and center point heat transfer are included in Figs. 8 and 10. The 99 percent confidence intervals for the measured Reynolds numbers, friction factors and Nusselt numbers are less than 7.1 percent, 15 percent, and 15 percent of the respective values.

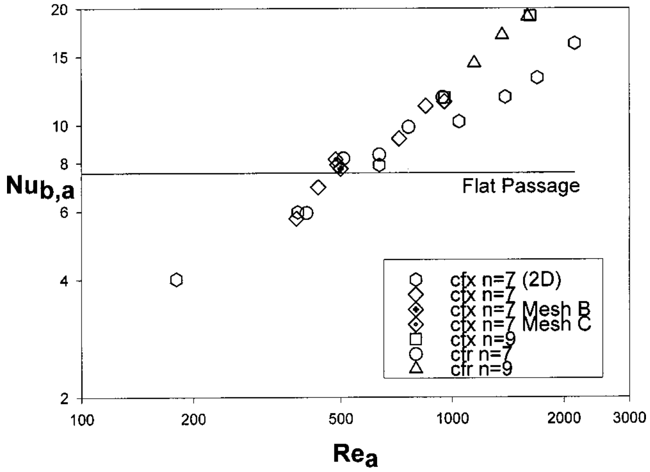

Fig. 9 Bulk Nusselt number versus Reynolds number

All two-dimensional and low Reynolds number ($\mathrm{Re}_a < 1000$) three-dimensional simulations employ seventh-order spectral elements $(N=7)$. Simulations for the more refined and wider meshes (B and C, respectively) at $\mathrm{Re}_a \approx 500$ also use $N=7$. Higher Reynolds number simulations use ninth-order elements $(N=9)$.

At $\mathrm{Re}_a \approx 500$, where the size of the dominant three-dimensional flow structures are fairly close to the dimensions of the computational domain, the results are independent of the domain width (mesh C) and the number of z-levels of the grid (mesh B). At $\mathrm{Re} \approx 950$, where the flow field is highly three-dimensional, the results are effectively independent of simulation order ($N=7$ or 9). The constant f_x (*cfx*) and constant flow rate (*cfr*) results in Figs. 8–10 are also nearly the same, except that the *cfr* correlations are slightly smoother than the *cfx* results. This indicates that flow rate unsteadiness has a much smaller effect on heat transfer at supercritical Reynolds number than it does at subcritical values. These results indicate that the numerical data are grid and forcing function independent for $\mathrm{Re}_a \lesssim 950$. However, the highest Reynolds number results must be regarded as somewhat speculative since no spatial resolution study was performed for $\mathrm{Re}_a > 1000$. On the other hand, the numerical results are in fair agreement with the available experimental data.

The two and three-dimensional friction factor results shown in Fig. 8 are essentially identical for Reynolds numbers at and below $\mathrm{Re}_a = 380$ but they diverge at higher flow rates. A solid line shows the fully developed Fanning factor for a laminar flat passage with the same minimum wall to wall spacing as the grooved channel. The two-dimensional simulations predict that the friction factor decreases with Reynolds number, similar to unmixed flow in a laminar flat passage. The three-dimensional simulations on the other hand predict that the friction factor rises from $\mathrm{Re}_a = 380$ to 490, drops by roughly ten percent from $\mathrm{Re}_a = 490$ to 720, and then gently increases from $\mathrm{Re} = 720$ to 1600.

At low Reynolds numbers, the grooved channel friction factors are *below* the flat passage values. We note that these passages have the same *minimum* wall to wall spacing. At low Reynolds numbers, the grooved passage flow field is steady and the grooves essentially act to relax the no-slip boundary conditions. The onset of unsteadiness at $\mathrm{Re}_a = 380$ causes its friction factor to increase beyond that of the flat passage. The experimental and numerical friction factor data overlap in a fairly narrow Reynolds number range, $1000 < \mathrm{Re}_a < 1600$. Within this range the numerically predicted values are roughly 20 percent below the measured values.

The bulk Nusselt numbers from the two and three-dimensional simulations shown in Fig. 9 are identical for Reynolds numbers less than $\mathrm{Re}_a=380$, similar to the friction factor behavior. At higher Reynolds numbers three-dimensional mixing causes the heat transfer to be greater than the level predicted from two-dimensional simulations. This divergence is much smaller for the bulk Nusselt number than it is for friction factor. At $\mathrm{Re}_a=1000$, the two-dimensional friction factor results are smaller than the three-dimensional result by a factor of more than two, while the heat transfer results are only 20 percent low. At low Reynolds numbers, the grooved channel Nusselt number is smaller than the flat passage value (shown using a solid line) due to the thermal resistance of the slow moving fluid in the grooves. The onset of unsteady mixing causes the grooved channel heat transfer to increase beyond the flat passage value for Reynolds numbers above $\mathrm{Re}_a=500$.

Figure 10 compares the center point Nusselt numbers from the current three-dimensional simulation with experimental data from [12]. As mentioned earlier, the experiments use the temperature at the center of the domain to characterize the fluid temperature instead of the bulk value. Our calculations show that the center point Nusselt number is 20 percent below the bulk value at $\mathrm{Re}_a=435$, but the two values are within ten percent at $\mathrm{Re}_a=849$, where the flow is well mixed. In the range $800<\mathrm{Re}<1000$ the numerically predicted Nusselt number is slightly above the experimental data. At higher Reynolds numbers, however, the slope of the numerical Nu_c versus Re dependence is significantly greater than the measured value. As mentioned in connection with Fig. 6, this difference may be traced to differences on the downstream groove lip.

Summary

Navier-Stokes simulations of three-dimensional flow and augmented convection in a fully developed, symmetrically grooved passage were performed using the spectral element technique. These simulations were performed over the Reynolds number range $180\leq\mathrm{Re}\leq1600$. Simulations were performed using both a constant body force and a constant flow rate condition to drive the flow. A method employing an exponentially decaying temperature scale was developed to calculate the fully developed heat transfer coefficient for constant temperature boundary conditions.

The evolution of the velocity and temperature fields as the Reynolds number is increased, from steady two-dimensional flow to coherent traveling wave structures to three-dimensional mixing, has been documented. The simulations exhibited good quantitative agreement with the measured local Nusselt number profile at $\mathrm{Re}_a=800$. However, at high Reynolds numbers the simulations predicted greater heat transfer levels than the experimental results on the downstream surface of the groove.

Two-dimensional simulations did not accurately predict the spatially and temporally averaged friction factor for $\mathrm{Re}_a>400$, or the heat transfer for $\mathrm{Re}_a>1000$. However, three-dimensional calculations predicted friction factor and heat transfer results that were within 20 percent of measured values in the range $800<\mathrm{Re}_a<1600$. The results from constant body force and constant flow rate simulations were nearly identical, indicating that flow rate unsteadiness has little effect on transport at supercritical Reynolds numbers.

Acknowledgment

National Science Foundation Grant CTS-9501502 supported this work. The work of P. F. Fischer was supported by the Mathematical, Information, and Computational Sciences Division subprogram of the Office of Advanced Scientific Computing Research, U.S. Department of Energy, under Contract W-31-109-Eng-38. The California Institute of Technology provided time on the Intel Paragon under NSF Cooperative Agreement CCR-8809616.

Nomenclature

a = groove depth, Fig. 1
b = channel periodicity length, Fig. 1
c = decay constant
D_h = hydraulic diameter of minimum cross section, $2H$
f = Fanning friction factor, $(f_x D_h)/(2U_a^2)$
f_x = fluid body force per unit mass in the x-direction
H = minimum channel wall to wall spacing, Fig. 1
k = fluid thermal conductivity, 0.0263 W/m°C
K = number of spectral elements
$\hat{n}$ = wall normal unit vector
N = spectral element order
Nu_b = bulk Nusselt number based on projected area
Nu_c = center point Nusselt number
Pr = fluid molecular Prandtl number, 0.70
Re = Reynolds number, UD_h/ν
Re_a = time-average Reynolds number, $U_a D_h/\nu$
t = time
T = temperature
T_b = bulk temperature
T_c = center point temperature
u, v, w = velocity components in the x, y, and z-directions
U = mean x-velocity at the minimum channel cross section
U_a = time-average U
V = volume
W = width of the computational domain, Fig. 1

Greek

α = thermal diffusivity, 2.63×10^{-5} m^2/s
ν = fluid kinematic viscosity, 1.84×10^{-5} m^2/s
θ = periodic temperature
ρ = fluid density, 1.006 kg/m^3
τ = period of local time variations
Ω = computational domain

References

[1] Webb, R. L., 1994, *Principles of Enhanced Heat Transfer*, John Wiley and Sons, New York.
[2] Ghaddar, N. K., Korczak, K., Mikic, B. B., and Patera, A. T., 1986, ''Numerical Investigation of Incompressible Flow in Grooved Channels. Part 1: Stability and Self-Sustained Oscillations,'' J. Fluid Mech., **168**, pp. 541–567.
[3] Greiner, M., 1991, ''An Experimental Investigation of Resonant Heat Transfer Enhancement in Grooved Channels,'' Int. J. Heat Mass Transf., **24**, pp. 1383–1391.
[4] Roberts, E. P. L., 1994, ''A Numerical and Experimental Study of Transition Processes in an Obstructed Channel Flow,'' J. Fluid Mech., **260**, pp. 185–209.
[5] Kozlu, H., Mikic, B. B., and Patera, A. T., 1988, ''Minimum-Dissipation Heat Removal by Scale-Matched Flow Destabilization,'' Int. J. Heat Mass Transf., **31**, pp. 2023–2032.
[6] Karniadakis, G. E., Mikic, B. B., and Patera, A. T., 1988, ''Minimum-Dissipation Transport Enhancement by Flow Destabilization: Reynolds Analogy Revisited,'' J. Fluid Mech., **192**, pp. 365–391.
[7] Amon, C. H., Majumdar, D., Herman, C. V., Mayinger, F., Mikic, B. B., and Sekulic, D. P., 1992, ''Experimental and Numerical Investigation of Oscillatory Flow and Thermal Phenomena in Communicating Channels,'' Int. J. Heat Mass Transf., **35**, pp. 3115–3129.
[8] Greiner, M., Chen, R.-F., and Wirtz, R. A., 1989, ''Heat Transfer Augmentation Through Wall-Shaped-Induced Flow Destabilization,'' ASME J. Heat Transfer, **112**, pp. 336–341.
[9] Greiner, M., Chen, R.-F., and Wirtz, R. A., 1991, ''Enhanced Heat Transfer/Pressure Drop Measured From a Flat Surface in a Grooved Channel,'' ASME J. Heat Transfer, **113**, pp. 498–500.
[10] Greiner, M., Spencer, G., and Fischer, P. F., 1998, ''Direct Numerical Simulation of Three-Dimensional Flow and Augmented Heat Transfer in a Grooved Channel,'' ASME J. Heat Transfer, **120**, pp. 717–723.
[11] Ghaddar, N. K., Magen, M., Mikic, B. B., and Patera, A. T., 1986, ''Numerical Investigation of Incompressible Flow in Grooved Channels. Part 2: Resonance and Oscillatory Heat Transfer Enhancement,'' J. Fluid Mech., **168**, pp. 541–567.
[12] Wirtz, R. A., Huang, F., and Greiner, M., 1999, ''Correlation of Fully Developed Heat Transfer and Pressure Drop in a Symmetrically Grooved Channel,'' ASME J. Heat Transfer, **121**, pp. 236–239.
[13] Patera, A. T., 1984, ''A Spectral Element Method for Fluid Dynamics; Laminar Flow in a Channel Expansion,'' J. Comput. Phys., **54**, pp. 468–488.
[14] Maday, Y., and Patera, A. T., 1989, ''Spectral Element Methods for the

Navier-Stokes Equations,'' *State of the Art Surveys on Computational Mechanics*, A. K. Noor and J. T. Oden, eds, ASME, New York, pp. 71–143.

[15] Orszag, S. A., and Kells, L. C., 1980, ''Transition to Turbulence in Plane Poiseuille Flow and Plane Couette Flow,'' J. Fluid Mech., **96**, pp. 159–205.

[16] Fischer, P. F., and Patera, A. T., 1992, ''Parallel Spectral Element Solutions of Eddy-Promoter Channel Flow,'' *Proceedings of the European Research Community on Flow Turbulence and Computation Workshop*, Lausanne, Switzerland, Cambridge University Press, Cambridge, UK, pp. 246–256.

[17] Patankar, S. V., Liu, C. H., and Sparrow, E. M., 1977, ''Fully Developed Flow and Heat Transfer in Ducts Having Streamwise Periodic Variations of Cross-Sectional Area,'' ASME J. Heat Transfer, **99**, pp. 180–186.

[18] Kays, W. M., and Crawford, M. E., 1993, *Convection Heat and Mass Transfer*, 3rd Ed., McGraw-Hill, New York.

[19] Fischer, P. F., and Patera, A. T., 1991, ''Parallel Spectral Element Solutions of the Stokes Problem,'' J. Comput. Phys., **92**, pp. 380–421.

[20] Fischer, P. F., and Ronquist, E. M., 1994, ''Spectral Element Methods for Large Scale Parallel Navier-Stokes Calculations,'' Comp. Meth. Mech. Eng., pp. 69–76.

M. R. D. Davies

D. T. Newport
e-mail: david.newport@ul.ie

T. M. Dalton

PEI Technologies,
Thermofluids Research Centre,
Department of Mechanical and
Aeronautical Engineering,
University of Limerick,
Limerick, Ireland

On Gaseous Free-Convection Heat Transfer With Well-Defined Boundary Conditions

The scaling of free convection heat transfer is investigated. The nondimensional groups for Boussinesq and fully compressible variable property free convection, driven by isothermal surfaces, are derived using a previously published novel method of dimensional analysis. Both flows are described by a different set of groups. The applicability of each flow description is experimentally investigated for the case of the isothermal horizontal cylinder in an air-filled isothermal enclosure. The approach taken to the boundary conditions differs from that of previous investigations. Here, it is argued that the best definition of the boundary conditions is achieved for heat exchange between the cylinder and the enclosure rather than the cylinder and an arbitrarily chosen fluid region. The enclosure temperature is shown both analytically and experimentally to affect the Nusselt number. The previously published view that the Boussinesq approximation has only a limited range of application is confirmed, and the groups derived for variable property compressible free convection are demonstrated to be correct experimentally. A new correlation for horizontal cylinder Nusselt number prediction is presented.
[S0022-1481(00)01604-2]

Keywords: Cylinder, Heat Transfer, Laminar, Natural Convection, Scaling

Introduction

The objective of this paper is to derive and experimentally confirm the correct nondimensional parameters for the prediction of the Nusselt number in free convection. The fundamental groups traditionally used in free convection are the Grashof and Prandtl numbers, and these are often combined as a product to reduce the number of variables to one, the Rayleigh number. Thus there are many published correlations and predictions for the Nusselt number as a function of the Grashof and Prandtl, or Rayleigh, numbers for particular geometries.

It is shown later that the functional dependence on the Grashof and Prandtl numbers arises from the Boussinesq approximation, and the isothermal surface boundary condition. Given that almost all correlations and predictions for the Nusselt number are presented as functions of parameters arising from the Boussinesq approximation, these are limited by the accuracy of that approximation. Leal [1] notes ''one should expect quantitative deviations from the Boussinesq predictions for systems in which the temperature differences are large (greater than 10–20 K).'' Analytical work by Gray and Giorgini [2], Zhong et al. [3], and Mahony et al. [4] predict the limits of the approximation. Zhong et al. [3] have it valid for surface to ambient temperature ratios up to 1.1, whereas Mahony et al. [4] place it up to 1.2. Given that many free convection applications involve temperature ratios exceeding these, there is a need to examine whether the Grashof and Prandtl numbers are suitable groups for free convection, and if not, to determine what groups are.

In this paper, the nondimensional groups for two types of flow, Boussinesq and compressible with variable properties, are derived using the novel method of Dalton and Davies [5]. The groups derived are applicable to any free convecting body, since it is the functional relationship between the groups that is dependent upon the geometry, not the groups themselves.

To test the results of the different flow descriptions, an experimental investigation was made into the horizontal isothermal cylinder, which was chosen as it represents one of the simplest geometries in free convection and has been subject to numerous analytical, experimental, and numerical investigations. McAdams [6] and Morgan [7] presented correlations based on the data of all previous experimental investigators into the geometry dating back to the start of this century. These correlations, with the thermophysical properties evaluated at the film temperature, are generally accepted as approximately true for moderate Rayleigh numbers, failing at lower Rayleigh numbers where the boundary layer is thick in comparison with the cylinder diameter, and at higher Rayleigh numbers, where transition to turbulence occurs. Hesse and Sparrow [8] experimentally investigated the lower Rayleigh number regime and produced a correlation to supercede McAdam's over this range. They also discuss the effect of evaluating the volumetric coefficient of thermal expansion as $1/T_\infty$, and not as $1/T_f$ as was previously done. The most recent experimental investigation was by Clemes et al. [9], who examined horizontal cylinders of various cross-sectional geometries. They also review four of the most widely cited correlations and predictions from the literature, and determine the prediction of Kuehn and Goldstein [10] to best predict their data. Interestingly, Clemes et al. [9] maintained a maximum temperature ratio of 1.1, thereby producing, according to Zhong et al. [3] and Mahony et al. [4], data which obey the Boussinesq approximation. Churchill and Chu [11] produced a Nusselt number prediction valid for a very wide range of Grashof and Prandtl numbers, based upon the Churchill and Usagi [12] model. Other predictions for the horizontal circular cylinder arose as limiting cases from investigations for more general geometries, such as Kuehn and Goldstein [10] and Raithby and Hollands [13]. Kuehn and Goldstein [10] discuss how turbulence and thick layer effects must be considered in the use of the conduction layer model. In the eighties and nineties, numerical work became more predominant, with work by Ghaddar [14] and Takeuchi et al. [15], among others. Saitoh et al. [16] presented a bench mark numerical solution, but did not produce a correlation for the overall Nusselt number.

In all the correlations and predictions in the literature the thermophysical properties are evaluated at the film temperature, although density and the thermophysical properties are derived by

---

Contributed by the Heat Transfer Division for publication in the JOURNAL OF HEAT TRANSFER. Manuscript received by the Heat Transfer Division, Sept. 15, 1999; revision received, Apr. 25, 2000. Associate Technical Editor: R. W. Douglass.

Schlichting [17] and Bejan [18], as being evaluated at the quiescent temperature in the Boussinesq form of the governing equations. The use of the film temperature in the literature is an approximation to account for the variation in fluid properties. As an alternative to the film temperature for gases, Sparrow and Gregg [19] propose

$$T_{\mathrm{ref}}=T_w-0.38(T_w-T_\infty) \tag{1}$$

Fand et al. [20] recommend a similar approach in which a best fit reference temperature is empirically determined to suit the data set.

A novel aspect of the present investigation is that the effect of enclosure temperature is examined which, to the authors' knowledge, has not been investigated since Rice [21], who took four data points at an ambient temperature of 103°C, and noted that ''the convection increases with the ambient temperature.'' The ambient temperature is generally a poorly controlled quantity in free convection experimentation, being generally defined as an arbitrary region outside the boundary layer. Quiescent temperatures used in the literature range from 10°C to 50°C, yet there appears to have been no systematic examination of the effect of this variation. In the more recent experimental investigations carried out, such as Clemes et al. [9], Hesse and Sparrow [8], and Tsubouchi et al. [22], the ambient temperature was not controlled. Investigations utilizing isothermal enclosures, such as Warrington and Powe's [23] examination of enclosure free convection, do not report at which temperature the measurements were made. From the literature, it would therefore appear that a well-defined ambient temperature is not an important criteria in free convection experimentation. It is shown later, both analytically and experimentally, that the enclosure temperature does affect the Nusselt number.

In the first section of the paper, the nondimensional groups for Boussinesq and variable property fully compressible free convection are derived, as well as a criteria for the consideration of variable property effects. An account of the experimental investigation into the horizontal isothermal cylinder suspended in the center of an isothermal cubical enclosure is then presented, followed by results, plotted to demonstrate the nondimensional groups.

Dimensional Analysis

The non-dimensional groups for two types of flow—fully compressible with variable properties and Boussinesq—are derived using the method of Dalton and Davies [5].

Schlichting [17] approximated the variation of viscosity, thermal conductivity, and specific heat capacity with a power law as

$$\frac{\mu}{\mu_{\mathrm{ref}}}=\left(\frac{T}{T_{\mathrm{ref}}}\right)^a;\quad \frac{c_p}{c_{p_{\mathrm{ref}}}}=\left(\frac{T}{T_{\mathrm{ref}}}\right)^b;\quad \frac{k}{k_{\mathrm{ref}}}=\left(\frac{T}{T_{\mathrm{ref}}}\right)^c \tag{2}$$

where a, b, and c are fluid specific.

Equation (2) may be expressed in the form

$$\mu=C_\mu T^a;\quad c_p=C_{c_p}T^b;\quad k=C_kT^c \tag{3}$$

If the variable property, compressible equations of mass momentum, energy, and state without viscous heating for a perfect gas, are expressed in nondimensional form with the following definitions of the nondimensional variables,

$$u^*=\frac{u}{\sqrt{Dg}};\quad v^*=\frac{v}{\sqrt{Dg}};\quad p^*=\frac{p}{\mu_{\mathrm{ref}}\left(\frac{gD}{RT_{\mathrm{ref}}}\right)^a}\sqrt{\frac{D}{g}};$$

$$\rho^*=\frac{\rho\sqrt{D^3g}}{\mu_{\mathrm{ref}}\left(\frac{gD}{RT_{\mathrm{ref}}}\right)^a};T^*=\frac{TR}{Dg};\quad \mu^*=\frac{\mu}{\mu_{\mathrm{ref}}}\left(\frac{gD}{RT_{\mathrm{ref}}}\right)^a; \tag{4}$$

$$c_p^*=\frac{c_p}{c_{p_{\mathrm{ref}}}}\left(\frac{gD}{RT_{\mathrm{ref}}}\right)^b;\quad k^*=\frac{k}{k_{\mathrm{ref}}}\left(\frac{gD}{RT_{\mathrm{ref}}}\right)^c$$

Then the only constants in the equations are a, b, c the modified Prandtl number,

$$\mathrm{Pr}_{\mathrm{mod}}=\frac{\mu_{\mathrm{ref}}c_{p_{\mathrm{ref}}}}{k_{\mathrm{ref}}}\left(\frac{gD}{RT_{\mathrm{ref}}}\right)^{a+b-c} \tag{5}$$

and the compressibility group

$$\gamma_{\mathrm{mod}}=\frac{R}{c_{p_{\mathrm{ref}}}}\left(\frac{gD}{RT_{\mathrm{ref}}}\right)^b \tag{6}$$

Similarly, if the compressibility is confined to the momentum equations, and the properties are constant, which is the Boussinesq approximation, then the governing equations of mass, momentum, and energy, expressed in nondimensional form with the following nondimensional variables,

$$u^*=\frac{\rho uD}{\mu};\quad v^*=\frac{\rho vD}{\mu};\quad \Delta T^*=\frac{\rho^2g\beta D^3(T-T_{\mathrm{ref}})}{\mu^2};\quad p^*=\frac{pD^2p}{\mu^2} \tag{7}$$

have only the Prandtl number as a constant.

Consider free convection between an isothermal surface of characteristic length D, and surface temperature T_w and a quiescent fluid at T_∞. An initial pressure p_i, is defined which sets the pressure datum. The boundary conditions for the compressible flow case leads to the following relationship for any independent variable. For example:

$$T^*=f_1\left(\begin{array}{l}\left(\frac{p_i}{\mu_{\mathrm{ref}}}\left\{\frac{gD}{RT_{\mathrm{ref}}}\right\}^a\sqrt{\frac{D}{g}}\right),\left(\frac{T_wR}{Dg}\right),\\ \left(\frac{T_\infty R}{Dg}\right),\left(\frac{\mu_{\mathrm{ref}}c_{p_{\mathrm{ref}}}}{k_{\mathrm{ref}}}\left\{\frac{gD}{RT_{\mathrm{ref}}}\right\}^{a+b-c}\right),\left(\frac{R}{c_{p_{\mathrm{ref}}}}\left\{\frac{gD}{RT_{\mathrm{ref}}}\right\}^b\right),\ a,b,c,x^*,y^*\end{array}\right) \tag{8}$$

Taking a heat balance at the heated surface it can be shown for the overall Nusselt number that,

$$\overline{\mathrm{Nu}}=f_2\left(\begin{array}{l}\left(\frac{p_i}{\mu_{\mathrm{ref}}}\left\{\frac{gD}{RT_{\mathrm{ref}}}\right\}^a\sqrt{\frac{D}{g}}\right),\left(\frac{T_wR}{Dg}\right),\\ \left(\frac{T_\infty R}{Dg}\right),\left(\frac{u_{\mathrm{ref}}c_{p_{\mathrm{ref}}}}{k_{\mathrm{ref}}}\left\{\frac{gD}{RT_{\mathrm{ref}}}\right\}^{a+b-c}\right),\left(\frac{R}{c_{p_{\mathrm{ref}}}}\left\{\frac{gD}{RT_{\mathrm{ref}}}\right\}^b\right),\ a,b,c\end{array}\right) \tag{9}$$

or with the order of terms preserved,

$$\overline{\mathrm{Nu}}=f_2(p_i^*,T_w^*,T_\infty^*,\mathrm{Pr}_{\mathrm{mod}},\gamma_{\mathrm{mod}},a,b,c) \qquad (10)$$

Similarly, it can be shown for a Boussinesq system that,

$$\overline{\mathrm{Nu}}=f_3\left(\left(\frac{\rho^2 g\beta D^3(T_{\mathrm{cyl}}-T_e)}{\mu^2}\right),\frac{\mu c_p}{k}\right) \qquad (11)$$

Having determined the groups for the two types of flow, a condition is derived for when property variation becomes important in buoyancy driven flow. Property variation in the momentum equation is expressed as

$$\frac{\partial}{\partial y}\left(\mu\frac{\partial u}{\partial v}\right)=\frac{\partial\mu}{\partial y}\frac{\partial u}{\partial y}+\mu\frac{\partial^2 u}{\partial y^2} \qquad (12)$$

and in the energy equation:

$$\frac{\partial}{\partial y}\left(k\frac{\partial t}{\partial y}\right)=\frac{\partial k}{\partial y}\frac{\partial T}{\partial y}+k\frac{\partial^2 T}{\partial y^2} \qquad (13)$$

The aim is to find under what conditions the first term on the right hand side of Eqs. (12) and (13) is significant. As the second term is always significant, a ratio of these terms gives a criteria.

$$R_\mu=\frac{(\partial\mu/\partial y)(\partial u/\partial y)}{\mu(\partial^2 u/\partial y^2)} \qquad (14)$$

$$R_k=\frac{(\partial k/\partial y)(\partial T/\partial y)}{k(\partial^2 T/\partial y^2)} \qquad (15)$$

To evaluate these ratios requires knowledge of the boundary layer profiles. Standard flat-plate free convection profiles from Holman [24] are

$$\frac{u}{u_x}=\frac{y}{\delta}\left(1-\frac{y}{\delta}\right)^2;\quad \frac{T-T_\infty}{T_w-T_\infty}=\left(1-\frac{y}{\delta}\right)^2 \qquad (16)$$

where u_x is a fictitious velocity. Property variations are as given by Schlichting ([17]) in Eq. (2). The greatest temperature, and hence property gradients, are found at the wall. Furthermore, the second order derivatives approach zero at the wall, which also makes the gradients maximum at the wall. So, if at $y=0$, the effect is insignificant, then it is also elsewhere. Differentiating Eq. (16) and substituting into Eqs. (14) and (15) at $y=0$ gives

$$R_{\mu_{y=0}}=\frac{a}{2}\left(1-\frac{T_\infty}{T_w}\right) \qquad (17)$$

$$R_{k_{y=0}}=2c\left(1-\frac{T_\infty}{T_w}\right) \qquad (18)$$

Setting an arbitrary 5 percent error limit, property variations may be ignored if

$$\frac{a}{2}\left(1-\frac{T_\infty}{T_w}\right)<0.05 \qquad (19)$$

$$2c\left(1-\frac{T_\infty}{T_w}\right)<0.05 \qquad (20)$$

Having derived the nondimensional groups for each flow for free convection between two isothermal surfaces, and obtained a criteria determining when property variations become significant, an experiment was performed to demonstrate the derived groups.

Experimentation

The case of the isothermal horizontal circular cylinder located in the center of a cubical isothermal enclosure was experimentally investigated, with Nusselt, Grashof, nondimensional wall temperature, cylinder temperature, and pressure number measurements being made. Nondimensional parameters were varied using the cylinder and enclosure temperatures and the cylinder diameter. Air was used as the working fluid, therefore the Prandtl number and the fluid specific constants *a*, *b*, and *c* were invariant.

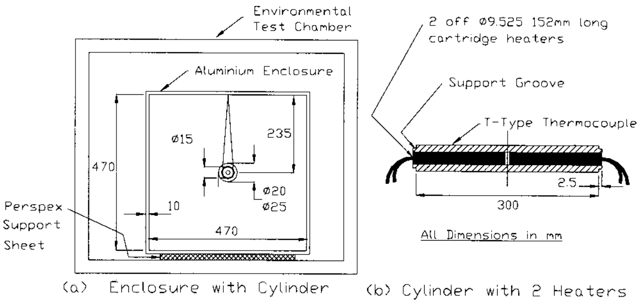

Fig. 1 Horizontal cylinder suspended within an isothermal enclosure

Figure 1 shows the apparatus used. Two cylinders made of aluminum, of 20 mm and 25 mm diameter, were used in the investigation. Each cylinder was 305 mm long, and powered by two 300 W N&P cartridge heaters, of ∅9.5 mm and 152 mm long, inserted into either end of the cylinders. The cylinder surface temperature was measured using two welded tip *T*-type thermocouples, calibrated to 0.1°C, mounted on the surface of the cylinder, which was found to be isothermal to within 1 percent. The thermocouples were located 50 and 100 mm from either end of the cylinder, one at the upper and the other at the lower cylinder stagnation point. Interferogrames by Newport et al. [25] verified the isothermality of the ∅20 mm cylinder. The power into the cylinders was measured as the product of the voltages across and current through the cartridge heaters. Voltages were measured using sense wires connected to a voltmeter, and current measured with an ammeter connected in series with the cartridge heaters.

To prevent the convective heat loss from the cylinders being influenced by random drafts, each cylinder was suspended in turn within a 470 mm sided and 10 mm thick cubical aluminum enclosure. The heat transfer was defined relative to the enclosure, ensuring a well defined system. In order to examine the influence of enclosure temperature, the system, comprising cylinder, and enclosure, was placed in an environmental test chamber. The enclosure temperature was controlled by the environmental test chamber and measured using six *T*-type thermocouples located at the center of each inner enclosure surface. Warrington et al. [26] present a criteria to determine whether the enclosure size will influence the Nusselt number. For the largest Rayleigh number obtained in the present investigation, the enclosure was over eight times the required minimum size as given by Warrington et al. [26]. Clemes et al. [9] placed their cylinder in a second enclosure, twice the size of the first, and reported no change in the Nusselt number. This indicated that the enclosure would have no influence on the results and that the Nusselt numbers would be identical to that of a cylinder in an extensive draft free atmosphere.

Prior to the test, the environmental test chamber temperature and the whole system was allowed three hours to reach equilibrium. Having reached the desired steady state ambient temperature, power was switched on to the heaters. Maximum power input to the heaters was 80 W and the cylinder temperature ranged from 5°C to 185.6°C. Steady state conditions were taken to be less than 0.1°C change over half an hour. Times to steady state were of the order of three hours. Approximately six data points were taken for each enclosure wall temperature and the process was repeated for enclosure wall temperatures of −10°, 20°, 50°, and 80°C. The second cylinder of ∅25 mm was then inserted and the process repeated for enclosure temperatures of 56°C and 93°C. These temperatures were chosen to produce two similar T_e^* as were obtained for the ∅20 mm cylinder. The Rayleigh number ranged from 1.55×10^3 to 7.05×10^4, which places the flow about the

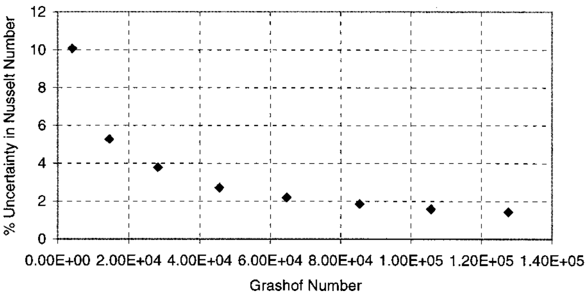

Fig. 2 Uncertainty in Nusselt number with increasing Grashof number for $T_e^*=3.99\times10^5$. Similar trends obtained for all other T_e^*.

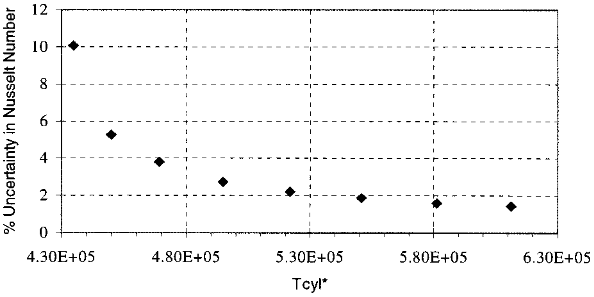

Fig. 3 Uncertainty in Nusselt number with increasing T_{cyl}^* for $T_e^*=3.99\times10^5$, and $\mathrm{Pr}_{\mathrm{mod}}p_i^*=4.97$. Similar trends obtained for all other T_e^* and $\mathrm{Pr}_{\mathrm{mod}}$.

cylinder in the laminar regime. Repeatability checks were made at one power setting for each enclosure temperature by monitoring the temperature rise of the cylinder, which was found to be repeatable to within 1°C.

Calculation of Results. The Nusselt number is given by

$$\overline{\mathrm{Nu}}=\frac{Q_{\mathrm{conv}}d}{kA_{\mathrm{cyl}}(T_{\mathrm{cyl}}-T_e)} \tag{21}$$

where

$$\begin{aligned}Q_{\mathrm{conv}}&=Q_{\mathrm{total}}-Q_{\mathrm{loss}}\\&=\mathrm{VI}-Q_{\mathrm{loss}}\end{aligned} \tag{22}$$

Losses are defined as heat transfer by any means other than free convection from the surface of the cylinder, such as radiation and conduction through the heater leads. Conduction through the leads is difficult to determine, but is considered small considering that the ratio of the cross-sectional area of the heater wires in comparison with the cylinder was 0.01. Because the cylinder area is considerably less than the enclosure area, the radiative heat loss is given by

$$Q_{\mathrm{rad}}=\sigma\varepsilon_{\mathrm{cyl}}A_{\mathrm{cyl}}(T_{\mathrm{cyl}}^4-T_e^4). \tag{23}$$

Radiation in free convection experimentation is, in general, rendered small by polishing the object, or objects, of interest to an emissivity of less than 0.1. However, in the present investigation, the cylinder surface was found to oxidize considerably, resulting in the radiative heat transfer not being fully determined. Therefore, the cylinder was painted black to a measured emissivity of 0.96, which also prevented oxidization.

Convection from the end faces and support grooves of the cylinder was also considered. Support groove convection is approximated by comparing the surface area of the support grooves to the total surface area of the cylinder. End face convection can be approximated by using a vertical flat plate correlation. This lead to a 5 percent reduction in the cylinder heat transfer coefficient.

Voltage, current, and temperatures were measured to an accuracy of 0.01 V, 0.01 A, and 0.1°C, respectively. This resulted in a maximum uncertainty of 10 percent in the Nusselt number at the smallest Grashof number and nondimensional cylinder number, arising out of the small temperature differences involved. This large uncertainty decayed rapidly to an average value of 2.5 percent for larger Grashof numbers, as shown in Figs. 2 and 3.

Results and Discussion

The results obtained from the experimental investigation are presented in Figs. 4, 5, and 6. The data is first plotted in the traditional form of Nusselt versus Rayleigh number, with the thermophysical properties evaluated at the film temperature, and the cylinder diameter, *d*, taken as the characteristic length. The plots

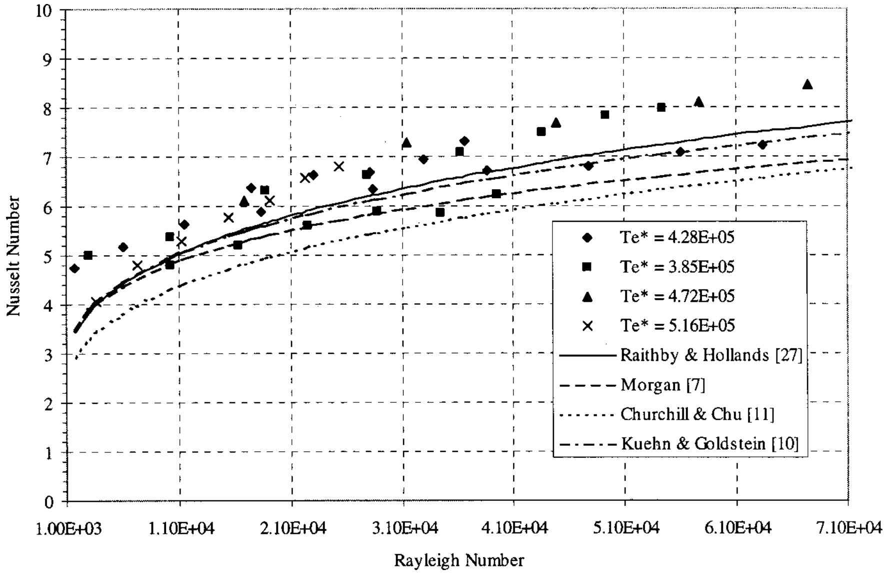

Fig. 4 Comparison of present data with correlations from the literature, with thermophysical properties evaluated at the film temperature

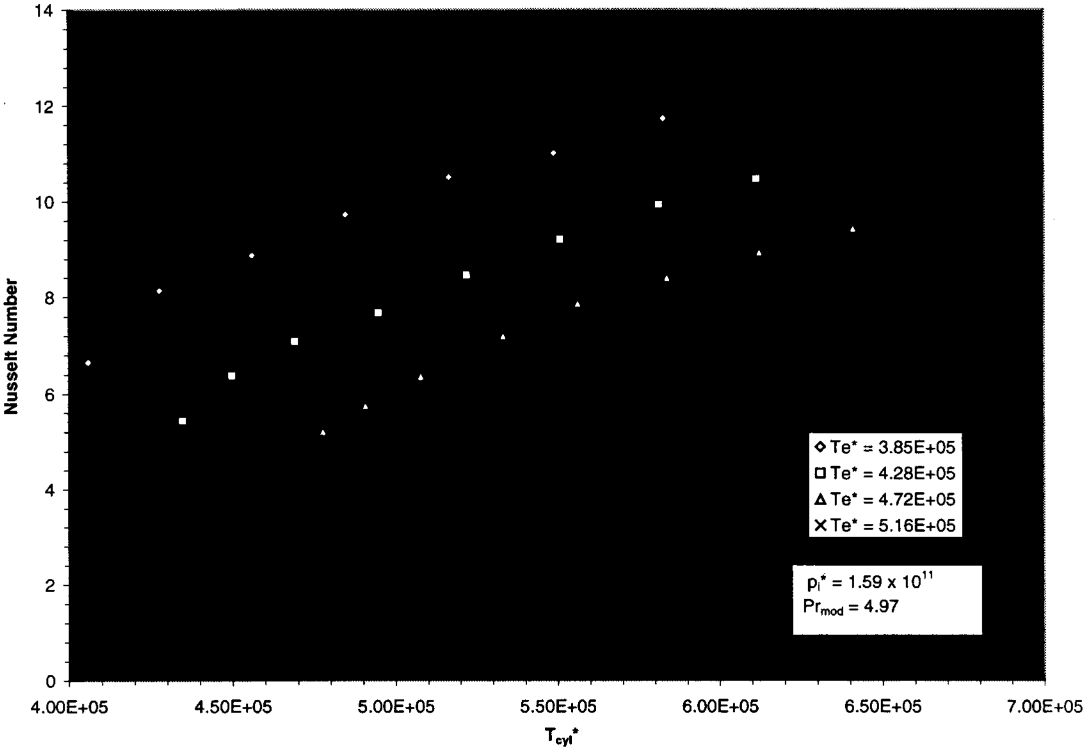

Fig. 5 Plot of Nu versus T^*_{cyl} with constant p^*_i and Pr_{mod}, showing the effect of varying T^*_e

are described and then discussed in terms of the dimensionless groups derived earlier. A table of the measured data is given in Table 1 for reference.

Figure 4 shows a comparison of the present experimental data with four of the most widely cited correlations in the literature: Raithby and Hollands [27], Morgan [7], Kuehn and Goldstein [10], and Churchill and Chu [11]. Considerable scatter, up to 30 percent, is present in the experimental data set. Below a Rayleigh number of 1.10×10^4, the scatter in the present data lies within the bounds of the experimental uncertainty given in Fig. 2. Therefore,

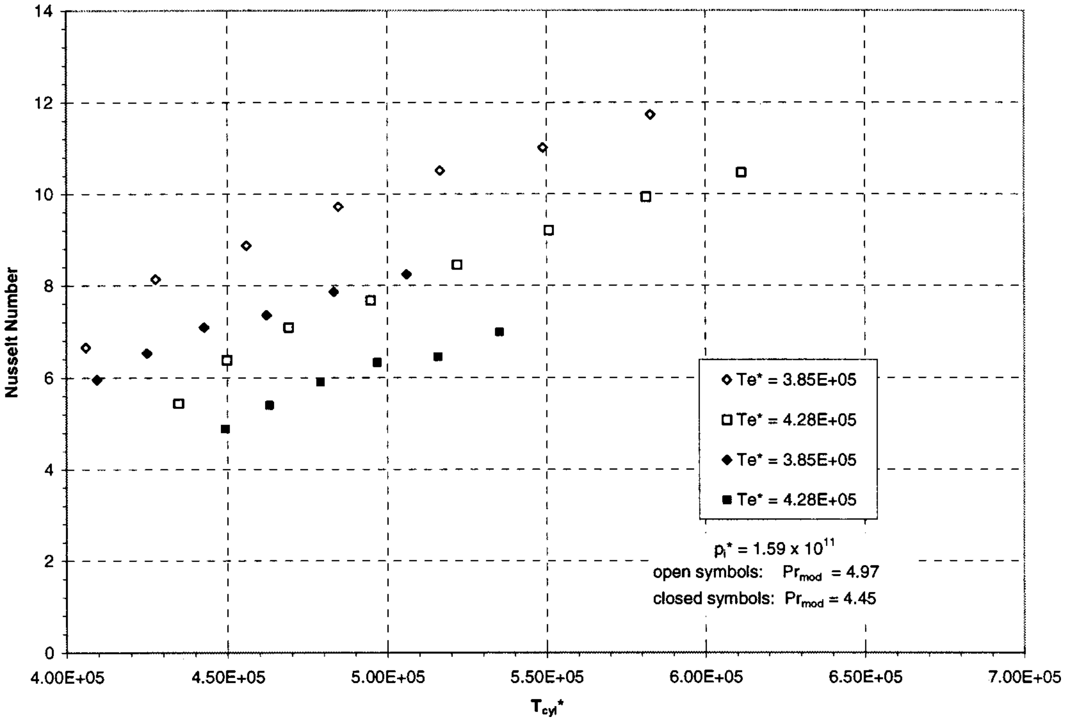

Fig. 6 Plot of Nu versus T^*_{cyl} with constant p^*_i, at two different T^*_e showing the effect of a change in Pr_{mod}

Table 1 Table of experimental data

d (m)	q (W/m^2)	T_{cyl} (deg C)	T_e (deg C)
0.020	25.58	24.25	20.20
0.020	98.60	34.55	20.28
0.020	228.84	47.70	20.06
0.020	402.51	65.25	20.32
0.020	626.93	83.80	20.20
0.020	895.31	103.50	19.90
0.020	1202.20	124.40	20.28
0.020	1513.89	144.90	19.92
0.020	22.62	53.60	50.16
0.020	88.45	62.50	50.34
0.020	196.79	74.20	49.74
0.020	371.56	89.85	50.10
0.020	566.28	107.25	50.56
0.020	777.09	126.10	50.84
0.020	1048.54	145.55	50.52
0.020	1363.12	165.30	50.78
0.020	107.51	4.60	-10.64
0.020	264.21	19.40	-11.20
0.020	460.64	38.70	-10.12
0.020	711.38	58.35	-10.72
0.020	1005.09	80.15	-10.20
0.020	1305.96	102.25	-10.28
0.020	1668.93	125.35	-9.92
0.020	66.19	91.40	80.78
0.020	162.11	101.80	80.16
0.020	297.78	115.75	80.16
0.020	478.83	130.85	79.54
0.020	693.76	148.35	79.96
0.020	941.04	164.65	79.86
0.020	1237.10	185.55	80.60
0.025	144.62	76.95	55.82
0.025	259.28	90.20	55.62
0.025	406.80	105.40	55.36
0.025	559.64	122.00	55.56
0.025	756.42	139.95	55.92
0.025	971.89	159.40	56.36
0.025	108.90	111.00	93.27
0.025	200.37	122.70	93.21
0.025	320.42	136.35	93.33
0.025	464.14	151.60	93.37
0.025	601.56	167.80	93.55
0.025	795.62	184.35	93.79

the Nusselt number can be said to exhibit a dependence on the Rayleigh number below a Rayleigh number of 1.10×10^4. Above this value, the experimental uncertainty reduces to a mean value of 2 percent. However, the scatter in the data set increases up to the order of 30 percent. The scatter in this region can only be attributed to a breakdown in the functional dependence of the Nusselt number on the Rayleigh number. This could result from a dependence of the Nusselt number on the enclosure temperature, or variable property effects. Fand et al. [20] note how an apparent dependence on diameter manifested itself in a comparison between Morgan's [7] data and their own. Interestingly, they postulate the existence of an extra correlating dimensionless group. Although the data could most probably be collapsed using an empirically determined reference temperature, which would better approximate the variation in fluid properties than the film temperature, a more rigorous approach, as will be shown, is to plot the data in terms of the dimensionless parameters derived for variable property free convection.

Comparing the present data set to the correlations in the literature, standard deviations of 9.6 percent, 13.3 percent, 19.2 percent, and 10.2 percent are obtained with the correlations of Raithby and Hollands [27], Morgan [7], Churchill and Chu [11], and Kuehn and Goldstein [10]. Morgan [28] extensively reviewed the existing experimental, numerical, and analytical correlations and noted that for Rayleigh numbers below 10^4, the mean deviation of experimental values of the Nusselt number to predicted was 4 percent, but increased from 8 percent to 11 percent with increasing Rayleigh numbers up to 10^7. Considering that the present data set includes a significant variation in absolute temperature which was never previously examined, the deviations in the data with the predictive correlations are relatively consistent with the deviations in previous experimental investigations.

Considering variable conductivity effects in a fully compressible fluid, the functional relationship of the Nusselt number is described by Eq. (8). The cylinder is of diameter d, and temperature T_{cyl}, and the enclosure of temperature T_e. In the experimental investigation, the working fluid was kept constant, therefore the groups a, b, and c did not change. Therefore,

$$\mathrm{Nu}=f_2\left(\begin{array}{c}\left(\frac{p_i}{\mu_{\mathrm{ref}}}\left\{\frac{RT_{\mathrm{ref}}}{gd}\right\}^a\sqrt{\frac{d}{g}}\right),\left(\frac{T_{\mathrm{cyl}}R}{dg}\right),\left(\frac{T_eR}{dg}\right)\\ \left(\frac{\mu_{\mathrm{ref}}c_{p_{\mathrm{ref}}}}{k_{\mathrm{ref}}}\left\{\frac{gd}{RT_{\mathrm{ref}}}\right\}^{a+b-c}\right),\left(\frac{R}{c_{p_{\mathrm{ref}}}}\left\{\frac{gd}{RT_{\mathrm{ref}}}\right\}^b\right)\end{array}\right) \tag{24}$$

or,

$$\mathrm{Nu}=f_2(p_i^*,T_{\mathrm{cyl}}^*,T_e^*,\mathrm{Pr}_{\mathrm{mod}},\gamma_{\mathrm{mod}}) \tag{25}$$

Over the range of temperatures considered in the present experiment, and in many applications, property variations may be approximated as

$$\mu=1.1\times 10^{-6}T^{0.5} \tag{26}$$

$$k=8.55\times 10^{-5}T \tag{27}$$

and c_p is constant. Therefore $a=0.5$, $b=0$, and $c=1$ in Eq. (2). Equations (19) and (20) may then be written as $T_{\mathrm{cyl}}/T_e>1.25$ for variable viscosity effects to be considered $T_{\mathrm{cyl}}/T_e>1.03$ for variable conductivity effects to be considered.

The maximum cylinder to enclosure temperature ratio in the experiment was 1.5. Therefore, variable conductivity and viscosity effects are present in the data set. It is interesting to note that the effect of variable conductivity is significant in almost all engineering applications involving air, whilst variable viscosity effects may be only sometimes significant.

Inserting $a=0.5$, $b=0$, and $c=1$, into Eq. (24), and defining T_e as the reference temperature gives

$$\mathrm{Nu}=f_2\left(\left(\frac{\rho_iR^{0.5}}{C_\mu g}\right),\left(\frac{T_{\mathrm{cyl}}R}{dg}\right),\left(\frac{T_eR}{dg}\right),\left(\frac{C_\mu C_{c_p}}{C_k}\sqrt{\frac{R}{gd}}\right),\left(\frac{R}{c_{p_{\mathrm{ref}}}}\right)\right) \tag{28}$$

or with the order of terms preserved,

$$\mathrm{Nu}=f_2(p_i^*,T_{\mathrm{cyl}}^*,T_e^*,\mathrm{Pr}_{\mathrm{mod}},\gamma^*) \tag{29}$$

The first and last terms in Eq. (28) are constant for the range of measured data, and the penultimate term varies only with the change in diameter of the cylinder. Thus the data should be described by

$$\mathrm{Nu}=f_2\left(\left(\frac{T_{\mathrm{cyl}}R}{dg}\right),\left(\frac{T_eR}{dg}\right),\left(\frac{C_\mu C_{c_p}}{C_k}\sqrt{\frac{R}{gd}}\right)\right) \tag{30}$$

Figures 5 and 6 show the measured data plotted to demonstrate the functional relationship indicated by Eq. (30). It can be seen that the data collapses on the predicted groups. From Fig. 5, it can be seen that for constant p_i^* and $\mathrm{Pr}_{\mathrm{mod}}$, the Nusselt number decreases with increasing nondimensional enclosure temperature. From Fig. 6 it can be seen that, for a given nondimensional wall temperature at constant p_i^*, a change in $\mathrm{Pr}_{\mathrm{mod}}$ results in a reduction in the Nusselt number and in the slope of the relationship. It was not possible to demonstrate the effect of changes in the p_i^* group owing to the lack of a facility to vary the initial pressure of the system.

The following correlation is presented for compressible variable property free convection from an isothermal horizontal cylinder in air, valid only over the present range of data.

$$\mathrm{Nu}=14.224\ln\left(\frac{T^*_{\mathrm{cyl}}}{T^{*1.35}_e}\right)+f(\mathrm{Pr}_{\mathrm{mod}}) \tag{31}$$

where

$$f(\mathrm{Pr}_{\mathrm{mod}})=03722\,\mathrm{Pr}_{\mathrm{mod}}-21.159$$

Using the fully compressible variable property nondimensional groups at large temperature differences, the Nusselt number for the horizontal cylinder can be predicted to within 2 percent, compared to a mean of 10 percent using Grashof–Prandtl number correlations. However, this gain in accuracy comes at the price of additional nondimensional parameters. At lower temperature differences, the Boussinesq approximation with properties evaluated at the film temperature offers a suitable means of predicting the Nusselt number. The choice of method will depend on the degree of accuracy desired by the user for the prediction of the Nusselt number.

Conclusions

The following conclusions are made:

- The dimensionless parameters governing Boussinesq and variable property fully compressible free convection flow have been derived, and a criteria determined for when variable property effects should be considered.
- The enclosure temperature has been shown, both analytically and experimentally, to have an effect on the Nusselt number, and the inability of the correlations and predictions in the literature to accurately predict the Nusselt number highlighted.
- The functional relationship derived for compressible variable property free convection has been verified experimentally.
- An accurate correlation for predicting the cylinder Nusselt number, valid only over the range of present data, has been presented.

Acknowledgments

The authors gratefully acknowledge PEI Technologies for their financial support, and the technical staff of the University of Limerick.

Nomenclature

Symbol

A = Area m^2
C_{cp} = Specific heat constant J/kg K^2
C_k = Conductivity constant W/m K^2
C_μ = Viscosity constant N/m^2 s K
D = Characteristic length m
I = Electric current A
L = Characteristic length m
Q = Power W
R = Gas constant J/kg K
R_μ = Viscosity ratio Term
R_k = Conductivity ratio Term
T = Temperature K
V = Voltage V
a = fluid specific constant
b = fluid specific constant
c = fluid specific constant
c_p = specific heat capacity J/kg K
d = diameter m
g = gravitational acceleration m/s^2
h = heat transfer coefficient W/m^2 K
k = thermal conductivity W/m K
p = Pressure N/m^2
r = radial displacement m
t = time s
u = velocity x m/s
v = velocity y m/s
ΔT = temperature difference K

Greek

β = Coeff. thermal expansion K^{-1}
δ = boundary layer thickness m
ε = emmisivity
μ = dynamic viscosity Ns^2/m
θ = angular displacement rad
ρ = density kg/m^3
σ = Stefan–Boltzman constant W/m^2 K^4

Subscripts

e = enclosure
i = initial
r = radial component
w = heated surface
θ = angular component
∞ = ambient
film = evaluated at film temp.
conv = convective
cyl = cylinder
mod = modified
rad = radiative
ref = reference
total = total

Superscript

$*$ = dimensionless parameter

Dimensionless Numbers

Nu = Nusselt Number
Gr = Grashof Number
Pr = Prandtl Number

References

[1] Leal, G. L., 1992, *Laminar Flow and Convective Transport Processes: Scaling Principles and Asymptotic Analysis*, 1st Ed., Butterworth–Heinemann, Newton MA, p. 673.
[2] Gray, D., and Giorgini, A., 1976, ''The Validity of the Boussinesq Approximation for Liquids and Gases,'' Int. J. Heat Mass Transf., **19**, pp. 545–551.
[3] Zhong, Z. Y., Yang, K. T., and Lloyd, J. R., 1985, ''Variable Property Effects in Laminar Natural Convection in a Square Enclosure,'' ASME J. Heat Transfer, **107**, pp. 133–138.
[4] Mahony, D. N., Kumar, R., and Bishop, E. H., 1986, ''Numerical Investigation of Variable Property Effects on Laminar Natural Convection of Gases Between Two Horizontal Isothermal Concentric Cylinders,'' ASME J. Heat Transfer, **108**, pp. 783–789.
[5] Dalton, T., and Davies, M. R. D., 1997, ''Convection Dimensional Analysis,'' ASME *Proceedings of the 32nd National Heat Transfer Conference*, HTD-Vol. 346, Vol. 8, Baltimore, Maryland, ASME, New York, pp. 33–41.
[6] McAdams, W. H., 1954, *Heat Transmission*, McGraw-Hill, New York.
[7] Morgan, V. T., 1975, ''The Overall Convective Heat Transfer From Smooth Circular Cylinders,'' Advances in Heat Transfer, Vol. 11, Academic Press, San Diego, CA.
[8] Hesse, G., and Sparrow, E. M., 1974, ''Low Rayleigh Number Natural Convection Heat Transfer From High Temperature Horizontal Wires to Gases,'' Int. J. Heat Mass Transf., **17**, pp. 796–798.
[9] Clemes, S. B., Hollands, K. G. T., and Brunger, A. P., 1994, ''Natural Convection Heat Transfer from Long Horizontal Isothermal Cylinders,'' ASME J. Heat Transfer, **116**, pp. 96–104.
[10] Kuehn, T. H., and Goldstein, R. J., 1976, ''Correlating Equations for Natural Convection Heat Transfer Between Horizontal Circular Cylinders,'' Int. J. Heat Mass Transf., **19**, pp. 1127–1134.
[11] Churchill, S. W., and Chu, H. H. S., 1975, ''Correlating Equations for Laminar and Turbulent Free Convection From a Horizontal Cylinder,'' Int. J. Heat Mass Transf., **18**, pp. 1049–1053.
[12] Churchill, S. W., and Usagi, R., 1972, ''A General Expression for the Correlation of Rates of Transfer and Other Phenomena,'' AIChE J., **18**, pp. 1121–1128.
[13] Raithby, G. D., and Hollands, K. G. T., 1976, ''Laminar and Turbulent Free Convection From Elliptic Cylinders, With a Vertical Plate and Horizontal Circular Cylinder as Special Cases,'' ASME J. Heat Transfer, **98**, pp. 72–80.
[14] Ghaddar, N., 1992, ''Natural Convection Heat Transfer Between a Uniformly Heated Cylindrical Element and its Rectangular Enclosure,'' Int. J. Heat Mass Transf., **35**, pp. 2327–2334.
[15] Takeuchi, Y., Hata, K., Shiotsu, M., and Sakurai, A., 1992, ''A General Cor-

relation for Natural Convection Heat Transfer From Horizontal Cylinders in Liquids and Gases,'' ASME *General Papers in Heat Transfer*, HTD-Vol. 204, ASME, New York, pp. 183–189.

[16] Saitoh, T., Sajiki, T., and Maruhara, K., 1993, ''Benchmark Solutions to Natural Convection Heat Transfer Problem Around a Horizontal Circular Cylinder,'' Int. J. Heat Mass Transf., **36**, No. 5, pp. 1251–1259.

[17] Schlichting, H., 1979, *Boundary Layer Theory*, 7th Ed., McGraw-Hill, London, p. 328.

[18] Bejan, A., 1995, *Convection Heat Transfer*, 2nd Ed., John Wiley and Sons, New York.

[19] Sparrow, E. M., and Gregg, J. L., 1958, ''The Variable Fluid Property Problem in Free Convection,'' Trans. ASME, **80**, pp. 879–886.

[20] Fand, R. M., Morris, E. W., and Lum, M., 1977, ''Natural Convection Heat Transfer from Horizontal Cylinders to Air, Water, and Silicone Oils for Rayleigh Numbers Between 3×10^2 and 2×10^7,'' Int. J. Heat Mass Transf., **20**, pp. 1173–1184.

[21] Rice, C. W., 1923, ''Free and Forced Convection of Heat in Gases and Liquids,'' Transactions of the Institute of American Electrical Engineers, **42**, pp. 653–706.

[22] Tsubouchi, T., and Masuda, H., 1966/1967, ''Natural Convection Heat Transfer From a Horizontal Circular Cylinder With Small Rectangular Grooves,'' Rept. Inst. High Sp. Mech. Japan, **19**, pp. 211–242.

[23] Warrington, R. O., and Powe, R. E., 1985, ''The Transfer of Heat by Natural Convection Between Bodies and Their Enclosures,'' Int. J. Heat Mass Transf., **28**, No. 2, pp. 319–330.

[24] Holman, J. P., 1992, *Heat Transfer*, 7th Ed., McGraw-Hill, London, pp. 231–381.

[25] Newport D., Dalton T., Davies M., Whelan M., and Forno C., 1999, ''An Optical and Numerical Investigation into the Thermal Interaction Between an Isothermal Cylinder and its Isothermal Enclosure,'' *Proceeding of the 33rd ASME National Heat Transfer Conference*, 15–17 August, Albuquerque, NM, ASME, New York.

[26] Warrington, R. O., Smith, S., Powe, R. E., and Mussulman, R., 1984, ''Boundary Effects on Natural Convection for Cylinders and Cubes,'' Transactions of the ASME, **39**, pp. 63–69.

[27] Raithby, G. D., and Hollands, K. G. T., 1985, *Handbook of Heat Transfer Fundamentals*. 2nd Ed., Rohsenow, Hartnett and Ganic, eds., McGraw-Hill, New York, Chapter 6.

[28] Morgan, V. T., 1997, ''Heat Transfer by Natural Convection From a Horizontal Isothermal Cylinder in Air,'' J. Heat Transf. Eng., **18**, No. 1, pp. 25–33.

Effect of Outflow Orientation on Heat Transfer and Pressure Drop in a Triangular Duct With an Array of Tangential Jets

J.-J. Hwang[1]
Professor, Mem. ASME
e-mail: jjhwang@chu.edu.tw

B.-Y. Chang
Graduate Student

Department of Mechanical Engineering,
Chung-Hua University,
Hsinchu, Taiwan 300, R.O.C.

Experiments are conducted to study the heat transfer and pressure drop characteristics in a triangular duct cooled by an array of tangential jets, simulating the leading-edge cooling circuit of a turbine blade. Coolant ejected from a high-pressure plenum through an array of orifices is aimed at the leading-edge apex and exits from the radial outlets. Three different outflow orientations, namely coincident with the entry flow, opposed to the entry flow, and both, are tested for various Reynolds numbers ($12600 \leqslant Re \leqslant 42000$). A transient liquid crystal technique is used to measure the detailed heat transfer coefficients on two walls forming the leading-edge apex. Flow rate across each jet hole and the crossflow development, which are closely related to the local heat transfer characteristics, are also measured. Results show that increasing Re increases the heat transfer on both walls. The outflow orientation affects significantly the local heat transfer characteristics through influencing the jet flow together with the crossflow in the triangular duct. The triangular duct with two openings is recommended since it has the highest wall-averaged heat transfer and the moderate loss coefficient among the three outflow orientations investigated. Correlations for wall-averaged Nusselt number and loss coefficient in the triangular duct have been developed by considering the Reynolds number for three different outflow orientations. [S0022-1481(00)01204-4]

Keywords: Augmentation, Heat Transfer, Impingement, Jets, Turbines

Introduction

To accommodate higher turbine inlet temperatures and still maintain the metal temperatures below acceptable limits, highly sophisticated cooling techniques are required, e.g., film cooling, jet impingement, and augmented convection via roughness elements or pin fins. The blade external shape demands a complex geometry for the internal cooling cavities near the leading edge, which is often simplified to triangular or cylindrical channels for analytical or experimental analyses. Conductive heat from the external pressure/suction surfaces is mostly convected away from the inner surfaces of the two walls forming the leading-edge apex to the internal coolant. In a common design, rib-turbulators are mounted on two or three walls of the triangular duct to enhance the convective heat transfer ([1,2]). In addition, using impingement jets to cool the blade leading-edge apex ([3]) is another alternative. In the present work, an array of tangential jets is employed to cool the blade leading-edge circuit. As shown in Fig. 1, an array of tangential jets injecting into the leading-edge triangular duct traverse one principal wall, then directly impinge on the apex as well as another principal wall, and finally exit radially from the blade tip. Thus, the tangential jets not only cool the leading-edge apex but also enhance the heat transfer on two principal walls of the triangular duct.

Chupp et al. ([4]) conducted an experiment to evaluate the internal heat transfer coefficient for impingement cooling on the leading edge of a turbine blade. Correlations for impingement heat transfer were developed in the presence of crossflow. Kercher and Tabakoff ([5]) measured the average flat-plate heat transfer coefficients for multiple, square array, round impinging air jets from a perforated plate. Their study included measurements of sixteen different combinations of hole spacing and channel height. Correlations of heat transfer performance in the semi-enclosed environment were presented in terms of individual spanwise row jet and crossflow velocity. Florschuetz et al. ([6–8]) experimentally studied the heat transfer characteristics for jet array impingement under different crossflow conditions. They presented correlations for both in-line and staggered holes patterns, including the effects of jet spacing, jet travel distance, and jet Reynolds number. Bunker and Metzger ([3]) employed a transient liquid crystal technique to measure detailed heat transfer around the blade leading-edge apex cooled by impinging jets. The effects of jet Reynolds number, leading-edge sharpness, jet spacing, and jet travel distance were examined. Results showed that the heat transfer increased with decreasing leading-edge sharpness and decreasing jet travel distance. Priedeman et al. ([9]) reported experimental results of liquid jet impingement heat transfer from several different configurations of arrays of extended surface using both water and FC-77 as coolant. Van Treuren et al. ([10]) measured the detailed heat transfer coefficients as well as the adiabatic wall temperatures under impinging jets by using the liquid crystal method. In their study, the liquid crystal color changes were analyzed by using the hue saturation intensity (HSI) methods. Huang et al. ([11]) measured the detailed heat transfer coefficient on the target wall with an array of orthogonal impinging jets by using a transient liquid crystal technique. The effects of jet Reynolds number and exit flow orientation were examined. It was found that the flow exiting from both sides of the duct performed the best heat transfer on the target surface.

Recently, Ligrani et al. ([12]), Moon et al. ([13]), Hedlund et al. ([14]), and Hedlund and Ligrani ([15]) examined heat transfer characteristics in a swirl pipe flow induced by lengthwise continuous tangential jets. Ligrani et al. ([12]) performed a flow visualization study to examine the relation between the generation of Göertler vortices and the augmented heat transfer characteris-

---

[1] Phone: 886-35374281 Ext. 8334, Fax: 886-35373771.

Contributed by the Heat Transfer Division for publication in the JOURNAL OF HEAT TRANSFER. Manuscript received by the Heat Transfer Division, Nov. 8, 1999; revision received, May 5, 2000. Associate Technical Editor: J.-C. Han.

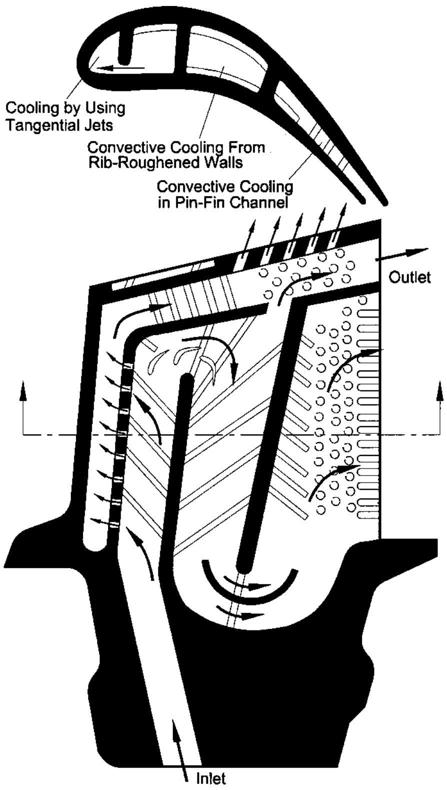

Fig. 1 Conceptual view of the internal-cooling circuit of the turbine blade

tics in the cooling passage. Additional details of the pressure distribution and heat transfer measurements in the swirl chamber closely simulating the flow and wall-to-coolant temperature ratio in the swirl-cooled blade are presented in a parallel study by Hedlund et al. ([14]). Then, Hwang and Chen ([16]) used the transient liquid crystal technique to study the local heat transfer characteristics in a modeled leading-edge triangular duct cooled by an array of swirling jets. The angles between the jet-flow directions and the duct axis varied from $\alpha' = 30$ deg to 75 deg. The outflow orientation along the triangular duct is the same as the entry-flow direction in the high-pressure plenum.

The purpose of the present work is to extend the study of Hwang and Cheng ([16]) to examine the effect of outflow orientation on heat transfer and pressure drop characteristics in a triangular duct cooled by multiple tangential jets. Three different outflow orientations are investigated, i.e., coincident with the entry flow, opposed to the entry flow, and both. Moreover, additions to the previous work and differences between the present and previous works are as follows. First, the angles between the jet-flow directions and the duct axis are inclined ($\alpha' = 30$ deg to 75 deg) in the previous work, while the tangential jets direct normally to the duct axis ($\alpha' = 90$ deg) in the present work. Then, higher Reynolds numbers $12600 \leqslant \mathrm{Re} \leqslant 42000$ selected in this study and those in the previous work ($8600 \leqslant \mathrm{Re} \leqslant 21000$) can complement each other. Furthermore, the loss coefficients in the triangular duct of different outflow orientations, which were not discussed previously, are studied in the present work. Finally, empirical correlations for average Nusselt number on the two principal walls have been developed in term of the Reynolds number for three different outflow orientations for the first time. The present results, in conjunction with those obtained in the previous work about the effect of jet inclined angle, provide a detailed information of heat transfer and pressure drop characteristics in a triangular duct cooled by an array of tangential jets. Such data are helpful in the design of highly effective turbine blades.

Experimental Program

Experimental Apparatus. The apparatus employed in the present work, as shown in Fig. 2, is the same as that in Hwang and Chen ([16]), including an open flow circuit, a test section, and instruments. Outdoor air from a blower passes through a rotameter that measures the air volumetric flow rate, and then flows into an electric heater to be heated to a required temperature. The hot air from the heater subsequently traverses a settling chamber for reducing the possible noise, a high-pressure plenum, then injects into the triangular test section from the side entry, and finally exits from the upstream and/or downstream ends of the triangular duct. Figure 3 shows the detailed configuration, the coordinate system, and dimensions of the test section. The entire test section including the triangular duct and the plenum is made of Plexiglas® plates. An array of equal-spacing ($s = 15$ mm) holes of diameter 5 mm (d) is drilled normally ($\alpha' = 90$ deg) through the low end of the wall between the plenum and the triangular duct that ensures they are tangent to the duct inner surface. With respect to these jets, the two walls that form a 45 deg apex (β) are referred to the ‘‘target wall’’ and the ‘‘bottom wall,’’ respectively; while the remainder wall facing the apex β is called the ‘‘divider.’’ Since conductive heat from the blade external pressure/suction surfaces

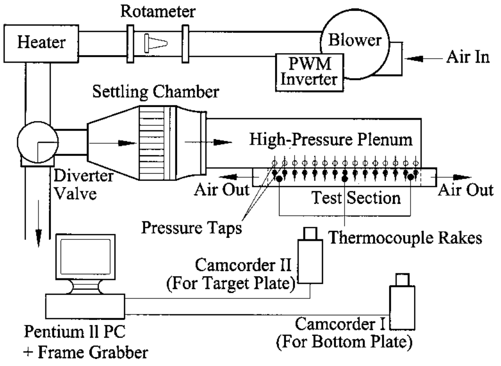

Fig. 2 Schematically drawing of the flow circuit, test section, and the instrumentation

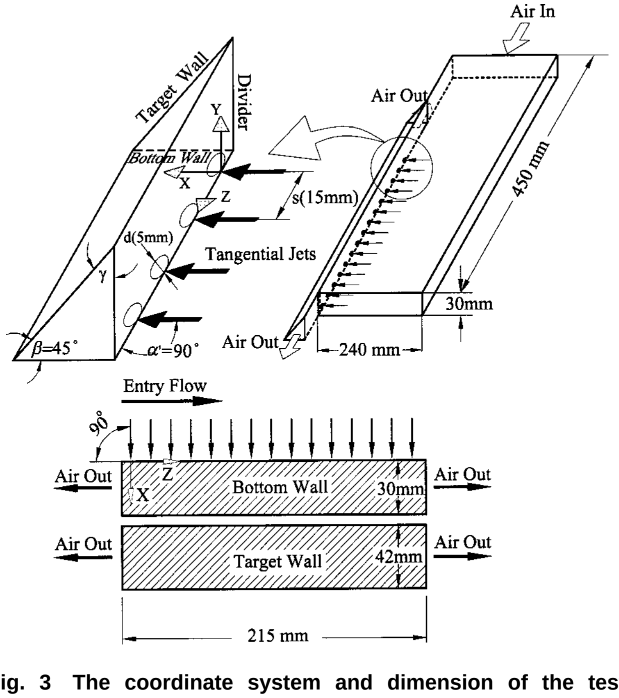

Fig. 3 The coordinate system and dimension of the test section

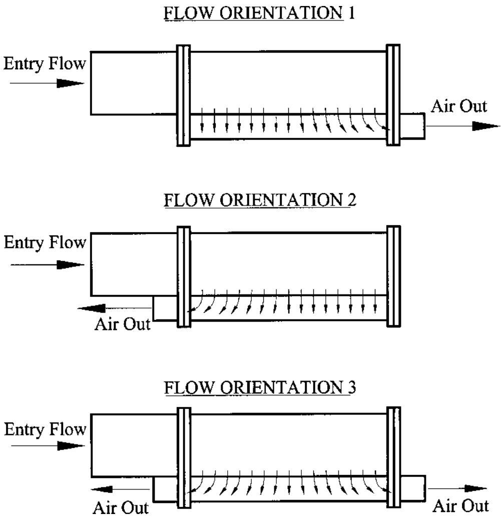

Fig. 4 Three different outflow orientations of the triangular duct

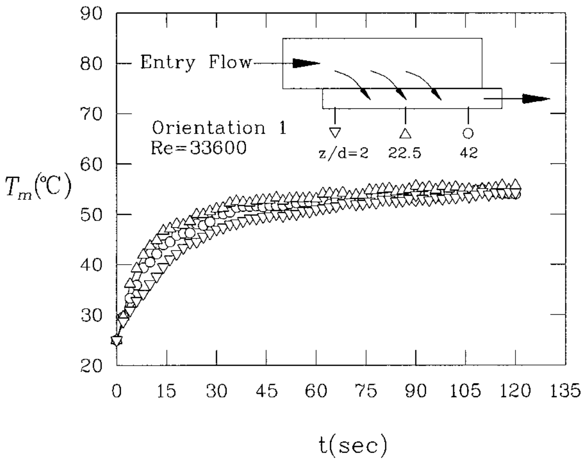

Fig. 5 Typical mainstream temperature history in the triangular duct of different axial locations

is mostly removed convectively from the surfaces of the bottom and target walls, only these two walls are coated with liquid crystals for heat transfer measurement. As shown in Fig. 4, this study changes the discharge openings of triangular ducts to test three different outflow orientations. The first one, as depicted in Fig. 1, has a radial outflow paralleled with the entry flow from the blade root. The second outflow direction is opposed to the entry flow, which simulates the cooling system that coolant is provided by a return flow passage. The last one has both outflows. Such orientation may be unpractical due to difficulty in routing the outflow through the blade root. However, it is very academically interesting and relevant in studying the heat transfer and friction characteristics affected by the crossflow of orientation 3.

Returning to Fig. 2, three thermocouple rakes located at the midway and two ends of the duct, respectively, are connected to a real-time analyzing recorder to measure the mainstream temperature history. In addition, the time of color change of the liquid crystals during a transient test is determined by using two digital color camcorders and a computer vision system (including a frame grabber interface associated with a Pentium II personal computer). These two camcorders are focused on the liquid-crystal-coated bottom and target walls to view and record their color changes during the transient test. A frame grabber interface is programmed to analyze the color changes using image-processing software. The software analyzes the picture frame-by-frame and simultaneously records the time lapse of the liquid crystals from colorless to green during the transient test. As for the static pressure measurement, the bottom and target walls of the triangular duct together with the bottom wall of the plenum are respectively installed 15 pressure taps. They are connected to a micro-differential transmitter to display the pressure signals.

Heat Transfer Theory and Procedure. Heat transfer coefficients on the surface of a semi-infinite solid can be obtained by assuming one-dimensional transient conduction. The solution of one-dimensional transient conduction can be shown as

$$\frac{T_w-T_i}{T_m-T_i}=1-\exp\left(\frac{h^2\alpha t}{k^2}\right)\operatorname{erfc}\left(\frac{h\sqrt{\alpha t}}{k}\right) \tag{1}$$

where k and α are the thermal conductivity and diffusivity of the material, respectively. By knowing the wall temperature (T_w), the initial surface temperature (T_i), the oncoming mainstream temperature (T_m), and the corresponding time (t) required to change the coated-surface color to green at any location, the heat transfer coefficient h can be calculated from the above equation. In a typical run, the time required for the color changes is about 15 to 90 s depending on the location, mainstream temperature, and through flow rate. This testing time is so short that the heat flow can hardly penetrate the depth of Plexiglas® plate. Typically, the maximum axial conduction on the region far away the jet holes is less than 5 percent of the convection heat transfer from fluid to the surface in the test duration ([17]). Therefore, the assumption of the semi-infinite solid on the test surface is valid.

To capture the real local mainstream temperature (T_m) in a long test duct for the transient analysis, a total five sections cutting from the length of test duct are analyzed individually. Figure 5 shows typical T_m histories measured at three locations of the duct, i.e., $z/d=2.0$, 22.5, and 42.0, respectively. The mainstream temperature for the transient analysis in each section is interpolated linearly from these three values. Since the mainstream temperature is time-dependent, the solution in Eq. (1) should be modified. First, the mainstream temperature history is simulated as a series of time step changes. Then, the time step changes of the mainstream temperature are included in the solution for the heat transfer coefficient using Duhamel's superposition theorem. The solution for the heat transfer coefficient at every location is therefore represented as

$$T_w-T_i=\sum_{j=1}^{n}\left\{1-\exp\left[\frac{h^2\alpha(t-\tau_j)}{k^2}\right]\times\operatorname{erfc}\left[\frac{h\sqrt{\alpha(t-\tau_j)}}{k}\right]\right\}[\Delta T_{m(j,j-1)}] \tag{2}$$

where $\Delta T_{m(j,j-1)}$ and τ_j are the temperature and time step changes obtained from the recorder output. Typically, τ_j is set to 2 s in the present study.

Transient test for the heat transfer measurement is carried out by the following procedures. First, the bottom and target surfaces are sprayed with liquid crystals and then black paints. After assembling the test section, the camcorders are set up and focused on these surfaces from outside. Before the test run, the hot air bypasses the test section so that the walls remain at the laboratory ambient temperature. The valve keeps in the diverted position until a required mainstream temperature has been achieved in the diversion flow loop. Then, the valve turns to route the hot air into the test section and, simultaneously, the recorder are switched on to record the mainstream temperature history. The image processing system records the transition time for the color change to green, and transfers the data into a matrix of time of the color change over the entire surface. The time and temperature data are entered into a computer program to obtain the local heat transfer coefficient.

Data Analysis and Uncertainty. To determine each jet flow rate, the static pressure drops between the plenum and the triangular duct are measured by placing the taps beside each orifice (Fig. 2). With the assumptions of temperature-independent fluid density and the same discharge coefficient for all orifices, the jet mass flow rate ($\dot{m}_j$) is thus proportional to square root of pressure drop (ΔP_j) across each jet hole ([18]), i.e.,

$$\frac{\dot{m}_1}{\sqrt{\Delta P_1}}=\frac{\dot{m}_2}{\sqrt{\Delta P_2}}=\cdots=\frac{\dot{m}_j}{\sqrt{\Delta P_j}}=\text{constant} \tag{3}$$

Thus, by knowing the total volumetric flow rate in the flow circuit ($\dot{V}$) and the pressure drop across each jet hole, the jet mass flow rate can be determined by the following equation:

$$\dot{m}_j=\frac{\Sigma \dot{m}_j}{\Sigma \sqrt{\Delta P_j}}\sqrt{\Delta P_j}=\frac{\rho \dot{V}}{\Sigma \sqrt{\Delta P_j}}\sqrt{\Delta P_j} \tag{4}$$

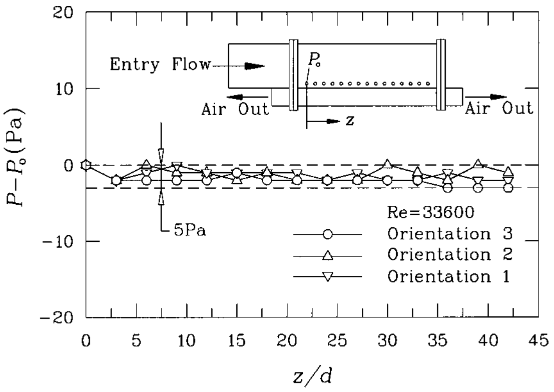

Fig. 6 Static pressure differences along the bottom wall of the plenum

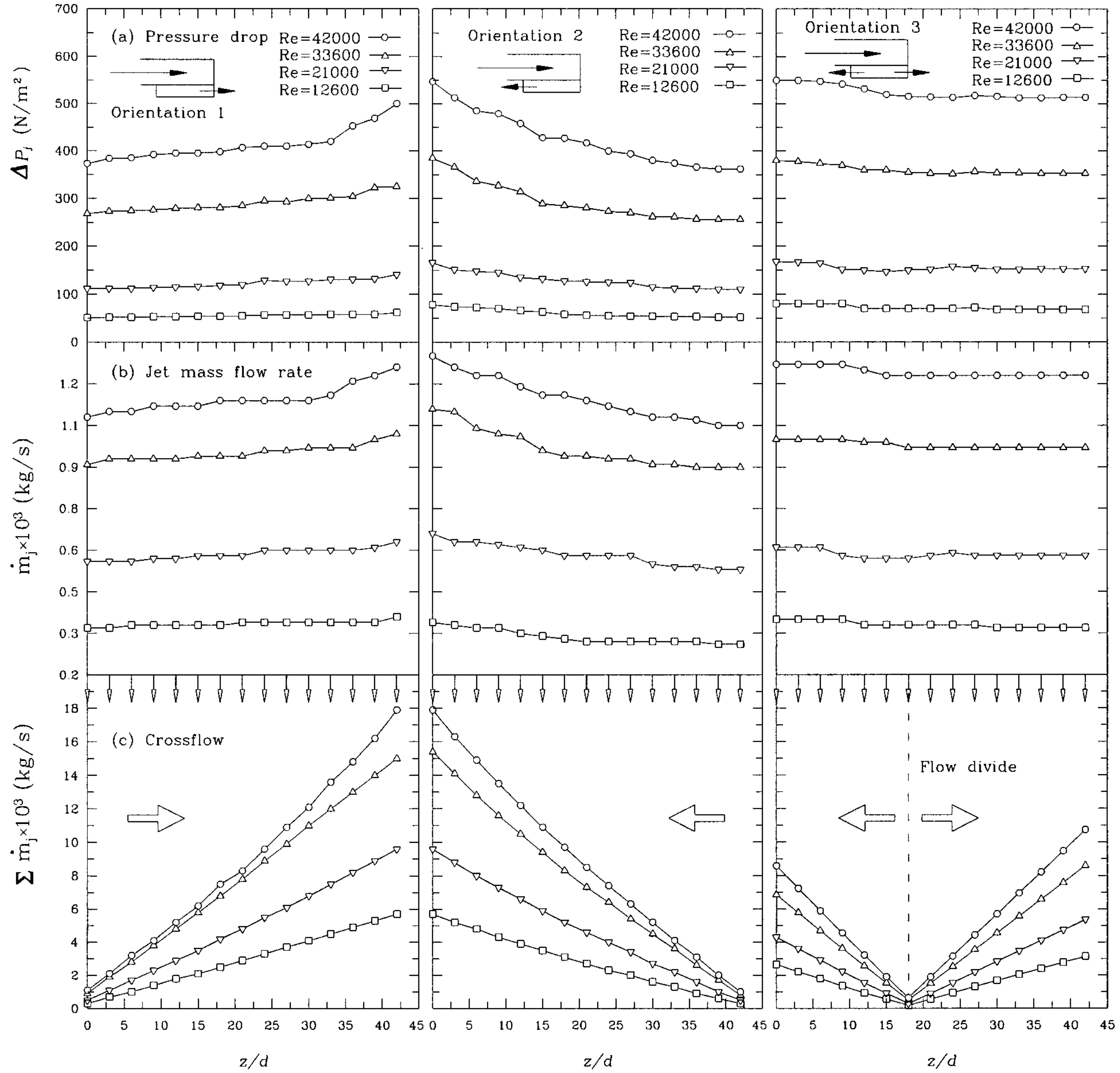

Fig. 7 Axial distributions of the pressure drop and jet mass flow rate across each jet hole, and the crossflow in the triangular duct

The nondimensional heat transfer coefficient on the target and bottom walls of the triangular duct with tangential jets is represented by the Nusselt number as

$$Nu = hD/k_f \tag{5}$$

where D is the hydraulic diameter of the triangular cross-sectional duct, and k_f is the conductivity of the air. The Reynolds number used herein is based on the duct parameters, i.e.,

$$\mathrm{Re} = G \times D/\mu \tag{6}$$

where G is the maximum mass flux in the triangular duct. The static pressure drops along the triangular duct, either on the bottom wall or on the target wall, are made dimensionless as

$$C_p = 2\rho(P_z - P_0)/G^2 \tag{7}$$

where P_0 is the reference wall static pressure at $z = 0$. In addition, it is important to determine the requirement of pressure drop that drives the flow across the multi-orifice divider and then to traverse the triangular duct for the design of the blade cooling circuit. To drive a fixed volumetric flow rate ($\dot{V}$) in the triangular duct with both openings, the pumping power required can be written as

$$\Delta P \dot{V} = \Delta P_1 \dot{V}_1 + \Delta P_2 \dot{V}_2 \tag{8}$$

where $\dot{V}_1$ and $\dot{V}_2$ are the volumetric flow rates and, ΔP_1 and ΔP_2, the pressure drops between the plenum and the two exits of the triangular duct, respectively. Moreover, if the density of the flowing air does not vary significantly in the test section, the head loss of a finite-length triangular duct with both outlets, can be made dimensionless using ([19])

$$K_L = 2\Delta P/(G^2/\rho) \tag{9}$$

All above pressure-drop data are based on adiabatic conditions (i.e., test with ambient-temperature mainstream).

By using the estimation method of Kline and McClintock ([20]), the maximum uncertainty of h is an order of ±8.2 percent. The individual errors contributed to the uncertainty of h for the measured or physical properties are: time of the color change t, ±0.2 s, mainstream temperature T_m, ±1.0 K, wall temperature, T_w, ±0.2 K and wall material properties α and k, ±3.0 percent. Noteworthy that in the region where the heat transfer coefficient varies significantly in spatiality, the data measured may be somewhat averaged by the axial conduction in Plexiglas® plate (i.e., two- or three-dimensional effect). The worst region for uncertainty of the present test section is in the region near the jet hole, where the heat transfer coefficients may be overpredicted by as much as 15 percent. The maximum uncertainties of the other nondimensional parameters are Re, 6.3 percent, C_p, 7.7 percent, and K_L, 8.1 percent, respectively.

Results and Discussion

Flow Distributions. Before the measurement of each jet flow rate, it is very important to check the static pressure distributions in the plenum, which strongly influence the local jet flow characteristics in the present long triangular duct. As shown in Fig. 6, static pressure tapes are placed on the plenum bottom wall adjacent each jet hole. The reference pressure P_0 is set to $z = 0$. It is seen that the values of $P - P_0$ slightly decrease downstream due to the viscous effect. However, this variation is so small, typically within 5 Pa for three different outflow orientations, which is only about 1.1 percent of the gage pressure in the plenum. This means that the plenum is large enough to act as a constant pressure chamber to provide coolant to the triangular test section.

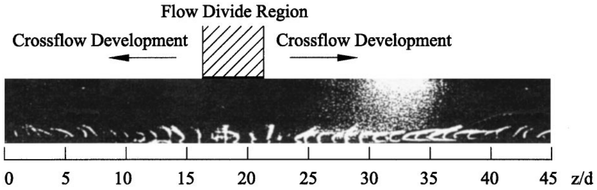

Fig. 8 Visualization of flow divide of orientation 3 by using the surface tuft method

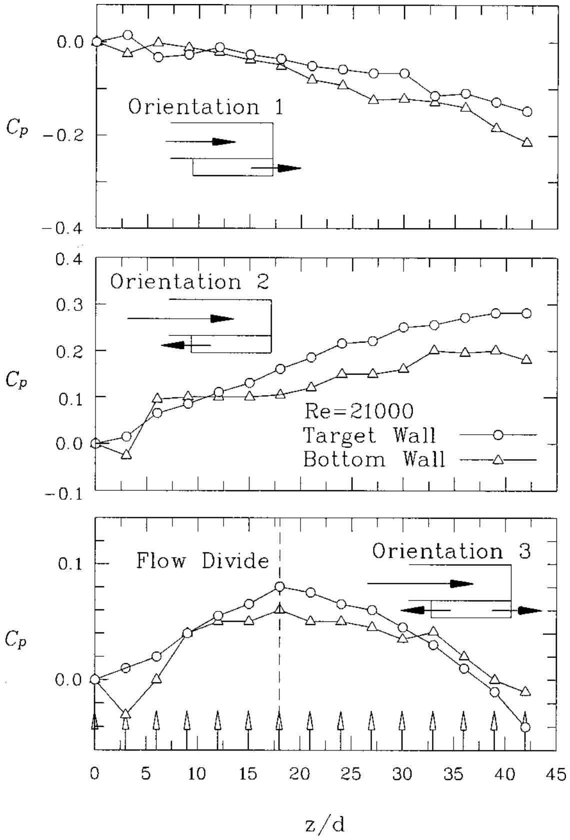

Fig. 9 Pressure-drop coefficient distributions along the triangular duct

The axial distributions of static pressure drop and mass flow rate across each jet hole are shown in Figs. 7(*a*) and (*b*) for various Re, respectively; while the crossflow rate at the corresponding axial station of the triangular duct is displayed in Fig. 7(*c*). It is seen that the larger the pressure drop across each jet hole is, the higher is the jet flow rate. In addition, the jet flow rate slightly increases with increasing the streamwise distance in the triangular duct for orientations 1 and 2. The increment becomes significant as the flow approaches the duct exit, especially for high Reynolds numbers. This is because the flow accumulation increases the mean velocity of the mainflow (or crossflow) downstream, and thus reduces the static pressures in the triangular duct. With an almost constant static pressure in the plenum (Fig. 6), the lower static pressure near downstream end of the triangular duct could entrain more fluid from the plenum. Figure 7(*c*) shows the crossflow rate increasing linearly almost with an increase in the channel distance for orientations 1 and 2. As for orientation 3, the axial distribution of jet flow rate (or static pressure drop) seems to be slightly uneven at the mid-channel region of $10 \leqslant z/d \leqslant 22$, where the flow is divided and develops toward both ends of the triangular duct. Figure 8 visualizes the flow divide of orientation 3 by using surface tufts. An array of the light tufts is attached to the bottom wall of the triangular duct. It is seen that the tufts in the region between $15 \leqslant z/d \leqslant 20$ lift vertically almost, while those beside the above region deflect toward the exits by crossflow. To precisely determine the flow divide for orientation 3, the distributions of static pressure-drop coefficient (C_p) along the bottom and

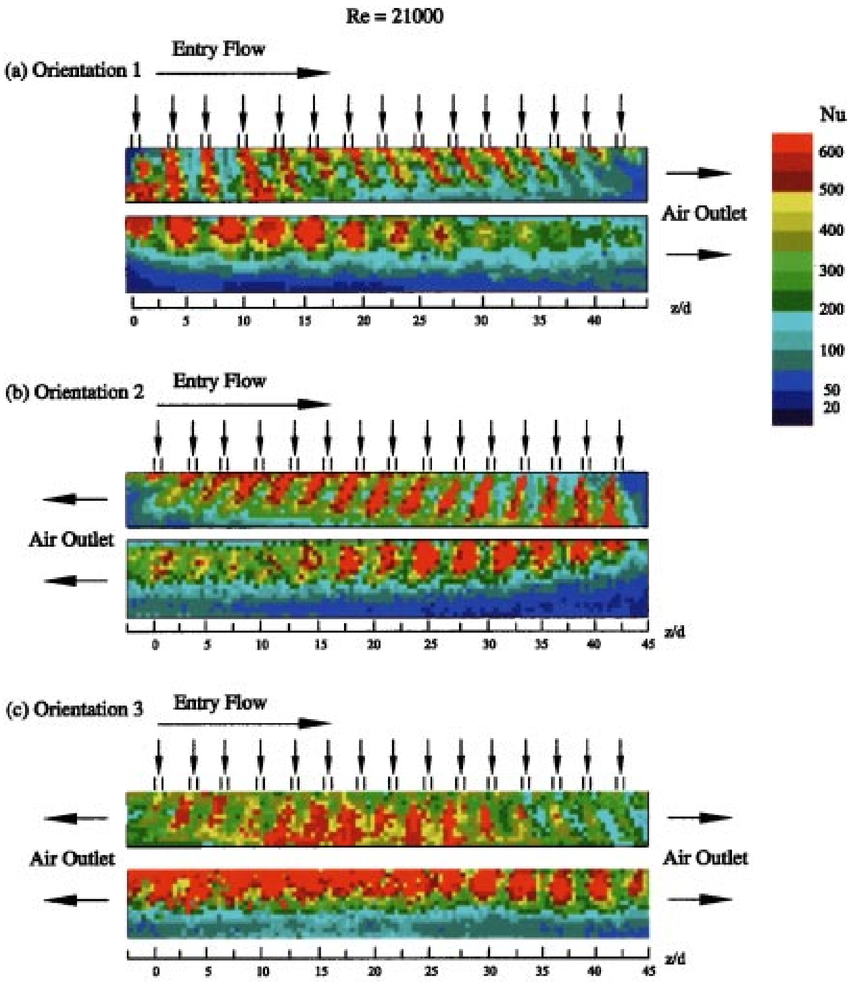

Fig. 10 Effect of the outflow orientation on the detailed heat transfer coefficient distribution on the bottom and target walls for Re=21000 and $s/d=3.0$, (*a*) orientation 1, (*b*) orientation 2, and (*c*) orientation 3

target walls of the triangular duct are further measured and displayed in Fig. 9. The reference pressure is also set at upstream most jet hole of orientation 1, i.e., $z/d=0$. It is seen that orientation 3 has the maximum pressure-drop coefficients at about $z/d=17.5$ for both bottom and target walls where the flow is divided. This location is not at the middle of the test duct but slightly closer to the flow entry, meaning that the crossflow develops unevenly toward two openings of the triangular duct. In fact, the lower value of C_p near the remote opening ($z/d=42$) than that close to the flow entry ($z/d=0$) has clearly illustrated the higher crossflow rate exiting from the remote exit as given Fig. 7(*c*). As for orientations 1 and 2 shown in Fig. 9, they have the highest values of C_p on both walls near the closed ends (i.e., upstream most). The values subsequently decrease monotonically along the mainflow direction. Noteworthy that the data range (position or negative) of C_p for each plot reflects the pressure drop across each duct, which will be shown later by the loss-coefficient distribution for different outflow orientations.

Detailed Heat Transfer Coefficient Distributions. Figures 10–12 show the detailed heat transfer coefficient distributions on the bottom and target walls for various outflow orientations and Reynolds numbers. The entry-flow is from the left, and an array of small arrows shown on each figure indicates the locations and directions of the jets. The throughflow exits from the right and/or left ends of the graphs.

Figure 10 shows the effect of outflow orientation on the detailed heat transfer coefficient distributions on the bottom and target walls of the triangular duct at a fixed Reynolds number of Re=21000. It is seen that the detailed distributions of Nu for orientations 1 and 2 are roughly symmetric about the mid-channel plane of $z/d=22.5$. Near the closed ends of orientations 1 and 2, wall jets wash the entire bottom-wall surfaces and create high heat transfer bends perpendicular to the duct axis from the jet inlet to the leading-edge apex. Meanwhile, the jet impingement on the target wall at the corresponding axial locations produces an oval zone of high heat transfer. As the flow develops along the axial direction, the jets are deflected toward the outflow direction by crossflow, and the penetrability of wall jet is gradually reduced. On the target wall, high heat transfer zones are also gradually reduced and move to the span center of the target wall as the flow develops downstream. Hwang and Cheng ([16]) observed similar trends for the duct with an array of inclined jets ($\alpha'=30$ deg, 45 deg, and 75 deg). As for the flow exits from both ends (orientation 3), the highest heat transfer coefficients are around the mid-location of the bottom wall, where the jets direct normally to the duct axis and the crossflow is severely small [Fig. 7(*c*)]. The high heat transfer region on the bottom wall is coincident with the flow-divide region shown in Fig. 8. The heat transfer coefficients on the bottom wall, again, decrease toward two exits with the crossflow development. However, due to less crossflow effect

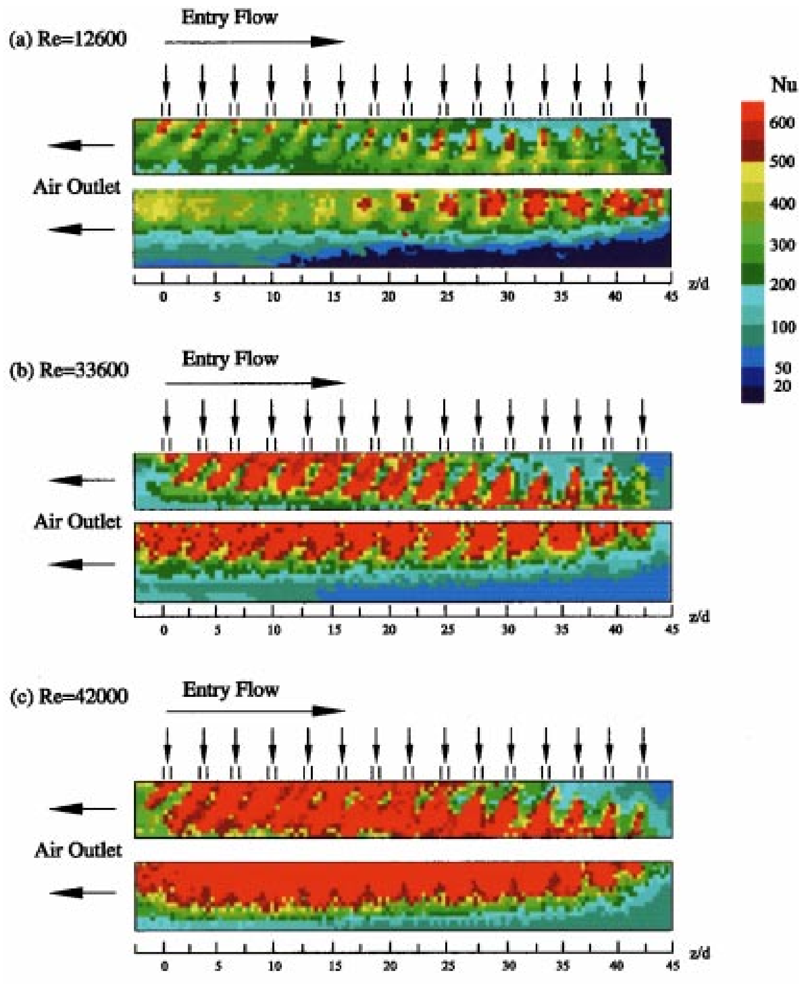

Fig. 11 Effect of the Reynolds number on the detailed heat transfer coefficient distribution on the bottom and target walls for orientation 2

[Fig. 7(*c*)] for orientation 3, the heat transfer coefficients near two exits, both for the bottom and the target walls, are higher than those of orientations 1 and 2.

Figures 11 and 12 together with Figs. 10(*b*) and (*c*) show the effect of Re on the detailed Nu distribution for orientations 2 and 3, respectively. The jet spacing is fixed at $s/d=3.0$, and the Reynolds number varies from Re=12600 to 42000. Results show an increase in Nu for an increase in Re for both orientations. As for the orientation 2, the heat transfer coefficients for Re⩽21000 are high near the duct upstream, especially on target wall, and then decreases downstream. In contrast, when Re⩾33600, the downstream heat transfer are higher than the upstream one. The above discrepancy is explained as follows. The flow rate across each jet shown in Fig. 7(*a*) is relatively uniform in the entire duct for Re ⩽21000. The crossflow herein plays the major role to influence the local heat transfer distribution, which decreases Nu along the axial direction as shown in Figs. 10(*b*) and 11(*a*). As for the high Reynolds numbers, say Re⩾33600 [Fig. 7(*b*)], the jet velocities are however no more uniform but increased with the axial distance, which becomes the predominant of the local heat transfer characteristics on both walls. The stronger jets near the downstream end of the duct produce higher local heat transfer coefficients, and the crossflow only deflects the wall jet and push away the impinged jet toward the downstream end. The above Re dependence of Nu distribution, however, is not observed in Fig. 12 for orientation 3.

Wall-Averaged Nusselt Number. Figure 13 shows the averaged Nusselt number ($\overline{\mathrm{Nu}}$) on the bottom and target walls as a function of Reynolds numbers. The value of $\overline{\mathrm{Nu}}$ is an area-average of the detailed results on the entire bottom or target wall. The previous results (dashed lines, ([16])) for the orientation 1 with an inclined jet angle $\alpha'=75\,\mathrm{deg}$ are also displayed for comparison. The present results for the three different orientations correlate for the Reynolds-number dependence as

$$\overline{\mathrm{Nu}}=a_1\,\mathrm{Re}^{a_2} \tag{10}$$

The coefficients of a_1 and a_2 for each orientation and the deviations between the actual experiments and these correlations are displayed in Table 1. It is seen that the bottom wall has a higher area-averaged heat transfer than the target wall for all flow orientations investigated. Under the same Reynolds number, the values of $\overline{\mathrm{Nu}}$ on the target and bottom walls follow the same trend in that orientations 1 and 2 have almost the same values of $\overline{\mathrm{Nu}}$, and both are lower than the values for orientation 3. Huang et al. ([11]) found a similar trend for an array of orthogonal jets impinging on the target wall of different crossflow directions. Further inspection of this figure shows that the present results of orientation 1 are higher than those of an inclined jet angle (dashed line) under the low Reynolds number conditions. After about Re⩾18000, the trend is reversed on the bottom wall. This indicates that the swirl-motioned mainflow induced by inclined jets can produce a higher

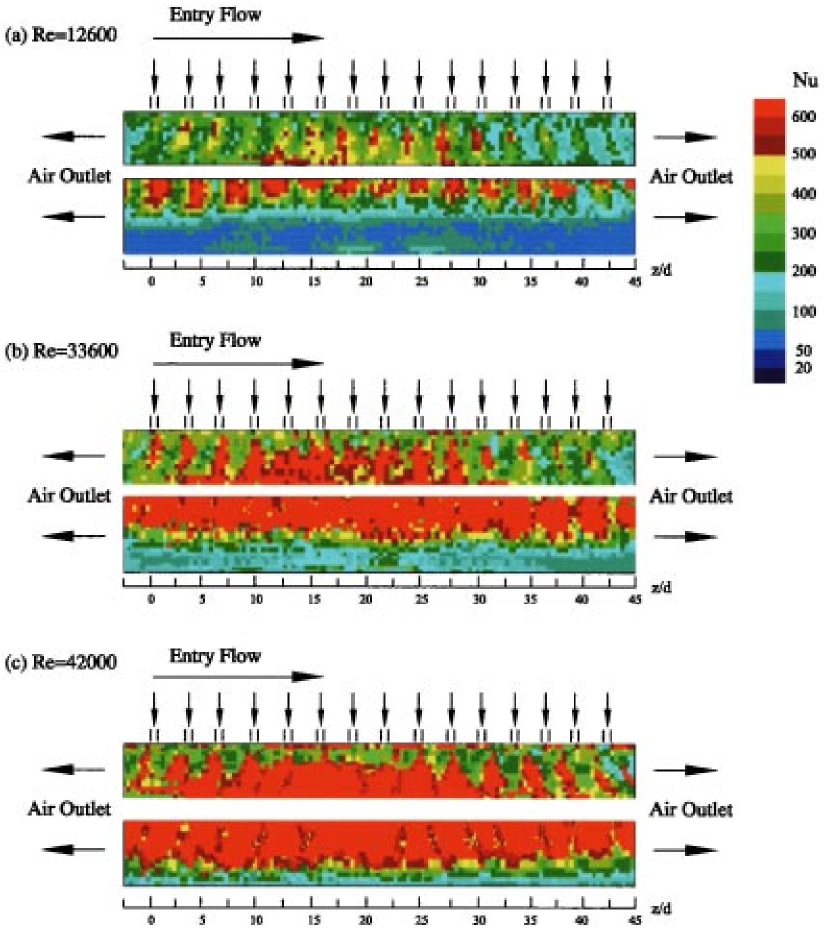

Fig. 12 Effect of the Reynolds number on the detailed heat transfer coefficient distribution on the bottom and target walls for orientation 3

heat transfer on the bottom wall than the orthogonal jets for high Reynolds numbers. To understand the level of heat transfer enhancement in the blade-leading triangular duct by using an array of tangential jets of different outflow orientations, Table 2 further shows a comparison of the area-averaged Nusselt number between the present data and those of the straight flow in a smooth duct. The fully developed heat transfer of a smooth pipe flow, $\overline{\mathrm{Nu}}_s$, is represented by the Dittus–Boelter correlation ([21]). The length-mean Nusselt number $\overline{\mathrm{Nu}}_d$ is a developing heat transfer coefficient averaged from the sharp-edge entrance of a triangular duct to an axial distance of 12*D* ([22]), which has the same streamwise length as the present triangular jet duct. It is seen that the heat transfer enhancement is more significant for lower Re. Typically, the enhancements of heat transfer are 2.1–4.7 and 3.1–7.6 times with respect to the developing and fully developed flow values, respectively.

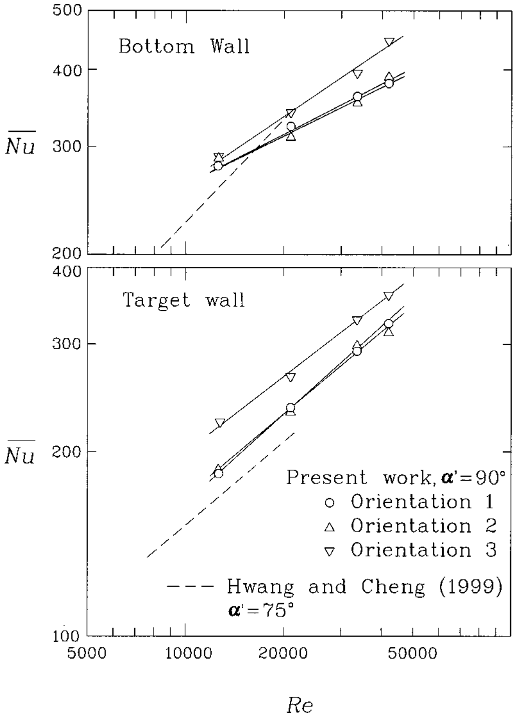

Fig. 13 Reynolds-number dependence of the area-averaged Nusselt number of the bottom and target walls

Table 1 Coefficients of wall-averaged heat transfer correlations

	$\overline{\mathrm{Nu}}=a_1\,\mathrm{Re}^{a_2}$							
	Target wall				Bottom wall			
	a_1	a_2	Error	Eq.	a_1	a_2	Error	Eq.
Orientation 1	2.49	0.457	9.8%	(10-1)	37.0	0.218	5.4%	(10-4)
Orientation 2	3.18	0.431	8.5%	(10-2)	31.1	0.236	8.2%	(10-5)
Orientation 3	4.39	0.414	7.2%	(10-3)	15.3	0.312	2.9%	(10-6)

Table 2 Comparison of the present area-averaged heat transfer with those in smooth pipes

				Orientation 1			Orientation 2			Orientation 3		
Re	$\overline{\mathrm{Nu}}_d$	$\overline{\mathrm{Nu}}_s$		$\overline{\mathrm{Nu}}$	$\frac{\overline{\mathrm{Nu}}}{\overline{\mathrm{Nu}}_s}$	$\frac{\overline{\mathrm{Nu}}}{\overline{\mathrm{Nu}}_d}$	$\overline{\mathrm{Nu}}$	$\frac{\overline{\mathrm{Nu}}}{\overline{\mathrm{Nu}}_s}$	$\frac{\overline{\mathrm{Nu}}}{\overline{\mathrm{Nu}}_d}$	$\overline{\mathrm{Nu}}$	$\frac{\overline{\mathrm{Nu}}}{\overline{\mathrm{Nu}}_s}$	$\frac{\overline{\mathrm{Nu}}}{\overline{\mathrm{Nu}}_d}$
12600	61	38	Bottom wall	281	7.40	4.61	287	7.55	4.71	289	7.61	4.74
			Target wall	185	4.87	3.03	187	4.92	3.07	221	5.82	3.62
21000	83	57	Bottom wall	326	5.72	3.93	304	5.33	3.66	341	5.98	4.11
			Target wall	236	4.14	2.84	232	4.07	2.80	267	4.68	3.22
36000	137	83	Bottom wall	362	4.36	2.64	351	4.22	2.56	390	4.48	2.85
			Target wall	292	3.52	2.13	299	3.60	2.18	329	3.96	2.40
42000	148	100	Bottom wall	380	3.80	2.57	393	3.93	2.66	449	4.49	3.03
			Target wall	323	3.23	2.18	310	3.10	2.10	361	3.61	2.44

Remarks: $\overline{\mathrm{Nu}}_s$: fully developed Nusselt number for the smooth pipe flow ([21])
$\overline{\mathrm{Nu}}_d$: length-mean Nusselt number from 90 deg sharp entry to $z/D=12.0$ of a triangular duct ([22])

Loss Coefficients. It is realized that a theoretical analysis to predict the detail of the flows to obtain the head loss in the present test section is not, as yet, possible. Thus, the head-loss information for essentially the present test rig is given in dimensionless form and based on experimental data. The most common method used to determine these head losses or pressure drops is to specify the loss coefficient K_L as defined in Eq. (9). Figure 14 shows the results for loss coefficients as a function of Reynolds number for different outflow orientations. For comparison, the loss coefficients developed from the friction factors of fully developed smooth pipe flows with the same axial length as the present test section (i.e., $12D$) are displayed in this figure, including the Blasius correlation and that developed by Petukhov ([23]). Both correlations are well represented fully developed flows in smooth ducts. As expected, the loss coefficients in the present cooling circuit are much higher than those of fully developed flows in straight smooth ducts due to significant pressure drop for flow through multiple orifices. The loss coefficients, in general, decrease with increasing Reynolds numbers for all three different orientations investigated and can be correlated using the equation given by

$$K_L=b_1\,\mathrm{Re}^{b_2} \tag{11}$$

where the coefficient b_1 and exponent b_2 for each orientation together the maximum error between the actual experiments and these correlations are displayed in Table 3. It is further seen that orientation 2 has the largest loss coefficient, and orientation 1 has a lower loss coefficient than the orientation 3. This is very reasonable since the mainflow has to turn 180 deg to exit from the duct for orientation 2, which yields the largest pressure drops.

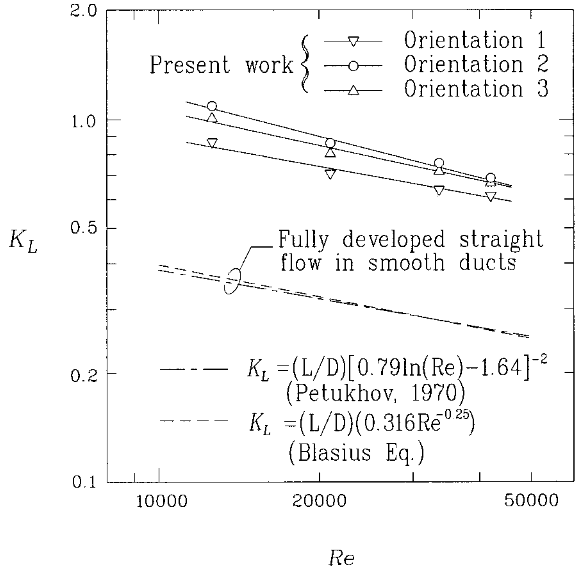

Fig. 14 Loss coefficients of the triangular duct as a function of Reynolds number

Table 3 Coefficients of loss-coefficient correlations of the present triangular duct

	$K_L=b_1\,\mathrm{Re}^{b_2}$			
	b_1	b_2	Error	Eq.
Orientation 1	12.01	−0.281	4.2%	(11-1)
Orientation 2	43.31	−0.390	6.9%	(11-2)
Orientation 3	22.15	−0.332	3.4%	(11-3)

Concluding Remarks

The effect of outflow orientation on heat transfer and pressure-drop characteristics in a triangular duct with multiple tangential jets impinged on the apex of the triangular duct is investigated experimentally. New information of detailed heat transfer coefficient distributions and pressure drop characteristics is provided for all outlet orientations. The most important application for this system is the leading-edge cavity of the turbine blade where heat loads are significant. Several findings based on the experiments are as follows.

1 For orientations 1 and 2, the jet flow rate increases slightly with increasing the axial distance. The high jet flow rate near the downstream end of the duct is induced by the significant crossflow of low static pressure. In contrast, orientation 3 has a relatively uniform jet flow rate because of the less crossflow.

2 According to the pressure-drop coefficient distributions in the triangular duct together with the flow visualization using the surface-tuft method, the flow divide for orientation 3 is slightly closer to the entry flow, typically at about $z/d=17.5$.

3 Continuing item (1), although the significant crossflow near the duct exit of orientation 1 or 2 reduces the local heat transfer coefficient, the strong jets entrained by the above crossflow enhance the local heat transfer. Under $\mathrm{Re}\leqslant 21000$, the former effect is more notable and thus produces a lower heat transfer coefficient in the duct downstream. However, as $\mathrm{Re}\geqslant 33600$, the latter effect overcomes the former effect and thus creates a higher heat transfer in the downstream region. The orientation 3 has the highest local heat transfer near the flow divide on the bottom wall for all Re investigated.

4 Under the same Reynolds number, the orientation 3 has the highest area-averaged heat transfer on two principal duct walls and moderate pressure loss among the three outflow orientations investigated.

5 Correlations of wall-averaged Nusselt numbers and loss coefficients in the present triangular duct with multiple tangential jets have been developed in terms of Reynolds number for three different outlet orientations.

Acknowledgment

The National Science Council under the contract number of NSC-89-2212-E-216-004 provides supports of this work.

Nomenclature

C_P = pressure-drop coefficient, $2\rho(P-P_0)/G^2$
G = mass flux at the triangular duct exit $[\mathrm{kg\,m^{-2}\,s^{-1}}]$
K_L = loss coefficient, $2\rho\Delta P/G^2$

Greek Symbols

α' = inclined angle between the jet and duct axis, Fig. 3

Subscripts

b = bottom wall
d = developing
i = initial
j = jet or index of time step
m = mainstream
o = reference
s = smooth

References

[1] Metzger, D. E., and Vedula, R. P., 1987, ''Heat Transfer in Triangular Channels with Angled Roughness Ribs on Two Walls,'' Exp. Heat Transfer, **1**, pp. 31–44.
[2] Zhang, Y. M., Gu, W. Z., and Han, J. C., 1994, ''Augmented Heat Transfer in Triangular Ducts with Full and Partial Ribbed Walls,'' AIAA, J. Thermophys. Heat Transfer, **8**, pp. 574–597.
[3] Bunker, R. S., and Metzger, D. E., 1990, ''Local Heat Transfer in Internally Cooled Turbine Airfoil Leading Edge Regions: Part I-Impingement Cooling Without Film Coolant Extraction,'' ASME J. Turbomach., **112**, pp. 451–458.
[4] Chupp, R. E., Helms, H. E., McFadden, P. W., and Brown, T. R., 1969, ''Evaluation of Internal Heat-Transfer Coefficients for Impingement-Cooled Turbine Airfoils,'' J. Aircr., **6**, pp. 203–208.
[5] Kercher, D. M., and Tabakoff, W., 1970, ''Heat Transfer by a Square Array of Round Air Jets Impinging Perpendicular to a Flat Surface Including the Effect of Spent Air,'' ASME J. Eng. Power, **92**, pp. 73–82.
[6] Florschuetz, L. W., Berry, R. A., and Metzger, D. E., 1980, ''Periodic Streamwise Variations of Heat Transfer Coefficients for Inline and Staggered Arrays of Circular Jet with Crossflow of Spent Air,'' ASME J. Heat Transfer, **102**, pp. 132–137.
[7] Florschuetz, L. W., Truman, C. R., and Metzger, D. E., 1981, ''Streamwise Flow and Heat Transfer Distributions for Jet Array Impingement with Crossflow,'' ASME J. Heat Transfer, **103**, pp. 337–342.
[8] Florschuetz, L. W., Metzger, D. E., and Su, C. C., 1984, ''Heat Transfer Characteristics for Jet Array Impingement with Initial Crossflow,'' ASME J. Heat Transfer, **106**, pp. 34–41.
[9] Priedeman, D., Callahan, V., and Webb, B. W., 1994, ''Enhancement of Liquid Jet Impingement Heat Transfer with Surface Modifications,'' ASME J. Heat Transfer, **116**, pp. 486–489.
[10] Van Treuren, K. W., Wang, Z., Ireland, P. T., Jones, T. V., 1994, ''Detailed Measurements of Local Heat Transfer Coefficient and Adiabatic Wall Temperature Beneath an Array of Impinging Jets,'' ASME J. Turbomach., **116**, pp. 369–374.
[11] Huang, Y., Ekkad, S. V., and Han, J. C., 1998, ''Detailed Heat Transfer Distributions Under an Array of Orthogonal Impinging Jets,'' AIAA. J. Thermophys. Heat Transfer, **12**, pp. 73–79.
[12] Ligrani, P. M., Hedlund, C. R., Thambu, R., Babinchak, B. T., Moon, H. K., and Glezer, B., 1998, ''Flow Phenomena in Swirl Chambers,'' Exp. Fluids, **24**, pp. 254–264.
[13] Moon, H. K., O'Connell, T., and Glazer, B., 1998, ''Heat Transfer Enhancement in a Circular Channel Using Lengthwise Continuous Tangential Injection,'' *International Heat Transfer Congress*, Seoul, South Korea.
[14] Hedlund, C. R., Ligrani, P. M., Moon, H.-K., and Glezer, B., 1999, ''Heat Transfer and Flow Phenomena in a Swirl Chamber Simulating Turbine Internal Cooling,'' ASME J. Turbomach., **121**, pp. 803–813.
[15] Hedlund, C. R., and Ligrani, P. M., 1999, ''Local Swirl Chamber Heat Transfer and Flow Structure at Different Reynolds Numbers,'' ASME Paper No. 99-GT-164.
[16] Hwang, J. J., and Cheng, C. S., 1999, ''Augmented Heat Transfer in a Triangular Duct by Using Multiple Swirling Jets,'' ASME J. Heat Transfer, **121**, pp. 683–690.
[17] Hwang, J. J., and Lui, C. C., 1999, ''Detailed Heat Transfer Characteristic Comparison in Straight and 90-deg Turned Trapezoidal Ducts with Pin-Fin Arrays,'' Int. J. Heat Mass Transf., **42**, pp. 4005–4016.
[18] Munson, B., Young, D., and Okiishi, T., 1994, ''Fundamental of Fluid Mechanics,'' 2nd Ed., John Wiley & Sons. Inc., New York.
[19] Hwang, J. J., Lai, D. Y., and Tsia, Y. P., 1999, ''Heat Transfer and Pressure Drop in Trapezoidal Pin-Fin Ducts,'' ASME J. Turbomach., **121**, pp. 264–272.
[20] Kline, S. J., and McClintock, F. A., 1953, ''Describing Uncertainties in Single-Sample Experiments,'' Mech. Eng. (Am. Soc. Mech. Eng.), **75**, pp. 3–8.
[21] Dittus, F. W., and Boelter, L. M. K., 1930, University of California at Berkeley, *Publications in Engineering*, Vol. 2, p. 443.
[22] Cheng, C. S., 1998, ''Enhancement of Heat Transfer and Friction in Triangular Ducts with an Array of Side-Entry Jets,'' Master Thesis, Chung-Hua University, Taiwan (in Chinese).
[23] Petukhov, B. S., 1970, *Advances in Heat Transfer*, Academic, New York, Vol. 6, pp. 503–504.

Natural Convection Heat Transfer and Entropy Generation From a Horizontal Cylinder With Baffles

B. A/K Abu-Hijleh
Department of Mechanical Engineering,
Jordan University of Science & Technology,
P. O. Box 3030,
Irbid 22110, Jordan
e-mail: bassam@just.edu.jo

The problem of laminar natural convection heat transfer from a horizontal cylinder with multiple, equally spaced, low conductivity baffles on its outer surface was investigated numerically. The effect of several combinations of number of baffles and baffle height on the average Nusselt number was studied over a wide range of Rayleigh numbers. The computed velocity and temperature fields were also used to calculate the local and global entropy generation for different cylinder diameters. The results showed that there was an optimal combination of a number of baffles and baffle height for minimum Nusselt number for a given value of the Rayleigh number. Short baffles slightly increased the Nusselt number at small values of the Rayleigh number. The global entropy generation increased monotonically with increasing Rayleigh number and decreased with increasing cylinder diameter, baffle height, and number of baffles. [S0022-1481(00)01203-2]

Keywords: Convection, Cylinder, Heat Transfer, Insulation, Numerical Methods

Introduction

Laminar convection from a heated cylinder is an important problem in heat transfer. It is used to simulate a wide range of engineering applications as well as provide a better insight into more complex systems of heat transfer. Accurate knowledge of the overall natural convection heat transfer around circular cylinders is important in many fields, including heat exchangers, hot water and steam pipes, heaters, refrigerators, and electrical conductors. Because of its industrial importance, this class of heat transfer has been the subject of many experimental and analytical studies. The problem received continuous attention since the early work of Morgan [1] and Churchill and Chu [2]. The most widely referenced work in this area is that of Kuehn and Goldstein [3] which included the first numerical solution of the fully elliptic governing equations. Although more recent work and more accurate work has been reported in the literature since then ([4–6]) the work of Kuehn and Goldstein [3] is still being referenced ([7,8]). Recent economic and environmental concerns have raised the interest in methods of reducing or increasing the natural heat transfer, depending on the application, from a horizontal cylinder. Classical methods, such as the use of insulation materials, are becoming a cost as well as an environmental concern. Researchers continue to look for new methods of heat transfer control. The use of porous materials to alter the heat transfer characteristics has been reported by several researchers including Vafai and Huang [9] and Al-Nimr and Alkam [10].

Recently, entropy generation (or production) has been used to gauge the significance of irreversibility related to heat transfer, friction, and other nonideal processes within thermal systems ([11]). The rate of useful energy lost owing to irreversibility is proportional to the rate of entropy generation. Entropy-generation calculations can be used to optimize the thermodynamic behavior of thermal systems both on the component level and as complete systems. Knowledge of the locations and levels of high entropy generation will help focus the designers' efforts on the regions or components that contribute most to the irreversibility and thus inefficiency of the system.

This paper presents the numerical results of placing very thin, low conductivity baffles on the cylinder's outer surface in order to suppress the natural convection currents around the cylinder which should translate into lower heat transfer rate. The baffles were distributed equally along the cylinder's outer surface. No baffles were located at the top nor bottom of the cylinder. Figure 1 shows a schematic of a cylinder with three baffles. The fluid under consideration is air, Pr=0.7. The numerical solution of the elliptic momentum and energy equations was performed using the stream function-vorticity method on a stretched grid. The computed velocity and temperature fields were used to compute the local and global entropy generation. This detailed study included varying the Rayleigh number from 1 to 10^6, number of baffles from 0 to 12, the nondimensional baffle height from 0.1 to 3, and the cylinder diameter from 10^{-4} to 10 meters.

Mathematical Analysis

The steady-state equations for two-dimensional laminar mixed convection over a cylinder, including the Boussinesq approximation, are given by

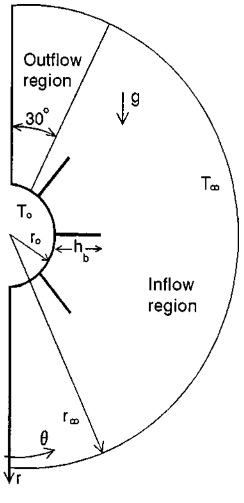

Fig. 1 Schematic of the problem, case of a cylinder with three baffles

---

Contributed by the Heat Transfer Division for publication in the JOURNAL OF HEAT TRANSFER. Manuscript received by the Heat Transfer Division, Sept. 23, 1999; revision received, Apr. 5, 2000. Associate Technical Editor: B. Chung.

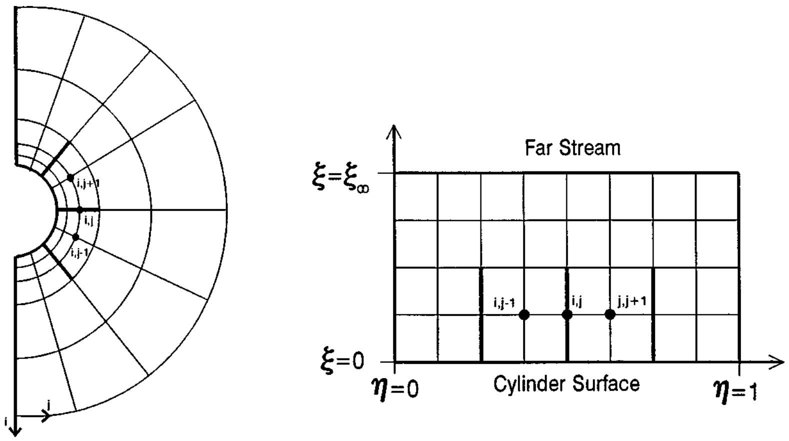

Fig. 2 Schematic of the computational grid in the physical (left) and computational (right) domains

$$\frac{1}{r}\frac{\partial(ru)}{\partial r}+\frac{1}{r}\frac{\partial v}{\partial\theta}=0 \tag{1}$$

$$u\frac{\partial u}{\partial r}+\frac{v}{r}\frac{\partial u}{\partial\theta}-\frac{v^2}{r}=\frac{1}{\rho}\left[\rho g\beta(T-T_\infty)\sin(\theta)-\frac{\partial p}{\partial r}\right]+\nu\left[\frac{\partial^2 u}{\partial r^2}+\frac{1}{r}\frac{\partial u}{\partial r}-\frac{u}{r^2}+\frac{1}{r^2}\frac{\partial^2 u}{\partial\theta^2}-\frac{2}{r^2}\frac{\partial v}{\partial\theta}\right] \tag{2}$$

$$u\frac{\partial v}{\partial r}+\frac{v}{r}\frac{\partial v}{\partial\theta}+\frac{uv}{r}=\frac{1}{\rho}\left[\rho g\beta(T-T_\infty)\cos(\theta)-\frac{1}{r}\frac{\partial p}{\partial\theta}\right]+\nu\left[\frac{\partial^2 v}{\partial r^2}+\frac{1}{r}\frac{\partial v}{\partial r}-\frac{v}{r^2}+\frac{1}{r^2}\frac{\partial^2 v}{\partial\theta^2}+\frac{2}{r^2}\frac{\partial u}{\partial\theta}\right] \tag{3}$$

$$u\frac{\partial T}{\partial r}+\frac{v}{r}\frac{\partial T}{\partial\theta}=\alpha\nabla^2 T \tag{4}$$

where

$$\nabla^2\equiv\left[\frac{\partial^2}{\partial r^2}+\frac{1}{r}\frac{\partial}{\partial r}+\frac{1}{r^2}\frac{\partial^2}{\partial\theta^2}\right].$$

Equations (1)–(4) are subject to the following boundary conditions:

1 On the cylinder surface, i.e., $r=r_o$; $u=v=0$ and $T=T_o$.

2 Far stream from the cylinder, i.e., $r\rightarrow\infty$; $\partial v/\partial r=0$. As for the temperature, and following the work of Kuehn and Goldstein [3] and Abu-Hijleh et al. [8], the far-stream boundary condition is divided into an inflow ($\theta\leq 150$ deg) and an outflow ($\theta>150$ deg) regions (Fig. 1). The far-stream temperature boundary conditions are $T=T_\infty$ and $\partial T/\partial r=0$ for the inflow and outflow regions, respectively.

3 Plane of symmetry; $\theta=0$ and $\theta=180$ deg; $v=0$ and $\partial u/\partial\theta=\partial T/\partial\theta=0$.

4 On the baffle surface; $u=v=0$. Since the baffles are assumed to be very thin and of very low conductivity, there will be no heat conduction along the baffles. Thus, the temperature at any point along the baffle will be the average temperature of the fluid just above and below the baffle, i.e., $T_{ij}=(T_{ij+1}+T_{ij-1})/2$ (see Fig. 2).

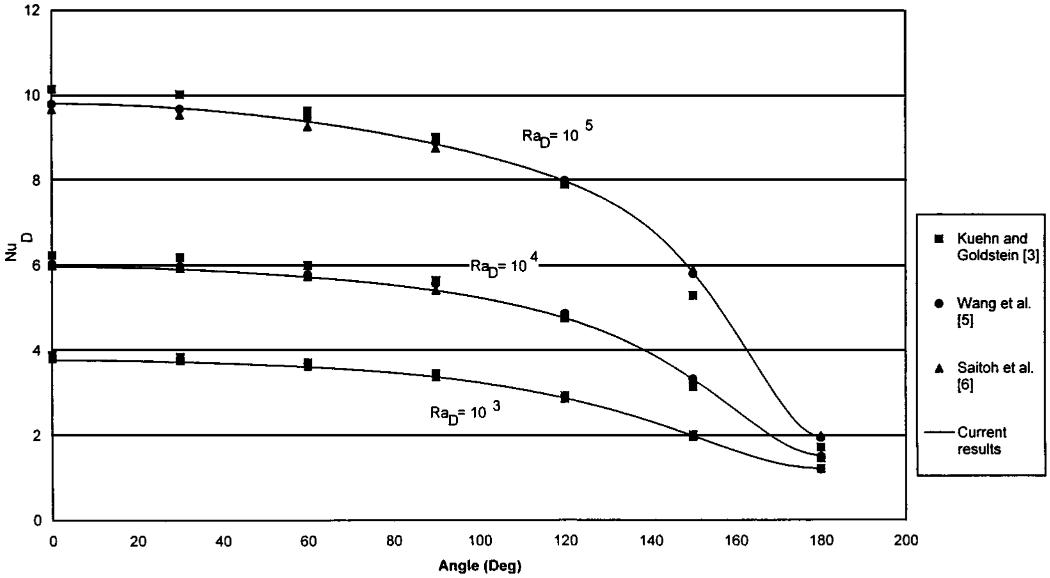

Fig. 3 Comparison of the local Nusselt number for the case of a smooth cylinder

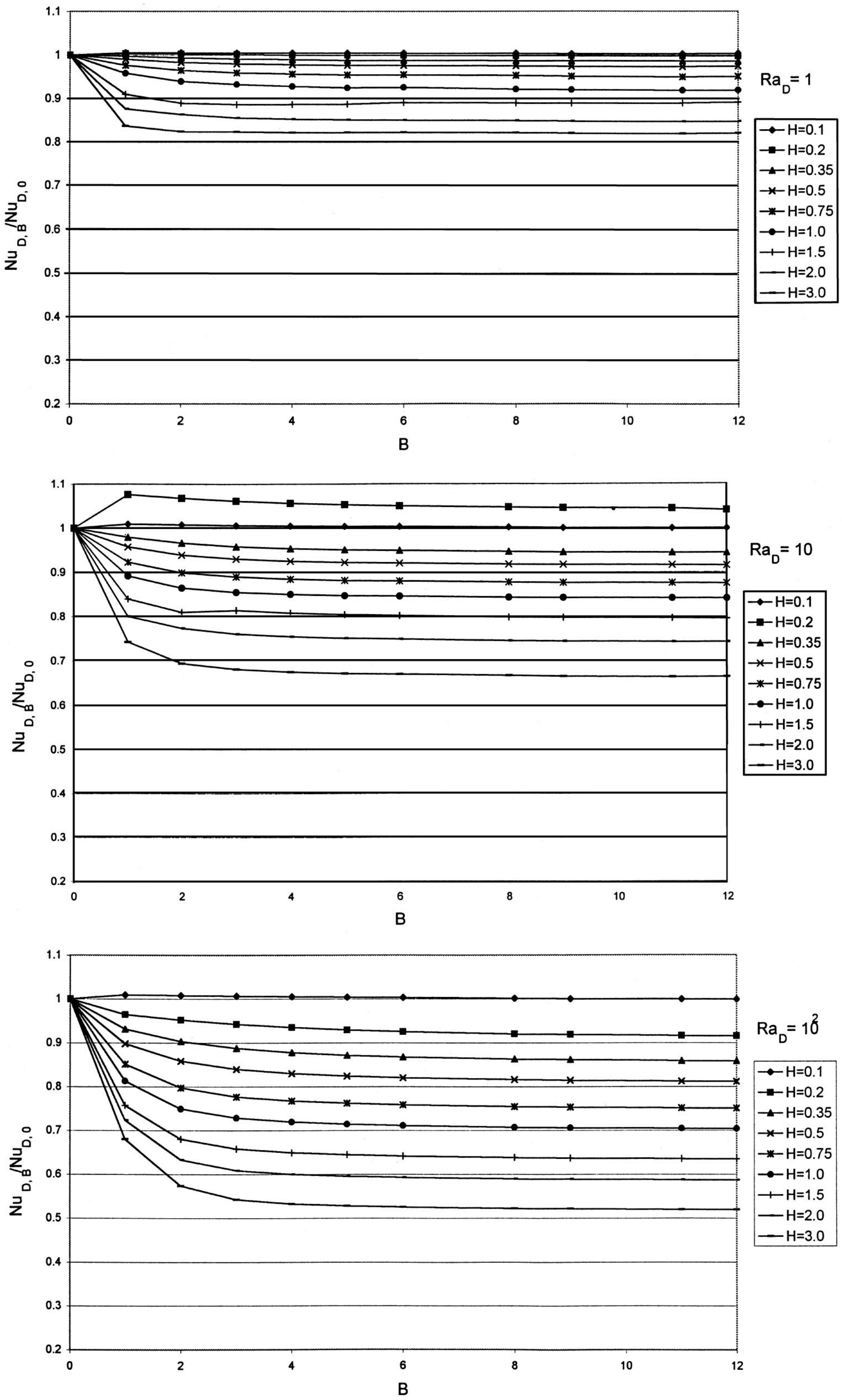

Fig. 4 Change in the average Nusselt number as a function of the number of baffles at different Ra_D

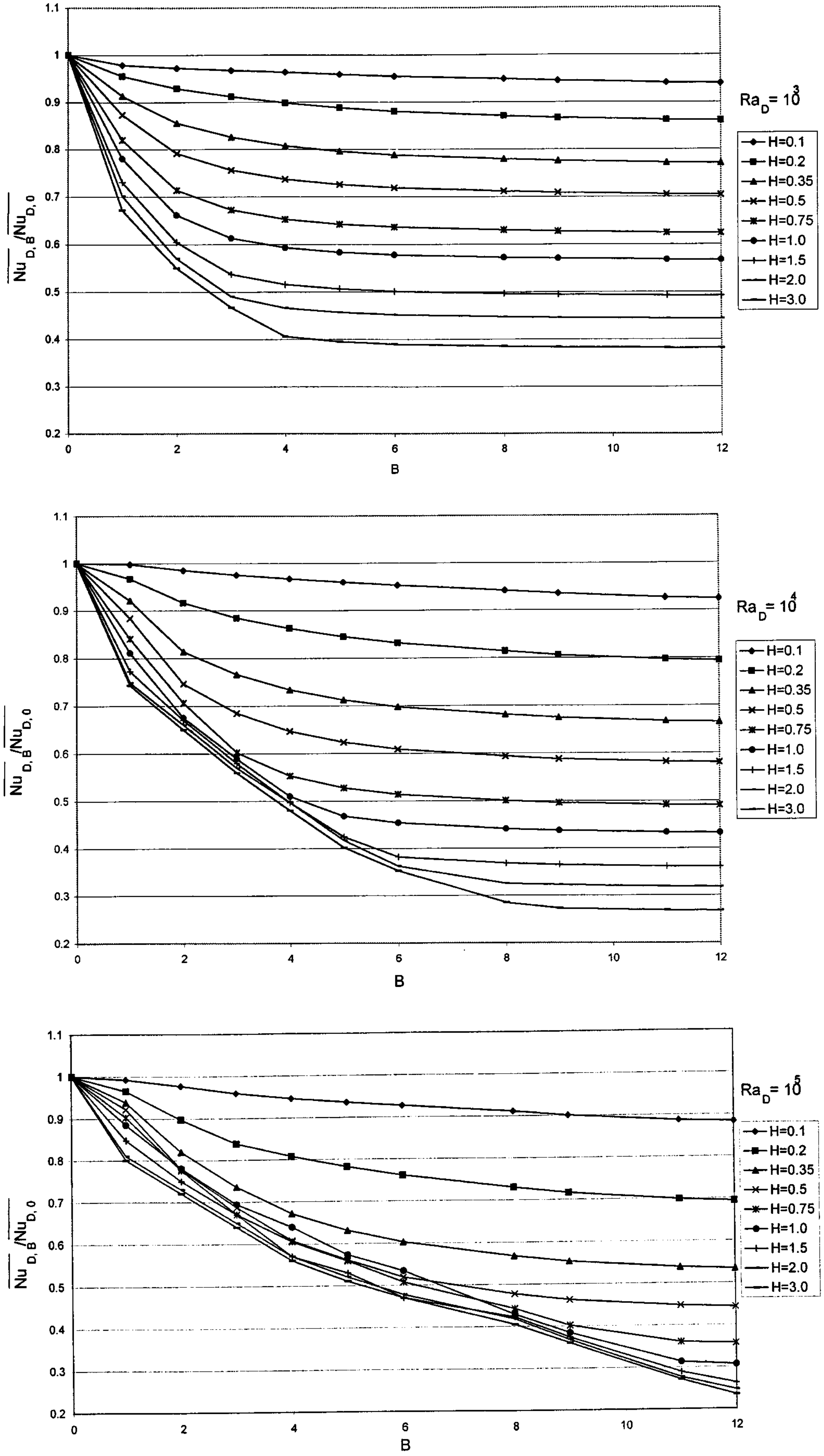

Fig. 4 (*Continued.*)

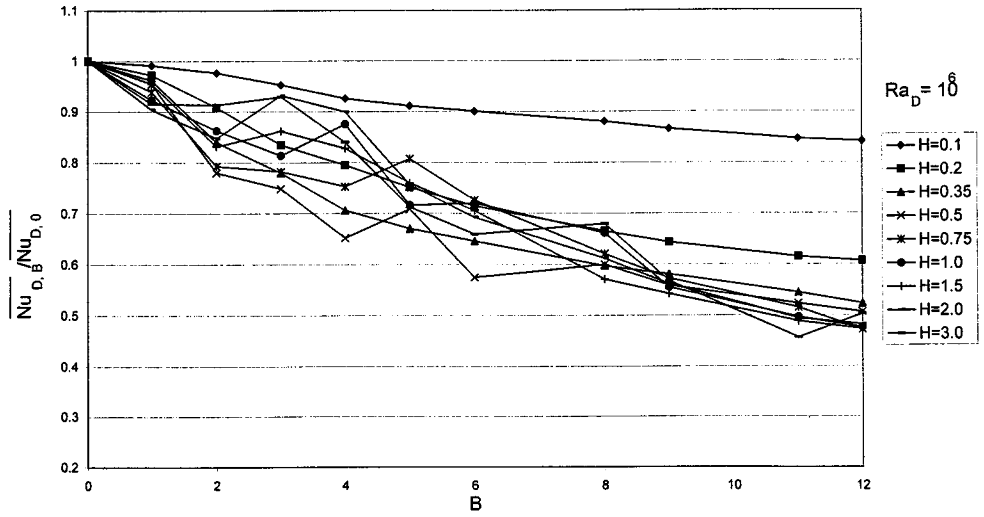

Fig. 4 (*Continued.*)

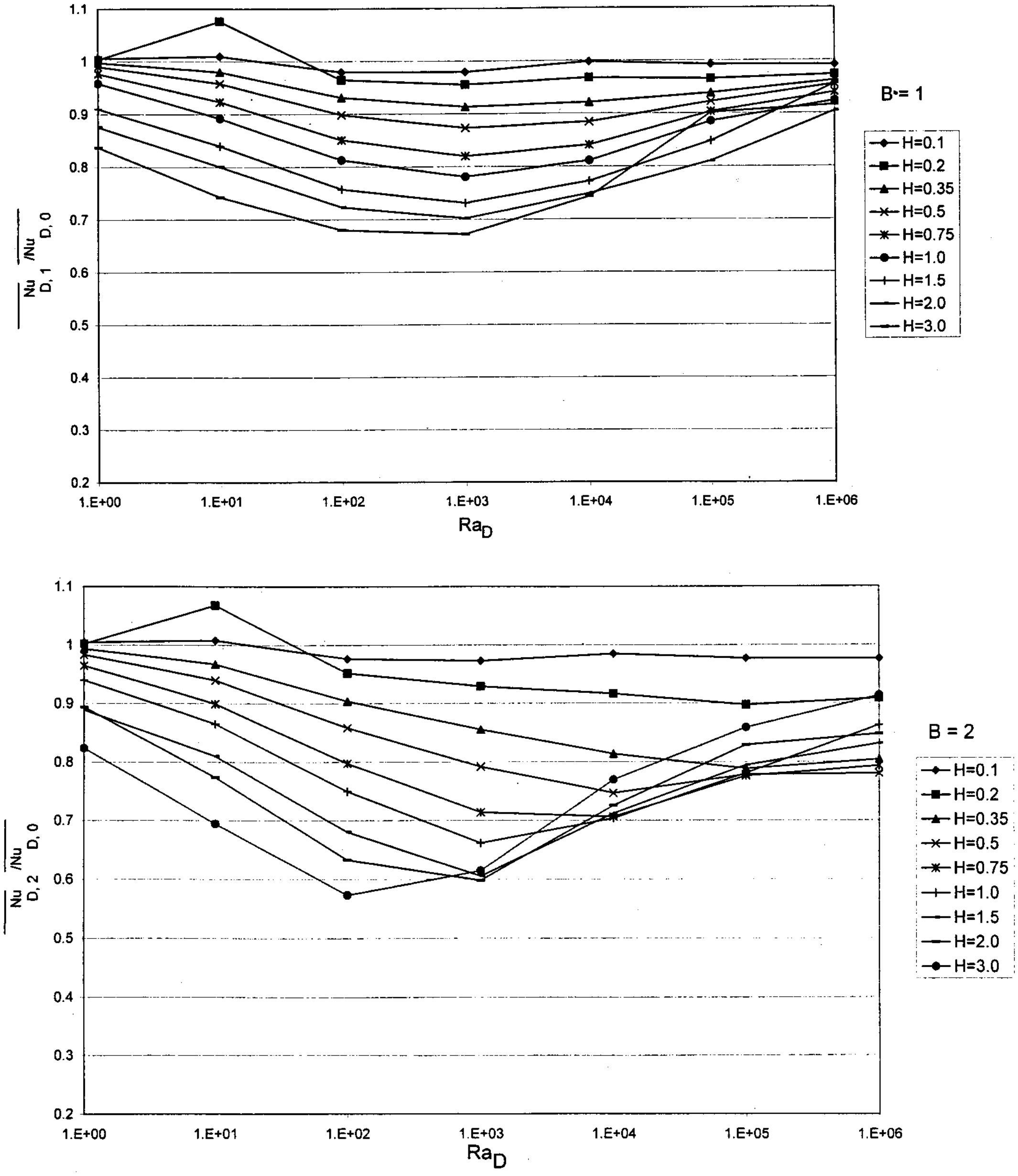

Fig. 5 Change in the average Nusselt number as a function of Ra_D at selective number of baffles

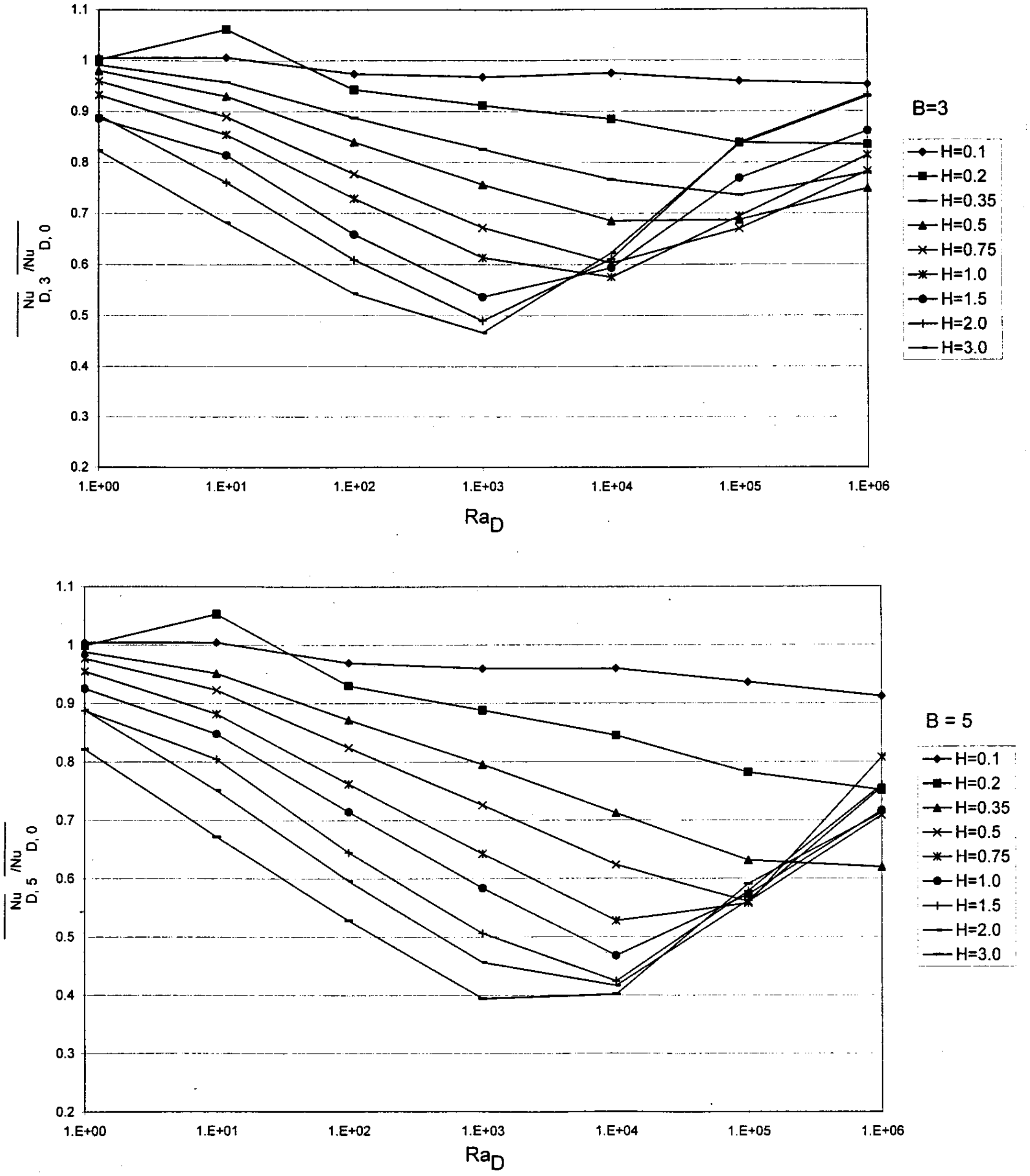

Fig. 5 (***Continued.***)

The local and average Nusselt number, based on diameter, are calculated as

$$\mathrm{Nu}_D=\frac{Dh(\theta)}{k};$$
$$\overline{\mathrm{Nu}_D}=\frac{1}{\pi}\frac{D}{k}\int_0^\pi h(\theta)d\theta=-\frac{D}{\pi}\int_0^\pi\frac{\partial T(r_o,\theta)/\partial r}{(T_o-T_\infty)}\partial\theta. \tag{5}$$

The following nondimensional groups are introduced:

$$R\equiv\frac{r}{r_o},\quad U\equiv\frac{ur_o}{\alpha},\quad V\equiv\frac{vr_o}{\alpha},\quad \phi\equiv\frac{T-T_\infty}{T_o-T_\infty},\quad P\equiv\frac{p-p_\infty}{\rho\alpha^2/r_o^2}. \tag{6}$$

Using the steam function–vorticity formulation, the nondimensional form of Eqs. (1)–(4) are given by

$$\omega=\nabla^2\psi \tag{7}$$

$$U\frac{\partial\omega}{\partial R}+\frac{V}{R}\frac{\partial\omega}{\partial\theta}=\mathrm{Pr}\,\nabla^2\omega+\mathrm{Ra}\,\mathrm{Pr}\left[\sin(\theta)\frac{\partial\phi}{\partial R}+\frac{\cos(\theta)}{R}\frac{\partial\phi}{\partial\theta}\right] \tag{8}$$

$$U\frac{\partial\phi}{\partial R}+\frac{V}{R}\frac{\partial\phi}{\partial\theta}=\nabla^2\phi \tag{9}$$

where

$$U\equiv\frac{1}{R}\frac{\partial\psi}{\partial\theta},\quad V\equiv-\frac{\partial\psi}{\partial R},\quad \mathrm{Ra}=\frac{g\beta r_o^3(T_o-T_\infty)}{\alpha\nu},$$
$$\mathrm{Ra}_D=\frac{g\beta D^3(T_o-T_\infty)}{\alpha\nu},\quad \mathrm{Pr}=\frac{\nu}{\alpha}. \tag{10}$$

The new nondimensional boundary conditions for Eqs. (7)–(9) are given by

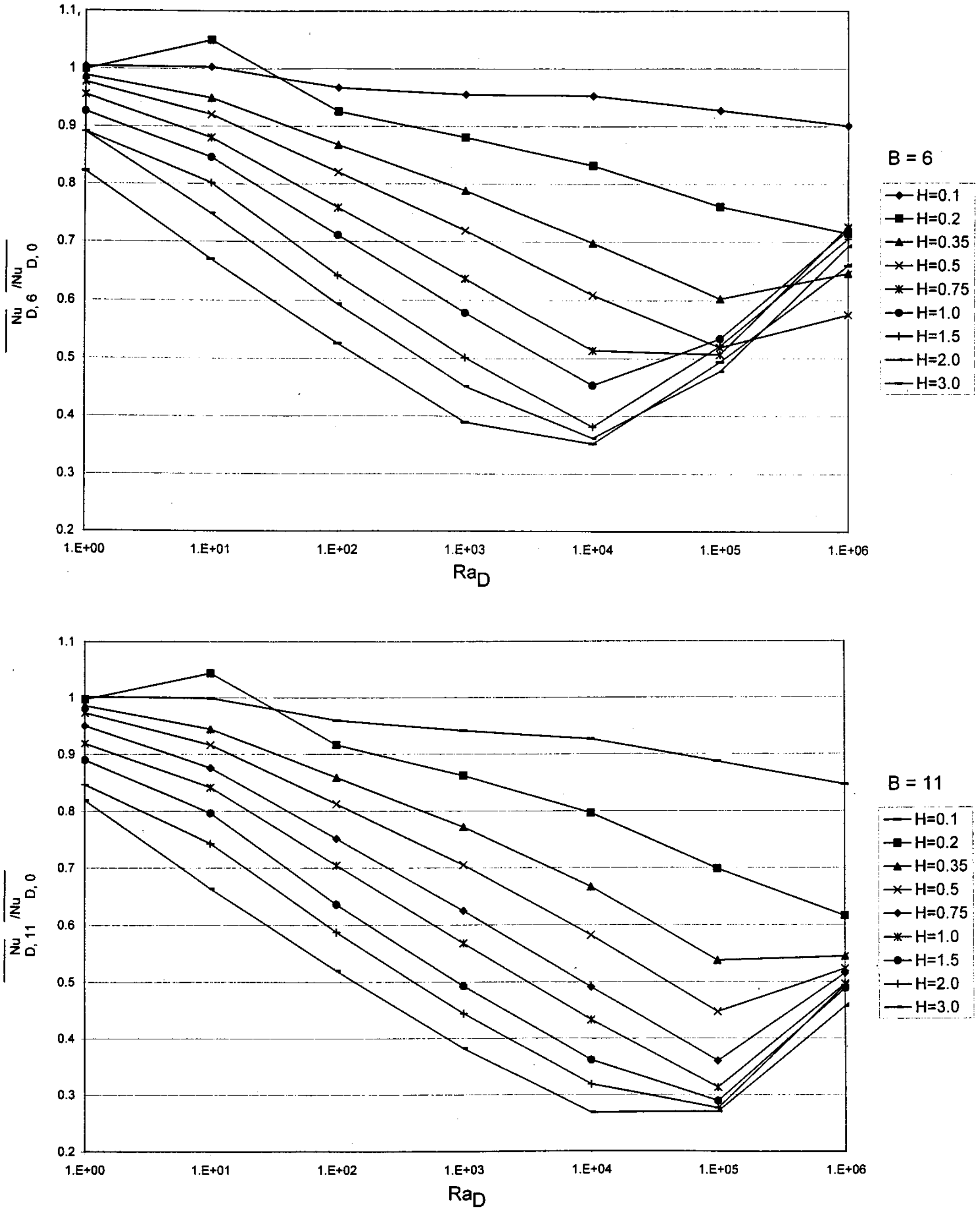

Fig. 5 (***Continued.***)

1 On the cylinder surface, i.e., $R=1.0$; $\psi=\partial\psi/\partial R=0$, $\omega=\partial^2\psi/\partial R^2$, and $\phi=1.0$.

2 Far stream form the cylinder, i.e., $R\rightarrow\infty$; $\partial^2\psi/\partial R^2=0$ and $\omega=-(1/R^2)(\partial^2\psi/\partial\theta^2)$. For the nondimensional temperature, $\phi=0$ and $\partial\phi/\partial R=0$, for the inflow and outflow regions, respectively.

3 Plane of symmetry; $\psi=\omega=\partial\phi/\partial\theta=0$.

4 On the baffle surface; $\psi=0$, $\omega=-(1/R^2)(\partial^2\psi/\partial\theta^2)$, and $\phi_{ij}=(\phi_{ij+1}+\phi_{ij-1})/2$.

In order to accurately resolve the boundary layer around cylinder, a grid with small radial spacing is required. It is not practical to use this small spacing as we move to the far-stream boundary. Thus a stretched grid in the radial direction is needed ([12]). This will result in unequally spaced nodes and would require the use of more complicated and/or less accurate finite difference formulas. To overcome this problem, the unequally spaced grid in the physical domain (R,θ) is transformed into an equally spaced grid in the computational domain (ξ,η) [12] (Fig. 2). The two domains are related as follows:

$$R=e^{\pi\xi},\quad \theta=\pi\eta. \tag{11}$$

Equations (7)–(9) along with the corresponding boundary conditions need to be transformed into the computational domain. In the new computational domain, the current problem will be given by

$$\omega=\frac{1}{E^2}\left[\frac{\partial^2\psi}{\partial\xi^2}+\frac{\partial^2\psi}{\partial\eta^2}\right] \tag{12}$$

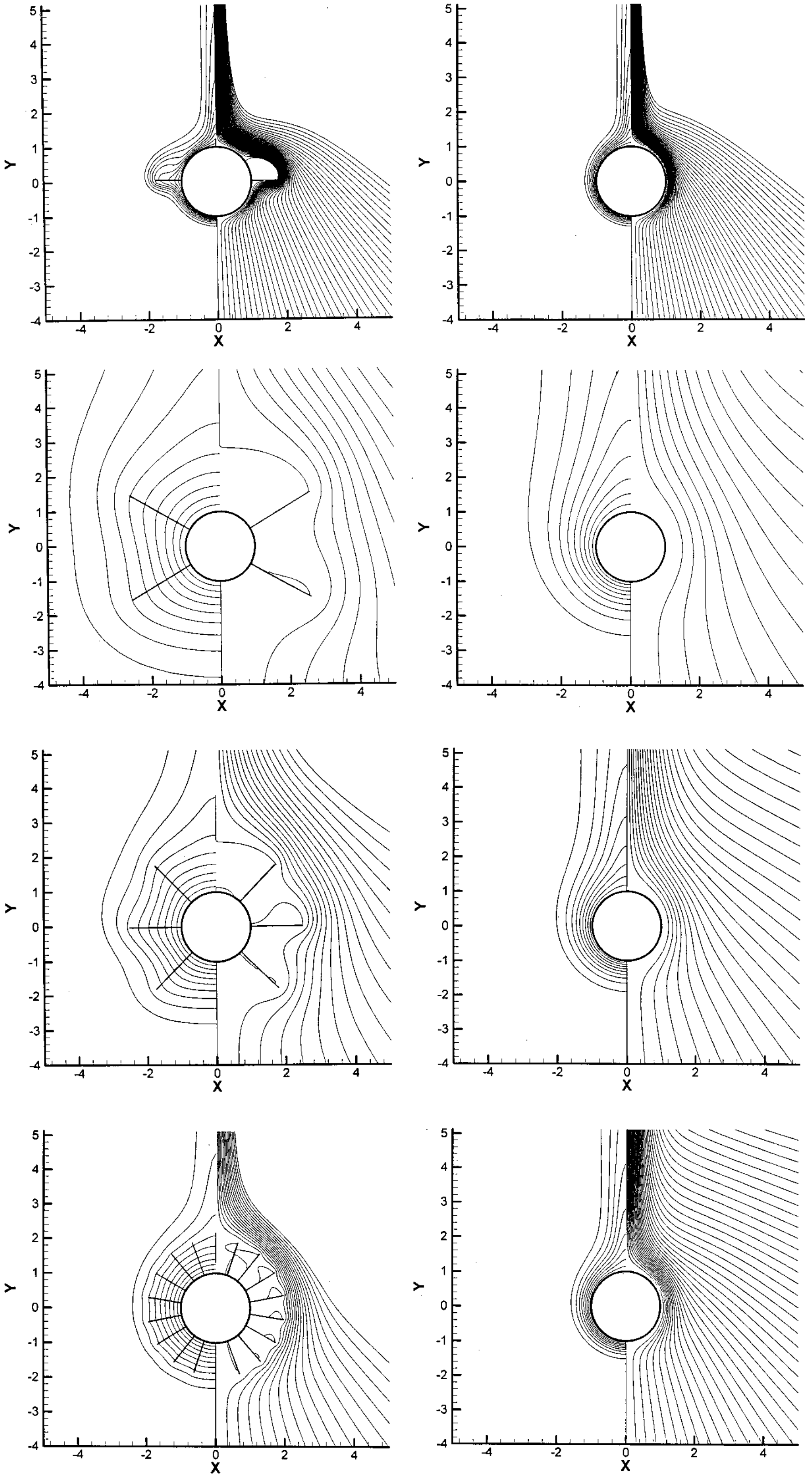

Fig. 6 Changes in the streamline and temperature contours between the case of a smooth cylinder (right) and a baffle equipped cylinder (left) for the cases (B,H,Ra_D) from top: (1,0.75,10^5), (2,2.0,10^2), (3,1.5,10^3), and (8,1.0,10^4)

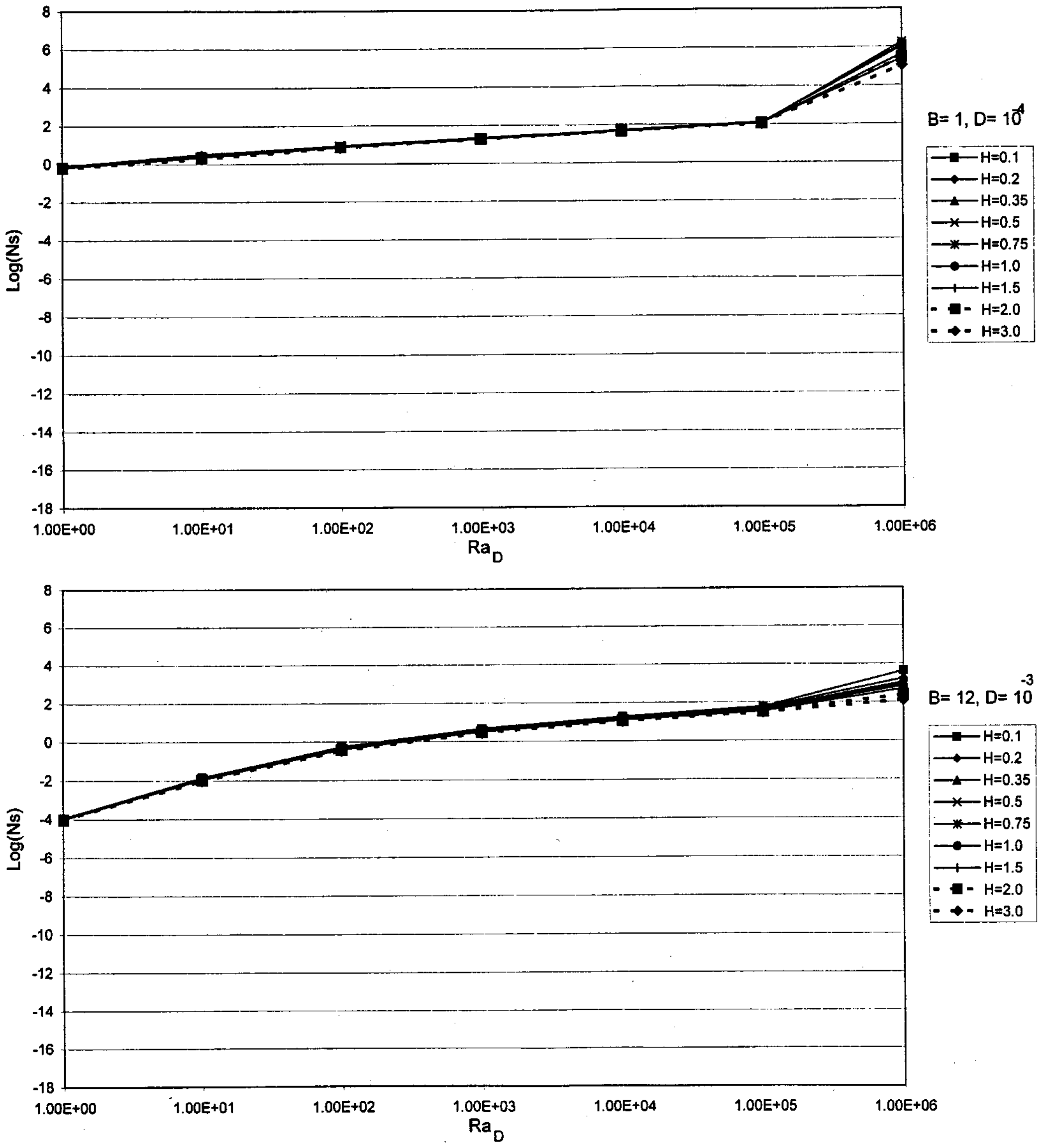

Fig. 7 Total entropy generation as a function of Ra_D at selective combinations of number of baffles and cylinder diameter

$$\frac{\partial^2\omega}{\partial\xi^2}+\frac{\partial^2\omega}{\partial\eta^2}=\frac{1}{\Pr}\left[\frac{\partial\psi}{\partial\eta}\frac{\partial\omega}{\partial\xi}-\frac{\partial\psi}{\partial\xi}\frac{\partial\omega}{\partial\eta}\right]$$

$$-E\mathrm{Ra}\left[\sin(\pi\eta)\frac{\partial\phi}{\partial\xi}+\cos(\pi\eta)\frac{\partial\phi}{\partial\eta}\right] \qquad (13)$$

$$\frac{\partial^2\phi}{\partial\xi^2}+\frac{\partial^2\phi}{\partial\eta^2}=\left[\frac{\partial\psi}{\partial\eta}\frac{\partial\phi}{\partial\xi}-\frac{\partial\psi}{\partial\xi}\frac{\partial\phi}{\partial\eta}\right] \qquad (14)$$

where

$$E=\pi e^{\pi\xi} \qquad (15)$$

The transformed boundary conditions are given by

1 On the cylinder surface, i.e., $\xi=0$; $\psi=\partial\psi/\partial\xi=0$, $\omega=(1/\pi^2)(\partial^2\psi/\partial\xi^2)$, and $\phi=1.0$.

2 Far stream form the cylinder, i.e., $\xi\rightarrow\infty$; $\partial^2\psi/\partial\xi^2=0$ and $\omega=-(1/E^2)(\partial^2\psi/\partial\eta^2)$. For the nondimensional temperature $\phi=0$ and $\partial\phi/\partial\xi=0$, for the inflow and outflow regions, respectively.

3 Plane of symmetry; i.e., $\eta=0$ and $\eta=1$; $\psi=\omega=\partial\phi/\partial\eta=0$.

4 On the baffle surface; $\psi=0$, $\omega=-(1/\pi^2)(\partial^2\psi/\partial\xi^2)$, and $\phi_{ij}=(\phi_{ij+1}+\phi_{ij-1})/2$.

The system of elliptic PDEs given by Eqs. (12)–(14) along with the corresponding boundary conditions was discretized using the finite difference method. The resulting system of algebraic equations was solved using the hybrid scheme ([13]). Such a method proved to be numerically stable for convection-diffusion problems. The finite difference form of the equations was checked for consistency with the original PDEs ([13]). The iterative solution procedure was carried out until the error in all solution variables (ψ,ω,ϕ) became less than a predefined error level (ϵ). Other predefined parameters needed for the solution method included the placement of the far-stream boundary condition (R_∞) and the number of nodes in both radial and tangential directions, N and M, respectively. Extensive testing was carried out in order to determine the effect of each of these parameters on the solution. This was done to insure that the solution obtained was independent of and not tainted by the predefined value of each of these parameters. The testing included varying the value of ϵ from 10^{-3} to

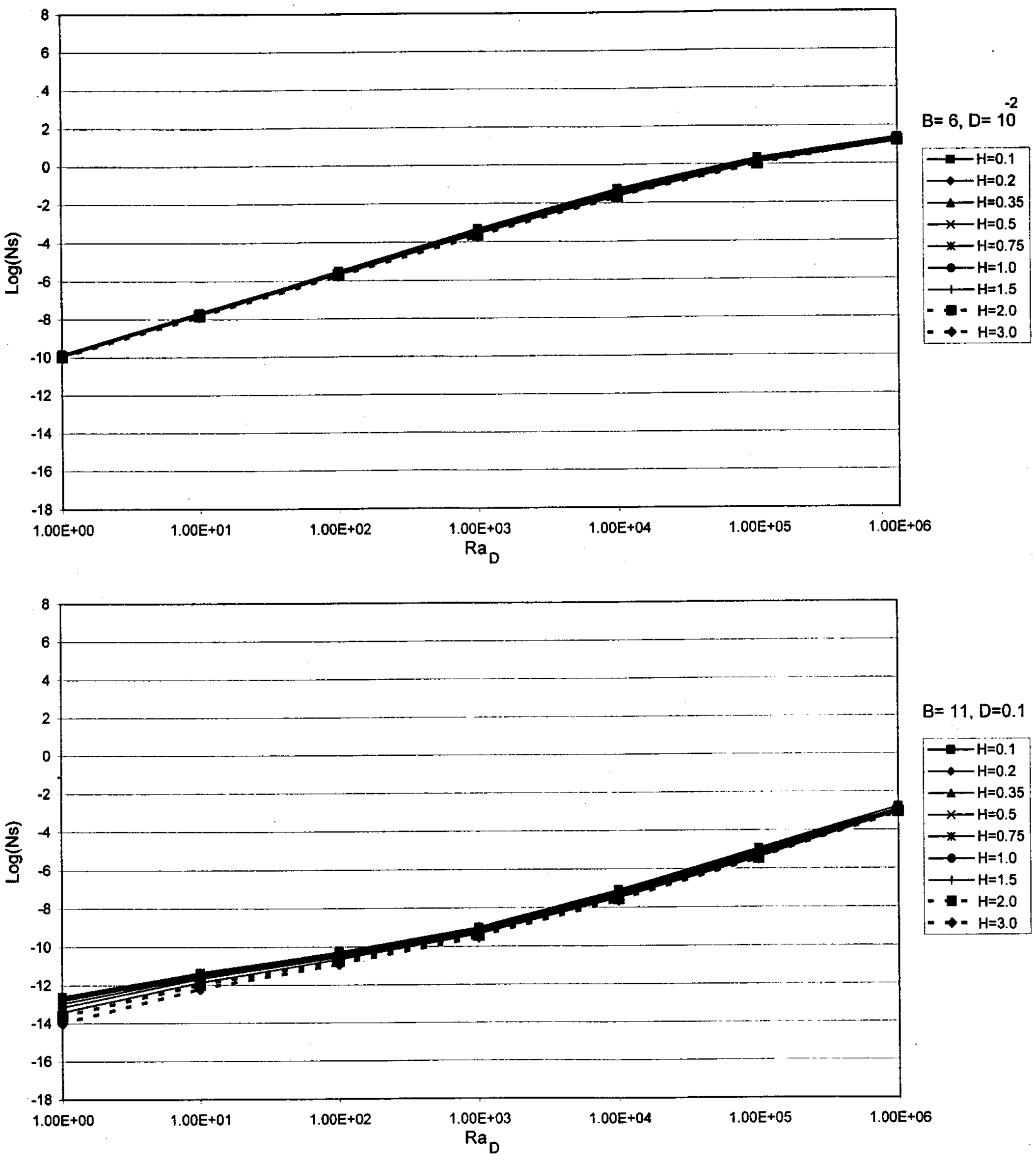

Fig. 7 (*Continued.*)

10^{-6}, R_∞ from 5 to 50, N from 60 to 150, and M from 60 to 144. The results reported herein are based on the following combination: $N=133-141$, $M=117-120$, $R_\infty=13$, and $\epsilon=10^{-5}$. The variation in the number of nodes used in the radial and tangential direction was baffle number and baffle height dependent. The variation was to insure that all baffles coincided with one of the grid's radial nodes and that the baffles end coincided with one of the grid's tangential nodes (see Fig. 2). The large number of tangential node ensured that the solution was grid independent even for the cases with baffles. The current grid resolution used is better than most grids used in published studies of natural ([6,8]) and forced convection from a heated cylinder ([14]). The accuracy of the local Nusselt number calculations (Nu_D) was important to insure the accuracy of the local entropy generation calculations. Figure 3 shows very good agreement between the profiles of the local Nusselt number calculated by the current code and the data reported by Kuehn and Goldstein [3], Wang et al. [5], and Saitoh et al. [6] for the case of cylinder with no baffles.

The nondimensional form of the local entropy generation equation in two-dimensional cylindrical coordinates can be written as ([11])

$$S''_{\mathrm{gen}}=\frac{1}{(\phi+T)^2}\left[\left(\frac{\partial\phi}{\partial R}\right)^2+\left(\frac{1}{R}\frac{\partial\phi}{\partial\theta}\right)^2\right]+\frac{\sigma}{(\phi+T)}\left\{2\left[\left(\frac{\partial U}{\partial R}\right)^2+\frac{1}{R^2}\left(\frac{\partial V}{\partial\theta}+U\right)^2\right]+\left[\frac{1}{R}\frac{\partial U}{\partial\theta}+R\frac{\partial}{\partial R}\left(\frac{V}{R}\right)\right]^2\right\} \tag{16}$$

where

$$\overline{T}=\frac{T_\infty}{T_o-T_\infty},\quad \sigma=\frac{\alpha^2\mu}{r_o^2k(T_o-T_\infty)},\quad \text{and}\quad S''_{\mathrm{gen}}=\frac{S''_{\mathrm{gen}}r_o^2}{k}. \tag{17}$$

The total nondimensional entropy generation is calculated by integrating S''_{gen} over the entire flow field:

$$N_s=\int_1^{R_\infty}\int_0^{\pi}S''_{\mathrm{gen}}(R,\theta)\,d\theta\,dR. \tag{18}$$

The range of N_s is very large, thus the logarithm to base ten is usually used, $\log(N_s)$ ([11]). There are two components in the

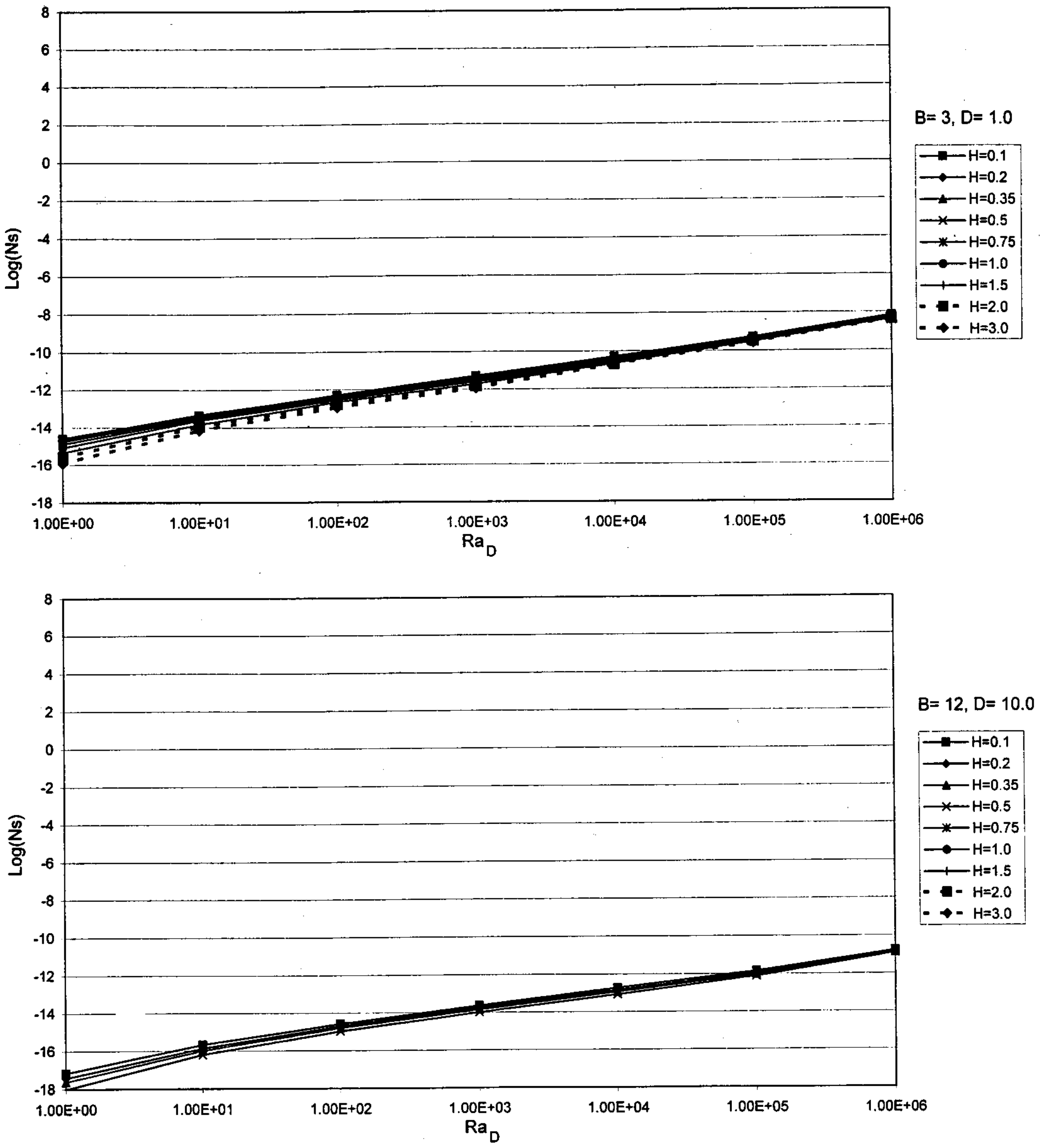

Fig. 7 (***Continued.***)

entropy generation equation: the conduction part and the viscous dissipation part, the first and second terms on the right-hand side of Eq. (8), respectively. The values of the local and total entropy generation were calculated after the velocity and temperature profiles were obtained from the numerical iterations. Thus there was no need to transform Eq. (15) into the computational domain.

Results

The effect of baffles on the natural heat transfer from a horizontal isothermal cylinder was studied for several combinations covering a wide range of number of baffles ($B=1,2,3,4,5,6,8,9,11,12$), nondimensional baffle height ($H=0.1$, 0.2, 0.35, 0.5, 0.75, 1.0, 1.5, 2.0, 3.0), and Rayleigh number (Ra=1, 10, 10^2, 10^3, 10^4, 10^5, 10^6). The change in the average Nusselt number, for a given value of Rayleigh number, due to the addition of B baffle(s) ($\overline{\mathrm{Nu}_{D,B}}$) was normalized by the Nusselt number of a smooth cylinder, no baffles, at the same Rayleigh number ($\overline{\mathrm{Nu}_{D,0}}$).

Figure 4 shows the change in the average Nusselt number as a function of number of baffles and baffle height for different values of Rayleigh number. There was up to 72 percent reduction in the value of average Nusselt number depending on the number and height of baffles as well as the Rayleigh number. There seems to be an optimal number of baffles for a given baffle height and Rayleigh number beyond which increasing the number of baffles does not reduce the average Nusselt number. This data can be used to optimize the thermal insulation design of baffle equipped cylinders. As the Rayleigh number increased, the optimal number of baffles increased. For $\mathrm{Ra}_D \geq 10^5$, the average Nusselt number continued to decrease as the number of baffles increased. Thus, there was no optimal number of baffles for $\mathrm{Ra}_D \geq 10^5$, at least for the number of baffles considered in this study. For $\mathrm{Ra}_D = 10^6$, the solution became unstable for baffle height (H)>0.35. The current code is valid for laminar flow only. The use of long baffle(s) coupled with high value of Rayleigh number could result in the transition of the flow into the turbulent regime. Thus, the results for $\mathrm{Ra}_D = 10^6$ are not reliable for long baffles. An interesting observation in Fig. 4 was that, at low Rayleigh number and for short baffles, the average Nusselt number actually increased. This was especially clear for the case of $\mathrm{Ra}_D = 10$ and $H=0.2$. At low Rayleigh number, the boundary layer is thick. Thus, it is possible that the short baffles ''energized'' the sublayer of the boundary layer

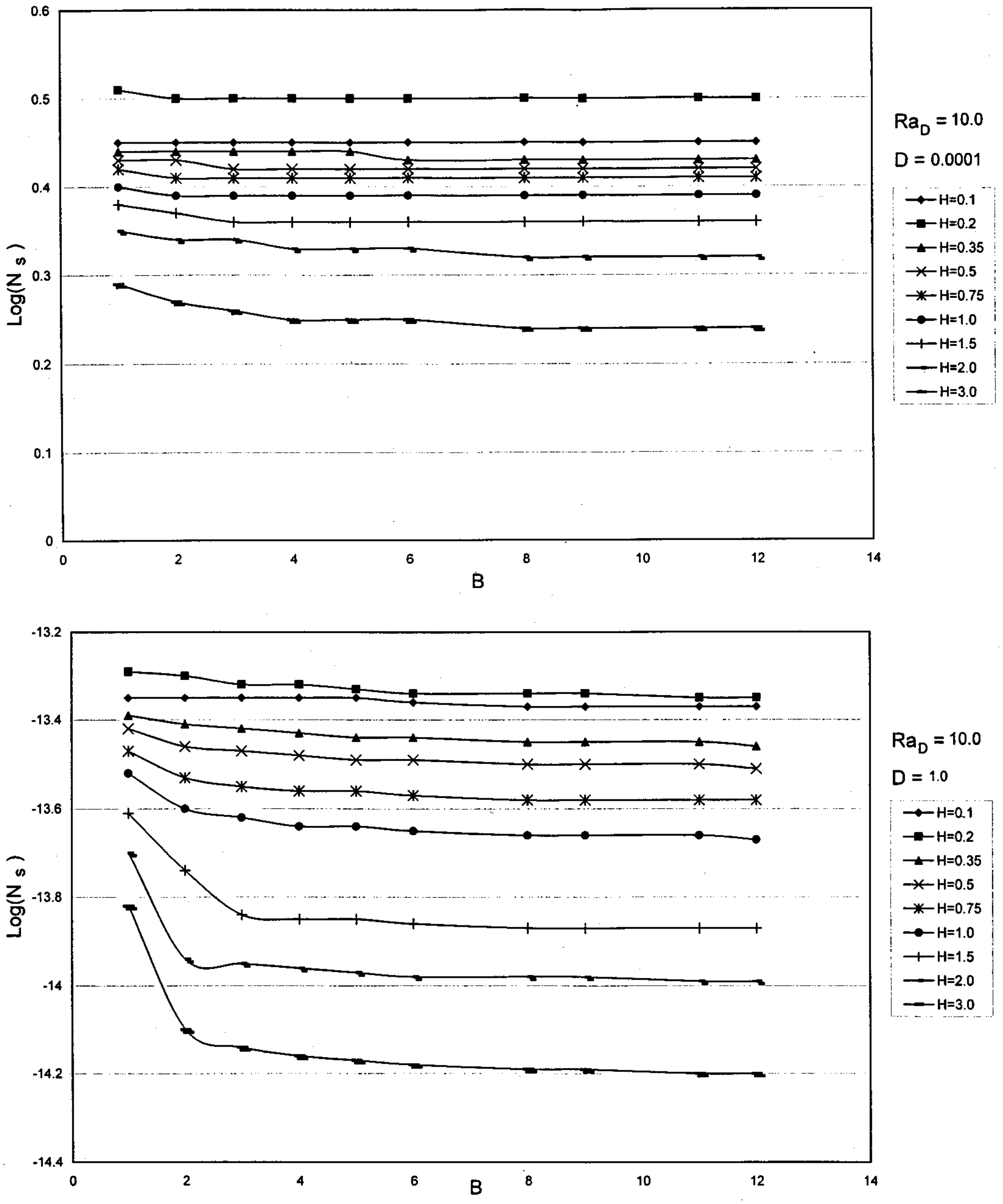

Fig. 8 Total entropy generation as a function of baffle height (*H*) at selective combinations of Rayleigh number and cylinder diameter

resulting in enchased heat transfer from the cylinder which translated to an increase in the average Nusselt number. Several mathematical models were tested in order to correlate the change in the Nusselt number with the number of baffles and baffle height but none was successful.

Figure 5 shows the change in the average Nusselt number as a function of Rayleigh number for a selective number of baffles. This figure contains the same data in Fig. 4 but rearranged in order to show the variation of the average Nusselt number for a given number of baffles as the Rayleigh number changes. This figure shows the effect of off-design conditions, i.e., variation in cylinder's and/or surrounding's temperature, on the average Nusselt number of a cylinder. The increase in the average Nusselt number at $\mathrm{Ra}_D=10$ and $H=0.2$ is clearly visible. Selective streamline (right half) and temperature (left half) contours are shown in Fig. 6 in order to give a better insight in the hydrodynamic and thermal changes in the flow due to the addition of the baffles.

Equation (16) introduces a new parameter in the calculation of entropy generation. The cylinder size has a direct effect on the entropy generation even at the same values of Rayleigh number, number of baffles, and baffle height. Entropy generation was calculated for several cylinder diameters ($D=10^{-4}$, 10^{-3}, 10^{-2}, 0.1, 1.0, 10.0 meters) at every combination of Rayleigh number, number of baffles, and baffle height. The resulting number of data and figures was huge. Thus, only a summary of the results, with some sample graphs, will be reported. The general trend was that an increase in the Rayleigh number resulted in an increase in the total entropy generation, $\log(N_s)$ (Fig. 7). This is consistent with Eq. (15) which shows entropy generation to increase with velocity and/or temperature gradients. High values of Rayleigh number result in stronger convection currents which translate to higher velocity gradients. At high Rayleigh number, the thickness of the thermal boundary layer becomes smaller which results in higher temperature gradients. Increasing the number of baffles and/or the

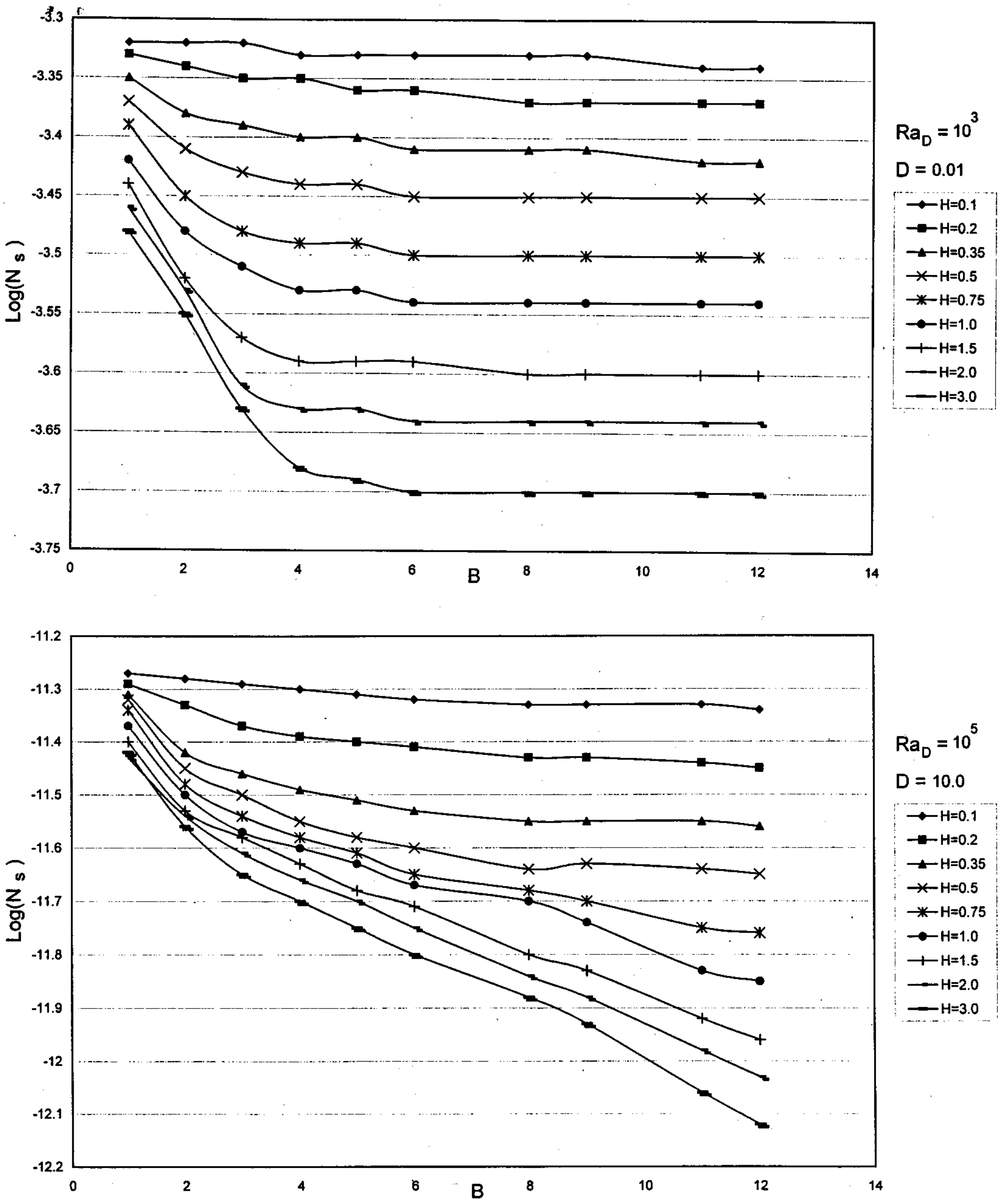

Fig. 8 (***Continued.***)

baffle height resulted in a small reduction in entropy generation. The baffles tended to reduce the heat transfer from the cylinder and thus the temperature gradients in the vicinity of the cylinder. A reduction in temperature gradients translates to a reduction in the entropy generation due to thermal effect, the first term on the right-hand side of Eq. (15). The presence of the baffles would result in higher velocity gradients near the baffles, which increases the entropy generation due to friction losses, the second term on the right hand side of Eq. (15). Previous work on natural convection from a smooth cylinder showed that the friction loss contribution to the total entropy generation was negligible even for highly viscous fluids ([15]). That is why the reduction in thermal entropy generation due to the addition of the baffles was not offset by the increase in friction loss entropy generation. Figure 8 shows the change in the total entropy generation as a function of baffle height, for selected combinations of Rayleigh number and cylinder diameter. The change in total entropy generation closely resembles that of the change in the average Nusselt number seen in Fig. 4. This confirms that the additional viscous entropy generated due to the addition of the baffles was negligible compared to the entropy generated due to changes in the thermal field.

Increasing the cylinder diameter resulted in a noticeable reduction in entropy generation. As the cylinder diameter increased, and for the same value of Rayleigh number, the temperature difference between the cylinder and the surroundings decreased, as per Eq. (10). This resulted in a reduction in the temperature gradients which translated into a reduction in thermal entropy generation. The change in entropy generation was monotonic with respect to all parameters studied (Re_D, B, H, and D). This is in contrast to the changes in the average Nusselt number as seen in Figs. 4 and 5. This is an important observation from a design point of view.

Figure 4 shows that the average Nusselt number does not change beyond a certain number of baffles. Thus, no additional thermal insulation is gained by increasing the number of baffles. Yet entropy generation continues to increase with increasing number of baffles even though the average Nusselt number remains constant. Thus, an over designed cylinder with extra baffles will not result in extra insulation but will be less efficient from a thermodynamic point of view. The combination of Figs. 4, 7, and 8 give the designer some guidelines as to the possible tradeoffs between increased insulation effect and reduced thermodynamic efficiency due to the addition of the baffles.

Conclusions

The problem of natural heat transfer from an isothermal horizontal cylinder with low conductivity, equally spaced baffles was studied numerically. Changes in the average Nusselt number at different combinations of number of baffles, baffle height, and Rayleigh number were reported. The local velocity and temperature data were used to calculate the local entropy generation around the cylinder. Selective results of the changes in the total entropy generation due to the presence of the baffles and at difference cylinder diameters were presented and discussed. The results can be used to optimize the design of baffle equipped cylinders for optimal thermal insulation behavior.

Nomenclature

B = number of equally spaced baffles
D = cylinder diameter (meters), $2r_o$
E = parameter in computational domain, $\pi e^{\pi\xi}$
g = gravity
H = nondimensional baffle height, h_b/r_o
h = local convection heat transfer coefficient
h_b = baffle height
k = conduction heat transfer coefficient
M = number of grid points in the tangential direction
N = number of grid points in the radial direction
N_s = total nondimensional entropy generation
Nu_D = local Nusselt number based on cylinder diameter, no baffles
$\overline{\mathrm{Nu}}_D$ = average Nusselt number based on cylinder diameter, no baffles
$\overline{\mathrm{Nu}_{D,B}}$ = average Nusselt number based on cylinder diameter, cylinder with B baffles
P = nondimensional pressure
p = pressure
Pr = Prandtl number
R = nondimensional radius
r = radius
Ra = Rayleigh number based on cylinder radius, $g\beta(T_o - T_\infty)r_o^3/\alpha\nu$
Ra_D = Rayleigh number based on cylinder diameter, $g\beta(T_o - T_\infty)D^3/\alpha\nu;\ = 8\ \mathrm{Ra}$
S''_{gen} = nondimensional local entropy generation
s''_{gen} = dimensional local entropy generation
T = temperature
U = nondimensional radial velocity
u = radial velocity
V = nondimensional tangential velocity
v = tangential velocity

Greek Symbols

α = thermal diffusivity
β = coefficient of thermal expansion
ϵ = measure of convergence of numerical results
η = independent parameter in computational domain representing tangential direction
θ = angle
ν = kinematic viscosity
ξ = independent parameter in computational domain representing radial direction
ρ = density
ϕ = nondimensional temperature
ψ = stream function
ω = vorticity function

Subscripts

D = value based on cylinder diameter
o = value at cylinder surface
∞ = freestream value

References

[1] Morgan, V. T., 1975, ''The Overall Convective Heat Transfer From Smooth Circular Cylinders,'' Adv. Heat Transfer, **11**, pp. 199–264.
[2] Churchill, S. W., and Chu, H. H. S., 1975, ''Correlating Equations for Laminar and Turbulent Free Convection From a Horizontal Cylinder,'' Int. J. Heat Mass Transf., **18**, pp. 1049–1053.
[3] Kuehn, T. H., and Goldstein, R. J., 1980, ''Numerical Solutions to the Navier-Stokes Equations for Laminar Natural Convection About a Horizontal Cylinder,'' Int. J. Heat Mass Transf., **23**, pp. 971–979.
[4] Farouk, B., and Guceri, S. I., 1981, ''Natural Convection From a Horizontal Cylinder-Laminar Regime,'' ASME J. Heat Transfer, **103**, pp. 522–527.
[5] Wang, P., Kahawita, R., and Nguyen, T. H., 1990, ''Numerical Computation of the Natural Convection Flow About a Horizontal Cylinder Using Splines,'' Numer. Heat Transfer, Part A, **17**, pp. 191–215.
[6] Saitoh, T., Sajik, T., and Maruhara, K., 1993, ''Bench Mark Solutions to Natural Convection Heat Transfer Problem Around a Horizontal Circular Cylinder,'' Int. J. Heat Mass Transf., **36**, pp. 1251–1259.
[7] Chai, J. C., and Patankar, S. V., 1993, ''Laminar Natural Convection in Internally Finned Horizontal Annuli,'' Numer. Heat Transfer, Part A, **24**, pp. 67–87.
[8] Abu-Hijleh, B. A/K, Abu-Qudais, M., and Abu-Nada, E., 1998, ''Entropy Generation due to Laminar Natural Convection From a Horizontal Isothermal Cylinder,'' ASME J. Heat Transfer, **120**, pp. 1089–1990.
[9] Vafai, K., and Huang, P. C., 1994, ''Analysis of Heat Transfer Regulation and Modification Employing Intermittently Emplaced Porous Cavities,'' ASME J. Heat Transfer, **116**, pp. 604–613.
[10] Al-Nimr, M. A., and Alkam, M. K., 1998, ''A Modified Tubeless Solar Collector Partially Filled With Porous Substrate,'' Renewable Energy, **13**, pp. 165–173.
[11] Bejan, A., 1982, *Entropy Generation Through Heat and Fluid Flow*, Wiley, New York.
[12] Anderson, J. D., 1994, *Computational Fluid Dynamics: The Basics with Applications*, McGraw-Hill, New York.
[13] Patankar, S. V., 1980, *Numerical Heat Transfer of Fluid Flow*, McGraw-Hill, New York.
[14] Ahmad, R. A., 1996, ''Steady-State Numerical Solution of the Navier-Stokes and Energy Equations Around a Horizontal Cylinder at Moderate Reynolds Numbers from 100 to 500,'' Heat Transfer Eng., **17**, pp. 1–81.
[15] Abu-Hijleh, B. A/K, Jadallah, I. N., and Abu-Nada, E., 1998, ''Entropy Generation due to Natural Convection From a Horizontal Isothermal Cylinder in Oil,'' Int. Commun. Heat Mass Transfer, **25**, pp. 1135–1143.

Velocity Statistics of Plane Self-Preserving Buoyant Turbulent Adiabatic Wall Plumes

R. Sangras

Z. Dai

G. M. Faeth
Mem. ASME
e-mail: gmfaeth@umich.edu

Department of Aerospace Engineering,
The University of Michigan,
Ann Arbor, MI 48109-2140

Measurements of the velocity properties of plane buoyant turbulent adiabatic wall plumes (adiabatic wall plumes) are described, emphasizing conditions far from the source where self-preserving behavior is approximated. The experiments involved helium/air mixtures rising along a smooth, plane, and vertical wall. Mean and fluctuating streamwise and cross-stream velocities were measured using laser velocimetry. Self-preserving behavior was observed 92–156 source widths from the source, yielding smaller normalized plume widths and larger near-wall mean velocities than observations within the flow development region nearer to the source. Unlike earlier observations of concentration fluctuation intensities, which are unusually large due to effects of streamwise buoyant instabilities, velocity fluctuation intensities were comparable to values observed in nonbuoyant turbulent wall jets. The entrainment properties of the present flows approximated self-preserving behavior in spite of continued development of the wall boundary layer. Measurements of temporal power spectra and temporal and spatial integral scales of velocity fluctuations are also reported. [S0022-1481(00)00504-1]

Keywords: *Heat Transfer, Natural Convection, Plumes, Turbulence, Turbulent*

Introduction

Plane turbulent wall plumes are caused by line sources of buoyancy along the base of flat walls. These flows are of interest because they are a classical buoyant turbulent flow having numerous practical applications for mixing during confined natural convection processes and in unwanted fires. These flows are also useful for gaining a better understanding of buoyancy/turbulence interactions, and the role of surfaces for inhibiting the large-scale motion mainly responsible for turbulent mixing, as part of developing methods of predicting the properties of buoyant turbulent flows. Motivated by these observations, the objective of the present investigation was to extend recent measurements of mixing processes (mixture fraction or composition statistics) in plane turbulent wall plumes along vertical surfaces, due to Sangras et al. [1] to consider the velocity statistics, i.e., the mean and fluctuating velocity properties, of these flows. Present observations were limited to turbulent wall plumes along smooth plane vertical surfaces for conditions where the streamwise buoyancy flux is conserved, which corresponds to flow along an adiabatic wall for a thermal plume.

Present measurements emphasize fully developed conditions far from the source where effects of source disturbances and momentum have been lost. Free line plumes become self-preserving at these conditions which simplifies reporting and interpreting measurements ([2,3]). Adiabatic wall plumes never formally approach self-preserving behavior, however, because the streamwise growth rates of the near-wall boundary layer and the outer plume-like region are not the same. For example, past measurements show that characteristic widths of turbulent adiabatic wall plumes relatively far from the source grow proportional to streamwise distance to the first power similar to free line plumes ([4,5]); whereas turbulent boundary layers along plane surfaces for nonbuoyant and buoyant flows grow proportional to streamwise distance to a power less than unity ([6]). Thus, the more rapid growth of the outer plume-like region than the near-wall boundary layer in adiabatic wall plumes implies that the outer plume-like region eventually dominates the flow and direct effects of wall friction are small far from the source, where adiabatic wall plumes approximate self-preserving behavior with scaling similar to free line plumes ([1,4]). Thus, self-preserving behavior of adiabatic wall plumes was sought in this approximate sense during the present investigation.

Early studies of turbulent plumes have been reviewed by Ellison and Turner [7], Lee and Emmons [8], List [9], Papanicolaou and List [10], Tennekes and Lumley [3], and Turner [11]. An interesting feature of the early studies is that the entrainment rates observed for wall plumes were much smaller than those observed for free line plumes; this behavior was attributed to both the wall preventing mixing on one side and inhibition of the large-scale cross-stream turbulent motion needed for effective mixing.

Grella and Faeth [4] report hot-wire probe measurements of temperatures and streamwise velocities within adiabatic wall plumes using a linear array of small flames as a thermal source of buoyancy. Self-preserving behavior was sought but was not achieved due to the limited dynamic range of hot wire probes while buoyancy fluxes are difficult to define accurately for this study due to near-source heat losses. Ljubaja and Rodi [12] subsequently predicted the properties of these flows using a turbulence model that allowed for buoyancy/turbulence interactions, finding good agreement far from the source where approximate self-preserving behavior was approached.

Lai et al. [5] and Lai and Faeth [13] carried out laser-induced fluorescence (LIF) and laser velocimetry (LV) measurements of mean and fluctuating concentrations and velocities in adiabatic wall plumes. Gas mixtures leaving a slot provided well-defined source dimensions and buoyancy fluxes. The observations were used to evaluate predictions based on simplified mixing length and higher-order turbulence models, finding good predictions for mean properties but relatively poor predictions for turbulence properties. These measurements were limited to near-source conditions in order to highlight effects of flow development; therefore self-preserving behavior was not achieved.

Sangras et al. [2] reconsidered the mixing properties (mixture fraction statistics) of adiabatic wall plumes during the initial phases of the present investigation. LIF was used to measure mean and fluctuating mixture fractions, emphasizing results for

---

Contributed by the Heat Transfer Division for publication in the JOURNAL OF HEAT TRANSFER. Manuscript received by the Heat Transfer Division Apr. 28, 1999; revision received May 18, 2000. Associate Technical Editor: C. Beckermann.

self-preserving conditions. In addition to large values of $(x-x_o)/b$ needed to avoid effects of source disturbances, approximate self-preserving behavior also requires large values of $(x-x_o)/l_{\mathrm{M}}$ to avoid effects of source momentum, where l_{M} is the Morton length scale ([11]). Noting that plume behavior dominates adiabatic wall plumes at self-preserving conditions, l_{M} can be defined by analogy to free line plumes having uniform source properties, as follows ([9]):

$$l_{\mathrm{M}}/b=(\rho_o/\rho_\infty)u_o^2/(bu_og|\rho_o-\rho_\infty|/\rho_\infty)^{2/3}. \tag{1}$$

Sangras et al. [1] found that self-preserving behavior was observed farther from the source than distances considered in earlier work, e.g., $(x-x_o)/b>92$ and $(x-x_o)/l_{\mathrm{M}}>12$, and yielded smaller normalized plume widths and near-wall mean mixture fractions than previously thought. This result also raises concerns about velocity properties used in various models of these flows, e.g., entrainment constants for simple integral models and turbulence structure for conventional and sub-grid-scale turbulence models. Thus, these findings provide strong motivation to find the velocity statistics of adiabatic wall plumes at similar conditions.

In view of these observations, the objective of the present investigation was to measure the mean and fluctuating velocity properties of adiabatic wall plumes, emphasizing conditions within the approximate self-preserving region far from the source. The experiments consisted of helium/air source flows along a smooth plane and vertical wall in still air at standard temperature and pressure, which provides straightforward specifications of source dimensions and plume buoyancy fluxes. Present work involved measurements of mean and fluctuating velocities using LV, to extend the earlier measurements of mean and fluctuating mixture fractions using LIF due to Sangras et al. [1].

Experimental Methods

Apparatus. The test apparatus was the same as the earlier adiabatic wall plume study of Sangras et al. [1]. The plumes were observed in an enclosure (3400 × 2000 × 3600 mm high) that had porous side walls (parallel to the source) and a porous ceiling made of filter material. This approach controlled room disturbances and ambient light leakage into the test enclosure while allowing free inflow of entrained air and free exhaust of the plume. The source slot (876 mm long × 9.4 mm wide) was mounted flush at a flat floor (876 mm long × 610 mm wide) with the vertical wall mounted adjacent to one edge of the slot. The floor/slot/wall assembly was mounted in turn normal to end walls (2440 mm high × 610 mm wide). A screen array (2 screens, 16 mesh × 0.20 mm wire diameter, separated by a distance of 38 mm) was installed across the outer edge of the end walls (facing the vertical wall) to further control room disturbances, following Gutmark and Wygnanski [14], Sangras et al. [1], and references cited therein. The entire floor/slot/wall assembly was traversed to accommodate rigidly mounted optical instruments in the same manner as Sangras et al. [1].

Gas supplies to the source were metered and measured using critical flow orifices in conjunction with pressure regulators. These flow rates were calibrated using either wet test or turbine flow meters. After mixing, the source flows passed through feed lines having length-to-diameter ratios of 1200 to ensure uniform source mixtures. Uniform source flow properties were provided by a bed of beads, a filter and a 3:4:1 contraction at the slot exit.

Instrumentation. Dual-beam frequency-shifted LV was used for velocity measurements, based on the 514.5 nm line of an argon-ion laser. The optical axis of the LV passed horizontally through the flow with off-axis signal collection to yield a measuring volume having a diameter of 400 μm and a length of 260 μm. Vertical and horizontal orientations of the plane of the laser beams were used to find the streamwise and cross-stream velocity components, similar to Lai and Faeth [13].

Table 1 Summary of plane buoyant turbulent adiabatic wall plume test conditions[a]

Source Properties	Case 1	Case 2
Helium concentration (percent by volume)	29.0	52.3
Density (kg/m^3)	0.871	0.639
Kinematic viscosity (mm^2/s)	22.1	31.3
Average velocity (mm/s)	868	1240
Buoyancy flux, B_o (m^3/s^3)	0.0200	0.0514
Density ratio ρ_o/ρ_∞	0.750	0.550
Reynolds number, Re_o	740	745
Froude number, Fr_o	3.50	3.20
Morton length scale, l_{M}/b	7.7	6.1

[a] Helium/air sources directed vertically upward at the base of a vertical smooth plane wall in still air with an ambient pressure of 99±0.5 kPa and temperature of 297±0.5 K. Pure gas properties as follows: air density of 1.161 kg/m^3, air kinematic viscosity of 15.9 mm^2/s, helium density of 0.163 kg/m^3, and helium kinematic viscosity of 122.5 mm^2/s. Source slot width and length of 9.4 and 876 mm. Virtual origin based on $\bar{f}$ of $x_o/b=0$ determined from present measurements in the range $(x-x_o)/b=92-155$ and $(x-x_o)/l_{\mathrm{M}}=12-21$.

The detector output was amplified and processed using a burst counter signal processor (TSI, model 1980B). Similar to past work, the low-pass filtered analog output of the signal processor was sampled at equal time intervals in order to avoid problems of velocity bias ([15,16]), whereas directional ambiguity and bias were controlled by frequency shifting. The detector output was sampled at rates more than twice the break frequency of the low-pass filter in order to control alias signals. Only the ambient flow was seeded because mixture fractions are small in the self-preserving region so that effects of concentration bias when seeded in this way are negligible. Effects of gradient bias were less than one percent because present measurements were made relatively far from the source where the flow widths were large compared to LV measuring volume dimensions. Seeding levels were sufficiently large that effects of step noise did not have a significant effect on determinations of rms velocity fluctuations; this will be quantified later based on measurements of temporal power spectral densities. Experimental uncertainties were evaluated considering effects of fundamental calibration of the velocity signal and effects of finite sampling times, similar to Dai et al. [15]; the latter dominated experimental uncertainties which are estimated to be less than five percent for mean streamwise velocities, less than 13 percent for rms velocity fluctuations and less than 20 percent for mean cross-stream velocities (the last being relatively large due to the small magnitudes of this velocity component).

Test Conditions. The test conditions were the same as the earlier adiabatic wall plume study of Sangras et al. [1] and are summarized in Table 1. Two source flows were considered in order to test scaling of source properties in the region of self-preserving behavior. Approximate self-preserving behavior for adiabatic wall plumes was only observed relatively far from the source where $(x-x_o)/b\leqslant 92$ and $(x-x_o)/l_{\mathrm{M}}\geqslant 12$; therefore, the locations of virtual origin could not be distinguished from $x_o/b=0$ within present experimental uncertainties. Finally, the source Froude numbers, Fr, defined for adiabatic wall plumes by analogy to free line plumes, as follows:

$$\mathrm{Fr}^2=\rho_o u_o^2/(2bg|\rho_\infty-\rho_o|) \tag{2}$$

were selected to approximate Froude numbers far from the source in order to enhance the development of the flow toward self-preserving behavior, following George et al. [17].

Self-Preserving Scaling

The state relationship for density as a function of mixture fraction, assuming an ideal gas mixture far from the source where the flow becomes self-preserving, is as follows ([18]):

$$\rho=\rho_\infty+f\rho_\infty(1-\rho_\infty/\rho_o),\quad f\ll 1. \tag{3}$$

Assuming approximate self-preserving behavior for adiabatic wall plumes, in the sense discussed earlier, yields the following expressions for mean and fluctuating mixture fractions and velocities ([9]):

$$F(y/(x-x_o)) \text{ or } F'(y/(x-x_o))=(\bar{f} \text{ or } \overline{f'})gB_o^{-2/3}(x-x_o) \times|1-\rho_\infty/\rho_o| \tag{4}$$

$$U(y/(x-x_o)) \text{ or } U'(y/(x-x_o))=(\bar{u} \text{ or } \overline{u'})/B_o^{1/3} \tag{5}$$

$$V(y/(x-x_o)) \text{ or } V'(y/(x-x_o))=(\bar{v} \text{ or } \overline{v'})/B_o^{1/3} \tag{6}$$

where $F(y/(x-x_o))$, $F'(y/(x-x_o))$, etc., are appropriately scaled cross-stream profile functions of mean and fluctuating mixture fractions and velocities, which approximate universal functions far from the source. Characteristic plume widths, l_f and l_u, based on $\bar{f}$ and $\bar{u}$ are also defined, similar to turbulent free line plumes, as follows ([18]):

$$F(l_f/(x-x_o))/F(0)=e^{-1};\quad U(l_u/(x-x_o))/U_{\max}=e^{-1}. \tag{7}$$

For plane turbulent adiabatic wall plumes, F decreases monotonically from its value of $F(0)$ at the wall and there is only one location where Eq. (7) is satisfied. In contrast, U satisfies Eq. (7) at two locations, in the boundary-layer-like region near the wall and in the outer plume-like region; the outer plume-like region is used when applying Eq. (7). The source buoyancy flux, B_o, is a conserved scalar of the flow which can be found as follows for plane plumes having uniform source properties ([9]):

$$B_o=bu_og|\rho_o-\rho_\infty|/\rho_\infty. \tag{8}$$

The corresponding characteristic plume Reynolds number can be written as follows for approximate self-preserving conditions ([1]):

$$\mathrm{Re}_c=\bar{u}_{\max}l_u/\nu_\infty=U_{\max}B_o^{1/3}l_u/\nu_\infty. \tag{9}$$

Values of $U_{\max}$ and l_u were available from measurements in the self-preserving region of the flow for the present test conditions; they were obtained from measurements farthest from the source for earlier studies.

Results and Discussion

Mean Velocities. Distributions of mean velocities in the approximate self-preserving region of the flow will be considered first. Present measurements of cross stream distributions of mean streamwise velocities for the two sources are illustrated in Fig. 1. The scaling parameters of Eq. (5) have been used when plotting the figure so that the value of the ordinate is $U(y/(x-x_o))$. Results for $z/Z=0$ and 1/4 (where z is measured from a position halfway between the ends walls), are in good agreement with each other which confirms the two-dimensionality of the flow. A least-squares correlation of present measurements is shown on this and the following plots to help indicate the trends of the measurements. The present measurements also yield universal distributions within experimental uncertainties for $92\leq(x-x_o)/b\leq155$ and $12\leq(x-x_o)/l_M\leq21$ with flow aspect ratios of $Z/l_u\geq7.9$, as required for self-preserving flow and in agreement with earlier findings for mean mixture fractions due to Sangras et al. [1]. Present conditions within the self-preserving region of the flow correspond to $3800\leq\mathrm{Re}_c\leq6700$ which is similar to the Reynolds number range considered for self-preserving round and plane turbulent plumes by Dai et al. [9,15,16], Dai and Faeth [19], and Sangras et al. [2]. These values are comparable to the largest values of Re_c that have been considered for wakes, which exhibit self-preserving turbulence properties for Re_c as small as 70 ([20]); therefore, present Reynolds numbers are large enough to be representative of fully developed turbulent flows. The adequacy of the present Reynolds number range is also confirmed by present measurements of turbulence spectra to be considered later.

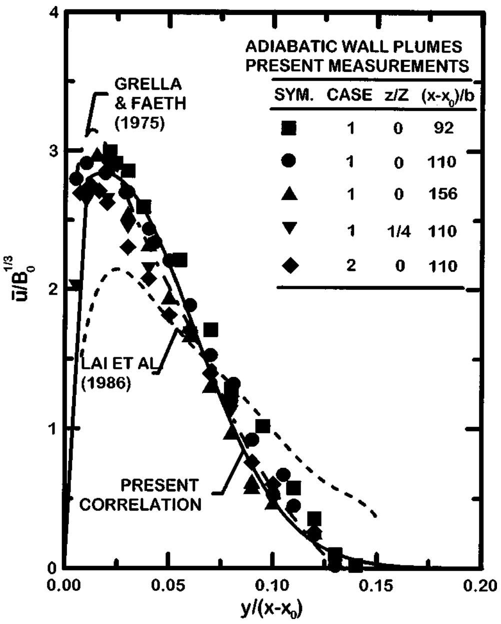

Fig. 1 Cross-stream distributions of mean streamwise velocities in plane adiabatic wall plumes on vertical surfaces. Measurements of Grella and Faeth [4] and Lai et al. [5] and the present investigation. Results from Grella and Faeth [4] and Lai et al. [5] are for their largest distances from the source.

Measurements of U from other studies of turbulent adiabatic wall plumes on vertical surfaces are also plotted in Fig. 1 for comparison with the present measurements, including results from Grella and Faeth [4] and Lai et al. [5]. The measurements of Grella and Faeth [4] and Lai et al. [5] exhibit streamwise variations of U implying that self-preserving behavior was not reached; therefore, their results plotted in Fig. 1 are for conditions farthest from the source.

Considering the three sets of measurements illustrated in Fig. 1, it is evident that the results of Lai et al. [5] are considerably broader than present results (33 percent broader at the $1/e$ points of the distributions) and that while the width of the distribution of Grella and Faeth [4] is comparable to present results, the maximum value of U is somewhat larger. The larger widths of U for the measurements of Lai et al. [5] are typical of conditions in developing plumes before self-preserving behavior is reached. This behavior affects results of Lai et al. [5] which were limited to $(x-x_o)/b\leq37.5$ whereas self-preserving behavior was only observed much farther from the source $(x-x_o)/b\geq92$, during the present study. This behavior is illustrated by the value of $l_f/(x-x_o)$ summarized in Table 2 for the measurements of Lai et al. [5] and the present investigation where the progressive reduction of $l_u/(x-x_o)$ with increasing distance from the source, tending toward values observed in the present investigation, is quite evident. Similar trends were observed with respect to F by Sangras et al. [1]. Distances from the source cannot be quantified for the measurements of Grella and Faeth [4] where an array of small flames was used for the source but consideration of flow widths suggest that their results farthest from the source are approaching self-preserving behavior. As pointed out by Sangras et al. [1], however, the results of Grella and Faeth [4] are still problematical because their evaluations of B_o were based on mean mixture fraction and streamwise velocity distributions which ignores the appreciable streamwise turbulent flux of B_o in the present plumes (found to be 28 percent of the total). This causes value of U from Grella and Faeth [4] to be somewhat overestimated (by roughly

Table 2 Development of plane turbulent adiabatic wall plumes[a]

Source	Condition	$(x-x_o)/b$	$l_u/(x-x_o)$
Lai et al. [5]	developing	10.0	0.183
		20.0	0.133
		37.5	0.108
present	self-preserving	92–156	0.081

[a] Plane turbulent adiabatic wall plumes along smooth vertical surfaces in still and unstratified environments

nine percent based on present measurements of the streamwise turbulent flux of mixture fraction) in agreement with the observations of Fig. 1.

The test conditions and results of various existing velocity measurements of wall plumes and free line plumes are summarized in Table 3. Studies considered include the adiabatic wall plume measurements of Grella and Faeth [4], Lai et al. [5], and the present investigation, the isothermal wall plume measurements of Liburdy and co-workers [21,22] and the free line plume measurements of Rouse et al. [23] and Ramaprian and Chandrasekhara [24]. Parameters are given in the table to the extent that they are known for each study, as follows: the aspect ratio of the source, Z/b, the range of streamwise distances, $(x-x_o)/b$, the smallest flow aspect ratio, $(Z/l_u)_{\min}$, the range of streamwise distances in terms of Morton length scale, $(x-x_o)/l_{\mathrm{M}}$, the characteristic flow width, $l_u/(x-x_o)$, the maximum normalized streamwise velocity, $U_{\max}$, the entrainment coefficient, E_o, and the maximum streamwise and cross-stream velocity fluctuations, $\overline{u}'_{\max}/\overline{u}_{\max}$ and $\overline{v}'_{\max}/\overline{u}_{\max}$. The earlier measurements of Grella and Faeth [4], Lai et al. [5], and Ramaprian and Chandrasekhara [24] continue to vary with increasing distance from the source so that only results farthest from the source are tabulated. The measurements of Rouse et al. [23], Grella and Faeth [4], and Liburdy and co-workers [21,22] employed linear arrays of flames as thermal sources for plumes so that source dimensions cannot be prescribed for these studies. The behavior of mean streamwise velocities for the various wall plumes is similar and has already been discussed in connection with Fig. 1. Earlier measurements of mixture fraction statistics in free-line plumes due to Sangras et al. [2] show that the measurements of Rouse et al. [23] and Ramaprian and Chandrasekhara [24] did not reach self-preserving behavior; nevertheless, it is still interesting to compare these results with present findings for adiabatic wall plumes. In particular, the characteristic plume widths, l_u, are up to 2.1 times larger for free line plumes than for the present adiabatic wall plumes because the presence of the wall inhibits the large-scale turbulent motions that are responsible for the lateral spread of the flow. Effect of the wall on mixing properties will be considered initially by assuming that B_o refers to the buoyancy flux of the entire flow for both wall plumes and free line plumes because this provides a direct indication of the effect of a surface as opposed to a gas mixing region on the mixing properties of the flow. Properties in Table 3 have been computed in this way and show that scaled values of $U_{\max}$ are up to 37 percent smaller for free line plumes than for the present adiabatic wall plumes which indicates a significant effect of the wall on inhibiting mixing of the plumes. The reduced mixing comes about because the wall is less effective in transferring momentum from the flow than mixing with ambient gas on the same side, with additional reduced mixing due to inhibition of large-scale turbulent motion that was mentioned earlier. Some workers seek to account for reduced mixing with the ambient gas on the wall side of an adiabatic wall plume by associating B_o with only the buoyancy flux in half the plume, see Lai et al. [5] and references cited therein. Using this reference condition yields $U_{\max}$ up to seven percent smaller for free line plumes than for the present adiabatic wall plumes as a direct effect of the wall on inhibiting mixing of the plumes. These effects have unfortunate implications for unwanted fires because reduced mixing rates allow heated regions containing toxic substances to extend farther from the source than would be the case for unconfined plumes ([1]).

Present measurements of cross-stream distributions of mean cross-stream velocities for the two sources are illustrated in Fig. 2. The scaling parameters used for the figure provide universal plots in the self-preserving region as well as a check of the internal consistency of the present measurements of $\overline{u}$ and $\overline{v}$. Carrying out this evaluation as described by Dai et al. [15] based on the present streamwise velocity measurements illustrated in Fig. 1, yields the prediction calculated from the continuity equation illustrated in Fig. 2. The measurements illustrated in Fig. 2 exhibit universal behavior for the two test plumes, as anticipated for the self-preserving region. Additionally, the measurements of $\overline{v}$ also are consistent with the present measurements of $\overline{u}$ through the continuity equation.

The asymptotic values of $\overline{v}$ at large values of $y(x-x_o)$ are proportional to the entrainment constant of the plumes, which is important for integral theories of plume scaling and as a measure of turbulent mixing rates ([7,11]). Entrainment behavior can be seen by integrating the continuity equation in the cross-stream direction to obtain an expression for the rate of change of the volumetric flow rate within the plume, per unit plume length, at self-preserving conditions where the density of the flow is nearly constant, as follows:

$$d/dx\int_0^\infty \overline{u}dy = dQ/dx = -\overline{v}_\infty . \tag{10}$$

Table 3 Summary of self-preserving properties of plane buoyant turbulent plumes[a]

Source	Present Study	Lai et al. [5][b]	Grella & Faeth [4][b,c]	Liburdy & Co-workers [21,22][b,c]	Ramaprian & Chandrasekhara [24][d]	Rouse et al. [23][b,c]
Plume Type	Adiabatic Wall	Adiabatic Wall	Adiabatic Wall	Isothermal Wall	Free-line	Free-line
Z/b	93	38	⋯	⋯	50	⋯
$(x-x_o)/b$	92–156	10–38	⋯	⋯	25–65	⋯
$(Z/l_u)_{\min}$	7.9	10.8	13.0	5.9	2.6[d]	⋯
$(x-x_o)/l_{\mathrm{M}}$	12–21	1–5	⋯	⋯	3–15	⋯
$l_u/(x-x_o)$	0.081	0.117	0.080	0.124	0.126	0.177
$U_{\max}$	2.84	2.14	3.16	2.90	2.10	1.80
E_o	0.068	0.071	0.067	0.096	0.11	0.14
$\overline{u}'_{\max}/\overline{u}_{\max}$	0.26	0.25	0.16	0.20	0.27	⋯
$\overline{v}'_{\max}/\overline{u}_{\max}$	0.17	0.18	⋯	0.11	0.20	⋯

[a] Plane buoyant turbulent plumes in still and unstratified environments. Range of streamwise distances are for conditions where quoted self-preserving properties were found from measurements over the cross section of the plumes. Entries are ordered chronologically.

[b] These flows were evolving over the range of the measurements and results shown pertain to distances farthest from the source.,

[c] Source was a linear array of round jets so that slot properties cannot be specified.

[d] This value is $(Z/(2l_u))_{\min}$ which is the full width of the flow, similar to wall plume entries.

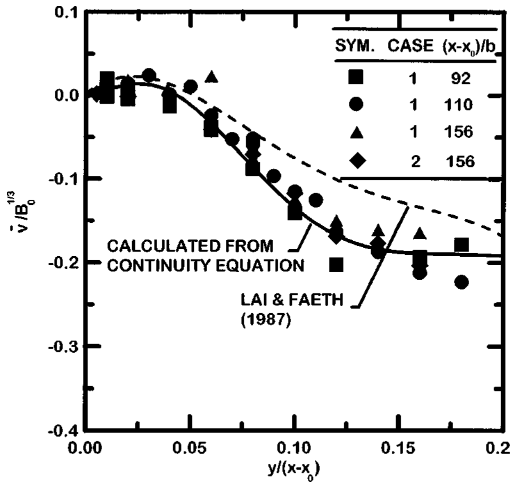

Fig. 2 Cross-stream distributions of mean cross-stream velocities in plane adiabatic wall plumes on vertical surfaces. Measurements of Lai and Faeth [13] and the present investigations. Results from Lai and Faeth [13] are for their largest distances from the source.

Then defining the entrainment constant based on $\overline{u}_{\max}$, there results

$$E_o = -\overline{v}_\infty / \overline{u}_{\max} \tag{11}$$

which provides the result summarized in Table 3. Notably, measured entrainment constants for the three adiabatic wall plume studies are in excellent agreement in spite of potential effects of flow development (problems of finding B_o accurately are not a factor here because this parameter does not appear in Eq. (11)). Values of E_o, however, are only roughly half as large for wall plumes than for free line plumes which is consistent with effects of the wall inhibiting turbulent mixing as mentioned earlier (with potential effects of flow development for the free-line plumes being a contributing factor).

Velocity Fluctuations. Measurements of cross-stream distributions of streamwise and cross-stream velocity fluctuations are illustrated in Fig. 3. In addition to the present measurements for the same conditions as the measurements of U in Fig. 1, other measurements for adiabatic wall plumes have been plotted from Grella and Faeth [4], Lai et al. [5], and Lai and Faeth [13]. As before, the earlier measurements do not extend to fully self-preserving conditions so that only their results farthest from the source are shown. The scaling used for the variables in Fig. 3 is the same as Figs. 1 and 2 and corresponds to the self-preserving variables, U' and V', of Eqs. (5) and (6).

Present measurements of U' and V' in Fig. 3 exhibit self-preserving behavior within experimental uncertainties over the test range. Values of U' and V' become small as the wall and the free stream are approached and reach a maximum near $y/(x-x_o) \approx 0.05$, which is in the region of the maximum mean streamwise velocity gradient (see Fig. 1) where turbulence production is a maximum. Maximum velocity fluctuations in adiabatic wall plumes and free-line plumes, and the value of anisotropy based on maximum velocity fluctuations of 3/2, are similar, see Table 3. In contrast, the effect of the wall on stabilizing mixing is more apparent for mixture fraction fluctuation intensities where maximum values are larger, 47 percent, for free-line plumes than for adiabatic wall plumes, 37 percent. Finally, present values of velocity fluctuations generally are larger than the earlier measurements of Grella and Faeth [4], Lai and Faeth [13], and Lai et al. [5]; this can be attributed to effects of flow development, with problems of using hot wires in strongly turbulent flows serving as a contributing factor for the measurements of Grella and Faeth [4].

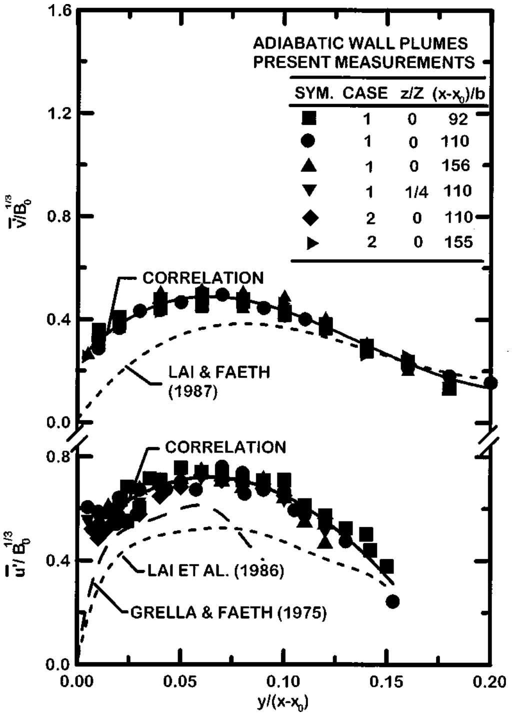

Fig. 3 Cross-stream distributions of fluctuating cross-stream and streamwise velocities in plane adiabatic wall plumes on vertical surfaces. Measurements of Grella and Faeth [4], Lai et al. [5], and Lai and Faeth [13] and the present investigation. Results from Grella and Faeth [4], Lai et al. [5], Lai and Faeth [13] are for their largest distances from the source.

Temporal Power Spectral Densities. Typical temporal power spectra of streamwise and cross stream velocity fluctuations are illustrated in Figs. 4 and 5 for self-preserving turbulent adiabatic wall plumes. These results are for various cross-stream positions, $y/(x-x_0)=0.02\text{–}0.08$, for $(x-x_0)/b=110$ and 156 for the case 1 plume but results for other self-preserving conditions are similar. The measurements of streamwise spectra are normal-

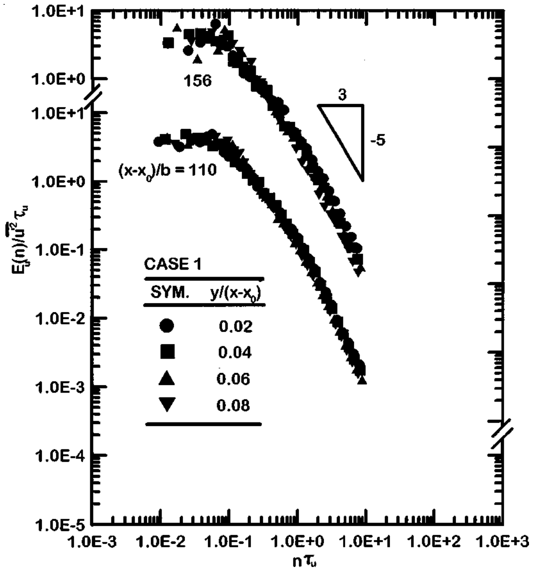

Fig. 4 Temporal power spectra of streamwise velocity fluctuations in the self-preserving region of plane adiabatic wall plumes on vertical surfaces

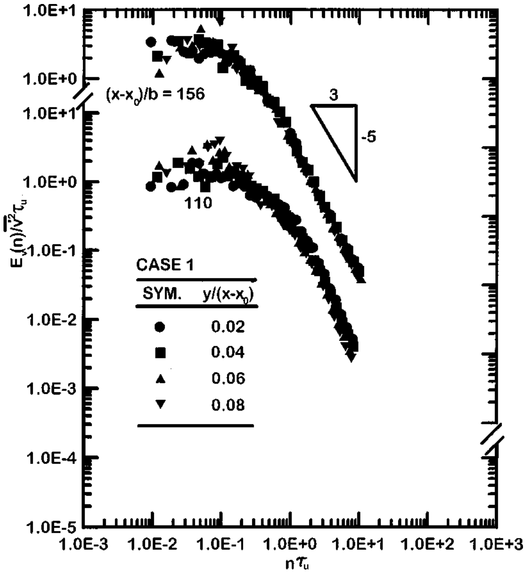

Fig. 5 Temporal power spectra of cross-stream velocity fluctuations in the self-preserving region of plane adiabatic wall plumes on vertical surfaces

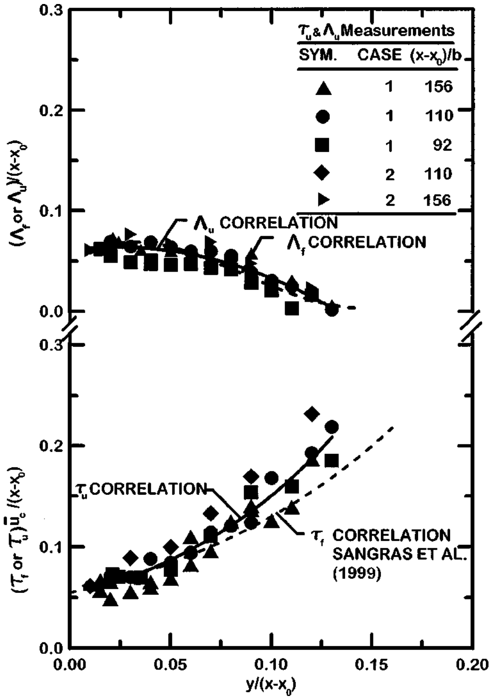

Fig. 6 Temporal and spatial integral scales of mixture fraction and streamwise velocity fluctuations in the self-preserving region of plane adiabatic wall plumes on vertical surfaces

ized by local turbulence properties as described by Hinze [6]; the measurements of cross-stream spectra are normalized using the same parameters. The spectra are relatively independent of both radial and streamwise position when normalized in the manner of Figs. 4 and 5. The spectra decay according to the $-5/3$ power of frequency, analogous to the well-known inertial-convective region for scalar property and velocity fluctuations in nonbuoyant turbulence ([3]), for the range of frequencies that could be considered during the present investigation. Usually, a decay according to the -3 power of frequency, analogous to the inertial-diffusion region seen for turbulence in buoyant flows, is observed at larger frequencies, see Sangras et al. [1]. Unfortunately, this region could not be observed during the present investigation due to dynamic range limitations of the present LV measurements ([25]). In spite of this limitation, however, it is evident that present spectra are noise-free for several decades implying reasonably accurate determinations of velocity fluctuations. An apparent exception is the scattering of the spectra for cross-stream velocity fluctuations at small frequencies seen in Fig. 5. This apparent scattering comes about due to a dip in the spectra of cross stream velocity fluctuations at small frequencies, see Hinze [6], which tends to look like noise when results for various positions in the flows are illustrated because the dip does not begin at exactly the same normalized frequency at all positions in the self-preserving region of the plumes.

Integral Scales. Measured values of temporal integral scales based on streamwise velocity fluctuations for the present self-preserving turbulent adiabatic wall plumes are illustrated in Fig. 6. Earlier measurements of temporal integral scales based on mixture fraction fluctuations, due to Sangras et al. [1], are also shown on the plot for comparison with the present measurements. Additionally, spatial integral scales were found from the temporal integral scale data using Taylor's hypothesis, e.g.,

$$\Lambda_u = \bar{u}\tau_u, \quad \Lambda_f = \bar{u}\tau_f \qquad (12)$$

and are also illustrated in Fig. 6. Self-preserving normalization has been used for all the integral scales, similar to earlier treatments of integral scales for round buoyant turbulent plumes ([15,16,18]). All the integral scales approximate universal behavior for self-preserving conditions when plotted in the manner of Fig. 6. Spatial integral sales progressively decrease as the cross-stream distance increases, which is expected considering the topography of the turbulence-containing region of the flow. The corresponding increase of temporal integral scales near the edge of the flow is caused by smaller mean velocities in this region through Taylor's hypothesis.

Conclusions

Velocity statistics were measured in turbulent adiabatic wall plumes rising along plane smooth vertical walls in still air. Conditions far from the source were emphasized where effects of source disturbances are lost and the outer plume-like region of the flow approximates self-preserving behavior with scaling similar to self-preserving free line plumes. The test conditions consisted of buoyant jet sources of helium and air mixtures to obtain the source properties summarized in Table 1 with measurements involving $(x-x_o)/b$ in the range 92–155 and $(x-x_0)/l_M$ in the range 12–21. The major conclusions of the study are as follows:

1 The present measurements yielded distributions of mean streamwise velocities in self-preserving plumes that were up to 22 percent narrower, with maximum scaled values up to 75 percent different, than earlier measurements in the literature. There were two main reasons for these differences: the results of Lai et al. [5] were limited to $(x-x_o)/b \leq 38$, which is not a sufficient distance from the source to observe self-preserving behavior in spite of effects to promote rapid streamwise development of the flow; and in the case of Grella and Faeth [4], estimations of buoyancy fluxes based on measured profiles of mean mixture fractions and velocities introduce significant experimental uncertainties and overestimate normalized streamwise velocities because the relatively large streamwise turbulent flux of B_o (comprising 28 percent of the total based on present measurements) is ignored.

2 Cross-stream distributions of velocity fluctuations are anisotropic near the maximum velocity condition ($\overline{u'}/\overline{v'} \approx 1.5$) with a tendency to become more isotropic near the edge of the flow. Maximum intensities of streamwise velocity fluctuations, 26 percent, are comparable to observations in free line plumes but are significantly smaller than maximum intensities of mixture fraction fluctuations, 47 percent, which are enhanced due to buoyancy/turbulence interactions. Present normalized values of velocity

fluctuations are also roughly 30 percent larger than earlier observations of Lai et al. [5] and Grella and Faeth [4] due to problems of flow development and buoyancy flux determinations for these earlier studies that were mentioned earlier.

3 Present measurements of velocity statistics support earlier findings based on mixture fraction statistics that the self-preserving plane turbulent adiabatic wall plumes mix much slower than comparable for free-line plumes having the same buoyancy flux. In particular, characteristic plume widths are up to 100 percent larger and scaled maximum mean streamwise velocities are up to 40 percent smaller for free-line plumes than for the present adiabatic wall plumes. These differences come about because the wall limits mixing to one side of the flow and inhibits the large-scale motion that is mainly responsible for turbulent mixing.

4 Temporal power spectra of velocity fluctuations scale in a relatively universal manner. The spectra exhibit the well known $-5/3$ power inertial-convective decay region but present measurements did not extend to sufficiently large frequencies to resolve the -3 power inertial-diffusive decay region that is generally observed in buoyant turbulent flows.

5 Temporal and spatial integral scales could be correlated in a relatively universal manner in terms of self-preserving parameters. Temporal integral scales were smallest near the maximum streamwise velocity condition which follows from Taylor's hypothesis in view of the relatively slow variation of integral length scales in this region.

Acknowledgments

This research was supported by the United States Department of Commerce, National Institute of Standards and Technology, Grant No. 60NANB4D1696, with H. R. Baum of the Building and Fire Research Laboratory serving as Scientific Officer.

Nomenclature

b = source width
B_o = source buoyancy flux
d = source diameter
E_o = entrrainment constant, Eq. (11)
$E_u(n), E_v(n)$ = temporal power spectral densities of u and v
f = mixture fraction
$F(y/(x-x_o))$ = normalized self-preserving cross stream distribution of $\overline{f}$
$F'(y/(x-x_o))$ = normalized self-preserving cross stream distribution of $\overline{f'}$
Fr_o = source Froude number, Eq. (2)
g = acceleration of gravity
l_f = characteristic plume width based on $\overline{f}$, Eq. (7)
l_M = Morton length scale, Eq. (1)
l_u = characteristic plume width based on $\overline{u}$, Eq. (7)
n = frequency
PDF(f) = probability density function of mixture fraction
Q = plume volumetric flow rate per unit length
Re_c = characteristic plume Reynolds number, Eq. (9)
Re_o = source Reynolds number, $2\overline{u}_o b/v_o$
u = streamwise velocity
$U(y/(x-x_o))$ = normalized self-preserving cross stream distribution of $\overline{u}$
$U'(y/(x-x_o))$ = normalized self-preserving cross stream distribution of $\overline{u'}$
$V(y/(x-x_o))$ = normalized self-preserving cross stream distribution of $\overline{v}$
$V'(y/(x-x_o))$ = normalized self-preserving cross stream distribution of $\overline{v'}$
v = cross stream velocity
x = streamwise distance
y = cross stream distance
z = distance along source from its midplane location
Z = source length
Λ_f = spatial integral scale of mixture fraction fluctuations
Λ_u = spatial integral scale of streamwise velocity fluctuations
ν = kinematic viscosity
ρ = density
τ_f = temporal integral scale of mixture fraction fluctuations
τ_u = temporal integral scale of streamwise velocity fluctuations

Subscripts

max = condition where the property reaches a maximum value
o = initial value or virtual origin location
∞ = ambient value

Superscripts

$\overline{(\ )}$ = time-averaged mean value
$(\ )'$ = root-mean-squared fluctuating value

References

[1] Sangras, R., Dai, Z., and Faeth, G. M., 1999, ''Mixture Fraction Statistics of Plane Self-Preserving Buoyant Turbulent Adiabatic Wall Plumes,'' ASME J. Heat Transfer, **121**, pp. 837–843.
[2] Sangras, R., Dai, Z., and Faeth, G. M., 1998, ''Mixing Structure of Plane Self-Preserving Buoyant Turbulent Plumes,'' ASME J. Heat Transfer, **120**, pp. 1033–1041.
[3] Tennekes, H., and Lumley, J. L., 1972, *A First Course in Turbulence*, M.I.T. Press, Cambridge, MA, pp. 113–124.
[4] Grella, J. J., and Faeth, G. M., 1975, ''Measurements in a Two-Dimensional Thermal Plume Along a Vertical Adiabatic Wall,'' J. Fluid Mech., **71**, pp. 701–710.
[5] Lai, M.-C., Jeng, S.-M., and Faeth, G. M., 1986, ''Structure of Turbulent Adiabatic Wall Plumes,'' ASME J. Heat Transfer, **108**, pp. 827–834.
[6] Hinze, J. O., 1975, *Turbulence*, 2nd Ed., McGraw-Hill, New York, pp. 175–319, pp. 614–638.
[7] Ellison, T. H., and Turner, J. S., 1959, ''Turbulent Entrainment in Stratified Flows,'' J. Fluid Mech., **6**, pp. 423–448.
[8] Lee, S. L., and Emmons, H. W., 1961, ''A Study of Natural Convection Above a Line Fire,'' J. Fluid Mech., **11**, pp. 353–368.
[9] List, E. J., 1982, ''Turbulent Jets and Plumes,'' Annu. Rev. Fluid Mech., **14**, pp. 189–212.
[10] Papanicolaou, P. N., and List, E. J., 1987, ''Statistical and Spectral Properties of Tracer Concentration in Round Buoyant Jets,'' Int. J. Heat Mass Transf., **30**, pp. 2059–2071.
[11] Turner, J. S., 1973, *Buoyancy Effects in Fluids*, Cambridge University Press, Cambridge, UK, pp. 165ff.
[12] Ljuboja, M., and Rodi, W., 1981, ''Prediction of Horizontal and Vertical Turbulent Buoyant Wall Jets,'' ASME J. Heat Transfer, **103**, pp. 343–349.
[13] Lai, M.-C., and Faeth, G. M., 1987, ''Turbulence Structure of Vertical Adiabatic Wall Plumes,'' ASME J. Heat Transfer, **109**, pp. 663–670.
[14] Gutmark, E., and Wygnanski, I., 1976, ''The Plane Turbulent Jet,'' J. Fluid Mech., **73**, pp. 465–495.
[15] Dai, Z., Tseng, L.-K., and Faeth, G. M., 1995, ''Velocity Statistics of Round, Fully-Developed Buoyant Turbulent Plumes,'' ASME J. Heat Transfer, **117**, pp. 138–145.
[16] Dai, Z., Tseng, L.-K., and Faeth, G. M., 1995, ''Velocity/Mixture-Fraction Statistics of Round, Self-Preserving Buoyant Turbulent Plumes,'' ASME J. Heat Transfer, **117**, pp. 918–926.
[17] George, Jr., W. K., Alpert, R. L., and Tamanini, F., 1977, ''Turbulence Measurements in an Axisymmetric Buoyant Plume,'' Int. J. Heat Mass Transf., **20**, pp. 1145–1154.
[18] Dai, Z., Tseng, L.-K., and Faeth, G. M., 1994, ''Structure of Round, Fully-Developed, Buoyant Turbulent Plumes,'' ASME J. Heat Transfer, **116**, pp. 409–417.
[19] Dai, Z., and Faeth, G. M., 1996, ''Measurements of the Structure of Self-

Preserving Round Buoyant Turbulent Plumes,'' ASME J. Heat Transfer, **118**, pp. 493–495.

[20] Wu, J.-S., and Faeth, G. M., 1993, ''Sphere Wakes in Still Surroundings at Intermediate Reynolds Numbers,'' AIAA J., **31**, pp. 1448–1455.

[21] Liburdy, J. A., and Faeth, G. M., 1978, ''Heat Transfer and Mean Structure of a Turbulent Thermal Plume Along Vertical Isothermal Walls,'' ASME J. Heat Transfer, **100**, pp. 177–183.

[22] Liburdy, J. A., Groff, E. G., and Faeth, G. M., 1979, ''Structure of a Turbulent Thermal Plume Rising Along an Isothermal Wall,'' ASME J. Heat Transfer, **101**, pp. 299–355.

[23] Rouse, H., Yih, C. S., and Humphreys, H. W., 1952, ''Gravitational Convection From a Boundary Source,'' Tellus, **4**, pp. 201–210.

[24] Ramaprian, B. R., and Chandrasekhara, M. S., 1989, ''Measurements in Vertical Plane Turbulent Plumes,'' ASME J. Fluids Eng., **111**, pp. 69–77.

[25] Adrian, R. J., and Yao, C. S., 1987, ''Power Spectra of Fluid Velocities Measured by Laser Doppler Velocimetry,'' Exp. Fluids, **5**, pp. 17–28.

An Experimental Study on Mixed Convection in a Horizontal Rectangular Channel Heated From a Side

C. Gau
Professor
e-mail: gauc@mail.ncku.edu.tw

Y. C. Jeng
Graduate Student

C. G. Liu
Graduate Student

Institute of Aeronautics and Astronautics,
National Cheng Kung University,
Tainan 70101, Taiwan, R.O.C.

Experiments are performed to study the mixed convection flow and heat transfer in a horizontal rectangular channel heated from a side. The channel is made of two vertical parallel plates with one of the plates heated uniformly and the opposite plate well insulated. The gap between the parallel plates is small and the height to gap ratio of the channel cross section is 6.67. Both flow visualization and the heat transfer along the heated wall are measured. The Reynolds number ranges from 317 to 2000, the buoyancy parameter, $\mathrm{Gr}/\mathrm{Re}^2$*, from 0 to 20000 and Pr of the air flow is 0.7. Flow structure inside the channel is visualized by injecting smoke at the inlet flowing along the heated side wall. The heated buoyant flow accumulates in the upper region of the channel, which grows in size as the buoyancy parameter increases. The accumulated flow is thermally stable and has a slower motion which can reduce the heat transfer enhancement by the buoyancy force. The effect of the Reynolds number and the buoyancy parameter on the heat transfer is presented and discussed. Comparisons of the Nusselt numbers with the case of the vertical channel flow and the prediction similar to the case of a horizontal flow through a heated vertical plate are also made. The normalized Nusselt numbers are found in proportion to the buoyancy parameter, correlations of the heat transfer data in terms of this parameter have been very successful.* [S0022-1481(00)01404-3]

Keywords: *Channel Flow, Heat Transfer, Mixed Convection*

Introduction

Mixed convection in channels has received great interest in the last three decades for its practical application in the solar energy collectors, heat exchangers, geothermal energy systems, chemical deposition of solid layer in the semiconductor industry, and the cooling of the nuclear reactor and modern electronic equipment. Most of the work in the past has been concerned with the mixed convection in a vertical parallel-plate channel ([1–5]), or a horizontal parallel-plate channel ([6–11]). Review on the relevant work can be found in Aung ([1]).

However, different orientations or heating conditions of the channel can induce different kinds of heated buoyant flows which enhance the heat transfer in different manners. For asymmetric heated vertical channel, when the buoyancy parameter is not large, the small amount of the buoyant flow induced along the heated wall can either assist or oppose the mainflow and cause either enhancement or reduction in the heat transfer. When the buoyancy parameter becomes large, the heated buoyant flow along the side wall become substantial. Depending upon the flow direction of the mainstream, the buoyant flow can cause different kinds of flow reversals which will alter the entire flow characteristic and enhance the heat transfer in different manners. For horizontal channel, the heating is usually from the below. Therefore, enhancement in the heat transfer can be obtained from the initiation of the secondary flow. This secondary flow is usually a heated buoyant flow which forms in mushroom shaped plumes associated with vortices. This kind of secondary flow is a laminar plume in the upstream and may have a transition into a two-dimensional convection rolls, a very irregular flow or even a turbulent flow in the downstream. The transition into different flows depends on the magnitudes of the Reynolds number and the buoyancy parameter. Therefore, it appears that the mixed convection in a channel with different orientations or heating conditions differs so drastically that studies on the flow and heat transfer in such a different channel must be carefully performed in a separate manner.

The current geometry of channel is a horizontal channel formed by two 20 cm×45 cm vertical parallel-plate with one of the walls heated uniformly and the other well insulted. The gap between the parallel-plate is narrow and is 3 cm. The current configuration of geometry has the potential application in the cooling of electronic equipment. When the circuit boards with electronic circuits printed in one side of the walls are arranged in parallel with passage in between for cooling air moving horizontally, one will have the current configuration of channel. It appears that the heat transfer data obtained before in both the heated vertical channel or the horizontal channel heated from below could not be used in the current geometry. Work in this kind of channel and heating condition is not found in literature. Therefore, a systematic study on the mixed convection flow and the heat transfer is needed. Both flow visualization and heat transfer measurements are performed to gain a good understanding of the physical process and to provide some useful data.

Experimental Apparatus and Procedures

Experiments are performed in a Plexiglas made parallel-plate channel, as shown in Fig. 1. The channel is 45 cm in length, 20 cm in height inside, and 3 cm in width (gap) at the entrance. All the Plexiglas walls have a thickness of 1.27 cm. This channel is very similar to the ones used in the reference ([11,12]), except that the channel is rotated 90° about the *x* axis. The vertical side wall is heated uniformly and the opposite wall is well insulated. The uniform heating of the wall is achieved by gluing a number of 0.015 mm thin stainless steel foil strips on the entire side wall and passing an electric current through the foil heater. DC power is

---

Contributed by the Heat Transfer Division for publication in the JOURNAL OF HEAT TRANSFER. Manuscript received by the Heat Transfer Division June 11, 1999; revision received May 1, 2000. Associate Technical Editor: A. Majumdar.

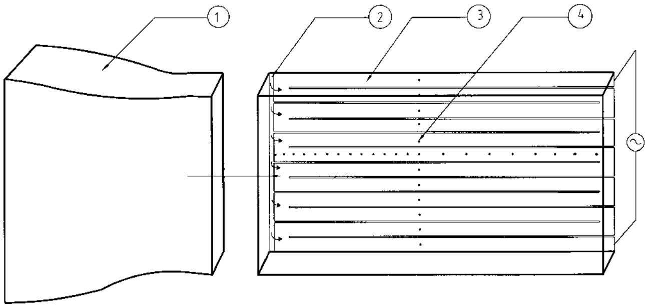

Fig. 1 Schematic diagram of the channel: 1) wind tunnel, 2) slot for smoke injection, 3) stainless steel foil, 4) 12 rows of thermocouples in the transverse direction

used to provide the electric energy for generating the desired heat flux. The heat flux can be determined by the electric voltage and current passing through the foil. The electric voltage drop due to the contact resistance between the heating strips and the terminals, which connect the heating strips with the DC power supply, has been taken into account. This kind of voltage drop is also noticed in other experiments ([13]). For better insulation, a 12 cm thick foamed rubber is glued on the back of the heated wall. All the other side walls are wrapped with 3 cm thick foam rubber.

Since the temperature variation of the heated wall may be large in the vertical direction, the heated wall is instrumented with 12 rows of chromel–alumel thermocouples. Each row has a total of 23 thermocouples. The vertical distance between two neighboring rows is 1.52 cm, and the longitudinal spacing between two neighboring thermocouples in the entrance region is 1.5 cm, while near the exit the spacing is 3 cm. Since the surface temperature of the insulated wall is needed for estimating the radiation loss from the heated wall, five additional thermocouple are embedded along the surface of the wall. All thermocouples are calibrated in a constant temperature bath and the measurement error is found to be within ±0.1°C. All the temperature signals are acquired with a FLUKE-2287A data logger connected to a computer for direct processing. The temperature data are taken when the entire system reaches steady state, usually in 3–4 hours.

The wind tunnel is a blowdown type which is similar to the one used in the studies of mixed convection in a heated vertical convergent or divergent channel ([4,11]) except that the insulated wall used here is not tilted, hence a detailed description is omitted here. The calibration needed for velocity measurement is also described in these reports. The total heat input in a single heating strip can be determined by the electric voltage and current passing through the strip. Since both conduction and radiation losses from each heating strip need to be accounted for and subtracted from the total energy supplied by the heater, the local heat transfer coefficient is evaluated by the following equation:

$$h_l=(q_t-q_{\mathrm{rad}}-q_{\mathrm{cond}})/(T_w-T_o) \tag{1}$$

where T_w is the temperature on the heating strip. The conduction loss from the heated wall is estimated by a one-dimensional conduction equation in a composite wall. The procedure to calculate the radiation loss from the heated wall is very similar to the one described in Webb and Hill ([13]) and will not be repeated here. The thermophysical properties used in the local Nusselt number are evaluated at the bulk mean temperature of the flow, while those in the Reynolds and Grashof numbers are evaluated at the inlet temperature.

Since the channel flow exits directly to the ambient, the heat loss is relatively large near the exit. Therefore, the last three heating strips are used only as guard heaters. Relatively large heat loss in the exit region is also found in other experiments ([5,13]). The uncertainty of the experimental data is determined according to the procedure proposed by Kline and McClintock ([14]). The maximum uncertainty of local Nusselt number is 5.6 percent, while that for the Reynolds and Grashof number are 6.2 percent and 7.8 percent, respectively.

During the flow visualization experiments, a smoke generator is used to supply smoke of fine particles. The smoke particles are measured to be in a scale of 2 μm and are small enough to trace the flow in the channel. Smoke enters the channel from a slot of 1 mm width located on the vertical side wall in the immediate upstream of the channel entrance. A vertical sheet of light perpendicular to the side insulated wall is used to visualize the circulation structure of secondary flow; while the sheet of light from the end parallel to the flow passage is used to visualize the flow structure from the side view. The flow patterns at the upstream, the central, and the downstream regions can be observed and recorded. The smoke particles injected were found to have no obvious effect on the heat transfer after rerunning the heat transfer measurements. During the experiments, the flow structure in the channel is sensitive to the circulation of ambient flow. Therefore, a wind shield is constructed around the exit of the channel to prevent this possible extraneous effect.

Results and Discussion

1. Flow Visualizations. The smoke exits from a vertical, narrow slot on the heated side wall at the inlet of the channel, and enters smoothly, as shown in Fig. 1, into the channel forming a vertical thin sheet of smoke along the side wall. As the thin-sheet smoke is heated, it moves upward, due to the buoyancy force, until reaching the top wall of the channel. The heated flow is essentially accumulated in the upper region of the channel as it moves downstream, as shown in Fig. 2. The accumulated flow circulates slowly in the upper region of the channel and grows in size due to the continuous supply of the heated buoyant flow along the side wall. The streamwise velocity of the accumulated flow is much slower than the mainstream. This is attributed to the heated buoyant flow along the vertical side wall which can create a higher pressure in the upper region of the downstream flow, and thus result in a lower pressure gradient in the upper region than in the lower region of the flow. This lower axial pressure gradient can reduce the streamwise velocity in the upper region. Therefore, one could expect a lower heat transfer inside the accumulated flow region than the outside. The smoke region shown in Fig. 3 is the

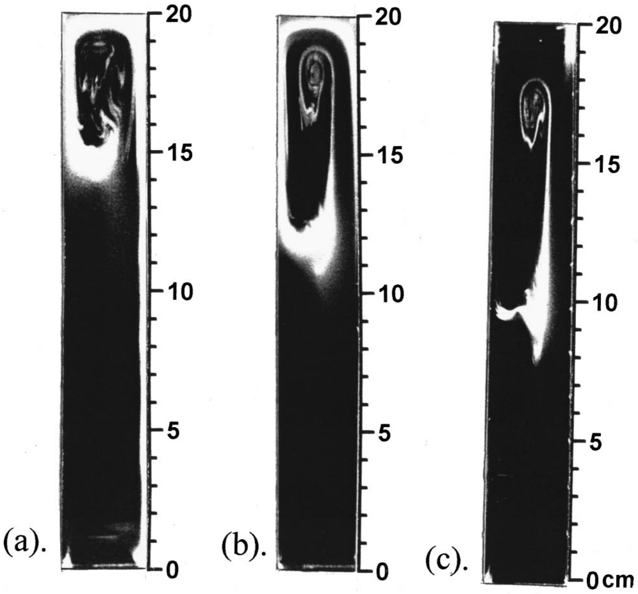

Fig. 2 Flow structure from the end view with Re=500 and Gr/Re^2=7700 at (*a*) x=10 cm, (*b*) x=20 cm, and (*c*) x=30 cm

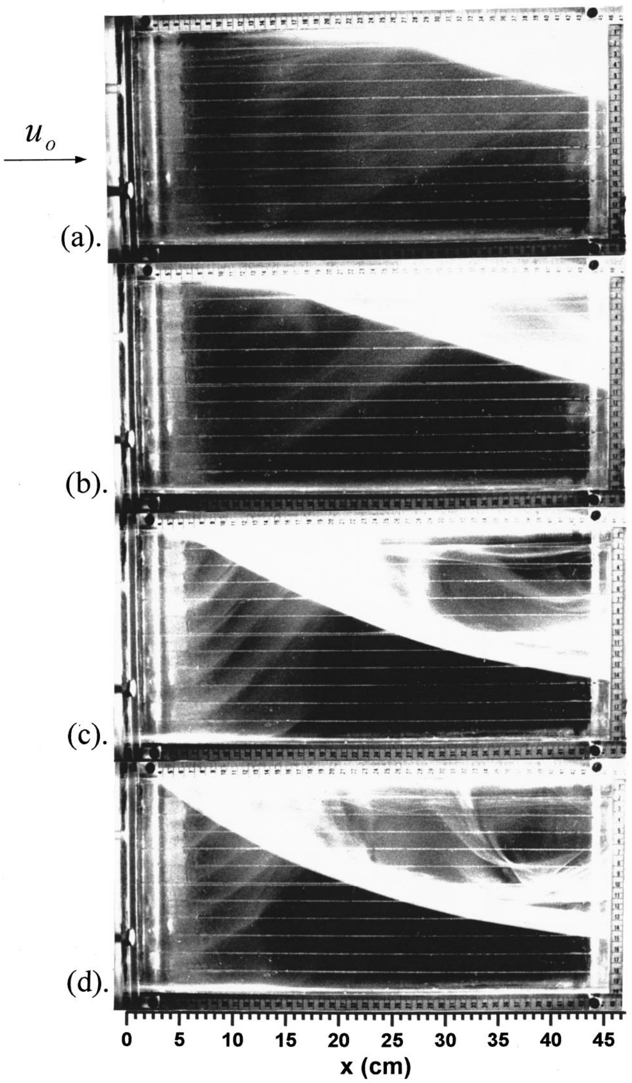

Fig. 3 Flow structure from the side view with Re=500 and (*a*) Gr/Re^2=1000, (*b*) Gr/Re^2=2000, (*c*) Gr/Re^2=6000, and (*d*) Gr/Re^2=7700

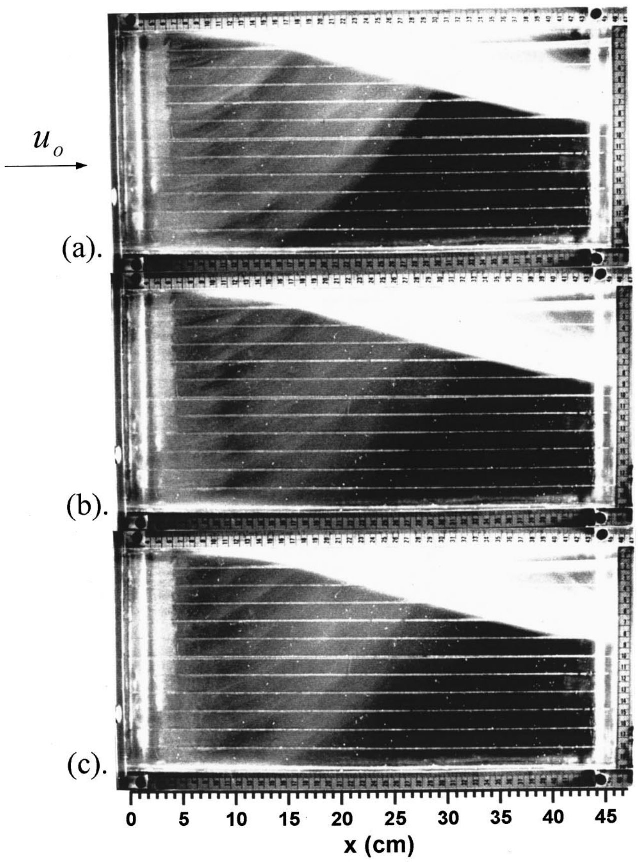

Fig. 4 Flow structure from the side view with Gr/Re^2=2000 and (*a*) Re=500, (*b*) Re=700, and (*c*) Re=1000

accumulated flow which occurs in the upper right portion of the channel as the flow enters the channel from the left end. Since the accumulated flow is warmer than the mainstream below, it is thermally stable. Therefore, the mainstream below will not break into the accumulated flow region, mix with it, and carry away even a small portion of the accumulated flow. Therefore, the accumulated flow maintains a very stable condition and does not vary in size or location with time.

As the buoyancy parameter increases, the accumulated flow region is initiated earlier and become larger in size, as shown in Figs. 3(*a*), (*b*), and (*c*). At the extreme condition, e.g., Gr/Re^2 =7700 as shown in Fig. 3(*d*), the heated buoyant flow starts accumulating at the entrance and the accumulated flow region has the largest size in the transverse direction. Even at this condition, the accumulated flow is still very stable. One can expect a reduction in the heat transfer in the region covered by the accumulated flow.

As the Reynolds number increases by increasing the flow velocity, one may expect that the entire accumulated flow region shifts downstream and leads to shrink in size. This may lead to the increase in the overall heat transfer enhancement by the buoyancy force. The downstream motion of the heated buoyant flow for mixed convection in a heated vertical channel indeed occurs ([3,4]) as the Reynolds number increases, but this leads to reduction in the heat transfer enhancement by the buoyancy force. In the current experiments, however, previous expectation is not true if the buoyancy parameter Gr/Re^2 is kept constant. As shown in Fig. 4, the entire accumulated flow region does not alter in size, shape, and location as the Reynolds number increases, but the buoyancy parameter is kept constant. This is attributed to the fact that by keeping Gr/Re^2 constant the increase in the Reynolds number is counterbalanced by the increase in Grashof number, i.e., the increase in the inertia force in the streamwise direction is counterbalanced by the increase in the buoyancy force in the transverse direction. This leads to a result that the entire accumulated flow region stays in the same shape and position as long as the buoyancy parameter is maintained constant. It means that the enhancement in the overall heat transfer by the buoyancy force will remain the same if the buoyancy parameter is kept constant.

2. Mixed Convection Heat Transfer. To validate the heat transfer data measured the Nusselt numbers for pure forced convection in the current channel are also measured and compared with the data and the prediction published in the literature ([4,15]). The current data follow the prediction of Natio ([15]) within graphical accuracy and agree well with the data of Huang et al. ([4]) and Jeng ([16]). This gives us confidence on the heat transfer data for the case of mixed convection. The entire distributions of the Nusselt numbers along the heated side wall are shown in Fig. 5. The Nusselt numbers vary not only along the streamwise direction, but also the transverse direction. The variation in the transverse direction is attributed only to the free convection effect which makes the heat transfer in the lower region of the channel higher than the upper region. The variation in the

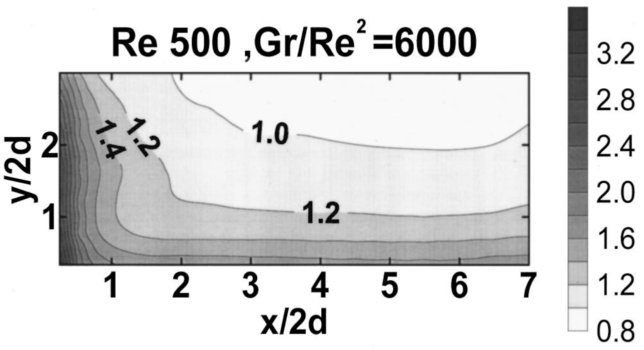

Fig. 5 The Nusselt number contours on the heated side wall with Gr/Re^2=6000 and Re=500

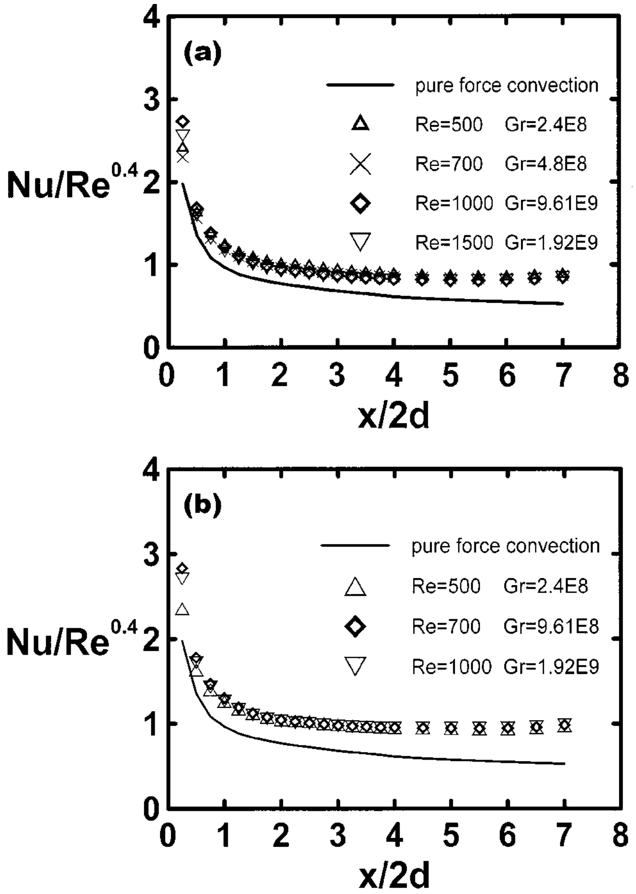

Fig. 6 The normalized Nusselt number distributions at different Reynolds numbers with (*a*) Gr/Re^2 very close to 1000 and (*b*) Gr/Re^2 very close to 2000

streamwise direction is attributed to the combined free and forced convection. By carefully examining the heat transfer data in the accumulated flow region and the region outside, one found that the heat transfer in the accumulated flow region is essentially lower, as expected, due to the lower velocity of the flow in both the transverse and the streamwise direction. At a given streamwise location, the Nusselt numbers at different heights differ due to the effect of the free convection and the accumulated flow. It appears that the Nusselt number distribution in the transverse direction can be averaged and the averaged value represents the mixed convection heat transfer with an averaged effect of free convection or the buoyancy force in the transverse direction. To simplify the presentation and the analysis, the Nusselt number distributions are averaged in the transverse direction. The averaged Nusselt numbers are then plotted along the streamwise direction at different buoyancy parameters. In this way, one can readily study the buoyancy effect on the heat transfer inside the channel in a clear fashion. Therefore, Figs. 6 to 9 are presented in this way.

For pure forced convection, it was found ([4]) that the normalized Nusselt number at different Reynolds numbers can collapse into a single line if Nusselt number is defined based on the air temperature at the inlet of the channel and is normalized by Re$^{0.4}$. By plotting the heat transfer data in this way, the Reynolds number effect can be eliminated. This is useful to study buoyancy effect on the heat transfer in a channel with mixed convection occurring inside. For mixed convection in a heated vertical channel, Huang et al. ([4]) found that the normalized Nusselt numbers for buoyancy opposed convection indeed can collapse into a single line in certain regions of the buoyancy parameters when Gr/Re^2 is kept constant. That is when the buoyancy parameter is small enough that the buoyant heated, reversed flow does not occur or when it is large enough that the buoyant heated, reversed flow occurs over the entire channel. When the buoyancy parameter Gr/Re^2 is not so large that the buoyant heated, reversed flow is initiated only in certain regions of the channel, then the normalized Nusselt numbers do not collapse into a single line. This was attributed to the fact that the buoyant heated, reversed flow region is significantly affected by the changes of the Reynolds number as Gr/Re^2 is kept constant. However, the previous flow visualization clearly indicates that the slower flow region accumulated by the buoyant heated flow is not affected at all by the Reynolds number if the buoyancy parameter is kept constant. One thus plots the normalized Nusselt number results, as shown in Figs. 6(*a*) and (*b*), under the same buoyancy parameter but different Re and Gr numbers. It appears that all the normalized Nusselt numbers at different Reynolds numbers collapse into a single line when Gr/Re^2 is kept constant. In the following presentation, therefore, one can study the buoyancy effect on the heat transfer. The variation of the buoyancy parameter can be made by changing either the values of Gr or the values of Re during the experiments. Figures 7 and 8 show that the normalized Nusselt numbers increases with increasing the buoyancy parameters. This is true within the ranges of current experiments. In Fig. 7, the increase of the buoyancy parameter is made by increasing the value of Gr. However, in Fig. 8 the increase of the buoyancy parameter is made by decreasing the value of Re. It appears that Gr/Re^2 is the only dimensionless parameter to affect the heat transfer enhancement as a result from the buoyancy force. As long as the value of Gr/Re^2 is kept constant, the enhancement in the heat transfer by the buoyancy force is the same.

It is interesting to see how different for the normalized Nusselt number in the horizontal channel heated from a side and the ones in the vertical channel heated from the side ([4]). Comparison of the normalized Nusselt numbers between the two different cases is made, as shown in Fig. 9. All the dimensionless parameters used in the work of Huang et al. ([4]) is transformed into the ones used in the current work. For the case of pure forced convection, the normalized Nusselt numbers from both cases agree very well. However, deviation between the two different cases occurs as natural convection sets in. The deviation increases as the buoyancy parameter increases, and it becomes very large when the buoyancy parameter becomes very high. It appears that natural convection in the current configuration has a better performance in the enhancement of the heat transfer. For mixed convection in the vertical channel, natural convection indeed can enhance the heat transfer when the buoyancy parameter is not large. When Gr/Re^2 becomes large, the entire heat transfer in the channel is actually dominated by natural convection while the force convection effect becomes insignificant. In other words, at this stage, the fan which was used to pump the air to cause forced convection is now used to furnish the air required to cause natural convection.

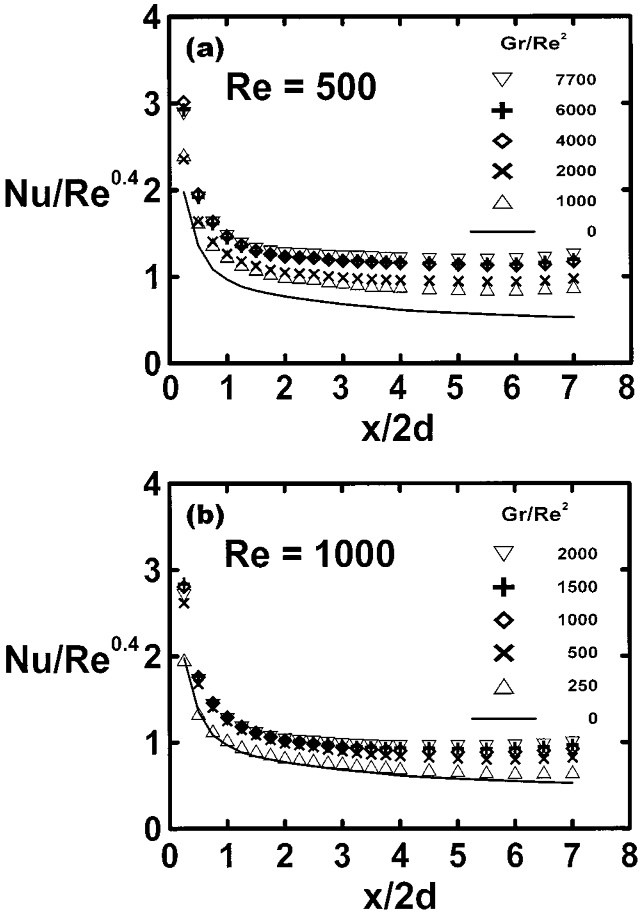

Fig. 7 The normalized Nusselt number distributions at different buoyancy parameters with (*a*) Re=500 and (*b*) Re=1000

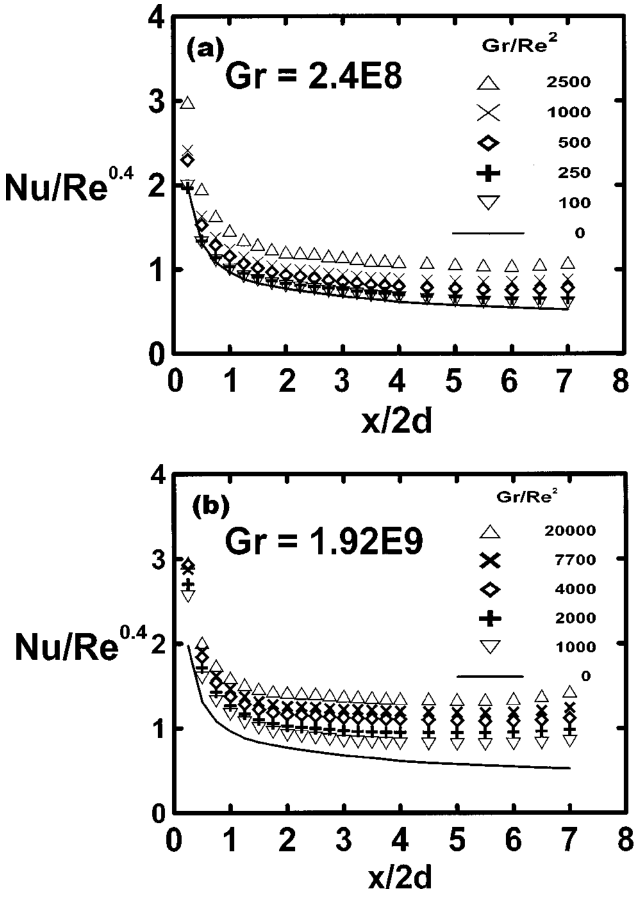

Fig. 8 The normalized Nusselt number distributions at different buoyancy parameters by changing the Reynolds numbers with (*a*) $Gr=2.4\times10^8$ and (*b*) $Gr=1.92\times10^9$

However, this is not the case in the current configuration. The total heat transfer is a geometrical addition of the heat transfer for the case of pure forced convection with the case of natural convection, no matter whether the buoyancy parameter is high or low.

For a horizontal flow passing through a vertical plate, Oosthuizen and Bassey ([17]) suggested

$$Nu_{mix}=[Nu_f^n+Nu_{nat}{}^n]^{1/n} \tag{2}$$

Different values of n have been tested. The best agreement with the data of mixed convection heat transfer was found when $n=3$ ([18]). For a horizontal channel heated from a side, the heat transfer along the heated side wall is very similar to the one along a vertical plate. Therefore Eq. (2) is adopted to estimate the heat transfer in the current configuration, while the Nusselt number for pure forced convection is adopted from the Ref. ([15]) and is written as follows:

$$\begin{aligned}Nu_f=0.461Gz^{1/2}[1+6.352Gz^{-1/2}-33.408Gz^{-1}\\+419.158Gz^{-3/2}-1537.84Gz^{-2}]\end{aligned} \tag{3}$$

where $Gz=RePr/(x/D_h)$. Equation (3) is the heat transfer result for a channel flow. The Nusselt number for natural convection along a vertical plate is adopted from Raithby and Hollands ([19]) and is written as follows:

$$Nu_{nat}=1.83/\log(1+1.83/(0.555[PrGr(y/w)^4]^{0.2})] \tag{4}$$

Comparison of the Nusselt numbers measured and the ones calculated from Eq. (2) with $n=3$ is shown in Fig. 10. The agreement is good except in the entrance region, and in the upper right region of the channel where the accumulated flow occurs which can reduce the heat transfer. In the entrance region, especially in the lower left corner of the channel, the heat transfer data is significantly higher than the prediction of Eq. (2), especially when the buoyancy parameter is high. It appears that in the entrance region, the thermal boundary layer is very thin and is very sensitive to the occurrence of natural convection which can further reduce the boundary layer thickness in the lower region of the channel and significantly increase the heat transfer.

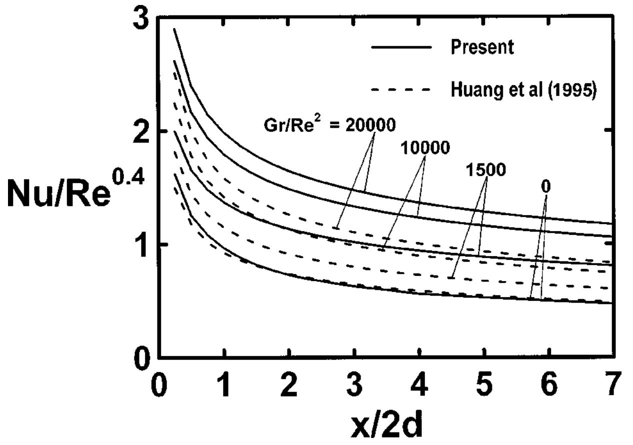

Fig. 9 Comparison of the normalized Nusselt numbers between the case of a vertical channel heated from the side and the case of horizontal channel heated from a side

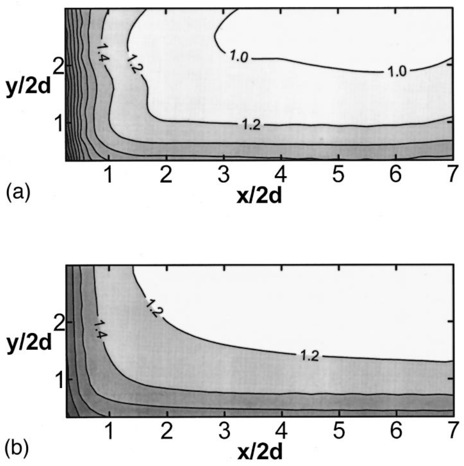

Fig. 10 Comparison of (*a*) the normalized Nusselt number contour measured with (*b*) the predicted with Eq. (2) (with $n=3$) at Re=500 and $Gr/Re^2=4000$

Other values of n have been tested for the current configuration of channel. However, the best agreement between the data and the prediction is found when $n=4$. To present the comparison with $n=4$ at different values of Gr/Re^2, the Nusselt numbers from both the measurements and the predictions are averaged in the transverse direction, and are plotted streamwisely at different values of Gr/Re^2, as shown in Fig. 11. It appears that the agreement between the data and the prediction is very good when the buoyancy parameter is not large. When Gr/Re^2 is greater than 10^4, the deviation of the Nusselt number measured from the predicted becomes large. This is attributed to the fact that at high buoyancy parameter, the accumulated flow region as indicated in the flow visualization section, becomes very large which can significantly reduce the heat transfer.

Since the normalized Nusselt number increases in proportion to the buoyancy parameter, one can expect that it can be correlated in terms of the buoyancy parameter. The correlation is very successful and the result is written as follows:

$$\mathrm{Nu}=0.94[1+0.0081(\mathrm{Gr}/\mathrm{Re}^2)]^{0.148}(x/D_h)^{-0.272} \tag{5}$$

which has a standard deviation of 0.042. The least-square fit of the data is presented in Fig. 12. The average Nusselt number, which is defined as $\overline{hD_h/k}$, is also correlated in terms of the buoyancy parameter, and the result is written as follows:

$$\overline{\mathrm{Nu}}/\mathrm{Re}^{0.4}=0.83[1+0.0081(\mathrm{Gr}/\mathrm{Re}^2)]^{0.126} \tag{6}$$

which has a standard deviation of 0.011. The least-square fit of the data is presented in Fig. 13. Both Eqs. (5) and (6) are valid for the Reynolds number in the range from 316 to 1500 and the buoyancy parameter is from 0 to 20000. Therefore, correlation (5) and (6) have included the heat transfer data of pure forced convection.

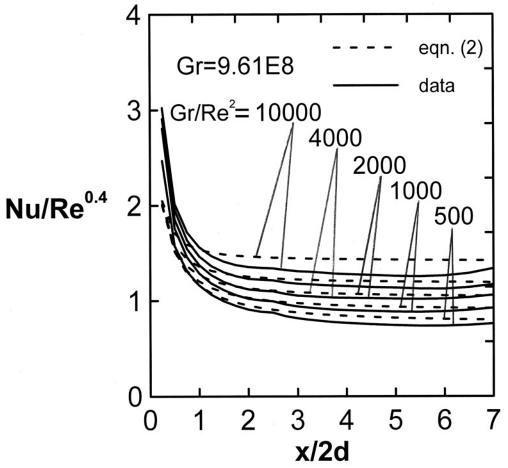

Fig. 11 Comparison of the average Nusselt numbers measured with the predicted with Eq. (2) (with $n=4$) at different buoyancy parameters and $Gr=9.61\times10^8$

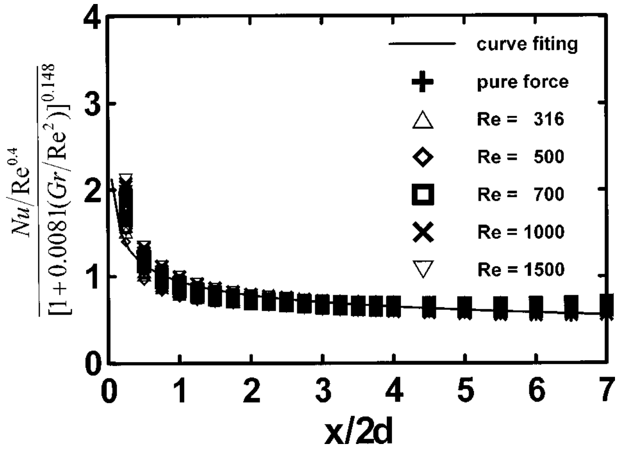

Fig. 12 Correlation of the normalized Nusselt numbers in terms of the buoyancy parameter and the nondimensional axial distance

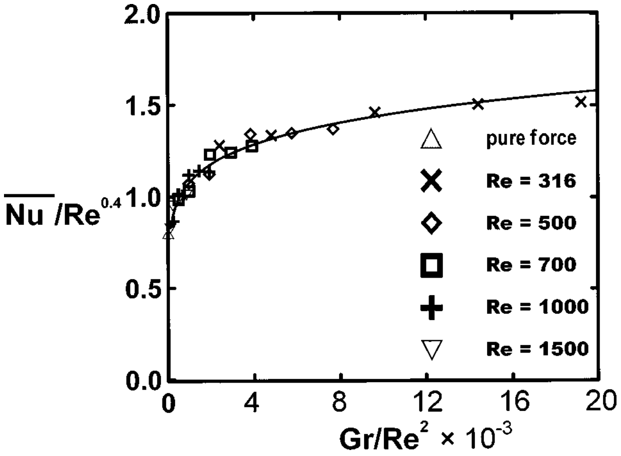

Fig. 13 Correlation of the average Nusselt numbers in terms of the buoyancy parameter

Conclusions

Mixed convection flow and the heat transfer process in a horizontal channel heated from a side is studied experimentally. Due to the vertical buoyancy force, the heated buoyant flow moves upward and accumulated in the upper region of the channel. The accumulated flow is thermally stable which grows in size as the buoyancy parameter increases. However, by keeping the buoyancy parameter constant, the variation of the Reynolds number does not have any effect on the size, shape, and location of the accumulated flow. This suggests that the buoyant heated flow and the heat transfer data can be properly presented in terms of the buoyancy parameter. The Reynolds number effect on the heat transfer can be eliminated by dividing the Nusselt number defined in the current report by $Re^{0.4}$. The increase of the buoyancy parameter either by increasing Gr or decreasing Re will identically lead to an increase in the normalized Nusselt number. The increase in the normalized Nusselt numbers are in proportion to the buoyancy parameter. Correlations of both the local (averaged in the transverse direction) and the averaged (over the entire channel) Nusselt number in terms of the buoyancy parameter are successfully obtained.

Due to the nature of the geometrical addition of the heat transfer for the case of pure forced with the case of natural convection, the Nusselt number in the current configuration is much greater than the case in a heated vertical channel flow. The Nusselt number results are very close to the prediction [Eq. (2)] similar to the case of a horizontal flow through a heated vertical plate. However, the accumulated flow in the upper region of the channel can significantly reduce the heat transfer and make it much lower than the prediction of Eq. (2), especially when the buoyancy parameter is high.

Acknowledgment

This research was sponsored by the National Science Council of Taiwan under contract No. NSC 87-2212-E006-088.

Nomenclature

d = channel gap (width)
D_h = hydrodynamic diameter, $2d$
g = gravitational acceleration
Gr = Grashof number, $g\beta q w^4/k\nu^2$
Gz = Graetz number, $\mathrm{RePr}(x/D_h)^{-1}$
h = transverse average in heat transfer coefficient
h_L = local heat transfer coefficient
$\bar{h}$ = overall average in heat transfer coefficient
k = thermal conductivity of air
Nu = transverse average in the Nusselt number, $h(D_h)/k$
Nu_l = local Nusselt number, $h_l(D_h)/k$
$\overline{\mathrm{Nu}}$ = overall average in the Nusselt number, $\bar{h}(D_h)/k$
Pr = Prandtl number, ν/α
q = heat flux
Re = Reynolds number defined at the inlet of the channel, $u_0(D_h)/\nu$
T = temperature
u_0 = inlet velocity
w = height of the channel
x,y = coordinate along the heated wall parallel, and normal to the streamwise direction

Greek Symbols

β = coefficient of thermal expansion
ν = kinematic viscosity

Subscript

b = refers to bulk mean
f = refers to pure forced convection
nat = refers to natural convection
o = refers to inlet

References

[1] Aung W., 1987, ''Mixed Convection in Internal Flow,'' *Handbook of Single Phase-Phase Convective Heat Transfer*, S. Kakac, R. K. Shah, and W. Aung, eds., John Wiley and Sons, New York, Chapter 15.

[2] Gau, C., Yih, K. A., and Aung, W., 1992, ''Reverse Flow Structure and Heat Transfer Measurements for Buoyancy-Assisted Convection in Heated Vertical Duct,'' ASME J. Heat Transfer, **114**, pp. 928–935.

[3] Gau, C., Yih, K. A., and Aung, W., 1992, ''Measurements of Heat Transfer and Flow Structure in Heated Vertical Channels With Buoyancy Assisted and Opposed Flows,'' AIAA J. Thermophys. Heat Transf., **6**, No. 4, pp. 707–712.

[4] Huang, T. M., Gau, C., and Aung, W., 1995, ''Mixed Convection Flow and Heat Transfer in a Vertical Convergent Channel,'' Int. J. Heat Mass Transf., **38**, No. 13, pp. 2445–2456.

[5] Wirtz, R. A., and McKinley, P., 1985, ''Buoyancy Effects on Downward Laminar Convection Between Parallel-Plates,'' *Fundamentals of Forced and Mixed Convection*, ASME HTD-Vol. 42, ASME, New York, pp. 105–112.

[6] Hwang, G. J., and Liu, C. L., 1976, ''An Experimental Study of Convective Instability in the Thermal Entrance Region of a Horizontal Parallel-Plate Channel Heated From Below,'' Can. J. Chem. Eng., **54**, pp. 521–525.

[7] Incropera, F. P., Knox, A. L., and Maughan, J. R., 1987, ''Mixed Convection Flow and Heat Transfer in the Entry Region of a Horizontal Rectangular Duct,'' ASME J. Heat Transfer, **109**, pp. 434–439.

[8] Maughan, J. R., and Incropera, F. P., 1990, ''Regions of Heat Transfer Enhancement for Laminar Mixed Convection in a Parallel Plate Channel,'' Int. J. Heat Mass Transf., **33**, pp. 555–570.

[9] Mahaney, H. V., Incropera, F. P., and Ramadhyani, S., 1987, ''Development of Laminar Mixed Convection in the Thermal Entrance Region of Horizontal Rectangular Ducts,'' Numer. Heat Transfer, **12**, pp. 137–155.

[10] Lee, F. S., and Hwang, G. J., 1991, ''The Effect of Asymmetric Heating on the Onset of Thermal Instability in the Thermal Entrance Region of a Parallel-Plate Channel,'' Int. J. Heat Mass Transf., **34**, pp. 2207–2218.

[11] Gau, C., Huang, T. M., Liu, C. W., and Aung, W., 1998, ''Mixed Convection Flow and Heat Transfer in a Horizontal Divergent Channel With Bottom Wall Heated,'' *Proceedings of the 11th International Heat Transfer Conference*, Korea, Vol. 3, pp. 257–262.

[12] Gau, C., Liu, C. W., Huang, T. M., and Aung, W., 1999, ''Secondary Flow and Enhancement of Heat Transfer in Horizontal Parallel-Plate and Convergent Channels Heating From Below,'' Int. J. Heat Mass Transf., **42**, pp. 2629–2647.

[13] Webb, B. W., and Hill, D. P., 1989, ''High Raleigh Number Laminar Natural Convection in an Asymmetrically Heated Vertical Channel,'' ASME J. Heat Transfer, **111**, pp. 649–656.

[14] Kline, S. J., and McClintock, F. A., 1953, ''Describing Uncertainties in Single-Sample Experiments,'' Mech. Eng. (Am. Soc. Mech. Eng.), **75**, pp. 3–12.

[15] Naito, E., 1975, ''Laminar Heat Transfer in the Entrance Region Between Parallel-Plate—The Case of Uniform Heat Flux,'' Heat Transf. — Japan. Res., **4**, No. 2, pp. 63–74.

[16] Jeng, Y. C., 1998, ''Mixed Convection in a Horizontal Duct Heated From a Side,'' MS thesis, National Cheng Kung University, Tainan, Taiwan, ROC.

[17] Oosthuizen, P. H., and Bassey, M., 1973, ''An Experimental Study of Combined Forced and Free Convective Heat Transfer on Flat Plates to Air at Low Reynolds Numbers,'' ASME J. Heat Transfer, **95**, pp. 120–121.

[18] Churchill, S. W., 1977, ''A Comprehensive Correlating Equation for Laminar Assisting Forced and Free Convection,'' AIChE J., **23**, pp. 10–16.

[19] Raithby, G. D., and Hollands, K. G. T., 1985, ''Natural Convection,'' *Handbook of Heat Transfer: Fundamental*, W. M. Rohsenow, J. P. Hartnett, and E. N. Ganic, eds., McGraw-Hill, New York, Chapter 6, pp. 16–20.

Pool Boiling Heat Transfer in Aqueous Solutions of an Anionic Surfactant

V. M. Wasekar

R. M. Manglik[1]
e-mail: Raj.Manglik@uc.edu
Mem. ASME

Thermal-Fluids and Thermal
Processing Laboratory,
Department of Mechanical, Industrial
and Nuclear Engineering,
University of Cincinnati,
Cincinnati, OH 45221-0072

Saturated nucleate pool boiling of aqueous surfactant solutions on a horizontal cylindrical heater has been experimentally investigated. Sodium dodecyl or lauryl sulfate (SDS or SLS), an anionic surfactant, is employed. Boiling performance, relative to that for pure water, is found to be enhanced significantly by the presence of SDS, with an early onset of nucleate boiling. An optimum level of enhancement is observed in solutions at or near critical micelle concentration of the surfactant; the enhancement, however, decreases considerably in higher concentration solutions. The dynamic surface tension measurements indicate a substantial influence of temperature on the overall adsorption isotherm. The diffusion kinetics of surfactant molecules and micelles is, therefore, expected to be quite different at boiling temperature than at room temperature. This greatly modifies the boiling mechanism that is generally characterized by the formation of smaller-size bubbles with increased departure frequencies, and a decreased tendency to coalesce which causes considerable foaming. [S0022-1481(00)00704-0]

Keywords: *Additives, Boiling, Enhancement, Experimental, Heat Transfer, Surface Tension*

Introduction

It is well established that nucleate boiling sustains considerably high heat transfer rates with relatively small temperature differences. Over the past 60 years there has been extensive research to address issues such as bubble growth, bubble dynamics, effects of heater surface characteristics, fluid-surface interaction, and fluid properties, among others. In recent years, given the energy conservation and economic imperatives, much attention has been directed towards techniques to enhance nucleate boiling heat transfer. Bergles [1], Webb [2], and Thome [3] document several active and passive techniques used for boiling enhancement. Amongst these, the use of additives, which lower the surface tension of liquids, has been a focus of current research ([4]).

Small concentrations of surfactant additive in water lower the solution's surface tension considerably, and its level of reduction depends on the amount and type of surfactant present in solution. The consequent heat transfer enhancement in pool boiling of this solution is found to be dependent upon the surfactant concentration. Higher heat transfer coefficients have generally been obtained in higher concentration solutions ([4–6]). However, the earlier attempts to correlate this enhancement primarily with the equilibrium surface tension of the aqueous solution have been inconclusive ([4,7]). For a boiling bubble in saturated water as well as in surfactant solutions, typical bubble growth times are in the range of 25 to 30 ms ([6,8]), and the characteristic surfactant diffusion time scale is of the order of 10 to 15 milliseconds ([9]). The comparable bubble growth and surfactant diffusion time scales suggest that perhaps the dynamic surface tension rather than the equilibrium value should be considered; though the dynamic surface tension alone may not be an adequate correlating variable ([6,10]). Also, the nature of surfactant additives, their solution chemistry (ionic character, molecular weight, wettability, diffusion-adsorption kinetics, and micelle behavior), and heater geometry have a significant impact on the boiling mechanism.

Morgan et al. [11] were perhaps the first to study the effects of surfactants on nucleate pool boiling of water. Their experiments with aqueous solutions of 0.1 percent and 1 percent Drene (triethanolamine alkyl sulfate) on a steam-heated copper tube indicated that boiling heat transfer was controlled more by the surface tension of newly formed surfaces rather than the equilibrium values of surface tension. The heat transfer enhancement increased with concentration, to a maximum of the order of 100 percent at $\Delta T_w = 15\,\mathrm{K}$. The role of dynamic surface tension appears to be further supported by the experimental results of Jontz and Myers [10] for aqueous solutions of Tergitol (25 percent sodium tetradecyl sulfate). In this case, dynamic surface tension was measured by passing air at different flow rates through a horizontal, circular orifice submerged in aqueous Tergitol solutions. It was found that the dynamic surface tension estimated in this manner approached the static value either by increasing the concentration or by decreasing the bubble-formation rate.

More recently, Wu et al. [6] have measured the dynamic surface tension for aqueous solutions of SDS (sodium dodecyl or lauryl sulfate, anionic surfactant) and Triton X-100 (polyoxyethylated t-octylphenol, a nonionic surfactant) using the maximum bubble pressure method. Iliev and Dushkin [12] have likewise reported data for SDS and Veranol H-10 (nonylphenol polyglycol ether with 10 mols of ethylene oxide, a nonionic surfactant). In all cases, the dynamic σ is generally higher than the equilibrium values at all surfactant concentrations. The SDS solutions also display a more rapid relaxation of surface tension than the Triton X-100 and Veranol H-10 solutions, indicating a lower surface activity and a smaller characteristic diffusion time of SDS monomers. Wu et al. [6], however, could not directly correlate the observed heat transfer enhancement for both SDS and Triton X-100 solutions with the depression in dynamic surface tension. This is probably because their measurements were made at room temperature, which do not reflect the effect of elevated temperature on the dynamic σ curves and surfactant characteristic diffusion times during boiling. Additionally, the ionic nature of the surfactant additive and its molecular weight also contribute to the dynamic characteristics of their solutions [13].

All surfactant-solvent systems have a characteristic surfactant concentration referred to as critical micelle concentration (c.m.c.), which differentiates the presence of surfactant in the solution ei-

---

[1] To whom correspondence should be addressed.

Contributed by the Heat Transfer Division for publication in the JOURNAL OF HEAT TRANSFER. Manuscript received by the Heat Transfer Division, Aug. 16, 1999; revision received, May 18, 2000. Associate Technical Editor: S. S. Sadhal.

ther as individual monomer or associated groups as micelles ([14,15]). A micelle is an aggregation of a large number of monomers and can have spherical, cylindrical, or lamellar type structure depending upon the nature of surfactant. Similar to monomers, the characteristic time of diffusion for micelles is in the range of milliseconds ([12]). At c.m.c., noticeable changes are observed in the physical properties (including σ) of the surfactant solutions ([14,15]). Podsushnyy et al. [16] were perhaps the first to report a ''peaking'' in the enhanced pool boiling heat transfer corresponding to the c.m.c. of solutions of PVS-6 polyvinyl alcohol, NP-3 sulfonol, and SV 1017 wetting agent in seawater. Although peaks in boiling heat transfer enhancement for aqueous surfactant solutions have been observed by others ([17–19]), they cannot be associated with the c.m.c. of respective solutions due to the lack of surface tension data reported in these studies.

The improved boiling heat transfer in surfactant solutions has been generally found to be associated with the reduction in bubble departure diameter, increased departure frequency, and reduced coalescence. A synthesis of several mechanisms (that include modified bubble dynamics, increase in active nucleation sites, and Marangoni convection, among others) has been proposed to explain the observed behavior, though the direct correlation of enhancement with these mechanisms still remains elusive. The present study attempts to address some of these issues by investigating the saturated nucleate boiling heat transfer for aqueous solutions of SDS on a horizontal cylindrical heater. The size of heater employed represents a larger class of commercially available tubes commonly used in industrial heat exchangers. A wide range of concentrations is used that extend to and above c.m.c. levels. Systematic measurements of dynamic surface tension at room and elevated temperatures were carried out to understand the temperature effects on the characteristic diffusion times for monomers and micelles. Additionally, in order to obtain further insight into the observed phase-change phenomena, photographic records of the evolution of boiling process are also presented.

Surface Tension Measurements

Surface tension measurements were carried out using a Sensa-Dyne QC6000 surface tensiometer (CSC Scientific Company) that employs the maximum bubble pressure method. This method measures the dynamic interfacial tension of an interface undergoing a steady, unsteady, or pulse expansion ([20]). Dry air is slowly bubbled through the small and large orifice probes immersed in the test fluid that produces a differential pressure signal proportional to the fluid surface tension. The surface age (time interval between the newly formed interface and the point of bubble breakoff) gives the measure of bubble growth time corresponding to the dynamic surface tension value at a given operating bubble frequency. By altering the bubble frequencies of air through the probes, both static and dynamic σ can be measured. In essence, the value of σ is governed by the rate of diffusion of surfactant molecules toward the growing air bubble.

The test fluids were prepared by dissolving weighed samples (± 0.1 mg accuracy) of SDS in distilled water to get the desired concentration [wppm]. The physico-chemical properties of the surfactant powder are listed in Table 1. The surface tensiometer was initially calibrated using deionized water and ethyl alcohol at room temperature, and the validity of measurements was established by comparing the data for deionized water at various temperatures with accepted values [21]. The dynamic surface tension measurements for surfactant solutions were then carried out at four different bubble frequencies (10, 2, 0.33, and 0.0167 Hz) at 23°C and 80°C.

Table 1 Physico-chemical properties of SDS (sodium dodecyl or lauryl sulfate)

Chemical formula	$C_{12}H_{25}SO_4Na$
Ionic nature	Anionic
Appearance	White in color
Molecular weight	288.3
Micelle aggregation number at 23°C	71
Micellar weight at 23°C	20470
Specific gravity	0.4
Krafft point*	16°C
Water solubility at 20°C	180 g/liter (180,000 wppm)

*Temperature at which solubility of the surfactant increases sharply ([23]).

Figure 1(*a*) shows the dynamic surface tension measurements for SDS solutions at 23°C, where the lowest bubble frequency gives the static or equilibrium value. Surface tension decreases with increasing SDS concentration to an asymptotic value beyond

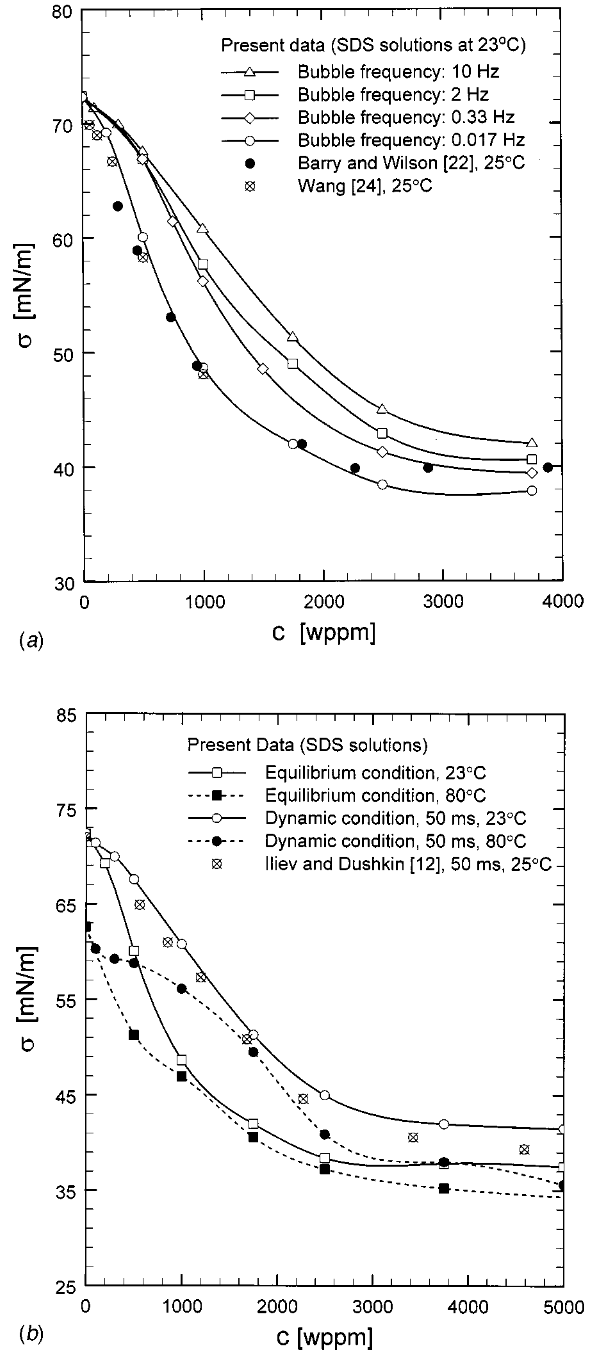

Fig. 1 Surface tension measurements for aqueous SDS solutions: (*a*) dynamic σ at room temperature, and (*b*) effect of temperature on the dynamic and equilibrium σ (values in *ms* refer to surface age)

a critical concentration (c.m.c.). With the increase in bubble frequency, c.m.c. is found to shift toward higher concentrations, and this is also seen in the Iliev and Dushkin [12] data for two different surfactants. The formation of a complete monolayer at the interface is a time-dependent process with a finite diffusion time scale ([12,14,15]). Thus, at higher bubble frequencies, larger bulk concentrations would be needed to initiate micelle formation and c.m.c. would tend to shift to the right. The value of c.m.c. at 23°C and a bubble frequency of 0.0167 Hz is ≈2500 wppm. Some of the reported values in the literature at 25°C are 2335 wppm ([22]), and 2306 wppm ([23]). The reasonable agreement with the static σ data given by Barry and Wilson [22] and Wang [24] validate the present measurements. However, it may be noted that measured interfacial properties can differ by an order of magnitude owing to their sensitivity to the physical state of the interface, trace impurities, and relative experimental ''cleanliness'' ([20]).

The effect of temperature on both the dynamic and equilibrium surface tension of aqueous SDS solutions is graphed in Fig. 1(*b*). The values of dynamic σ are for a surface age of 50 ms, which is comparable to the boiling bubble growth time. While both equilibrium and dynamic σ decrease with increasing temperature for all surfactant concentrations, this reduction is not uniform. The reduction in dynamic σ is more pronounced for low concentrations (<1000 wppm) and for those above c.m.c. (>2500 wppm). For the intermediate concentration range, the effect of temperature appears to be negligible. This reflects the different adsorption-diffusion kinetics of SDS monomers at low and intermediate concentrations, and of SDS micelles at concentrations above c.m.c. As shown by Dushkin and Iliev [9], there is a substantial increase in the characteristic diffusion time scale at intermediate concentration levels with the development of an adsorption barrier. The temperature effect is also dependent on the bubble frequency with a relatively larger decrease in σ at higher bubble frequencies. Furthermore, c.m.c. at 80°C is around 3750 wppm, which is considerably higher than c.m.c. at room temperature (2500 wppm). A similar increase in c.m.c. (from 2335 wppm to 2566 wppm) has been observed by Barry and Wilson [22] over a temperature range of 20°C to 50°C.

Experimental Setup and Procedure

Figure 2(*a*) gives a schematic of the experimental setup used for the pool boiling studies. The inner tank that contains the test liquid pool and cylindrical heater, is housed in an outer tank that has circulating mineral oil fed from a constant-temperature recirculating bath (not shown in figure). Both tanks are transparent and allow visual observation and photographic recordings of the boiling process, and the test pool is maintained at its saturation temperature at atmospheric pressure. A pressure gage (±0.0025 bar precision), mounted on top of the boiling vessel, monitors the atmospheric pressure in the pool throughout the experiment. A water-cooled reflux condenser cools the excess vapor, vents the noncondensable gases, and returns the condensate back to the boiling vessel. A second coiled-tube water-cooled condenser provides additional condensation surface for instances of large vapor generation. The pool level, with free surface about 100 mm above the heater centerline, is maintained such that no liquid comes in contact with the coil and directly cooled when the pool is highly agitated.

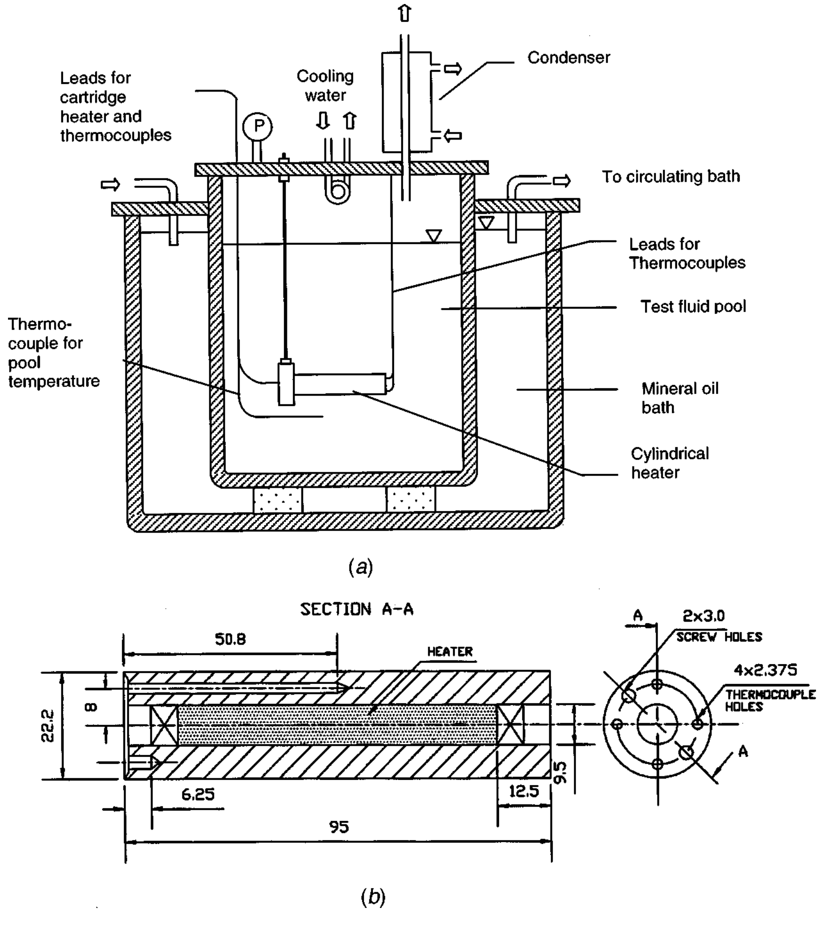

Fig. 2 (*a*) **Schematic of experimental facility, and** (*b*) **cross-sectional view of cylindrical heater assembly**

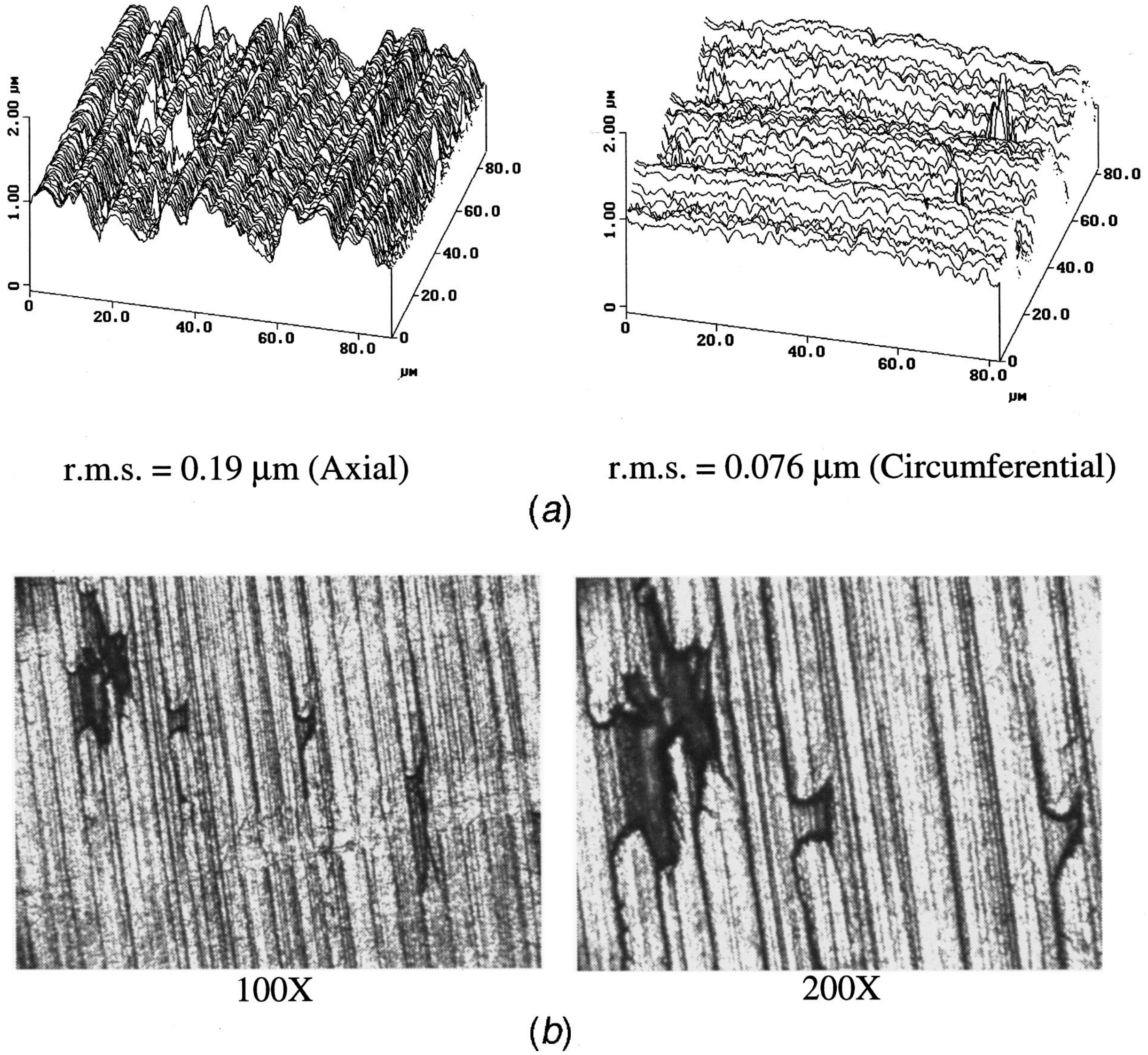

r.m.s. = 0.19 µm (Axial)

r.m.s. = 0.076 µm (Circumferential)

(*a*)

100X

200X

(*b*)

Fig. 3 Roughness characteristic of heater surface: (*a*) three-dimensional roughness profiles using AFM, and (*b*) optical microscope images

The heater test section, shown in Fig. 2(*b*), consists of a horizontal, gold plated, hollow copper cylinder of 22.2-mm outer diameter, 9.5-mm inner diameter, with a length of 95 mm and a tight-fit cavity for the immersible electric cartridge heater. The 0.0127-mm-thick gold plating on the outer boiling surface mitigated any surface degradation and oxidation from chemicals in the fluids. The inner-to-outer diameter of the cartridge heater was selected such that it ensured a uniform temperature distribution on the outer surface ([25]), and it provided a peak heat flux of about 225 kW/m^2. The 88.9-mm long, 240 V, 1500 W cartridge heater with insulated lead wires was press-fitted with conductive grease to fill any remaining air gaps, and provide good heat transfer contact. It is centrally located inside the copper tube, and the gaps at each end are filled with silicone rubber to prevent water contact. Also, because the heater surface roughness significantly influences the boiling behavior, it was examined using an atomic force microscope (AFM) as well as an optical microscope. Figure 3(*a*) shows a typical AFM scan, where r.m.s. roughness values in the axial and circumferential directions are 0.19 μm and 0.076 μm, respectively. The overall r.m.s. roughness, measured at four different locations, range from 0.076 μm to 0.347 μm. In addition, the optical microscope images of the heated surface in Fig. 3(*b*) show a random distribution of pits, cavities, and machining grooves of varying shapes and sizes along the heater surface.

The primary measurements consist of heater wall and pool bulk temperatures, and power input to the heater. Four ‘‘T’’ type precision thermocouples (calibrated to ±0.2°C), located as shown in Fig. 2(*b*), are used to measure the heater surface temperature. Two thermocouples, one below the heater surface and one near the free surface of the pool are used to monitor the pool temperatures, and the test fluid was maintained at its saturation temperature at atmospheric pressure. A variac-controlled AC power supply, a current shunt (0.15 Ω with one percent accuracy), and two precision multimeters (for current and voltage measurements) provided the controls and measurement of the input electric power. All data recordings were interfaced with a HP-75,000 data acquisition system and a PC.

Prior to each boiling test run for a test fluid, the pool was thoroughly degassed to remove dissolved non-condensables. This was done by heating it to saturation temperature, through the temperature controlled oil bath, and then boiling it at a heat flux of 30 kW/m^2 for at least half an hour while constantly maintaining it at T_{sat}. Power to the heater was then turned off and the system was allowed to attain stable, saturation conditions. The boiling experiments were then carried out by varying the wall heat flux in a stepwise manner, first by increasing the heat flux from zero to 225 kW/m^2 and then by decreasing it back to zero. At each heat flux increment, the corresponding voltage drop V and current I were recorded to give the dissipated wall heat flux $(q''_w=VI/A)$. At the same time, the heater wall surface temperature was recorded as the average of the four wall thermocouple readings $(T_{R,i})$ after accounting for the radial temperature gradient between the thermocouple locations and outer surface of the cylinder from

$$T_w=\left\{\sum_{i=1}^{4}[T_{R,i}-(q''_wR_o/k)\ln(R_o/R)]/4\right\}. \qquad (1)$$

Thus, the wall superheat was determined as $\Delta T_w=(T_w-T_{\mathrm{sat}})$. At each q''_w step, data were recorded only when the boiling system was stable, and this was determined when none of the measured variables changed by more than 0.1 percent over time. The pool temperature measured beneath the heater decreased slightly during an increase of heat flux, and vice versa due to the mixing of subcooled condensate with the bulk. The maximum variation in the pool temperature occurring at the highest q''_w was negligible ($\sim$0.5 K), and the pool was essentially at saturation temperature. The measurement precision in the experimental variables V, T, D, and L, respectively, were ± 0.1 V, ± 0.2 K, ± 0.025 mm, and ± 0.025 mm, and the maximum measurement uncertainty in the computed values of I was ± 1.41 percent. Correspondingly, the maximum experimental uncertainties in q''_w and ΔT_w, computed by the method outlined by Moffatt [26], were 1.44 percent and 0.5 percent, respectively.

Aqueous surfactant solutions of seven different SDS concentrations (200 to 10,000 wppm) were prepared by dissolving weighed samples in distilled water. Also, the boiling curve for pure distilled water was first established over a period of four months to verify its repeatability and the effects of heater surface aging. These water data provide the baseline reference for the surfactant solution results, as well as validate the experimental reliability of the apparatus, and data acquisition and reduction procedures.

Results and Discussion

Figure 4 shows the nucleate boiling data for pure distilled water taken over a period of four months, and its comparison with the cylindrical copper-heater/water data available in the literature. Excellent repeatability is observed with runs 2 and 3, indicating stabilization of the nucleation cavities; these runs were carried out, respectively, after three and four months of the first run. Boiling heat transfer measurements from the same apparatus often show considerable variations due to ''aging'' effects of impurities and any chemical actions that may occur on the heater surface ([7,27,28]). The present stabilized data are well within the experimental scatter of the literature data ([29–32]). Comparisons are also made with the correlations due to Borishanskii [33] and Cornwell and Houston [34]. Borishanskii's correlation is based on the principles of thermodynamic similitude, and Cornwell and Houston [34] give a generalized correlation that accounts for the diameter effects of the horizontal cylindrical heater. The present data agree very well with both correlations, and they provide an accurate baseline reference for the nucleate boiling performance of the surfactant solutions.

With the addition of surfactant to water the nucleate boiling curve shifts to the left, indicating enhancement in heat transfer. This is seen in Fig. 5, which gives the experimental data for pool boiling of various concentrations of aqueous SDS solutions (results for 200 and 1750 wppm are not shown for the sake of clarity). Except for the 10,000 wppm data, all other results are with increasing heat flux. An early onset of nucleate boiling (ONB) or incipience was observed for all surfactant solutions; incipience was determined by visual observation of nucleating bubbles on the heater surface. This conforms to the incipient superheat criteria proposed by Griffith and Wallis [35]; i.e., for a given cavity size and liquid properties, incipient superheat decreases with decrease in surface tension. In distilled water, ONB was observed at a heat flux of 12.83 kW/m^2 with the wall superheat of 5.13 K, which is in agreement with the generally observed ΔT_w of 4 K $\sim$8 K for saturated, atmospheric boiling of water on copper cylinders ([3]). With aqueous SDS solutions, ONB was observed at lower levels of q''_w and ΔT_w. For example, ONB for 2500 wppm SDS solution was seen at $q''_w \cong 8.3\,\mathrm{kW/m^2}$ and $\Delta T_w \cong 3.35\,\mathrm{K}$. Wetting behavior is also expected to improve with the presence of surfactants ([14,15,36]), and an appreciable hysteresis has been reported for pure fluids having low surface tension and high wettability ([37,38]). In the present study, however, boiling of solutions with $c \leqslant 3750$ wppm SDS showed no significant thermal hysteresis. The results for 10,000 wppm SDS solution, however, show a strong hysteresis that is akin to the boiling of refrigerants and other highly wetting fluids.

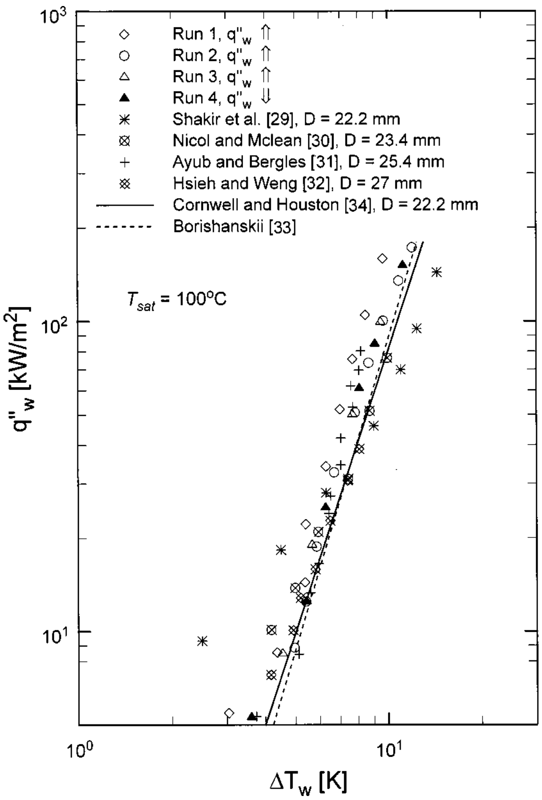

Fig. 4 Nucleate pool boiling data for distilled water

An explanation for the observed enhancement in boiling heat transfer coefficient seen in Fig. 5 can perhaps be given by considering the role of dynamic surface tension and subsequent modification of bubble dynamics. With the nucleation of vapor bubble and during its subsequent growth, diffusion of surfactant molecules and their adsorption/desorption rates at the interface govern the extent of dynamic surface tension. The dynamic σ is appreciably lower than the solvent's σ (see Fig. 1(*b*)), which helps promote large number of active nucleation sites. Lower values of dynamic σ also allow departure of smaller-sized bubbles because of the reduction in surface tension force at the heater surface that counters the buoyancy force trying to pull the bubble away from the surface. This is consistent with the well-established Fritz equation ([39]), and its variants ([40,41]), which suggest bubble departure diameter is directly proportional to σ. The bubble growth time could consequently be expected to reduce and lead to an increase in bubble departure frequency. Furthermore, the performance envelope for aqueous SDS solutions tends to get narrower with increasing heat flux, especially in the fully developed boiling

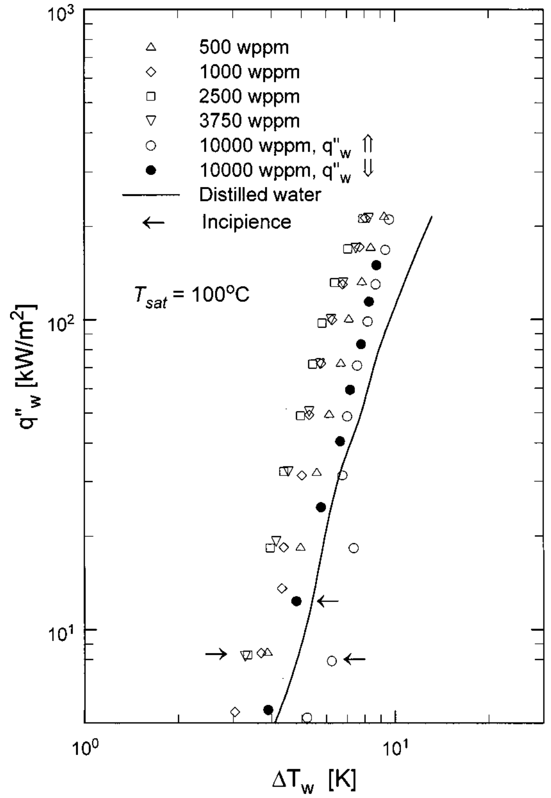

Fig. 5 Pool boiling data for aqueous SDS solutions; arrows indicate incipience, and, except for 10,000 wppm, all data are for increasing heat flux

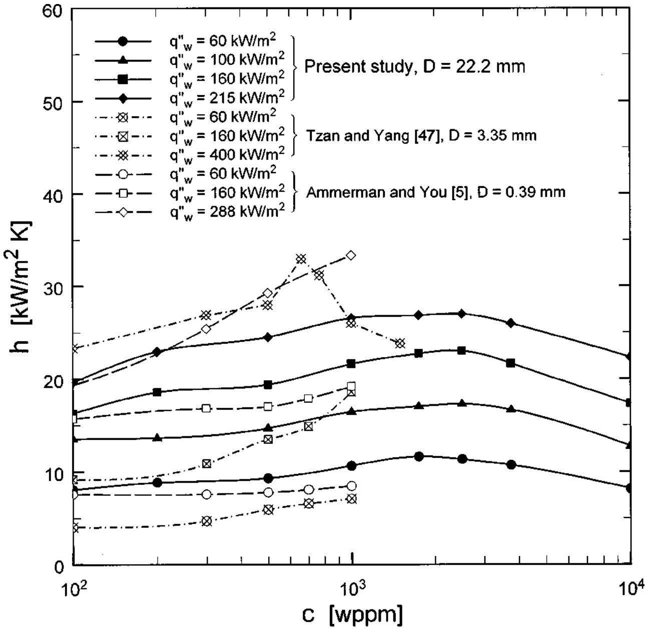

Fig. 6 Effect of heater diameter and heat flux on the nucleate pool boiling performance of aqueous SDS solutions

regime (Fig. 5). This is perhaps due to the ''bubble sliding'' mechanism ([42–44]) becoming substantially more important in this regime. In boiling of pure liquids over large diameter heaters, it has been observed that a bubble boundary layer is developed over the heater surface. This is essentially made up of bubbles nucleated at the bottom of the cylinder, which then slide upward along its surface before departing ([42–44]). These sliding vapor bubbles contribute significantly towards enhancing heat transfer through the various mechanisms of seeding adjacent nucleation sites, evaporation of thin liquid layer at the bubble base, and enhanced convection in the adjacent wake region.

The surfactant behavior in aqueous solution becomes markedly different at or around c.m.c. as a result of the formation of micellar structures in the solution ([14,15,36]). A micelle is an aggregate of surfactant molecules, and for SDS it is usually spherical in shape with a diameter of about 5 nm. Typical value of aggregation number for a SDS micelle at 23°C is 71 ([23]), and the corresponding micellar weight (product of aggregation number and the molecular weight of the surfactant) is 20470. The presence of large number of micelles leads to an increase in the apparent viscosity and density of the solution ([45]), and it may perhaps contribute towards altering the thermal conductivity and molecular weight of the solution as well. As seen in Figs. 5 and 6, nucleate pool boiling of aqueous SDS solutions with concentrations above c.m.c. ($>$ 2500 wppm) show a deterioration in heat transfer at all heat flux levels, thereby indicating an optimum in heat transfer enhancement around c.m.c. For the 10,000 wppm SDS ($\gg$ c.m.c.) solution, pronounced nucleate boiling hysteresis is also observed, with ONB at a heat flux of 7.92 kW/m^2 and the corresponding wall superheat of 6.26 K. Furthermore, for this solution, the boiling performance up to a heat flux level of $\sim$40 kW/m^2 is much poorer than that of distilled water; at higher q''_w, however, the performance improves substantially.

Figure 6 also gives a comparison between the nucleate boiling heat transfer performance of aqueous SDS solutions for three different cylindrical heater sizes. For the heat flux range of the new data, the larger diameter heater (22.2 mm) is seen to give higher heat transfer coefficients followed, in order, by the platinum wire heater (0.39 mm) and the smaller diameter stainless steel heater (3.35 mm). Cornwell and Houston [34] have pointed out such a dependence of heater size on the nucleate boiling of R113, and they attribute this to the formation of bubble boundary layer and the subsequent bubble sliding at detachment. More recently, in pool boiling of propane and n-hexane on cylindrical heaters, Gorenflo et al. [44] have reported an improvement in nucleate boiling heat transfer with larger diameter (88.4 mm) heater in comparison with that of smaller diameter (7.6 mm); both heaters were made of mild steel and had the same mean surface roughness. This enhancement is once again ascribed to the vigorous motion of large buoyancy-driven bubbles sliding over the cylindrical heater surface. A similar bubble sliding mechanism appears to promote the higher large-diameter-heater boiling performance for the aqueous surfactant solutions as well.

In order to quantify the extent of enhancement in nucleate boiling of surfactant solutions, the results are graphed in Fig. 7 in the form of a relative heat transfer coefficient defined as

$$\frac{(h-h_{\text{water}})}{h_{\text{water}}}=\left[\frac{(q''_w/\Delta T_w)-(q''_w/\Delta T_w)_{\text{water}}}{(q''_w/\Delta T_w)_{\text{water}}}\right]. \tag{2}$$

Figure 7 shows a maximum enhancement of 65 percent for 2500 wppm aqueous SDS solution. The trends in the results for solutions with $c < 2500$ wppm, however, seem to suggest that this optimum in heat transfer enhancement may be dependent upon q''_w as well. At higher q''_w there may be a peak performance for slightly lower concentration solutions, though this could not be ascertained in the present experiments where the highest attainable heat flux was 215 kW/m^2. A similar heat flux dependence of maximum enhancement has been observed by Manglik [46] for boiling of aqueous alkyl glyceryl sulfonate solutions on a 25.4-mm cylindrical heater, and by Tzan and Yang [47] for aqueous SDS solutions on a 3.35-mm heater. Additionally, Fig. 7 clearly shows the decrease in boiling heat transfer enhancement in 3750 wppm and

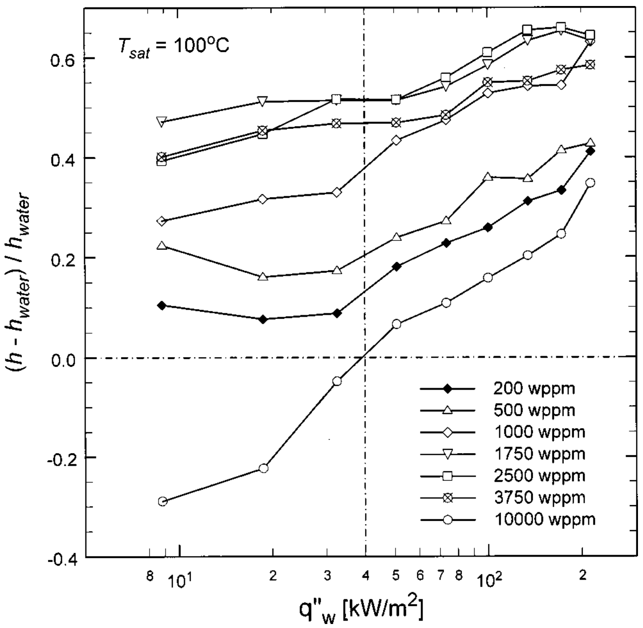

Fig. 7 Relative heat transfer performance of aqueous SDS solutions and its variation with heat flux and surfactant concentration

10,000 wppm SDS solutions ($c >$ c.m.c.). In the latter case, the degradation in performance relative to that for pure water at $q''_w < 40\,\mathrm{kW/m^2}$ is also evident.

To understand qualitatively the boiling behavior of aqueous surfactant solutions, the boiling history for 1000 wppm and 2500 wppm SDS solutions was photographed using a CCD camera. These images for $q''_w = 20$, 50, and 100 kW/m^2 are shown in Fig. 8 along with those for distilled water. Boiling in surfactant solutions, in comparison with that in pure water, is observed to be more vigorous with clusters of smaller-sized and more regularly shaped bubbles. In both surfactant solution and pure water, the bubbles mostly originate from the underside of the cylindrical heater, and then slide along the heater surface before departure. These sliding bubbles tend to knock off the bubbles growing on the top surface of the heater causing their early departure, and this tendency was observed to increase with increasing bubble departure frequency. With surfactant solutions, the lowering of surface tension promotes nucleation of smaller sized bubbles and activation of nucleation sites in a clustered fashion, especially at lower heat fluxes. The bubbles depart at much higher frequencies and the coalescence between two neighboring bubbles or between the sliding bubbles along the heater surface is minimal. The departing bubbles were seen to reach the pool free surface and form a foam layer, whose thickness increased with increasing heat flux. At high heat fluxes (~200 kW/m^2), due to the vigorous bubbling motion, the liquid free surface in the pool oscillated mildly. This was also observed with the boiling of pure water. Furthermore, except for the thermal overshoot seen in very high SDS concentration (10,000 wppm) solution, no significant differences were observed in the boiling evolution in surfactant solutions having SDS concentrations below and above c.m.c.

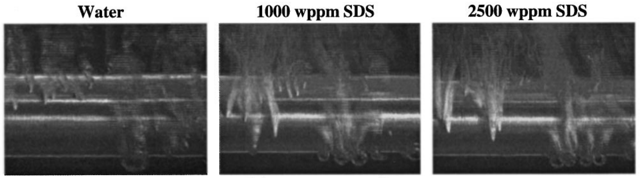

(*a*) $q''_w = 20$ kW/m^2

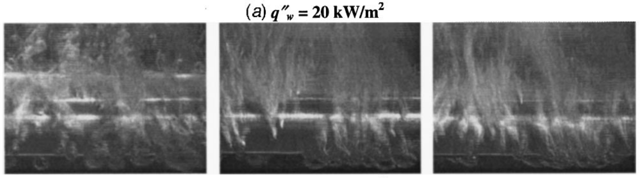

(*b*) $q''_w = 50$ kW/m^2

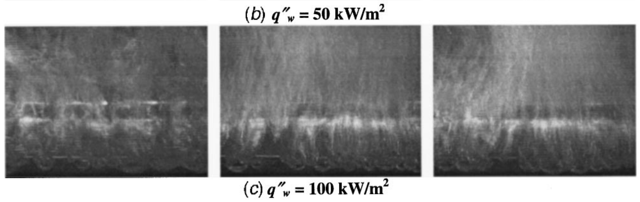

(*c*) $q''_w = 100$ kW/m^2

Fig. 8 Boiling history for distilled water, and aqueous SDS solutions of 1000 and 2500 wppm

Conclusions

Saturated nucleate boiling of aqueous surfactant solutions show a considerable enhancement in heat transfer coefficient (10 percent–65 percent, depending upon c and q''_w) relative to that for pure water. This enhancement is characterized by an early incipience, followed by a rapid departure of smaller-sized, regularly shaped bubbles from the heater surface, and an increase in the number of active nucleation sites. The dynamic surface tension has a primary role in the modification of the bubble dynamics and associated heat transfer, and it is dictated by the adsorption kinetics of the surfactant molecules at boiling temperatures. As such, in order to develop viable models for the boiling mechanism, the influence of surfactant kinetics on bubble growth rates needs further investigation.

Acknowledgment

This study was supported by the National Science Foundation CAREER Award (Grant No. CTS-9502128).

Nomenclature

A = heater surface area ($=\pi DL$) (m^2)
c = concentration (wppm, or g/lit)
D = cylindrical heater outer diameter (mm, or m)
h = boiling heat transfer coefficient (kW/m^2 K)
h_{water} = boiling heat transfer coefficient of pure water (kW/m^2 K)
I = current (A)
k = thermal conductivity of heater material (kW/m K)
L = length of heated cylinder (m)
q''_w = wall heat flux (W/m^2, or kW/m^2)
R = radius of wall thermocouple location (m)
R_o = cylindrical heater outer radius (m)
T = temperature (°C, or K)
ΔT_w = wall superheat (K)
V = voltage (V)
σ = surface tension (mN/m)

Subscripts

o = outer surface
sat = saturation
w = wall

References

[1] Bergles, A. E., 1997, ''Enhancement of Pool Boiling,'' Int. J. Refrig., **20**, pp. 545–551.
[2] Webb, R. L., 1994, *Principles of Enhanced Heat Transfer*, John Wiley and Sons, New York.
[3] Thome, J. R., 1990, *Enhanced Boiling Heat Transfer*, Hemisphere, New York.
[4] Wasekar, V. M., and Manglik, R. M., 1999, ''A Review of Enhanced Heat Transfer in Nucleate Pool Boiling of Aqueous Surfactant and Polymeric Solutions,'' J. Enhanced Heat Transf., **6**, pp. 135–150.

[5] Ammerman, C. N., and You, S. M., 1996, ''Determination of Boiling Enhancement Mechanism Caused by Surfactant Addition to Water,'' ASME J. Heat Transfer, **118**, pp. 429–435.

[6] Wu, W.-T., Yang, Y.-M., and Maa, J.-R., 1998, ''Nucleate Pool Boiling Enhancement by Means of Surfactant Additives,'' Exp. Therm. Fluid Sci., **18**, pp. 195–209.

[7] Westwater, J. W., 1956, ''Boiling of Liquids,'' *Advances in Chemical Engineering*, Vol. I, T. A. Drew and J. W. Hoopes, Jr., eds., Academic, New York, pp. 1–76.

[8] Hahne, E., and Ribeiro, R., 1998, ''Single Bubble Heat Transfer in Nucleate Pool Boiling,'' *Heat Transfer 1998*, Vol. 2, KSME, Seoul, pp. 503–508.

[9] Dushkin, C. D., and Iliev, Tz. H., 1994, ''Dynamic Surface Tension of Micellar Solutions Studied by the Maximum Bubble Pressure Method: 2. Theory of the Solutions below CMC,'' Colloid Polym. Sci., **272**, pp. 1157–1165.

[10] Jontz, P. D., and Myers, J. E., 1960, ''The Effect of Dynamic Surface Tension on Nucleate Boiling Coefficients,'' AIChE J., **6**, No. 1, pp. 34–38.

[11] Morgan, A. I., Bromley, L. A., and Wilke, C. R., 1949, ''Effect of Surface Tension on Heat Transfer in Boiling,'' Ind. Eng. Chem., **41**, pp. 2767–2769.

[12] Iliev, Tz. H., and Dushkin, C. D., 1992, ''Dynamic Surface Tension of Micellar Solutions Studied by the Maximum Bubble Pressure Method,'' Colloid Polym. Sci., **270**, pp. 370–376.

[13] Wasekar, V. M., and Manglik, R. M., 2000, ''Pool Boiling Heat Transfer in Aqueous Anionic Surfactant Solutions: Effect of Additive Molecular Weight,'' *Heat and Mass Transfer 2000*, M. S. Loknath et al., eds., Tata McGraw-Hill, New Delhi, pp. 783–788.

[14] Adamson, A. W., 1982, *Physical Chemistry of Surfaces*, 4th Ed., John Wiley and Sons, New York.

[15] Rosen, M. J., 1989, *Surfactants and Interfacial Phenomena*, 2nd Ed., John Wiley and Sons, New York.

[16] Podsushnyy, A. M., Minayev, A. N., Statsenko, V. N., and Yakubovskiy, Yu. V., 1980, ''Effect of Surfactants and of Scale Formation on Boiling Heat Transfer to Sea Water,'' Heat Transfer—Sov. Res., **12**, No. 2, pp. 113–114.

[17] Filippov, G. A. and Saltanov, G. A., 1982, ''Steam-Liquid Media Heat-Mass Transfer and Hydrodynamics With Surface-Active Substance Additives,'' *Heat Transfer 1982*, Vol. 4, Hemisphere, Washington DC, pp. 443–447.

[18] Saltanov, G. A., Kukushkin, A. N., Solodov, A. P., Sotskov, S. A., Jakusheva, E. V., and Chempik, E., 1986, ''Surfactant Influence on Heat Transfer at Boiling and Condensation,'' *Heat Transfer 1986*, Vol. 5, Hemisphere, Washington DC, pp. 2245–2250.

[19] Liu, T., Cai, Z., and Lin, J., 1990, ''Enhancement of Nucleate Boiling Heat Transfer With Additives,'' *Heat Transfer Enhancement and Energy Conservation*, T. N. Veziroglu et al., eds., Hemisphere, New York, pp. 417–424.

[20] Edwards, D. A., Brenner, H., and Wasan, D. T., 1991, *Interfacial Transport Processes and Rheology*, Butterworth-Heinemann, Boston, Chapter 6.

[21] CRC Press, 1986, *CRC Handbook of Chemistry and Physics*, 67th Ed., CRC Press, Boca Raton, FL.

[22] Barry, B. W., and Wilson, R., 1978, ''C. M. C., Counterion Binding and Thermodynamics of Ethoxylated Anionic and Cationic Surfactants,'' Colloid Polym. Sci., **256**, pp. 251–260.

[23] Porter, M. R., 1994, *Handbook of Surfactants*, 2nd Ed., Blackie, London, Chapter 6.

[24] Wang, T. A. A., 1993, ''Influence of Surfactants on Nucleate Pool Boiling of Aqueous Polyacrylamide Solutions,'' Ph.D. thesis, University of Illinois, Chicago, IL.

[25] Chyu, M.-C., and Bergles, A. E., 1988, ''Thermal Analysis of the Electrically Heated Cylindrical Test Section for Heat Transfer Experiments,'' Exp. Therm. Fluid Sci., **1**, pp. 19–27.

[26] Moffatt, R. J., 1988, ''Describing the Uncertainties in Experimental Results,'' Exp. Therm. Fluid Sci., **1**, pp. 3–17.

[27] Gaertner, R. F., 1965, ''Photographic Study of Nucleate Pool Boiling on a Horizontal Surface,'' ASME J. Heat Transfer, **87**, pp. 17–29.

[28] Miaw, C. B., 1978, ''A Study of Heat Transfer to Dilute Polymer Solutions in Nucleate Pool Boiling,'' Ph.D. thesis, University of Michigan, Ann Arbor, MI.

[29] Shakir, S., Thome, J. R., and Lloyd, J. R., 1985, ''Boiling of Methanol-Water Mixtures on Smooth and Enhanced Surfaces,'' Multiphase Flow and Heat Transfer, ASME, New York, pp. 1–6.

[30] Nicol, A. A., and Mclean, J. T., 1968, ''Boiling Heat Transfer From a Rotating Horizontal Cylinder,'' Can. J. Chem. Eng., **46**, pp. 304–308.

[31] Ayub, Z. H., and Bergles, A. E., 1987, ''Pool Boiling From GEWA Surfaces in Water and R-113,'' Waerme-und Stoffuebertrag., **21**, pp. 209–219.

[32] Hsieh, S.-S., and Weng, C.-J., 1997, ''Nucleate Pool Boiling Heat Transfer Coefficients of Distilled Water (H_2O) and R-134a/Oil Mixtures From Rib-Roughened Surfaces,'' ASME J. Heat Transfer, **119**, pp. 142–151.

[33] Borishanskii, V. M., 1969, ''Correlation of the Effect of Pressure on the Critical Heat Flux and Heat Transfer Rates Using the Theory of Thermodynamic Similarity,'' *Problems of Heat Transfer and Hydraulics of Two-Phase Media*, S. S. Kutateladze, ed., Pergamon Press, New York, pp. 16–37.

[34] Cornwell, K., and Houston, S. D., 1994, ''Nucleate Pool Boiling on Horizontal Tubes: A Convection-Based Correlation,'' Int. J. Heat Mass Transf., **37**, Suppl. 1, pp. 303–309.

[35] Griffith, P., and Wallis, J. D., 1960, ''The Role of Surface Conditions in Nucleate Boiling,'' Chem. Eng. Prog., Symp. Ser., **56**, pp. 47–62.

[36] Tsujii, K., 1998, *Surface Activity: Principles, Phenomena, and Applications*, Academic, San Diego.

[37] Jung, C., and Bergles, A. E., 1989, ''Evaluation of Commercial Enhanced Tubes in Pool Boiling,'' Heat Transfer Laboratory Report No. HTL-2, Rensselaer Polytechnic Institute, Troy, NY.

[38] Bar-Cohen, A., 1992, ''Hysteresis Phenomena at the Onset of Nucleate Boiling,'' *Pool and External Flow Boiling*, ASME, New York, pp. 1–14.

[39] Fritz, W., 1935, ''Berechnung des Maximalvolume von Dampfblasen,'' Phys. Z., **36**, pp. 379–388.

[40] Caery, V. P., 1992, *Liquid-Vapor Phase-Change Phenomena*, Hemisphere, Washington DC.

[41] Jensen, M. K., and Memmel, G. J., 1986, ''Evaluation of Bubble Departure Diameter Correlations,'' *Heat Transfer 1986*, Vol. 4, C. L. Tien et al., eds., Hemisphere, Washington, DC, pp. 1907–1912.

[42] Yan, Y., Kenning, D., and Cornwell, K., 1997, ''Sliding and Sticking Vapor Bubbles Under Inclined Plane and Curved Surfaces,'' Int. J. Refrig., **20**, pp. 583–591.

[43] Cornwell, K., and Grant, I. A., 1998, ''Heat Transfer to Bubbles Under a Horizontal Tube,'' Int. J. Heat Mass Transf., **41**, pp. 1189–1197.

[44] Gorenflo, D., Luke, A., and Danger, E., 1998, ''Interactions Between Heat Transfer and Bubble Formation in Nucleate Boiling,'' *Heat Transfer 1998*, Vol. 1, KSME, Seoul, pp. 149–174.

[45] Tokiwa, F., and Ohki, K., 1967, ''Micellar Properties of a Series of Sodium Dodecylpolyoxyethylene Sulfates From Hydrodynamic Data,'' J. Phys. Chem., **71**, pp. 1343–1348.

[46] Manglik, R. M., 1998, ''Pool Boiling Characteristics of High Concentration Aqueous Surfactant Emulsions,'' *Heat Transfer 1998*, Vol. 2, KSME, Seoul, pp. 449–453.

[47] Tzan, Y. L., and Yang, Y. M., 1990, ''Experimental Study of Surfactant Effects on Pool Boiling Heat Transfer,'' ASME J. Heat Transfer, **112**, pp. 207–212.

Diffusion Layer Modeling for Condensation With Multicomponent Noncondensable Gases

P. F. Peterson
Department of Nuclear Engineering,
University of California,
Berkeley, CA 94720-1730
e-mail: peterson@nuc.berkeley.edu

Many condensation problems involving noncondensable gases have multiple noncondensable species, for example, air (with nitrogen, oxygen, and other gases); and other problems where light gases like hydrogen may mix with heavier gases like nitrogen. Particularly when the binary mass diffusion coefficients of the noncondensable species are substantially different, the noncondensable species tend to segregate in the condensation boundary layer. This paper presents a fundamental analysis of the mass transport with multiple noncondensable species, identifying a simple method to calculate an effective mass diffusion coefficient that can be used with the simple diffusion layer model. The results are illustrated with quantitative examples to demonstrate the potential importance of multicomponent noncondensable gas effects. [S0022-1481(00)01104-X]

Keywords: *Condensation, Heat Transfer, Multicomponent, Multiphase, Nucleonics*

Introduction

Noncondensable gases are well known to degrade condensation heat transfer rates for pure vapors, by generating a mass transfer resistance as shown in Fig. 1. Stagnant film models (SFM), also referred to as Couette flow models, have long been available for multicomponent phase change and are described in standard texts ([1,2]). Considerable simplification of the SFM approach is possible when all species except the vapor are noncondensable. For noncondensable gas systems, the diffusion layer model (DLM) ([3]) allows the gas degradation to be expressed in the form of a simple effective condensation thermal conductivity which is only a weak function of the liquid-vapor interface temperature, allowing rapid convergence to the correct condensation heat flux in a few iterations.

Due to its simplicity, DLM has been subsequently applied extensively for nuclear reactor thermal hydraulics modeling, being incorporated into the RELAP5/MOD3 code ([4]), used for condensation analysis for the AP-600 reactor ([5]), and providing a basis for assessing the validity of the commonly used Uchida correlation ([6]).

A variety of DLM formulations are possible which introduce varying degrees of approximation. Brouwers [7] provided modifications to account for the effects of suction and fog formation on sensible heat transfer.

This paper discusses the extension of DLM to multicomponent noncondensable-gas mixtures. The correct treatment of multicomponent noncondensables becomes particularly important for mixtures like air and helium or nitrogen and hydrogen, where the different noncondensable species have much different mass diffusion coefficients. Examples include fission reactor severe accidents, where hydrogen can mix with air or nitrogen ([5]), and where helium may be used as an inert substitute for hydrogen in experiments. Likewise, while air is a multicomponent gas, the theory developed here demonstrates that the averaged diffusion coefficient can be used for air with negligible error due to the similar diffusion coefficients of nitrogen and oxygen, the major air components.

Diffusion Layer Model

The diffusion layer model provides a convenient approach for predicting condensation rates in the presence of a single noncondensable gas species, Fig. 1, by expressing the mass transfer coefficient in terms of an equivalent condensation heat transfer coefficient h_c. The total heat flux q_t'' is then controlled by the parallel resistance with the sensible heat transfer coefficient h_s, and the series resistance with the film-and-wall-heat-transfer coefficient h_w ([3]),

$$q_t''=\frac{h_c(T_b^s-T_\infty)+\theta_T' h_s(T_b-T_\infty)}{1+\dfrac{h_c+\theta_T' h_s}{h_w}} \tag{1}$$

This allows the total heat flux q_t'' to be expressed as a simple function of the temperature difference between the cooling me-

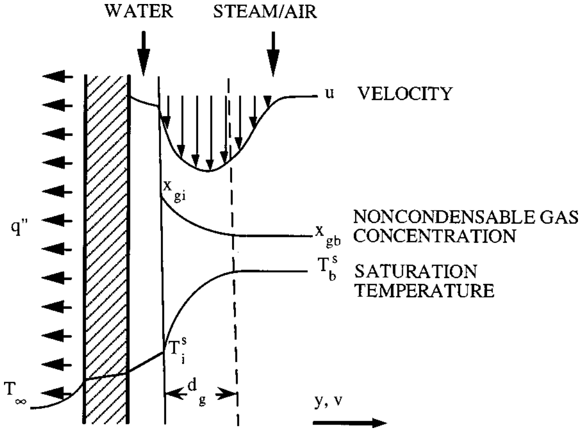

Fig. 1 Schematic illustration of condensation with noncondensable gas

---

Contributed by the Heat Transfer Division for publication in the JOURNAL OF HEAT TRANSFER and presented at the 1999 NHTC, Albuquerque, NM. Manuscript received by the Heat Transfer Division, Sept. 10, 1999; revision received, May 19, 2000. Associate Technical Editor. D. Poulikakos.

dium T_∞ and the bulk sensible temperature T_b and saturation temperature T_b^s, where the bulk saturation temperature is evaluated based on the bulk vapor partial pressure. The sensible heat transfer should be corrected by a modified Ackermann correction, θ_T', discussed later, as well as a correction for fog formation ([7]).

To derive the effective condensation heat transfer coefficient, the diffusion layer model introduces the Clausius–Clapeyron approximation for the difference between the vapor saturation partial pressures at the bulk and interface temperatures,

$$\frac{P_{vb}-P_{vi}}{T_b^s-T_i^s} \approx \frac{h_{fg}x_{v,\mathrm{ave}}P_tM_v}{RT_{\mathrm{ave}}^2} \tag{2}$$

and the molar density of the condensing vapor is approximated using the ideal gas law,

$$c=\left(\frac{\rho_v}{P_v}\right)_{\mathrm{ave}}\frac{P_t}{M_v}\approx\frac{P_t}{RT_{\mathrm{ave}}} \tag{3}$$

These assumptions permit derivation of an ''effective condensation thermal conductivity,'' ([3])

$$k_c=\frac{1}{\phi T_{\mathrm{ave}}}\left(\frac{h_{fg}h_{fg}'P_oM_v^2D_{o,\mathrm{eff}}}{R^2T_o^2}\right) \tag{4}$$

where M_v is the molecular weight of the condensing vapor, R the ideal gas constant, and T_{ave} the arithmetic average of the bulk and interface saturation temperatures $(T_b^s+T_i^s)/2$. In this paper it is also noted that greater accuracy can be obtained by using the following values for the latent heats: $h_{fg}=h_{fg}(T_{\mathrm{ave}})$, and $h_{fg}'=h_{fg}(T_i)+c_{pv}(T_b-T_i)$, where c_{pv} is the specific heat of the vapor species. The condensation thermal conductivity increases with decreasing noncondensable gas concentration due to the factor ϕ, the ratio of the log-mean gas and vapor mole fractions,

$$\phi=\frac{x_{g,\mathrm{ave}}}{x_{v,\mathrm{ave}}} \tag{5}$$

where the log-mean concentration is given in terms of the bulk and interface concentrations as

$$x_{\mathrm{ave}}=\frac{x_b-x_i}{\ln(x_b/x_i)} \tag{6}$$

Interestingly, like the sensible thermal conductivity and dynamic viscosity of gases, the condensation thermal conductivity depends only weakly on pressure, unlike the mass diffusion coefficient D.

Alternatively, to avoid these approximations tabulated data for the saturation pressures P_v and vapor density over saturation pressure ρ_v/P_v can be used, and the effective condensation thermal conductivity without approximation becomes

$$\begin{aligned} k_c&=\frac{q_c''\delta_g}{T_b^s-T_i^s}=\frac{h_{fg}'cM_v\tilde{v}\delta_g}{T_b^s-T_i^s}\\ &=\frac{h_{fg}'D}{x_{g,\mathrm{ave}}P_t}\left(\frac{\rho_v}{P^s}\right)_{\mathrm{ave}}\frac{P_{vb}-P_{vi}}{T_b^s-T_i^s} \end{aligned} \tag{7}$$

Using the heat and mass transfer analogy, the condensation heat transfer coefficient h_c can be predicted from standard heat transfer correlations using the Sherwood number $\mathrm{Sh}_L(\mathrm{Sc})=\mathrm{Nu}_L(\mathrm{Pr})$, as

$$\mathrm{Sh}_L=\frac{L}{\delta_g}=\frac{h_cL}{k_c} \tag{8}$$

just as the sensible heat transfer coefficient comes from $\mathrm{Nu}_L=L/\delta_T=h_sL/k_s$, where δ_g and δ_T are the effective diffusion layer thicknesses for mass and heat transfer. The convenience of the diffusion layer model occurs because the ''condensation thermal conductivity'' k_c is only a weak function of the interface temperature T_i, and thus rapid convergence is possible even with a crude initial guess for T_i.

Multiple Gas Species Mass Diffusion

When mass diffusion occurs with multiple species, Wilke [8] provides a relationship for the diffusion of gas A into a mixture of gases $B,C,D\ldots$,

$$\frac{dx_A}{dy}=\frac{x_Ax_B}{D_{AB}}(v_A-v_B)+\frac{x_Ax_C}{D_{AC}}(v_A-v_C)+\frac{x_Ax_D}{D_{AD}}(v_A-v_D)+\cdots \tag{9}$$

where y is position, D_{AB} is the binary mass diffusion coefficient for species A into species B, and v_A is the average velocity of species A. Now we let the condensing species be $x_v=x_B$ and all the other species be noncondensable, and then let the n noncondensable species take values $x_j=x_A$ to obtain separate equations for each species. Noting that the noncondensing species are stagnant in the diffusion layer and thus $v_j=v_A=0$ and $v_C=v_D=\ldots=0$, then Eq. (9) gives n equations, one for each of the noncondensable species j,

$$\tilde{v}=x_vv_v=\frac{D_{jv}}{x_j}\frac{dx_j}{dy}=D_{jv}\frac{d}{dy}\ln(x_j) \tag{10}$$

where $\tilde{v}$ is the mole average velocity toward the wall and D_{jv} is the binary diffusion coefficient of noncondensable species j into the vapor. For one-dimensional flow, mass conservation requires that

$$\frac{d}{dy}(c\tilde{v})=c\frac{d\tilde{v}}{dy}+\tilde{v}\frac{dc}{dy}=0 \tag{11}$$

Because the pressure is constant through the diffusion layer, and because the temperature change through the layer is typically small compared to the absolute temperature, it is valid to assume that the molar density c is constant, so that $dc/dy=0$. Equation (11) then requires that the mole average velocity $\tilde{v}$ is also a constant in the diffusion layer. This allows Eq. (10) to be integrated from the condensing interface through the diffusion layer thickness δ_g,

$$\tilde{v}=\frac{D_{jv}}{\delta_g}[\ln(x_{jb})-\ln(x_{ji})]=\frac{D_{jv}}{\delta_g}\frac{(x_{jb}-x_{ji})}{x_{j,\mathrm{ave}}} \tag{12}$$

providing n equations, where x_{jb} is the bulk mole fraction, x_{ji} the interface mole fraction, and $x_{j,\mathrm{ave}}$ the log mean average given by Eq. (6) for noncondensable species j.

Because $\tilde{v}$ and δ_g are constants, and Eq. (12) applies for all of the n noncondensable species, it is important to note that the concentration gradient of high-mass-diffusivity species like helium and hydrogen will be significantly smaller than for lower-diffusivity species like nitrogen, and therefore the lower diffusivity species will tend to accumulate to higher concentrations at the condensing interface. Figure 2 illustrates this effect, showing the diffusion-layer mole fraction distributions that can occur for condensing helium/air/steam mixtures.

The bulk and the interface total noncondensable mole fractions are given by

$$x_{gb}=\sum_{j=1}^{n}x_{jb} \tag{13}$$

$$x_{gi}=\sum_{j=1}^{n}x_{ji}=1-\frac{P_v(T_i)}{P_t} \tag{14}$$

Multiplying the n equations of Eq. (12) by $x_{j,\mathrm{ave}}$, summing the n equations, and rearranging then gives the condensation velocity as

$$\tilde{v}=\left(\frac{x_{g,\mathrm{ave}}}{\sum_{j=1}^{n}(x_{j,\mathrm{ave}}/D_{jv})}\right)\frac{1}{\delta_g}\frac{(x_{gb}-x_{gi})}{x_{g,\mathrm{ave}}} \tag{15}$$

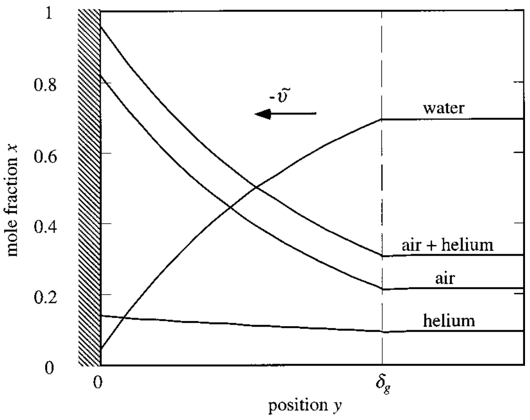

Fig. 2 Illustration of typical gas and vapor mole fraction distributions in the diffusion layer (case 1 from Table 1)

For a single noncondensable gas species, Eq. (15) reduces to the same equation derived by Peterson et al. [their Eq. (6)] ([3]), and earlier by Bird et al. ([1]) [their Eq. (21.5-36), with their flux $N_{B0}=0$], or

$$\tilde{v}=\frac{D_{gv}}{\delta_g}\frac{(x_{gb}-x_{gi})}{x_{g,\mathrm{ave}}} \tag{16}$$

Comparing Eqs. (15) and (16), it is readily seen that the single-noncondensable-species diffusion layer theory, which results in a condensation thermal conductivity given in Eq. (4), can be used for multiple noncondensable species simply by using an effective mass diffusion coefficient, originally derived by Wilke [8] and confirmed experimentally by Fairbanks and Wilke [9]

$$D_{\mathrm{eff}}=\frac{x_{g,\mathrm{ave}}}{\sum_{j=1}^{n}(x_{j,\mathrm{ave}}/D_{jv})}. \tag{17}$$

Evaluating the effective mass diffusion coefficient requires knowledge of the binary mass diffusion coefficients of each of the noncondensable gas species into the vapor species, D_{jv}, as well as the bulk and interface noncondensable species mole fractions x_{jb} and x_{ji}. While the binary mass diffusion coefficients can be evaluated from correlations, and the bulk noncondensable gas composition is usually known, the interface gas composition must be determined by an iterative procedure. Because a small number of iterations are often needed anyhow to determine the interface temperature and the resulting interface noncondensable gas concentration from Eq. (14), for example using the iterative procedure outlined by Kuhn et al. [10], these iterations can also allow rapid convergence to the correct effective diffusion coefficient D_{eff}.

If not known, the interface temperature can initially be assumed to equal the wall temperature, and then an initial estimate of the interface total gas mole fraction x'_{gi} calculated from Eq. (14). A first estimate of the interface mole fraction of each of the *n* noncondensable species can then assume the same relative proportions of gas species at the interface and in the bulk, or $x'_{ji}=x_{jb}x'_{gi}/x_{gb}$.

With an initial estimate for the interface concentration of each of the *n* noncondensable species, convergence to the correct interface concentrations can be achieved in three to ten iterations. Combining Eqs. (12) and (16),

$$x''_{ji}=\exp\left[\ln(x_{jb})-\frac{D'_{\mathrm{eff}}}{D_{jv}}\frac{(x_{gb}-x'_{gi})}{x_{g,\mathrm{ave}}}\right] \tag{18}$$

Table 1 Example diffusion coefficient calculations for air/helium/water systems, with comparison of averaging methods (A,B,C).

Case	1	2	3	4	5
Input parameters					
T_b(C)	90.0	90.0	131	131	131
T_i(C)	30	30	120	120	30
P(atm)	1.0	1.0	3.0	3.0	3.0
$x_{\mathrm{He},b}/x_{gb}$	0.30	0.80	0.30	0.90	0.90
Calculated parameters					
x_{gb}	0.308	0.308	0.083	0.083	0.083
x_{gi}	0.958	0.958	0.346	0.346	0.973
$x_{\mathrm{He},i}/x_{gi}$	0.144	0.611	0.118	0.529	0.306
$D_{\mathrm{He\text{-}H_2O}}(T_{\mathrm{ave}})(10^4\ \mathrm{m^2/s})$	1.017	1.017	0.464	0.464	0.376
$D_{\mathrm{Air\text{-}H_2O}}(T_{\mathrm{ave}})(10^4\ \mathrm{m^2/s})$	0.305	0.305	0.139	0.139	0.113
(A)$D_{(\mathrm{A})}(10^4\ \mathrm{m^2/s})$	0.519	0.946	0.237	0.432	0.350
(B)$D_{(\mathrm{B})}(10^4\ \mathrm{m^2/s})$	0.386	0.824	0.176	0.376	0.305
(C)$D_{\mathrm{eff}}(10^4\ \mathrm{m^2/s})$	0.359	0.670	0.162	0.291	0.206

(A) bulk mole-fraction-weighted average $(x_{\mathrm{He},b}D_{\mathrm{He\text{-}H_2O}}+x_{\mathrm{Air},b}D_{\mathrm{Air\text{-}H_2O}})/x_{gb}$.
(B) inverse bulk mole-fraction-weighted average $x_{gb}/x(x_{\mathrm{He},b}/D_{\mathrm{He\text{-}H_2O}}+x_{\mathrm{Air},b}/D_{\mathrm{Air\text{-}H_2O}})$.
(C) effective mass diffusion coefficient, Eq. (17).

$$x'_{ji}=x''_{ji}\frac{x'_{gi}}{\sum_{j=1}^{n}x_{ji}} \tag{19}$$

The procedure then involves the following steps: (1) calculate an estimate for D'_{eff} using Eq. (17) and the current estimates x'_{ji}; (2) calculate the vector of *n* values x''_{ji} using Eq. (18); (3) normalize the results using Eq. (19) to give the desired total gas mole fraction x'_{gi} and obtain a new estimate for x'_{ji}; and (4) iterate to step (1) until converged on D_{eff}.

Table 1 provides several example cases for a steam/air/helium system. The correct effective diffusion coefficient (C) is compared with a simple bulk mole fraction weighted average (A) and inverse bulk mole fraction weighted average (B), and is found to be substantially lower. The helium is remarkably ineffective in augmenting the mass transfer. Even at bulk helium concentrations of 90 mole percent, the effective diffusion coefficient remains much closer to the lower value for pure air than the higher helium value, showing the importance of the accumulation of higher air concentrations close to the condensing surface. *Proper calculation of the effective diffusion coefficient makes a substantial difference in the predicted mass transfer rate.*

Air is also a multicomponent mixture of nitrogen, oxygen, argon, small amounts of carbon dioxide, and traces of other gases. Because the mass diffusion coefficients of nitrogen, oxygen, and argon are quite similar, negligible concentration of any of these species occurs in the boundary layer when Eqs. (17)–(19) are applied.

Similarity of H_2-Air and He-Air Combinations

Condensation heat transfer with mixtures of air and hydrogen is commonly of interest for analysis of light water reactor containment response during severe accidents, due to the potential for cladding oxidation with steam to create hydrogen that can subsequently mix with air or nitrogen in the containment. Due to the flammability hazard, helium is often substituted for hydrogen in experiments.

Table 2 shows a comparison of the effects of hydrogen and helium on condensation, for the same cases considered above in Table 1. The mass diffusion coefficient for hydrogen, $D_{\mathrm{H_2\text{-}H_2O}}$, is typically almost 10 percent higher than that of helium. This causes a larger depletion of hydrogen in the diffusion layer, with the relative interface mole fraction, $x_{\mathrm{H_2},i}$, being around 3 to 11 per-

Table 2 Comparison of hydrogen/air and helium/air systems (same input parameters as Table 1)

Case	1	2	3	4	5
Input parameters					
T_b(C)	90.0	90.0	131	131	131
T_i(C)	30	30	120	120	30
P(atm)	1.0	1.0	3.0	3.0	3.0
$x_{\mathrm{He},b}/x_{gb}$	0.30	0.90	0.30	0.90	0.90
Calculated parameters					
x_{gb}	0.308	0.308	0.083	0.083	0.083
x_{gi}	0.958	0.958	0.346	0.346	0.973
$(D_{\mathrm{H_2\text{-}H_2O}}/(D_{\mathrm{He\text{-}H_2O}})$	1.096	1.096	1.098	1.098	1.098
$(x_{\mathrm{H_2},i}/x_{gi})/(x_{\mathrm{He},i}/x_{gi})$	0.965	0.954	0.958	0.949	0.889
$(D_{\mathrm{eff,H_2}})/(D_{\mathrm{eff,He}})$	1.004	1.029	1.004	1.026	1.005
$(\Delta\rho/\rho)_{\mathrm{H_2}}/(\Delta\rho/\rho)_{\mathrm{He}}$	1.008	1.048	1.007	1.059	1.068
$\dfrac{[D_{\mathrm{eff}}^{2/3}(\Delta\rho/\rho)^{1/3}]_{\mathrm{H_2}}}{[D_{\mathrm{eff}}^{2/3}(\Delta\rho/\rho)^{1/3}]_{\mathrm{He}}}$	1.007	1.0045	0.006	0.046	0.127

cent lower than for helium. Interestingly, for the effective diffusion coefficient, D_{eff}, this depletion effect cancels, in part, the higher mass diffusion coefficient of hydrogen, so that $D_{\mathrm{eff,H_2}}$ is less than 3 percent higher than for helium. Thus, for forced convection, helium reproduces the effects of hydrogen with only small distortions, as long as a similar number moles (not kilograms) is used in the experiment.

For natural convection the difference between the bulk and interface densities, $\Delta\rho$, depends on the molecular weight of the light gas, as well as the depletion that occurs in the diffusion layer. The density of the mixture is relatively insensitive to the molecular weight of the light species, as long as it is present at the same mole fraction, since the total density is dominated by the heavy species. The relatively higher depletion of hydrogen in the diffusion layer reduces the effect of its lower molecular weight, so as shown in Table 2 the bulk to interface density difference $\Delta\rho/\rho$ typically increases by 7 percent or less. For turbulent natural convection the Sherwood number typically varies with the Rayleigh number to the 1/3 power, so that the condensation mass transfer coefficient varies as $D_{\mathrm{eff}}^{2/3}(\Delta\rho/\rho)^{1/3}$. For the cases shown in Table 2, hydrogen at the same mole fraction increases natural convection mass transfer by less than 5 percent, again showing that helium is an acceptable simulant gas for hydrogen if used at the same molar concentrations.

Multiple Gas Species Sensible Heat Transfer

Next the question of sensible heat transfer is discussed. Convection augments sensible heat transfer, giving a sensible heat transfer balance in the diffusion layer as

$$q_s''=(T-T_i)c\tilde{v}M_v c_{pv}-k_s\frac{dT}{dy} \tag{20}$$

Noting that the sensible heat flux is constant through the boundary layer, and assuming that sensible thermal conductivity k_s is constant and equal to the average mixture value,

$$k_s=\frac{1}{\dfrac{x_{v,\mathrm{ave}}}{k_v}+\displaystyle\sum_{j=1}^{n}\frac{x_{j,\mathrm{ave}}}{k_j}} \tag{21}$$

then Eq. (20) can be integrated through the thermal boundary layer thickness δ_T, giving

$$1-\frac{(T_b-T_i)c\tilde{v}M_v c_{pv}}{q_s''}=\exp\left(\frac{c\tilde{v}M_v c_{pv}\delta_T}{k_s}\right) \tag{22}$$

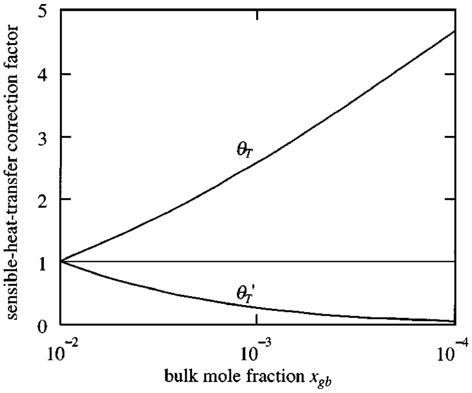

Fig. 3 Comparison of Ackermann correction θ_T with modified form for small bulk gas concentrations x_{gb}, with $x_{gi}=0.01$ and $(cM_v c_{pv}D_{\mathrm{eff}}/k_s)$ Sh/Nu=1

In Eq. (4) for the condensation thermal conductivity, it is recommended to use $h_{fg}'=h_{fg,i}+c_{pv}(T_b-T_i)$, which is equivalent to adding an additional energy flux to the condensation heat transfer coefficient of $-c\tilde{v}M_v c_{pv}(T_b-T_i)$. Therefore, the net sensible heat flux, which is positive for condensation (since $\tilde{v}$ is negative), is $q_{sn}''=c\tilde{v}M_v c_{pv}(T_b-T_i)-q_s''$, which gives

$$q_{sn}''=\frac{c\tilde{v}M_v c_{pv}}{1-\exp\left(-\dfrac{c\tilde{v}M_v c_{pv}\delta_T}{k_s}\right)}(T_b-T_i)$$

$$=\theta_T'\frac{k_s}{\delta_T}(T_b-T_i)=\theta_T' h_s(T_b-T_i) \tag{23}$$

where θ_T' is a *modified* Ackermann correction, given by

$$\theta_T'=\frac{\Phi}{1-\exp(-\Phi)} \tag{24}$$

Figure 3 shows the magnitude of the two forms of the Ackermann correction, showing that when the modified form is used, the correction is smaller.

Using Eq. (12) with D_{eff} and noting that $\delta_T/\delta_g=\mathrm{Sh/Nu}$,

$$\Phi=-\left(\frac{D_{\mathrm{eff}}}{k_s/cM_v c_{pv}}\right)\frac{\mathrm{Sh}}{\mathrm{Nu}}[\ln(x_{gi}+\varepsilon)-\ln(x_{gb}+\varepsilon)] \tag{25}$$

where ε is a small number (i.e., 10^{-10}) which allows computer models to treat pure vapor, $x_{gb}=0$, gracefully.

Under conditions where fog formation can occur, an additional correction to the sensible heat transfer contribution becomes warranted. Brouwers [8,11] discusses this correction and the tangency condition where it should be applied ([12]).

Conclusions

When noncondensable gases consist of mixtures of heavy, low mass diffusion species and light, high mass diffusion species, then during condensation the heavy species accumulates preferentially at the condensing interface. This effect alters substantially the effective mass diffusion, making even large fractions of light gases remarkably ineffective in augmenting condensation heat transfer in the presence of heavy gases. A relatively straightforward iterative procedure can be applied to predict the effective mass diffusion coefficient under these conditions.

When one of the gas species has a particularly high mass diffusion coefficient, like hydrogen or helium, mass transfer can cause it to be substantially depleted in the diffusion layer compared to the heavier noncondensable species. In the cases considered here, helium gives mass transfer rates less than five percent lower than hydrogen, for both forced and turbulent natural convection, making it an effective, inert simulant gas for condensation experiments, if it is used at the same *molar* concentrations. The depletion of the lighter species in the boundary layer may create a distortion when natural convection correlations for heat transfer are applied to condensation problems using the heat and mass transfer analogy; these potential effects provide an interesting area for future study.

Air is also a multicomponent noncondensable gas mixture, but the mass diffusion coefficients of the principal species are sufficiently similar that negligible relative concentration of any of the species occurs in the diffusion layer. Thus for air the commonly used average mass diffusion coefficient provides accurate prediction of condensation heat transfer.

Nomenclature

c = molar density (kmol/m^3)
c_p = constant pressure specific heat (J/kg K)
D = mass diffusivity (m^2/s)
h = heat transfer coefficient (W/m^2 K)
h_{fg} = latent heat of vaporization (J/kg)
h'_{fg} = $h_{fg}(T_i)+c_{pv}(T_b-T_i)$
k = thermal conductivity (W/m K)
L = length scale (m)
$\dot{m}''$ = mass flux for mass (ρ) or mole (c) formulations (kg/m^2 s)
M = molecular weight (kmol/kg)
n = number of noncondensable species
Nu = Nusselt number, $h_s L/k_s$
P = absolute pressure (Pa)
q'' = heat flux (W/m^2)
R = universal gas constant (J/kmol K)
Sh = Sherwood number, $h_c L/k_c$
T = absolute temperature (K)
v = velocity (m/s)
$\tilde{v}$ = molar average velocity (m/s)
x = mole fraction
x_{ave} = average mole fraction, Eq. (6)
y = coordinate normal to interface (m)
δ = diffusion layer thickness (m)
ϕ = gas/vapor log mean concentration ratio, Eq. (5)
Φ = Eq. (28)
θ'_T = modified Ackermann correction, Eq. (27)

Subscripts

ave = average of bulk and interface
b = bulk
c = condensation
eff = effective value
g = noncondensable gas species
i = liquid/vapor interface
o = value at reference temperature T_o
s = sensible heat
t = total
v = vapor species
w = wall, film, and external resistance
∞ = bulk cooling medium

Superscripts

s = saturation

References

[1] Bird, R. B., Stewart, W. E., and Lightfoot, E. N., 1960, *Transport Phenomena*, John Wiley & Sons, New York.
[2] Kays, M. K., and Crawford, M. E., 1993, *Convective Heat and Mass Transfer*, 3rd Ed., McGraw-Hill, New York.
[3] Peterson, P. F., Schrock, V. E., and Kageyama, T., 1993, ''Diffusion Layer Theory for Turbulent Vapor Condensation With Noncondensable Gases,'' ASME J. Heat Transfer, **115**, pp. 998–1003.
[4] Hassan, Y. A., and Banerjee, S., 1996, ''Implementation of a Non-Condensable Model in RELAP5/MOD3,'' Nucl. Eng. Des., **162**, pp. 281–300.
[5] Herranz, L. E., Anderson, M. H., and Corradini, M. L., 1998, ''A Diffusion Layer Model for Steam Condensation Within the AP600 Containment,'' Nucl. Eng. Des., **183**, pp. 133–150.
[6] Peterson, P. F., 1996, ''Theoretical Basis for the Uchida Correlation for Condensation In Reactor Containments,'' Nucl. Eng. Des., **162**, pp. 301–306.
[7] Brouwers, H. J. H., 1996, ''Effect of Fog Formation on Turbulent Vapor Condensation With Noncondensable Gases,'' ASME J. Heat Transfer, **118**, pp. 243–245.
[8] Wilke, C. R., 1950, ''Diffusional Properties of Multicomponent Gases,'' Chem. Eng. Prog., **46**, No. 2, pp. 95–104.
[9] Fairbanks, D. F., and Wilke, C. R., 1950, ''Diffusion Coefficients in Multicomponent Gas Mixtures,'' Ind. Eng. Chem., **42**, No. 3, pp. 471–475.
[10] Kuhn, S. Z., Schrock, V. E., and Peterson, P. F., 1997, ''An Investigation of Condensation from Steam-Gas Mixtures Flowing Downward Inside a Vertical Tube,'' Nucl. Eng. Des., to appear.
[11] Brouwers, H. J. H., 1992, ''A Film Model for Heat and Mass Transfer With Fog Formation,'' Chem. Eng. Sci., **47**, pp. 3023–3036.
[12] Brouwers, H. J. H., 1991, ''An Improved Tangency Condition for Fog Formation in Condenser-Coolers,'' Int. J. Heat Mass Transf., **34**, pp. 2387–2394.

Combustion-Thermoelectric Tube

C.-W. Park

M. Kaviany[1]
e-mail: kaviany@umich.edu

Department of Mechanical Engineering,
The University of Michigan,
Ann Arbor, MI 48109-2125

In direct combustion-thermoelectric energy conversion, direct fuel injection and reciprocation of the air flowing in a solid matrix are combined with the solid-gas interfacial heat transfer and the solid conduction to allow for obtaining superadiabatic temperatures at the hot junctions. While the solid conductivity is necessary, the relatively large thermal conductivity of the available high-temperature thermoelectric materials (e.g., Si–Ge alloys) results in a large conduction loss from the hot junctions and deteriorates the performance. Here, a combustion-thermoelectric tube is introduced and analyzed. Radially averaged temperatures are used for the fluid and solid phases. A combination of external cooling of the cold junctions, and direct injection of the fuel, has been used to increase the energy conversion efficiency for low thermal conductivity, high-melting temperature thermoelectric materials. The parametric study (geometry, flow, stoichiometry, materials) shows that with the current high figure of merit, high temperature $Si_{0.7}Ge_{0.3}$ properties, a conversion efficiency of about 11 percent is achievable. With lower thermal conductivities for these high-temperature materials, efficiencies about 25 percent appear possible. This places this energy conversion in line with the other high efficiency, direct, electric power generation methods. [S0022-1481(00)01304-9]

Keywords: *Combustion, Energy Conversion, Heat Transfer, Optimization, Thermoelectric*

Introduction

Local, superadiabatic temperatures are obtained in premixed combustion in porous media by gas preheating (i.e., heat recirculation) through the solid matrix. Hanamura et al. [1] have designed a reciprocating premixed fluid flow-porous medium system to create such super-adiabatic temperatures. The release of the heat of combustion in the gas phase is followed by the solid-gas interfacial heat transfer and solid-phase conduction and radiation. The interfacial heat transfer to the upstream cold gaseous stream completes the heat recirculation and the formation of local, superadiabatic temperatures in the flame region ([2–5]). The important roles of the interfacial surface area per unit volume, the Nusselt number, and the reciprocation of the flow, are evident in this heat recirculation. As compared to the unidirectional flow arrangement used for achieving a superadiabatic flame temperature by solid conduction (and surface radiation), the reciprocation of the flow allows for heat recirculation using the storage/release of the thermal energy in the solid. The lack of solid conductivity and surface radiation would assist the process.

Echigo et al. [6] have also suggested that such a system can be harvested for thermoelectric energy conversion by placing the hot junction in the flame region and the cold junction in the entrance region (one on each side). A relatively short combustion region separates the two thermoelectric regions. Critical to the high efficiency of this combustion-thermoelectric system is the solid conductivity in the thermoelectric region. The currently available high-temperature thermoelectric materials ([7]), have relatively high figure of merits (e.g., Si–Ge alloys), while also having relatively high thermal conductivities which prevent high energy-conversion efficiencies. These high-temperature ceramics are fabricated from powders and the effective conductivity of the sintered powder mixture is much smaller than the bulk thermal conductivity of each of the components and depends on their grain sizes. It has been shown by Chen [8] that the effective conductivity can be reduced by using very fine grains. The search for low conductivity thermoelectric materials continues.

The use of direct fuel injection, as compared to premixing, allows for a better control of the flame location and further increases the maximum gas and solid temperatures avoiding any premature ignition ([9]).

Here in order to identify the potential and limitation of this energy conversion system, a combustion-thermoelectric tube is introduced and analyzed. The tube is shown in Fig. 1(*a*). The reciprocating oxidant (here air is used) flow is represented by a radially averaged fluid velocity $\langle u \rangle_g$ which alters in direction at the end of each half cycle. The tube consists of two thermoelectric regions (designated by TE) and one combustion region (designated by *C*). The combustion region is much shorter than each of the thermoelectric regions. The tube inside and outside diameters are uniform throughout. In the thermoelectric region, the tube wall is made of a layer of *p*-type and a layer of *n*-type semiconductor materials with a very thin (neglected thickness) dielectric layer (such as a silicon oxide) separating these two layers. The thermoelectric and combustion regions are connected with an assumed negligible thermal contact resistance.

The fuel (gaseous methane) is injected laterally in a short combustion region. Due to the small diameter tube (order of one millimeter), the fuel is expected to mix over a short distance. Using radial diffusion only, the distance needed for the penetration of the fluid supplied at the periphery is $0.01\langle u \rangle_{g,o} D_1^2/D_m$. For the range of $\langle u \rangle_{g,o}$, D_1, and D_m (and T_g) considered here, this distance is less than the tube diameter D_1. Also, due to the high temperature of the combustion region and the availability of the oxidant (i.e., low stoichiometry, fuel-limited combustion), the fuel is completely burned.

There are geometrical parameters (diameters and lengths), flow parameters (velocity and cycle period), heat transfer parameters (Nusselt number, surface emissivity), fuel parameters (stoichiometric ratio), thermoelectric material properties (Seebeck coefficient, thermal conductivity, electrical resistivity), and power-circuit parameter (external resistance). Through parametric variations, the role of these parameters on the thermoelectric energy conversion is studied using the properties of one of the current high-temperature thermoelectric materials, i.e., $Si_{0.7}Ge_{0.3}$ alloys. Then further increase in the efficiency is demonstrated with a reduction in the thermal conductivity.

---

[1] To whom correspondence should be addressed.

Contributed by the Heat Transfer Division for publication in the JOURNAL OF HEAT TRANSFER. Manuscript received by the Heat Transfer Division, Feb. 20, 1999; revision received, June 5, 2000. Associate Technical Editor: J. P. Gore.

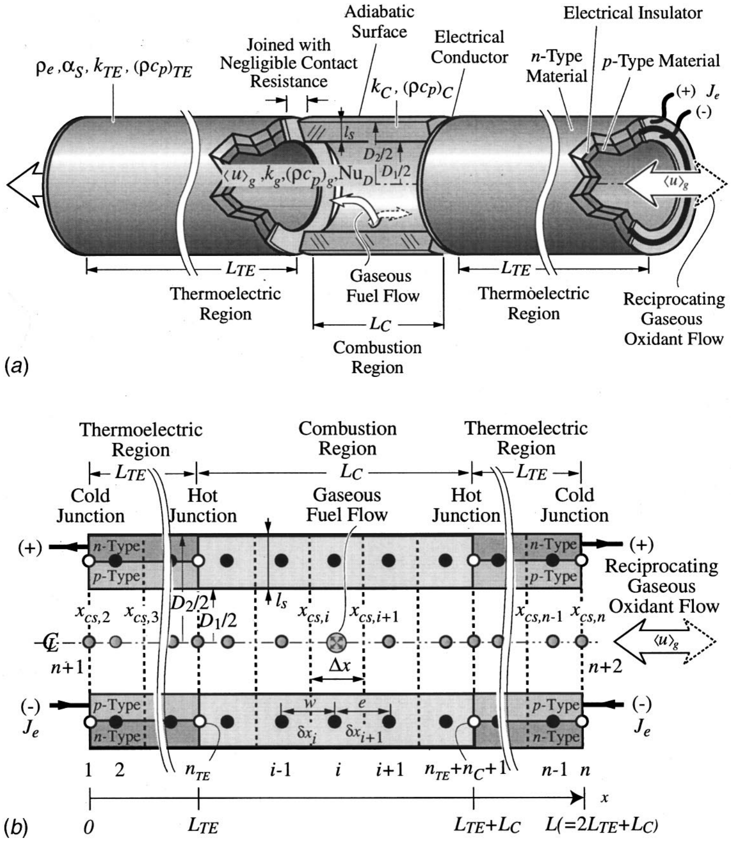

Fig. 1 (***a***) **A schematic of the combustion-thermoelectric tube; (*b*) thermal nodal model of the combustion-thermoelectric tube.**

Analysis

Radially averaged temperatures are used for the gas and solid phases. The various regions are axially divided into small, finite volumes. These volumes are shown in Fig. 1(*b*). The surface nodes are shown with open circles and they are at the cold and hot junctions, i.e., at $i=1$, n_{TE}, $n_{\mathrm{TE}}+n_C+1$, and n. Constant thermophysical properties and a unity Lewis number (Le=1), are assumed.

Using the radially averaged velocity $\langle u\rangle_g$, the mass conservation equation for the gas phase is

$$A_g\Delta x\,\frac{d\rho_{g,i}}{dt}=(\rho A\langle u\rangle)_{g,w,i}-(\rho A\langle u\rangle)_{g,e,i}. \tag{1}$$

The density is given by the ideal gas law, $\rho_g=pM_g/\overline{R}T_g$, and a constant, atmospheric pressure is assumed.

The finite-volume species mass conservation equation for the product-species P in i gas-phase node is

$$\begin{aligned}A_g\Delta x\,\frac{d}{dt}\,\frac{\rho_{\mathrm{P},i}}{\rho_g}&=A_g[(\rho_{\mathrm{P}}\langle u\rangle_g)_{w,i}-(\rho_{\mathrm{P}}\langle u\rangle_g)_{e,i}]\\&\quad+D_mA_g\left(\frac{\rho_{\mathrm{P},i-1}-\rho_{\mathrm{P},i}}{\delta x_i}-\frac{\rho_{\mathrm{P},i}-\rho_{\mathrm{P},i+1}}{\delta x_{i+1}}\right)\\&\quad+\dot{n}_{r,\mathrm{P},i}A_g\Delta x,\end{aligned} \tag{2}$$

where i is the axial node index.

For the product species generation terms $\dot{n}_{r,\mathrm{P},i}$, a first-order, Arrhenius relation ([10]) is used, i.e.,

$$\dot{n}_{r,\mathrm{P},i}=a_r(\rho_g-\rho_{\mathrm{P},i})e^{-\Delta E_a/\overline{R}T_{g,i}}, \tag{3}$$

where $\rho_{g,i}=\rho_{\mathrm{R},i}+\rho_{\mathrm{P},i}$, $\rho_{\mathrm{R},i}=\rho_{\mathrm{F},i}+\rho_{\mathrm{O},i}$ and $(\rho_{g,i}-\rho_{\mathrm{P},i})$ is the local reactant density in the gas phase. Since the amount of the injected fuel (2.36 percent of the oxidant mass flow rate for the baseline conditions) is small, it is assumed that the injected fuel is well mixed and the change in ρ_g due to the fuel injection is negligible and a premixed reaction begins after the injection.

The two medium model is used here to allow for the thermal nonequilibrium caused by the gaseous combustion. The radially averaged temperatures $\langle T\rangle_r^g=T_g$ and $\langle T\rangle_r^s=T_s$ are used, where $\langle\ \rangle_r^g$ and $\langle\ \rangle_r^s$ indicate radially, phase averaged quantities ([11]).

The finite-volume energy conservation equation for the i gas-phase node [shown in Fig. 1(*b*)] is

$$A_g\Delta x\frac{d}{dt}(\rho c_pT)_{g,i}=Q_{g,u,i}+Q_{g,k,i}+Q_{g,ku,i}+\dot{S}_{r,c,i}, \tag{4}$$

where

$$Q_{g,u,i}=(\rho c_p\langle u\rangle AT)_{g,w,i}-(\rho c_p\langle u\rangle AT)_{g,e,i} \tag{5}$$

$$Q_{g,k,i}=k_gA_g\left(\frac{T_{g,i-1}-T_{g,i}}{\delta x_i}-\frac{T_{g,i}-T_{g,i+1}}{\delta x_{i+1}}\right) \tag{6}$$

$$Q_{g,ku,i}=\mathrm{Nu}_D\frac{k_g}{D_1}A_{sg}(T_{s,i}-T_{g,i}) \tag{7}$$

$$\dot{S}_{r,c,i}=-\Delta h_{r,F}\frac{\nu_{\mathrm{F}}M_{\mathrm{F}}}{\nu_{\mathrm{R}}M_{\mathrm{R}}}\dot{n}_{r,\mathrm{P},i}A_g\Delta x. \tag{8}$$

The hydrodynamic dispersion is neglected, because of the small Péclet number and the dominance of the surface convection over gaseous conduction and dispersion. The energy equation for the i solid-phase node [shown in Fig. 1(*b*)] is

$$(\rho c_p)_{s,i}A_s\Delta x\,\frac{dT_{s,i}}{dt}=Q_{s,k,i}-Q_{s,ku,i}-Q_{s,r,i}+(\dot{S}_{e,J})_i+(\dot{S}_{e,P})_i\,, \tag{9}$$

where

$$Q_{s,k,i}=k_sA_s\left(\frac{T_{s,i-1}-T_{s,i}}{\delta x_i}-\frac{T_{s,i}-T_{s,i+1}}{\delta x_{i+1}}\right) \tag{10}$$

$$Q_{s,ku,i}=\mathrm{Nu}_D\frac{k_g}{D_1}A_{sg}(T_{s,i}-T_{g,i}) \tag{11}$$

$$Q_{s,r,i}=\frac{E_{b,i}-(q_{r,o})_i}{\left(\dfrac{1-\epsilon_r}{A_r\epsilon_r}\right)_i} \tag{12}$$

$$(\dot{S}_{e,J})_i=\left[\left(\frac{\rho_e\Delta x}{A}\right)_{p,i}+\left(\frac{\rho_e\Delta x}{A}\right)_{n,i}\right]J_e^2\quad\text{for TE region} \tag{13}$$

$$(\dot{S}_{e,P})_i=\mp\alpha_ST_{s,i}J_e\quad\text{at hot/cold junctions of TE region,} \tag{14}$$

where the Nusselt number, Nu_D, is taken to be for laminar, fully developed fields, occuring $\mathrm{Re}_D<2300$, $\mathrm{Nu}_D=3.66$. The Peltier heat absorption/release $(\dot{S}_{e,P})_i$ occurs at the hot/cold junctions and is used in the surface nodes.

Using simple mean beam length analysis ([12]), it can be shown that for small (order of one millimeter diameter) tubes, the gas radiation is less than one half percent of the surface radiation. The surface radiation heat flow rate $Q_{s,r,i}$ is written as

$$Q_{s,r,i}=\frac{E_{b,i}-(q_{r,o})_i}{\left(\dfrac{1-\epsilon_r}{A_r\epsilon_r}\right)_i}=\sum_{j=1}^{n+2}\frac{(q_{r,o})_i-(q_{r,o})_j}{\dfrac{1}{A_{r,i}F_{i-j}}}, \tag{15}$$

where $E_{b,i}=\sigma_{\mathrm{SB}}T_{s,i}^4$ is the total hemispherical blackbody emissive power. The inlet $(i=n+1)$ and outlet region $(i=n+2)$ of the tube as shown in Fig. 1(*b*), are treated as imaginary blackbody surfaces. The view factor F_{i-j} is obtained by the kernel approximation ([2,12]) and is

$$\begin{aligned}F_{i-j}=&\frac{D_1}{4\Delta x}[e^{2(x_{cs,i}+\Delta x)/D_1}-e^{2x_{cs,i}/D_1}]\\&\times[e^{-2x_{cs,j}/D_1}-e^{-2(x_{cs,j}+\Delta x)/D_1}]\\&i,j=1,\ldots,n\quad\text{ring to another ring}\end{aligned} \tag{16}$$

$$\begin{aligned}F_{i-j}=&\frac{D_1}{4\Delta x}[e^{-2x_{cs,i}/D_1}-e^{-2(x_{cs,i}+\Delta x)/D_1}]\\&i=1,\ldots,n,\ j=n+1,n+2\quad\text{ring to end disk.}\end{aligned} \tag{17}$$

Figure 2(*a*) shows a bundle of the combustion-thermoelectric tubes with its electrical connections. Figure 2(*b*) also shows the electrical circuit for such a bundle. The voltage $\Delta\varphi$ for an N_t-tube bundle shown in Fig. 2(*b*), is

$$\Delta\varphi=J_eR_{e,o}=2N_t[\alpha_S\Delta T_s-J_e(R_{e,p}+R_{e,n})], \tag{18}$$

where $\Delta T_s=T_{s,h}-T_{s,c}$, $T_{s,h}=(T_{s,n_{\mathrm{TE}}}+T_{s,n_{\mathrm{TE}}+n_C+1})/2$, $T_{s,c}=(T_{s,1}+T_{s,n})/2$, $\alpha_S=\alpha_{S,p}-\alpha_{S,n}$, $R_{e,p}=(\rho_eL/A)_p$ and $R_{e,n}=(\rho_eL/A)_n$.

For the case of $A_p=A_n=A_s/2$, $\rho_{e,p}=\rho_{e,n}=\rho_e$ and $L_p=L_n=L_{\mathrm{TE}}$, the internal electrical resistance of the left side of a thermoelectric tube, shaded in Fig. 2(*b*), is

$$R_e=R_{e,p}+R_{e,n}=\left(\frac{\rho_eL}{A}\right)_p+\left(\frac{\rho_eL}{A}\right)_n=4\,\frac{\rho_eL_{\mathrm{TE}}}{A_s}, \tag{19}$$

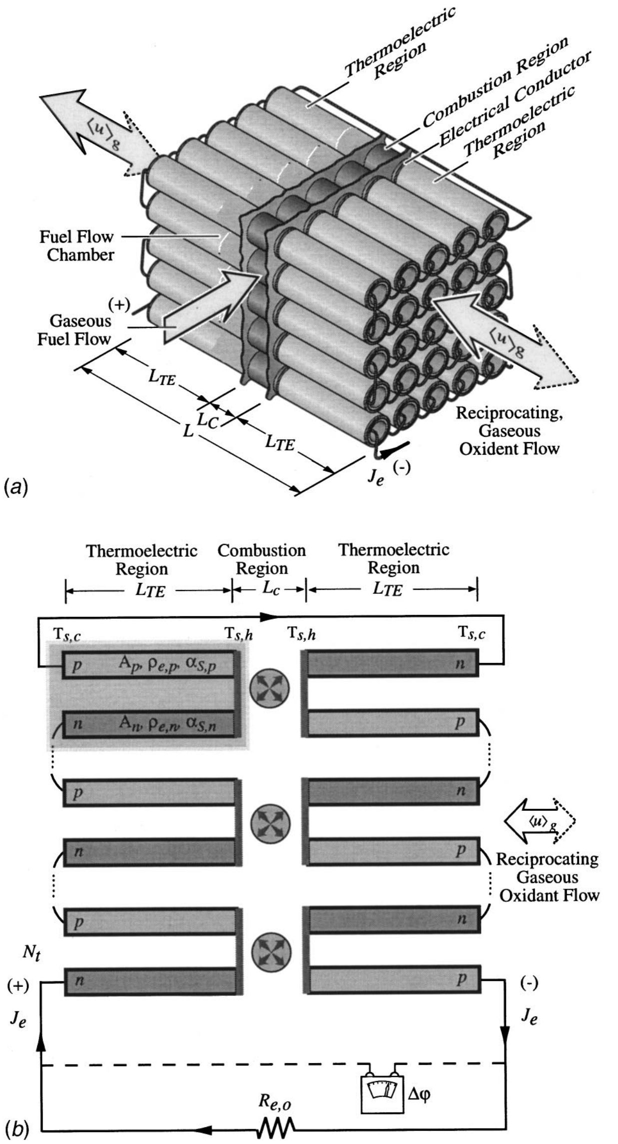

Fig. 2 (*a*) Tube-bundle module of the combustion-thermoelectric energy converter; (*b*) electrical circuit for the combustion-thermoelectric energy converter

where A_p and A_n are the cross-sectional areas of the *p*-type and *n*-type thermoelectric materials, and A_s is the total solid cross-sectional area.

Using the voltage relation, Eq. (18), the current is

$$J_e=\frac{2N_t\alpha_S\Delta T_s}{2N_tR_e+R_{e,o}}=\frac{\alpha_S\Delta T_e}{R_e(1+R_{e,o}^*)}=\frac{\alpha_S\Delta T_s}{4\rho_eL_{\mathrm{TE}}(1+R_{e,o}^*)}A_s\,, \tag{20}$$

where $R_{e,o}^*$ is the ratio of the external resistances to the internal resistance, i.e., $R_{e,o}/(2N_tR_e)$.

The electric power generated is

$$\begin{aligned}J_e^2R_{e,o}&=2N_t(J_e\alpha_S\Delta T_s-J_e^2R_e)\\&=N_t\frac{\alpha_S^2\Delta T_s^2R_{e,o}^*}{2\rho_eL_{\mathrm{TE}}(1+R_{e,o}^*)^2}A_s\,.\end{aligned} \tag{21}$$

The gas-phase energy and species-*P* conservation equations for the inlet and outlet fluid nodes, for the gas flowing from left to right, are

$$-k_g A_g \frac{T_{g,1}-T_{g,2}}{\delta x_2}+(\rho c_p A)_g \langle u\rangle_g (T_o - T_{g,1})=0 \quad \text{at } i=1 \tag{22}$$

$$T_{g,n}=T_{g,n-1} \quad \text{at } i=n \tag{23}$$

$$-D_m A_g \frac{\rho_{\mathrm{P},1}-\rho_{\mathrm{P},2}}{\delta x_2}-A_g\langle u\rangle_g\, \rho_{\mathrm{P},1}=0 \quad \text{at } i=1 \tag{24}$$

$$\rho_{\mathrm{P},n}=\rho_{\mathrm{P},n-1} \quad \text{at } i=n. \tag{25}$$

Similar equations are written for the gas flow from right to left.

The energy equations for the left-side cold junction is

$$-k_{\mathrm{TE}} A_s \frac{T_{s,1}-T_{s,2}}{\delta x_2}-\epsilon_r \sigma_{\mathrm{SB}} A_s (T_{s,1}^4 - T_o^4)+J_e \alpha_s T_{s,1} - \mathrm{Nu}_e \frac{k_g}{D_2} A_s (T_{s,1}-T_o)=0, \tag{26}$$

where Nu_e is the external Nusselt number for the external air cooling at cold junctions. A similar equation is written for the right-side cold junction.

Table 1 Physical, chemical, and geometrical properties and the baseline magnitude of parameters.

Parameter	Magnitude
fuel (methane):	
$\rho_{F,o}$	0.02746 kg fuel/m^3
$(\rho_{F,o})_{\mathrm{st}}$	0.06424 kg fuel/m^3
Φ	0.414
$\Delta h_{r,F}$	−55.53 MJ/kg fuel
ΔE_a	131 MJ/kmole
a_r	2.8×10^8 1/*s*
T_{ad}/T_o	4.0
oxidant (air):	
$\rho_{g,o}$	1.164 kg/m^3
$c_{p,g}$	1099 J/kg K
k_g	0.0573 W/m K
μ_g	369.8×10^{-7} N s/m^2
$\langle u\rangle_{g,o}$	0.75 m/s
$T_{g,o}, T_o$	298 K, 298 K
$\mathrm{Nu}_D, \mathrm{Nu}_e$	3.66, 1.5
Re_D	54.5
τ_c	10 s
Le	1
tube bundle module:	
length, $2L_{\mathrm{TE}}+L_C$	127.5 mm
cross-sectional area, $a\times a$	30×30 mm^2
number of tubes, N_t	$a^2/D_2^2=144$
electrical resistance ratio	$R_{e,o}^*=1$
power generated	24.0 W, 26.7 kW/m^2
voltage	93.7 V
current	256.3 mA
thermoelectric region Si$_{0.7}$Ge$_{0.3}$:	
$Z_e T_o$	0.59
$\alpha_{S,p}, \alpha_{S,n}, \alpha_S(=\alpha_{S,p}-\alpha_{S,n})$	195.3, −207.3, 402.6 μV/K
ρ_e	19.1 μOhm m
ρ_s	2990 kg/m^3
$c_{p,s}$	816.7 J/kg K
C_{TE}	1908.8
k_{TE} (k_{TE}^*)	4.3 W/m K (75)
D_1	1.3 mm
l_s (D_2)	0.6 mm (2.5 mm)
L_{TE}	60 mm
ϵ_r	1.0
T_{sl}	2000 K
combustion region	
SiC (CVD fabrication):	
ρ_s	3160 kg/m^3
$c_{p,s}$	1310 J/kg K
C_C	3236.0
k_C (k_C^*)	30 W/m K (523.6)
L_C	7.5 mm
ϵ_r	1.0
T_{sl}	3100 K

The thermoelectric conversion efficiency is the ratio of the electric power generated to the combustion heating rate, i.e.,

$$\eta=\frac{J_e^2 R_{e,o}}{-N_t \Delta h_{r,\mathrm{F}} \dfrac{\nu_{\mathrm{F}} M_{\mathrm{F}}}{\nu_{\mathrm{R}} M_{\mathrm{R}}} \rho_g \langle u\rangle_{g,o} A_g}=\frac{\dfrac{\alpha_S^2 \Delta T_s^2 R_{e,o}^*}{2\rho_e L_{\mathrm{TE}}(1+R_{e,o}^*)^2} A_s}{-\Delta h_{r,\mathrm{F}} \rho_{\mathrm{F},o} \langle u\rangle_{g,o} A_g}. \tag{27}$$

The power consumed for the reciprocating flow and in other components (e.g., valves), are neglected.

Considering the existence of many parameters, they are made dimensionless reducing their number. The nondimensional parameters are

$$Z_e T_o=\frac{\alpha_S^2}{\rho_e k_{\mathrm{TE}}} T_o, \quad R_{e,o}^*=\frac{R_{e,o}}{2N_t R_e}, \quad \mathrm{Re}_D=\frac{\rho_g \langle u\rangle_{g,o} D_1}{\mu_g},$$

$$C=\frac{\rho c_p}{(\rho c_p)_g}, \quad k^*=\frac{k}{k_g}, \quad \Phi=\frac{\rho_{\mathrm{F},o}}{(\rho_{\mathrm{F},o})_{\mathrm{st}}} \frac{(1-\rho_{\mathrm{F},o}/\rho_g)_{\mathrm{st}}}{(1-\rho_{\mathrm{F},o}/\rho_g)}.$$

The magnitude for the baseline parameters (i.e., conditions) are listed in Table 1 (properties from ([13])). From these magnitudes, the magnitudes of the nondimensional parameters are $Z_e T_o = 0.59$, $R_{e,o}^*=1$, $\mathrm{Re}_D=54.5$, $C_{\mathrm{TE}}=1908.8$, $C_C=3236.0$, $k_{\mathrm{TE}}^*=75$, $k_C^*=523.6$, and $\Phi=0.414$.

The species and energy conservation equations [Eqs. (2), (4) and (9)] are discretized with a central-difference scheme with respect to space, and an implicit-difference scheme with respect to time and are solved simultaneously using iterations ([14]). The grid-net size dependence is tested and for an 85 node (uniform gridnet), an asymptotic solution is obtained. For a typical case, the computation time is about 90 min with HP B160L. The convergence at each time step is obtained by evaluating the residues in the species and energy conservation equations and requiring the maximum residues be below 0.00001. The quasi-steady solution is obtained when the error in the overall energy balance is below 1∼2 percent.

Results and Discussion

Typical results for the distributions of the solid- and gas-phase temperatures, the mass fraction of the combustion products, and the reaction rate at the end of a half cycle, with gas flowing from left to right, are shown in Fig. 3. The results show that for Si$_{0.7}$Ge$_{0.3}$ alloy with an assumed melting temperature of $T_{\mathrm{sl}} = 2000$ K, the conversion efficiency is 11.3 percent and the power converted is 24.0 W, under the baseline conditions listed in Table 1.

As was indicated in the introduction, the pure lateral diffusion transport of the fuel is expected to occur in a very short distance. The lateral momentum of the fuel can further assist in the mixing. As shown in Fig. 3, due to the high oxidant temperature, the flame temperature reaches a local, superadiabatic temperature right at the fuel-injection site in the combustion region. The adiabatic flame temperature T_{ad} is also shown in Fig. 3.

The conduction heat flow towards, and the Peltier heat release at the cold junctions, are removed by the intensive external cooling [the product of the total solid cross-sectional area A_s and the external Nusselt number Nu_e is large in Eq. (26)]. A Nusselt number $\mathrm{Nu}_e=150$ (based on the outside diameter) and a surface area A_s are used as a baseline values. When an extended surface (fins) is used with an area of $A=100A_s$, the Nusselt number Nu_e is then reduced to 1.5 which can readily be achieved using low speed air flow over fins.

For $R_{e,o}^*=1$ [obtained as the optimum value for a maximum power from Eq. (21)], the current is independent of the number of tubes, as evident from Eq. (20). The number of tubes in a tube-bundle module, which is an elemental unit circuit, is chosen to meet electrical specifications such as a desired current-voltage. A

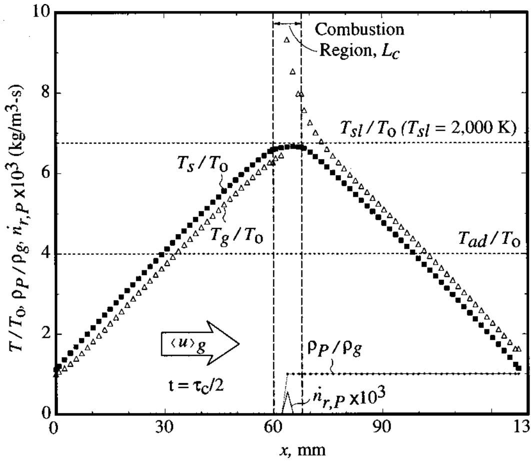

Fig. 3 Typical axial distributions of normalized gas and solid temperatures, reaction rate, and product species mass fraction. $Z_eT_o=0.59$, $R^*_{e,o}=1$, $\tau_c=10$ s, $\langle u\rangle_{g,o}=0.75$ m/s, $D_1=1.3$ mm, $l_s=0.6$ mm, $L_{TE}=60$ mm, $L_C=7.5$ mm, $C_{TE}=1908.8$, $C_C=3236.0$, $k^*_{TE}=75$, $k^*_C=523.6$, $\Phi=0.414$.

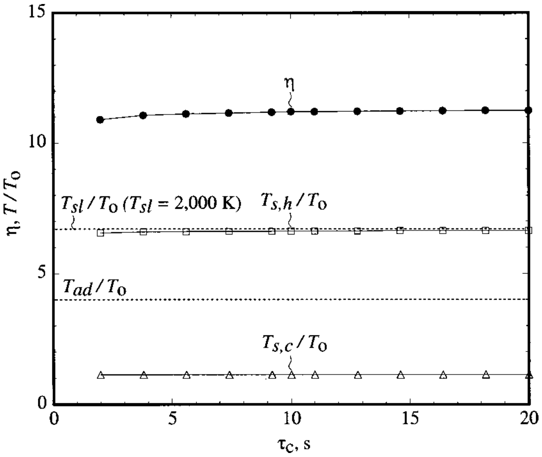

Fig. 4 Effect of the cycle period τ_c on the conversion efficiency and the junction temperatures. $Z_eT_o=0.59$, $R^*_{e,o}=1$, $\langle u\rangle_{g,o}=0.75$ m/s, $D_1=1.3$ mm, $l_s=0.6$ mm, $L_{TE}=60$ mm, $L_C=7.5$ mm, $C_{TE}=1908.8$, $C_C=3236.0$, $k^*_{TE}=75$, $k^*_C=523.6$, $\Phi=0.414$.

tube-bundle module of 144 tubes gives a current of $J_e=256.3$ mA and a voltage of $\Delta\varphi=93.7$ V. For nine such modules connected in parallel, the power is $J_e\Delta\varphi=216.1$ W and the current is $J_e=2.31$ A. Each tube-bundle module has a length $2L_{TE}+L_C=127.5$ mm and a cross-sectional area $a\times a=30$ (mm)×30 (mm), in a close-pack, square-array arrangement of the tubes, giving the power density of 26.7 kW/m^2. These results are not far to the design results of the $2L_{TE}+L_C$ of 50 ~100 mm and power density of 5~10 kW/m^2 suggested by Echigo et al. [6].

Effect of Various Parameters. A parametric study is performed using the fluid flow, thermoelectric-region, and combustion-region parameters. The baseline conditions are listed in Table 1.

Figure 4 shows that the conversion efficiency η, defined by Eq. (27), and the hot and cold junction temperatures of the thermoelectric region, do not change noticeably with the cycle period τ_c. This is because the flame location is fixed at the fuel injection site and due to the intensive external cooling of the cold junction, the transient variations are diminished, as compared to the case of the premixed combustion. For mechanical maintenance purposes, less mechanical movement of the parts (e.g., valves) is desirable. Here, a longer period of $\tau_c=10$ s is used as the baseline condition.

Figure 5 shows that for the gas velocities $\langle u\rangle_{g,o}>0.75$ m/s, the efficiency no longer increases and the hot junction temperature reaches the melting temperature T_{sl}. The pressure drop under the baseline conditions is about 178 Pa, and therefore, is considered rather small.

The combustion region provides as an extended surface to the hot junctions (joined with an assumed negligible contact resistance to the combustion region) for the transfer of the heat released by combustion. Figure 6 shows the effect of the combustion region length L_C (with the fuel injection located at the center of the region), on the conversion efficiency. The effect is not significant, because of the relatively high thermal conductivity for the combustion region, which results in a uniform temperature. For complete combustion, only a short combustion region is needed, i.e., $L_C=7.5$ mm. The efficiency is not very sensitive to the thermal conductivity and the heat capacity of the combustion region. Here, SiC has been used, due to its high melting temperature. The thermal conductivity of SiC varies depending on the fabrication technique (e.g., CVD, sintered powder, etc.). Here a value close to the CVD fabrication is used ([11]).

Figure 7 shows the effect of the stoichiometric ratio Φ on the conversion efficiency η, for several tube wall thicknesses. As the stoichiometric ratio increases, the efficiency and the hot junction temperatures $T_{s,h}$ increase. Above a tube wall thickness $l_s=0.6$ mm used as the baseline value, the efficiency reaches an asymptotic value, with $T_{s,h}$ kept below $T_{sl}=2000$ K. The maximum flame temperature for the tube wall thickness $l_s=0.8$ mm and 0.9 mm, are also shown in Fig. 7. Since the maximum flame temperature depends on the gas preheating temperature (determined by the maximum temperature of the thermoelectric region, i.e., the hot junction temperature $T_{s,h}$), it is much higher than the adiabatic flame temperature. Note that due to the preheating, the flammability limit is reduced significantly. The smallest equivalence ratio for a stable flame in ceramic foams is 0.026 reported by Hoffmann et al. [5].

The oxidant preheating temperature is determined by the length of the thermoelectric region L_{TE}. The flame has a superadiabatic temperature and as compared to the premixed combustion, the flame position is determined by the fuel injection location, instead of the ignition temperature. In addition, with the fuel injection the maximum flame temperature is only limited by the allowable maximum temperature of the combustion region, i.e., its the melt-

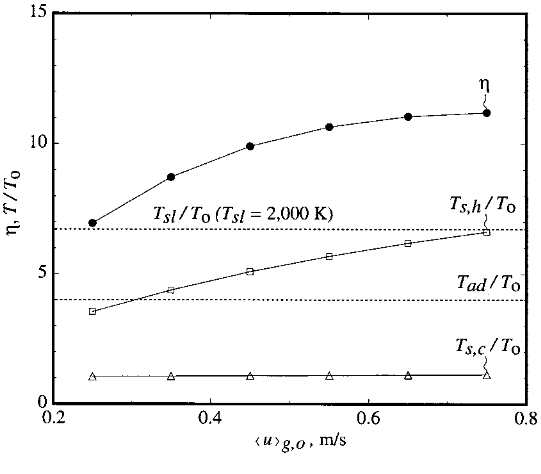

Fig. 5 Effect of the gas velocity $\langle u\rangle_{g,o}$ on the conversion efficiency and the junction temperatures. $Z_eT_o=0.59$, $R^*_{e,o}=1$, $\tau_c=10$ s, $D_1=1.3$ mm, $l_s=0.6$ mm, $L_{TE}=60$ mm, $L_C=7.5$ mm, $C_{TE}=1908.8$, $C_C=3236.0$, $k^*_{TE}=75$, $k^*_C=523.6$, $\Phi=0.414$.

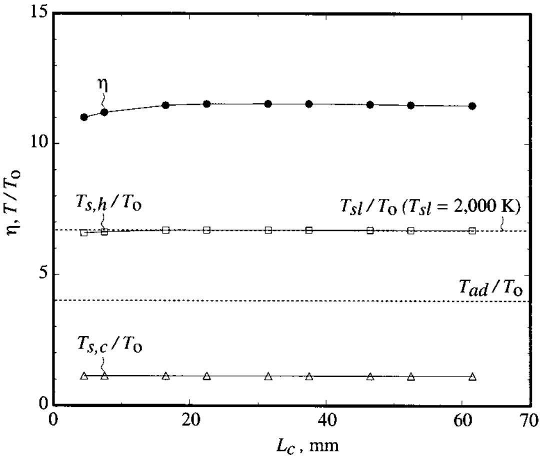

Fig. 6 Effect of the combustion region length L_C on the conversion efficiency and the junction temperatures. $Z_eT_o=0.59$, $R^*_{e,o}=1$, $\tau_c=10$ s, $\langle u\rangle_{g,o}=0.75$ m/s, $D_1=1.3$ mm, $l_s=0.6$ mm, $L_{TE}=60$ mm, $C_{TE}=1908.8$, $C_C=3236.0$, $k^*_{TE}=75$, $k^*_C=523.6$, $\Phi=0.414$.

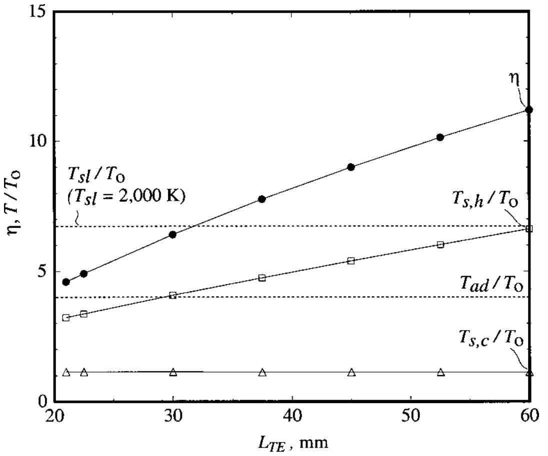

Fig. 8 Effect of the thermoelectric region length L_{TE} on the conversion efficiency and the junction temperatures. $Z_eT_o=0.59$, $R^*_{e,o}=1$, $\tau_c=10$ s, $\langle u\rangle_{g,o}=0.75$ m/s, $D_1=1.3$ mm, $l_s=0.6$ mm, $L_C=7.5$ mm, $C_{TE}=1908.8$, $C_C=3236.0$, $k^*_{TE}=75$, $k^*_C=523.6$, $\Phi=0.414$.

ing temperature. Then within the chemical kinetic considered, there is no limit on the achievable maximum flame temperature.

The efficiency increases with an increase in the length of the thermoelectric region, as shown in Fig. 8. Here, $L_{TE}=60$ mm is used to optimize the efficiency and keep $T_{s,h}\leqslant T_{sl}=2000$ K.

Improved surface convection between the gas and solid phase results in the higher temperature and the higher efficiency. This requires large specific interfacial area [in the surface convection terms $Q_{g,ku}$ and $Q_{s,ku}$ of Eqs. (4) and (9) respectively] and large Nusselt number. The specific interfacial area $A_{sg}/V(=4D_1/(2l_s+D_1)^2)$ have a maximum value at $D_{1,\mathrm{opt}}=2l_s$ for a fixed l_s. However, the optimum inside diameter for the maximum efficiency will be different from than $D_{1,\mathrm{opt}}$, since the relative magnitude of the other terms in the energy conservation equations of Eqs. (14) and (19), are dependent on D_1 and l_s. As shown in Fig. 9, the maximum efficiency is achieved near $D_1=1.3$ mm, for $l_s=0.6$ mm, which is close to the optimum diameter $D_{1,\mathrm{opt}}=1.2$ mm. The optimum diameter is also restricted by the allowable hot junction temperature being below the melting temperature T_{sl}.

As the tube thickness l_s decreases, the conduction heat loss decreases and thus the hot junction temperature increase. While keeping the hot junction temperature $T_{s,h}\leqslant T_{sl}$, $l_s=0.6$ mm gives the highest efficiency, as shown Fig. 10. If a higher melting temperature is allowed, the tube wall thickness smaller than 0.6 mm would give even higher efficiency. However, as the l_s is decreased beyond a threshold, the Joule heating becomes very significant and the efficiency begins to decrease.

Figure 11 shows the effect of the electrical resistance ratio on the conversion efficiency. The efficiency does not increase noticeably for $R^*_{e,o}>1.27$. For simplicity, $R^*_{e,o}=1$ is used to optimize the efficiency. For the unity $R^*_{e,o}$, the total internal resistance $2N_tR_e$ is matched with the external resistance $R_{e,o}$. The power generated, and the current and voltage, are regulated by combining modules in parallel or series arrangements to meet the requirement.

In general, the surface radiation in the tube deteriorates the conversion efficiency by lowering the hot junction temperature. Here, the blackbody emissivity, $\epsilon_r=1$, is used for the surface

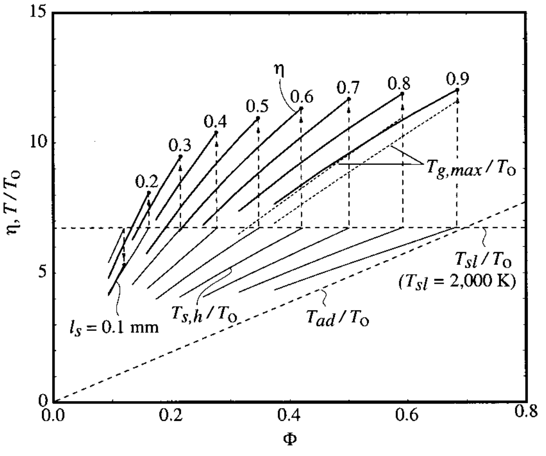

Fig. 7 Effect of the stoichiometric ratio Φ on the conversion efficiency and the hot junction temperature, for various tube wall thicknesses. $Z_eT_o=0.59$, $R^*_{e,o}=1$, $\tau_c=10$ s, $\langle u\rangle_{g,o}=0.75$ m/s, $D_1=1.3$ mm, $L_{TE}=60$ mm, $L_C=7.5$ mm, $C_{TE}=1908.8$, $C_C=3236.0$, $k^*_{TE}=75$, $k^*_C=523.6$.

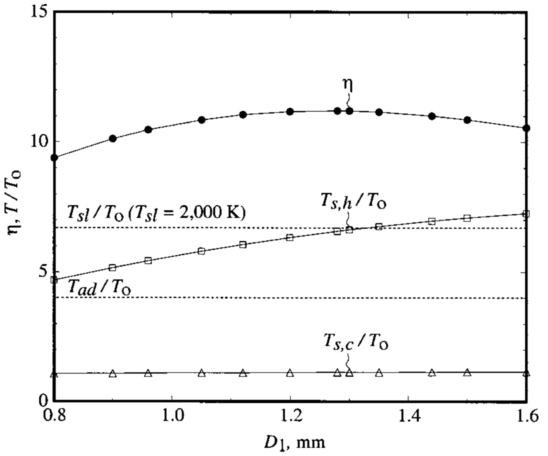

Fig. 9 Effect of the diameter D_1 of the thermoelectric regions on the conversion efficiency and the junction temperatures. $Z_eT_o=0.59$, $R^*_{e,o}=1$, $\tau_c=10$ s, $\langle u\rangle_{g,o}=0.75$ m/s, $l_s=0.6$ mm, $L_{TE}=60$ mm, $L_C=7.5$ mm, $C_{TE}=1908.8$, $C_C=3236.0$, $k^*_{TE}=75$, $k^*_C=523.6$, $\Phi=0.414$.

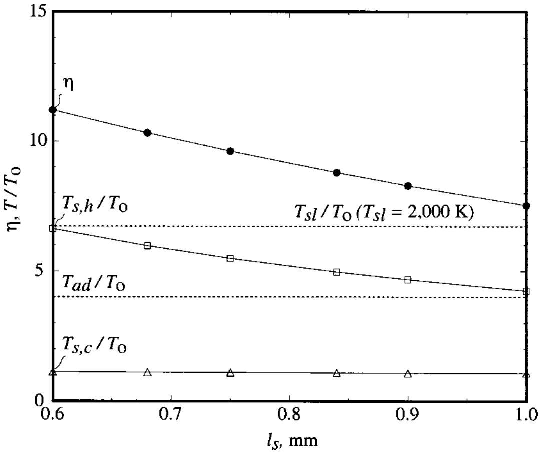

Fig. 10 Effect of the tube thickness l_s on the conversion efficiency and the junction temperatures. $Z_eT_o=0.59$, $R^*_{e,o}=1$, $\tau_c=10$ s, $\langle u\rangle_{g,o}=0.75$ m/s, $D_1=1.3$ mm, $L_{TE}=60$ mm, $L_C=7.5$ mm, $C_{TE}=1908.8$, $C_C=3236.0$, $k^*_{TE}=75$, $k^*_C=523.6$, $\Phi=0.414$.

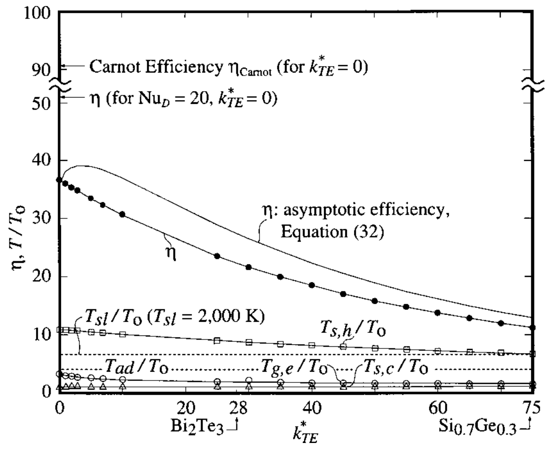

Fig. 12 Effect of the thermal conductivity k_{TE} of the thermoelectric region on the conversion efficiency and the junction temperatures. $R^*_{e,o}=1$, $\tau_c=10$ s, $\langle u\rangle_{g,o}=0.75$ m/s, $D_1=1.3$ mm, $l_s=0.6$ mm, $C_{TE}=1908.8$, $C_C=3236.0$, $L_{TE}=60$ mm, $L_C=7.5$ mm, $k^*_C=523.6$, $\Phi=0.414$.

radiation within the tube. The tube length to diameter ratio is very large, and therefore, the radiation heat transfer is rather local.

Effect of Thermal Conductivity and Melting Temperature. A good thermoelectric material should have a large Seebeck coefficient α_S, and a low thermal conductivity k_{TE} to keep a large temperature difference. It should also have a low electrical resistance ρ_e to minimize the Joule heating. These properties are embodied in a figure-of-merit $Z_e=\alpha_S/(k_{TE}\rho_e)$. The thermal conductivity of the thermoelectric region is a key parameter in limiting the thermoelectric conversion efficiency. Figure 12 shows the effect of thermal conductivity of the thermoelectric region k_{TE} on the efficiency and the junction temperatures. The efficiency increases rapidly as the thermal conductivity decreases.

For lower thermal conductivity, (such as that of the low-temperature thermoelectric materials, e.g., bismuth telluride Bi_2Te_3, $k_{TE}=1.6$ W/m K, $k^*_{TE}=28$), higher efficiencies are possible. Currently the highly melting temperature material is used.

The asymptotic, quasi-steady, overall energy equation, neglecting radiation losses, gives

$$\eta=\frac{J_e^2R_{e,o}/N_t}{Q_e+Q_{g,u}+J_e^2R_{e,o}/N_t}. \tag{28}$$

The neglected radiation losses to the ambient are less than 1 ~3 percent of the combustion heating rate. This is because due to the high aspect ratio, the high temperature region of the tube is barely exposed to the ambient and the cold ends.

Assuming a linear solid temperature distribution, the external heat removal rate at the cold junctions Q_e is approximated by the sum of the conduction loss and the cold-junction Peltier loss. Then from Eq. (26) we have

$$\begin{aligned}Q_e&=\mathrm{Nu}_e\frac{k_g}{D_2}A_s[(T_{s,1}-T_o)+(T_{s,n}-T_o)]\\&=2k_{TE}A_s\frac{\Delta T_s}{L_{TE}}+J_e\alpha_S(T_{s,1}+T_{s,n}).\end{aligned} \tag{29}$$

The exhaust gas heat loss $Q_{g,u}$ is

$$Q_{g,u}=(\rho c_pA)_g\langle u\rangle_g(T_{g,e}-T_o), \tag{30}$$

where $T_{g,e}$ is the exhaust gas temperature.

The power generated from a tube $J_e^2R_{e,o}/N_t$ is, from Eq. (21)

$$J_e^2R_{e,o}/N_t=\frac{\alpha_S^2\Delta T_s^2R^*_{e,o}}{2\rho_eL_{TE}(1+R^*_{e,o})^2}A_s. \tag{31}$$

Then, the efficiency given by Eq. (28), becomes

$$\begin{aligned}\eta^{-1}=1+\frac{1}{Z_eT_o}\frac{4(1+R^*_{e,o})}{R^*_{e,o}}\frac{T_o}{\Delta T_s}+\frac{1+R^*_{e,o}}{R^*_{e,o}}\frac{T_{s,c}}{\Delta T_s}+\frac{2}{Z_eT_o}\\ \times\frac{(1+R^*_{e,o})^2}{R^*_{e,o}}\frac{(\rho c_p\langle u\rangle T)_{g,e}-(\rho c_p\langle u\rangle T)_{g,o}}{k_{TE}\dfrac{\Delta T_s}{L_{TE}}}\frac{D_1^2}{D_2^2-D_1^2}\frac{T_o}{\Delta T_s}.\end{aligned} \tag{32}$$

The prediction of Eq. (32) is also shown in Fig. 12. The difference between Eq. (32) and the numerical results is mainly due to the underestimation of the conduction loss due to the convex, nonlinear solid temperature distribution. The convex solid temperature profile becomes more pronounced for the low thermal conductivity materials. In Eq. (32), the underestimation of the conduction loss leads to an overestimation of the asymptotic efficiency. In Fig. 12, as the thermal conductivity decreases, and therefore, the conduction loss decreases, the asymptotic efficiency

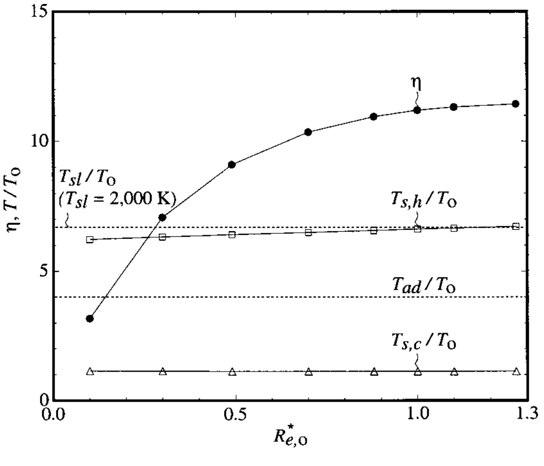

Fig. 11 Effect of the dimensionless external resistance $R^*_{e,o}$ on the conversion efficiency and the junction temperatures. $Z_eT_o=0.59$, $\tau_c=10$ s, $\langle u\rangle_{g,o}=0.75$ m/s, $D_1=1.3$ mm, $l_s=0.6$ mm, $C_{TE}=1908.8$, $C_C=3236.0$, $L_{TE}=60$ mm, $L_C=7.5$ mm, $k^*_{TE}=75$, $k^*_C=523.6$, $\Phi=0.414$.

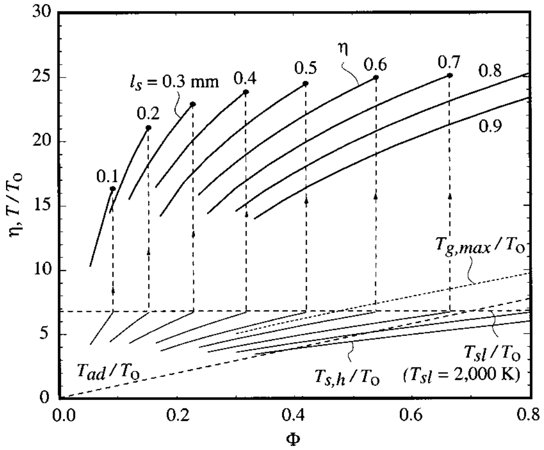

Fig. 13 Effect of the stoichiometric ratio Φ on the conversion efficiency and the hot junction temperature, for various tube wall thicknesses for low thermal conductivity material (Bi_2Te_3). $Z_eT_o=1.58$, $R^*_{e,o}=1$, $\tau_c=10$ s, $\langle u\rangle_{g,o}=0.75$ m/s, $D_1=0.63$ mm, $L_{TE}=60$ mm, $L_C=7.5$ mm, $C_{TE}=1908.8$, $C_C=3236.0$, $k^*_{TE}=28$, $k^*_C=523.6$.

becomes close to that obtained numerically. Figure 12 shows that due to the exhaust gas enthalpy loss, the maximum efficiency for zero thermal conductivity, $k^*_{TE}=0$, is 37 percent, under the baseline conditions listed in Table 1. Note that the maximum efficiency is lower than the Carnot efficiency (due to the exhaust gas enthalpy, the Joule heating, and the cold-junction Peltier heating losses). Also note that for a larger Nusselt number, say $Nu_D=20$ (that is, for enhanced surface convection), resulting in a reduction in the exhaust gas enthalpy loss, the maximum efficiency increases substantially (but is still lower than the Carnot efficiency, due to the Joule and the cold-junction Peltier heating losses).

The solid conduction is always unfavorable for achieving a higher junction temperature difference and a higher conversion efficiency. This is in contrast to the unidirectional flow arrangement in which the solid conduction is the main mechanism for the heat recirculation for achieving a superadiabatic temperature (along with surface radiation).

Figure 13 shows that for a low thermal conductivity material, say $k^*_{TE}=28$, a conversion efficiency over 25 percent is achievable, while $T_{s,h}$ is kept below $T_{sl}=2000$ K. Optimizations have shown that for this k^*_{TE} a smaller tube diameter, $D_1=0.63$ mm, is needed and the results shown in Fig. 13, use this diameter. Note that using $k^*_{TE}=28$, with $D_1=0.63$ mm and $\Phi=0.53$, the electrical power generated is the same as that for $k^*_{TE}=75$, $D_1=1.3$ mm and $\Phi=0.414$. However, much less fuel is used. The smaller gas flow cross-sectional area results in a saving of 61 percent of the fuel. This is due to the smaller solid conduction loss.

The reduction in the effective thermal conductivity, potentially achievable using small powders (small grain size), should lead to a high efficiency thermoelectric converter. Experimental verification of the high efficiency thermoelectric power generator is needed.

Conclusion

The proposed combustion-thermoelectric tube allows for harvesting of the local superadiabatic temperature and the analysis of the combustion-thermoelectric energy conversion efficiency. Direct fuel injection is effective in controlling the flame position and in increasing the flame and the hot junction temperatures. For the current high-temperature $Si_{0.7}Ge_{0.3}$ thermoelectric alloy, a conversion efficiency of 11.3 percent is predicted. For a thermal conductivity equal to that of bismuth telluride Bi_2Te_3, and a melting temperature of 2000 K, a conversion efficiency of about 25 percent is predicted.

Nomenclature

a = frequency factor (s^{-1}) or length (mm)
A_g = cross-sectional area of gas phase $\pi D_1^2/4$ (m^2)
A_s = cross-sectional area of solid phase $\pi(D_2^2-D_1^2)/4$ (m^2)
A_r = surface area for surface radiation $\pi D_1\Delta x$ (m^2)
A_{sg} = interfacial surface area $\pi D_1\Delta x$ (m^2)
c_p = specific heat capacity (J/kg K)
C = heat capacity ratio $\rho c_p/(\rho c_p)_g$
D_1, D_2 = inside and outside diameter (m)
D_m = diffusion coefficient (m^2/s)
E_b = blackbody emissive power (W/m^2)
F_{i-j} = view factor
J_e = current (A)
k = thermal conductivity (W/m K)
l_s = tube wall thickness $(D_2-D_1)/2$ (m)
L = length (m)
Le = Lewis number $D_m/\alpha_g=(\rho c_p)_g D_m/k_g$
M = molar weight (kg/kmole)
n = n-type material or number of grid nodes
$\dot{n}_{r,P}$ = volumetric production rate of species P (kg/m^3 s)
N_t = number of thermoelectric tube
Nu_D = internal Nusselt number
Nu_e = external Nusselt number
p = p-type material or pressure (Pa)
P = combustion product species
q = heat flux (W/m^2)
Q = heat flow rate (W)
Q_k = conduction heat flow rate (W)
Q_{ku} = surface-convection heat flow rate (W)
Q_u = convection heat flow rate (W)
Q_r = surface radiation heat flow rate (W)
R_e = internal electrical resistance per a tube (Ohm)
$R_{e,o}$ = external electrical resistance (Ohm)
R = universal gas constant 8.3145 kJ/kmole K
Re_D = Reynolds number $\rho_g\langle u\rangle_{g,o}D_1/\mu_g$
$\dot{S}$ = energy conversion rate (W)
t = time (s)
T = temperature (K)
$\langle u\rangle_g$ = average gas velocity (m/s)
V = nodal volume of gas and solid phases (m^3)
x = coordinate axes (m)
x_{cs} = coordinate of control surface of a grid (m)
Z_e = figure of merit of the thermoelectric material $\alpha_S^2/(\rho_e k_{TE})$(1/K)

Greek

α_S = Seebeck coefficient (V/K)
δx = distance between nodes (m)
ΔE_a = activation energy (kJ/kmole)
$\Delta h_{r,F}$ = heat of reaction of fuel (J/kg fuel)
ΔT_s = $T_{s,h}-T_{s,c}$ (K)
Δx = length of nodal control volume (m)
$\Delta\varphi$ = voltage (V)
ϵ_r = emissivity
Φ = stoichiometric ratio
η = conversion efficiency $(J_e^2R_{e,o}/N_t)/(-\Delta h_{r,F}\rho_{F,o}\langle u\rangle_g A_g)$
ν = stoichiometric coefficient
ρ = density (kg/m^3)
ρ_e = internal electric resistivity (Ohm m)
σ_{SB} = Stefan–Boltzmann constant 5.670×10^{-8} W/m^2-K^4
τ_c = period of reciprocation (s)

Subscripts

$1,2,...,n+2$ = node index
a = activation
ad = adiabatic
b = blackbody
c = cold or combustion or cycle
cs = control surface
C = combustion
D = diameter
e = electric or external or east or exhaust
F = fuel
g = gas phase
h = hot
i,j = node index
J = Joule
k = conduction
ku = surface convection
l = left
m = mass diffusion
n = n-type material or last node
o = reference or outgoing
opt = optimum value
O = oxidant
p = pressure or p-type material
P = Peltier or product species
r = radiation or reaction or right
R = reactant species
s = solid phase
sg = solid-gas interface
sl = solid-liquid phase change
st = stoichiometry
S = Seebeck
SB = Stefan–Boltzmann
t = tube
TE = thermoelectric
u = convection
w = west
x = x-component

Other symbols

$\langle\,\rangle$ = local spatial averaged
$*$ = dimensionless quantity

References

[1] Hanamura, K., Echigo, R., and Zhdanok, S. A., 1993, ''Superadiabatic Combustion in a Porous Medium,'' Int. J. Heat Mass Transf., **36**, No. 13, pp. 3201–3209.

[2] Min, D. K., and Shin, H. D., 1991, ''Laminar premixed flame stabilized inside a honeycomb ceramic,'' Int. J. Heat Mass Transf., **34**, No. 2, pp. 341–356.

[3] Sahraoui, M., and Kaviany, M., 1994, ''Direct simulation vs volume-averaged treatment of adiabatic, premixed flame in a porous medium,'' Int. J. Heat Mass Transf., **37**, No. 18, pp. 2817–2834.

[4] Hoffmann, J. G., Echigo, R., Tada, S., and Yoshida, H., 1996, ''Analytical Study of Flame Stabilization in Reciprocating Combustion in Porous Media with High Thermal Conductivity,'' *26th Symposium (International) on Combustion*, pp. 2709–2716.

[5] Hoffmann, J. G., Echigo, R., Yoshida, H., and Tada, S., 1997, ''Experimental Study on Combustion in Porous Media with a Reciprocating Flow System,'' Combust. Flame, **111**, pp. 32–46.

[6] Echigo, R., Hanamura, K., Yoshida, H., Koda, M., and Tawata, K., 1992, ''Sophisticated Thermoelectric Conversion Devices of Porous Materials by Super-Adiabatic Combustion of Reciprocating Flow and Advanced Power Generation System,'' *11th International Conference on Thermoelectrics*, pp. 45–50.

[7] Rowe, D. M., Editor, 1995, *CRC Handbook of Thermoelectrics*, CRC Press, Boca Raton.

[8] Chen, G., 1998, ''Thermal conductivity and ballistic-phonon transport in the cross-plane direction of superlattices,'' Phys. Rev. B, **57**, No. 23, pp. 14958–14973.

[9] Kesting, A., Pickenacker, O., Trimis, D., and Drust, F., 1999, ''Development of a Radiation Burner for Methane and Pure Oxygen Using the Porous Burner Technology,'' *5th International Conference on Technologies and Combustion for a Clean Environment (Clean Air V)*, Lisbon, Portugal.

[10] Yoshizawa, Y., Sasaki, K., and Echigo, R., 1988, ''Analytical study of the structure of radiation controlled flame,'' Int. J. Heat Mass Transf., **31**, No. 2, pp. 311–319.

[11] Kaviany, M., 1999, *Principles of Heat Transfer in Porous Media*, Corrected Second Edition, Springer-Verlag, New York.

[12] Siegel, R., and Howell, J. R., 1992, *Thermal Radiation Heat Transfer*, Third Edition, Hemisphere, Washington, D.C.

[13] Kaviany, M., 2000, *Principles of Heat Transfer*, Course Pack, University of Michigan.

[14] Patankar, S. V., 1980, *Numerical Heat Transfer and Fluid Flow*, Hemisphere, Washington, DC.

Partially Premixed Flame Structure and Stability of Twin Droplets in Flows

W. H. Chen
Department of Environmental
Engineering and Sanitation,
Foo Yin Institute of Technology,
Taliao, Kaohsiung Hsien,
Taiwan 831, R.O.C.
e-mail: whchen@cc.fy.edu.tw

The flame structure and stability, as well as the vaporization rates of twin droplets exposed to a high-temperature, partially premixed flow are investigated in the present study. Two important parameters of the Reynolds number and ambient equivalence ratio are taken into consideration to account for the influence of fuel vapor in the upstream far field on those of burning mechanisms around the twin droplets. When increasing the ambient equivalence ratio, the chemical reactivity in the upstream can be classified into three types; weakly, moderately, and obviously reactive flows, according to the distribution of the vaporization rate of the leading droplet versus the Reynolds number. In particular, if the flow is moderately reactive, say, $\phi = 0.2$, a double-peak profile is observed in the vaporization rate of the leading droplet, and it clearly depicts that by increasing the Reynolds number the vaporization is sequentially dominated by the envelope flame, reactive flow, and convective flow. With regard to the trailing droplet, because of the multiple effects stemming from the leading droplet, the impact of the ambient equivalence ratio on the vaporization rate distribution is similar, except for in the purely oxidizing environment in which the twin droplets behave as a single droplet. As a whole, the evaluated results illustrate that the partially premixed flow is conducive to promoting the vaporization and aides the flame stability in a twin-droplet system, while some burning characteristics in a counterflow system can also be obtained in front of the leading droplet. [S0022-1481(00)01504-8]

Keywords: Droplet, Flame, Flow, Stability, Vaporization

Introduction

For laminar gas-phase combustion the flame is often classified to be either premixed or nonpremixed, however many kinds of flame structures based on various geometric configurations have been conducted in the past. Behind those of the flame structures, the boundary condition plays a key factor in determining the intrinsic burning characteristics such as flame stability and extinction. For this reason, partial mixing of fuel and air prior to reaction is frequently applied in practice to stabilize combustion and reduce pollution formation. The fundamental behaviors of partially premixed flame have been widely reported in the literature. For instance, in the earlier investigations of Yamaoka and Tsuji ([1–3]) concerning a partially premixed, burning counterflow system, a double-flame structure consisting of premixed and diffusion flames with separation has been observed. Similar to the preceding result, the separate flames have been also obtained by Peters ([4]), Seshadri et al. ([5]), and Hamins et al. ([6]). In their studies ([4–6]) after reducing the system Damköhler number by increasing the stretch rate, it was found that two individual flames would merge into a diffusion flame when the state of extinction was brought about. This result implies that the extinction occurred in the merged flame configuration. In addition, the study of Peter ([4]) revealed that partial premixing would make the flamelet more sensitive to stretch, where the concept of the laminar diffusion flamelet was adopted into a turbulent flow field. Furthermore, by performing asymptotic analysis the theoretical investigation of Law et al. ([7]) found that three types of flame structures were identified in terms of fuel concentrations in two streams. The results indicated that only a single merged flame behaving as a diffusion flame developed when the system was a nonpremixed or a weakly premixed environment. Alternatively, if the system was a moderately reactive environment, a binary flame consisting of premixed and nonpremixed flames should appear, while in a strongly reactive environment two premixed flames appear. In contrast to the previous works ([4–6]), however, the extinction of the binary flame might occur under the situation of individual flame separation or single merged flame ([7]). Besides the double-flame structure, another interesting flame relating to the partially premixed environment is the triple flame structure, which consists of two premixed wings and a trailing diffusion flame. According to the theoretical analysis of Buckmaster and Matalon ([8]), Dold ([9]), and Ruetsch et al., ([10]), this specific flame structure can appear as a laminar flame propagates in a partially premixed flow or nonuniform mixture.

Aside from the flame structure and stability, partially premixed flame is also relevant to the heat transfer and combustion production. In this aspect, recent study of Gore and Zhan ([11]) the attention was placed on a partially premixing methane-air coflow system. The experimental results illustrated that the flame height, radiative heat loss fractions, stable gas species, and pollutant emission of the jet flame were significantly affected by the level of partial premixing, and therefore an optimum level of partial premixing existed. In other words, adequate control of partial premixing can provide a beneficial situation concerning combustion and pollutant formation. More recent investigations, Aggarwal and co-workers ([12,13]) dealt with transient partially premixed flames, in which a fuel-rich methane-air annular jet was sandwiched between an axisymmetric air jet (on the inside) and a coflowing air (on the outside). They ([12]) found that the fuel-rich annular ring close to the nozzle exit was dominated by premixed combustion, and once oxygen was depleted inside the annular ring, diffusion flames were established on both sides of the ring. Afterward, the two high temperature nonpremixed regions merged into a single surface in the plume, causing shear-layer rollup, and subsequently leading to the formation of toroidal vortex rings. It was also elucidated that the vortex rollup process could be de-

---

Contributed by the Heat Transfer Division for publication in the JOURNAL OF HEAT TRANSFER. Manuscript received by the Heat Transfer Division, July 13, 1999; revision received, June 5, 2000. Associate Technical Editor: J. P. Gore.

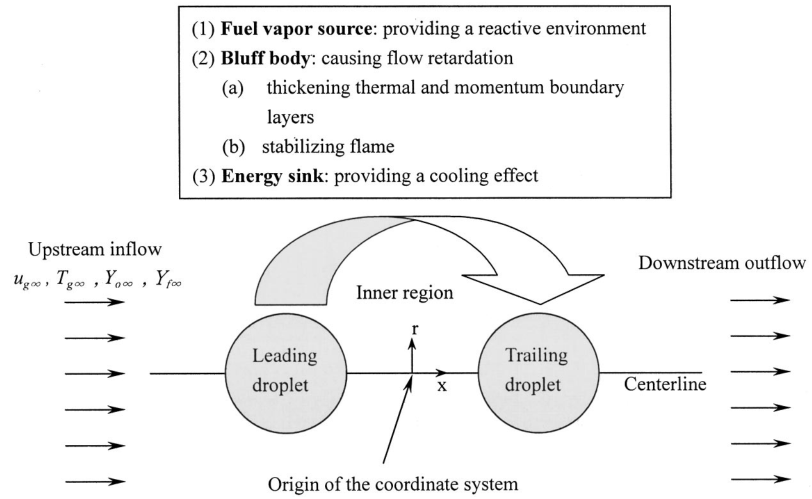

Fig. 1 Schematic illustrations of twin droplets interaction in a hot convective flow and coordinate system

layed by increasing either the Froude or Reynolds numbers, and the plume flicker frequency increased as the Froude number was decreased. Furthermore, the investigation ([13]) focused on the chemical and fluid dynamic interactions between the premixed flame in the upstream and downstream nonpremixed flame. As a result, the reaction rate profiles showed that the synergistic interaction between the inner and outer layers leaded to the formation of complex composite flames.

As far as a convective droplet with combustion is concerned, conceptually, we are capable of conceiving the local flowing behavior in front of the droplet as a counterflow. Nevertheless, the contact boundary between the far field stream and the Stefan flow stemming from droplet vaporization is a curved interface rather than a strange one, as in the counterflow ([7]). Reviewing previous studies ([14–20]), when the droplet with respect to ambience moved slowly while the ambience had no fuel vapor or just contained a little, whenever the droplet was ignited by spark in a room-temperature environment or by autoignition in a high-temperature flow, a single envelope flame surrounding the droplet developed. Under this situation, if the Reynolds number was increased or the Damköhler number was decreased continuously, the envelope flame tended to approach the front stagnation point of the droplet and then broke down. Subsequently, extinction occurred for the droplet ignited initially by spark as a result of room-temperature surrounding ([14–16]), whereas, for combustion originally excited by autoignition, a wake flame established resulting from the energy accumulated behind the droplet ([19,20]). The foregoing behaviors on the whole, resemble that of the single merged flame in the counterflow ([7]). On the other hand, if the droplet within a flow in the presence of upstream fuel vapor had a concentration which was large enough, a double-flame, composed of a premixed flame and a nonpremixed flame, existed ahead of the droplet during steady burning ([17,18]). By consecutively increasing the velocity of the approaching flow, these double flames would merge together and then be destroyed. Concerning the flame stability around a droplet, the experimental observation of Gore et al. ([17]) and the numerical prediction of Jiang et al. ([18]) demonstrated that the enhancement in extinction velocity due to fuel gases in the ambience was always significant. Accordingly, there are remarkable similarities in flame structure and stability between the convective droplet and the counterflow system. On the other hand, because the droplet vaporization rate is deeply affected by the flame around the droplet, it results in the partially premixed flow being conducive to the gasification of the droplet all the time.

In practical spray combustion processes, spray droplets are always generated from the fuel nozzle and therein a dense spray forms. This leads to droplets in close proximity to produce a noticeable droplet interaction effect due to their closeness in vicinity. In examining the two-droplet system shown in Fig. 1, essentially, the leading droplet simultaneously acts as a fuel vapor source, a bluff body, and an energy sink with respect to the trailing one. This is because the fuel vaporized from the leading droplet is convected toward the trailing droplet, plunging the latter into a partially premixed flow. However, for a high-temperature flow stream, the temperature of the fuel vapor originating from the leading droplet is generally lower than the ambience, causing a cooling effect upon the trailing droplet. Moreover, the fluid velocity ahead of the trailing droplet will be slowed down as a consequence of the flow retardation effect coming from the leading droplet. Therefore, the thermal and momentum boundary layers along the trailing droplet surface will be thickened and the flame may be stabilized behind the leading droplet if the envelope flame breaks down. As a result of the thickened thermal boundary layers and the cooling effect, the trailing droplet's vaporization rate will be suppressed ([21,22]), but the stabilized flame promotes vaporization ([23]). Meanwhile, the retarded flow field will make two droplets collide together or move apart from each other, depending on initial conditions ([24,25]).

Recently, some burning phenomena in conjunction with the complicated interactive mechanisms mentioned above, such as the hysteresis effect, and the multiplicity on vaporization rate and flame configuration, in two-droplet systems have been explored ([23,26]). The obtained results illustrated that, by varying the ambient temperature, under certain boundary conditions the vaporization rates and flame configurations of the two droplets are multivalued. Moreover, in the two-droplet systems the double, triple, and tetra-brachial flame structures ([27]) have been observed. These studies have already provided a practical observation and estimation on droplet burning mechanisms in sprays. As stated previously, however, due to the short distances between droplets in sprays, any droplet may be bathed in an environment that contains the fuel vapor from other droplets. Therefore, the reactive flow will be excited in the upstream if the far field temperature is high enough. This will give a more realistic investigation on droplet combustion with regard to the effect of fuel vapor in ambience. For this reason, the present study is intended to exploit the partially premixed flame structure and stability, as well as the vaporization rate of twin droplets. In the meantime, some similarities associated with the burning characteristics between twin-droplet and counterflow systems will also be emphasized.

Theoretical Model

The present study considers the flame structure and stability of twin 100 μm-diameter *n*-octane (C_8H_{18}) droplets, being exposed in tandem to a partially premixed flow that contains fuel vapor, as shown in Fig. 1. The ambient pressure and temperature are unitary atmosphere and 1000 K, respectively. When the distance between twin droplets is small, the interaction between the droplets is very strong thereby significantly reducing the droplets' vaporization rates ([28,29]). Meanwhile, the flame's location surrounding the two droplets quite resembles that of a single droplet, and hence the two droplets burning globally can be thought of as a single droplet. On the contrary, if the droplet spacing is large the interaction apparently decays so that the two droplets can be regarded to be two isolated droplets. In order to provide an adequate observation on a twin-droplet combustion with moderate interaction, 6 radii of droplet spacing is thus selected as the basis in this work. Intrinsically, this physical problem involves the fluid dynamics, heat and mass transfer, as well as combustion reaction in the flow stream. In order to obtain these transport phenomena, the conservation equations of continuity, momentum, energy, and species are taken into account. However, since the transport processes mentioned above couple together in the equations, resulting in extremely complex predictions, the following assumptions are included.

1 The gas-phase flow field is axisymmetric and laminar because of low Reynolds numbers' simulations, and it abides by the ideal gas law.

2 The Reynolds numbers investigated presently are below 50. It is known that the characteristic time of the approaching flow through the droplets is much smaller than those of the droplets' lifetime and those of the movements between the two droplets which is induced by drag force, therefore a quasi-steady flow over the twin droplets is assumed.

3 The burning twin droplets are in a period of full vaporization. It has been realized ([30]) that the above assumption can give a satisfactory result in predicting the droplet burning behavior in the later two-third period of the droplet lifetime. In other words, in this specific period, the assumption of gas-phase heat transfer completely used for vaporization is acceptable.

4 The gas-liquid interface is in a state of thermodynamic equilibrium. The droplet size, in this study, is very small thus the effects of Soret, Dufort, body force, radiation, and droplet deformation are ignored, owing to the negligible import in the low-pressure environment.

Before the simulation is performed, a dimensionless procedure will be carried out. The physical variables are first nondimensionalized in terms of the upstream far field conditions, and they are expressed below:

$$x=\frac{x'}{r'_s},\quad r=\frac{r'}{r'_s},\quad u=\frac{u'}{u'_\infty},\quad v=\frac{v'}{u'_\infty},\quad T=\frac{T'}{T'_\infty}$$

$$\rho=\frac{\rho'}{\rho'_\infty},\quad \mu=\frac{\mu'}{\mu'_\infty},\quad k=\frac{k'}{k'_\infty},\quad Cp=\frac{Cp'}{Cp'_\infty},\quad D=\frac{D'}{D'_\infty}$$

$$Y_f=Y'_f,\quad Y_o=Y'_0,\quad p=\frac{p'-p'_\infty}{p'_\infty},\quad h=\frac{h'}{h'_\infty},\quad Q=\frac{Q'}{h'_\infty}$$

According to the above variables, the dimensionless governing equations are then cast into a general form and given in axisymmetric coordinate (x,r) as follows:

$$\frac{\partial}{\partial x}\left(\rho u_g\Phi-\Gamma^\Phi\frac{\partial\Phi}{\partial x}\right)+\frac{1}{r}\frac{\partial}{\partial r}\left(r\rho v_g\Phi-\Gamma^\Phi\frac{\partial\Phi}{\partial r}\right)=S^\Phi \qquad (1)$$

where the fixed origin of the axisymmetric coordinate is located at the center between the twin droplets, as shown in Fig. 1. The general form of the preceding equation represents either of the mass, momentum, energy, and species conservation equations. The transport coefficient Γ^Φ and the source terms S^Φ appearing in the governing equations are provided in Table 1. Meanwhile, the dimensionless groups involved in the governing equation are presented in Table 2. Fick's law is followed in the species conservation equations to describe the species diffusion velocity of a gas mixture. In the energy equation, the gaseous enthalpy is represented by

$$h=\frac{\sum_{i=1}^{N}Y_i\int_{T_{\mathrm{ref}}}^{T}Cp_\infty dT}{Cp_\infty T_\infty} \qquad (2)$$

For gas-phase combustion, which is included in the energy and species conservation equations, the model is a single-step global finite-rate chemical reaction that is established by using the laminar flame model ([31]), and it is demonstrated as:

$$\dot{\omega}=\frac{\mathrm{Da}}{\mathrm{Re}}\rho^{1.75}Y_f^{0.25}Y_o^{1.5} \qquad (3)$$

In examining the above equation, it is evident to see that the chemical reaction is inversely proportional to the Reynolds number. It follows that the chemical reaction will be decreased if the Reynolds number is enlarged. Physically, the greater the Reynolds number a flow has, the less is the energy accumulated around the droplets. Consequently, increasing Reynolds number plays a role of anti-reaction. The anti-reaction played by convection will be later addressed. Variable thermophysical and transport properties are taken into consideration to provide a more realistic prediction. Therefore, the variations of species heat capacities with respect to

Table 1 Transport coefficients and source terms appearing in governing equations

Equations	Φ	Γ^Φ	S^Φ
Continuity	1	0	0
Axial momentum	u_g	$\frac{2\mu_g}{\mathrm{Re}}$	$-\mathrm{Eu}\frac{\partial p_g}{\partial x}+\frac{2}{\mathrm{Re}}\frac{\partial}{\partial x}\left\{-\frac{2}{3}\mu_g\left[\frac{\partial u_g}{\partial x}+\frac{1}{r}\frac{\partial}{\partial r}(rv_g)\right]+\mu_g\frac{\partial u_g}{\partial x}\right\}+\frac{1}{r}\frac{2}{\mathrm{Re}}\frac{\partial}{\partial r}\left(r\mu_g\frac{\partial v_g}{\partial x}\right)$
Radial momentum	v_g	$\frac{2\mu_g}{\mathrm{Re}}$	$-\mathrm{Eu}\frac{\partial p_g}{\partial r}+\frac{2}{\mathrm{Re}}\left\{\frac{\partial}{\partial x}\left(\mu_g\frac{\partial u_g}{\partial r}\right)-2\mu_g\frac{v_g}{r^2}+\frac{2}{3}\frac{\mu_g}{r}\left(\frac{\partial u_g}{\partial x}+\frac{1}{r}\frac{\partial}{\partial r}(rv_g)\right)\right\}+\frac{1}{r}\frac{2}{\mathrm{Re}}\frac{\partial}{\partial r}\left\{r\mu_g\frac{\partial v_g}{\partial x}-\frac{2}{3}r\mu_g\left[\frac{\partial u_g}{\partial x}+\frac{1}{r}\frac{\partial}{\partial r}(rv_g)\right]\right\}$
Energy	h	$\frac{2k_g}{\mathrm{RePr}Cp}$	$\mu_g\frac{2\mathrm{Ec}}{\mathrm{Re}}\left\{2\left[\left(\frac{\partial u_g}{\partial x}\right)^2+\left(\frac{\partial v_g}{\partial r}\right)^2+\left(\frac{v_g}{r}\right)^2\right]+\left(\frac{\partial u_g}{\partial r}+\frac{\partial v_g}{\partial x}\right)^2\right\}+Q\dot{\omega}$
Species	Y_i	$\frac{2\rho D_g}{\mathrm{ReSc}}$	$-\nu_i W_i\dot{\omega}$

Table 2 Definition of dimensionless groups

Parameter	Definition
Re	$\dfrac{2\rho'_\infty u'_\infty r'_s}{\mu'_\infty}$
Eu	$\dfrac{p'_\infty}{\rho'_\infty u'^2_\infty}$
Pr	$\dfrac{Cp'_\infty \mu'_\infty}{k'_\infty}$
Ec	$\dfrac{u'^2_\infty}{Cp'_\infty T'_\infty}$
Sc	$\dfrac{\mu'_\infty}{\rho'_\infty D'_\infty}$
Da	$\dfrac{2r'^2_s \rho'^{1.75}_\infty}{\mu'_\infty W_f^{0.25} W_o^{1.5}} A \exp\left(-\dfrac{Ar}{T}\right)$
Ar	$\dfrac{E'_a}{R_u T'_\infty}$

temperature are established by polynomials, and those in gas mixture are assumed to abide by the ideal gas mixing rule. The kinetic theory models and correlation ([28,32]) are respectively applied to account for species viscosity and diffusion coefficient versus temperature. Furthermore, based on the calculation of viscosity, the gas thermal conductivity is obtained by means of a modified Eucken method, and the effect of temperature on diffusion coefficient is accounted for through the Fuller et al. method. To evaluate gas mixture viscosity and conductivity, Wilke's formulation is used.

As far as the boundary conditions are concerned, four different parts including upstream inflow, downstream outflow, axis of symmetry, and gas-liquid interface are defined individually. The values of the upstream inflow are given directly. It has been illustrated that the region near the outflow exhibits local one-way behavior if the Peclet number is sufficiently large, thereby no boundary-condition information is needed ([33]). In the present study for the downstream outflow, because the local one-way behavior that prevails there, hence the boundary conditions are extrapolated from the inner region. With regard to the axis of symmetry, the absence of the mass and energy fluxes are taken into account. At gas-droplet interface, it is necessary to simultaneously satisfy the mass conservation of fuel and oxidizer, the heat balance, and the no-slip condition. Additionally, on account of the assumption of thermodynamic equilibrium at droplet surface, the Clausius–Clapeyron relation is employed to relate the vapor pressure and temperature of the vaporizing droplets. Consequently, the interface boundary conditions are expressed to be:

$$\rho v_{gn} = \rho v_{gn} Y_f - \rho D \frac{2}{\text{Re Sc}} \left(\frac{dY_f}{dr_s} \right) \tag{4}$$

$$\rho v_{gn} Y_o = \rho D \frac{2}{\text{Re Sc}} \left(\frac{dY_o}{dr_s} \right) \tag{5}$$

$$\rho v_{gn} L = k \frac{2}{\text{Re Pr}} \left(\frac{dT}{dr_s} \right) \tag{6}$$

$$v_{g\theta} = 0 \tag{7}$$

$$\ln\left(\frac{p_s}{p_{\text{ref}}} \right) = L_1 \left(\frac{1}{T_{\text{ref}}} - \frac{1}{T_s} \right) \tag{8}$$

where $L = L'/Cp'_\infty T'_\infty$ and $L_1 = L'/R_u T'_\infty$.

The ambient equivalence ratio, interpreting the influence of the fuel vapor of far field environment on the combusting droplets, is defined as:

$$\phi = \frac{(y_f/y_o)_\infty}{(y_f/y_o)_{\text{st}}} \tag{9}$$

where the subscripts ∞ and st stand for the upstream far field and stoichiometric state, respectively. For the droplet vaporization rate that will be discussed later, it is normalized and expressed to be:

$$\dot{m} = \frac{2\pi r_l'^2 \int_0^\pi \rho'_s v'_s \sin\theta d\theta}{4\pi r_l'^2 \rho'_{\text{ref}} v'_{\text{ref}}} = \frac{\rho'_\infty v'_\infty}{2\rho'_{\text{ref}} v'_{\text{ref}}} \int_0^\pi \rho_s v_s \sin\theta d\theta \tag{10}$$

In the above equation, the reference states of density and velocity represent room temperature (298 K) air density and unitary velocity (1 m/s), respectively.

Numerical Method

The physical geometry for a flow through twin droplets, as shown in Fig. 1, is highly irregular. Hence a computational model consisting of a body-fitted technique and a nonorthogonal curvilinear coordinate ([34,35]) is employed for solution. Before generating the body-fitted coordinate system, a hyperbolic tangent function is first applied to distribute the grid location outward from the droplet surface to the far field region along the centerline. Meanwhile, the uniform grid profiles are produced along with the twin-droplet surfaces, the far field boundary, and the centerline between the twin droplets. Next, based on the preceding generated boundary grids, the body-fitted grid system is established by using the elliptic differential equation technique ([34]) wherein the Poisson equations are solved to obtain the curvilinear coordinates in the interior of the specified physical region. During development of the entire grid system, two singular points, *viz*., the near stagnation point of the leading droplet and the front stagnation point of the trailing droplet, should be noted that by adjusting the proper parameters the grid distribution near the singularities can be made as smooth as possible. Then, according to the finite volume method ([33]), the physical coordinate governing equations are transformed and discretized into the nonorthogonal curvilinear coordinate counterparts, in terms of the contravariant velocity components ([35]). In other words, the physical domain is transformed into a computational domain of equal-space and square grids where the transformed equations are solved.

As far as the computational procedure is concerned, the SIMPLER algorithm ([33]) is followed to solve the transformed governing equations. The power-law scheme is used for evaluating the convective and diffusive fluxes over the control volume surface. The line-by-line tridiagonal-matrix algorithm (TDMA) is applied as the equation solver, while the block correction procedure ([36]) is used to enhance the computational efficiency. At the gas-liquid interface, it is found that the number of variables is greater than that of discretized equations as a result of the utilization of the Clausius–Clapeyron relation, the Newton–Raphson scheme is thus adopted to overcome the numerical difficulties. It is known that the governing equations are not only highly nonlinear but also coupled to each other, hence the solution is obtained by an iterative procedure with underrelaxing each variable. A nonuniform staggered grid system of 41×65 is employed to avoid zigzag pressure and velocity distributions. Accordingly, all scalar quantities such as temperature and density are stored at the nodal points of cells, whereas velocity components are stored on the cell faces. Rigorous convergence is assured by requiring the relative difference of the vaporization rate of each droplet between two iterations being smaller than 10^{-6}. Validation of the numerical code has been performed previously ([35]) by making detailed comparison with the experimental and the numerical results where the nonreacting low Reynolds number flows around a tandem pair of spheres were simulated. Validation of the adopted chemical model has also been made with a burning droplet ([18]).

Results and Discussion

In the following discussion, effects of two important parameters, including the Reynolds number and ambient equivalence ratio (ϕ) on the flame structure and stability, as well as the vaporization rates of twin droplets are investigated. In particular, the attention will be placed on some physical scales, such as the chemical reaction rate, temperature, and the fuel and oxidizer concentrations, along the centerline in front of the leading droplet, since the local flowing behaves as a counterflow system. The Reynolds number and ambient equivalence ratio studied range from 1 to 50 and 0 to 0.25, respectively, therefore the flame variation and its influence on droplet vaporization can be observed. In order to provide a reference for comparison, first the distributions of vaporization rate and flame configuration of two droplets versus the Reynolds number under a purely oxidizing environment, namely, $\phi=0$, are shown in Fig. 2. Clearly, the twin droplets are encompassed by envelope flames at lower Reynolds numbers ($\mathrm{Re} \leqq 10$). When the Reynolds number grows, the heat generation due to combustion is increasingly difficult to accumulate. In other

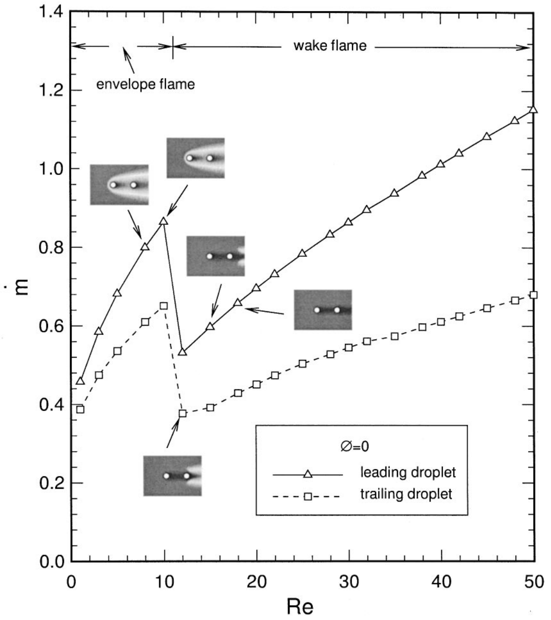

Fig. 2 Distributions of vaporization rate and flame configuration of twin droplets versus the Reynolds number in a purely oxidizing environment ($\phi=0$)

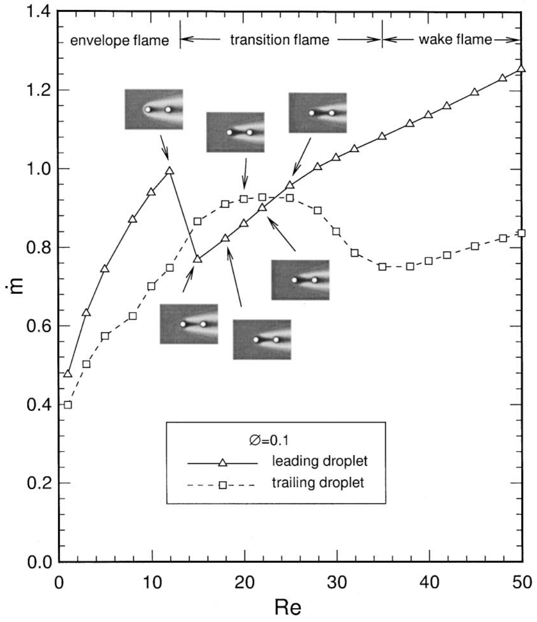

Fig. 3 Distributions of vaporization rate and flame configuration of twin droplets versus the Reynolds number at $\phi=0.1$

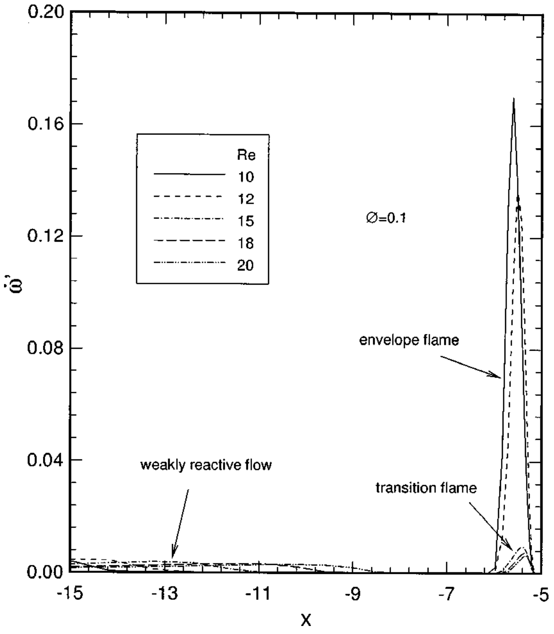

Fig. 4 Reaction rate distributions along the centerline in front of the leading droplet for various Reynolds numbers at $\phi=0.1$

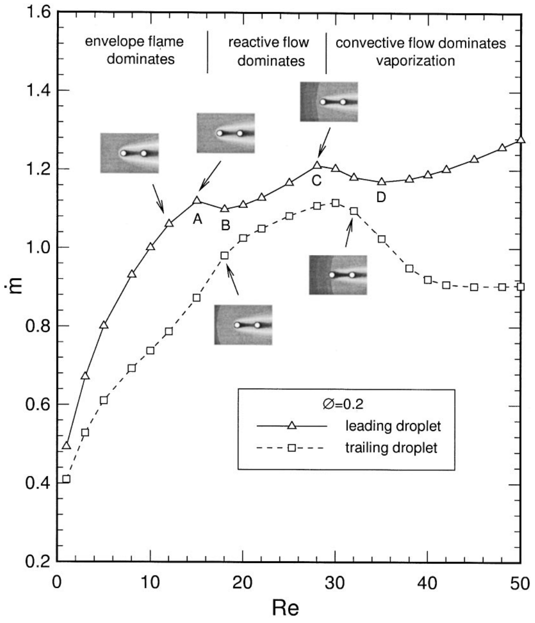

Fig. 5 Distributions of vaporization rate and flame configuration of twin droplets versus the Reynolds number at $\phi=0.2$

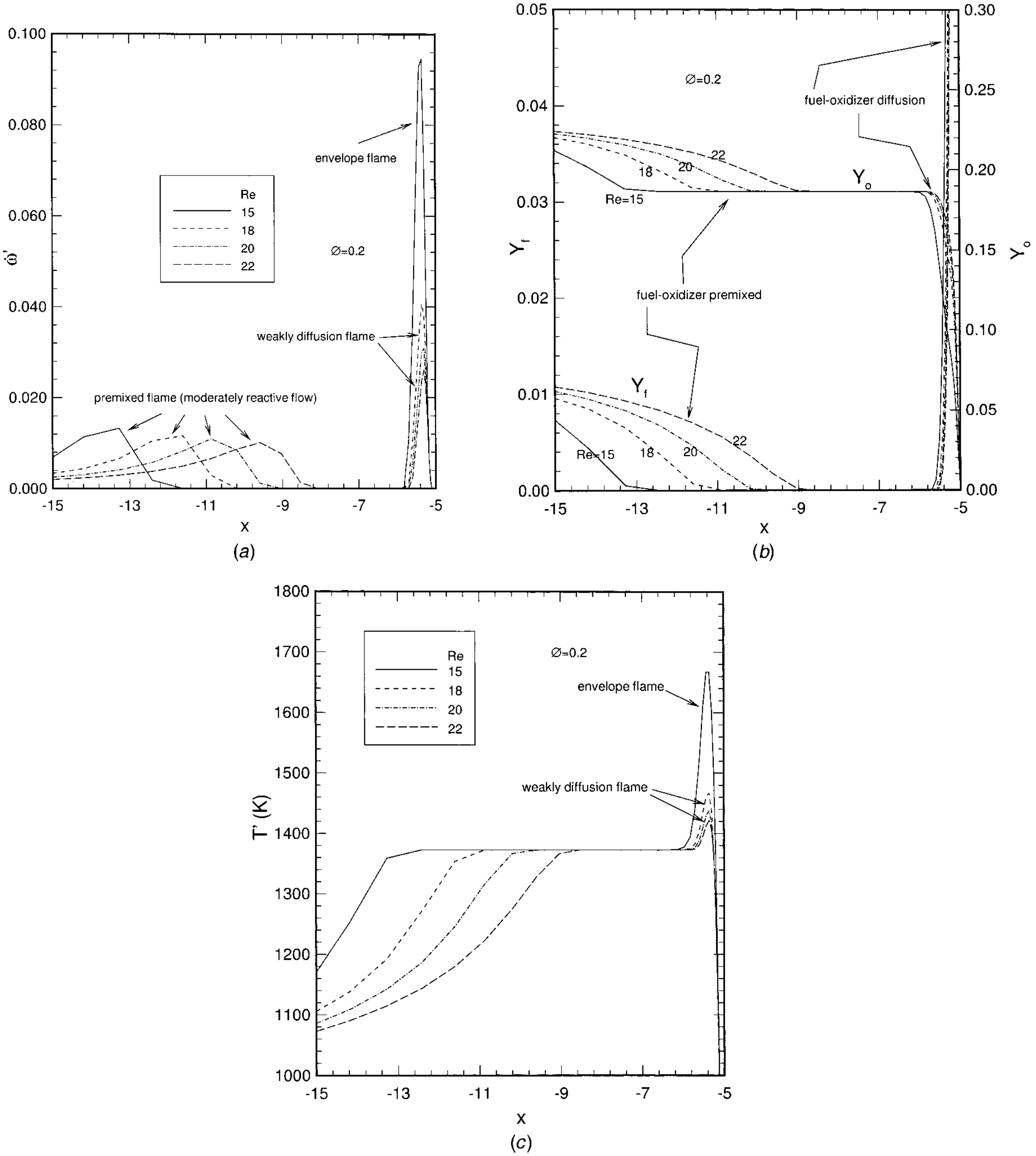

Fig. 6 Distributions of (*a*) reaction rate, (*b*) mixture-concentrations, and (*c*) temperature along the centerline in front of the leading droplet for various Reynolds numbers at $\phi=0.2$

words, the role played by anti-reaction of convection is enlarged, thereby destroying the envelope flame at Re=12 and a sudden drop in both droplets' vaporization rates is obtained. Thereafter, a wake flame behind the twin droplets develops and it prevails throughout the higher Reynolds number region. As a result, the trend of vaporization rate distribution between the leading droplet and the trailing one is identical and this characteristic coincides with that of a single droplet ([14–20]). Upon inspection of the preceding result, we are able to regard the twin-droplet system as a single droplet.

When the ambient equivalence ratio is equal to 0.1, the vaporization rate distribution of the leading droplet shown in Fig. 3 is similar to that of $\phi=0$. In examining the centerline reaction rate distributions in front of the leading droplet, as shown in Fig. 4, the reactive flows have been slightly excited in the upstream far field. Nevertheless, in contrast to the reaction rates near the front stagnation point of Re=10 and 12, the reactivity in the upstream is so small that it is negligible. As a result of this, it is not difficult to see that the partially premixed flow with $\phi=0.1$ influencing the leading droplet vaporization rate distribution is slight. In comparison to the result of Law et al. ([7]), it is revealed that the burning feature of the envelope flame ahead of the leading droplet with $\phi=0.1$ resembles that of the counterflow system in weakly reactive condition which renders a merged flame ([7]). Concerning the trailing droplet, it is interesting to find that after the envelope flame breaks down, the vaporization rate distribution associated with $\phi=0.1$ is far different from that of $\phi=0$. It has been mentioned previously that a droplet within a partially premixed flow is conducive to flame stability ([17,18]). Basically, a leading droplet acts as a fuel vapor source for a trailing droplet. It follows that the

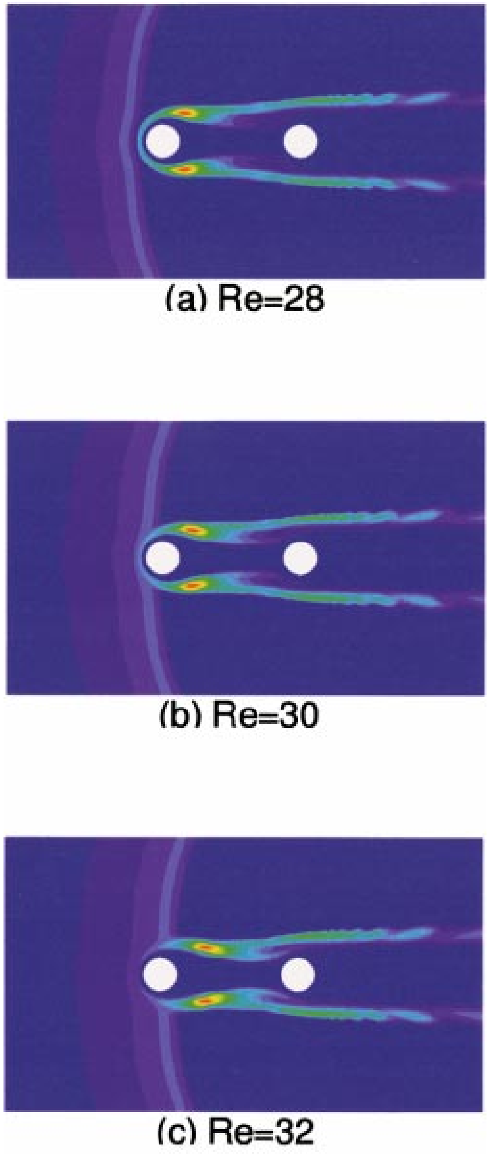
(a) Re=28

(b) Re=30

(c) Re=32

Fig. 7 Reaction rate contours around twin droplets at $\phi=0.2$ for various Reynolds numbers: (*a*) 28, (*b*) 30, and (*c*) 32

latter is bathed in an environment whose fuel vapor concentration is richer than that of the upstream far field. In addition, by virtue of the flow retardation effect stemming from the leading droplet, which can be thought of as a bluff body, the opportunity for a flame stabilized behind the droplet is enhanced. For these reasons, instead of the wake flame being behind the twin droplets for $\phi=0$, a flame experiencing destruction can still be sustained ahead of the trailing droplet, resulting in transformation into a transition flame, as shown in Fig. 2. Under this situation, in spite of the energy sink played by the leading droplet, it should be emphasized that when the Reynolds number is within the range of 15 and 22 the vaporization rate of the trailing droplet is even higher than that of the leading droplet. After that $(25\leqq\mathrm{Re}\leqq35)$, the vaporization rate of the trailing droplet decays slowly as a result of growth from the cooling effect by the leading droplet.

In Fig. 5, the ambient equivalence ratio of 0.2 indicates that the vaporization rate of the leading droplet versus the Reynolds number, globally exhibits a double-peak distribution, and the vaporization rate of a leading droplet preceded by that of a trailing one, with $\phi=0.1$, does not appear any more here. In this diagram, the stability of envelope flame has been promoted to $\mathrm{Re}=15$, where the first peak (point A) appears. It is worthy to note that though the envelope flame breaks down at $\mathrm{Re}=18$, unlike $\phi=0$ and 0.1, the vaporization rate of the leading droplet only decreases a little (point B). This arises from the flame being retained beside the leading droplet. In the meantime, because the cooling effect from the leading droplet is reduced slightly at $\mathrm{Re}=18$, the vaporization rate of the trailing droplet keeps increasing there. The foregoing characteristic is also observed for the ambient equivalence ratio of 0.1 at $\mathrm{Re}=15$, as shown in Fig. 3. To proceed farther into the recognition of flame evolution with increasing Reynolds number, the centerline reaction rate distributions in front of the leading droplet are shown in Fig. 6(*a*). According to the profiles in Fig. 6(*a*), the partially premixed flow in the upstream has already produced considerable chemical reaction, relative to that of the envelope flame at $\mathrm{Re}=15$, and thus a double-reaction zone, consisting of a front and a near reaction zones, is established. Upon inspection of the fuel and oxidizer concentration profiles shown in Fig. 6(*b*), it is apparent to know that the corresponding burning of the front and the rear reaction zones are the premixed flame and the diffusion flame, respectively. The double-reaction zone obtained in Fig. 6(*a*) is consistent with the theoretical and experimental study of Gore et al. ([17]) on a single droplet. The present results are also in good agreement with the predictions of Jiang et al. ([18]). With further increasing the Reynolds number, it should be emphasized that the double-reaction zone is still featured despite the fact that the envelope flame has broken down at $\mathrm{Re}=18$, but the near reaction zone withers rapidly and a weakly diffusion flame is thus characterized. On the other hand, for the front reaction zones, they lead to a decrease in the anti-reaction effect of convection and an enlargement of the approaching flow temperature. Accordingly, as shown in Fig. 6(*c*), the ambient temperature of 1000 K in the upstream far field is promoted to approximately 1370 K as the approaching flow closes in on the leading droplet. By continuously increasing the Reynolds number in Fig. 5, the vaporization rate of the leading droplet will climb to the second peak of $\mathrm{Re}=28$ (point C) and then descend to the local minimum of $\mathrm{Re}=35$ (point D). By observing the reaction rate contours in Fig. 7, it is clearly depicted that, corresponding to the Reynolds numbers of 28, 30, and 32, the reactive flow will approach, be in contact with, and then cross the front stagnation point of the leading droplet sequentially. As a result, the double reaction zones, as shown in Fig. 8(*a*) for $\mathrm{Re}=25$ and 28, merge together at $\mathrm{Re}=30$. The variations of fuel and oxidizer concentration profile in Fig. 8(*b*) illustrate that these profiles vary drastically during the reactive flow through the leading droplet, and the fuel vapors of the upstream and of the leading droplet connect at $\mathrm{Re}=30$. After the reactive flow passes through the front stagnation point of the leading droplet, the chemical reaction rates of $\mathrm{Re}=32$ and 35 ahead of the leading droplet decrease in a significant way, as shown in Fig. 8(*a*). Consequently, the temperature distributions with $\mathrm{Re}=32$ and 35 at the same position decay markedly, as shown in Fig. 8(*c*). This merged behavior is extremely similar to that of the counterflow system ([4–6]) around its extinction, however, the reactive flow beside the leading droplet is exhibited in flame rather than disappearing as in the counterflow system.

If we further analyze the double-peak vaporization rate distribution of the leading droplet sketched in Fig. 5, we are able to partition the profile into three sections with increasing Reynolds number. For the first section $(\mathrm{Re}\leqq15)$, the leading droplet's vaporization is mainly a contribution of the envelope flame, partially by convection, and slightly by reactive flow. In other words, the reactive flow is so far away from the leading droplet that it is relatively unimportant to vaporization. In the second section $(18\leqq\mathrm{Re}\leqq28)$, as long as the envelope flame is destroyed and replaced by a transition flame (or side flame) at a higher Reynolds number, the reactive flow will propagate toward the leading droplet and progressively dominate gasification, whereas the importance of the flame beside the leading droplet will gradually diminish. Furthermore, if the Reynolds number is high enough (Re

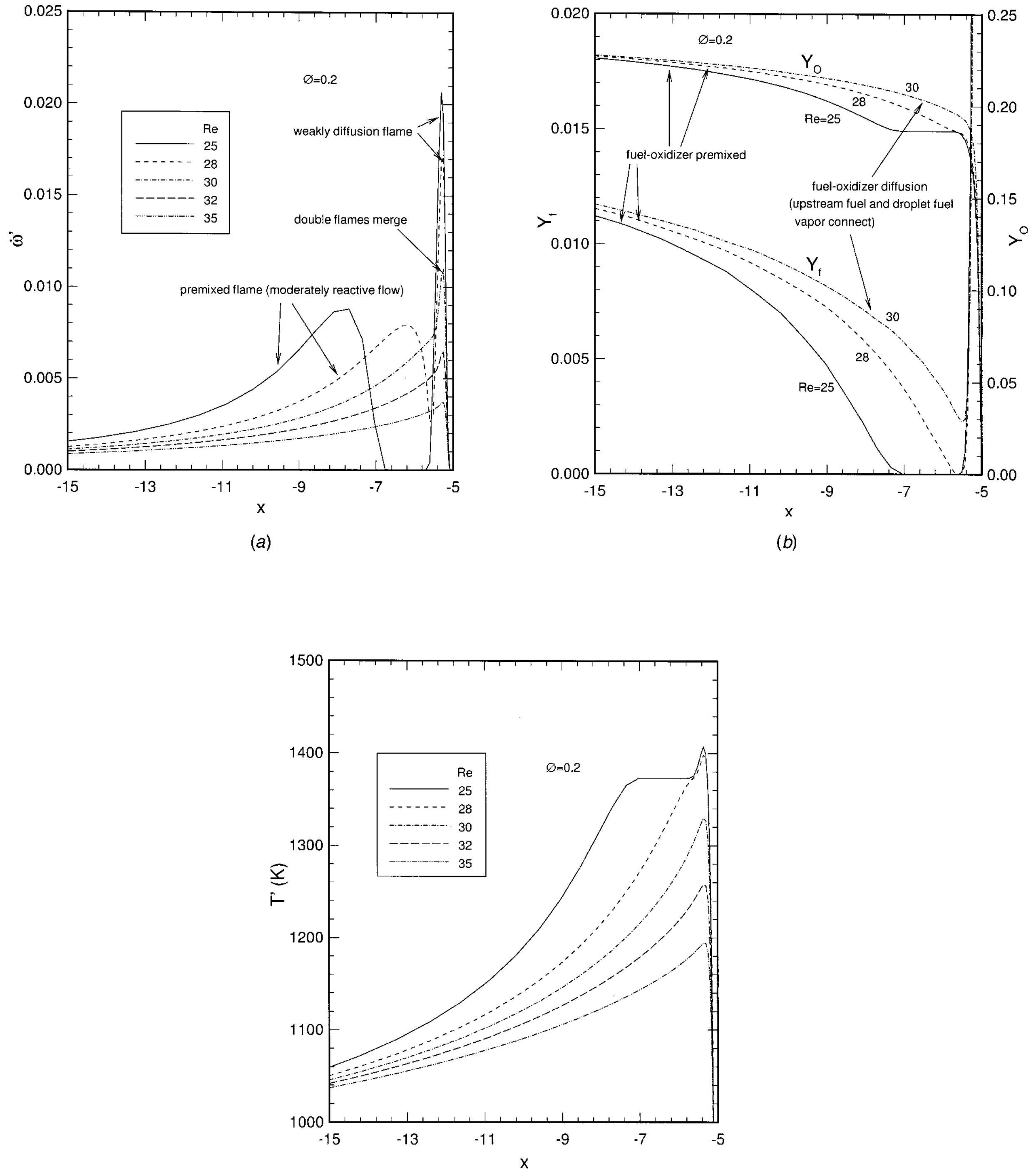

(*a*)

(*b*)

(*c*)

Fig. 8 Distributions of (*a*) reaction rate, (*b*) mixture-concentrations, and (*c*) temperature along the centerline in front of the leading droplet for various Reynolds numbers at $\phi=0.2$

≧30), convection will eventually control the leading droplet's vaporization in consequence of both flame and reactive flow being located behind the leading droplet. In summary, with increasing the Reynolds number the vaporization rate of the leading droplet is governed mainly by the envelope flame, the reactive flow, and the convective flow sequentially. When the ambient equivalence ratio is as high as 0.25, as shown in Figs. 9 and 10, the variations in flame configuration and centerline reaction rate versus the Reynolds number indicate that the flame destruction distinction becomes ambiguous. Similar to Fig. 8(*a*), the merged behavior of the double reaction zones, in Fig. 10, is also obtained at Re=30. Meanwhile, it is of interest to see that, in Fig. 9, the originally declining vaporization characteristic after destroying the envelope flame for $\phi \leqq 0.2$ disappears. This is attributed to the fact that the upstream reactive flow plays a key factor in determining the leading droplet's vaporization.

In order to assess the impact of the ambient equivalence ratio on the gasification of twin droplets, the variations of vaporization rates in the leading and the trailing droplets with respect to the Reynolds number are demonstrated in Figs. 11 and 12, respec-

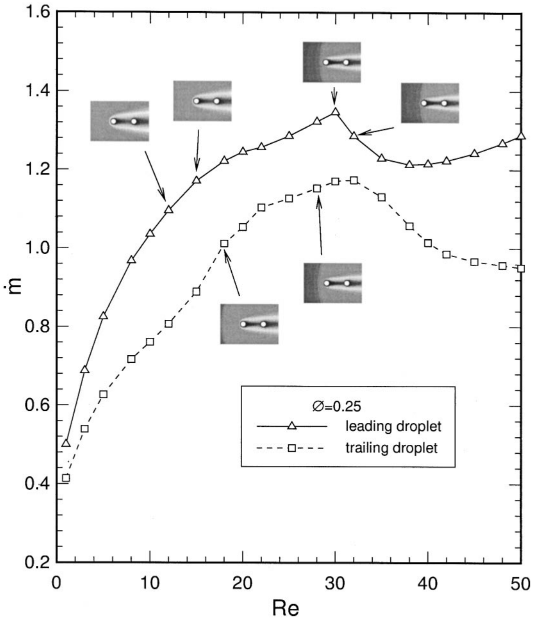

Fig. 9 Distributions of vaporization rate and flame configuration of twin droplets versus the Reynolds number at $\phi=0.25$

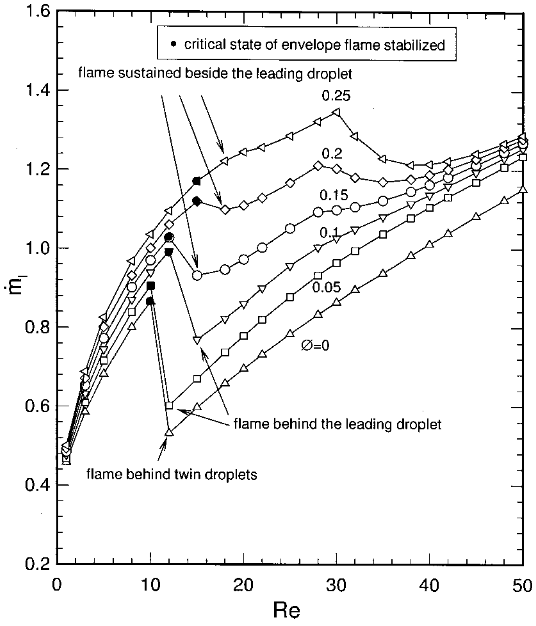

Fig. 11 Distributions of the vaporization rate of the leading droplet versus the Reynolds number under various ambient equivalence ratios

tively. It is known that a higher temperature of the approaching flow will enlarge the droplet vaporization rate, resulting from amplifying the transfer number. In this study the ambient temperature is high (1000 K). When the upstream far field contains fuel vapor ($\phi>0$), the vapor will prereact with surrounding oxidizer, thereby promoting temperature of the approaching flow. The greater the ambient equivalence ratio is, the higher is the temperature of the approaching flow. Because of this, as a whole, with increasing the ambient equivalence ratio the burning rates of the twin droplets become higher, as shown in Figs. 11 and 12. On the other hand, according to the vaporization rate distributions of the leading droplet under various ambient equivalence ratios, three different situations including weakly, moderately, and obviously reactive flows are identified when the destruction of envelope flame is brought about. In the case of $\phi\leqq 0.1$, once the envelope flame surrounding the twin droplets breaks down, the flame is transported to a place behind the two droplets ($\phi=0$) or behind the leading droplet ($\phi=0.05$ and 0.1). This arises mainly because the upstream chemical reactivity is too weak to stabilize the flame beside the leading droplet at higher Reynolds numbers. Consequently, the weakly reactive flow is induced ($\phi\leqq 0.1$) and the convection is the controlling flame stability and vaporization mechanism. On the other hand, it is important to recognize that, for $\phi=0.15$ and 0.2, the envelope flame after destruction can be

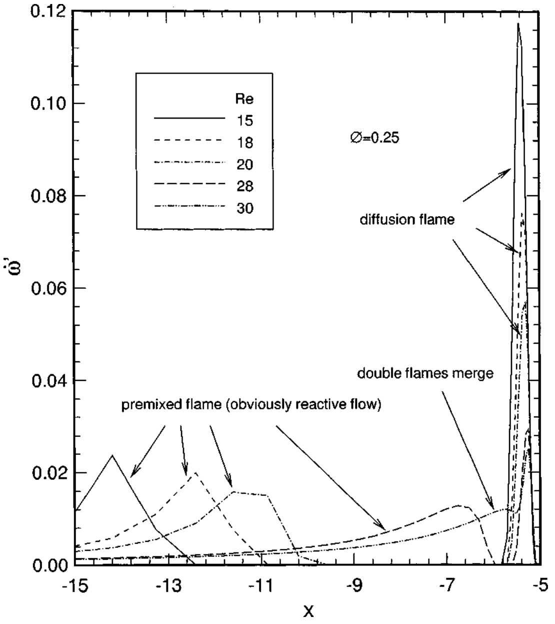

Fig. 10 Reaction rate distributions along the centerline in front of the leading droplet for various Reynolds numbers at $\phi=0.25$

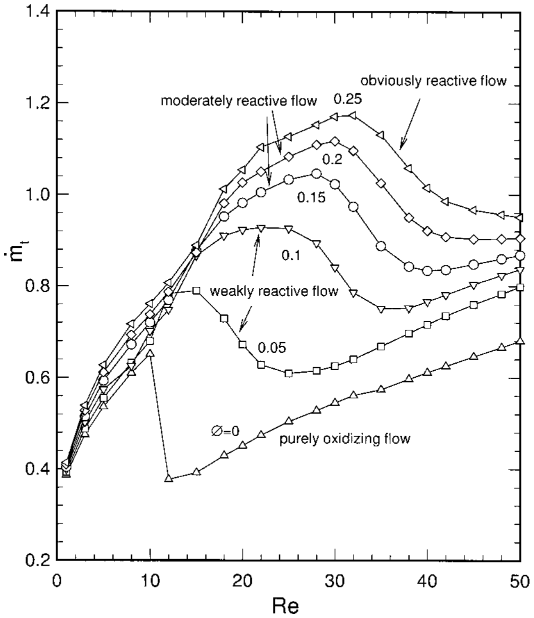

Fig. 12 Distributions of the vaporization rate of the trailing droplet versus the Reynolds number under various ambient equivalence ratios

sustained beside the leading droplet, arising from remarkable growth of reactivity in the approaching flow. This results in a slight decay in the vaporization rate of the leading droplet, and the moderately reactive flow is identified. Accordingly, near the critical state of the flame burst, below the state the envelope flame mainly excites the vaporization, whereas beyond the critical state it is mainly by the reactive flow. As the ambient equivalence ratio is further amplified, say, to $\phi = 0.25$, the characteristics of envelope flame destruction decreasing the vaporization rate disappears. This implies, in turn, that the chemical reaction in a partially premixed flow is strong enough so that the influence of the envelope flame on the vaporization of the leading droplet tend to be minimal. The reactive flow, therefore, becomes the controlling vaporization mechanism and elicits the obviously reactive flow. When attention is placed on the trailing droplet, no matter what the ambient equivalence ratio is, except for $\phi = 0$, the envelope flame ahead of the leading droplet burst influencing the vaporization rate of the trailing droplet tends to slow down, as shown in Fig. 12. As mentioned previously, the trailing droplet is located in a flow containing the fuel vapors coming from the upstream far field and the leading droplet, so that the reactivity in front of the trailing droplet is always stronger than the leading droplet. However, for purely oxidizing environment, even if the fuel vapor source and bluff body simultaneously played by the leading droplet, the flow velocity retardation and fuel vapor accumulation behind the leading droplet are insufficient to counteract the cooling effect of the same droplet and the anti-reaction effect of the convection. As a result, the flame is located behind the twin droplets but not stabilized between them, and an abrupt drop in the vaporization rate distribution after the envelope flame breaks down is obtained. In summary, the enlargement of the ambient equivalence ratio will promote the flame stability and increase the vaporization rates of the twin droplets in a significant way, as shown in Figs. 11 and 12.

Conclusions

The analysis on flame structure and stability, as well as the vaporization rates of twin droplets exposed to a high-temperature, partially premixed flow has been performed through numerical method by employing the body-fitted technique in cooperation with the curvilinear coordinate system. A brief summary of the results is drawn below:

1 According to the vaporization rate distribution of the leading droplet, the reactivity in the approaching flow can be classified into three different results, including weakly, moderately, and obviously reactive flows, in terms of ambient equivalence ratio.

2 With twin droplets in a purely oxidizing environment ($\phi = 0$), there is an abrupt drop in the vaporization rate distribution of both droplets that results from the destruction of the envelope flame, which is brought about at a place behind the droplets. The two droplets can then be globally thought of as a single droplet system, however, owing to the cooling and flow retardation effects of the leading droplet, the vaporization rate of the trailing droplet tends to always be lower than that of the leading one.

3 For the case of the weakly reactive flow, since the roles of fuel vapor source and the bluff body played by the leading droplet associated with upstream weak reactivity becomes considerable. After the envelope flame breaks down the flame can still be stabilized in front of the trailing droplet. In this specified situation, the vaporization rate of the trailing droplet may surpass that of the leading droplet under certain Reynolds numbers. As a whole, the convective flow is an important factor in determining flame stability, and the flame structure in front of the leading droplet resembles the merged flame in a counterflow.

4 Increasing the ambient equivalence ratio enlarges the upstream reactivity, for the moderately reactive flow this results in a bit of a reduction on the leading droplet's vaporization once the envelope flame breaks down. This is attributed to the fact that the flame is sustained beside the leading droplet. Throughout the entire vaporization rate distribution, a double-peak profile, say, of $\phi = 0.2$, may appear, where with increasing the Reynolds number, the envelope flame, reactive flow, and convective flow sequentially dominate the vaporization.

5 As the ambient equivalence ratio is large enough, namely, $\phi = 0.25$, the transition during the envelope flame bursts becomes ambiguous and the envelope flame destruction declining the leading droplet's vaporization rate for $\phi \leqq 0.2$ disappears here. Accordingly, the obviously reactive flow is elicited, in which the vaporization rate of the leading droplet decays only after the reactive flow goes through the front stagnation point of the leading droplet. It follows that the upstream chemical reaction plays a key factor in flame stability and vaporization. In both moderately and obviously reactive flows, the double reaction zones, composed of the front premixed flame and the near diffusion flame, are clearly characterized until the front and the rear reaction zones merge, even though the envelope flame is destroyed. Consequently, this foregoing behavior is similar to that of the separate flames in the counterflow.

6 Regarding the trailing droplet, except for $\phi = 0$ therein the twin-droplet behaves as a single droplet, the roles played by the leading droplet on the fuel vapor source and bluff body always keep up with the combined effects of the energy sink from the same droplet and the anti-reaction of convection. As a consequence, after disruption the flame can be stabilized in front of the trailing droplet, and a leisurely decay of the vaporization rate appears rather than a sudden decline as in $\phi = 0$, where the cooling effect is a controlling mechanism.

Finally, the global observation of the vaporization rate distributions of the leading and trailing droplets elucidates that the enlargement of the ambient equivalence ratio will pronouncedly promote the flame stability and vaporization rates of the twin droplets. Meanwhile, some burning features in the counterflow system can be found in the two-droplet system as well.

Acknowledgments

This research is supported by the National Science Council, Taiwan, ROC, under contract NSC 88-2212-E-242-001. Computational resources for this work is in part provided by the National Center for High-Performance Computing in Taiwan.

Nomenclature

A = Preexponential factor ($= 4.6 \times 10^{11}$)
Ar = Arrhenius number
Cp = Specific heat of constant pressure
d = The distance between twin droplets' center
D = Diffusivity
Da = Damköhler number
E_a = Activation energy ($E_a' = 30$ Kcal/mole)
Ec = Eckert number
Eu = Euler number
h = Sensitive enthalpy
k = Thermal conductivity
L = Latent heat of droplet
N = Number of species
$\dot{m}$ = Droplet vaporization rate
p = Pressure
Q = Heat of combustion
r = Radial coordinate
r_s = Droplet radius
Pr = Prandtl number
R_u = Universal gas constant
Re = Reynolds number
S = Source term
Sc = Schmidt number
T = Temperature
u = Axial velocity

v = Radial velocity
v_n = Fuel droplet surface normal velocity
v_θ = Fuel droplet surface tangential velocity
W = Molecular weight
x = Axial coordinate
Y = Mass fraction

Greek Symbols

θ = Polar angle
μ = Viscosity
ν_i = Stoichiometric coefficients of ith species
ρ = Gas density
ϕ = Ambient equivalence ratio
$\dot{\omega}$ = Specific chemical reaction rate
Γ = Transport coefficient

Superscripts

$'$ = Dimensional scale
n = nth iteration

Subscripts

f = Fuel
g = Gas phase
i = ith species
l = Leading droplet
n = Normal direction
o = Oxidizer
ref = Reference
s = Droplet surface
st = Stoichiometric state
t = Trailing droplet
θ = Tangential direction
∞ = Upstream far field

References

[1] Yamaoka, I., and Tsuji, H., 1974, ''The Structure of Rich Fuel-Air Flames in the Forward Stagnation Region of a Porous Cylinder,'' *Fifteenth Symposium (International) on Combustion*, pp. 637–644.
[2] Yamaoka, I., and Tsuji, H., 1976, ''Structure Analysis of Rich Fuel-Air Flames in the Forward Stagnation Region of a Porous Cylinder,'' *Sixteenth Symposium (International) on Combustion*, pp. 1145–1154.
[3] Yamaoka, I., and Tsuji, H., 1978, ''An Experimental Study of Flammability Limits Using Counterflow Flames,'' *Seventeenth Symposium (International) on Combustion*, pp. 843–855.
[4] Peters, N., 1984, ''Partially Premixed Diffusion Flamelets in Non-Premixed Turbulent Combustion,'' *Twentieth Symposium (International) on Combustion*, pp. 353–360.
[5] Seshadri, K., Puri, I., and Peters, N., 1985, ''Experimental and Theoretical Investigations of Partially Premixed Diffusion Flames at Extinction,'' Combust. Flame, **61**, pp. 237–249.
[6] Hamins, A., Thridandam, H., and Seshadri, K., 1985, ''Structure and Extinction of a Counterflow Partially Premixed, Diffusion Flame,'' Chem. Eng. Sci., **40**, pp. 2027–2045.
[7] Law, C. K., Zhu, D. L., Li, T. X., Chung, S. H., and Kim, J. S., 1989, ''On the Structure and Extinction Dynamics of Partially-Premixed Flames: Theory and Experiment,'' Combust. Sci. Technol., **64**, pp. 199–232.
[8] Buckmaster, J., and Matalon, M., 1988, ''Anomalous Lewis Number Effects in Tribrachial Flames,'' *Twenty-Second Symposium (International) on Combustion*, pp. 1527–1535.
[9] Dold, J. W., 1989, ''Flame Propagation in a Nonuniform Mixture: Analysis of a Slowly Varying Triple Flame,'' Combust. Flame, **76**, pp. 71–88.
[10] Ruetsch, G. R., Vervisch, L., and Linan, A., 1995, ''Effects of Heat Release on Triple Flames,'' Phys. Fluids, **7**, No. 6, pp. 1447–1454.
[11] Gore, J. P., and Zhan, N. J., 1996, ''NO_x Emission and Major Species Concentrations in Partially Premixed Laminar Methane/Air Co-flow Jet Flames,'' Combust. Flame, **105**, pp. 414–427.
[12] Shu, Z., Aggarwal, S. K., Katta, V. R., and Puri, I. K., 1997, ''A Numerical Investigation of the Flame Structure of an Unsteady Inverse Partially Premixed Flame,'' Combust. Flame, **111**, pp. 296–311.
[13] Aggarwal, S. K., and Puri, I. K., 1998, ''Flame Structure Interactions and State Relationships in an Unsteady Partially Premixed Flame,'' AIAA J., **36**, No. 7, pp. 1190–1199.
[14] Spalding, D. B., 1953, ''The Combustion of Liquid Fuels,'' *Fourth Symposium (International) on Combustion*, pp. 847–864.
[15] Gollahalli, S. R., and Brzustowski, T. A., 1973, ''Experimental Studies on the Flame Structure in the Wake of a Burning Droplet,'' *Fourteenth Symposium (International) on Combustion*, pp. 1333–1344.
[16] Gollahalli, S. R., and Brzustowski, T. A., 1975, ''The Effect of Pressure on the Flame Structure in the Wake of a Burning Hydrocarbon Droplet,'' *Fifteenth Symposium (International) on Combustion*, pp. 409–417.
[17] Gore, J. P., Meng, W. H., and Jang, J. H., 1990, ''Droplet Flames in Reactive Environments,'' Combust. Flame, **82**, pp. 126–141.
[18] Jiang, T. L., Chen, W. H., Tsai, M. J., and Chiu, H. H., 1994, ''Double Flame and Multiple Solution Computations for a Wetted Porous Sphere Vaporizing in Reactive Flows,'' Combust. Sci. Technol., **102**, pp. 115–143.
[19] Jiang, T. L., Chen, W. H., Tsai, M. J., and Chiu, H. H., 1995, ''A Numerical Investigations of Multiple Flame Configurations in Convective Droplet Gasification,'' Combust. Flame, **103**, pp. 221–238.
[20] Chiu, H. H., and Huang, J. S., 1996, ''Multiple-State Phenomena and Hysteresis of a Combusting Isolated Droplet,'' Atomization Sprays, **6**, pp. 1–26.
[21] Tsai, J. S., and Sterling, A. M., 1990, ''The Combustion of Linear Droplet Arrays,'' *Twenty-Third Symposium (International) on Combustion*, pp. 1405–1411.
[22] Tsai, J. S., and Sterling, A. M., 1991, ''The Combustion of a Linear Droplet Array in a Convective, Coaxial Potential Flow,'' Combus. Flame, **86**, pp. 189–202.
[23] Chen, W. H., Liu, C. C., and Jiang, T. L., 1998, ''Hysteresis Effects of Two Interactive Droplets Burning in Convective Flows,'' *Twenty-Seventh Symposium (International) on Combustion*, pp. 1923–1932.
[24] Raju, M. S., and Sirignano, W. A., 1987, ''Unsteady Navier-Stokes Solution for Two Interacting, Vaporizing Droplets,'' *AIAA 25th Aerospace Sciences Meeting*, AIAA-87-0300.
[25] Raju, M. S., and Sirignano, W. A., 1990, ''Interaction Between Two Vaporizing Droplets in an Intermediate Reynolds Number Flow,'' Phys. Fluids, **2**, No. 10, pp. 1780–1796.
[26] Chen, W. H., 2000, ''Combustion Hysteresis and Vaporization Interaction of Two Burning Droplets With Different Sizes,'' Combust. Sci. Technol., **154**, pp. 229–257.
[27] Chen, W. H., and Jiang, T. L., 2000, ''Double, Triple, and Tetra-Brachial Flame Structures Around a pair of Droplets in Tandem,'' Combust. Sci. Technol., **151**, pp. 105–132.
[28] Labowsky, M., 1978, ''A Formalism for Calculating the Evaporation Rates of Rapidly Evaporting Interacting Particles,'' Combust. Sci. Technol., **18**, pp. 145–151.
[29] Labowsky, M., 1980, ''Calculation of the Burning of Interacting Fuel Droplets,'' Combust. Sci. Technol., **22**, pp. 217–226.
[30] Chen, W. H., Liu, C. C., and Jiang, T. L., 1999, ''Numerical Investigation of Droplet Vaporization and Combustion Models Spray Combustion,'' *17th International Colloquium on the Dynamics of Explosions and Reactive Systems*, July 25–30, Heidelberg, Germany.
[31] Westbrook, C. K., and Dryer, F. L., 1981, ''Simplified Reaction Mechanisms for the Oxidation of Hydrocarbon Fuel in Flames,'' Combust. Sci. Technol., **27**, pp. 31–43.
[32] Reid, R. C., Prausnitz, J. M., and Poling, B. E., 1985, *The Properties of Gases and Liquids*, McGraw-Hill, New York.
[33] Patankar, S. V., 1980, *Numerical Heat Transfer and Fluid Flow*, Hemisphere, Washington, D.C.
[34] Thompson, J. F., Warsi, Z. U., and Mastin, C. W., 1985, *Numerical Grid Generation: Foundations and Applications*, North-Holland, Amsterdam.
[35] Jiang, T. L., Liu, C. C., and Chen, W. H., 1994, ''Convective Fuel Droplet Burning Accompanied by an Oxidizer Droplet,'' Combust. Sci. Technol., **97**, pp. 271–301.
[36] Patankar, S. V., 1981, ''A Calculation Procedure for Two-Dimensional Elliptic Situations,'' Numer. Heat Transfer, **4**, pp. 409–425.

Falling Film and Spray Evaporation Enhancement Using an Applied Electric Field

J. Darabi
Mem. ASME

M. M. Ohadi
Fellow ASME

S. V. Desiatoun

Thermal Miniaturization/Enhanced Heat Transfer Laboratory,
Department of Mechanical Engineering,
University of Maryland,
College Park, MD 20742

The effect of an electric field on the falling-film evaporation of refrigerant R-134a on a vertical plate and three commercially available tubes was investigated experimentally. The plate test section was 25.4 mm wide and 76.2 mm long, and each tube test section was 19 mm in diameter and 140 mm long. Experiments were conducted in both falling film and spray evaporation modes. The effects of various parameters such as heat flux, refrigerant flow rate, electrode gap, and applied voltage were investigated. It was found that in the presence of an applied electric field, the maximum enhancement in the heat transfer coefficient for both falling film and spray evaporation modes on a plate was nearly the same. A maximum enhancement of fourfold in the heat transfer coefficient with the plate, 90 percent with the smooth tube, 110 percent with the Turbo BIII, and 30 percent with 19 fpi tube were obtained. The electrohydrodynamic power consumption in all cases was less than 0.12 percent of the total energy exchange rate in the test section.
[S0022-1481(00)03003-6]

Keywords: Augmentation, Electric Fields, Enhancement, Film, Heat Transfer, Thin Films

Introduction

This paper presents the results of an experimental study that investigated the feasibility of using the electrohydrodynamic (EHD) technique for heat transfer enhancement of falling film evaporation on vertical surfaces. The falling film evaporation process has been widely employed in various industries such as refrigeration/HVAC, chemical processing, petroleum refineries, desalination, and food processing. Falling film evaporation on horizontal tubes has also been used for ocean thermal energy conversion systems (OTEC). In falling film evaporation, the liquid is introduced through distributors to the top of a bundle, evaporating as it falls down on the periphery of the tubes. The excess liquid drips from the bottom of the tubes to the lower ones. This process continues until the falling film reaches the lowest tube in the array. Often, the objective is to increase the evaporative capacity or to reduce the required temperature driving force. Also, the total mass of liquid charge is reduced because there is no liquid pool, and the effect of hydrostatic head is also eliminated ([1]).

The effect of electrohydrodynamics (EHD) on heat transfer has been under investigation for the past three decades. Previous work involves studies for single-phase, phase-change (boiling, condensation, melting, and freezing), pumping, and spraying. However, due to their greater potential for practical applications, boiling and condensation have attracted more attention from industrial and academic researchers. Phase-change heat transfer enhancement using an electric field was first investigated by Bochirol et al. [2] who conducted experiments with pool boiling. Several other researchers performed similar work ([3–6]). Additional discussion of the related research is given in Ohadi [7] and Yabe [8].

The (EHD) enhancement of heat transfer refers to the coupling of an electric field with the fluid field in a dielectric fluid medium. The net effect is the production of secondary motions that destabilize the thermal boundary layer near the heat transfer surface, leading to heat transfer coefficients that are often an order of magnitude higher than those achievable by the conventional enhancement techniques. The driving force behind the electrically induced secondary motions responsible for the EHD effect is the electric body force. For a dielectric fluid of electric permittivity ε, mass density ρ, and temperature T, when subjected to applied electric field strength E, this body force can be expressed as ([9])

$$\mathbf{f}=\rho_c\mathbf{E}-\frac{1}{2}E^2\nabla\varepsilon+\frac{1}{2}\boldsymbol{\nabla}\left[E^2\rho\left(\frac{\partial\varepsilon}{\partial\rho}\right)_T\right] \tag{1}$$

where ρ_c is the electric field charge density. The first term on the right side of the above equation is the electrophoretic force that results from the net free charges within the fluid. This term is usually of importance in single-phase flows where the EHD current discharge is predominantly responsible for the generation of electrically induced secondary motions and the resulting enhancement mechanism. The second term, known as the dielectrophoretic force, arises from the polarization of matter and produces the transnational motion of neutral matter in a nonuniform electric field. The third term is called the electrostrictive force and represents a volume force whenever there is an inhomogeneous electric field within the dielectric. The second and third terms contribute substantially to the EHD body force in a phase-change process. Note that in two-phase heat transfer processes, $\boldsymbol{\nabla}\varepsilon$ becomes singular at liquid-vapor interface, resulting in the liquid-vapor surface instability.

When the electric field is applied to a liquid, the liquid experiences electrical stress. This stress depends on the dielectric constant of the working fluid, spatial variations in the electric field, and the distribution of the free charges in the liquid. The effect of the dielectric constant is more pronounced in the liquid-vapor interface, due to a significant difference between the liquid and vapor dielectric constants. In the case of falling film evaporation, normal stresses at the liquid-vapor interface extract the falling film from the surface, resulting in locally concentrated films over a small region of the heat transfer surface, and a thinner film thickness over the remaining surface. Note that in doing so, a uniformly thick film is replaced by a concentrated film over a small region of the heat transfer surface with lesser evaporation, and a very thin film over the remaining surface with more rapid evaporation. Overall, the average heat transfer coefficient for the

---

Contributed by the Heat Transfer Division for publication in the JOURNAL OF HEAT TRANSFER. Manuscript received by the Heat Transfer Division, July 3, 1999; revision received, April 10, 2000. Associate Technical Editor: P. Ayyaswamy.

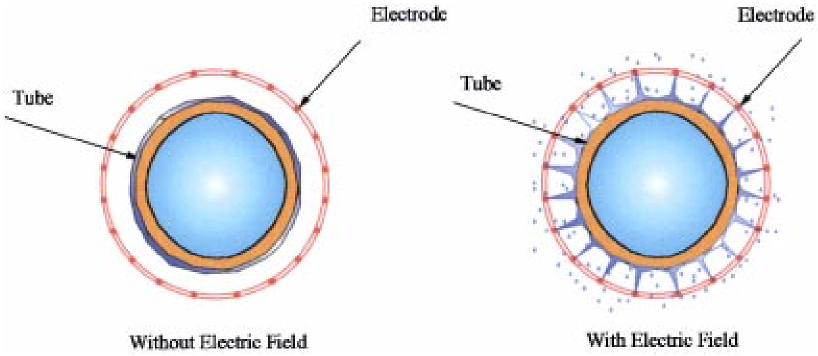

Fig. 1 The effect of electric field on the film distribution

surface can be substantially greater than if the surface were covered with a uniform film of greater thickness. This mechanism is shown schematically in Fig. 1.

Experimental Apparatus

The experimental facility is shown schematically in Fig. 2. The setup includes a test chamber, a feed refrigerant loop, a water loop, and a parasitic losses control system. The test chamber was made of a tempered-glass cylindrical wall with aluminum flanges covering both ends. The entire structure was reinforced by four stainless steel rods. The chamber could sustain up to 690 kPa pressure. The condenser was mounted horizontally on the upper flange and removed the heat generated in the test chamber. A pressure transducer, safety valve, and access valve for refrigerant charging were also mounted on the upper flange. The bottom flange was the base support for the copper coils and the test section. Access fittings for thermocouples, electrical wiring, and a refrigerant discharge valve were also installed on the bottom flange. Figure 3 shows a schematic of the test chamber.

The refrigerant loop consisted of a magnetic gear pump, a subcooler, a copper coil, and a liquid distributor. The refrigerant was passed through a subcooler before entering the pump. The subcooler was a tube-in-tube heat exchanger where the liquid refrigerant flowed in the tube side and the chilled water in the annulus. When the refrigerant leaves the pump, its temperature can be slightly lower than the saturation temperature. To eliminate this problem, the refrigerant was passed through a copper coil, which was submerged in a pool of liquid refrigerant. The liquid refrigerant was then passed through the liquid distributor and sprayed onto the heat transfer surface.

The water loop included a chiller, a pump, a stepper motor, and a flowmeter. This loop provided chilled water to the condenser to remove the heat generated by the test section. The water exited the chiller at the desired temperature and was then pumped into the condenser. The water then exited the condenser and flowed back to the chiller unit. The pressure of the test chamber was controlled by adjusting the temperature and flow rate of the water passing through the condenser.

To minimize heat losses to the surroundings, both the test chamber and the feed refrigerant loop were placed inside a parasitic losses control chamber. This chamber included a R-12 chiller unit, a heater, and a fan. All the units were interfaced with a computer for precise monitoring and control. The temperature of the chamber was controlled by a computer and was kept close to the saturation temperature at which the experiments were run.

Figure 4 shows the schematic diagram of the plate section. The heat transfer surface was a smooth copper plate with dimensions of 76.2 mm × 25.4 mm × 2.54 mm (3. in. ×1 in. ×0.1 in.). The plate was soldered on a 76.2 mm × 25.4 mm ×25.4 mm (3 in.×1 in.×1 in.) brass block. This arrangement allowed the placement of six thermocouples evenly between the copper plate and the brass block. A cartridge heater 3.2 mm in diameter and 50.8 mm in length (1/8 in.×2 in.) was placed inside the brass block. All surfaces of the brass block (except the front surface) were insu-

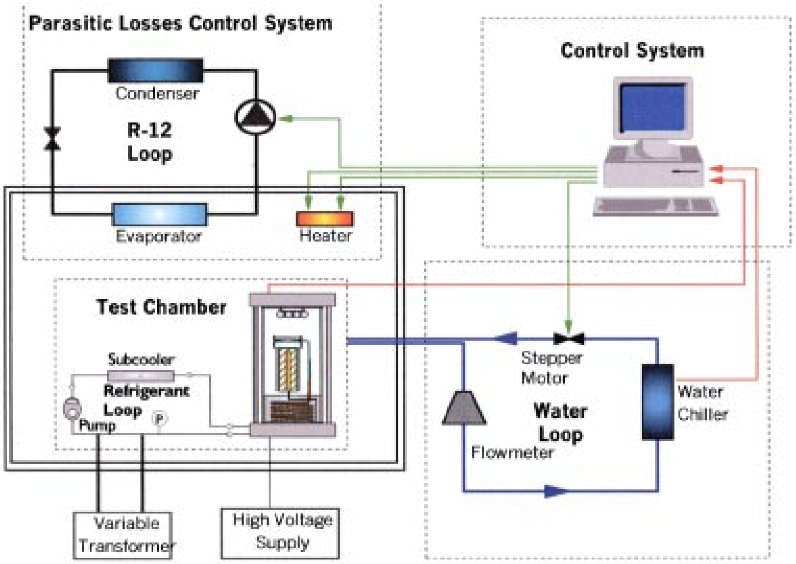

Fig. 2 Schematic of the experimental setup

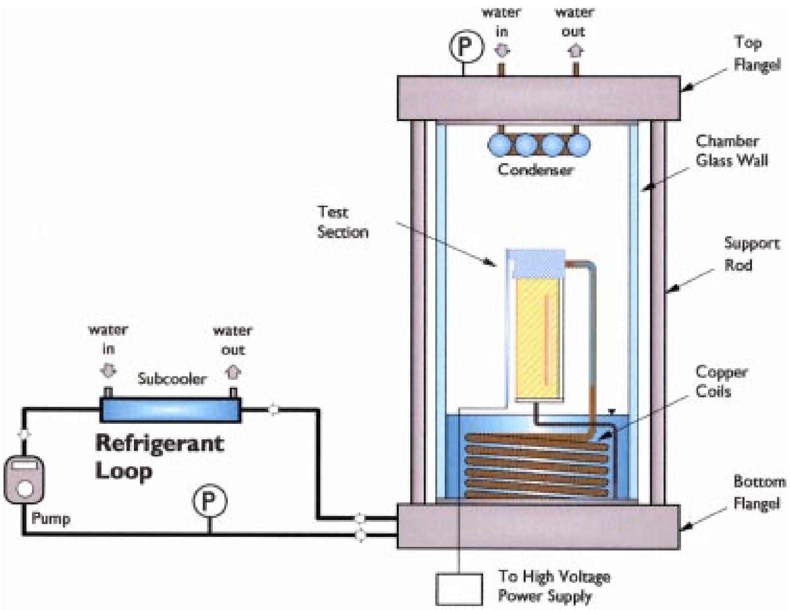

Fig. 3 Schematic of the test chamber

lated by 6.35-mm (1/4 in.) thick Teflon sheets. The gap between the brass block and Teflon sheets was filled with epoxy glue to prevent the seepage of the liquid between the test section and insulation materials. A 3 in.×1 in.×0.1 in. aluminum plate was used as the charged electrode and was oriented parallel to the heat transfer surface. Liquid refrigerant flowed downward on the copper plate from the liquid distributor located on the top of the test section. The distributor was made of a Delrin block. An entry hole with a diameter of 6.35 mm (1/4 in.) was made in the Delrin block to supply the liquid to the distributor. Six small holes, 4 mm apart and 0.9 mm in diameter, were made perpendicular to the entry hole to distribute the liquid evenly to the plate.

Three test section tubes were also designed and fabricated: a smooth tube, 19 fpi tube, and Turbo BIII tube. Figure 5 shows the schematic diagram of the test section. Each test section was 19 mm (3/4 in.) in diameter and 140 mm (5.5 in.) long. To facilitate wall temperature measurement, 12 thermocouple grooves of 1-mm width, 0.6-mm depth, and 30 deg apart from each other were made on the outer surface of the sleeve. The thermocouple wires were mounted on the inside wall of the test section. They were placed at three axial locations of 35 mm, 70 mm, 105 mm along the test section. At each axial location, four thermocouples were evenly placed 90 deg apart from each other. Heat was supplied to the test section by an electric cartridge heater with an outside diameter of 6.35 mm (1/4 in.) and a length of 127 mm (5 in.). Figure 5 also shows a schematic diagram of the feed refrigerant distributor at the top of the test section tube. Feed refrigerant was distributed by a 1/4 in. O-ring copper tube with 12 small holes, each set 30 deg apart. To ensure a well distributed refrigerant flow rate over the tube, the O-ring distributor was carefully aligned with the tube. The O-ring distributor was placed on the Derlin block and fastened with four screws.

Three different types of electrodes were tested in this study: a tubular electrode, a slitted electrode, and an IWF electrode. Schematics of these electrodes are shown in Fig. 6. The slitted electrode was made of a thin stainless steel plate. The length and width of the slits were 25.4 mm (1 in.) and 3.2 mm (1/8 in.), respectively. The thin plate was then rolled to form a cylindrical geometry. Also, two tubular electrodes with inside diameters of 24 mm and 26 mm were fabricated. The electrodes were made of stainless steel, and the gaps between the tube and the electrodes were 2.5 mm and 3.4 mm, respectively. The IWF electrode was made of nickel-chromium wire with a diameter of 0.24 mm and wrapped with a nylon strand with a diameter of 0.4 mm as an insulator to keep the electrode wire away from the tube surface.

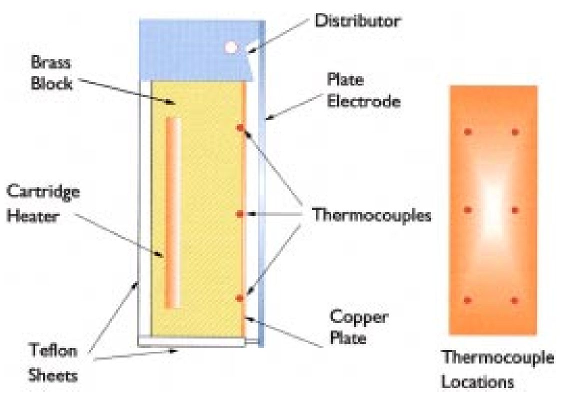

Fig. 4 Schematic of the vertical plate test section

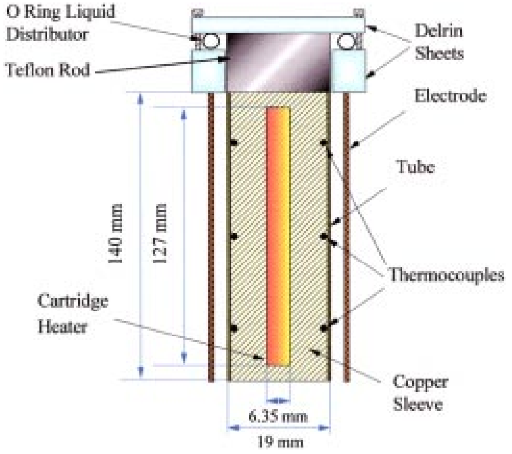

Fig. 5 Schematic of the vertical tube test section

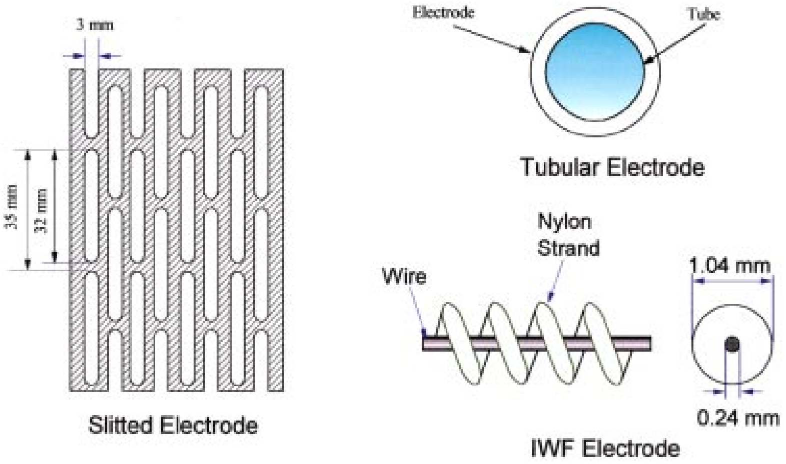

Fig. 6 Schematic of the electrodes tested

The pitch of the insulator was such that a significant portion of the electrode was exposed. The electrode was wound into the root region of the tube fins. This design required much lower applied voltage for a given electric field strength.

Experimental Procedure

A typical experimental run began by switching on the chiller pump. After several minutes the pressure of the test chamber was brought within a predetermined margin, and the feed refrigerant pump was switched on. Next, power to the cartridge heater was controlled with a variac and was fixed at a predetermined value. The DC high-voltage power supply was then turned on and adjusted to the predetermined voltage level. The pressure of the test chamber was controlled by adjusting the flow rate and temperature of the chilled water. Preliminary adjustments were done until the pressure of the chamber stabilized within one percent of the predetermined value. From then on, the computerized pressure control system took over control of the chamber pressure by adjusting the water flow rate and temperature. In general, it took approximately two to three hours for the system to reach steady-state condition, where the fluctuation of saturation pressure, temperature, and EHD current were less than one percent of the reading. Once steady-state conditions were achieved, the wall temperatures at 12 different locations, the saturation vapor and liquid temperatures at three different locations, and the EHD current were recorded. The applied EHD voltage was then set to the next level to be tested, and the above procedure was repeated. In general, eight to ten data points were taken in a given experimental run.

Data Reduction

The input power to the heater, $Q=VI$ was calculated from the measured voltage V and current I. The average heat flux, $q''=Q/A=Q/\pi D_o L$ was then calculated from the area of the heat transfer surface, A, and the input power, Q, to the cartridge heater. The average heat transfer coefficient h was found from

$$h=\frac{q''}{T_{\mathrm{wall}}-T_{\mathrm{sat}}} \tag{2}$$

where T_w and T_{sat} are the mean wall and saturation temperatures, respectively. The wall temperature was taken as the average of the 12 thermocouple readings on the wall. The outer wall surface temperatures were then obtained from the inner wall temperatures assuming one-dimensional conduction through the tube wall. Spatial variation in wall temperatures was less than 0.15°C. The saturation temperature was calculated as the mean of three thermocouple readings for saturation temperature. The average refrigerant flow rate per unit width was calculated as

$$\Gamma=\frac{\dot{m}}{L} \tag{3}$$

where Γ and $\dot{m}$ are refrigerant flow rate per unit length and refrigerant flow rate, respectively. L is the width for the plate test section and the tube perimeter for the tube test section.

A heat transfer enhancement factor η was defined to quantify the effectiveness of the EHD-assisted falling film evaporation process as compared to the conventional falling film evaporation:

$$\eta=\frac{h}{h_0} \tag{4}$$

where h is the average heat transfer coefficient for EHD-assisted falling film evaporation, and h_0 represents the average heat transfer coefficient in the absence of the EHD effect. The EHD power consumption for the heat transfer process was determined from the applied voltage ϕ and the associated electrical current I_{EHD}:

$$Q_{\mathrm{EHD}}=\phi I_{\mathrm{EHD}} \tag{5}$$

Finally, the EHD power consumption ratio α, was defined as

$$\alpha=\frac{Q_{\mathrm{EHD}}}{Q}\times 100\ \text{percent} \tag{6}$$

which quantifies the electrical power consumption of the electrodes relative to the total energy exchange rate in the test section.

Uncertainty Analysis

The directly measured quantities were temperature, voltage, and current. The heater voltmeter and ammeter had accuracies of 0.7 percent and 0.1 percent of the reading, respectively. All thermocouples were calibrated with an accuracy of ±0.1°C. The EHD voltage and current had an accuracy of ±0.1 percent of the reading. The uncertainties were calculated using the method of propagation of error suggested by Kline and McClintock [10] and Moffat [11]. The uncertainty in the heat transfer coefficient results from the uncertainties in total power to the heater, the surface area, and wall superheat. The uncertainty in the total power to the heater arises from the uncertainty in measured voltage and current across the heater, which was estimated to be 1.22 percent. The accuracy of the calipers used for measuring the dimensions of the test section was 0.01 mm, resulting in an uncertainty of 0.016 percent in the surface area. The uncertainty in temperature, however, was the main cause of the uncertainties in the heat transfer coefficient. For example, at low heat fluxes where the wall super-

Table 1 Results of the uncertainty analysis

Heat Transfer Surface	Uncertainty in q''	Uncertainty in h
Flat plate	1.27%	2.0% to 17.1%
Smooth tube	1.27%	4.7% to 7.2%
Turbo BIII	1.27%	11.9% to 26.9%
19 fpi tube	1.27%	6.1% to 8.9%

heat was as low as 0.5°C, the uncertainty in heat transfer coefficient due to temperature alone can be as high as 20 percent. The maximum uncertainty was at the lowest heat flux where the wall superheat was small, and the minimum uncertainty was at the highest heat flux. The heat flux was calculated based on the nominal outside diameter of the tubes. The uncertainties of heat flux and corresponding heat transfer coefficient are listed in Table 1.

Results and Discussion

For the flat-plate geometry, experiments were performed in both falling film and spraying modes. In falling film mode, the feed liquid was supplied to the heat transfer surface, whereas in the spraying mode the liquid was supplied to the plate electrode. These two cases are schematically shown in Fig. 7. For the spraying case, however, a minimum applied voltage is required to extract the liquid from the electrode to the heat transfer surface.

The effect of heat flux on the heat transfer coefficient with the plate geometry for the falling film case is demonstrated in Fig. 8. All of the data were taken at a refrigerant flow rate of 0.138 kg/m.s and an electrode spacing of 2.5 mm. The results indicate that the heat transfer coefficient initially increases with increasing applied voltage, reaches a peak, and then decreases with further increase in applied voltage. This can be explained by the fact that at low to moderate applied voltages, the electric field extracts the liquid from the heat transfer surface, forming a thin and well distributed liquid film on the surface. As a result, heat is removed more effectively by the evaporation process. At high applied voltages, however, visual inspection showed that the field was so strong that it prevented the liquid from falling down, causing the liquid to become trapped between the plate and electrode at the lower half of the test section. As a result, the lower half of the test section was partially filled with liquid. This is believed to be the main reason for the sharp drop in the heat transfer coefficient at high applied voltages. The maximum enhancement in the heat transfer coefficient was 390 percent, which took place at a refrigerant flow rate of 0.184 kg/m.s.

Another observation from Fig. 8 is that the heat transfer coefficient initially increases with heat flux up to a certain applied voltage and then the trend is reversed at moderate or high applied voltages. This trend is due to the fact that without the electric field, or with a weak field, the thickness of the film covering the surface decreases with an increase in heat flux, leading to a higher heat transfer coefficient at higher heat fluxes. However, for a given liquid mass flow rate, further increase in applied potential will extract too much liquid from the heat transfer surface, causing a dry out to occur on some parts of the surface at high heat fluxes. As a result, the formation of dry-out patches at high heat fluxes will lead to deterioration in heat transfer coefficient.

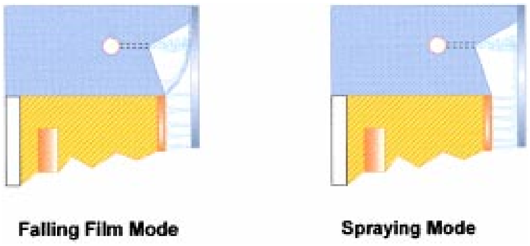

Fig. 7 Schematic illustration indicating the falling film and spraying modes

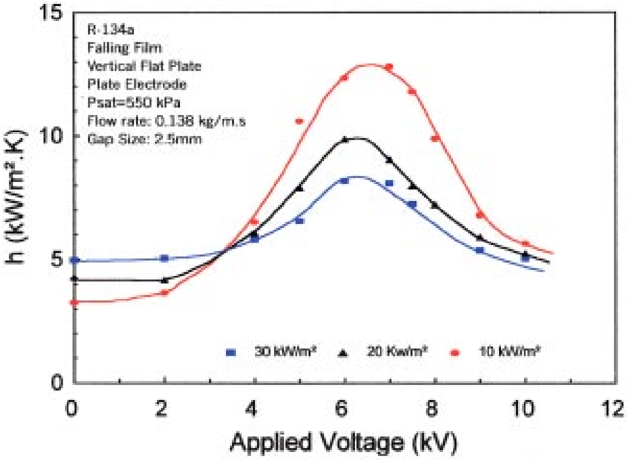

Fig. 8 Effect of heat flux on heat transfer coefficient for the falling film case

Figure 9 shows the effect of electrode spacing on the heat transfer coefficient. All of the data were obtained at a heat flux of 10 kW/m^2 and at a refrigerant flow rate of 0.138 kg/m.s. The results indicate that there is an optimum gap (here 2.5 mm) at which the EHD is most effective. Note that the optimum applied potential decreases from 10 kV to 6 kV as the electrode spacing decreases from 4 mm to 2 mm.

The effect of heat flux on the heat transfer for the spray evaporation case is shown in Fig. 10. For the range of heat fluxes tested, the results indicate that the heat transfer coefficient decreases with an increase in heat flux. This trend is consistent with the falling film case. This figure also reveals that the optimum applied voltage is more or less the same for the three heat fluxes tested. However, the optimum applied voltage tends to shift slightly to the left as the heat flux increases.

Figure 11 depicts the effect of flow rate for the spray evaporation case. The results indicate that the heat transfer coefficient increases with flow rate. This is believed to be due to the fact that when the liquid falls along the electrode, the interfacial instability increases with the flow rate, providing more potential for liquid jets to impinge on the heat transfer surface. As a result, the majority of the heat transfer surface is covered with a thin film of liquid, leading to an increased heat transfer coefficient. The power consumption in all cases was less than 0.12 percent of the total heat exchange in the test section.

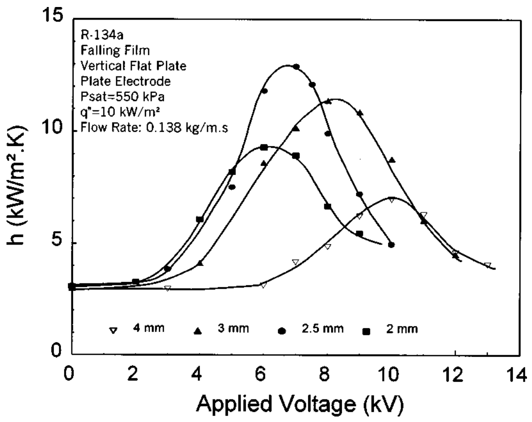

Fig. 9 Effect of electrode spacing on heat transfer coefficient for the falling film case

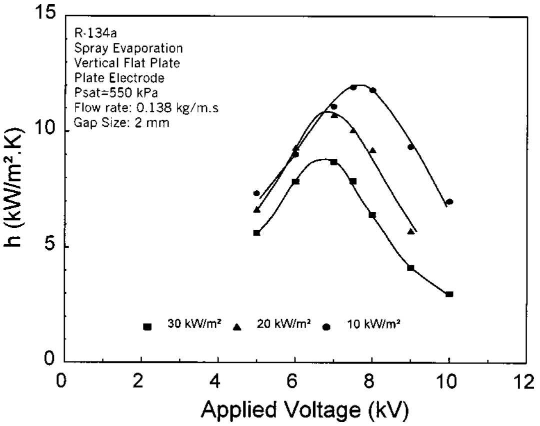

Fig. 10 Effect of heat flux on heat transfer coefficient for the spraying case

Experiments were also performed with falling film evaporation of R-134a on three commercially available tubes using R-134a as the working fluid. However, to compare our results with the previously published data, a few runs were also performed with R-123. The heat flux was calculated based on the nominal outside diameter of the tubes. Detailed specifications of the heat transfer surface/electrodes are listed in Table 2.

Figure 12 presents the results with R-123 on a smooth tube and a slitted electrode. Up to a sevenfold enhancement in heat transfer coefficient was obtained at an applied voltage of 14 kV. Results from Yamashita and Yabe [12] for similar conditions are shown for comparison. The comparison is satisfactory and deviations are within the experimental uncertainty.

Heat transfer enhancement results with R-134a on a smooth tube and a tubular electrode are shown in Fig. 13. A heat transfer enhancement factor is defined as the ratio of the average heat transfer coefficient for EHD-assisted falling film evaporation (h) over the average heat transfer coefficient in the absence of the EHD effect (h_0). Results indicate that the enhancement factor initially increases with applied voltage, reaches a maximum, and then decreases. At low or moderate applied voltages, the electric field tends to extract the liquid from the heat transfer surface, forming a thin and well-distributed liquid film on the surface. However, similar to the results obtained with the plate geometry, visual observation showed that further increase in applied potential caused the liquid to become trapped between the electrode and heat transfer surface, resulting in a reduction in heat transfer coefficient. This suggests that for a given set of operating conditions, there is an optimum applied voltage at which the EHD is most effective. The results also indicate that for a given applied potential the enhancement factor decreases as the heat flux increases due to the formation of dry-out spots at high heat fluxes. A higher potential allows a higher degree of liquid extraction, leading to a

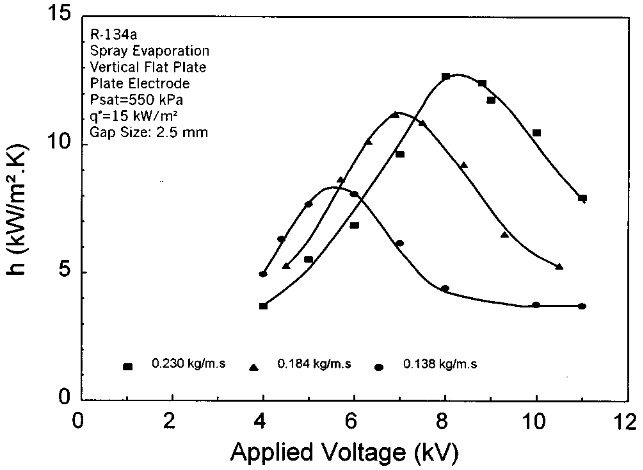

Fig. 11 Effect of flow rate on heat transfer coefficient for the spraying case

Table 2 Heat transfer surface/electrode configurations tested

Heat Transfer Surface	Electrode
Smooth tube Diameter=19 mm Length=140 mm	Tubular electrode Electrode gap=2.5 mm and 3.5 mm
Turbo BIII tube Diameter=19 mm Length=140 mm	Slitted electrode Slit length=25.4 mm Slit width=3.2 mm Electrode gap=3.4 mm
19 fpi tube Diameter=19 mm Length=140 mm	IWF electrode Wire diameter=0.24 mm Nylon strand diameter=0.4 mm

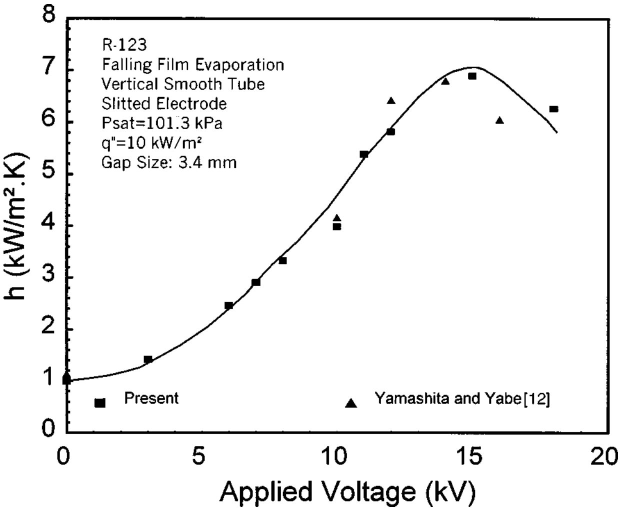

Fig. 12 Heat transfer coefficient versus applied voltage on a smooth tube and a slitted electrode

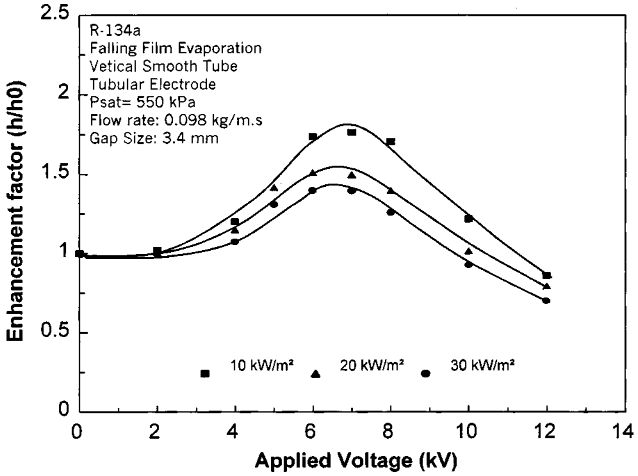

Fig. 13 Enhancement factor versus applied voltage on a smooth tube and a tubular electrode

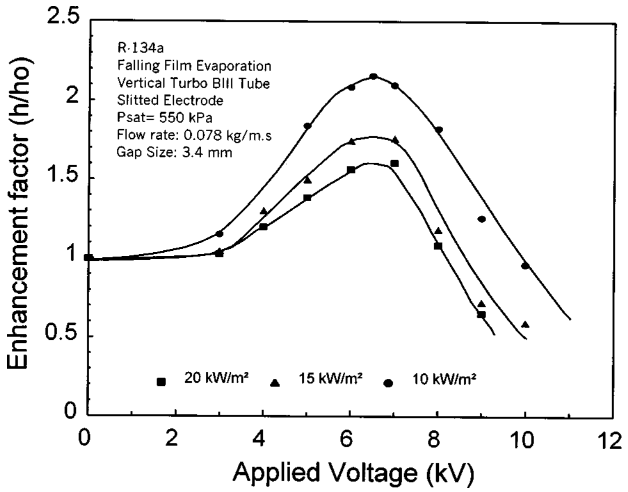

Fig. 14 Enhancement factor versus applied voltage on a Turbo Bill tube and a slitted electrode

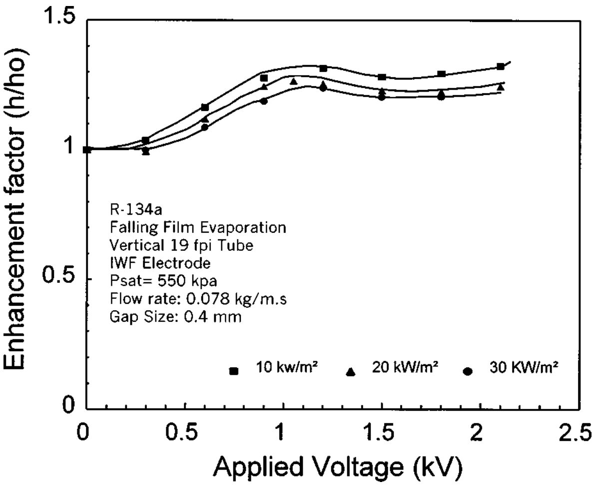

Fig. 15 Enhancement factor versus applied voltage on a 19 fpi tube and an IWF electrode

thinner liquid film on the heat transfer surface and higher heat transfer coefficients. On the other hand, when the film is too thin, dry out occurs more easily at the surface, leading to lower heat transfer coefficients. The results demonstrate 90 percent enhancement in the heat transfer coefficient at a heat flux of 10 kW/m^2 and a refrigerant flow rate of 0.098 kg/m.s. The absolute values of the non-EHD (base case) heat transfer coefficient for smooth, Turbo BIII, and 19 fpi tubes were 3103 W/m^2.K, 10157 W/m^2.K, and 4687 W/m^2.K, respectively. The data are for R-134a at a heat flux of 10 kW/m^2 and a flow rate of 0.078 kg/m.s.

Figure 14 shows the enhancement factor results as a function of applied voltage with the Turbo BIII tube and a slitted electrode. The trend is consistent with the results obtained with the smooth tube. The results also indicate that the higher value of enhancement ratios corresponds to the smaller value of heat fluxes. This is due to dry patch zones formed on the tube surface facing the slots at high heat fluxes. Maximum enhancement in the heat transfer coefficient was 110 percent at a heat flux of 10 kW/m^2 and a refrigerant flow rate of 0.078 kg/m.s.

In the EHD-enhanced falling film evaporation, the objective is to keep a very thin film of liquid close to the heat transfer surface. The enhancement mechanism is mainly governed by the Maxwell instability at the liquid-vapor interface and the electro-convection in the liquid ([13]). The Maxwell stress has a tangential component of nearly zero and a normal component that is proportional to the square of the electric field. As a result, the normal component of the Maxwell stress at the liquid-vapor interface extracts the thin-film from the heat transfer surface towards the electrodes, leading to locally concentrated films over a small region of the heat transfer surface, and thinner films over the remaining surface (see Fig. 1). This phenomenon is referred to as the liquid extraction phenomenon. Other effects of electric fields on enhancement of falling film evaporation include spraying of small liquid droplets by electrostatic atomization and surface perturbation and waviness.

Experiments were also conducted on a 19 fpi tube and IWF electrode. Figure 15 demonstrates the heat transfer enhancement factor at various heat flux levels. The magnitude of enhancement (20–30 percent) is about the same for all three heat fluxes. The low enhancement can be attributed to the lack of harmony between the gravity and buoyancy forces for the present case. It is possible that trapped bubbles beneath the electrode block the flow of fresh liquid to the heat transfer surface. However, this drawback may be reduced by certain modifications in the fin geometry of the 19 fpi tube. Due to the lack of optimum balance between gravity and buoyancy forces, vertical orientation does not appear to be a proper configuration for falling film evaporation on a 19 fpi tube and IWF electrode. For the range of parameters tested, the EHD power consumption ratio in all cases was less than 0.15 percent of the total heat transfer rate in the test section.

Conclusions

An experimental investigation was undertaken to study the effect of an applied electric field on heat transfer enhancement of falling film evaporation. A vertical flat plate and three commercially available tubes were tested. The effects of heat flux, refrigerant flow rate, electrode gap, and applied voltage were investigated. It was found that for the plate geometry, supplying liquid either to the heat transfer surface or the electrode resulted in more or less the same magnitude of the enhancement. Up to a fourfold enhancement in the heat transfer coefficient was obtained with the plate configuration, and it took place at a heat flux 10 kW/m^2 and a refrigerant flow rate of 0.138 kg/m.s.

For the representative tube geometries, the following results were documented: up to a sevenfold enhancement with R-123 on a smooth tube, 80 percent with R-134a on a smooth tube, 110 percent on a Turbo BIII tube, and 30 percent on 19 fpi tube. For a given flow rate, the enhancement factor decreased with increasing heat flux due to dryout spots at the heat transfer surface at high heat fluxes. It was found that for a given set of operating conditions, there was an optimum flow rate at which the EHD was most effective. A strong dependence of the heat transfer coefficient on the applied voltage was observed in all experiments. It was found that in EHD-enhanced falling film evaporation, the heat transfer coefficient is improved by forming a thin well-distributed layer of liquid on the heat transfer surface, increasing evaporation surface area, electro-convection in the liquid, and atomization of the falling liquid into small droplets. Despite the notable improvement in heat transfer coefficient, the maximum power consumption did not exceed 0.15 percent of the total heat transfer rate.

Nomenclature

A = heat transfer surface area (m^2)
E = electric field (V/m)
f_e = electric body force (N/m^3)
h = average heat transfer coefficient (W/m^2.K)
h_o = base case heat transfer coefficient, no EHD (W/m^2.K)
I = current (A)
k = thermal conductivity (W/m.K)
L = test section length (m)
q'' = heat flux (W/m^2)
Q = test section heat transfer rate (W)

T_w = average wall temperature (°C)
T_{sat} = average saturation temperature (°C)
V = voltage (V)
W = test section width (m)

Greek Symbols

α = EHD power consumption ratio (percent)
Γ = refrigerant flow rate per unit width (kg/m.s)
ε = dielectric permittivity (F/m)
η = enhancement ratio (h/h_o)
ρ = mass density (kg/m^3)
ρ_c = electric charge density (C/m^3)
Φ = electric field potential (V)

References

[1] Minton, P. E., 1986, *Handbook of Evaporation Technology*, Noyes Publications, Park Ridge, NJ.
[2] Bochirol, L., Bonjour, E., and Weil, L., 1960, A Echanges thermiques ''Etude de l'Action de Champs Electriques sur les Transferts de Chaleur dans les Liquides Bouillants,'' C. R. Hebd. Seances Acad. Sci., Paris **250**, pp. 76–78.
[3] Choi, H. Y., 1962, ''Electrohydrodynamic Boiling Heat Transfer,'' Ph.D. thesis, Massachusetts Institute of Technology, Cambridge, MA.
[4] Winer, M., 1967, ''An Experimental Study of the Influence of Nonuniform Electric Field on Heat Transfer in a Dielectric Fluid,'' TRW Systems Report, Report No. EM17-14.
[5] Zhorzholiani, A. G., and Shekriladze, I. G., 1972, ''Study of the Effect of an Electrostatic Field on Heat Transfer With Boiling Dielectric Fluids,'' Heat Transfer-Sov. Res., **4**, No. 4, pp. 81–98.
[6] Jones, T. B., 1978, ''Electrohydrodynamically Enhanced Heat Transfer in Liquids—A Review,'' Adv. Heat Transfer, **14**, pp. 107–148.
[7] Ohadi, M. M., 1991, ''Heat Transfer Enhancement in Heat Exchangers,'' ASHRAE J., **3**, No. 12, pp. 42–50.
[8] Yabe, A., 1991, ''Active Heat Transfer Enhancement by Applying Electric Fields,'' *Proceedings of the Third ASME/JSME Thermal Engineering Conference*, Vol. 3, ASME, New York, pp. xv–xxiii.
[9] Panofsky, W. K. H., and Phillips, M., 1962. *Classical Electricity and Magnetism*, Addison-Wesley, Reading, MA, p. 110.
[10] Kline, S. J., and McClinock, F. A., 1953, ''Describing Uncertainties in Single Sample Experiments,'' Mech. Eng. (Am. Soc. Mech. Eng.), **75**, No. 1, pp. 3–8.
[11] Moffat, R. J., 1988, ''Describing the Uncertainties in Experimental Results,'' ASME J. Fluids Eng., **107**, pp. 250–260.
[12] Yamashita, K., and Yabe, A., 1997, ''Electrohydrodynamic Enhancement of Falling Film Evaporation Heat Transfer and its Long Term Effect on Heat Exchanger,'' ASME J. Heat Transfer, **119**, pp. 339–347.
[13] Darabi J., Ohadi, M. M., and Dessiatoun, S. V., 1998, ''Heat Transfer Enhancement With Falling Film Evaporation on Vertical Tubes Using Electric Fields,'' *Proceedings of the ASME Heat Transfer Division*, Vol. 1, ASME, New York, pp. 331–38.

Mist/Steam Cooling in a 180-Degree Tube Bend

Tao Guo[1]

Ting Wang[2]

J. Leo Gaddis

Department of Mechanical Engineering,
Clemson University,
Clemson, SC 29634-0921

An experimental study on mist/steam cooling in a highly heated, horizontal 180-deg tube bend has been performed. The mist/steam mixture is obtained by blending fine water droplets (3~15 microns) with the saturated steam at 1.5 bar. The test section consists of a thin wall (~0.9 mm), welded, circular, stainless steel 180-deg tube (20-mm inside diameter) with a straight section downstream of the curved section, and is heated directly by a DC power supply. The experiment was conducted with steam Reynolds numbers ranging from 10,000 to 35,000, wall superheat up to 300°C, and droplet to steam mass ratio at about 1~2 percent. The results show that the heat transfer performance of steam can be significantly improved by adding mist into the main flow. The highest enhancement occurs at a location about 45-deg downstream of the inlet of the test section. Generally, only a small number of droplets can survive the 180-deg turn and be present in the downstream straight section, as observed by a phase Doppler particle analyzer (PDPA) system. The overall cooling enhancement of the mist/steam flow ranges from 40 percent to 300 percent. It increases as the main steam flow increases, but decreases as the wall heat flux increases. [S0022-1481(00)02003-X]

Keywords: Augmentation, Cooling, Droplet, Heat Transfer, Two-Phase

Introduction

Closed-loop steam cooling has been adopted by two major gas turbine manufacturers for their heavy-frame advanced turbine system (ATS) engines ([1–3]). The major advantage of closed-loop steam cooling is that it can eliminate the need for film cooling. According to Bannister [4], as the turbine inlet temperature is raised to 1400°C (~2600°F), excessive film cooling is the major obstacle to a further increase in gas turbine thermal efficiency. This is because as the cooling air is injected from the airfoil into the main hot gas flow, it interferes with the main flow field and subsequently causes aerodynamic and thermal losses. In the meantime, less air is available for combustion and therefore the work output will be reduced. Furthermore, excessive film cooling will force the combustion temperature to be raised in order to achieve higher turbine inlet temperature and further compound the issue of reducing NOx and controlling emissions.

As a result, for the heavy frame ATS, using the closed-loop steam cooling scheme allows achievement of a higher thermal efficiency than those using air film cooling ([5]). One of the most challenging problems of closed-loop steam cooling is that a very large amount of steam will be needed ([6,3,7]). The reason is that in order to eliminate film cooling, the coolant side heat transfer coefficient must be greatly increased (to about 8000–10,000 W/m^2K). To reach such high heat transfer coefficients, a very high steam Reynolds number (thus a very high steam flow rate) must be maintained. Drawing this large amount of steam out from the bottom steam cycle would decrease the thermal efficiency of the bottom steam turbines since the normal steam expansion process would be interrupted ([8]). Furthermore, high steam flow rate will significantly increase the pressure losses.

To deal with these problems, the concept of controlled closed-loop mist/steam cooling is explored in this study. As a first step toward verifying the validity of using mist/steam cooling, an experimental system under low pressure (1.5 bar) and low heat flux conditions, instead of high pressure and high heat flux conditions as in a real gas turbine environment, has been set up in the laboratory. Four test conditions have been performed: a horizontal tube, a 180-deg curved tube, impingement jets on a flat surface, and impingement jets on a curved surface. In this paper, the results for the 180-deg tube bend are reported. The results for the straight tube have been reported in separate papers ([9,10]).

Previous Work

Fluid flows and heat transfer in curved ducts are of importance in many engineering applications such as pipe bends, cooling and heating coils, blade passages of turbomachinery, and aircraft intakes. Under the effect of centrifugal force, the flow in curved ducts differs from that in a straight pipe by exhibiting a secondary flow in planes normal to the main flow. Descriptions of the flow and heat transfer behaviors in a curved duct have been shown by Mori and Nakayama [11] and Patankar et al. [12].

As indicated in Guo et al. [9], no experimental studies can be found in the open literature of internal mist/steam flow where the mist is generated by atomizing water and then injected into the *steam* under *controlled* conditions. Previous studies in two related areas, namely, the post-dryout dispersed flow and the two-component two-phase mist/air internal flow, have been reviewed by Guo et al. [9] and provide guidance to the current study. Both of them have the characteristic of a dispersed liquid phase flowing within a gas phase, as in the case of the mist/steam flow. The main difference between the post-dryout dispersed flow and the present mist/steam flow is that they have different inlet conditions. The droplet size and distribution as well as the liquid mass fraction at the critical heat flux point for post-dryout flow depend on the flow conditions prior to the critical heat flux point and are usually difficult to control. The inlet conditions for the mist/steam internal flow in the present study are controlled mainly by the atomizing system, the droplet size and distribution as well as the liquid mass fraction and liquid temperature can be systematically controlled. The droplets in the post-dryout flow are usually generated from the breakup and entrainment of liquid layers and the droplet sizes are quite large. The radial temperature profile is more developed in the post-dryout flow than in the current flow in which the mist/steam mixture is introduced homogeneously into a highly heated test section.

---

[1] Currently with General Electric Power Generating, Schenectady, NY.

[2] To whom correspondence should be addressed. Currently at Energy Conversion and Conservation Center, University of New Orleans, New Orleans, LA 70148-2000. e-mail: twang@uno.edu

Contributed by the Heat Transfer Division for publication in the JOURNAL OF HEAT TRANSFER. Manuscript received by the Heat Transfer Division, Aug. 4, 1999; revision received, Jan. 28, 2000. Associate Technical Editor: T. Avedisian.

The difference between the mist/air flow and the mist/steam flow is that they are thermodynamically different. Mist/air is a two-component two-phase flow where the evaporation process of the water droplets is controlled by the partial pressure of the water vapor in the air, not by the total pressure of the mixture. Mist/steam is a one-component two-phase flow in which the evaporation process of the water droplets is controlled by the steam pressure. Generally, under the same pressure and the same temperature, the droplets within mist/air flow are more likely to evaporate than those within mist/steam flow. For example, for mist/steam flow under saturated pressure and temperature, no evaporation would occur. However, for mist/air flow under the same pressure and temperature, if the air is dry, the water droplets would be in a superheated state and evaporate immediately because the partial pressure of the vapor is lower than the saturated pressure. Review of related mist/air and post-dryout studies in straight pipes was conducted by Guo et al. [9]. In this paper only the related work in a curved tube is selectively reviewed.

Post-Dryout Dispersed Flow in Curved Pipes. Although a considerable number of papers have been published on two-phase flow in curved pipes, there have been relatively few detailed studies of heat transfer, especially in dispersed flow. One of the earlier studies was due to Cumo et al. [13] who studied the effect of curvature on the onset of the critical heat flux in post-dryout flow. Another study was conducted by Lautenschlager and Mayinger [14]. They studied the post-dryout dispersed flow heat transfer of F-12 in an electrically heated circular 90-deg tube bend. It has been observed that when dispersed flow enters a bend, separation of liquid from vapor phase occurs due to the effect of centrifugal force. This leads to an increase in heat transfer at the outer wall and a decrease at the inner wall. Rewetting of the outer wall is possible. Due to the circumferential secondary flow induced by the centrifugal force, heat transfer at the inner wall strongly depends on the conditions at the outer wall. Therefore, after an axial distance heat transfer at the inner wall is improved and, in some cases, even rewetting can be observed.

A recent study of post-dryout dispersed flow in circular bends was performed by Wang and Mayinger [15]. They observed that the curvature induced centrifugal force and secondary flow can significantly change the behavior of droplet dynamics and phase distribution of the dispersed flow. Droplets in the vapor stream reveal a general trend of centrifugal migration towards the outer wall and may even impinge directly on the wall. The effects of the secondary flow and turbulent dispersion are found to bring about a better circumferential transportation of liquid.

Mist/Air Cooling in Curved Pipes. Very few studies can be found in the open literature regarding the flow and heat transfer of mist/air mixtures in curved pipes. Mori et al. [16] performed the experimental study of the mist/air cooling of a highly heated coil-tube. The experiment was conducted in a highly heated stainless steel coil-tube of 1.8-mm inside diameter with a bending radius of 27 mm. The air/water droplets was obtained by blending the compressed air and the water droplets within a mixer. The water droplets were generated by forcing the pressurized water through a very small tube of 0.4-mm inside diameter. Local wall temperatures were measured by thermocouples directly welded to the tube. It was found that due to the effect of centrifugal force, the heat transfer performance on the outer wall of the coil-tube is different from that on the inner wall. The heat transfer along the tube axis could be divided into four typical regions. The first region is the liquid film region where an annular liquid film (diminishing thickness along the tube axis) flows on the wall surface and the wall temperatures (being essentially quenched to the liquid temperature) are the same on both the inner and outer walls of the tube. Further downstream in the second region, the liquid film becomes thinner and thinner and the dryout is considered to occur at the outer wall first. Consequently, in the second region, the outer wall temperature increases more rapidly than that at the inner wall. In the third region, the dryout occurs even at the inner wall of the coil-tube. At this region, the whole tube is dry but droplets exist in the main stream. The centrifugal force will throw the existing droplets towards the outer wall. So the inner wall temperature in this region (as well as in the next region) rises more rapidly than that of the outer wall. It is usually in this region that the inner wall temperature becomes higher than the outer wall temperature. In the fourth region, the water droplets have completely evaporated and the heat transfer is essentially the single-phase heat transfer.

It must be noted that due to the very small tube used by Mori et al., the liquid film region in the above experiment is unavoidable because many water droplets' sizes are in the same order of magnitude as the tube diameter and tend to block the flow path. The flow in the liquid film region is suspected to be an annular two-phase flow, and the flow in the dryout region is therefore independent of the atomizing system, as in the case of post-dryout flow.

Experimental Facility

The current experiment is conducted on the same experimental facility as the previous study on a heated straight tube ([9]). A schematic of the overall experimental facility is shown in Fig. 1. Basically, the experimental setup consists of four systems: the steam system, the water system, the atomizing system, and the test section. The steam system consists of two subsystems: a low-pressure steam system (~1.5 bar) which provides the main steam flow for the experiment, and a high-pressure steam system (~8.5 bar) which furnishes the energy source for the ''steam-assist'' pneumatic atomizer to generate mist from water. The water sys-

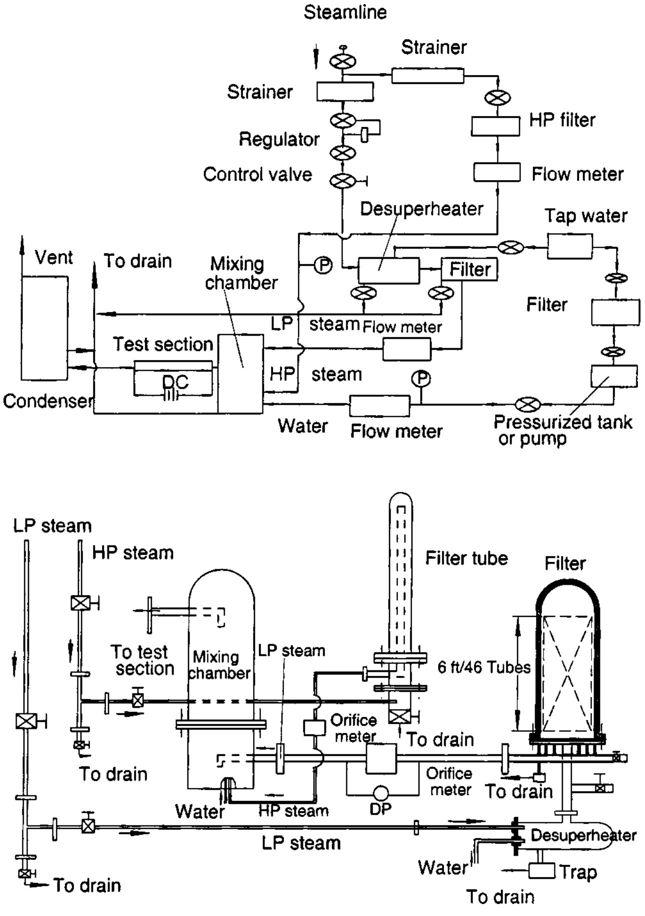

Fig. 1 Diagrams of the experimental facility; (*a*) flow diagram, (*b*) layout of the experimental facility

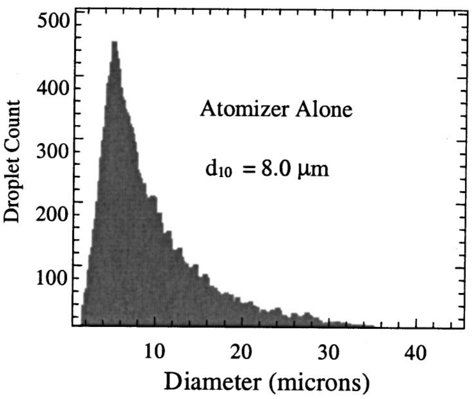

Fig. 2 PDPA result of a typical particle size distribution at the exit of the mixing chamber

tem also consists of two subsystems: a low-pressure water system (~5 bar) which is used by the ''steam-assist'' pneumatic atomizer, and a high-pressure water system (~70 bar) which is used by the pressure atomizer. The atomizing system, combined with the mixing chamber, is designed to generate the needed steam/fine water-droplet flow for the test section. Two mist generation systems have been designed and tested. It has been found that for the pneumatic atomizer, only very small droplets (0~10 μm in diameter) exist at the exit of the mixing chamber. For the pressure atomizer, relatively larger droplets (5~30 μm in diameter) can follow the main steam flow and come out of the mixing chamber. As a result, the pressure atomizer system is finally adopted in this study because the mean droplet diameter (3~4 μm) and the droplet mass ratio (less than one percent of the main steam flow) from the pneumatic atomizer are less ideal for heat transfer enhancement. A typical particle size distribution at the exit of the mixing chamber is shown in Fig. 2.

Test Section. A plan view of the test section design is shown in Fig. 3. The main part of the test section consists of a thin wall, welded, circular stainless steel tubing. The outside diameter of the tubing is 22.2 mm (7/8 in.), the wall thickness is 0.889 mm (0.035 in.), and the length is about 177.8 mm (8 in.). The bending radius of the tube is 57 mm (2.25 in.). The tube with an outer diameter of 22.2 mm was selected for three reasons: (1) this is a typical air cooling hole size in some of the current industrial gas turbines; (2) the tubes used in many previous experiments (for example, ~1 mm in Mori et al. [16]) were too small to remove the liquid film formed near the entrance region of the test sections; and (3) it is easier to measure the particle sizes and velocity distribution.

The test section is placed horizontally and is directly heated by a high-current power supply system. Copper wires with electrodes on the ends are used to connect the power supply and the test section. To isolate the test section from the possible power short-cuts, the test section is mounted on a wooden table. Besides, at both ends of the test section, reinforced dielectric silicone tubes are used to connect to the other parts of the experimental system.

Instrumentation

Temperature Measurement. All of the temperatures are measured by using Omega gage 30 (0.2546 mm in diameter) Iron/Constantan thermocouples with braided fiberglass insulation. The measured temperatures are monitored by a FLUKE data logger. The thermocouples, along with the data logger, were calibrated against a standard resistance temperature device (RTD) system by attaching the thermocouple junctions to a copper block and placing them in a furnace.

Wall Temperature of the Test Section. Since a high-current DC power supply is used to heat the test section, direct contact between the thermocouple junction and the test section wall surface should be avoided to eliminate the possible electrical voltage drop across the thermocouple junctions. To ensure there is no direct contact between the thermocouple junction and the wall, the test section is first wrapped with a thin layer (<0.1 mm) of mica tape, which is a dielectric tape with insignificant temperature drop across the tape thickness, manufactured by Cogebi, Inc. Then, the thermocouples are mounted onto the external surface of the test section using Omega high temperature cement, which has a thermal conductivity of 0.5 W/m°K and a dielectric constant of 6.

The detailed thermocouple arrangement for the test section is shown in Fig. 3. At each cross section along the curved section, four thermocouples, 90 deg apart are mounted on the outside wall surface. Other thermocouples are strategically deployed to measure the average room temperature and the insulator surface temperatures for calculating radiation and external convection losses.

Pressure Measurement. Steam pressure is measured by using Bourdon tube pressure gage in the inlets and outlets of the low-pressure filter and the high-pressure filter, respectively.

Heating Power. The heating power for the test section is calculated by obtaining the electrical current and voltage across the test section. The current is obtained by measuring the voltage across the shunt (with a pure resistance of $1.3333\times10^{-4}\ \Omega$) of the power supply. The voltage across the test section is measured directly by a voltmeter. The uncertainty for the heating power

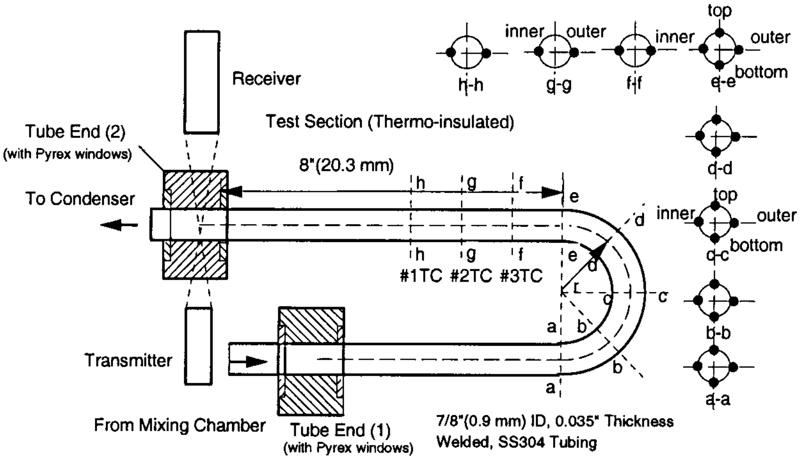

Fig. 3 A plan view of the 180-deg tube bend test section design

measurement is estimated to be less than three percent of a typical heat flux of 10,000 W/m^2.

Droplet Size Measurement. Droplet size and distributions are monitored by a phase Doppler particle analyzer (PDPA) system at the centerline of the test section outlet. The theory and technique of PDPA were well documented by Bachalo et al. [17,18]. The detail of the system setup was provided by Guo [7]. Due to the difficulty in moving the present PDPA system along the full length of the 180-deg tube bend, the measurements of particle size distribution were made only at the inlet and exit of the tube. The information of PDPA measurements is very helpful for modeling droplet dynamics and for interpreting the data.

Flow Measurement. Two orifice flow meters are used for the measurements of the flow rates of both the high-pressure and the low-pressure steam systems. The uncertainties of using the orifice meters for the flow measurement are estimated to be less than 0.4 percent. The water flow coming into the atomizer is measured by an Omega rotameter FL-112, which is calibrated by using the catch-and-weigh method. The uncertainty of the rotameter is estimated to be less than five percent for a typical flow of 15 kg/hr.

Since not all the mist generated by the atomizers enters the test section, the mass flow rate of the mist entering the test section is calculated using mass balance by measuring the mass flow rates of steams, mist and liquid at the mixer inlet, mixer drain, test section outlet, and condenser outlet. Since the steam continues to condense and mixes with the precipitated mist, the method to calculate the mist mass flow is not straightforward. A detailed description of the mass flow balance calculation was documented by Guo [7]. Besides, the PDPA measured droplet size distribution at the test section inlet is integrated across the test section to cross check the liquid mass flow rate. Generally, these two methods agree within five percent of each other.

Experimental Procedure

The experimental runs for two-phase mist/steam flow heat transfer were conducted in the following sequence. For each experimental run, the main steam flow rate was fixed. Under this fixed main steam flow rate, the test section was first heated with a certain heat flux and the wall temperature distribution of the test section for steam only was measured. After this, a certain amount of water was added into the main steam flow through the atomizing system, and the wall temperatures for the two-phase mist/steam flow were measured. This concluded one case for this specific experimental run. Then for a different case, a different heat flux value was applied to the test section and the above procedure was repeated. By doing so, the wall temperature for mist/steam flow under the same main steam flow (Re number) and same droplet mass ratio were obtained for this experimental run, but heat fluxes were different. For another experimental run, the main steam flow rate was changed, and the aforementioned process was repeated.

Experimental Conditions. The experiment was performed under the following conditions: The Reynolds numbers for the main steam flow range from 10,000 to 35,000. The liquid droplet mass ratio is at about two percent. The wall heat fluxes range from 3,000~25,000 W/m^2 (with the highest wall superheat up to 300°C). The average droplet diameter (d_{10}) at the inlet of the test section is around 6~8 μm. Totally, three experimental runs have been conducted. Generally, the increase of the main steam Reynolds number downstream due to continuous droplet evaporation in each run is small (less than two percent) because of the relatively low droplet mass ratios in all the cases.

Data Reduction

To evaluate the heat transfer enhancement of mist/steam flow over the single-phase steam-only flow, the following definition is used to calculate the heat transfer coefficient of the mist flow:

$$h_{\text{mist}}(x)=\frac{q''(x)}{T_w(x)-T_{\text{sat},in}} \tag{1}$$

where q'' is the local wall heat flux after various corrections are made as described below, T_w is the local wall temperature, and $T_{\text{sat},in}$ is the saturation temperature of steam at the inlet of the test section. For the sake of comparison, the heat transfer coefficient of the single-phase flow is also evaluated under the reference temperature of $T_{\text{sat},in}$, i.e.,

$$h_o(x)=\frac{q''(x)}{T_w(x)-T_{\text{sat},in}} \tag{2}$$

where T_w is the local wall temperature for the corresponding single-phase steam flow. The cooling enhancement is thus evaluated as h_{mist}/h_o.

Wall Temperature. The temperatures measured by the thermocouples are the tube outside surface temperatures of the test section (not outside of the insulator). The temperature drop across the tube wall, approximately 0.5°K, is included in the data reduction process.

Heat Flux. There are several factors that affect the local wall heat flux in a curved test section. One factor arises from the fact that due to the bending process, the outer wall of the tube is lengthened and becomes thinner, while the inner wall is shortened and becomes thicker. This results in an increase of electrical resistance and the surface area at the outer wall and a decrease of the electrical resistance and the surface area at the inner wall. With a constant voltage imposed on the two ends of the tube, the electrical current does not uniformly distribute in the circumferential direction of the tube. In the current study, a maximum deviation of two percent in wall thickness due to the tube-bending process has been measured over a cutaway cross section of a similarly bent tube. It has been estimated that the variations of the wall thickness, combined with the corresponding surface area change, result in an increase in the local wall heat flux of about 20 percent at the inner wall, and a decrease of about 20 percent at the outer wall.

Another factor which causes the change of local wall heat flux is the variation of the electric resistance of the wall due to the nonuniformity of the wall temperature. The resistance changes of SS 304 tube under different temperatures have been measured and documented by Guo [7]. It has been estimated that the maximum variation of the local heat flux in the circumferential direction caused by the temperature variation in the current study is about five percent, with the outer wall being lower than the inner wall.

The local wall heat flux can also be affected by thermal conductions in the axial and circumferential directions. Since the outer wall generally has lower temperatures than the inner wall, thermal conduction in the circumferential direction produces an opposite effect to those caused by electric resistance variations. By using a simple one-dimensional heat conduction analysis, it has been estimated that the circumferential thermal conduction significantly causes the local heat flux at the outer wall to be 10~15 percent higher than the average heat flux, while the inner wall to be 10~15 percent lower.

It is interesting to see that the corrections of local heat flux for the effects of bending, resistance changing with temperature, and the circumferential heat conduction have shown that the corrected heat flux is closed to the uncorrected heat flux within five percent. Radiation and external convection heat transfer losses, about two percent, are also included in the correction formula.

Uncertainty Analysis

The uncertainty analysis is conducted based on the theory of the Moffat [19] and closely follows the method used by Wang and

Table 1 Results of *N*th-order uncertainty analysis

Variables	*N*th-order Uncertainty (Percent)
$T_w/(T_w - T_{\mathrm{sat},in})$	1.2
Orifice flow meter (LP), kg/s	5.5
Pressure transducer (LP), mA	2.6
Orifice flow meter (HP), kg/s	0.4
Pressure transducer (HP), mA	0.4
Rotameter, kg/s	4.7
Steam flow, kg/s	6.1
Water flow, kg/s	4.7
Total heating power, W	2.8
Heat transfer coefficient, W/m^{2}K	6.7

Simon [20]. The results of the uncertainty analysis are summarized below in Table 1. The detailed analysis was documented by Guo [7].

Results and Discussions

Wall Temperature Distribution. Figures 4, 5 and 6 show the measured wall temperature distributions of the test section for two-phase mist/steam flow under various steam Reynolds numbers and wall heat fluxes. In particular, each figure gives the temperature distributions for various heat fluxes under a fixed Reynolds number and a fixed mist/steam mass ratio, along with the corresponding temperature distributions for steam-only flow for comparison.

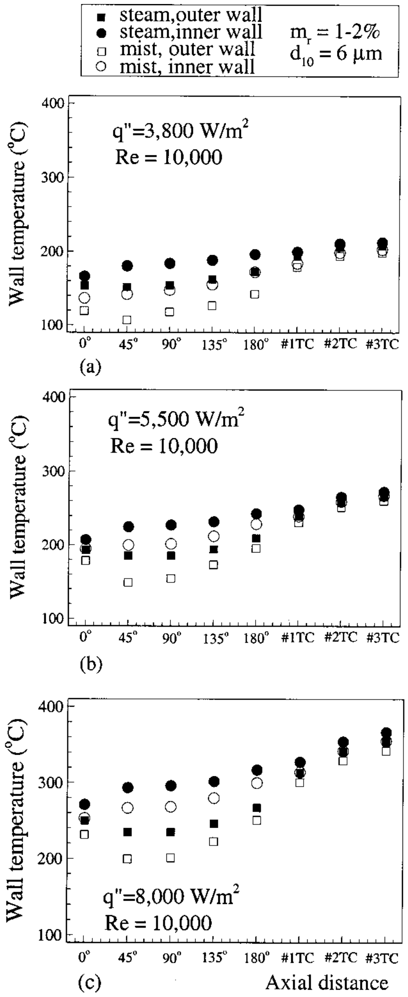

Fig. 4 Comparison of wall temperature variations between steam-only and mist/steam at Re=10,000 with various heat fluxes

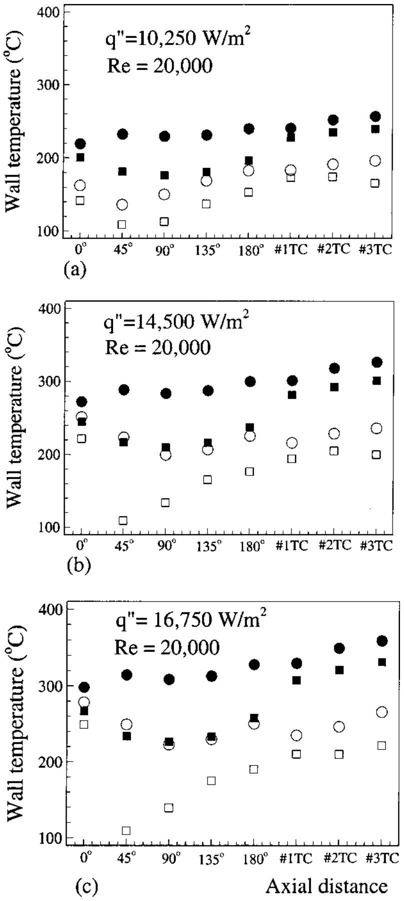

Fig. 5 Comparison of wall temperature variations between steam-only and mist/steam at Re=20,000 with various heat fluxes (same legend as Fig. 4)

In the steam-only flow condition, it can be seen that within the curved section, the outer wall always exhibits a better heat transfer (i.e., lower wall temperature) than the inner wall due to the centrifugal force effect. Generally, the outer wall always has a maximum cooling effectiveness (i.e., lowest wall temperature) at a location near 90 deg from the inlet. This is believed to be caused by the centrifugal force induced ''impingement'' effect. Another observation is that under the effect of secondary flow, the inner wall temperature increases rather mildly after a distinct increase at the beginning. Also it can be seen that at the inlet of the curved section, the outer wall temperature is different from that of the inner wall, indicating that the curved section has obviously affected the upstream flow condition. Since the inner wall temperature is higher than at the outer wall, the nonsymmetric temperature distribution persists in the downstream straight wall section.

For mist/steam flow, Fig. 4 shows an obvious decrease of local wall temperature of 20~30°C (40~60°F) at Re=10,000 with mist/steam mass ratios of two percent. Similar results are observed for the cases of higher main steam flows at Re=20,000 and Re=35,000 in Figs. 5 and 6, respectively. In both cases, a significant decrease in wall temperature (80~100°C) is detected after mist is added. These figures also show that the wall temperature difference between mist and steam-only cases increases as the Reynolds number increases.

Based on the wall temperature measurements, it can be seen that under low main steam flow (Fig. 4, Re=10,000) the extra cooling due to the mist decreases significantly as the heat flux

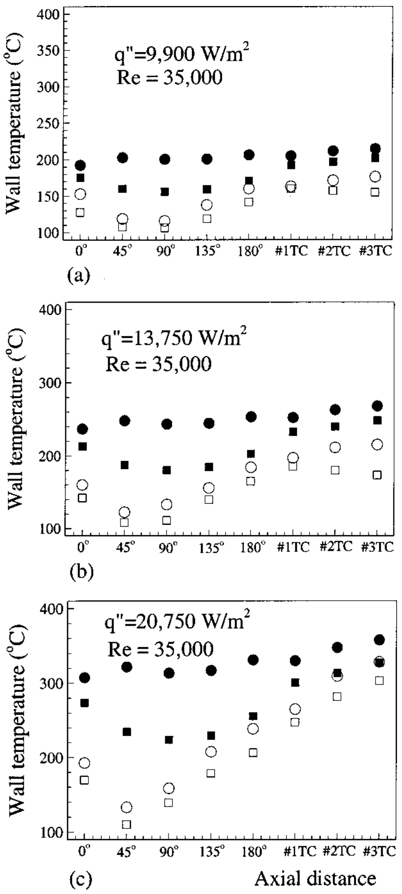

Fig. 6 Comparison of wall temperature variations between steam-only and mist/steam at Re=35,000 with various heat fluxes (same legend as Fig. 4)

increases. This is expected because as the heat flux increases the wall temperature also increases. As the wall temperature becomes higher, fewer droplets can attach to the wall surface. The major heat transfer path in such a case is by steam convection, with the heat transfer enhancement coming from (a) a lower steam bulk temperature, (b) a progressively increasing steam mass flow rate resulting from the added steam mass from droplet evaporation inside the steam flow, and (c) enhanced turbulence mixing induced by droplet dynamics.

For the cases of medium and high steam flows (Figs. 5 and 6, Re=20,000 and 35,000, respectively), the heat transfer enhancement is significant. Actually, in both cases, a ''quench'' effect is observed to occur at the first half of the outer wall in the curved section, where the local wall temperature is close to the saturation temperature of water. This quench effect, not observed in the low steam flow case, is caused by two reasons: (1) under higher Reynolds numbers higher droplet deposition rates occur (see [10]), thus a thicker deposited liquid film is formed at the inlet of the test section and (2) since the main steam flow has higher velocities, more droplets are entrained into the steam flow and are thrown onto the outer wall surface due to higher centrifugal forces. Under these two effects, the outer wall is always wetted at the inlet region of the curved section.

Another observation for the cases of medium and high steam flow is that after the ''quench'' point at the outer wall, the average temperature differences between the inner and outer wall at any cross section in the curved tube is smaller than those of the corresponding single-phase steam flow, particularly in the case of high-steam flow case (Re=35,000). This can be explained by that the secondary flow helps augment circumferential heat transfer and partially even out the nonuniform circumferential temperature distribution.

Heat Transfer Coefficient Ratio Distribution. Heat transfer enhancement is shown as the ratio of h_{mist}/h_o in Figs. 7–9. They show that the heat transfer coefficient ratios increase with the increase of Reynolds number under the same droplet mass ratio and heat flux.

The average heat transfer enhancement achieved so far in the curved section is about 400 percent ($h_{\text{mist}}/h_o = 500$ percent). It should be noted that under the current definition, the calculated

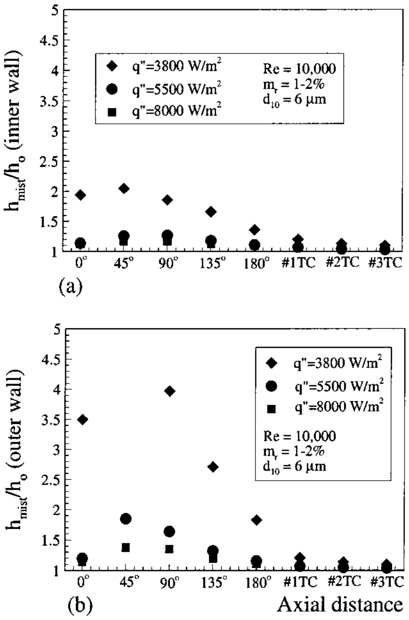

Fig. 7 Heat transfer coefficient ratios for Re=10,000; (*a*) inner wall, (*b*) outer wall (enhancement higher than 500 percent at 45-deg location is not shown)

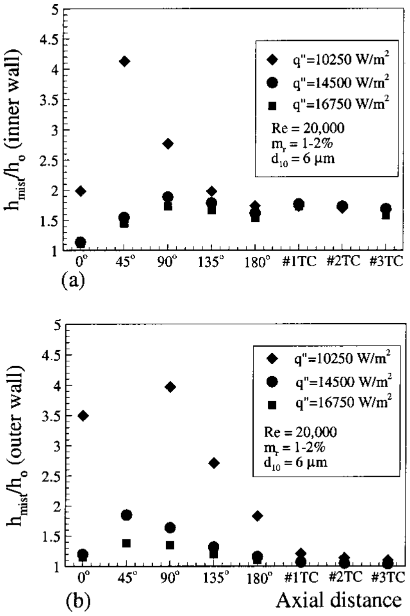

Fig. 8 Heat transfer coefficient ratios for Re=20,000; (*a*) inner wall, (*b*) outer wall (enhancement higher than 500 percent at 45-deg location is not shown)

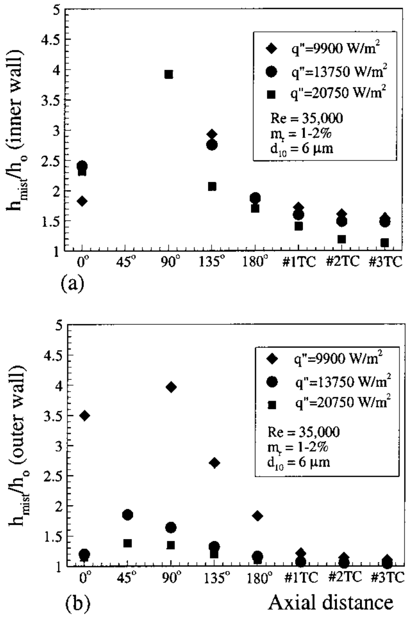

Fig. 9 Heat transfer coefficient ratios for Re=35,000; (*a*) inner wall, (*b*) outer wall (enhancement higher than 500 percent at 45-deg location is not shown)

heat transfer coefficient ratios at several locations are very large (500 percent~3,000 percent) due to the ''quench'' effect. Owing to the present definition of h_{mist} in Eq. (1), the h_{mist} would approach infinity as T_w is quenched towards T_{sat}. In order to clearly show the cooling enhancement values within the range that most of the data reside, data points larger than 500 percent enhancement at the 45-deg location are omitted in Figs. 7–9. It is interesting to see that even though the outer wall consistently has better cooling than does the inner wall, the inner wall obtains better cooling enhancement downstream of the 45-deg location at medium and high steam rates.

Conclusions

The results indicate the following:

1 For both steam-only and mist/steam conditions, the outer wall has better cooling than the inner wall. However, the inner wall can achieve better cooling enhancement downstream of the 45-deg bend at medium and high Reynolds numbers. The inner-outer wall temperature difference reduces as Reynolds number increases for the mist cases.

2 On the mist-cooled outer wall, the maximum cooling occurs near the 45-deg location due to the direct mist impingement on the outer wall. This impingement is believed to be caused by the inertia of water droplets coming from the upstream straight section and was further augmented by the centrifugal force. The secondary flow contributed to transporting the liquid droplets from the outer wall to the inner wall region and significantly increased the inner wall cooling, especially at the 45-deg location.

3 The overall cooling enhancement ranged from 40 to 300 percent with some local maximum enhancement being over 500 percent.

4 The mist cooling enhancement increased with the increased Reynolds number but decreased with the increased heat flux.

5 The nonsymmetrical cooling in the curved section persists in the downstream straight section.

It is hypothesized that even at the high wall temperature condition in the real engine environment, significant mist cooling enhancement could be achieved because of the high Reynolds number and increased steam density under a high-pressure condition (see Guo et al., [10] for details). The results of this study can also be applied to cooling in nuclear facility.

Acknowledgments

The authors would like to thank Graver Separations (Wilmington, DE) for donating the steam filters for the experiment. We also want to thank Mee Industries, Inc. (El Monte, CA) for donating the pressure atomizers and the high-pressure pump. We appreciate the help from Mr. X. Li in setting up the test facility. This research is sponsored by the U.S. Department of Energy under the contract DOE/AGTSR 95-01-SR-034, and is managed by Dr. N. Holcombe at the Federal Energy Technology Center and by Dr. L. Golan at the South Carolina Institute for Energy Studies.

Nomenclature

A = cross-sectional area
d_{10} = arithmetic mean droplet diameter
D = tube or channel diameter
h_0 = heat transfer coefficient for single-phase flow
h_{mist} = heat transfer coefficient for mist/steam flow
m_r = droplet mass flow ratio
q'' = heat flux
Re = UD/ν, Reynolds number
T_{sat} = saturation temperature of steam
T_w = wall temperature
U = mean flow velocity
x = streamwise flow direction
ν = kinematic viscosity

Subscripts

in = inlet
sat = saturation
w = wall

References

[1] van der Linden, S., 1992, ''Advanced Turbine Design Program,'' *Proceedings of the Ninth Annual Coal-Fueled Heat Engines, Advanced Pressurized Fluid-Bed Combustion (PFBC), and Gas Stream Cleanup Systems Contractors Reviewing Meeting*, Oct. 27–29, Morgantown, WV, Department of Energy, Morgantown, WV, pp. 215–227.
[2] Bannister, R. L., and Little, D. A., 1993, ''Development of Advanced Gas Turbine System,'' *Proceedings of the Joint Contractor Meeting: FE/EE Advanced Turbine System Conference*; FE Fuel Cells and Coal-Fired Heat Engine Conference,'' Aug. 3–5, Morgantown, WV, Department of Energy, Morgantown, WV, pp. 3–15.
[3] Mukavetz, D. W., Wenglarz, R., Nirmalan, N., and Daehler, T., 1994, ''Advanced Turbine System (ATS) Turbine Modification for Coal and Biomass Fuels,'' *Proceedings of the Advanced Turbine System Annual Program Review Meeting*, Nov. 9–11, ORNL/Arlington, VA, Department of Energy, Morgantown, WV, pp. 91–95.
[4] Bannister, R. L., Cheruvu, N. S., Little, D. A., and McQuiggan, G., 1994, ''Development Requirements for an Advanced Gas Turbine System,'' ASME Paper 94-GT-388.
[5] Farmer, R., and Fulton, K., 1995, ''Design 60 Percent Net Efficiency in Frame 7/9H Steam-Cooled CCGT,'' Gas Turbine World, May-June, pp. 12–20.
[6] Mukherjee, D., 1984, ''Combined Gas Turbine and Steam Turbine Power Station,'' patented by ABB, U.S. Patent No. 4424668.
[7] Guo, T., 1998, ''Mist/Steam Cooling in a Heated Horizontal Tube,'' Ph.D dissertation, Mechanical Engineering Department, Clemson University, Clemson, SC.
[8] Alff, R. K., Manning, G. B., and Sheldon, R. C., 1978, ''The High Temperature Water Cooled Gas Turbine in Combined Cycle with Integrated Low BTU Gasification,'' Combustion, **49**, pp. 27–34.
[9] Guo, T., Wang, T., and Gaddis, J. L., 2000, ''Mist/Steam Cooling in a Heated Horizontal Tube, Part 1—Experimental System,'' ASME J. Turbomach., **122**, pp. 360–365.
[10] Guo, T., Wang, T., and Gaddis, J. L., 2000, ''Mist/Steam Cooling in a Heated Horizontal Tube, Part 2—Results and Modeling,'' ASME J. Turbomach., **122**, pp. 366–374.
[11] Mori, Y., and Nakayama, W., 1967, ''Study on Forced Convective Heat Transfer in Curved Pipes (2nd Report, Turbulent Region),'' Int. J. Heat Mass Transf., **10**, pp. 37–59.
[12] Patankar, S. V., Pratap, V. S., and Spalding, D. B., 1975, ''Prediction of Turbulence Flow in Curved Pipes,'' J. Fluid Mech., **67**, Part 3, pp. 583–595.
[13] Cumo, M., Farello, G. E., and Ferrari, G., 1971, ''The Influence of Curvature

in Post Dryout Heat Transfer,'' Represented at XXVI National ATI Annual Meeting, L'Aquilia, Italy.

[14] Lautenschlager, G., and Mayinger, F., 1982, ''Post-Dryout Heat Transfer to R12 in a Circular 90-Deg-Tube-Bends'', 7th Int. Heat Transfer Conference, Munich, Germany.

[15] Wang, M. J., and Mayinger, F., 1995, ''Post-Dryout Dispersed Flow in Circular Bends,'' Int. J. Multiphase Flow, **21**, No. 3, pp. 437–454.

[16] Mori, Y., Hijikata, K., and Yasunaga, T., 1982, ''Mist Cooling of Very Hot Tubules With Reference to Through-Hole Cooling of Gas Turbine Blades,'' Int. J. Heat Mass Transf., **25**, No. 9, pp. 1271–1278.

[17] Bachalo, W. D., 1980, ''Method for Measuring the Size and Velocity of Spheres by Dual-Beam Light Scatter Interferometry,'' Appl. Opt., **19**, No. 3, pp. 363–372.

[18] Bachalo, W. D., and Houser, M. J., 1984, ''Phase Doppler Spray Analyzer for Simultaneous Measurements of Drop Size and Velocity Distributions,'' Opt. Eng., **23**, No. 5, pp. 583–597.

[19] Moffat, R. J., 1985, ''Using Uncertainty Analysis in the Planning of an Experiment,'' ASME J. Fluids Eng., **107**, pp. 173–178.

[20] Wang, T., and Simon, T. W., 1989, ''Development of A Special-Purpose Test Surface Guided by Uncertainty Analysis,'' Int. J. Thermophys., **3**, No. 1, pp. 19–26.

Laser-Based Measurement of Temperature or Concentration Change at Liquid Surfaces

C. H. Fan
Graduate Student Researcher,
Assoc. Mem. ASME
e-mail: cfan@ic.sunysb.edu

J. P. Longtin[1]
Assistant Professor,
Mem. ASME
e-mail: jlongtin@ms.cc.sunysb.edu

Department of Mechanical Engineering,
State University of New York,
Stony Brook, NY 11794-2300

This work presents a noncontact laser-based thermoreflectance technique to measure changes in temperature or concentration at a liquid surface. Changes in temperature and, for multi-component liquid mixtures, concentration result in a change in the liquid index of refraction, which alters the reflectivity of the liquid surface. An intensity-stabilized diode laser and silicon photodiode are used to monitor the surface reflectivity. Temperature variations in 1-propanol, methanol, ethanol, and water are measured with uncertainties of 0.5, 0.7, 0.7, and 3.7°C, respectively. For binary mixtures, the concentration of a methanol-propanol mixture is measured with an uncertainty of 0.3 percent. The experimental configuration is noninvasive, simple in design, and inexpensive. The technique can be used over a wide range of time scales, ranging from micro-seconds to minutes, and can achieve high spatial resolution by focusing the probe laser beam to a small spot size on the liquid surface. [S0022-1481(00)02803-6]

Keywords: Heat Transfer, Laser, Liquid, Measurement Techniques, Temperature and Concentration

Introduction

Noncontact measurement techniques have played a significant role in the investigation of thermal and fluid phenomena. Their distinct advantages over direct-contact counterparts include the noninvasive nature of the measurement, high spatial and temporal resolution, high reliability, and imperviousness to harsh and corrosive environments. The temperature and concentration at a liquid surface are two important parameters that are traditionally difficult to measure with conventional techniques, and thus are ideal candidates for noncontact measurement methods.

One popular noncontact instrument for temperature measurement is the commercial infrared thermometer, which measures infrared radiation emitted from an object to determine its temperature. These devices, however, are difficult to use for low-emissivity materials, such as transparent liquids, and objects with relatively small surface area. Furthermore, radiation emitted well below the liquid surface contributes to the measured temperature, making measurement of the liquid *surface* temperature very difficult. Infrared techniques also cannot measure concentration changes.

A laser-based temperature measurement technique is presented in this work that successfully avoids these disadvantages. Laser-based temperature measurement research has progressed rapidly in the past decade, though much of the research has focused on solids, while liquids have received relatively little attention. Sensitive laser-based optical techniques for noncontact solid-surface temperature measurements were presented by Qiu et al. [1], Chen and Grigoropoulos [2], and Lee et al. [3,4]. Longtin and Fan [5] presented a technique to measure temperature at liquid surfaces, but their system required both probe and reference beams, and was sensitive to background light.

Regarding concentration, Bergman et al. [6] developed an optical-based probe that relied on changes in the index of refraction to measure concentration in bulk liquids. The probe, however, was still required to be immersed in the liquid. Bergman et al. [7] also developed an optical deflection technique for measuring salt concentration based on the image distortion of a fine wire as it passed through a variable-concentration liquid. This technique measured concentration in the bulk liquid as an integrated effect of concentration variation along the light path. An accurate laser-based technique for bulk concentration measurements in liquids was recently developed by Longtin and Fan [8]; however, it cannot measure surface concentration.

In the present work, a high spatial and temporal resolution measurement technique is presented that is capable of measuring *temperature* or, for binary mixtures, *concentration* at a liquid surface in real time. The experimental theory and technique are discussed, followed by results presented for four liquids: 1-propanol, methanol, ethanol, and water. Results for both the temperature and concentration are in good agreement with reference values. Uncertainties of 0.5°C for 1-propanol, 0.7°C for ethanol and methanol, and 3.7°C for water have been obtained.

Experimental Theory and Setup

The reflectivity R of a liquid surface depends on the liquid index of refraction n, which, in turn, depends on the surface temperature T, and, for mixtures of liquids, the concentration C as well. The liquid surface is taken to be in contact with a gas, e.g., air, with $n=1$. Using a laser beam as the light source, the reflectivity variations from the liquid surface are recorded as the surface temperature or concentration changes. For single-component liquids, the technique measures temperature fluctuations only. For binary or multi-component mixtures, variations in both temperature and concentration will change the reflectivity of the surface.

The experimental configuration is shown in Fig. 1. A Hitachi HL6316G 3 mW laser diode with a nominal wavelength of 635 nm serves as the light source. The laser diode is housed in a small cylindrical container that includes an aspheric lens to focus the beam, and is driven by a Wavelength Electronics LFI-4505 laser diode driver. The liquid resides in a thin steel container, 4 cm in diameter, and 4 cm deep, which is itself surrounded by a closed water jacket connected to a hot/cold water bath to change the liquid temperature as desired. The beam is sent directly to the liquid surface, and the reflected beam is sent to an aluminum mirror and then a UDT PIN-6D silicon PIN photodiode (PD).

The diode has an active area of 20.3 mm^2 and is operated in photoconductive mode with a 15 V reverse bias voltage applied

---

[1] To whom correspondence should be addressed.

Contributed by the Heat Transfer Division for publication in the JOURNAL OF HEAT TRANSFER. Manuscript received by the Heat Transfer Division, July 3, 1999; revision received, Apr. 19, 2000. Associate Technical Editor: A. Majumdar.

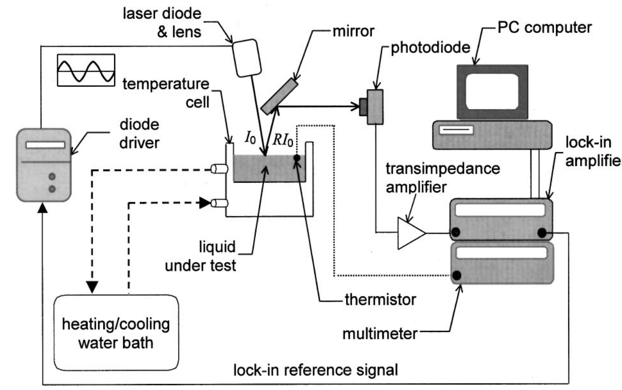

Fig. 1 Experimental setup for laser-based measurement of temperature or concentration at liquid surfaces

across the diode ([9]). The photodiode generates a current, which is sent to a transimpedance (current-to-voltage) amplifier and converted to a voltage. An EG&G 7260 lock-in amplifier provides a sinusoidal reference signal to the laser diode driver, which modulates the diode output intensity. The photodiode amplifier voltage is then sent to the lock-in amplifier input. Since the lock-in amplifier measures only signals with the reference frequency, effects such as background light and electrical noise will not affect the measurement. The lock-in amplifier is connected to a PC computer using a GPIB interface for data acquisition.

For a typical liquid, e.g., methanol, $R \sim 0.02$; for a 1°C temperature increase, the change in reflectivity, ΔR, is $\sim 4 \times 10^{-5}$, which is very difficult to measure. The experimental design, however, actually measures small voltage changes, ΔV, in the presence of a large, nearly constant nominal voltage, V_0. Referring to Fig. 1, if I_0 is the incident laser intensity, the reflected beam intensity at the PD will be RI_0. The photodiode/amplifier system generates a voltage that varies linearly with the intensity of the incident PD radiation:

$$V = GI_0R \tag{1a}$$

or

$$\Delta V = GI_0 \Delta R \tag{1b}$$

where G represents the intensity-to-voltage gain (V/W) of the photodiode/amplifier system. Dividing Eq. (1a) by (1b),

$$\frac{\Delta V}{V} = \frac{\Delta R}{R}. \tag{2}$$

Using methanol as an example, $\Delta R/R \sim 2 \times 10^{-3}$, thus the digital multimeter (DMM) used for the photodiode amplifier voltage needs only to resolve to 1 part in 1000, i.e., three displayed digits for a 1°C temperature resolution. In this experiment, 6.5 digit DMMs are used.

Both R and dR/dn vary with the laser beam angle of incidence, θ ([10]). Choosing a near-normal angle of incidence ($\theta \approx 0$) as done in the present work yields several advantages, including large values for $\Delta R/R$, no dependence on beam polarization, and ease of beam delivery. At normal incidence, R and n are related according to Fresnel's laws of reflection as follows for both s and p-polarized light ([10])

$$R = \left(\frac{n-1}{n+1}\right)^2 \tag{3a}$$

$$\frac{dR}{dn} = \frac{4(n-1)}{(n+1)^3}. \tag{3b}$$

These expressions result in an error of less than 0.01°C compared to the more complicated expressions for θ less than $\sim$6 deg, which is the actual angle of incidence used in the experiment. Therefore, Eq. (3) is used in the present work.

For monochromatic light, and in the absence of strong pressure variations, the index of refraction is function only of temperature in pure liquids, $n = n(T)$. The change in n with temperature, dn/dT, determines the sensitivity of R to temperature:

$$\Delta R \cong \left(\frac{dR}{dn}\right)\Delta n = \frac{4(n-1)}{(n+1)^3}\frac{dn}{dT}\Delta T \tag{4}$$

where ΔT is a small finite temperature change at the liquid surface. Often dn/dT can be treated as a constant if the total temperature change is small ([11,12]).

For a liquid mixture, the index of refraction depends on both temperature and concentration such that

$$n = n(T,C) \quad \Delta n \cong \frac{\partial n}{\partial T}\Delta T + \frac{\partial n}{\partial C}\Delta C \tag{5}$$

and, from Eq. (4),

$$\Delta R \cong \frac{dR}{dn}\left[\frac{\partial n}{\partial T}\Delta T + \frac{\partial n}{\partial C}\Delta C\right]. \tag{6}$$

Temperature Measurement. The technique measures the *change* in the surface reflectivity to obtain the temperature change at the liquid surface, thus at the start of the experiment, the system is allowed to reach thermal equilibrium at a known reference temperature with a corresponding reference reflectivity from the liquid surface, V_0. Using Eqs. (2)–(4), the temperature change becomes

$$\Delta T = \frac{n^2-1}{4}\left(\frac{dn}{dT}\right)^{-1}\frac{\Delta V}{V_0}. \tag{7}$$

Concentration Measurement. For the concentration measurement, the experiment configuration is identical to that for the temperature measurement, except that the water bath is not used. Note that from Eq. (5) changes in the index of refraction occur from changes in both temperature *and* concentration. It is not possible, in general, to distinguish between temperature and concentration changes based solely on this technique. If, however, the concentration term dominates, i.e.,

$$\frac{\partial n}{\partial C}\Delta C \gg \frac{\partial n}{\partial T}\Delta T \tag{8}$$

then concentration can successfully be measured. Alternately, temperature fluctuations can be accounted for in R by measuring temperature independently, e.g., with a thermocouple (Eq. (6)).

Temperature and Concentration Validation. To validate the laser-based measurement technique, experiments are performed on liquids whose temperature (or concentration) is measured by a separate independent technique. A small thermistor is placed just under the test liquid surface to monitor the temperature of the liquid (Fig. 1). The thermistor has a diameter $\sim$2 mm, and is calibrated against a NIST-traceable RTD over a temperature range of 15 to 50°C. During the laser-based measurement, the thermistor resistance is monitored by a Keithley 2000 multimeter and converted to temperature. This contact-based thermistor temperature measurement is then taken as the true temperature for the system with which the laser-based technique is compared.

For the concentration measurements, two liquids, A and B, are mixed together in different volume fractions. The volume concentrations C_A and C_B of liquids A and B are, respectively,

$$C_A = \frac{v_A}{v_A + v_B} \quad C_B = \frac{v_B}{v_A + v_B}. \tag{9}$$

Table 1 Liquid Properties

	n (λ = 632.8 nm, 25 °C)	dn/dT ($\times 10^4$ K^{-1})	dn/dT ($\times 10^4$ K^{-1}) (average)	R (%)[a]	dR/dn[a]	ρ (g/cm^3)
water	1.331 [11]	−0.8 [11] −1.04 [12]	−0.92 ± 0.12	2.02	0.105	
ethanol	1.358 [11]	−3.9 [11] −3.6 [12] −4.38 [13] −4.29 [14] −4.53 [15]	−4.14 ± 0.47	2.31	0.109	
methanol	1.325 [11]	−3.9 [11] −3.9 [12] −4.68 [13] −4.36 [14] −4.32 [15]	−4.32 ± 0.39	1.95	0.103	0.792 [16]
1-propanol	1.384 [11]	−3.9 [11] −3.8 [12] −4.33 [15]	−4.01 ± 0.27	2.59	0.113	0.804 [16]

[a] Calculated from Eq. (3)

In order to keep a constant liquid surface height, the concentration of the liquid mixture under test is changed by gradually replacing one of the liquid components in the test cell by another with the same volume, using a precision scale and the liquid density. The index of refraction dependence on concentration for the liquids tested, dn/dC, was measured in a separate experiment ([8]).

Results and Discussion

The liquids used in this experiment are 1-propanol, methanol, ethanol, and water. The relevant liquid properties for each of these liquids are shown in Table 1 ([11–16]). Reported values for dn/dT can vary by over ten percent; for this work, average values from Table 1 are used.

The spatial resolution of the technique is determined by the beam spot size on the liquid surface, which can be adjusted with the aspheric lens in the laser diode housing. The laser diode has a slightly rectangular beam profile whose size dimensions were roughly (0.5 mm)×1.0 mm at the liquid surface. The temporal resolution of the technique is limited by the electrical components, rather than the optical components. The photodiode and transresistance amplifier have a response time on the order of 1 μs or less; the DMMs have a response time of ~1 ms. For the results in this work the maximum sample rate was 100 samples/s. Faster response times can be obtained by using a fast digital oscilloscope or high-speed DMM to capture the PD voltage.

Surface Temperature Results. For the temperature measurements, pure 1-propanol, methanol, ethanol, and water are used. The test liquid, initially ~25°C, is cooled and then heated; the test is stopped when the liquid returns to 25°C. Typical test times range from 15 to 18 minutes. Before each test, the system is powered on and the test liquid is introduced and allowed to stabilize thermally for at least 20–30 minutes. At the start of the test, the liquid temperature and reflectivity signal are measured and stored as reference values.

The 4-cm-high test liquid container (Fig. 1) is filled with only ~1 cm of liquid, so that the container walls above the liquid retain the vapor that comes off the surface, and a vapor buffer layer is established over the liquid-vapor interface. Care is made to minimize air currents near the liquid container to avoid disturbing this buffer vapor layer. Note that this is done for validation only: Since the reference thermometer cannot accurately capture surface temperature transients, attempts are made to minimize evaporation during the temperature measurement. In fact, the technique will accurately capture surface temperature fluctuations due to evaporation; indeed, it is a strength of the method.

The temperature results for 1-propanol, methanol, ethanol, and water are shown in Figs. 2–5, respectively. In each graph the solid line represents the laser-based measurement, and the dashed line represents the calibrated thermistor temperature measurement. For the laser-based experiment, a 10-point moving average (20-point for water) is used to reduce noise in the results. The sampling rate is 5 samples/s, which introduces at most a 2 s history (4 s for water) in the measurement, which is negligible for the test duration used. As can be seen, the results from the laser-based technique are generally in good agreement with the calibrated thermistor temperature values for both heating and cooling, and for all liquids.

Note that the agreement for 1-propanol is the best, while the discrepancy for water is the largest. The tests for each liquid are repeated several times, with similar results found. The larger noise for water occurs because its refractive index temperature coefficient, dn/dT, is only 25 percent that of the other liquids, resulting in a correspondingly weaker signal for a given temperature change. Despite the higher noise for water, however, the temperature still agrees well with the thermistor values. The agreement and noise of the results for 1-propanol, methanol, and ethanol are comparable in their agreement.

Surface Concentration Results. To demonstrate the technique for concentration measurement, methanol and 1-propanol are used, as n varies linearly with concentration for these two liquids, as opposed to, e.g., ethanol and water ([17,18]). The index of refraction as a function of concentration for this liquid system was measured with an independent technique by Longtin and Fan [8] and found to be $dn/dC = -5.9\times10^{-4}$ 1/%, which is the value

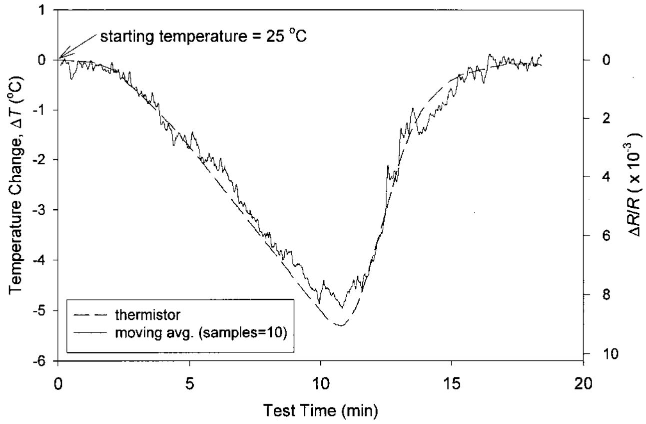

Fig. 2 1-propanol surface temperature measurement

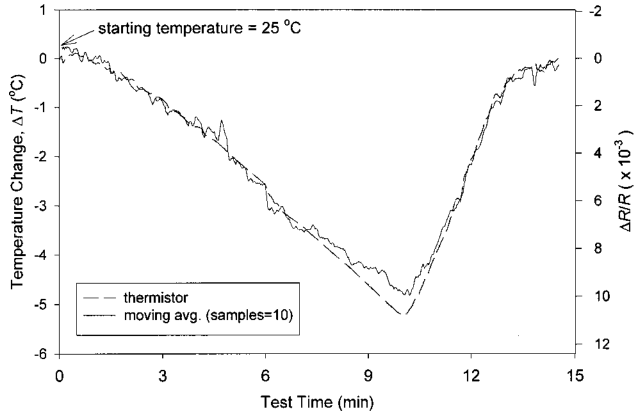

Fig. 3 Methanol surface temperature measurement

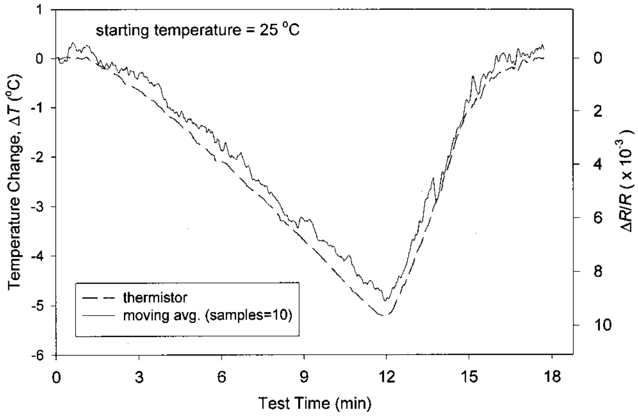

Fig. 4 Ethanol surface temperature measurement

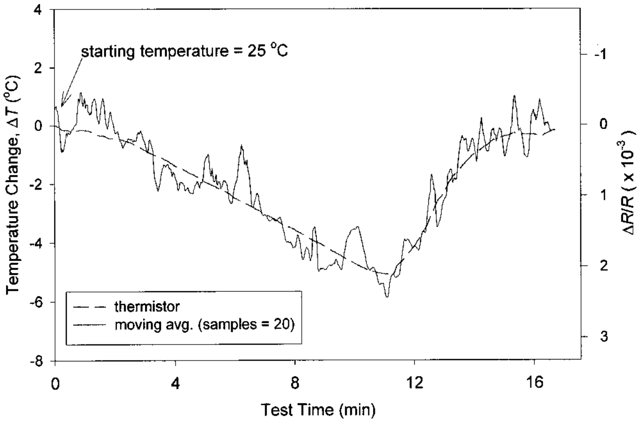

Fig. 5 Water surface temperature measurement

used in Eq. (6). The liquid temperature is also measured with the thermistor during the experiment, and used to compensate R for temperature in Eq. (6). The temperature drift in all cases was less than 0.3°C during a given run.

Results are presented over three concentration ranges, 0–10, 50–60, and 90–100 vol % methanol in Fig. 6. For each range, a known liquid concentration was prepared at the low end of the range, e.g., 50 vol % methanol for the 50–60 vol % range, using a precision scale and the liquid densities. This served as the reference value, from which the concentration was increased by two percent to the higher end of the range. The concentration was varied for each step by removing a volume of the mixture and adding the appropriate amount of methanol, which also served to keep the liquid height constant for the reflected beam.

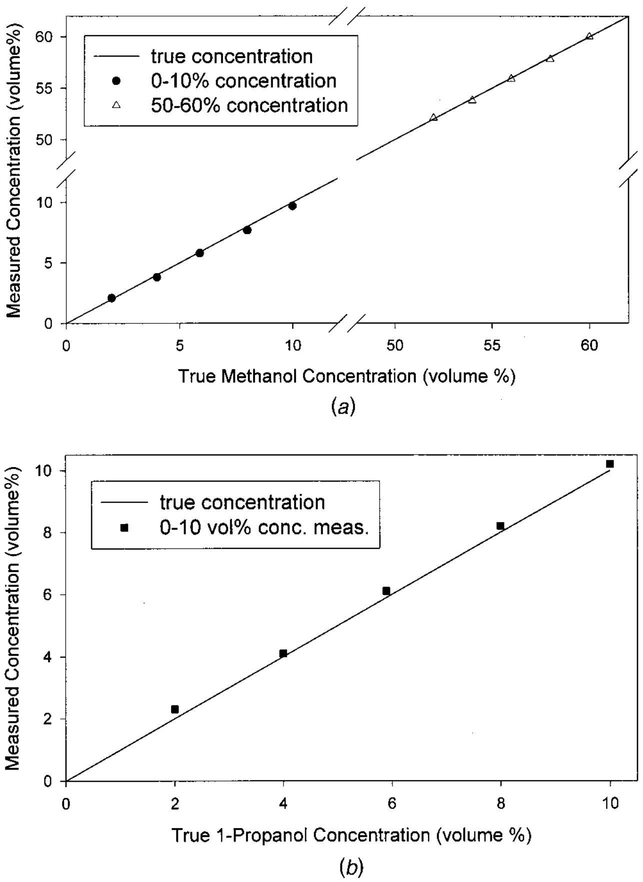

(*a*)

(*b*)

Fig. 6 (*a*) Concentration of methanol in 1-propanol-based mixture; (*b*) concentration of 1-propanol in methanol-based mixture

For each plot in Fig. 6, the x-axis represents the true concentration (by volume) of methanol, and the y-axis represents the measured concentration from the laser technique. The ideal results should follow the line $y = x$, as shown in the figure. The actual data from the experiment are shown as symbols. For all results, the difference between the measured and true concentration is less than 0.3 percent.

Experimental Uncertainty. The thermistor in Fig. 1 is calibrated using a NIST-traceable platinum resistance thermometer over a temperature range of 15–50°C. The resulting thermistor uncertainty is less than 0.05°C. For the concentration measurements, the liquid mixtures were prepared by weighing each liquid component using a digital scale with a resolution of 0.01 g. To convert to volume percent, liquid densities from the literature were used ([14]).

Uncertainty in ΔT in Eq. (7) depends on the uncertainty in thermophysical properties n and dn/dT, and measurements of $\Delta V/V_0$. Values of n in the literature typically vary by less than 0.5 percent (at the same temperature and wavelength); however, variation in dn/dT can exceed ten percent (Table 1), resulting in a corresponding uncertainty in ΔT. The average values of dn/dT were used, and their uncertainties were obtained using all values reported in Table 1. Variations in $\Delta V/V_0$ arise from fluctuations in the incident laser intensity, slight motion of the liquid surface, which displaces the position slightly in the photodiode, and cooling effects from evaporation (see above). Typical variation in

$\Delta V/V_0$ was 0.1–0.2 percent for all liquids, with water having the highest and 1-propanol the lowest values. Fluctuations in $\Delta V/V_0$ for the concentration measurements were comparable.

Considering the above uncertainties using a root-sum-square uncertainty analysis, the uncertainties for the temperature measurements were 0.5, 0.7, 0.7, and 3.7°C for 1-propanol, methanol, ethanol, and water, respectively. The large uncertainty in water results from its small value of dn/dT, which yields low signal-to-noise ratios. The uncertainty in the concentration measurements is ~0.3 percent for all liquids tested.

Applications. Since the same technique can be used to capture very fast (~1 μs) temperature and concentration variations as well as longer time scale phenomena (~minutes), the technique can be used in a variety of applications. Examples include:

(a) Measurement of Surface Concentration During Addition of Other Materials. The technique can be used to measure the time-varying surface concentration of a liquid when a second material is added, e.g., a surfactant, solid, or another liquid. To illustrate this, a 10-ml beaker 2.5 cm in diameter is filled with 1-propanol, and the laser beam directed onto the center of the liquid surface. One drop (~0.01 ml) of methanol is added to the side of the beaker above the liquid. The methanol flows down the beaker wall into the 1-propanol, resulting in concentration-induced surface tension gradients that cause surface motion. The measured surface concentration of methanol at the probe beam location is shown in Fig. 7. The liquid is added near $t=0$ s, and, after about 1 s, there is a large increase in the methanol surface concentration, presumably due to surface-tension-induced flow of the methanol across the surface. After ~3 s, the methanol surface concentration again drops to nearly zero. A sampling rate of 100 samples/s was used for these measurements.

(b) Measuring Surface Concentration in a Binary (Water and Ethanol) Solution Undergoing Both Thermal and Concentration-Induced Marangoni Convection. The beam is passed through a window into a sealed container containing only the liquid mixtures and their vapors. One of the container walls is heated and the opposite wall cooled to generate buoyancy and Marangoni-induced convection. The beam is reflected off the liquid surface to measure concentration changes as a function of position away from either wall.

(c) Measurement of Surface Temperature During Laser-Induced Surface Tension Flows. Another application under investigation is the time-dependent measurement of surface temperature during laser-induced surface tension driven flows. A laser pulse strikes the liquid surface, causing heating and subsequent fluid motion due to the temperature-dependent surface tension ([19]). The fast noncontact nature of the presented technique is well suited for such measurements, and can be used to measure time-dependent surface temperature at various positions from the laser heated region. Deformation of the liquid surface may result in the reflected beam being repositioned over different parts of the photodiode, causing some measurement noise. However, if the diode has a uniform response across its detecting area, these variations will be minimized. Second, if the surface deformation is oscillatory then the beam will traverse the detector in a periodic fashion, and the resulting data can be averaged and processed to account for this variation. Finally, keeping the beam angle of incidence near 0 deg will minimize beam deflection due to surface deformation.

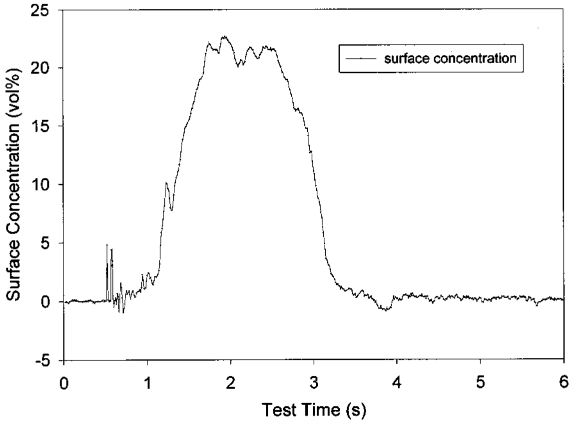

Fig. 7 Transient methanol concentration measurement at 1-propanol surface

(d) Measurement of Crystal Melt Temperature During Crystal Growth. A more challenging potential application of the technique is to measure surface temperature of semiconductor materials during the growth phase. Accurate high-spatial-resolution temperature information is critical for high purity and low-defect crystals. The incident and reflected laser beams would pass through a sight glass in the growth chamber for the measurement.

Conclusions

This work presents a laser-based noncontact technique to measure the temperature or concentration of liquid surfaces. The change in index of refraction of the liquid due to temperature or concentration changes results in a change of the intensity of reflected light from the surface, which is measured and recorded. A 3 mW diode laser serves as the light source, and reflected light is monitored with a photodiode. The technique is demonstrated using four pure liquids: 1-propanol, methanol, ethanol, and water with good results found. Liquid surface concentration can also be measured, and results for a methanol-propanol mixture are found to be in very good agreement with expected results. The technique shows potentials for a variety of applications requiring noncontact remote monitoring of surface temperature or concentration, and preliminary results are shown for the transient surface concentration of a drop of methanol spreading on a volume of 1-propanol.

Acknowledgments

The authors gratefully acknowledge financial support for this work from the National Science Foundation through contact CTS-9702644.

Nomenclature

C = concentration (volume percent)
G = amplifier/photodiode gain factor (V/W)
I = laser intensity (W)
n = index of refraction
R = reflectivity of liquid surface
T = temperature (K, °C)
V = voltage (V)
v = volume (m^3)

Greek Symbols

ρ = density (kg/m^3)
θ = laser beam angle of incidence (deg)

Subscripts

A,B = liquid A, liquid B
0 = initial

References

[1] Qiu, T. Q., Grigoropoulos, C. P., and Tien, C. L., 1993, ''Novel Technique for Noncontact and Microscale Temperature Measurements,'' Exp. Heat Transfer, **6**, pp. 231–241.
[2] Chen, S., and Grigoropoulos, C. P., 1997, ''Noncontact Nanosecond-Time-

Resolution Temperature Measurement in Excimer Laser Heating of Ni-P Disk Substrates,'' Appl. Phys. Lett., **71**, pp. 3191–3193.

[3] Lee, A. S., Hostetler, J. L., and Norris, P. M., 1996, ''Temperature Measurement by Thermoreflectance at Near Grazing Angles,'' *Proceedings of the 1996 ASME International Mechanical Engineering Congress and Exposition*, Vol. 59, , Atlanta, GA, Nov. 17–22, ASME, New York, pp. 77–82.

[4] Lee, A. S., and Norris, P. M., 1997, ''A New Optical Method for Measuring Surface Temperature at Large Incident Probe Angles,'' Rev. Sci. Instrum., **68**, pp. 1307–1311.

[5] Longtin, J. P., and Fan, C. H., 1998, ''Laser-Based Temperature Measurement at a Liquid Surface,'' *Proceedings, 11th International Heat Transfer Conference*, Vol. 4, Kyongju, Korea, Taylor and Francis, London, pp. 119–123.

[6] Bergman, T. L., Incropera, F. P., and Stevenson, W. H., 1985, ''Miniature Fiber-Optic Refractometer for Measurement of Salinity in Double-Diffusive Thermohaline Systems,'' Rev. Sci. Instrum., **56**, pp. 291–296.

[7] Bergman, T. L., Munoz, D. R., Incropera, F. P., and Viskanta, R., 1986, ''Measurement of Salinity Distributions in Salt-Stratified, Double-Diffusive Systems by Optical Deflectometry,'' Rev. Sci. Instrum., **57**, pp. 2538–2542.

[8] Longtin, J. P., and Fan, C. H., 1998, ''Precision Laser-Based Concentration and Refractive Index Measurement of Liquids,'' Microscale Thermophys. Eng., **2**, pp. 261–272.

[9] Graeme, J., 1996, *Photodiode Amplifiers—Op Amp Solutions*, McGraw-Hill, New York.

[10] Jenkins, F. A., and White, H. E., 1976, *Fundamentals of Optics*, 4th Ed., McGraw-Hill, New York.

[11] Solimini, D., 1966, ''Loss Measurements of Organic Materials at 6328 Å,'' J. Appl. Phys., **37**, pp. 3314–3315.

[12] Stone, J., 1972, ''Measurements of the Absorption of Light in Low-Loss Liquids,'' J. Opt. Soc. Am., **62**, pp. 327–333.

[13] Lusty, M. E., and Dunn, M. H., 1987, ''Refractive Indices and Thermo-Optical Properties of Dye Laser Solvents,'' Appl. Phys. B: Photophys. Laser Chem., **44**, pp. 193–198.

[14] Fan, C. H., 1998, ''Laser-Based Measurement of Liquid Refractive Index, Concentration, and Temperature,'' Master thesis, State University of New York, Stony Brook, NY, pp. 29–30.

[15] Sun, J., Longtin, J. P., and Irvine, Jr., T. F., 2000, ''Laser-Based Thermal Pulse Measurement of Liquid Thermophysical Properties,'' Int. J. Heat Mass Transf., to be published.

[16] Beaton, C. F., and Hewitt, G. F., 1988, *Physical Property Data for the Design Engineering*, Hemisphere, New York.

[17] Dean, J. A., 1973, *Lange's Handbook of Chemistry*, 11th Ed., J. A. Dean, ed., McGraw-Hill, New York.

[18] Lide, D. R., 1998, *CRC Handbook of Chemistry and Physics*, D. R. Lide, ed., CRC Press, Boca Raton, FL.

[19] Longtin, J. P., Hijikata, K., and Ogawa, K., 1999, ''Laser-Induced Surface-Tension-Driven Flows in Liquid,'' Int. J. Heat Mass Transf., **42**, pp. 85–93.

Transport Phenomena and Droplet Formation During Pulsed Laser Interaction With Thin Films

D. A. Willis

X. Xu[1]
e-mail: xxu@ecn.purdue.edu

School of Mechanical Engineering,
Purdue University,
West Lafayette, IN 47907

This work investigates transport phenomena and mechanisms of droplet formation during a pulsed laser interaction with thin films. The surface of the target material is altered through material flow in the molten phase induced by a tightly focused laser energy flux. Such a process is useful for developing a laser-based micromachining technique. Experimental and numerical investigations of the laser-induced fluid flow and topography variations are carried out for a better understanding of the physical phenomena involved in the process. As with many machining techniques, debris is often generated during laser-material interaction. Experimental parametric studies are carried out to correlate the laser parameters with the topography and droplet formations. It is found that a narrow range of operation parameters and target conditions exists for ''clean'' structures to be fabricated. The stop action photography technique is employed to capture the surface topography variation and the melting development with a nanosecond time resolution and a micrometer spatial resolution. Numerical simulations of the laser-induced surface deformation are also performed to obtain the transient field variables and to track the deforming surface. The comparison between the numerical and experimental work shows that, within the energy intensity range investigated in this work, the surface deformation and droplet formation are attributed to the surface-tension-driven flow, and the recoil pressure effect plays an insignificant role in the surface topography development. [S0022-1481(00)02903-0]

Keywords: Heat Transfer, Instability, Laser, Surface Tension, Visualization

1 Introduction

Droplet formation is a common problem in laser machining. Many studies have attributed droplet formation to fluid flow instabilities that develop from disturbances in the molten surface of the target ([1]). These disturbances lead to a wavy surface due to thermocapillary effects, which grow into surface structures due to the capillary wave instability. Droplets may then form from the capillary wave instability itself, or due to other instability mechanisms. The initial temperature disturbances can be attributed to a number of factors, including laser spatial intensity distributions that oscillate over time, as is the case with non-Gaussian laser beams, or a surface roughness that may cause nonuniform absorption of the incident laser beam.

The purpose of this work is to study the transport phenomena and droplet formation in a pulsed laser thin film interaction. Little work has been done on analyzing droplet formation arising from the use of lasers with Gaussian intensity distribution where the fluid flow is dominated in the radial direction. Because of the intensity distribution of the Gaussian laser beams, it is doubtful that capillary wave instabilities are contributing factors to droplet formation. Balandin et al. [2] studied the flow of iron containing surface active impurities irradiated by a nanosecond pulsed laser. No discussion of droplet formation was included. Dimitrov [3] observed droplets in his study but gave no explanations or theories to the droplet mechanisms either. Bennett et al. [4] used a finite element method to study the fluid flow and heat transfer in a nanosecond pulsed laser texturing process of magnetic disk substrates. Fluid flow was attributed to both thermocapillary and chemicapillary forces. The chemicapillary forces resulted from mass diffusion of phosphorous due to a concentration gradient caused by depletion of phosphorous at the free surface. Willis et al. [5] performed a parametric study which demonstrated that for a narrow range of laser pulse energy, holes could be formed due to the flow in the radial direction as shown in Fig. 1, with no debris found in the surrounding area. However, above this narrow energy range, the strong radial flow could lead to droplet formation.

In a pulsed laser micromachining process, flow acceleration is high. Common instability mechanisms such as Rayleigh-Taylor or Kelvin-Helmholtz can occur. The Rayleigh-Taylor instability occurs when two superposed fluids of different densities are accelerated toward each other. If the density of the overlying fluid is less than the underlying fluid, the motion will be unstable for disturbance wavelengths greater than the critical wavelength, Λ_c, which is calculated by ([6]):

$$\Lambda_c = 2\pi\left(\frac{\gamma}{g(\rho_1-\rho_2)}\right)^{1/2} \qquad (1)$$

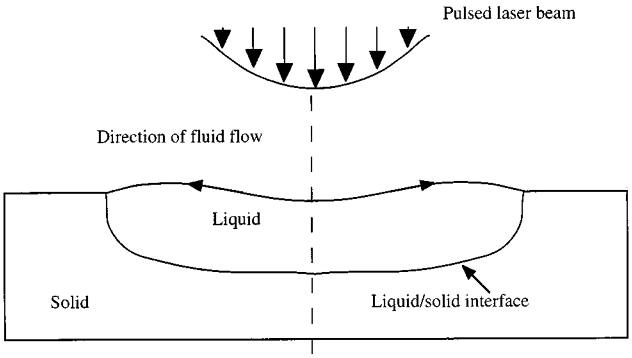

Fig. 1 Laser-induced phase change and Marangoni flow

---

[1] To whom correspondence should be addressed.

Contributed by the Heat Transfer Division for publication in the JOURNAL OF HEAT TRANSFER. Manuscript received by the Heat Transfer Division, Aug. 16, 1999; revision received, Apr. 19, 2000. Associate Technical Editor: A. Majumdar.

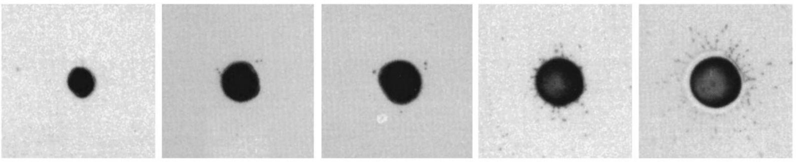
(a) 0.95 μJ (b) 1.6 μJ (c) 2.0 μJ (d) 2.7 μJ (e) 3.6 μJ

Fig. 2 Results of experimental parametric study for 0.3 μm chromium film on quartz substrate

where ρ_1 is the density of the underlying fluid, ρ_2 is the density of the overlying fluid, γ is the surface tension, and g is the acceleration of gravity.

The Kelvin-Helmholtz instability can occur at the interface of two fluids of different density in relative horizontal motion. Flows will be stable for relative velocities given by the criteria

$$(v_1-v_2)^2<\frac{2(\rho_1+\rho_2)\{\gamma g(\rho_1-\rho_2)\}^{1/2}}{\rho_1\rho_2}. \tag{2}$$

The critical wavelength above which instability can develop for the Kelvin-Helmholtz instability is also given by Eq. (1). It should be noted that Eqs. (1)–(2) are approximations developed for inviscid, two-dimensional flows. In reality, flow instabilities will be three dimensional in nature, possibly due to nonuniform heating by the laser, which will lead to nonuniform velocity, density, and recoil pressure distributions.

In the pulsed laser-induced fluid flow, the gravitational force is small compared to the acceleration forces that result from the large surface tension gradient at the molten surface. The gravitational term in the above equations therefore should be replaced with a flow acceleration term in a flow stability analysis.

In this work, the possible mechanisms of droplet formation during pulsed laser interaction with thin chromium films are investigated. An in situ photography technique with a nanosecond time resolution is employed. This experiment shows the transient topography changes of a thin chromium film irradiated by a pulsed Nd:YLF laser with a 20-nsec pulse width. A numerical code is used to calculate the transient velocity and temperature fields and free surface motion. Results of experimental and numerical work are used to analyze the possible mechanisms of droplet formation.

2 Experimental Study

A parametric study ([5]) was performed on laser machining of thin chromium films deposited on glass substrates. Topography changes and debris formation patterns induced by a pulsed Nd:YLF laser were investigated. A narrow range of energy density levels was found in which debris-free surface structures could be obtained. This energy range lies between a threshold for hole formation at low energy, and a threshold for droplet formation. At low pulse energy, above the threshold for hole formation, the pulse energy is large enough that surface-tension gradients induce hole opening. As pulse energy increases, radial flow becomes rapid enough that inertial effects dominate and cause droplets to separate from the molten pool. A summary of the resulting topography changes and droplet formations resulting from 20-nsec pulses focused to a 9.5-μm radius is shown in the microphotographs in Fig. 2. A debris-free 7.5-μm diameter hole created in the chromium film by a 0.95-μJ pulse is shown in Fig. 2(*a*). Increasing pulse energy to 1.6 μJ resulted in a 10-μm hole diameter and formation of droplets. At this energy level the holes are still relatively clean since few droplets are formed; however, increasing the energy further increases the number of droplets. This is seen in Fig. 2(*c*) for an 11-μm hole created by a 2.0-μJ laser pulse. Figure 2(*d*) again shows an increased number of droplets for a 13-μm hole resulting from a 2.7-μJ pulse. This pattern continues as energy increases, and the droplets become uniformly dispersed around the outer edge of the hole, as seen in Fig. 2(*e*) for a 15-μm hole created by a 3.6-μJ pulse. Atomic Force Microscopy verified that the surface deformations seen in Fig. 2 are holes. The holes created by 0.9 and 2.1-μJ pulses are shown in Fig. 3. The 0.9-μJ pulse energy is just above the threshold for hole formation, and the resulting hole is asymmetric. However, the hole does show that material is displaced to the outer edge of the hole and built up around the edges due to the surface-tension-driven flow as illustrated in Fig. 1. The 2.1-μJ pulse energy shows a similar pattern with improved symmetry. Power densities in this study are on the order of 62 MW/cm^2 for the highest energy used. No plasma is formed at the highest laser power density.

An in situ photography technique, the stop action photography, is developed to capture the transient melting and fluid flow processes ([5]). The experimental diagram is shown in Fig. 4. A pulsed nitrogen laser pumped dye laser with a visible wavelength of 600 nm and pulse width of 2.5 nsec was used to illuminate the surface of the specimen. The dye laser illuminates the specimen through a long working distance microscope objective system, which magnifies the specimen surface by 400x. Both the dye laser and the Nd:YLF laser are triggered by a pulse-delay generator. The delay between the two laser pulses is controlled by the pulse-delay generator, such that the dye laser is triggered after the Nd:YLF laser and exposes the film at the desired time. A 35-mm camera captures the illumination of the dye laser and stops the motion of the fluid on film. A 600-nm filter with a 40-nm bandwidth is placed in front of the camera to remove any light from sources other that the nitrogen laser pumped dye laser. This elimi-

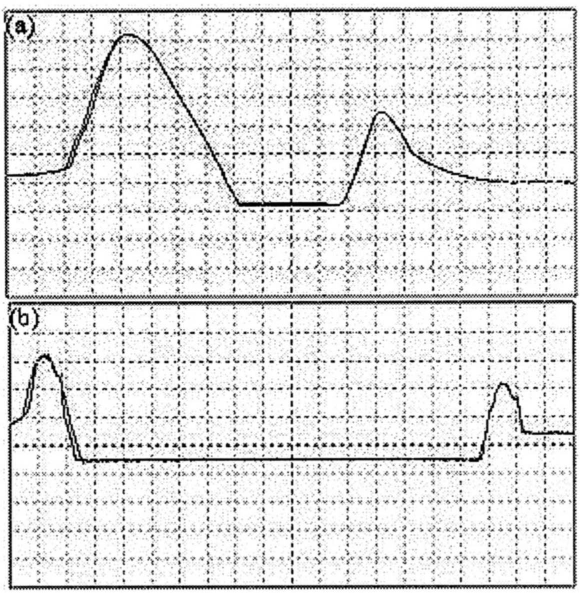

Fig. 3 AFM results: (*a*) 0.9 μJ pulse. Vertical scale is 0.4 μm/div., horizontal scale is 0.86 μm/div. (*b*) 2.1 μJ pulse. Vertical scale is 0.3 μm/div., horizontal scale is 1.1 μm/div.

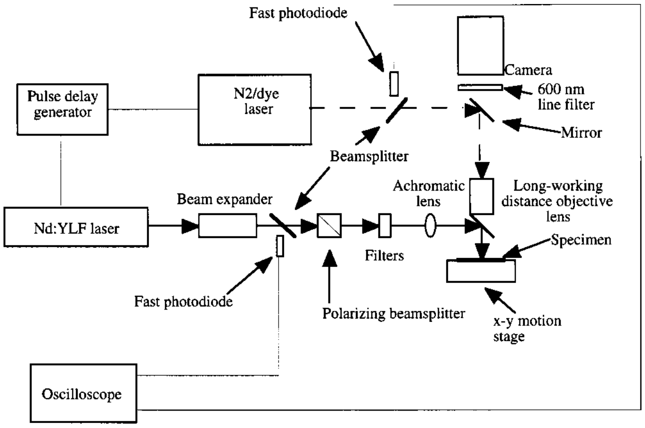

Fig. 4 Experimental diagram of stop-action photography

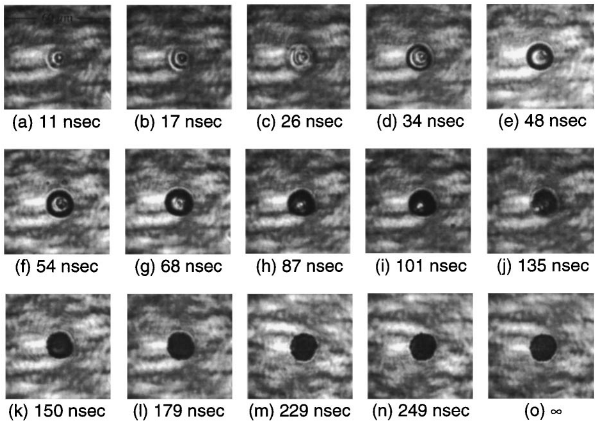

Fig. 5 Transient micrographs of 0.3-μm chromium film irradiated by 2.0-μJ 20-nsec laser pulses. Indicated time is with respect to the beginning of the laser pulse at $t=0$.

nates infrared light from the Nd:YLF laser that is reflected from the specimen surface, and thermal emission from the specimen surface and hot vapor. Only one photograph can be taken of each hole resulting from a laser pulse, therefore many photographs were taken at each pulse energy level and trigger delay setting. The experiments were repeatable, and the photos shown are representative of the results of several experiments at each delay time. The actual delay is measured by two fast photodiodes, and corrections are made for differences in optical path lengths and times for signals to reach the oscilloscope through cables. The measured delay is between laser peaks by approximating temporal distributions of the lasers as triangles. Two photographs are taken of each hole, one in situ, and the other several seconds after the laser pulse has ended (∞). Comparison of the two photographs allows the determination of the time at which changes in the hole geometry have ended. The 35-mm camera views an area of approximately $250\times250\ \mu$m, which limits the resolution of the optical system since only a small area of approximately $60\times60\ \mu$m is of interest in experiment. Only enlargements of the area of interest are presented.

The stop action photography is performed for 20-nsec full-width half-maximum (FWHM) laser pulses incident on 0.3-μm chromium films deposited by DC sputtering in ultrahigh vacuum. The focused laser radius is again 9.5 μm. The parametric study (Fig. 2) showed that randomly dispersed droplets were created around the outer edge of the hole for the 1.6, 2.0, and 2.7-μJ pulses, with the number of droplets increasing with pulse energy. The 3.6-μJ pulse increased the number of droplets and scattered them further away from the edge of the hole as seen in Fig. 2(*e*). The in situ photographs for a 2.0-μJ experiment are shown in Fig. 5. Surface deformation within the laser-irradiated zone is seen at 11 nsec. The deformed region within the laser-irradiated zone undergoes a rapid change between 17 and 34 nsec as shown in Figs. 5($b-d$). There is also a central region which has a higher reflectivity than the rest of the deformed area, Figs. 5($d-j$). This central region decreases in brightness with time until it is not visible in the 150-nsec photo in Fig. 5(*k*). The explanation for the high reflectivity spot is that the surface tension gradient is lower near the center of the laser-irradiated zone than it is near the outer edge of the laser-irradiated zone. Therefore, the center area of the irradiated zone does not begin to flow as early as the outer region. As time progresses, the flow pulls the chromium away from the center of the molten pool, leaving only glass in the center and thus decreasing the reflectivity. After 249 nsec no changes are seen in the surface geometry, indicating that the surface deformation process is complete. The final hole diameter is approximately 11 μm. Note that the photographs taken by the stop action photography (Fig. 5) have slightly poorer spatial resolution than those taken under an optical microscope after the process is complete (Fig. 2). Individual droplets are not clearly seen in Fig. 5.

Photographs of the transient surface topography resulting from 2.7-μJ laser pulses are shown in Fig. 6. Surface deformation is visible at 14 nsec and the hole size increases little after this time. Similar to the 2.0-μJ experiment, a central high reflectivity spot appears within the laser-irradiated zone that dissipates in brightness with time. The modified area becomes distorted at the outer edge between 98 and 184 nsec. This is the unstable fluid flow leading to the formation and separation of droplets. This distortion is due to scattering of light by droplets in all directions, making less light incident on and reflected off the target. This results in a blurring effect, making the holes appear larger, thus the final holes are smaller when compared to those in the intermediate times. Thermal lensing may also contribute to this blurring, but it only affects the very vicinity of the hole since the heat-affected zone, on the order of 1 micron, is much smaller than the blurred area. Individual droplets become visible in the photograph at 184 nsec. After 283 nsec no changes are seen in the hole diameter or droplet patterns surrounding the hole, indicating that the surface modification process is complete. The final hole diameter is approximately 13 μm.

Photographs of the transient surface topography induced by 3.6-μJ laser pulses are shown in Fig. 7. Surface deformation is seen at 14 nsec followed by expansion of the deformed area until 25 nsec. A central high reflectivity spot, similar to those seen in

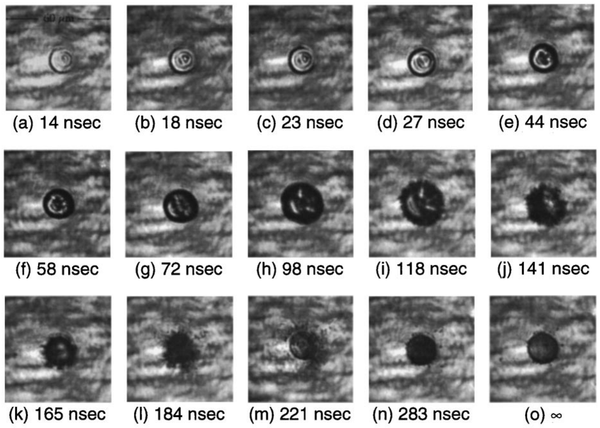

Fig. 6 Transient micrographs of 0.3-μm chromium film irradiated by 2.7-μJ 20-nsec laser pulses. Indicated time is with respect to the beginning of the laser pulse at $t=0$.

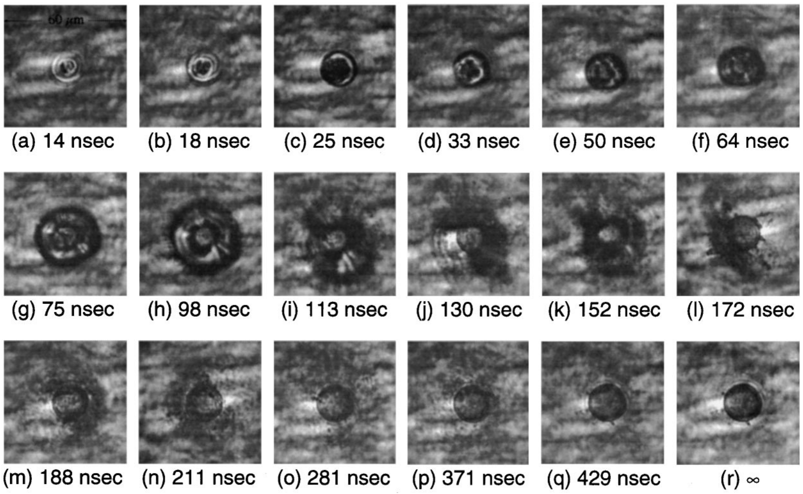

Fig. 7 Transient micrographs of 0.3-μm chromium film irradiated by 3.6-μJ 20-nsec laser pulse. Indicated time is with respect to the beginning of the laser pulse at $t=0$.

Figs. 5–6, is also seen in the photographs at 3.6 μJ, but this bright spot diminishes after 50 nsec. Similar to the previous experiments, the outer edge becomes distorted from 64 to 152 nsec due to the separation of droplets from the edge of the hole. Changes in the surface topography continue much longer in this experiment, and droplets are not seen until 281 nsec, as seen in Fig. 7(*o*). The flow has ceased at 429 nsec since no changes in the surface topography are seen after this time. The final hole diameter is approximately 15 μm.

The three in situ experiments presented here all indicate melting within the first 20 nsec of the laser pulse, with rapid hole expansion while the laser pulse is incident on the surface. Fluid flow is observed long after the laser pulse is completed at 40 nsec and lasts for over 250 nsec. Solidification time increases with increasing pulse energy, ranging from approximately 249 nsec for a 2.0-μJ pulse, to about 429 nsec for a 3.6-μJ pulse. The experiments show rapid flow development and droplet formation *after* the end of the laser pulse. The flow lasts longer with increasing pulse energy.

3 Numerical Modeling

A numerical model of the pulsed laser surface modification process is developed. The energy transfer and fluid flow induced by the laser irradiation are governed by the mass, momentum, and energy conservation equations

$$\nabla\cdot\mathbf{v}=0 \tag{3}$$

$$\rho\frac{\partial\mathbf{v}}{\partial t}+\rho(\mathbf{v}\cdot\nabla)\mathbf{v}=-\nabla p+\nabla(\mu\nabla\cdot\mathbf{v}) \tag{4}$$

$$\rho\frac{\partial h}{\partial t}+\rho(\mathbf{v}\cdot\nabla h)=\nabla\cdot\left(\frac{k}{c_p}\nabla h\right)+Q \tag{5}$$

In these equations, $\mathbf{v}$ is the velocity vector, p the pressure, and h the enthalpy. The thermophysical properties ρ, μ, k, and c_p are, respectively, the density, viscosity, thermal conductivity, and specific heat. The enthalpy method ([7]) is employed in the energy equation, Eq. (5), to calculate the solid-liquid phase change. Phase transition in the glass substrate is neglected, and flow of the softened glass is neglected due to its high viscosity. The volumetric heating term Q is used to describe the nonuniform absorption of the laser energy in the target, since the laser energy is absorbed exponentially along the optical axis, and is Gaussian in distribution along the radius of the laser beam. The absorption of laser energy is modeled as instantaneous heating with a triangular temporal distribution of 20 nsec (FWHM). Therefore, the entire length of the laser pulse is 40 nsec. The absorbed laser energy is estimated by calculating the reflectivity of chromium at the laser wavelength, which is calculated from the complex index of refraction of chromium to be 63 percent.

At the surface of the laser melted region, fluid flow is induced due to the tangential forces of the surface tension gradient created by the temperature gradient along the free surface. Therefore, the boundary condition at the free surface in the tangential direction is expressed as

$$\mathbf{t}\cdot\tau=\mathbf{t}\cdot\nabla\gamma+(\mathbf{t}\cdot\nabla T)\frac{\partial\gamma}{\partial T}=\mu\mathbf{n}\cdot\nabla(\mathbf{v}\cdot\mathbf{t}) \tag{6}$$

The boundary condition normal to the free surface is the balance between the normal component of the surface traction vector and the surface tension forces due to the curved free surface and the pressure

$$\mathbf{n}\cdot\tau=-\frac{\gamma}{R_c}-p_r \tag{7}$$

where R_c is the radius of curvature, p_r is the recoil pressure, and γ is the surface tension. The equation that governs variations of the free surface with time is given by

$$\frac{\partial\Sigma}{\partial t}+\mathbf{v}\cdot\nabla\Sigma=0 \tag{8}$$

where Σ is the free surface geometry.

At the free surface, the recoil pressure is related to surface temperature by the kinetic theory ([8]) as

$$p_r=p_o\exp\left\{\frac{\Delta H_{lv}(T-T_{lv})}{RTT_{lv}}\right\} \tag{9}$$

The molar mass flux, $\overline{j_v}$ due to evaporating atoms at the free surface is given by ([8])

$$\overline{j_v}=Ap_r(2\pi MRT)^{-1/2} \tag{10}$$

and this molar mass flux is related to the thermal boundary condition at the evaporating surface as

$$k_l\nabla T=-\Delta H_{lv}\overline{j_v}\,. \tag{11}$$

Equations (9)–(11) are used as boundary conditions for the energy equation. p_o is the atmospheric pressure, ΔH_{lv} is the enthalpy of vaporization, T_{lv} is the equilibrium boiling temperature, T is the

Table 1 Thermophysical properties of chromium ([10,18–22])

Melt Temperature	2133 K	Enthalpy of Fusion	16.933 kJ/mol
Equilibrium Boiling Temperature	2953 K	Enthalpy of Vaporization	344.3
Refractive Index @ $\lambda=1.047\ \mu$m	$4.52+i4.29$	Molar Weight	52.01 kg/kmol
Activation Energy	$E=55$ kJ/mol	Density	7100 kg/m^3
Viscosity at Melt Temperature	$\mu=0.000684$ kg/m·sec		
Surface tension	$\gamma=1.700-0.00032(T-T_m)$ N/m		
Thermal Conductivity	$k=69.9+0.15979T-0.0004212T^2+3.9265\times10^{-7}T^3-1.5974\times10^{-10}T^4+2.4025\times10^{-14}T^5$ W/m·K		
Specific Heat	$c_p=236.23+1.0788T-0.0015052T^2+9.7379\times10^{-7}T^3-1.8628\times10^{-10}T^4$ J/kg·K		

surface temperature, and R is the universal gas constant. In Eq. (10), A is a ''sticking coefficient,'' which is the fraction of vapor particles hitting the surface that stick to it. For metals, the value of A is approximately unity ([8]).

Boundary conditions at the far field are given by

$$\mathbf{v}=0 \tag{12}$$

$$\nabla T=0. \tag{13}$$

A no-slip boundary condition is used at the chromium/glass interface, because the dynamics of three-phase interface is not well known and thus not considered in this work. Numerical calculations are carried out using the computational fluid dynamics code, FIDAP (Fluent Inc., Lebanon, NH). The system is modeled as two-dimensional axisymmetric due to the symmetry of the incident laser beam. Thermophysical properties used in the simulations are listed in Table 1. Whenever possible, temperature-dependent material properties are used. The temperature dependence of viscosity is modeled as an Arrenhius relationship given by ([9,10])

$$\mu=\mu_o \exp(E/RT) \tag{14}$$

where μ_o is a reference viscosity which is normalized such that Eq. (14) results in the viscosity at the melting temperature given in Table 1 when the melting temperature is used in Eq. (14). E is the activation energy and is estimated by ([9])

$$E=0.431T_m^{1.348} \tag{15}$$

The surface tension data are for pure chromium obtained from Brandes and Brook [10]. The original values are from Allen ([11,12]) which were measured at the melting temperature ([11]) and calculated for higher temperatures ([12]). The surface tension of metals that have been exposed to atmospheric conditions will have chemically active surface impurities such as oxygen and sulfur. It has been reported that these surface active impurities will alter the surface tension significantly, such that the surface tension can actually increase at temperatures slightly above the melting temperature ([13–15]). Bostanjoglo and Nink [16] and Balandin et al. [2] reported that the effect of an increased surface tension above the melting point in metals during laser melting of thin films could cause thickening of the thin film at the center of the laser spot. Therefore, the effect of oxidation could be significant.

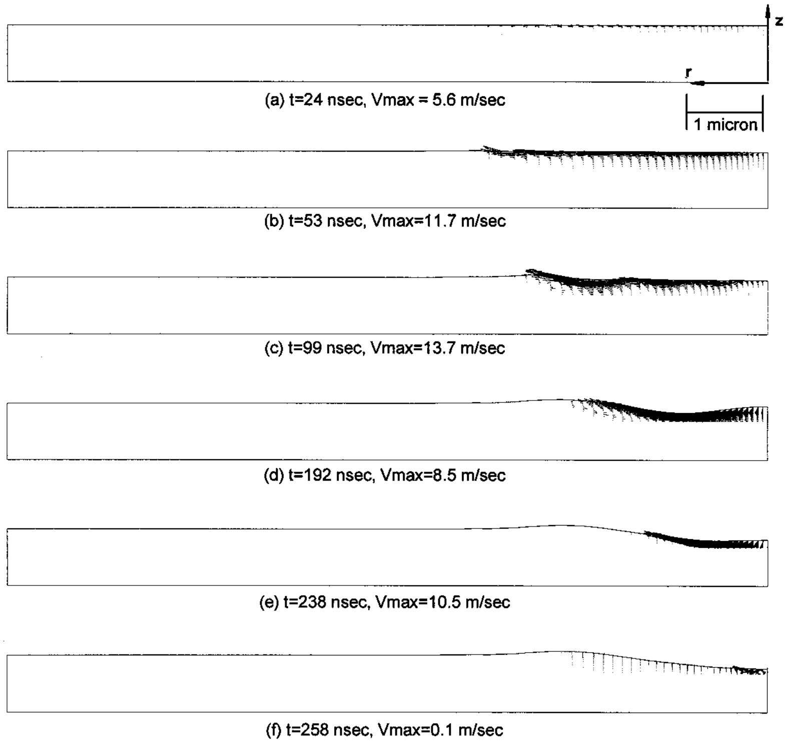

(a) t=24 nsec, Vmax = 5.6 m/sec

(b) t=53 nsec, Vmax=11.7 m/sec

(c) t=99 nsec, Vmax=13.7 m/sec

(d) t=192 nsec, Vmax=8.5 m/sec

(e) t=238 nsec, Vmax=10.5 m/sec

(f) t=258 nsec, Vmax=0.1 m/sec

Fig. 8 Calculated transient velocity field of a 0.3-μm chromium film irradiated by a 2.0-μJ, 20-nsec laser pulse

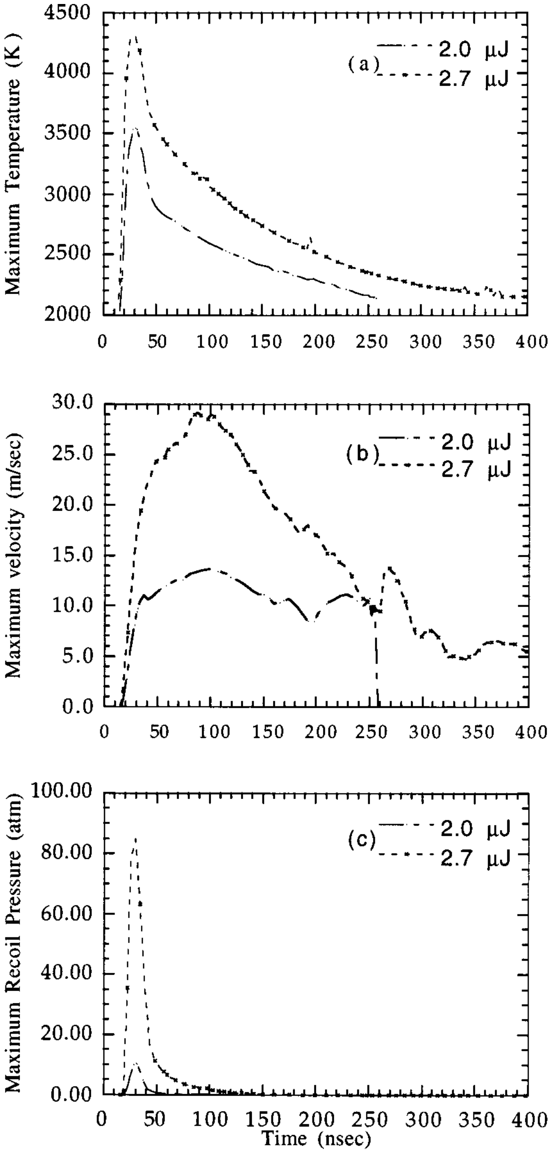

Fig. 9 Transient (*a*) center node temperature, (*b*) maximum velocity, and (*c*) center node recoil pressure of 0.3-μm chromium film irradiated by 2.0 and 2.7-μJ 20-nsec pulses

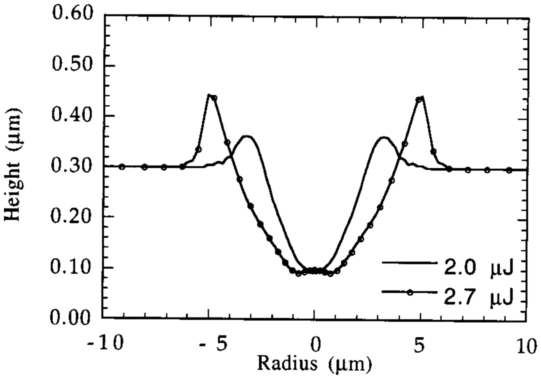

Fig. 10 Final surface topography of 0.3-μm chromium film irradiated by 2.0 and 2.7-μJ 20-nsec incident laser pulses

However, for chromium with oxygen and sulfur impurities, the only experimental data in literature shows a negative temperature coefficient ([17]). Therefore, only a negative temperature coefficient of surface tension is considered in the simulation.

Calculations are performed for incident laser pulse energies of 2.0 and 2.7 μJ with 20 nsec pulse width (FWHM) and a radius of 9.5 μm incident on a 0.3 μm chromium film. A domain with a radius of 12 μm and axial depth of 0.9 μm is used. The axial depth consists of the 0.3-μm thin chromium film and a 0.6-μm glass substrate. The glass substrate is much thinner than that used in the experiments; however, the thermal penetration depth into the glass is very small within the time period of interest, approximately 0.13 μm. Due to the same reason, the domain size in the radial direction, 12 μm, is large enough to contain the temperature and fluid field development. The grid size of the thin film is 60 nodes in the radial direction and 12 nodes in the axial direction. A grid independence study is performed for the 2.0 μJ, 20 nsec laser pulse by varying the number of grids in the radial direction. Grid sizes of 60×12 and 80×12 were tested and little differences were found. The Quasi-Newton (Broyden's update) method is used to solve the system of nonlinear equations. Time integration is performed by the backward Euler method. Approximately 200 hours of CPU time is required to complete each simulation on a Hewlett Packard 715/50.

The transient velocity field resulting from a 2.0 μJ pulse is plotted as a half-domain in Fig. 8, with the z-axis as the axis of symmetry. The velocity field begins to develop on the thin melted surface layer halfway into the laser pulse, seen at 24 nsec in Fig. 8(*a*), and flows away from the center of the irradiated area due to the surface tension gradient along the free surface. The flow accelerates to 11.7 m/sec at a time of 53 nsec in Fig. 8(*b*), and the velocity peaks at 13.7 m/sec at 99 nsec, and decreases slowly after this time. The velocity is still well developed with a maximum velocity of 8.5 m/sec at a time of 192 nsec, as seen in Fig. 8(*d*). At 238 nsec, the maximum velocity has actually increased when the location of the maximum velocity is moving toward the center of the irradiated zone. The size of the velocity field has decreased significantly since the molten pool is solidifying. The maximum velocity decreases rapidly until it is almost zero at 258 nsec, as seen in Fig. 8(*f*). Note that the fluid flow field does not develop until after the laser pulse has ended (40 nsec) and topography development occurs long after the laser pulse has ended. This can be seen in Figs. 8(*c–f*). These results compare well with the experimental results. The experimental study showed droplets outside of the holes, resulting from the high velocity radial flow away from the center of the molten pool. (This will also be discussed in Section 4.) The numerical results also correlate well with the in situ photography experiment, which showed flow development during the later half of the laser pulse, and rapid changes in the laser-irradiated area after completion of the laser pulse. The numerical model also shows that the center of the laser-irradiated zone will be thicker than the remaining modified area early in the process because the surface tension gradient is the lowest there, resulting in the lower velocity fluid flow.

The transient maximum temperature, velocity, and recoil pressure are plotted in Figs. 9(*a*), (*b*), and (*c*), respectively, for the 2.0 and 2.7-μJ laser pulses. The maximum temperature is reached at approximately 30 nsec, however, the fluid flow in the molten pool is still accelerating at this time for both laser energy levels. Figure 9(*b*) shows that the velocity continues to increase long after the end of the laser pulse. Note that the radial velocity in the molten pool increases rapidly when pulse energy increases, increasing inertial effects. Recoil pressure peaks at the same time as the maximum temperature (see Eq. (9)), and is only significant during the first 60 nsec of the process. Figure 8 shows that the topography of the free surface developed long after the laser pulse ended, therefore, it is unlikely that recoil pressure contributes significantly to the process. This is due to the fact that the topography development occurs long after the laser pulse has ended, while the recoil pressure is negligible after 50–60 nsec. In order to determine if recoil pressure has an impact on the results, simulations are performed with and without the recoil pressure term in Eq. (7) for both 2.0 and 2.7-μJ laser pulses. Due to the time required to perform a simulation with a temperature-dependent viscosity, the tests are performed using a constant viscosity. The results of the simulations show no changes in the transient velocity field or in the final surface topography. It is thus concluded that surface tension dominates the fluid flow, and that the recoil pressure has no significant influence on the processes studied in this work.

Plots of the final surface topography are shown in Fig. 10 for 2.0 and 2.7-μJ 20-nsec incident laser pulses. The 2.0-μJ pulse results in a hole that is approximately 8 μm in diameter and 0.2 μm deep. The 2.7-μJ pulse results in a hole that is approximately 12 μm in diameter and 0.2 μm deep. These diameters are smaller than the experimental values of approximately 11 μm for the 2.0-μJ pulse, and 13 μm for the 2.7-μJ pulse. The differences between the experimental and numerical hole sizes could be attributed to limitations of the numerical model. One of the limitations of the model is the limited knowledge of material properties. This is because thin film thermal properties and high-temperature thermal properties are not well known. The current model uses bulk material properties that are linearly extrapolated for high temperatures. Another limitation of the model is that the density change from the solid to liquid phase is not accounted for, which may affect the surface topography and the velocity field development.

4 Instability of the Laser-Induced Fluid Flow

The results of the experimental and numerical studies are used to analyze the instability mechanisms and droplet formation in the laser-induced molten pool. Although flow instabilities and droplet formation are not simulated due to their three-dimensional nature, the results of the two-dimensional model can be used to obtain acceleration data for an order of magnitude estimation. The calculations for the 2.0 and 2.7-μJ pulses predict maximum flow accelerations of approximately $3.53\times10^{8}\,\mathrm{m/sec}^{2}$ and $1.29\times10^{9}\,\mathrm{m/sec}^{2}$, respectively. Replacing the gravitational acceleration term in Eq. (1) with these acceleration values gives critical wavelengths of approximately 5.5 μm for the 2.0-μJ pulse and 2.9 μm for the 2.7-μJ pulse. These values are on the same order of magnitude as the molten pool diameter in the present study, therefore, perturbation in the molten pool can lead to a Rayleigh-Taylor instability development. Growth of such an instability could lead to a wavy surface, allowing droplets to initiate from the peaks of the waves. Inspection of Figs. 2(*d–e*) shows that the ridges of material around the holes have a wavy pattern, and Fig. 2(*e*) shows droplets connected to the peaks of the wavy ridge.

For the Kelvin-Helmholtz instability, if gravitational acceleration is used, Eq. (2) predicts flows to be stable for relative velocities less than 24 m/sec, which is on the same order of the calculated maximum velocity. However, the critical wavelength is on the order of 33 mm, much larger than the domain of interest in this study. On the other hand, if acceleration of the melt is used in Eqs. (1)–(2), the critical wavelength will decrease to the order of several microns; however, the relative velocity below which the flow is stable increases to values over 1000 m/s, much higher than the velocities encountered in the present study. Therefore, it is unlikely that the Kelvin-Helmholtz instability is present in the process.

The microphotographs of the laser-irradiated surface shown in Fig. 2 show droplets outside the edge of the holes. Numerical simulations and in situ photographs suggest that these droplets are due to the high radial flow velocity moving fluid away from the center of the molten pool after the laser pulse has ended. Droplets may form when the high velocity flow gains enough inertia to overcome the surface tension forces which hold the fluid together, allowing material to shear away from the ridge built up at the outer edge of the holes. The Weber number is a nondimensional ratio of inertial forces to surface tension forces and is defined as

$$\mathrm{We}=\frac{\rho_1 v^2 L_c}{\gamma} \tag{16}$$

where v is the velocity, γ is the surface tension, and L_c is a characteristic length scale. Since resolutions of the current in situ experimental techniques are not good enough to measure the melt velocity, the calculated velocity values are used to estimate the Weber number. A value of 0.5 μm is used for the characteristic length, which is approximately the diameter of the droplets measured by SEM. For the 2.0-μJ simulation, a maximum velocity of 13.7 m/sec is achieved, and the Weber number is calculated to be approximately 0.34, which indicates that surface tension forces dominate. The Weber number for the 2.7-μJ simulation is calculated to be 1.56 at a maximum velocity of 29.1 m/sec, indicating that inertial forces dominate. These calculations of the Weber number correlate well with experiments, which show that a large increase of the number of droplets occurs when the laser pulse energy varies from 2 to 2.7 μJ.

5 Conclusions

Fluid flow and droplet formation occurring in a pulsed laser thin film interaction have been studied. Experimental in situ photography of the process shows rapid fluid flow after completion of the laser pulse with evidence of flow instability at the outer edges of the melted region. Results of a numerical model including the flow development and total time duration correlate well with experimental results. Instability analysis shows that the critical instability wavelength is smaller than the molten pool. Thus, perturbations in the molten pool larger than the critical wavelength may lead to instability development. The calculated Weber number also correlated well with droplet formation. It is concluded that the fluid flow and droplet formation are due to the surface-tension-driven flow, and the recoil pressure due to surface evaporation plays a minor role in the laser fluence range used in the work.

Acknowledgment

Support for this work by the National Science Foundation (CTS-9624890) and by the IBM Shared University Research Program are gratefully acknowledged. The authors also wish to thank Mr. Stephen Montgomery of the Ray W. Herrick Laboratories Atomic Force Microscopy Center at Purdue University for performing Atomic Force Microscopy measurements.

Nomenclature

A = sticking coefficient
c_p = specific heat
E = activation energy
G = gravitational acceleration
H = enthalpy
$\bar{j}_v$ = molar mass flux
k = thermal conductivity
L_c = characteristic length scale
M = molar weight
$\mathbf{N}$ = surface normal vector
P = pressure
P_r = recoil pressure
p_o = ambient pressure
Q = volumetric heat generation
R = universal gas constant
R_c = radius of curvature
$\mathbf{T}$ = surface tangential vector
T = temperature
T_{lv} = equilibrium boiling temperature
T_m = equilibrium melting temperature
$\mathbf{V}$ = velocity vector
V = velocity
We = Weber number

Greek Symbols

ΔH_{lv} = enthalpy of vaporization
Σ = free surface geometry
γ = surface tension
Λ_c = critical instability wavelength
ρ = density
τ = surface traction vector
μ = viscosity

Subscripts

1 = underlying fluid
2 = overlying fluid
l = liquid
s = solid

References

[1] Brailovsky, A. B., Gaponov, S. V., and Luchin, V. I., 1995, ‘‘Mechanisms of Melt Droplets and Solid-Particle Ejection From a Target Surface by Pulsed Laser Action,’’ Appl. Phys. A: Mater. Sci. Process., **61**, pp. 81–86.

[2] Balandin, V. Yu., Otte, D., and Bostanjoglo, O., 1995, ‘‘Thermocapillary Flow Excited by Focused Nanosecond Laser Pulses in Contaminated Thin Liquid Iron Films,’’ J. Appl. Phys., **78**, No. 3, pp. 2037–2044.

[3] Dimitrov, D. A., 1995, ‘‘Some Observations on Laser Trimming Platinum Thin Films,’’ Platinum Met. Rev., **39**, No. 3, pp. 129–132.

[4] Bennett, T. D., Krajnovich, D. J., Grigoropoulos, C. P., Baumgart, P., and Tam, A. C., 1997, ‘‘Marangoni Mechanism in Pulsed Laser Texturing of Magnetic Disk Substrates,’’ ASME J. Heat Transfer, **119**, pp. 589–596.

[5] Willis, D. A., Xu, X., Poon, C. C., and Tam, A. C., 1998, ‘‘Laser-Assisted Surface Modification of Thin Chromium Films,’’ Opt. Eng., **37**, No. 3, pp. 1033–1041.

[6] Chandrasekhar, S., 1961, *Hydrodynamic and Hydromagnetic Stability*, Oxford University Press, London.

[7] Shamsundar, N., and Sparrow, E. M., 1975, ‘‘Analysis of Multidimensional Conduction Phase Change Via the Enthalpy Model,’’ ASME J. Heat Transfer, **97**, pp. 333–340.

[8] von Allmen, M., 1987, *Laser-Beam Interactions With Materials* (Springer Series in Materials Science 2), Springer-Verlag, Berlin, pp. 146–151.

[9] Grosse, A. V., 1963, ‘‘High Temperature Research,’’ Science, **140**, pp. 781–789.

[10] Brandes, E. A., and Brook, G. B., 1992, *Smithells Metals Reference Book*, 7th Ed., Butterworth-Heinemann, Oxford.

[11] Allen, B. C., 1964, ‘‘The Surface Tension of Liquid Chromium and Manganese,’’ Trans. Metall. Soc. AIME, **230**, pp. 1357–1361.

[12] Allen, B. C., 1972, ‘‘The Surface Tension of Liquid Metals,’’ *Liquid Metals, Chemistry and Physics*, S. Z. Beer, ed., Marcel Dekker, New York, pp. 161–212.

[13] Vitol, E. N., and Orlova, K. B., 1984, ‘‘The Surface Tension of Liquid Metals,’’ Russ. Metall., **4**, pp. 34–40.

[14] Tret'yakova, E. E., Baum, B. A., Tyagunov, G. V., Klimenkov, E. A., and Tsepelev, V. S., 1986, ‘‘Surface Tension of Molten Steel,’’ Russ. Metall., **4**, pp. 25–28.

[15] Filippov, K. S., 1992, ‘‘Density and Surface Tension of Iron and Fe-Cu-S Melts,’’ Russ. Metall., **1**, pp. 46–48.

[16] Bostanjoglo, O., and Nink, T., 1997, ‘‘Liquid Motion in Laser Pulsed Al, Co and Au Films,’’ Appl. Surf. Sci. , **109/110**, pp. 101–105.

[17] Chung, W. B., Nogi, K., Miller, W. A., and McLean, A., 1992, ‘‘Surface Tension of Liquid Cr-O System,’’ Mater. Trans., JIM, **33**, No. 8, pp. 753–757.

[18] Martynyuk, M. M., 1983, ‘‘Critical Constants of Metals,’’ Russ. J. Phys. Chem., **57**, No. 4, pp. 494–501.

[19] Barin, I., 1993, *Thermochemical Data of Pure Substances, Part I, Ag–Kr*, VCH, Weinheim, Germany, pp. 418–419.

[20] Incropera, F. P., and DeWitt, D. P., 1990, *Fundamentals of Heat and Mass Transfer*, 3rd Ed., John Wiley and Sons, New York, p. A3.

[21] Hunter, W. R., and Lynch, D., 1991, ‘‘An Introduction to the Data for Several Metals,’’ *Handbook of the Optical Constants of Solids II*, E. D. Palik, ed., Harcourt Brace Jovanovich, Boston, Part II, Subpart I, pp. 374–385.

[22] Boyer, H. E., and Gall, T. L., 1983, *Metals Handbook Desk Edition*, American Society for Metals, Metals Park, OH, p. 2.19.

Determination of Kinetic Energy Distribution in a Laser-Ablated Titanium Plume by Emission and Laser-Induced Fluorescence Spectroscopy

S. S. Chu

C. P. Grigoropoulos
e-mail: cgrigoro@me.berkeley.edu

Department of Mechanical Engineering,
University of California,
Berkeley, CA 94720

Pulsed laser deposition (PLD) of thin films has become a viable technique for a wide range of applications over the last few decades. As kinetic energy of the ablated plume is an important parameter in determining the quality of the film; consequently there is great interest in nonintrusive evaluation of the plume kinetic energy. Spectroscopic techniques such as optical time-of-flight (TOF) utilizes emission spectroscopy or laser-induced-fluorescence (LIF) and is an excellent method for this purpose since they offer temporal and spatial resolution as well as the capability of distinguishing different species. In this paper, the effects of laser fluence and background gas pressure on the kinetic energies of the ablated species are found by the optical time-of flight technique and by emission imaging. Laser-induced-fluorescence is employed for spectrally resolved imaging. The axial velocity of neutral titanium is found to be as high as 2×10^4 m/s. The distribution of species within the plume is also determined. [S0022-1481(00)01704-7]

Keywords: Ablation, Heat Transfer, Laser, Thin Films

Introduction

Pulsed laser deposition (PLD) is one among many thin film deposition techniques currently available. It works by exposing a source material to a high power laser that operates at about 20 ns per pulse. The energy delivered by the pulsed laser beam ablates a small amount of material from the target surface, and the ablated material is then deposited on a substrate placed opposite the target. PLD offers several distinct advantages over other deposition techniques. Since only a minute amount of film is deposited per laser pulse, varying the number of laser pulses used can easily control the thickness of the film. The nanosecond laser pulse delivers a great amount of energy to the source material in a short span of time thus making it more likely to deposit a multicomponent film that has the exact stoichiometry as the source. Furthermore, the vapor plume created by the short laser pulse is highly energetic. This enables lower temperatures to be used for the substrate and still form crystalline films ([1]). Additionally, the forward-peaking tendency of the velocity of the plume is excellent for bottom coverage of features with large aspect ratios. Titanium has been a material of great research interest since titanium based thin films have a great range of uses in microelectronic devices, optics, and tribology ([2–5]).

Kinetic energy of the ablated plume is a key parameter in determining the quality of the deposited film; consequently, there is a need to develop a technique quantifying the velocity of the plume propagation. Furthermore, it is important to know the spatial distribution of the plume since it directly relates to the thickness variation in the film. Spectroscopic methods offer great promise for these purposes because they are nonintrusive. With fast detectors, it is possible to obtain time-resolved spectroscopic information on the nanosecond scale. Furthermore, spectroscopic methods can effectively distinguish between different neutral and ionized species. This experiment employs a number of such techniques including emission optical time-of-flight, emission imaging, and laser-induced fluorescence imaging to investigate pulsed excimer laser-ablated titanium plumes.

Experimental Setup

Figure 1 shows the schematic of the experimental setup. The ablation source used in this experiment is a Lumonics Index 210 KrF ($\lambda = 248$ nm) excimer laser with a full width at half maximum (FWHM) pulse width of 20 ns. A tunnel-type homogenizer was used in the beam delivery system to eliminate hot spots and to improve the energy uniformity on the target surface. The focused spot size on the titanium target was $0.34\,\mathrm{mm}\times0.05\,\mathrm{mm}$ to yield fluences ranging from 3 to 8 J/cm^2. A polycrystalline titanium target of 99.99 percent purity was mounted inside a stainless steel high vacuum chamber on a rotational feedthrough rotating at 0.7 Hz in order to avoid deep drilling of the same location. The pressure inside the chamber was controlled between $<10^{-6}$ Torr to 20 Torr by filling the chamber with high purity (99.99 percent) argon.

The emission from the plume was detected by two different methods. Spectrally integrated and temporally gated images of the plume were captured via a Princeton Instruments ITE 576 intensified charge-coupled device (ICCD) camera with 576×384 pixels. Although the minimum gate width for this ICCD can be as short as 5 ns, a gate width of 10 ns was used to optimize the intensity while maintaining good temporal resolution. Since the majority of titanium line emission are in the UV range, a Nikkor 105 mm/f4.5 UV photo lens was used in conjunction with the ICCD. Spatial resolution of the combined imaging system was 100 μm, and the sensitive spectral range is between 300 and 850 nm. In order to synchronize the firing of the excimer laser and the delay in the gating of the ICCD, a Stanford Research DG535 programmable pulse generator with variable delay was used to trigger both the laser and the ICCD. The timing jitter of the imaging system was 3 ns under this configuration.

Spectrally resolved time-of-flight (TOF) data were acquired by projecting the plume by an 150 mm focal-length quartz UV lens

---

Contributed by the Heat Transfer Division for publication in the JOURNAL OF HEAT TRANSFER. Manuscript received by the Heat Transfer Division, Nov. 11, 1999; revision received, June 2, 2000. Associate Technical Editor: F. Cheung.

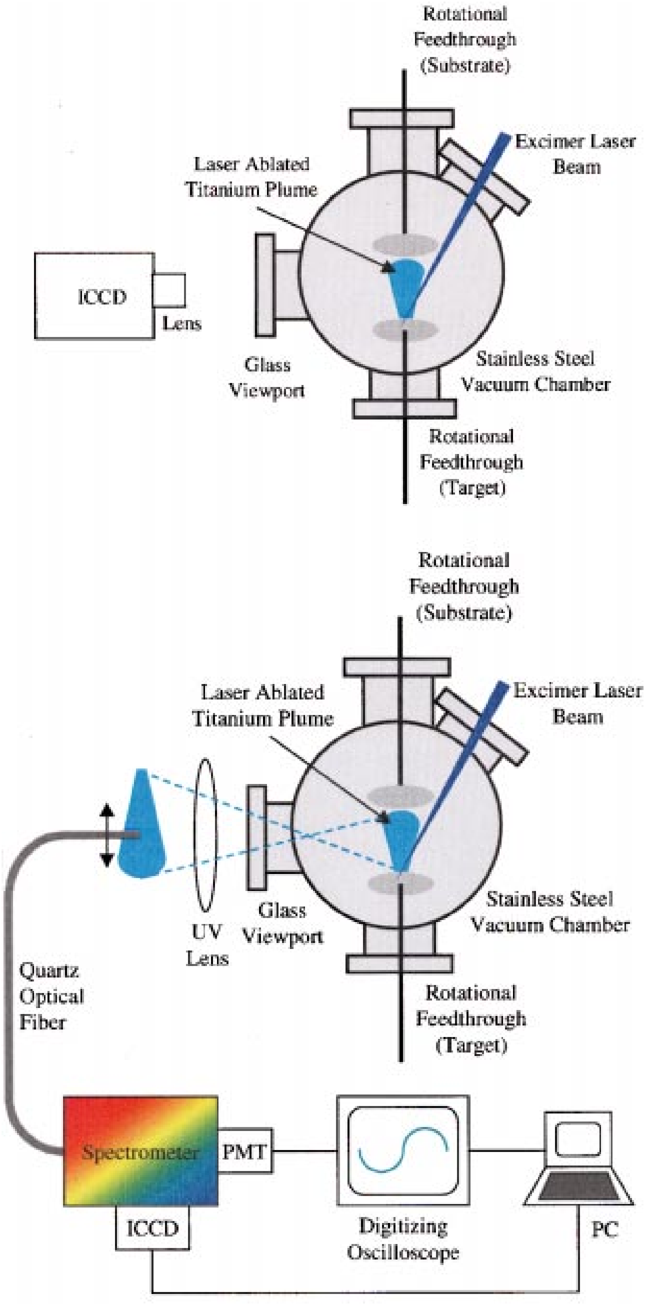

Fig. 1 Experimental setups for imaging plume emission and capturing emission lines

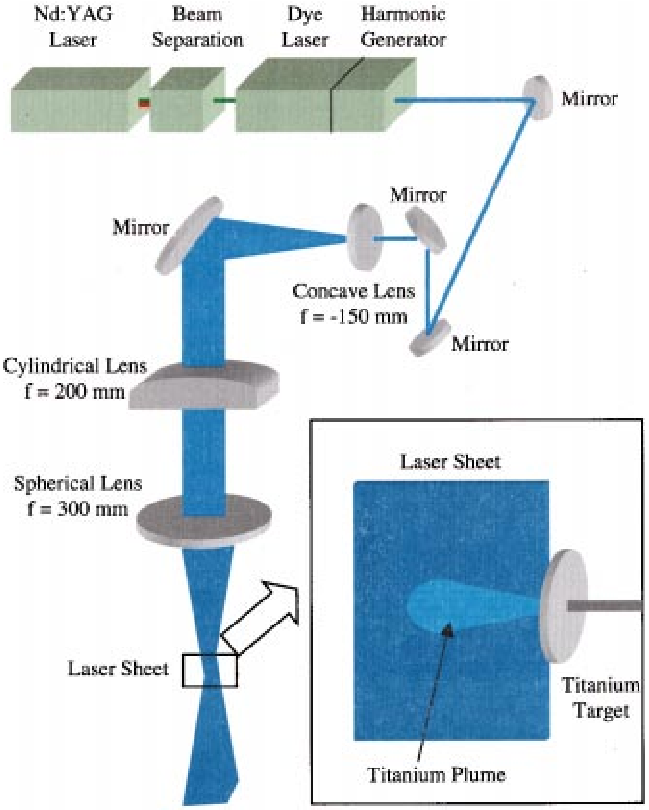

Fig. 2 Schematic of excitation laser setup. The output from the Nd:YAG laser contains both the fundamental (1064 nm) and doubled harmonic (532 nm). The fundamental portion is disposed in the beam separation package, and the remainder second harmonic is used to pump the dye laser. The vacuum chamber in which the titanium sample resides is omitted from this diagram.

to a magnification of 3.12 X. A fused silica optical fiber with 1.6-mm aperture was placed on the image plane and mounted on a micrometer stage so that different locations of the plume could be probed. The spatial resolution of this setup was 300 μm. The other end of the optical fiber was connected to a McPherson Model 2035 monochromator with a 1800 grooves/mm grating. The variable slits of the monochromator were adjusted so that the spectral resolution of the monochromator is 0.3 nm. The 399.86-nm emission line from neutral titanium was monitored. This emission line corresponds to $3d^24s^2a^3F^4 \rightarrow 3d^24s^14p^1y^3F^4_o$ transition. A Hamamatsu R928 photomultiplier tube (PMT) with 2.2 ns rise time was mounted on the exit slit of the monochromator to monitor the transient emission intensity from the plume. The PMT signals were digitized by a HP 54510 250 MHz digital oscilloscope and then downloaded to a PC. In order to enhance the signal-to-noise ratio, accumulations of 20 to 500 signals were taken for each data point.

A Continuum ND6000 Dye laser provided the excitation source for fluorescence generation. The dye laser was pumped by a Continuum Surelite II-10 Nd:YAG laser. The output of the dye laser was frequency-doubled by a KD*P crystal installed in a Continuum UVX Harmonic Generator, which produces the desired wavelength for creating fluorescence. A combination of UV optics were used to transform the laser beam into a sheet with a waist of approximately 0.25 mm. The width of the sheet was 25 mm, and the depth of focus was 5 mm. The dye laser sheet was aligned so that it passes through the centerline of the plume and covers the entire field-of-view of the ICCD camera, which was placed at 90 deg from both the target surface normal and the dye laser sheet to capture the image of the fluorescence. The dye laser was tuned to the excitation wavelength of 293.355 nm for the $3d^24S^2\,{}^3F_2 \rightarrow 3d^24s4p^3F_3 \rightarrow 3d^24s^2\,{}^3F_4$ transitions, and the fluorescence was observed at 296.722 nm. The experimental arrangement for laser-induced fluorescence is depicted in Fig. 2.

Results and Discussions

The typical lifetimes of titanium emission lines are on the order of several tens of ns ([6]). However, the emission was observed even 5 μs after the ablating laser pulse as seen in Fig. 6. The apparent discrepancy was due to the fact that the emission was a result of collisional excitation of titanium atoms and the subsequent release of photons when the excited atoms relax to lower energy states. As these collisional events are significant through

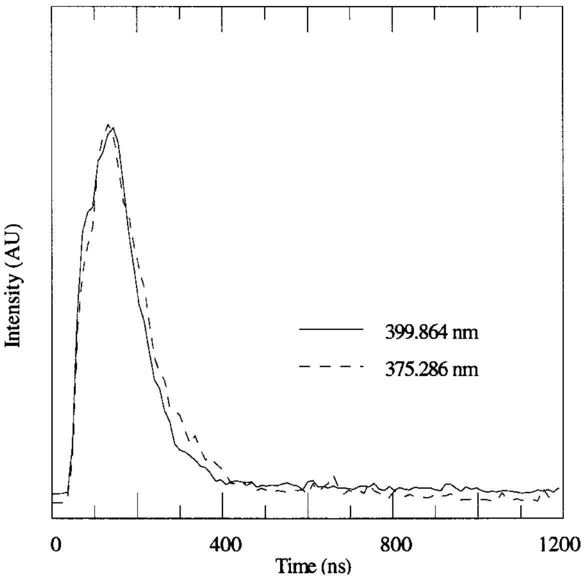

Fig. 3 Two representative TOF signals of neutral titanium. The signals for 375.286 nm and 399.864 nm are in excellent agreement.

the first few μs, the observable luminescence also persists. Two typical emission signals of neutral titanium as captured by a PMT at two strong emission lines of neutral titanium are shown in Fig. 3. The two signals were nearly identical proving that the TOF of neutral titanium is independent of the wavelength of the emission line monitored. The maximum emission intensity at a particular location in the plume corresponds to the peak concentration of titanium. The fluences used in this experiment were well above the ablating threshold and sufficient for the formation of a Knudsen layer ([7]). Hence, the intensity signal of the ablated titanium follows the full-range Maxwellian distribution ([8]).

X-t diagrams can be constructed by plotting location versus time corresponding to peak emission signal. The most-probable velocity is found by taking the slope of this curve. Figure 4 shows *x-t* curves for neutral titanium ablated by several different laser

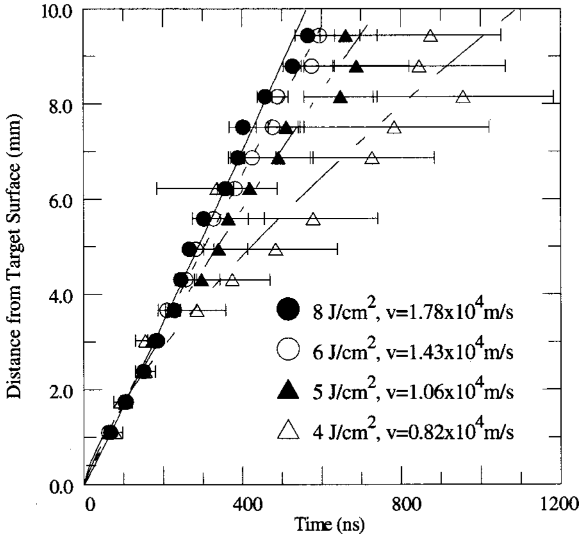

Fig. 4 Effects of laser fluence on the most probable centerline velocity of neutral titanium atoms in an expanding plume in vacuum. The velocities shown are average values over the measurement range.

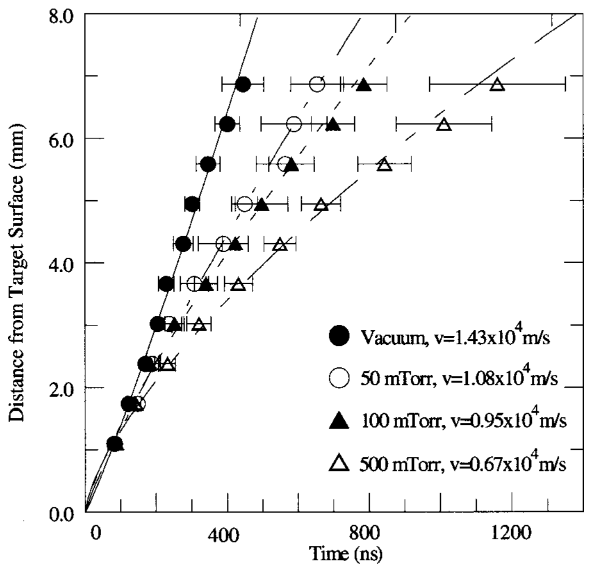

Fig. 5 Effects of background Ar pressure on the most-probable centerline velocity of neutral titanium atoms in the plume. $\phi = 7$ J/cm^2. The velocities shown are average values over the measurement range.

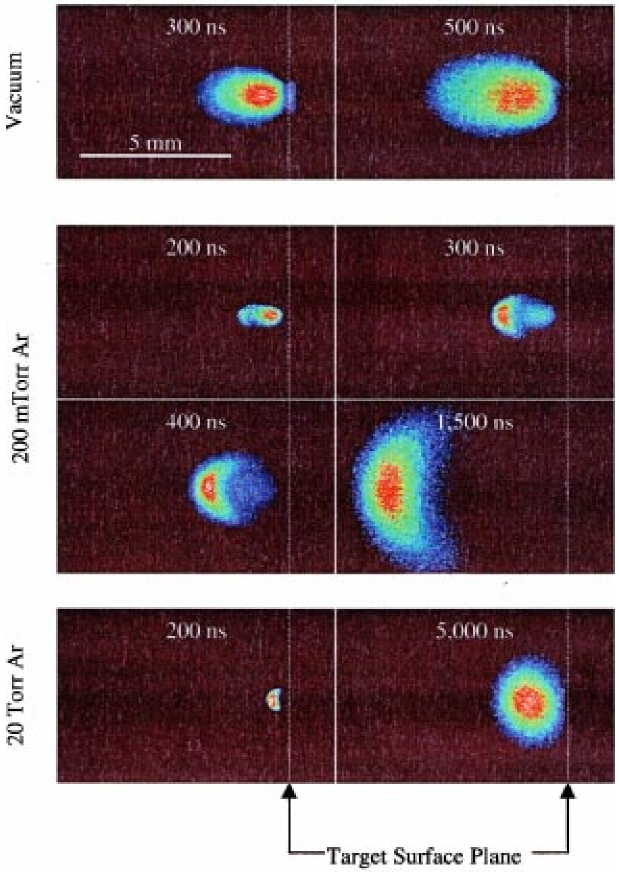

Fig. 6 Temporally resolved emission images of laser ablated titanium plume. Images are shown in normalized pseudocolor according to intensity.

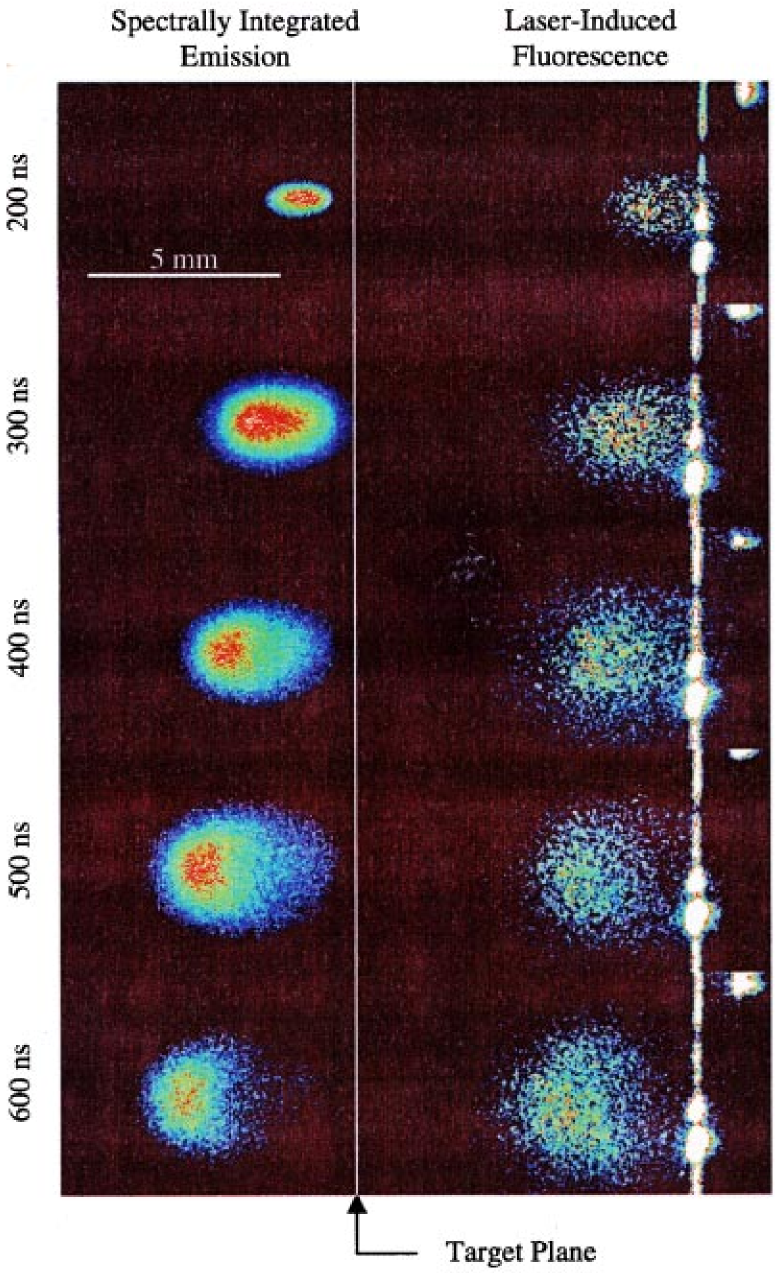

Fig. 7 Normalized pseudocolor PLIF images at $\lambda_{\text{fluorescence}}=296.355$ nm juxtaposed to emission images. The bright streaks in the PLIF images are reflections off the titanium target surface. The vacuum chamber is back filled with Ar at 100 mTorr. $\phi=3$ J/cm^2.

fluences under vacuum. Since x is the distance above the target surface on the centerline of the plume, the velocities derived are the axial centerline velocities. Collisions occur in the laterally expanding plume; therefore the centerline velocity can be expected to decrease with time and distance. The decrease in centerline velocity is more significant for the lower fluence as shown in Fig. 4. The effects of the background argon pressure on the centerline velocity are shown in Fig. 5 for a fluence of 7 J/cm^2. The background pressure suppresses plume expansion and consequently enhances collisions within the plume. This is evident in the decrease in centerline velocity and as will be seen later, the overall emission intensity. The error bars shown in Figs. 4 and 5 represent the uncertainty in determining the peak intensity from the low signal-to-noise ratio of the PMT signal.

Spectrally integrated and temporally resolved images of plumes ablated at 5 J/cm^2 under background argon pressures ranging from vacuum to 20 Torr have been acquired. Some selected images are shown in Fig. 6. Since the images are spectrally integrated over the near-UV to visible range, they include emission from both neutral and ionized species. A spectrum taken of the plume revealed that only emission from Ti and Ti$^+$ are detectable. No appreciable emission was detected from higher ionized Ti or the background Ar. The intensity of the emission increases at higher background pressure due to a greater number of collisions. At pressures above 50 mTorr, a separation of faster and slower moving components occurs in the plume. Similar results were also observed by other investigators ([9]). The location at which the separation of faster and slower moving components occurs is closer to the target surface at higher pressures. Additional imaging

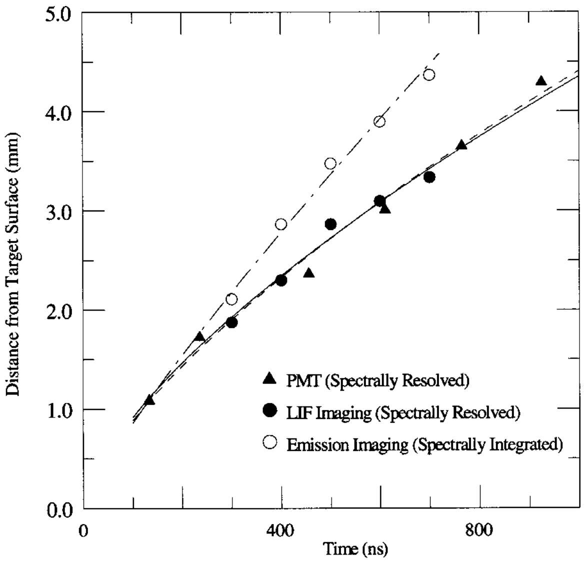

Fig. 8 TOF data acquired from emission imaging, LIF imaging, and PMT measurements. The velocities derived from LIF are consistent with the PMT data of neutral titanium (399.860 nm).

also revealed that the threshold for the separation to occur varies with the laser fluence and therefore the ablation flux. These observations have a strong dependence on the number of collisions. Thus it is reasonable to suggest that this occurrence is highly dependent on the Knudsen number. The plumes take on a crescent shape shortly after the separation occurs. The greatest concentration of titanium is found in the forward portion of plume. However, when pressures are sufficiently high, the number of collisions within the plume increases, and the concentration of titanium is redistributed to take on a Maxwellian shape as evidenced by the images taken at 20 Torr.

Figure 7 shows fluorescence images taken at 100 mTorr of Ar juxtaposed to emission images taken at the same pressure. The fluorescence images reveal that the forward-peaking distribution of titanium observed in the spectrally integrated emission images is conspicuously absent from the laser-induced fluorescence (LIF) images. Since only the neutral titanium atoms in the plume fluoresce at 296.722 nm, the comparison of emission and LIF images suggest that neutral species of titanium do not occupy the leading portion of the plume in any significant numbers. Since only neutral Ti and Ti^+ lines are detectable with the imaging system, it is reasonable to conclude that Ti^+ occupies the front portion of the plume expansion. Most probable velocities can be derived from these images by noting the location of peak intensity at different times. The velocities obtained from the images in Fig. 7 are plotted in Fig. 8. The average centerline velocity obtained from the emission images is 0.56×10^4 m/s while the velocity derived from the LIF images is 0.36×10^4 m/s. Also plotted in Fig. 8 are TOF data acquired by monitoring the progression of neutral titanium emission at $\lambda = 399.86$ nm by using a PMT installed on a monochromator. It is evident that the TOF data are in exceptional agreement with LIF data. This further confirms the fact that the bulk of neutral titanium is found in the center and aft portion of the plume, and the forward part of the plume is primarily composed of titanium ions. This observation is most likely due to the fact that the titanium ions acquire greater kinetic energy than the atoms through the absorption of the incident laser energy.

Conclusions

The effects of ablation laser fluence and background pressure were investigated using temporally integrated and temporally resolved imaging. A separation of faster and slower moving particles in the plume was observed. The separation was collision-driven and governed by the Knudsen number. The LIF images revealed that titanium ions occupied the front portions of the expanding plume, the neutral species were slower-moving and occupied the center and back portions of the plume. The effects of the laser fluence and background gas pressure on the centerline axial velocity of the plume were studied via emission time-of-flight measurements. Velocities higher than 1×10^4 m/s were recorded for neutral titanium ablated in vacuum at a fluence of 8 J/cm^2. The centerline axial velocity declined gradually as the plume moved away from the target surface. The decline in the velocity was more dramatic with lower fluence and higher background pressure because the lower laser fluence created atoms with smaller initial axial momentum, and the higher background pressure provided more resistance against the plume.

Acknowledgment

Support to this work by NSF and DOE under grant # DE-FG03-95ER14562 is gratefully acknowledged.

References

[1] Ohring, M., 1992, *The Materials Science of Thin Films*, Academic Press, Boston.
[2] Hems, J., 1990, ''Barrier Layers: The Advantages of Titanium Nitride,'' Semicond. Int., **13**, pp. 100–102.
[3] Narayan, J., 1992, ''Epitaxial Growth of TiN Films on (100) Silicon Substrates by Laser Physical Vapor Deposition,'' Appl. Phys. Lett., **61**, pp. 1290–1292.
[4] Sundgren, J. E., 1985, ''Structure and Properties of TiN Coatings,'' Thin Solid Films, **128**, pp. 21–29.
[5] Valkonen, E., 1983, ''Selective Transmission of Thin TiN-Films,'' *Proceedings of the SPIE 1983 International Conference*, Vol. 401, pp. 375–381.
[6] Wiese, W. L., and Fuhr, J. R., 1975, ''Atomic Transition Probabilities for Scandium and Titanium,'' J. Phys. Chem. Ref. Data, **4**, pp. 263–353.
[7] Hermann, J., Thomann, A. L., Boulmer-Leborgne, C., Dubreuil, B., De Giorgi, M. L., Perrone, A., Luches, A., and Mihailescu, I. N., 1995, ''Plasma Diagnostics in Pulsed Laser TiN Layer Deposition,'' J. Appl. Phys., **77**, pp. 2928–2936.
[8] Kelly, R., and Dreyfus, R. W., 1988, ''Reconsidering the Mechanisms of Laser Sputtering with Knudsen-Layer Formation Taken into Account,'' Nucl. Instrum. Methods Phys. Res. B, **32**, pp. 341–348.
[9] Wood, R. F., Chen, K. R., Leboeuf, J. N., Puretzky, A. A., and Geohegan, D. B., 1997, ''Dynamics of Plume Propagation and Splitting during Pulsed-Laser Ablation,'' Phys. Rev. Lett., **79**, pp. 1571–1574.

A.-S. Marchand

M. Raynaud
e-mail: raynaud@cethil.insa-lyon.fr

INSA de Lyon,
Centre de Thermique de Lyon,
ESA CNRS 5008,
Batiment 404,
20, avenue Albert Einstein,
69621 Villeurbanne Cedex,
France

Numerical Determination of Thermal Contact Resistance for Nonisothermal Forging Processes

A numerical study is conducted to estimate the thermal contact resistance (TCR) between the tool and the workpiece during slow nonisothermal forging processes. A finite difference method is used to determine the TCR from a thermomechanical microscopic model. Correlations of the numerical results are developed for the TCR as a function of the interface geometry and the thermal properties. The method used to introduce these correlations in forging softwares, to account for a time and space-dependent TCR instead of a constant arbitrary value, is given. The predictive capability of the correlations is partially validated by comparing their outputs with TCR results from the literature.
[S0022-1481(00)00903-8]

Keywords: Contact Resistance, Heat Transfer Interface, Modeling, Stress

1 Introduction

Heat transfer at solid/solid interfaces is a problem which has many practical applications: microelectronics, metal cutting, aerospace, forming, etc. The heat transfer processes which occur in forging operations are of considerable practical significance. Important aspects of the forming process, such as the geometrical integrity, the mechanical properties of the material or the required press capacity are both affected by the workpiece temperature. Kellow et al. [1] were among the first to point out that both workpiece and tool behaviors are strongly affected by the temperature field (high temperatures occasioned in production are detrimental to the life of forging dies). They concluded that the problem of imperfect interfacial contact, resulting from both the contact area effects and the presence of lubricant and oxide layers, can be treated analytically by assuming a contact resistance at the contact interface. Recently, algorithms and analytical tools have been developed to predict flow patterns and mechanical behaviors ([2,3]). Many analytical and experimental thermal studies are reported on thermal contact resistance (TCR) ([4–8]), but few investigations have been reported regarding procedures that estimate the TCR in forging processes. Numerous thermal-mechanical models have been proposed with an arbitrary constant value of the TCR ([3]). However, the determination of the TCR was not one of their main interests. Nevertheless it is obvious that if accurate and consistent predictions of the temperature distribution in hot metal forging processes are to be attempted, any numerical model would need to be supplied with consistent data on the heat transfer coefficient at the contacting surfaces. This is why this paper proposes a numerical approach to estimate the TCR between the tool and the workpiece during slow nonisothermal forging processes.

In order to obtain accurate values of the TCR, several experimental and numerical investigations have already been performed. Essentially four approaches allow determination of the TCR for forging processes:

1 The first one consists in choosing a constant value of the TCR such that the calculated and the measured temperatures agree as closely as possible. This method was used by Dadras and Wells [9] for forging processes. Burte et al. [10] gave several calibration curves for a set of experimental conditions (interface pressure, lubricant, etc.). These curves show theoretical temperature versus time plotted for different values of the TCR. This approach does not take into account the possible variation of the TCR during the process.

2 The second approach is based on the definition of the TCR, i.e., the ratio of the contact surface temperature difference to the heat flux through the interface:

$$R=\frac{Tc_2-Tc_1}{\varphi_1}. \tag{1}$$

Using this method, Vinod [11] measured a contact heat transfer coefficient between a tool and an aluminum workpiece under dry and lubricated conditions. The interface temperatures were obtained by linearly extrapolating the temperatures measured in the two samples far from the interface, whereas the heat flux is calculated from the temperature measurements in one sample at two locations:

$$\varphi=k\frac{T_2-T_1}{x_2-x_1}. \tag{2}$$

This heat flux determination is only valid for steady state. Since it was used to study the time variation of the heat transfer coefficient, these results are not reliable. Another method was commonly used for the assessment of the surface temperatures in transient state and thus of the TCR (using Eq. (1)). It requires the use of surface thermocouples. However, numerous researchers ([12,13]) underlined the difficulty of the direct measurement of surface temperatures due to the presence of very high stress concentration near the interface.

3 The third method to determine the TCR uses an inverse technique. Malinowski et al. [14] used a nonlinear optimization technique to minimize the squared difference between the experimental and the computed temperatures. In their work, the conductance is given by

$$h'(t)=h'(t-to)+\dot{h}'(t-to) \tag{3}$$

where $\dot{h}'$ is the h' variation over a period of time $[t-to]$. $\dot{h}'$ is obtained by minimizing, for each time interval, the following cost function J:

$$J(\dot{h}')=\int_{to}^{t}(T_i-T_m)^2dt \tag{4}$$

where T_i is the average of the computed temperatures and T_m the average of the temperatures measured by the thermocouples. The time variation of the thermal contact conductance, for 303 stainless steel, is obtained as a function of the interfacial pressure and

---

Contributed by the Heat Transfer Division for publication in the JOURNAL OF HEAT TRANSFER. Manuscript received by the Heat Transfer Division, Feb. 25, 1999; revision received, Feb. 15, 2000. Associate Technical Editor: S. Sadhal.

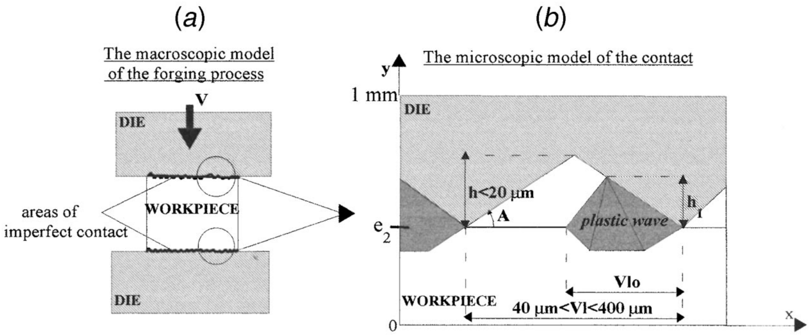

Fig. 1 Microscopic model of the contact. Note that usually $A<15$ deg.

the initial temperature of the die. It varies in a broad range from 50 to 20,000 $W/m^2 \cdot K$. A correlation was proposed with differences in temperatures reaching the magnitude of 10–20 percent from the numerical results, obtained using a finite element method. This methodology of the TCR determination is the most recent and effective one. Indeed it allows one to obtain a time-dependent TCR using remote thermocouples. This method was also used by Goizet et al. [15].

4 The fourth approach which is used herein is purely numerical. As a matter of fact, the conditions of a real hot forging process (force, temperature) are very hostile and detrimental to the life of the instrumentation. Furthermore, the interface quality depends upon the surface conditions, lubricant, and tool speed among other parameters. The influences of these variables, combined with plastic deformations are highly correlated and thus it is difficult to characterize accurately the interface heat transfer, for a wide range of forging conditions, with an experimental approach. Consequently, it was decided to estimate the TCR from a thermo-mechanical microscopic model, using a finite difference method. This procedure allows one to find correlations that give the TCR as a function of the asperity geometry and the thermal properties of the two solids.

This paper is divided into three parts. The microscopic model of the contact followed by the method to determine the TCR and the sensitivity of the model to the interface location are presented first. Then the TCR correlations are given. Finally, numerical results are discussed and compared with the theoretical TCR obtained from previous studies.

2 Thermal Contact Modeling

2.1 The Microscopic Model of the Contact. Several models have already been proposed ([16]), most of which consider uniformly distributed circular contact spots ([17,18]). The representative heat flux tube represents the heat transfer across a single contact area. This kind of geometrical schematization has also been used in previous studies where plastic, elastic, or elasto-plastic deformation models allow one to obtain the equivalent geometrical parameters (the mean contact spot radius, the ratio of the real area to the apparent one, etc.) and to deduce the thermal contact resistance (TCR) ([19,20]). In the present study, the TCR is deduced from the mechanical microscopic model proposed by Challen et al. [21]. This model assumes that during the relative motion between the tool and the workpiece, the perfectly rigid tool asperities create plastic waves on the workpiece contact surface (Fig. 1). The plastic wave model is developed, using either the upper bound theorem or the sliding lines theorem. The sliding lines theory allows analysis of nonhomogeneous plane-strain deformation in a perfectly rigid plastic isotropic solid with velocity fields compatible with an assumed plastic flow of the material ([22]). The plastic wave model was used by Baillet and Boyer [2] to design a macroscopic friction law for forging processes. The geometry of the tool surface is made of periodic triangular two-dimensional asperities (infinite in the z-direction). The height h, and the spatial periodicity Vl, can be easily deduced from the tool roughness measurement. Figure 2 shows an example of a real tool roughness. Note that the y-axis scale is dilated six times in regard to the x-axis one. According to this figure, the plastic wave model seems to give a quite good representation of the interface geometry (at least better than with rectangular asperities). The wave geometry is given by the two parameters h_1 and Vlo, which vary during the forging process. These parameters are calculated from the mechanical model, as functions of the interface normal stress and of the yield stress. Plastic wave deformations and friction between the workpiece and the tool are at the origin of heat generation. Considering nonisothermal forging processes, the tool is usually heated from 100°C to 600°C, and the workpiece temperature is about 1000°C. In that context, simulations on POLLUX forging code have shown that, whatever the initial temperature difference between the tool and the workpiece, the heat generation is much smaller than the heat flux crossing the contact interface. Consequently, even if the use of a thermal contact model that takes into account heat generation is necessary ([6]), an accurate determination of the heat generation coefficient, α, is not needed for the modeling of nonisothermal forging. That would not be the case for isothermal forging or for sliding contacts such as gears, ball bearings, or metal cutting, where friction can be the preponderant heat flux at the interface ([23]). In Bardon's ''macroscopic'' thermal interface model, α represents the fraction of the heat flux generated at the tool surface, while $(1-\alpha)$ represents the fraction generated on the workpiece surface. In most forging codes, the heat generation is taken into account considering a constant and arbitrary α value equal to 0.5. In nonisothermal forging, this value is accurate enough; thus this study focuses on the estimation of the TCR. In isothermal forging, where the heat generation can be of the same order as the heat flux crossing the interface, it might be necessary to estimate both the TCR and α. This problem of α determination is not addressed herein.

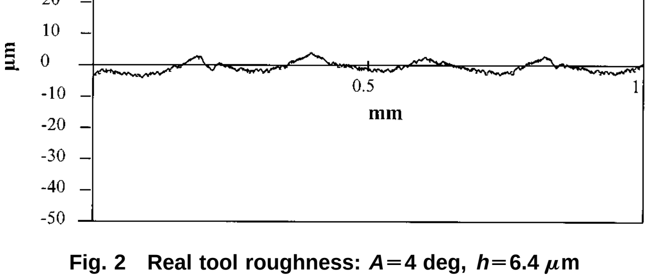

Fig. 2 Real tool roughness: $A=4$ deg, $h=6.4$ μm

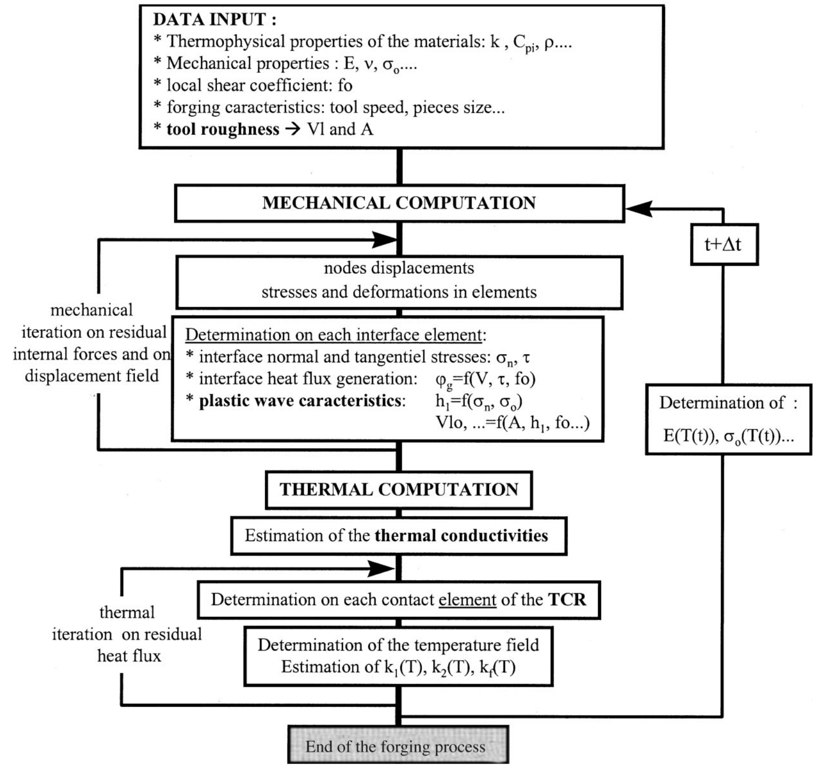

Fig. 3 Forging code flow chart

The aim of this study is to introduce the TCR variations in forging software packages and to study their influence on the thermomechanical behavior during nonisothermal forging. A shortened flow chart of the finite element forging code POLLUX is presented in Fig. 3. POLLUX is a finite element code, based on the elastoviscoplastic theory, which has been developed by the Solids Mechanic Laboratory of I.N.S.A. Lyon (France). Until now, most software packages have considered a constant TCR value as interface thermal condition. With the methodology proposed here, the triangular microscopic model will be used for each macro element of tool-workpiece contact, in order to estimate the thermal parameters of the contact. The advantages of this plastic wave model, in the context of this study, are as follows:

- The triangular tool asperities' sizes are obtained from profile analyses. Therefore, for each macro element of the contact, the microscopic model is used with the geometrical tool characteristics which leads to variations of thermal interface parameters all along the contact.
- The plastic wave parameters are directly dependent on the forging parameters and on the thermomechanical properties (tool speed, yield stress, etc.). Consequently they change during the process and along the interface of contact. For each time increment of the forging process, the plastic wave characteristics are updated as functions of the interface normal stress and of the yield stress. Thus the microscopic model and therefore the TCR varies.

As shown by the flowchart of Fig. 3, within each time-step, iterations are done on both the mechanical and thermal problems. Consequently, the TCR can be time and space-dependent, and a good coupling is realized between thermal and mechanical behaviors of the materials. If a three-dimensional microscopic interface model were to be used in order to be more representative of the real contact geometry, it would require a global three-dimensional approach (mechanical and thermal). The plastic wave model would then be replaced by another model capable of good mechanical behavior prediction. This model does not exist yet. Furthermore, most of the forging simulation are done presently with a two-dimensional model. One reason is that there are a great number of workpieces that are axisymmetric thus the third dimension is not modeled explicitly. The other reason is that the analysis done with a three-dimensional model requires a huge computational time.

Since the TCR estimation from the microscopic model represents a heavy computational cost, correlations were developed so that they can be easily included in the forging software. This paper proposes such correlations which give the TCR as a function of the thermomechanical properties and the geometrical interface characteristics.

2.2 Numerical Determination of the Thermal Contact Resistance.

The temperature field of the two solids, shown in Fig. 1(*b*), are governed by the following set of equations:

$$\rho_i c_{pi} V \frac{\partial T_i(x,y)}{\partial x} = k_i \left(\frac{\partial^2 T_i(x,y)}{\partial x^2} + \frac{\partial^2 T_i(x,y)}{\partial y^2} \right) + g \qquad (5)$$

$$\left.\frac{\partial T_i(x,y)}{\partial x}\right|_{x=0} = \left.\frac{\partial T_j(x,y)}{\partial x}\right|_{x=Vl} \quad y \in [0, e_1 + e_2] \qquad (6)$$

$$T_i(0,y) = T_i(Vl,y) \quad y \in [0, e_1 + e_2] \qquad (7)$$

$$-k_i \frac{\partial T_i(x,y)}{\partial n} = h_{\infty i}(T_i(x,y) - T_{\infty i})$$

$$y = 0 \text{ and } y = e_1 + e_2; \quad x \in [0, Vl] \qquad (8)$$

where n is the outward normal to the surface. Equations (6) and (7) represent periodicity conditions.

A finite difference method was implemented in order to calculate the temperature field in the tool and the workpiece near the contact interface. The volume source term g represents the heat source due to friction and deformations of the plastic wave. But, as shown by Chantrenne and Raynaud [24], this term does not influence the TCR value. Thus it can be set equal to zero in the microscopic model that is used to determine the TCR. The heat source distribution should be taken into account if we wanted to determine an accurate value of α, which as indicated before, is not necessary for nonisothermal forging processes. The temperature field is calculated in steady state for each microscopic interface geometry, using Gauss elimination with backsubstitution method.

In forging codes, the overall temperature field is calculated from the transient state. Nevertheless, Beck and Keltner [25] showed that the constriction phenomenon (and thus the TCR) is fully developed very quickly (around 10^{-3} s in our case) in regard to the thermal state. Since the TCR is an intrinsic property of the contact (function of the thermal properties and of the contact geometry), for each interface geometry it can be determined from the steady-state, considering that it is instantaneously established. The steady temperature field is not representative of the real temperature field obtained in forging processes. It is only used to calculate the local TCR that will be introduced in the forging codes to model the thermal contact of the two solids. That is why it is possible to suppose that the thermal properties are constant. When the process is slow ($V < 100$ mm/s), this steady-state model is realistic. Indeed, the time needed for the development of the constrictions is, in that case, one or two orders of magnitude smaller than the time-step, Δt, used in the forging code (Fig. 3). On the other hand, for quicker processes (forging time lower than 1 s), the method proposed herein does not allow to be representative of the transient interface phenomena. Nevertheless, in such a situation, only adiabatic conditions are presently considered between the tool and the workpiece in forging codes. As soon as the tool roughness and the thermal interface properties are well known, the mean TCR, estimated with this method, provides values of the interface condition that are more realistic than adiabatic ones.

The following assumptions are made:

- In most forging conditions, the velocity of the matter in the vicinity of the interface is small, thus the transport term can be neglected compared to the conductive heat flux. Equation (5) reduces to

$$k_i\left(\frac{\partial^2 T_i(x,y)}{\partial x^2}+\frac{\partial^2 T_i(x,y)}{\partial y^2}\right)=0. \tag{9}$$

- As the nominal gap between the contact surfaces is sufficiently small, the heat transfer within the fluid occurs only by conduction ([18]).

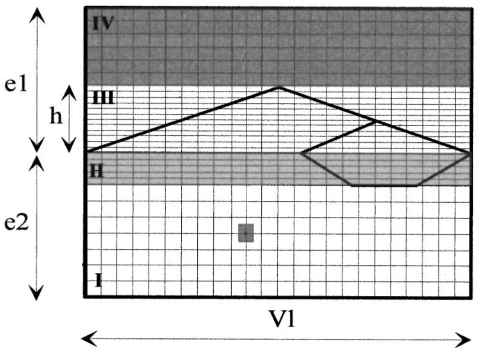

Fig. 4 Mesh of the microscopic model

- It was verified, as done by Sadhal [26] for similar case, that the radiation exchanges within the fluid (air or lubricant) or the cavity are negligible.
- The contact at the interface is supposed to be perfect because it is made between a perfectly rigid tool and a plastically deformed workpiece.
- The oxide layers are not taken into account because of lack of accurate knowledge. Indeed, very few models of oxide behaviors have already been proposed ([27]) and the oxide properties are not well known yet. It was preferred to ignore the oxide layers rather than introduce inaccurate data.

An example of the finite difference mesh is presented (Fig. 4). As in Fig. 1(*b*), in order to improve clarity, this figure is not to scale since $Vl \approx 200\ \mu$m and $e_1 + e_2 = 1$ mm. This mesh corresponds to 775 nodes whereas the mesh used for the computation has 17,825 nodes. The mesh was refined until the difference between the two successive calculated TCR was less than 0.5 percent. The results were validated by comparing, for two interface geometries, the temperature field obtained with the finite difference method with the one calculated with finite elements codes (Mfield, Matlab PDE toolbox).

A temperature distribution around the interface is shown in Fig. 5(*a*) for a 10 μm high and 75 μm wide asperity (angle 15 deg). The distances e_1 and e_2 are large enough to ensure that the perturbed zone height is smaller than the height of the zone under study. Far from the theoretical interface π_o, the temperature field

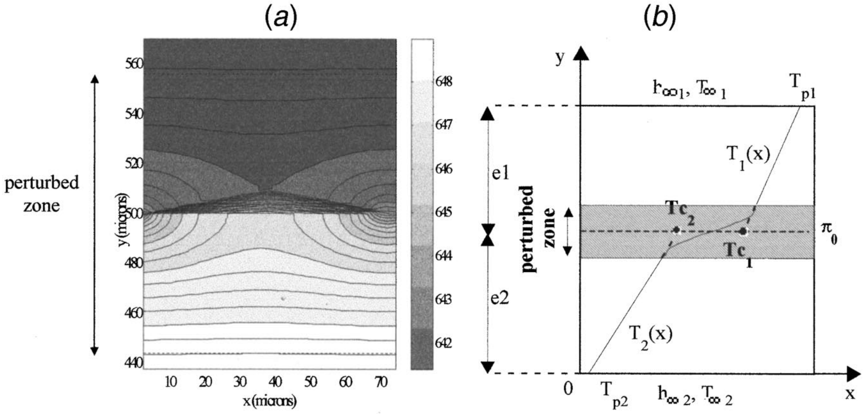

Fig. 5 (*a*) Example of temperature field near the interface without heat generation. $h=10\ \mu$m, $A=15$ deg, $k_1=20$ W/m·K, $k_2=10$ W/m·K, $h_1=1.43\ \mu$m. (*b*) Linear extrapolation of the temperature field to determine the temperature jump ($T_{c1}-T_{c2}$) at the theoretical interface.

in the system is one dimensional. But, due to the presence of the asperities, constrictions occur and the temperature field becomes two-dimensional near the interface.

Equation (1) is used to estimate the TCR. In this equation, Tc_1 and Tc_2 are two fictitious interface temperatures which do not have any physical significance from a microscopic point of view. As shown in Fig. 5(*b*), these temperatures are determined by extrapolating the one-dimensional temperature field toward the theoretical interface in the tool and in the workpiece:

$$T_{ci}=T_{pi}+\varphi_i\frac{e_i}{k_i} \tag{10}$$

where φ_i is the heat flux across the contact interface. It is determined from the boundary conditions on the backward surface of the solids 1 or 2 (Eq. (8)).

Recall that the TCR depends neither on the external boundary conditions nor on the macroscopic geometry. It only depends on the microscopic geometry of the contact and on the local thermophysical properties.

2.3 Influence of the Contact Interface Geometry. The numerical determination of the TCR is based on the choice of the theoretical interface π_o. In most studies the contact between a smooth and a rough surface is considered. For example, with the square periodic asperities model ([24]), the choice of the theoretical interface is obvious. This choice is not obvious in forging processes since, due to the temperature and the pressure levels, the two solids interpenetrate. Depending on the plastic wave height, the location of the theoretical interface, π_o (Fig. 5(*b*)), can be chosen at a Y location varying from e_2 to e_2+h which leads to different TCR values. Indeed, if π_o is placed at e_2 then the TCR obtained from Eqs. (1) and (10) is

$$R_{(\pi_o=e_2)}=\frac{T_{p2}-T_{p1}}{\varphi_1}-\frac{e_1}{k_1}-\frac{e_2}{k_2}=R_t-R_p \tag{11}$$

where R_t is the thermal resistance for the real contact and R_p is the thermal resistance for the perfect contact case. Equation (11) is also commonly used to define the thermal contact resistance.

Similarly, if π_o is placed at $(e_2+\delta)$, with $(0<\delta\leqslant h)$, then the TCR is given by

$$R_{(\pi_o=e_2+\delta)}=\frac{T_{p2}-T_{p1}}{\varphi_1}-\frac{e_1-\delta}{k_1}-\frac{e_2+\delta}{k_2}=R_{(\pi_o=e_2)}+\delta\left(\frac{1}{k_1}-\frac{1}{k_2}\right). \tag{12}$$

Three cases are considered:

- If $k_1=k_2$ whatever the theoretical interface position, the TCR values, given by Eqs. (11) and (12), are equal.
- If $k_1>k_2$ the maximal numerical TCR value is obtained with an interface defined at $y=e_2$. The TCR value can be negative if $R_{(\pi_o=e_2)}$ is lower than the absolute value of $\delta(1/k_1-1/k_2)$. That is why, in order to avoid negative numerical TCR values, the interface must be defined at $y=e_2$.
- If $k_1<k_2$, for the same reason, the interface location must be chosen at $y=e_2+h$, so as to calculate the maximal numerical TCR value and to avoid obtaining a negative TCR value. The choice of the interface location can lead to negative numerical TCR because the difference between the two extrapolated temperatures Tc_1 and Tc_2 can be positive or negative. If δ is such that $\delta=(1/k_2-1/k_1)^{-1}R_{(\pi_o=e_2)}$ then the macroscopic resistance is zero.

An example with a large angle asperity illustrates this situation. Figure 6(*a*) shows the temperature field near the asperity. Figure 6(*b*) shows the extrapolated contact temperatures. It can be observed that if the interface location is chosen at $y=e_2$ then the interface temperature jump (Tc_2-Tc_1) is equal to 0.35 K and the TCR is $8\cdot10^{-7}\ \mathrm{m^2\cdot K/W}$, whereas if the theoretical interface is located at $y=e_2+h$ then the TCR is $-1.7\cdot10^{-7}\ \mathrm{m^2\cdot K/W}$, for an interface gap temperature of -0.07 K. For this example, the TCR would be zero if the theoretical interface location were equal to $y=e_2+8.23\ \mu\mathrm{m}$.

It is important to note that whatever the choice of the theoretical interface, the corresponding value of the TCR, introduced in the macroscopic model, leads to the same temperature variations inside and outside the perturbed zone. Since it is more common to have positive TCR, it was decided to develop two correlations. The first one is for $k_1\geqslant k_2$ (Case 1) whereas the other one is for $k_1<k_2$ (Case 2).

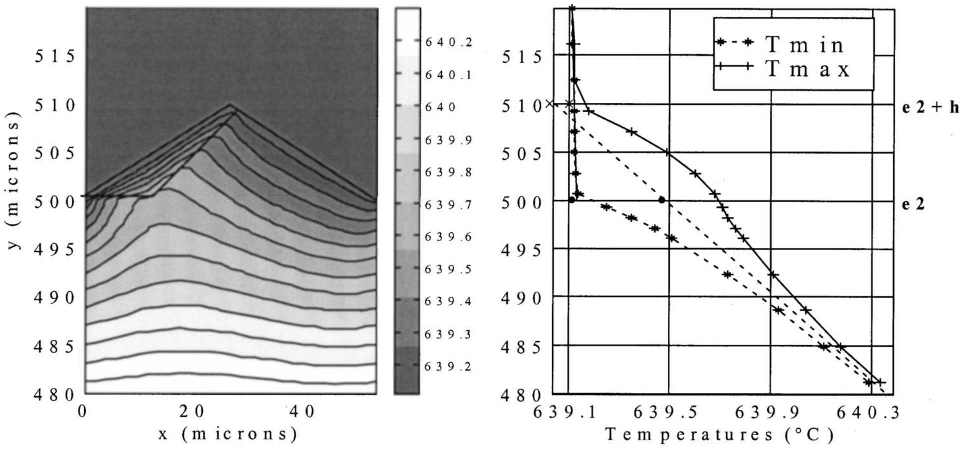
(*a*)

(*b*)

Fig. 6 Example of numerical simulation. $k_1=400$ W/m·K, $k_2=10$ W/m·K, $h=10\ \mu$m, $h_1=9.28\ \mu$m, $A=20$ deg, $T_{\infty 1}=200°$C, $T_{\infty 2}=1100°$C. (*a*) Temperature field near the interface without heat generation. (*b*) Linear extrapolation of the temperature field used to determine the temperature jump at the theoretical interface. Minimal (*), maximal (+) and extrapolated temperatures (-----) near the interface. Macroscopic interface temperatures determined at $\pi_o=e_2$ (●) and $\pi_o=e_2+h$ (×) locations.

3 Determination of the Thermal Contact Resistance (TCR) Correlations

The thermal contact resistance (TCR) can be calculated, from the methodology defined in Section 2.2, for a wide range of geometrical and thermophysical parameters. It depends on:

- the conductivities of the tool, the workpiece and the lubricant near the interface,
- the tool roughness which is represented by the height of the asperity h, and its periodicity Vl, and
- the real contact area and consequently, the size of the workpiece plastic wave (which is represented by its height h_1).

Correlations have been developed in order to estimate the TCR as a function of these parameters. Thus, numerous numerical tests ($\cong$220) were conducted, varying successively each of these parameters. All the tests were done with

$$5\ \mu\text{m} \leqslant h \leqslant 20\ \mu\text{m}$$

$$40\ \mu\text{m} \leqslant Vl \leqslant 400\ \mu\text{m}$$

$$3\ \text{deg} \leqslant A \leqslant 15\ \text{deg}$$

$$10\ \text{W/m}\cdot\text{K} \leqslant \lambda_{1,2} \leqslant 400\ \text{W/m}\cdot\text{K}$$

$$k_f \leqslant 10\ \text{W/m}\cdot\text{K} \ \text{ and } \ k_f \leqslant \frac{\text{Min}(k_1,k_2)}{10}.$$

This range of values corresponds to the asperity sizes encountered in forging processes. In most of the cases, the asperity angles are less than 5 deg as shown in Fig. 2. Since the TCR, denoted by R_{cor}, depends on six parameters $(h, Vl, h_1, k_1, k_2, k_f)$, it was difficult to find a global fit function that had a physical significance. It was preferred to assume that the TCR is the combination of

- the resistance to heat transfer through the asperity due to the constriction of the heat flux line toward the contact spot, which gives rise to the constriction resistance, R_s.
- the resistance to heat transfer, R_f, in the interstitial fluid whose thermal conductivity is usually lower than the thermal conductivity of the solids in contact. R_f represents the influence of the interstitial medium.

These two heat transfer modes do not interact if the interstitial medium conductivity is much lower than the contacting material conductivities and if the real contact area is much smaller than the apparent contact area ([17]). If the two previous conditions are valid then R_f and R_s are two parallel resistances and the TCR is given by Eq. (13):

$$\frac{1}{R_{\text{cor}}} = \frac{1}{R_f} + \frac{1}{R_s}. \tag{13}$$

In this study, the larger the plastic wave, the more R_f and R_s interact and Eq. (13) becomes theoretically not applicable. However, it is shown in Section 4.2 that this equation still allows to estimate R_{cor} with less than a ten percent mean deviation from the exact value, whatever the value of h_1.

R_s is estimated first, considering that no heat is transferred through the interstitial medium ($k_f \approx 0$ W/m·K). This TCR depends on the material conductivities and on the interstitial geometry. It was shown that R_s varies linearly with $1/k_1$ and $1/k_2$ ([17]):

$$R_s = \frac{Vl}{k_1}\cdot F_1 + \frac{Vl}{k_2}\cdot F_2 \tag{14}$$

where F_1 and F_2 are the dimensionless constriction coefficients which depend on the contact geometry. These two coefficients are estimated from the numerical simulations, independently for Case 1 and Case 2 (defined in Section 2.3). Their values are as follows: Case 1:

$$F_1 = \left(-0.268 - 0.692\cdot\frac{h}{Vl}\right)\cdot\log\left(\frac{h_1}{h}\right) - 0.338\cdot\frac{h}{Vl} + 0.0959 \tag{15}$$

$$F_2 = -0.273\cdot\log\left(\frac{h_1}{h}\right) + 0.227\cdot\frac{h}{Vl} + 0.129\cdot\frac{h_1}{Vl} + 0.0985 \tag{16}$$

Case 2:

$$F_1 = \left(-0.269 - 0.661\cdot\frac{h}{Vl}\right)\cdot\log\left(\frac{h_1}{h}\right) + 0.460\cdot\frac{h}{Vl} + 0.0999 \tag{17}$$

$$F_2 = -0.272\cdot\log\left(\frac{h_1}{h}\right) - 0.453\cdot\frac{h}{Vl} - 0.238\cdot\frac{h_1}{Vl} + 0.298\cdot\frac{h_1^2}{h\cdot Vl} + 0.0945 \tag{18}$$

Similarly R_f depends on the medium thermal conductivity and on the contact geometry (h, Vl, h_1). For the lubricant regime in the forging processes, it is considered that the initial lubricant film thickness is large enough to fill the cavities completely. This is the most commonly encountered case in forging processes. Thus, R_f can be expressed as

$$R_f = \frac{Vl}{k_f}\cdot F_f \tag{19}$$

where F_f is another constriction coefficient determined from the numerical results. Practically, the total resistance is determined and the value of R_f is obtained from Eq. (13) since R_s is known. For Case 1, F_f is such that

$$F_f = 0.427\cdot\frac{h}{Vl} - 0.00639\cdot\frac{h_1}{Vl} - 0.300\cdot\frac{h_1^2}{h.Vl}. \tag{20}$$

For Case 2 F_f is given by

$$F_f = 0.502\frac{h}{Vl} + 0.250\frac{h_1}{Vl} - 0.654\frac{h_1^2}{h\cdot Vl}. \tag{21}$$

The geometrical parameters are the height of the asperities, h, their periodicity, Vl, and the height of the plastic wave h_1 (Fig. 1). Using Eqs. (13) to (21) it is possible to determine immediately R_{cor}, as a function of the microscopic parameters and thermophysical properties near the interface.

4 Results and Discussion

The thermal contact resistance (TCR) values for an empty cavity ($R_{\text{cor}} = R_s$) or for a cavity full of lubricant are given. Several numerical tests were conducted with different values of the thermal properties and of the interface geometry. For each test, the TCR, denoted by R, is calculated from the methodology defined in Section 2.2 and is compared with R_{cor}. Then a validation of the correlations is obtained by comparing, for the same interface geometry, the correlation results with the TCR obtained in the literature.

4.1 Thermal Contact Resistance Without Lubricant. The case of cavities filled by a gas, i.e., when $1/R_f$ is negligible compared to $1/R_s$, is studied first. Figure 7 shows the thermal contact resistances, obtained by the correlation or by the numerical calculations, versus the plastic wave height h_1 for different values of solid conductivities; the asperity angle is $A = 8.13$ deg and the periodicity $Vl = 140\ \mu$m. Numerous numerical tests ($\cong$ 300) were conducted. The correlation values are satisfactory since the mean difference between R and R_{cor} is 1.09 percent with a mean square

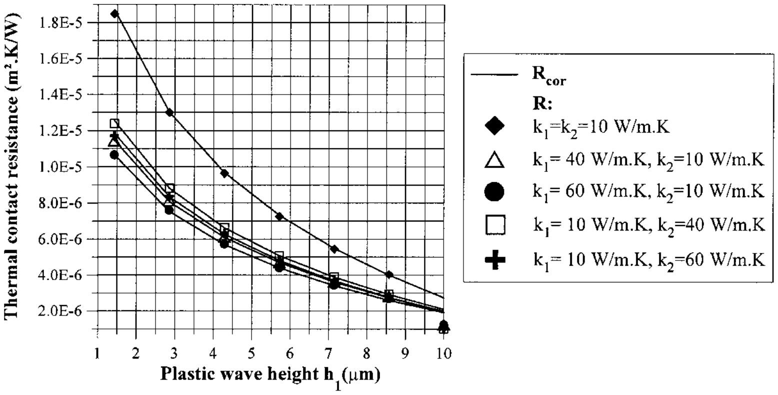

Fig. 7 Thermal contact resistances R_{cor} and R versus the plastic wave height for $h=10\ \mu m$, $Vl=140\ \mu m$ ($A=8.13$ deg), $k_f \approx 0$ W/m·K and for different values of k_1 and k_2

deviation of 0.98 percent. It is the constriction resistance in the solid with the lowest conductivity that dominates. Moreover, Fig. 7 underlines the influence of the plastic wave height on the TCR. Indeed, the TCR values, for low plastic wave heights, are an order of magnitude larger than those calculated for high plastic wave heights.

4.2 Thermal Contact Resistance Results With the Presence of an Interstitial Lubricant. Similar results are obtained with a lubricant. Figure 8 shows the TCR values R and R_{cor} versus the lubricant conductivity for different plastic wave heights h_1 under two different forging conditions. This figure underlines the influence of the plastic wave height on the TCR, as in the case of unlubricated contact. Furthermore, these results show the importance of the lubricant on the TCR: The proportion of heat transferred by conduction through the fluid, compared with that through the plastic wave depends upon the ratio of thermal conductivities of the fluid and the solids. The lubricant conductivity controls the proportion of the heat flux which tends to converge to the metal-metal contact, especially when the difference between the conductivities of the solids and the lubricant is small. More than 300 tests were performed. The mean difference between R and R_{cor} is six percent with a mean square deviation of seven percent.

4.3 Confidence Intervals. The dispersion of the TCR determined with the correlations is larger for lubricated contacts than for dry contacts. Indeed, the maximal deviation is as much as 37 percent. Moreover, the most important deviations are obtained when the fluid conductivity is not very small compared to that of the solids ($k_f \cong \mathrm{Min}(k_1, k_2)/10$) and when the plastic wave height is important. This is due to the hypothesis used in the development of the TCR correlations, in which it is assumed that heat transfer through the solid contact and through the fluid does not interact (Eq. (13)). This hypothesis is all the more valid since the interstitial medium conductivity is much lower than the contacting material conductivities and the plastic wave height is low. However, the worst relative differences occur for very tiny absolute TCR values ($\cong 10^{-7}$ to 10^{-8} m^2·K/W) and have consequently almost no influence on the heat transfer rate.

All the geometrical parameters and the thermophysical properties are known or determined with an uncertainty which leads to an uncertainty in the TCR. A Monte Carlo method was used to quantify the uncertainty in the TCR, predicted with the correlations, due to the uncertainty in these parameters. If a ten percent uncertainty in each parameter (the conductivities k_1, k_2, and k_f, the tool roughness, represented by the two parameters Vl and h, and the plastic wave characteristic h_1) is considered, then the uncertainty in R_{cor} varies from 20 percent to 50 percent. This uncertainty is consistently much larger than the difference between R and R_{cor}. Consequently it is of little use to develop a more complicated thermal model or correlations in view of the mean difference of six percent between the nominal values of R and R_{cor}. The results show that the correlations are sufficiently accurate approximations of the numerical results.

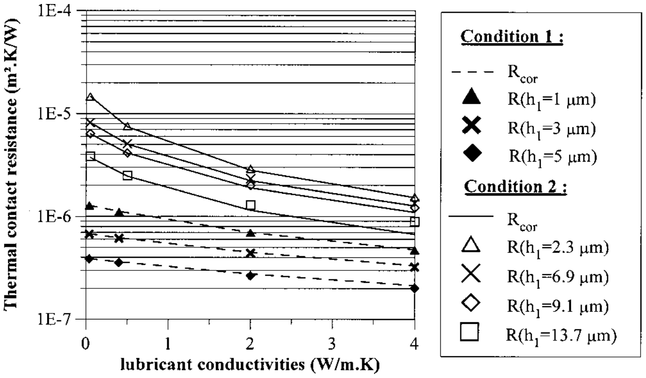

Fig. 8 Thermal contact resistances R_{cor} and R versus the lubricant conductivities. Condition 1: $k_1=80$ W/m·K, $k_2=60$ W/m·K, $h=7\ \mu m$, $A=12$ deg, $Vl=65.9\ \mu m$. Condition 2: $k_1=10$ W/m·K, $k_2=40$ W/m·K, $h=16\ \mu m$, $A=9.09$ deg, $Vl=200\ \mu m$.

4.4 Validation by Comparison With Results From the Literature. Numerous studies have already been presented in the literature to estimate the constriction resistance in solids for a given interface geometry. The aim of this section is to compare these published TCR values to the ones obtained by the present

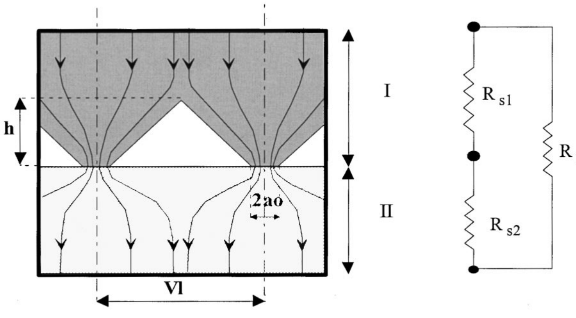

Fig. 9 Thermal contact model for the R_{th} estimation

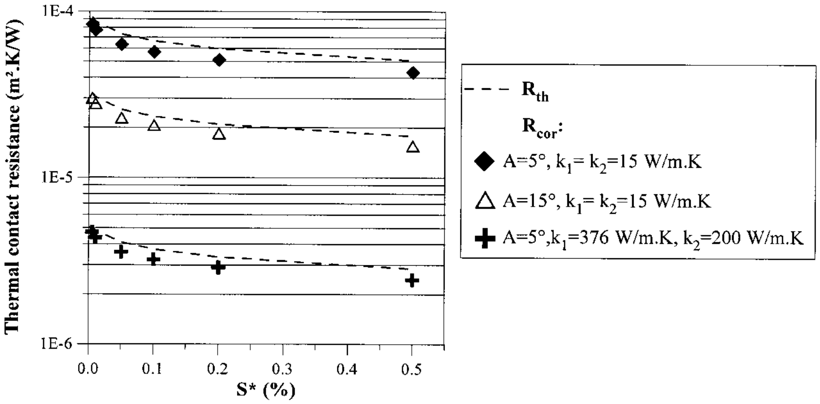

Fig. 10 Thermal contact resistances R_{cor} and R_{th}, versus $S*$ for an asperity height of 10 μm

correlations. As a first approximation, the TCR obtained here for the forging contact geometry (R_{cor}) (Fig. 1), with a very low plastic wave height h_1, can be compared to the ones previously obtained for the geometry shown in Fig. 9 (R_{th}). This geometry can be modeled with thermal resistances, as shown on Fig. 9: R_{s1} and R_{s2} are the constriction resistances and R_f the resistance due to the interstitial medium. Only comparisons of the constriction resistances can be realized, i.e., dry contacts ($k_f \approx 0$ W/m·K) are considered. In that case

$$R_{th}=R_{s1}+R_{s2}. \tag{22}$$

Several investigations have been carried out to determine correlations which give R_{s1} and R_{s2} as a function of the thermophysical properties and of the asperity sizes, for two-dimensional or three-dimensional contact geometries. For dry sliding contacts, Laraqi [7] and Chantrenne and Raynaud [28] proposed correlations which give R_{s2} as a function of the material conductivity and of $S*$. Their relations for the case of a static contact respectively reduce to Eqs. (23) and (24):

$$R_{s2}=\frac{Vl}{k}\,\frac{1}{\pi^3\left(\dfrac{S*}{100}\right)^2}\sum_{p=1}^{\infty}\frac{\sin^2(p\pi S*/100)}{p^3} \tag{23}$$

$$R_{s2}=\frac{Vl}{k}\left(-0.234\,\frac{S*}{100}+0.2847\right)\ln\left(\frac{100}{S*}\right). \tag{24}$$

The difference between Eqs. (23) and (24) is less than eight percent and is due to the models used by the authors which are not identical, as explained by Chantrenne and Raynaud [28].

Wong [29] considers that it is more realistic to model the contact junctions as conic frusta instead of circular cylinders. Consequently, he proposed a correlation for the estimation of the constriction resistance of a conic frustum. This correlation gives an approximate value of R_{s1} for three-dimensional geometries. A similar reasoning allows one to determine R_{s1} for the two-dimensional geometry (Fig. 9):

$$R_{s1}=\frac{Vl/2}{k\cdot\arctan\left(\dfrac{Vl-2a_o}{2h}\right)}\ln\left(\frac{1}{S*}\right). \tag{25}$$

Figure 10 shows R_{th} and R_{cor} versus $S*$ for different values of the geometrical and thermophysical properties, considering vacuum environment ($1/R_f=0$). Equations (24) and (25) are used to calculate R_{s2} and R_{s1}. The mean difference between R_{th} and R_{cor} is equal to 12 percent. This difference between R_{th} and R_{cor} tends to increase with $S*$ due to the difference between the two contact geometries (Figs. 1 and 9). For very low values of $S*$, the agreement is better. This difference is mainly due to

- the approximation of R_{s1} by Wong's correlation. If R_{s1} is calculated by a finite element code (MATLAB, PDE Toolbox for example), the difference between R_{th} and R_{cor} is less than five percent.
- the difference between the two interface geometries (Figs. 1 and 9) which tends to increase with $S*$.

5 Conclusion

The numerical determination of thermal contact resistance (TCR) between the tool and the workpiece for nonisothermal forging processes was studied. The microscopic model of the contact surfaces proposed by Challen et al. [21] was used. This two-dimensional microscopic model allows to couple the mechanical and the thermal behaviors of the solids as well as possible. The TCR was obtained as a function of the interface geometry and the thermal properties. Due to the interpenetration of the two solids, the theoretical interface was chosen depending on the solid conductivities to obtain, in every case, a positive TCR. Correlations were proposed, which give the TCR as a function of these parameters. Those correlations and the numerical results agreed reasonably well. Indeed the mean deviation between them did not exceed six percent. The correlations were compared with relationships proposed in other investigations and were in good agreement. It was shown that it is not much use developing more effective prediction of the TCR since the uncertainty, due to inaccurate thermal and mechanical properties, introduces larger discrepancies. Furthermore, phenomena such as oxidation, which strongly affects the interface heat transfer and thus the TCR, are not yet taken into consideration because of the lack of oxide layer modeling. The correlations have been introduced in a forging software (POLLUX) to take into account a time and space-dependent TCR instead of a constant arbitrary value. The first results of the simulations are presented in Marchand et al. [30]. A global validation of the approach proposed herein (the microscopic model used and the correlations) will be realized by comparing the TCR estimated by POLLUX thanks to the correlations, with the experimental ones measured by Goizet et al. [15]. Since the experimental tool roughness and the thermal conductivities of the materials and of the lubricant are well known, the comparison between experimental and numerical TCR will be possible for each forging condition (tool speed, initial tool temperature, etc).

Nomenclature

A = asperity angle, deg
C_{pi} = specific heat, J/kg.K

E = Young's modulus, MPa
e_i = height of the solid i, m
F = constriction coefficient
fo = local constant shear coefficient
g = heat source term, W/m^3
h = height of the asperity, m
h_1 = height of the plastic wave, m
h_∞ = heat transfer coefficient, W/m^{2}K
k = thermal conductivity, W/m·K
P = interface pressure, MPa
R = thermal contact resistance, m^2·K/W
S^* = ratio of the real contact area to the apparent one, percent
T_c = interface temperature, K
T_∞ = reference temperature, K
V = tool velocity, m/s
Vl = periodicity of the asperity, m
Vlo = length of the plastic wave, m

Greek Symbols

α = heat generation coefficient
δ = incremental length, m
φ = heat flux, W/m^2
ν = Poisson ratio
π_o = theoretical location of the contact interface
ρ = density, kg/m^3
σ_n = normal stress, MPa
σ_o = yield stress, MPa

Subscripts

1 = tool
2 = workpiece
cor = correlated
f = lubricant
p = perfect contact
t = total
s = solid
th = theoretical

References

[1] Kellow, M. A., Bramley, A. N., and Bannister, F. K., 1969, ''The Measurement of Temperatures in Forging Dies,'' Int. J. Mach. Tool Des. Res., **9**, pp. 239–260.

[2] Baillet, L., and Boyer, J. C., 1994, ''A Friction Model for Closed-Die Forging F.E.M. Simulation,'' *Metal Forming Process Simulation in Industry*, Vol. 1, Int. Com. Thugensorganisation Münchengladbach, Baden-Baden, Germany, pp. 132–145.

[3] Jinka, G. K., Fourment, L., and Bellet, M., 1995, ''Numerical Simulation of Hot Powder Forging of Connecting Rod,'' *Simulation of Materials Processing: Theory, Methods and Applications*, Shen and Dawson, eds. pp. 833–838.

[4] Fenech, H., and Rohsenow, W. M., 1963, ''Prediction of the Thermal Conductance of Metallic Surfaces in Contact,'' ASME J. Heat Transfer, **85**, pp. 15–24.

[5] Fletcher, L. S., 1988, ''Recent Developments in Contact Conductance Heat Transfer,'' ASME J. Heat Transfer, **110**, pp. 1059–1070.

[6] Bardon, J. P., 1994, ''Bases physiques des conditions de contact thermique imparfait entre milieux en glissement relatif,'' Rev. Gen. Therm., **386**, pp. 85–91.

[7] Laraqi, N., 1997, ''Velocity and Relative Contact Size Effects on the Thermal Constriction Resistance in Sliding Solids,'' ASME J. Heat Transfer, **119**, No. 1, pp. 173–177.

[8] Lambert, M. A., and Fletcher, L. S., 1997, ''Review of Models for Thermal Contact Conductance of Metals,'' J. Thermophys. Heat Transfer, **11**, No. 2, pp. 129–140.

[9] Dadras, P., and Wells, W. R., 1984, ''Heat Transfer Aspects of Nonisothermal Axisymmetric Upset Forging,'' J. Eng. Ind., **106**, pp. 187–195.

[10] Burte, P. R., Yong-Taek, I. M., Altan, T., and Semiatin, S. L., 1990, ''Measurement and Analysis of Heat Transfer and Friction During Hot Forging,'' J. Eng. Ind., **112**, pp. 332–339.

[11] Vinod, K. J., 1990, ''Determination of Heat Transfer Coefficient for Forging Applications,'' J. Mater. Shap. Technol., **8**, No. 3, pp. 193–202.

[12] Dean, T. A., and Silva, T. M., 1979, ''Die Temperatures During Production Drop Forging,'' J. Eng. Ind., **101**, pp. 385–390.

[13] Lenard, J. G., and Davies, M. E., 1995, ''The Distribution of Temperature in a Hot/Cold Die Set: The Effect of the Pressure, Temperature and Material,'' J. Eng. Mater. Technol., **117**, pp. 220–227.

[14] Malinowski, Z., Lenard, J. G., and Davies, M. E., 1994, ''A Study of Heat Transfer Coefficient as a Function of Temperature and Pressure,'' J. Eng. Mater. Technol., **41**, pp. 125–142.

[15] Goizet, V., Bourouga, B., and Bardon, J. P., 1998, ''Experimental Study of the Thermal Boundary Condition at the Workpiece-Die Interface During Hot Forging,'' *Proceedings of 11th IHTC*, Vol. 5, Kyongju, Korea, Aug. 23–28, Taylor and Francis, London, pp. 15–20.

[16] Mikic, B. B., 1974, ''Thermal Contact Conductance, Theoretical Considerations'' Int. J. Heat Mass Transf., **17**, No. 22, pp. 205–214.

[17] Bardon, J. P., 1972, ''Introduction à l'étude des résistances thermiques de contact,'' Rev. Gen. Therm., **125**, pp. 429–446.

[18] Snaith, B., Probert, S. D., and O'Callaghan, P. W., 1986, ''Thermal Resistances of Pressed Contacts,'' Appl. Energy, **22**, pp. 31–84.

[19] Sridhar, M. R., and Yovanovich, N. M., 1994, ''Review of Elastic and Plastic Contact Conductance Models: Comparison With Experiment,'' J. Thermophys. Heat Transfer, **8**, No. 4, pp. 633–640.

[20] Sridhar, M. R., and Yovanovich, N. M., 1996, ''Elastoplastic Contact Conductance Model for Isotropic Conforming Rough Surfaces and Comparison With Experiments,'' ASME J. Heat Transfer, **118**, pp. 3–9.

[21] Challen, J. M., Mc Lean, L. J., and Oxley, P. L. B., 1984, ''Plastic Deformation of a Metal Surface in Sliding Contact With a Hard Wedge: Its Reaction to Friction and Wear,'' Proc. R. Soc. London, Ser. A, **394**, pp. 161–181.

[22] Johnson, W., Sowerby, R., and Venter, R. D., 1982, *Plane Strain Slip Line Fields for Metal Deformation Processes: A Source Book and Bibliography*, Pergamon, Tarrytown, NY.

[23] Kennedy, F. E., 1984, ''Thermal and Thermomechanical Effect in Dry Sliding,'' Wear, **100**, pp. 453–476.

[24] Chantrenne, P., and Raynaud, M., 1997, ''A Microscopic Thermal Model for Dry Sliding Contact,'' Int. J. Heat Mass Transf., **40**, No. 5, pp. 1083–1094.

[25] Beck, J. V., and Keltner, N. R., 1982, ''Transient Thermal Contact of Two Semi-Infinite Bodies Over a Circular Area,'' Spacecraft Radi. Transfer Temp. Control, **83**, pp. 61–80.

[26] Sadhal, S. S., 1981, ''Unsteady Heat Flow Between Solids With Partially Contacting Interface,'' ASME J. Heat Transfer, **103**, pp. 32–35.

[27] Li, Y. H., and Sellars, C. M., 1996, ''Evaluation of Interfacial Heat Transfer and Friction Conditions and Their Effects on Hot Forming Processes,'' *37th MWSP Conf. Proc., ISS*, **33**, pp. 385–393.

[28] Chantrenne, P., and Raynaud, M., 1996, ''Détermination numérique de la résistance thermique de contact entre deux solides en frottement sec à partir d'un modèle thermique microscopique,'' *Annual Congress of the SFT*, Elsevier, New York.

[29] Wong, H. Y., 1968, ''Fundamental Studies of the Thermal Conductance of Metallic Contacts,'' *Proceedings of the 8th Conference on Thermal Conductivity*, Plenum, New York, pp. 495–511.

[30] Marchand, A. S., Salle, E., Raynaud, M., and Boyer, J. C., 1999, ''Influence of a Time and Space TCR on the Workpiece Thermo-Mechanical Behavior During Hot Forming Process,'' ESAFORM Congress, Portugal.

Fabry-Perot Resonators Built With $YBa_2Cu_3O_{7-\delta}$ Films on Si Substrates

A. R. Kumar
Department of Mechanical Engineering,
University of Florida,
Gainesville, FL 32611

V. A. Boychev
Department of Physics,
University of Florida,
Gainesville, FL 32611

Z. M. Zhang[1]
Department of Mechanical Engineering,
University of Florida,
Gainseville, FL 32611
e-mail: zzhang@cimar.me.ufl.edu

D. B. Tanner
Department of Physics,
University of Florida,
Gainesville, FL 32611

Fabry-Perot resonators were built from two superconductive $YBa_2Cu_3O_{7-\delta}$ (YBCO) films separated by a spacer. Each film of 35-nm thickness was deposited on a Si substrate, about 204 μm thick. A slow-scan Michelson interferometer was employed to measure the transmittance of the resonator in the far-infrared frequency region from 10 to 90 cm^{-1} at temperatures between 10 and 300 K. Measurements showed that in the normal state the peak (or resonant) transmittance decreases as temperature is lowered, whereas in the superconducting state it can increase with decreasing temperature. The transmittance of the resonator was calculated using properties of individual reflectors obtained previously. When the effect of partial coherence is taken into consideration, the calculated transmittance is in good agreement with the experiments. Furthermore, the maximum possible resonant transmittance was predicted based on an optimization analysis in which the cavity length is varied. The effect of the YBCO film thickness on the transmittance peaks was also studied, showing that the resonant transmittance decreases but the finesse increases as the film thickness is increased. This study should help improve the future design of Fabry-Perot resonators based on HTSC thin films. [S0022-1481(00)00604-6]

1 Introduction

Observations in the far-infrared region play an important role in the fields of astrophysics, chemical analysis, and molecular spectroscopy. Far-infrared studies in astrophysics include the cooling lines of star forming regions, associated cold dust, and spectra of giant planets ([1]). The pure rotational spectra of molecules and absorption bands in solids and liquids generally fall in the far-infrared region. Most of these studies require high precision measurements of the far-infrared radiation in a very narrow band; this can be achieved with the help of Fabry-Perot resonators ([2]). Fabry-Perot resonators can also be used as adaptable interferometers and in laser-line analysis ([2,3]). A simple resonator consists of two reflecting mirrors facing each other separated by a medium that is usually air or vacuum or a gas which needs to be analyzed. The most commonly employed reflectors in the far-infrared region are metallic meshes ([4,5]).

High-temperature superconducting (HTSC) thin films on transparent substrates have been considered as a potential substitute for the metallic mesh reflectors in far-infrared resonators ([6]). Metallic meshes show absorption at infrared frequencies due to the ohmic losses from the current induced in the wires ([5]). This absorption within the metallic mesh limits the finesse of the resonators. In the superconducting state, the thin films have no ohmic losses (i.e., no absorption) for frequencies up to their superconducting energy gap, which lies in the far-infrared region for HTSC materials. Hence, Fabry-Perot resonators built with HTSC thin films should offer a higher finesse than those with metallic meshes, although some residual absorption still exists at low temperatures due to noncondensing electrons. Another advantage is the suppression of high-frequency radiation, as HTSC materials are more opaque than the metallic-mesh at high frequencies.

Renk et al. [6] reported the use of HTSC thin films for the construction of far-infrared resonators in the frequency range up to 300 cm^{-1}. They used 100-nm-thick YBCO films on 1-mm thick MgO substrates as reflectors and a cavity length of 44 μm. The obtained peak transmittance was 0.016 with a finesse $F=30$ for the first-order resonance. The lower transmittance was due to the relatively thick YBCO film. Wiese et al. [7] measured the transmittance of a resonator made from two reflectors: a 50-nm-thick YBCO film on a 0.35-mm-thick MgO substrate and a 70-nm-thick film on a 0.25-mm-thick MgO substrate. The reported peak transmittance was 0.16 and $F=55$ for the first-order resonance located near 80 cm^{-1}. In order to obtain a high peak transmittance, the HTSC films should be thin enough so that the transmittance will not be too low and the substrates should effectively transmit in the frequency region of interest. Pechen et al. [8] measured the transmittance of a resonator built from 30-nm-thick YBCO films deposited on 0.5-mm-thick Si substrates. The measured peak transmittance at 10 K was about 0.6 with $F=20$ at the first-order resonance frequency of 60 cm^{-1}. Although this peak transmittance is much higher than that obtained in the previous studies, the resonance in the substrates has caused strong sidebands that overlap the main resonance peaks.

In the present paper, we describe the transmittance measurement of resonators built from two reflectors, each consisting of a 35-nm-thick YBCO film deposited on a Si substrate (about 204 μm thick). Measurements were carried out in the frequency region from 10 to 90 cm^{-1} at fixed temperatures between 10 and 300 K. The smaller thickness of the substrate used in the current work allows the distinction of the main resonance from the sidebands caused by interference effects in the substrates. In addition, the optimum cavity length that results in maximum peak transmittance was computed by coupling the cavity resonance with the resonance in the substrate. The effect of the YBCO film thickness on the peak transmittance of the resonator was also studied.

2 Theoretical Background

A simple plane Fabry-Perot resonator consists of two parallel mirrors separated by a gap, with their reflecting surfaces facing each other. In the present experiments, two Si substrates coated with YBCO films were used to form a resonator as shown in Fig. 1(*a*). The transmittance through this multilayer structure was derived using the two-effective-interface method. The transmittance of the resonator is ([2])

---

[1] To whom correspondence should be addressed.

Contributed by the Heat Transfer Division for publication in the JOURNAL OF HEAT TRANSFER and presented at the 1999 IMECE, Nashville, TN. Manuscript received by the Heat Transfer Division, July 9, 1999; revision received, May 25, 2000. Associate Technical Editor: D. Poulikakos.

$$\mathcal{T}=\frac{\dfrac{T_1T_2}{(1-\sqrt{R_1R_2})^2}}{1+\dfrac{4\sqrt{R_1R_2}}{(1-\sqrt{R_1R_2})^2}\sin^2\left(\dfrac{\beta+\phi_1+\phi_2}{2}\right)} \tag{1}$$

where subscripts 1 and 2 indicate the first and the second film/substrate composite, T and R are the transmittance and the film-side reflectance of the composite, $\beta=4\pi\omega d$ is the phase shift of the radiation at frequency ω (in cm^{-1}) for one round trip inside the cavity of length d (in cm) with a refractive index equal to 1, and ϕ is the phase shift upon refection at the film surface. Equation (1) can be expressed in a more compact form using the definitions of finesse,

$$F=\frac{\pi(R_1R_2)^{1/4}}{1-\sqrt{R_1R_2}}, \tag{2}$$

and resonant transmittance,

$$\mathcal{T}_{\text{res}}=\frac{T_1T_2}{(1-\sqrt{R_1R_2})^2}. \tag{3}$$

Hence, the transmittance of the resonator is

$$\mathcal{T}=\frac{\mathcal{T}_{\text{res}}}{1+\dfrac{4F^2}{\pi_2}\sin^2\left(\dfrac{\psi}{2}\right)} \tag{4}$$

where $\psi=\beta+\phi_1+\phi_2$. The transmittance reaches its maxima ($\mathcal{T}_{\text{res}}$) for $\psi=2m\pi$ and its minima for $\psi=(2m+1)\pi$ where m is the order of the interference fringe. If the change in $\mathcal{T}_{\text{res}}$ is small, for locations of the half maxima can be calculated by setting the denominator in Eq. (4) to be 2, i.e., $F^2\sin^2(\psi/2)=\pi^2/4$. For large values of F, $\psi=2m\pi\pm\pi/F$. If changes in ϕ_1 and ϕ_2 are neglected, the full-width-at-half-maximum (FWHM) bandwidth is $(2dF)^{-1}$. This is consistent with the definition of finesse F, which is the ratio of fringe separation or free spectral range, $\Delta\omega=(2d)^{-1}$, to the FWHM bandwidth. For a given cavity length, F is inversely proportional to the bandwidth of the transmittance peak. The effects of interference inside the substrate are included in the T and R terms, which can cause additional oscillations (sidebands) in the transmittance spectra and/or interfere with the resonant transmittance peaks. Hence, the actual bandwidth and finesse may differ significantly from the simplified calculations. It is noteworthy that the transmittance of the resonator can also be calculated using the transfer-matrix method ([9,10]). Because Eqs. (2)–(4) clearly distinguish the influence of the cavity resonance from the properties of each individual reflector, they are employed in the present analysis.

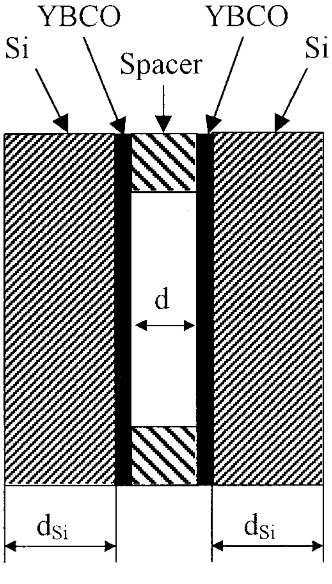

Fig. 1 The cross-sectional view of the resonator structure (not to scale)

3 Experiments

In the present study, each reflecting surface was made of a 35-nm-thick YBCO film deposited on a 12 mm × 12 mm Si substrate of 204 μm (± 1 μm) thickness. The superconductive films were deposited at the National Institute of Standards and Technology by a laser ablation technique using yttria-stabilized zirconia and CeO_2 buffer layers ([11,12]). The YBCO films were a-b plane oriented with a critical temperature (T_c) between 80 and 82 K. The spacer that separates the two films was either a polyimide sheet of 132-μm thickness or a copper plate of 550-μm thickness, with a hole at the center. The cross-sectional view of the resonator arrangement is shown in Fig. 1. The distance between the two films, i.e., the cavity length d, is determined by the spacer.

Two identical copper plates with equally sized apertures (6 mm in diameter) were mounted at a right angle on the sample holder; one is used to mount the resonator structure and the other is left blank for reference measurements, as shown in Fig. 2. Slightly curved beryllium copper strips (2 mm wide, 0.2 mm thick, and 5 mm long), fastened with screws on the corners of one plate, acted like springs (due to their high elasticity) to hold the films along with the spacer to the copper plate. This sample holder was mounted on the cold finger inside the cryostat. The cold finger was kept in high vacuum and cooled by liquid helium, resulting in conductive cooling of the films. The transmittance spectra were measured using a slow-scan Michelson interferometer with a mercury-arc lamp source and a liquid-helium-cooled silicon bolometer. The construction details of this particular interferometer were reported by Sanderson and Scott [13]. The transmittance spectra of individual films were measured with the same experimental arrangements and analyzed to obtain the dielectric function of individual films at various temperatures ([12]).

The transmittance of the resonator structure was measured at temperatures of 10, 50, 100, 200, and 300 K in the frequency region from 10 to 90 cm^{-1}. The measured transmittance spectra for the resonator with a polyimide spacer are shown in Fig. 3. The transmittance peaks resulting from the resonance within the cavity are located at $\omega_m=m/2d$, where $m=1,2,\ldots$. Therefore, the transmittance peaks of the first and second-order resonance for this spacer are approximately located at 39 cm^{-1} and 76 cm^{-1}, respectively. The actual resonance frequency are determined by ψ, which is influenced by ϕ_1 and ϕ_2. The resonant transmittance

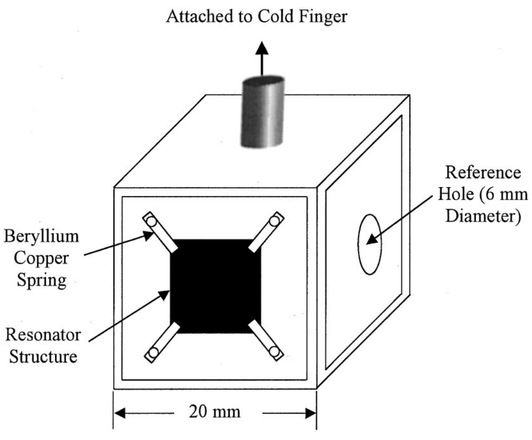

Fig. 2 Schematic of the sample holder

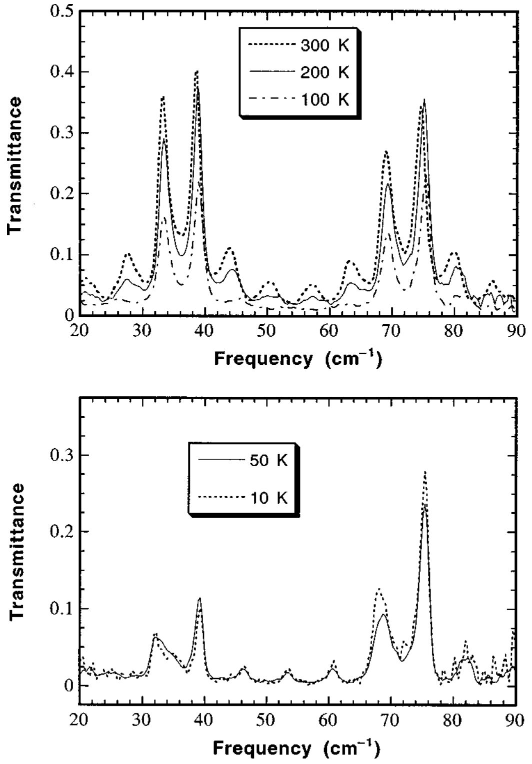

Fig. 3 Measured transmittance of the Fabry-Perot resonator with the polyimide spacer at various temperatures

peaks are shifted toward higher frequencies as the temperature is lowered. This can be explained by the decrease in the refractive index of the Si substrate as the temperature is lowered. The resonance (or interference) within the Si substrates is coupled to the main resonance inside the cavity, resulting in complex fringes. The sidebands include additional transmittance peaks near the main resonance and ripples in the spectra.

Above 100 K the peak transmittance associated with sidebands is comparable to that of the main resonance. In the normal state $\mathcal{T}_{\text{res}}$ decreases with temperature, by a factor of two from 300 to 100 K. If both the YBCO films were identical, then $\mathcal{T}_{\text{res}}$ given by Eq. (3) is reduced to ([4])

$$\mathcal{T}_{\text{res}}=\frac{1}{(1+A/T)^2} \tag{5}$$

where $A=1-T-R$ is the absorptance of the film/substrate composite. The smaller the value of A/T, the higher the resonant transmittance $\mathcal{T}_{\text{res}}$. The YBCO material exhibits a metallic behavior in the normal state. Its electrical conductivity will increase as the temperature decreases, yielding a reduction in the transmittance and an increase in the reflectance. The absorptance for radiation incident on the film side does not change significantly with temperature in the normal state ([14]). Therefore, as the temperature is lowered, the resonant transmittance decreases whereas the finesse increases, which means a decrease in the bandwidth. The transmittance associated with the sidebands shows a relatively higher percentage of reduction than the main resonant transmittance, because the increase in the reflectance of the YBCO films has suppressed the interference effects within the Si substrates.

In the superconducting state, the sidebands are suppressed even more significantly in comparison with the main resonance and this difference becomes larger at the second-order resonance. Another feature associated with the superconducting state is that at some frequencies, the peak transmittance increases as the temperature is lowered. This is particularly true at the second-order resonance (76 cm^{-1}), where $\mathcal{T}_{\text{res}}$ is increased from 0.24 at 50 K to 0.28 at 10 K. Similar behavior was observed in the transmittance spectra of a single film/substrate composite due to the resonance in the Si substrate ([12]). The radiative properties of YBCO in the superconducting state differ greatly from those in the normal state. In the superconducting state, HTSC materials tend to show perfect reflection and little absorption for radiation at frequencies up to the energy gap. Decreasing the temperature causes an increase in the fraction of superconducting electrons and a decrease in the far-infrared absorptance ([15]). Hence, the increase in the peak transmittance from 50 K to 10 K can be attributed to the decrease in the absorptance within the YBCO films. Similar to the normal state, the bandwidth also decreases with the decrease in temperature, because of the increase in the reflectance. The measured finesse at 76 cm^{-1} is approximately 20 at 50 K and 23 at 10 K.

4 Calculation and Comparison

The transmittance T, film-side reflectance R, and phase shift ϕ of each reflector can be calculated using the optical constants of the film and substrate, assuming it is composed of a thin absorbing film on a thin (coherent) transparent substrate ([14]). There exists a large difference between the film-side reflectance and the back-side reflectance ([16]). Calculation of the transmittance and reflectance requires prior knowledge of the frequency-dependent dielectric function of the thin-film materials. The dielectric function of YBCO in the far-infrared region is computed using the Drude model in the normal state and a two-fluid model in the superconducting state ([15]). By comparison with the experiments, best fitting parameters (such as the plasma frequency and scattering rate) were obtained and reported in the work of Kumar et al. [12] for each individual reflector. The fitted parameters obtained for the two films are not the same because of variation in the conditions of deposition and post treatment. There exists a large fraction of residual normal electrons at temperatures below T_c. The buffer layers have negligible effect to either the phase shift or the transmittance and reflectance.

The refractive index of Si depends on the frequency, increasing by about 0.1 percent from 10 to 100 cm^{-1} ([17]). Such small variation is negligible in the frequency region considered here; therefore, the refractive index of Si is assumed to be dependent only on temperature. The refractive index of Si changes from 3.42 at 300 K to 3.39 at 10 K as obtained by fitting the interference fringes in the transmittance and reflectance spectra of a bare Si substrate ([12,18]). The substrate thicknesses are $d_{\text{Si}}=203.6\ \mu\text{m}$ and 204.3 μm for the two reflectors, respectively. Changes in d_{Si} due to thermal expansion are within 0.024 percent throughout the temperature range, which is negligibly small. The uncertainty in the refractive index and thickness of Si is approximately 0.5 percent. The surfaces are optically smooth with a root-mean-square roughness of a few nanometers. Because the wavelength is longer than 100 μm, the effect of surface roughness can be neglected.

For the sake of brevity, only the results at 300 K and 10 K are presented. The transmittance of the resonator is very sensitive to the optical path length introduced by the spacer. The thickness of the polyimide spacer measured with a micrometer was 132 μm. To obtain a good agreement with the measured fringes, in the computation, the cavity length was adjusted to 138 μm at 300 K and 134 μm at 10 K. This discrepancy may be due to the beryllium copper springs not being tight enough. Excessive tightening was avoided as it might break the samples. At low temperatures, there may be a decrease in the cavity length due to thermal contraction of the polyimide film (about 1–2 μm) and the effect of the beryllium copper springs. The cavity length is the only adjustable parameter in the calculation using Eq. (1) or (4).

Another important issue is the parallelism between the two reflecting surfaces. Only manual adjustments were done before the experiments to maintain the two reflectors as parallel as possible. Parallelism between the two reflecting surfaces also might have suffered from the uneven tightening of the springs. Equations from thin-film optics are strictly applicable to completely coherent

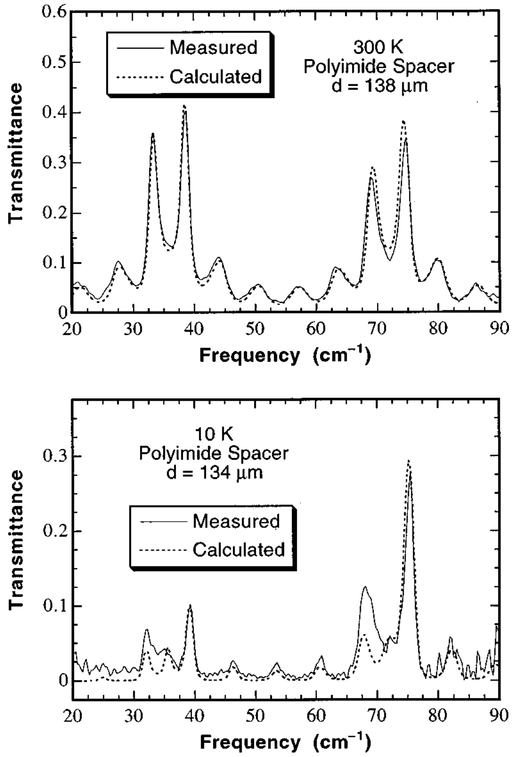

Fig. 4 Comparison between the measured and calculated transmittance, where *d* indicates the cavity length used in the calculation

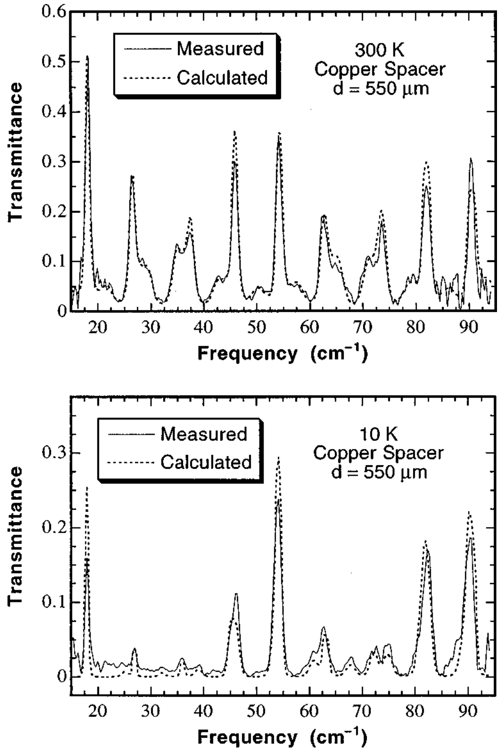

Fig. 5 Measured and calculated transmittance of the resonator with the copper spacer at 300 and 10 K

cases but nonparallelism can significantly reduce the fringe contrast and peak transmittance. The effect of partial coherence on the radiative properties of thin films were studied by many authors ([19–22]). The finite spectral resolution and beam divergence also reduce the coherence ([20]). In the experiments, the frequency interval between data points was 0.28 cm^{-1} and the spectral resolution was 0.56 cm^{-1}. The spatial incoherence caused by the nonparallelism (between the two films) and by the beam divergence (due to the finite solid angle) increases towards higher frequencies ([21]). Therefore, an empirical relation is introduced for the frequency-dependent effective resolution ($\delta\omega$):

$$\delta\omega=\sqrt{0.56^2+(0.02\omega)^2}. \tag{6}$$

Equation (6) gives an effective resolution from about 0.6 to 2.1 cm^{-1} as ω changes from 10 to 100 cm^{-1}. In the computation, the transmittance is integral averaged from $\omega-\delta\omega/2$ to $\omega+\delta\omega/2$ for each point. Figure 4 shows the comparison between the measured transmittance and calculated transmittance which includes the effect of partial coherence. The measured and calculated values agree closely except for the spectra at 10 K in the regions from 30 to 37 cm^{-1} and from 65 to 72 cm^{-1}. The reason for this disagreement needs further investigation.

The measured and calculated transmittance at 300 K and 10 K for the resonator with the copper spacer is shown in Fig. 5. The main resonant peaks are located at approximately 9 cm^{-1} (which is below the cutoff frequency), 18 cm^{-1}, 27 cm^{-1}, etc. The interference in the Si substrates has a strong effect on the peak transmittance because $\mathcal{T}_{\mathrm{res}}$ changes drastically with frequency, which will be discussed in the following section. The measured peak transmittance is 0.51 at 300 K and 0.16 at 10 K for the second-order resonance. The FWHM bandwidth for this transmittance peak is 1.1 cm^{-1} and 0.9 cm^{-1} at 300 K and 10 K, respectively.

To demonstrate the effect of partial coherence, the transmittance calculated directly from thin-film optics (complete coherence) with a frequency interval of 0.05 cm^{-1} is compared with that calculated considering partial coherence in Fig. 6. The effect of partial coherence is particularly large for sharp transmittance peaks. It is not surprising that the agreement in Fig. 5 is not as good as that in Fig. 4. Notice that the bandwidth of the transmittance peak broadens due to partial coherence. Higher spectral

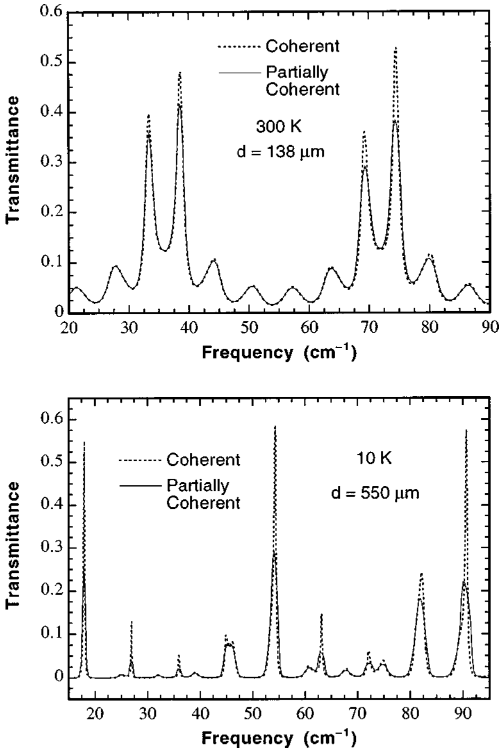

Fig. 6 The effect of partial coherence on the resonant transmittance

resolution with improved alignment between the two reflecting surfaces should be used in future measurements.

5 Discussion

Optimization of the Resonant Transmittance. The radiative properties of individual reflectors, which are related to the interface effects in the substrates, strongly influence the transmittance characteristics of the resonator. The resonant transmittance $\mathcal{T}_{\mathrm{res}}$, determined from Eq. (3), depends entirely on the two reflectors but not on the cavity length. Figure 7 plots the calculated T_1, R_1 and ϕ_1 of the first reflector, together with $\mathcal{T}_{\mathrm{res}}$ at 300 K and 10 K for completely coherent situation. The properties of the second reflector are very similar to these of the first one since the substrate thickness is nearly the same. All spectra oscillate due to interference in the substrate with a period (free spectral range) of $\Delta\omega_{\mathrm{Si}}=(2n_{\mathrm{Si}}d_{\mathrm{Si}})^{-1}$, where d_{Si} is the thickness and n_{Si} the refractive index of Si. In the normal sate, the fringe contrast in the reflectance is much larger than that in the transmittance. Therefore, the maxima of both $\mathcal{T}_{\mathrm{res}}$ and R_1 are located at the same frequencies, given by

$$\omega_{m_{\mathrm{Si}}}=\frac{2m_{\mathrm{Si}}+1}{4n_{\mathrm{Si}}d_{\mathrm{Si}}}, \tag{7}$$

where m_{Si} is the order of resonance in the Si substrate. At frequencies equal to $\omega_{m_{\mathrm{Si}}}$, ϕ_1 is approximately zero. In order to achieve the maximum peak transmittance, the particular resonance in the cavity must be coincident with one of the resonances in the substrates. Since $\phi_1\approx\phi_2\approx 0$ at the substrate resonance, Eq. (4) suggests that β must equal $2\pi m$, corresponding to the main resonant frequencies $\omega_m=m/2d$. By equating ω_m and $\omega_{m,\mathrm{Si}}$, we have

$$d=\frac{2n_{\mathrm{Si}}m}{2m_{\mathrm{Si}}+1}d_{\mathrm{Si}} \tag{8}$$

which is a criterion for obtaining maximum resonant transmittance.

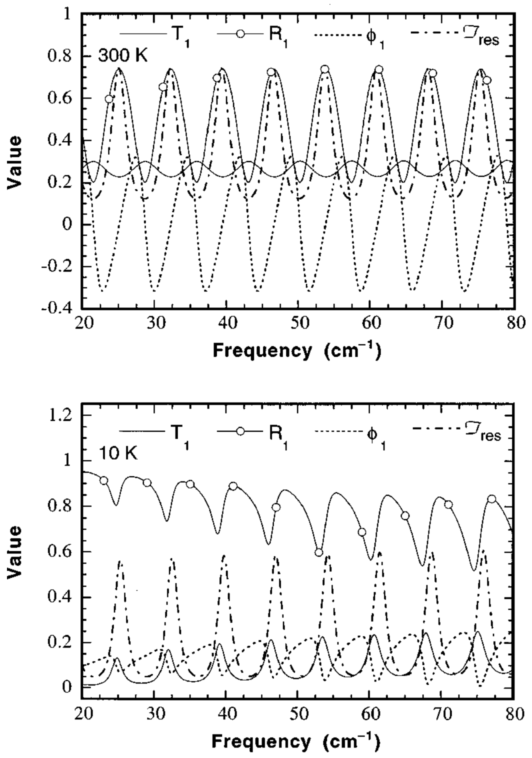

Fig. 7 Calculated transmittance *T*, reflectance *R*, and phase shift upon reflection ϕ for the first reflector, together with $\mathcal{T}_{\mathrm{res}}$

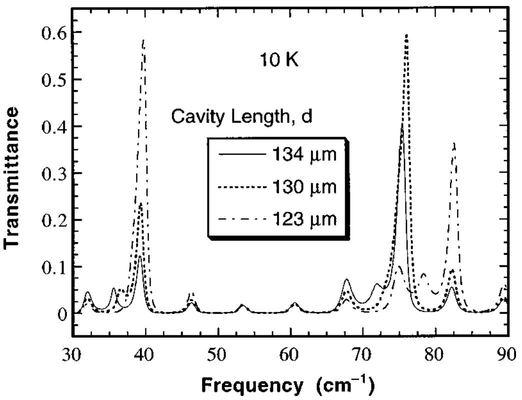

Fig. 8 The effect of cavity length on the peak transmittance for the first and second-order resonance

In the superconducting state, Fig. 7(*b*) shows that ϕ_1 is always greater than zero and the behavior of T_1 and R_1 are quite different from those in the normal state. The maxima of $\mathcal{T}_{\mathrm{res}}$, however, are still located near $\omega_{m_{\mathrm{Si}}}$, where ϕ_1 is close to zero. Therefore, Eq. (8) provides a good approximation for getting the best performance. The actual value of optimum d may be slightly different from that given by Eq. (8).

Equation (8) was originally obtained by Malone et al. [9]. They adjusted the substrate thickness in the computation to predict the maximum resonant transmittance. Here, we have provided detailed derivations of Eq. (8) by analyzing the resonator transmittance equation and the properties of each individual reflector. In practice, it is often easier to adjust the cavity length. In our experiments, the value of d was chosen at random and was kept constant. In order to show that HTSC films on transparent substrates are indeed good candidates for far-infrared resonators, the cavity length d is varied to compute the optimal characteristics of the resonator.

The peak transmittance is optimized for the first and second-order of the cavity resonance (i.e., $m=1,2$) for 10 K. The value of m_{Si} is chosen so that the value of d lies in the close vicinity of 134 μm, the value obtained from the experiment. Using $n_{\mathrm{Si}}=3.39$ and $d_{\mathrm{Si}}=204$ μm, which is the average thickness of the two substrates, Eq. (8) gives the values of d that yield the maximum transmittance to be 126 μm ($m_{\mathrm{Si}}=5$) and 133 μm ($m_{\mathrm{Si}}=10$), respectively, for the first and second-order resonance. The actual optimized cavity lengths are $d=123$ μm and 130 μm. Figure 8 compares the calculated transmittance for the cavity lengths optimized for the first and second-order resonance with that obtained from the experiment. All three cases are assumed to be completely coherent. The optimized peak transmittance is near 0.6, which is 400 percent higher than the peak transmittance for the first-order resonance obtained from the experiment. Another important feature in the optimized situation is that the sidebands have been substantially reduced, which is the advantage of using thin Si substrates as compared with the 0.5 mm thick Si substrates used by Pechen et al. [8]. The value F calculated from Eq. (2) also oscillates. Because $\mathcal{T}_{\mathrm{res}}$ and ϕ_1 change drastically with frequency, the value of F calculated from Eq. (2) is not an indicator of the finesse anymore. The finesse is calculated by dividing the free spectral range by the FWHM bandwidth.

The above method can be applied to optimize the performance for various ranges of d and at different temperatures. These calculations demonstrate that HTSC materials are promising candidates for constructing far-infrared resonators. The performance of the resonator, however, is a strong function of the cavity length. Therefore, a mechanism that can adjust the cavity length within a few micrometers during the measurement is required and is currently under development to achieve the optimal performance.

The Effect of the YBCO Film. The YBCO film thickness affects the transmittance, reflectance, and absorptance of the individual reflectors, which in turn affect the transmittance characteristics of the resonator. Increasing the film thickness will decrease the transmittance of the film/substrate composite, yielding a reduction in the peak transmittance of the resonator as can be seen from Eq. (3). However, increasing the film thickness will increase the reflectance of the film/substrate composite, which in turn will improve the finesse, see Eq. (2).

The effect of the YBCO film thickness is studied by a computer simulation, in which the film thickness is varied on one or both reflectors, under conditions that facilitate the maximum possible first-order resonant transmittance. Only a brief summary is given here. As the YBCO thickness decreases, the peak resonant transmittance increases and reaches 1 for zero thickness (i.e., only Si substrates). The height of the sidebands also increases as the YBCO film thickness decreases. The bandwidth of the transmittance peaks shows a decreasing trend with the increase in the YBCO film thickness, indicating that the finesse is increasing. Hence, in the resonator design, a compromise must be made between high resonant transmittance and high finesse with suppressed sidebands. The thickness of the YBCO film should generally be equal to or less than 50 nm in order to have acceptable resonant transmittance. The quality of the YBCO film also affects the resonator's performance. High-quality films with little residual absorption in the superconducting state will improve the peak transmittance and finesse.

6 Conclusions and Future Work

We have measured the transmittance of Fabry-Perot resonators using YBCO films on Si substrates as the reflecting surfaces in the far-infrared region at temperatures between 10 and 300 K. The sidebands observed in previous studies have been suppressed by the use of thin substrates. The resonant transmittance decreases with temperature in the normal state but can increase in the superconducting state as the temperature goes down. The calculated transmittance, considering partial coherence, is in good agreement with the experimental data. An optimization analysis was performed to predict the maximum resonant transmittance by examining the interference effects in the cavity and substrates. The transmittance characteristics of the resonator are very sensitive to the thickness of each layer that forms the resonator. The maximum resonant transmittance is obtained when a particular resonance in the cavity is coincident with one of the substrate resonances. An increase in the YBCO film thickness will improve the finesse but reduce the peak transmittance.

This work demonstrates the potential of using YBCO thin films on thin Si substrates to construct Fabry-Perot resonators and can serve as the basis for the future design of such resonators. We are developing a mechanism that will improve the alignment between the two reflectors and will allow fine-tuning of the cavity length during the measurement. A higher spectra resolution should be used to discern sharp transmittance peaks. The quality of the YBCO film should be improved with reduced residual absorption to achieve a better performance.

Acknowledgments

The authors would like to thank Dr. Leila Vale and Dr. David Rudman of the National Institute of Standards and Technology for providing the superconducting film samples. This work has been supported by the National Science Foundation (NSF) through grant CTS-9812027. Z.M.Z. is also grateful to the NSF support through a PECASE award (CTS-9875441).

Nomenclature

A = absorptance
d = cavity length, cm
d_{Si} = thickness of the Si substrate, cm
F = finesse
m = order of resonance (or interference fringe)
n = refractive index
R = reflectance of the film/substrate composite
T = transmittance of the film/substrate composite
T_c = critical temperature, K
$\mathcal{T}$ = transmittance of the resonator
$\mathcal{T}_{\mathrm{res}}$ = resonant transmittance
β = phase shift inside the cavity, rad
ϕ = phase shift upon reflection, rad
ψ = $\beta+\phi_1+\phi_2$, Eq. (4)
ω = frequency, cm^{-1} ($1\ \mathrm{cm}^{-1}=2.9979\times10^{10}$ Hz)
ω_m = resonance frequency, cm^{-1}
$\Delta\omega$ = fringe separation (or free spectral range), cm^{-1}
$\delta\omega$ = spectral resolution, cm^{-1}

Subscripts

1 = first film
2 = second film
Si = silicon

References

[1] Brodbeck, R., Pepe, F. A., Tognina, C., Bhend, D., Zimmerman, E., and Kneubuhl, F. K., 1998, ''Balloon-Borne Far-Infrared Fabry-Perot Spectrometers for Astrophysical Observations,'' Infrared Physics and Technology, **39**, pp. 393–414.

[2] Vaughan, J. M., 1989, *The Fabry-Perot Interferometer*, Adam Hilger Publishers, Philadelphia, PA.

[3] Komm, D. S., Blanken, R. A., and Brossier, P., 1975, ''Fast-Scanning Far-Infrared Fabry-Perot Interferometer,'' Appl. Opt., **14**, pp. 460–464.

[4] Renk, K. F., and Genzel, L., 1962, ''Interference Filters and Fabry-Perot Interferometers for the Far Infrared,'' Appl. Opt., **1**, pp. 643–648.

[5] Belland, P., and Lecullier, J. C., 1980, ''Scanning Fabry-Perot Interferometer: Performance and Optimum Use in the Far Infrared Range,'' Appl. Opt., **19**, pp. 1946–1952.

[6] Renk, K. F., Betz, J., Schützmann, J., Prückl, A., Brunner, B., and Lengfellner, H., 1990, ''Use of High T_c Superconductors for Far-Infrared Fabry-Perot Resonators,'' Appl. Phys. Lett., **57**, pp. 2148–2149.

[7] Wiese, P., Riederer, X., Schützmann, J., Gorshunov, B., Betz, J., and Renk, K. F., 1992, ''Far-Infrared Fabry Perot Filter of High Transmission With High-T_c Superconductor Reflectors,'' Int. J. Infrared Millim. Waves, **13**, pp. 65–70.

[8] Pechen, E. V., Vent, S., Brunner, B., Prückl, A., Lipp, S., Linder, G., Alexandrov, O., Schützmann, J., and Renk, K. F., 1992, ''Far-Infrared Fabry-Perot Resonator With High T_c $\mathrm{YBa_2Cu_3O_{7-\delta}}$ Films on Silicon Plates,'' Appl. Phys. Lett., **61**, pp. 1980–1982.

[9] Malone, C. G., Zhang, Z. M., Flik, M. I., and Cravalho, E. G., 1993, ''Optimized Design of Far-Infrared Fabry-Perot Resonators Fabricated From $\mathrm{YBa_2Cu_3O_7}$,'' IEEE Trans. Appl. Supercond., **3**, pp. 2852–2855.

[10] Kumar, A. R., and Zhang, Z. M., 1999, ''Far-Infrared Spectroscopy of High-Temperature Superconducting Films on Silicon Substrates,'' *Recent Research Developments in Applied Spectroscopy*, Vol. 2, S. G. Pandalai, ed., Research Signpost, India, pp. 99–112.

[11] Rice, J. P., Grossman, E. N., and Rudman, D. A., 1994, ''Antenna-Coupled High-T_c Air-Bridge Microbolometer on Silicon,'' Appl. Phys. Lett., **65**, pp. 773–775.

[12] Kumar, A. R., Zhang, Z. M., Boychev, V. B., Tanner, D. B., Vale, L. R., and Rudman, D. A., 1999, ''Far-Infrared Transmittance and Reflectance of $\mathrm{YBa_2Cu_3O_{7-\delta}}$ Films on Si Substrates,'' ASME J. Heat Transfer, **121**, pp. 844–851.

[13] Sanderson, R. B., and Scott, H. E., 1971, ''High Resolution Far Infrared Interferometer,'' Appl. Opt., **10**, pp. 1097–1102.

[14] Kumar, A. R., Zhang, Z. M., Boychev, V. B., and Tanner, D. B., 1999, ''Temperature-Dependent Far-Infrared Absorptance of Thin $\mathrm{YBa_2Cu_3O_{7-\delta}}$ Films in the Normal State,'' Microscale Thermophys. Eng., **3**, pp. 5–15.

[15] Tanner, D. B., and Timusk, T., 1992, ''Optical Properties of High-Temperature Superconductors,'' *Physical Properties of High-Temperature Superconductors*, Vol. 3, D. M. Ginsberg, ed., World Scientific Publishing, Singapore, pp. 363–469.

[16] Zhang, Z. M., Kumar, A. R., Boychev, V. B., Tanner, D. B., Vale, L. R., and Rudman, D. A., 1998, ''Back-Side Reflectance of High T_c Superconducting Thin Films in the Far Infrared,'' Appl. Phys. Lett., **73**, pp. 1907–1909.

[17] Loewenstein, E. V., Smith, D. R., and Morgan, R. L., 1973, ''Optical Constants of Far-Infrared Materials, 2: Crystalline Solids,'' Appl. Opt., **12**, pp. 398–406.

[18] Kumar, A. R., 1999, ''Far-Infrared Radiative Properties of Superconducting YBCO Films Deposited on Silicon Substrates,'' Ph.D. Dissertation, University of Florida, Gainesville, FL.

[19] Chen, G., and Tien, C. L., 1992, ''Partial Coherence Theory of Thin Film Radiative Properties,'' ASME J. Heat Transfer, **114**, pp. 636–643.

[20] Zhang, Z. M., 1994, ''Optical Properties of Layered Structures for Partially Coherent Radiation,'' *Proc. Tenth Intl. Heat Transfer Conf.*, Vol. 2, G. F. Hewitt, ed., Taylor and Francis, London, pp. 177–182.

[21] Grossman, E. N., and McDonald, D. G., 1995, ''Partially Coherent Transmittance of Dielectric Lamellae,'' Opt. Eng., **34**, pp. 1289–1295.

[22] Anderson, C. F., and Bayazitoglu, Y., 1996, ''Radiative Properties of Films Using Partial Coherence Theory,'' J. Thermophys. Heat Transfer, **10**, pp. 26–32.

Heat Transfer Coefficient in Rapid Solidification of a Liquid Layer on a Substrate

P. S. Wei
Professor,
e-mail: pswei@mail.nsysu.edu.tw

F. B. Yeh
Graduate Student

Institute of Mechanical Engineering,
National Sun Yat-Sen University,
Kaohsiung Taiwan, R.O.C.

The heat transfer coefficient at the bottom surface of a splat rapidly solidified on a cold substrate is self-consistently and quantitatively investigated. Provided that the boundary condition at the bottom surface of the splat is specified by introducing the obtained heat transfer coefficient, solutions of the splat can be conveniently obtained without solving the substrate. In this work, the solidification front in the splat is governed by nonequilibrium kinetics while the melting front in the substrate undergoes equilibrium phase change. By solving one-dimensional unsteady heat conduction equations and accounting for distinct properties between phases and splat and substrate, the results show that the time-dependent heat transfer coefficient or Biot number can be divided into five regimes: liquid splat-solid substrate, liquid splat-liquid substrate, nucleation of splat, solid splat-solid substrate, and solid splat-liquid substrate. The Biot number at the bottom surface of the splat during liquid splat cooling increases and nucleation time decreases with increasing contact Biot number, density ratio, and solid conductivity of the substrate, and decreasing specific heat ratio. Decreases in melting temperature and liquid conductivity of the substrate and increase in latent heat ratio further decrease the Biot number at the bottom surface of the splat after the substrate becomes molten. Time-dependent Biot number at the bottom surface of the splat is obtained from a scale analysis.
[S0022-1481(00)01004-5]

Keywords: *Coatings, Contact Resistance, Heat Transfer, Phase Change, Solidification*

Introduction

Rapid solidification takes place in splat cooling, plasma or powder spray deposition, single and twin-roller melt-spinning, strip and slab casting, melt-extraction, etc. Extensive reviews have been presented by Anantharaman and Suryanarayana [1], Jones [2], Zaat [3], and Cahn [4]. In all these processes, the molten metal is brought in contact with a cold substrate, and heat is transferred from the melt into the substrate. Advantages of rapid solidification are that the workpiece surface can improve resistances to abrasion, wear, corrosion, or oxidation. Microstructures including grain sizes, spacings, and morphologies of dendrites and cells and solute segregation in the deposition are related to the heat transfer and kinetics of solidification.

Rapid solidification differs from slow equilibrium solidification ([5,6]) in the fact that the temperature at the solid-liquid interface is allowed to vary and the growth rate is governed by supercooling between the melting and interface temperatures ([7,8]). Rapid freezing takes place as the interface temperature is decreased to the nucleation temperature. Hence, a sudden increase in solidification rate results in recalescence, provided that the latent heat evolution is much greater than the dissipation of heat ([9]). The contact heat transfer coefficient between the liquid splat and substrate should reflect a strong variation of temperature and phase change near the substrate at an initial stage. In castings it has been known that contact heat transfer coefficient depends on the roughness of contact surfaces, impurities and properties on surfaces, gas entrapment, etc. ([10]). Contact heat transfer coefficient between the casting and mold decreases with time, first rapidly then much more slowly until an almost constant value is reached. This behavior can be related to the formation of an air gap at the contact surfaces upon shrinkage of the metals and or due to surface displacement. In view of the complexity of the process for rapid solidification, a study of the contact heat transfer coefficient affected by significant heat transfer, distinct properties in different phases, and kinetic effect becomes the objective of this work.

Cooling rates in a splat of aluminum, silver, and a gold alloy rapidly solidified on a cold substrate of nickel were first measured by Predecki et al. [11]. Referring to the measured thermo-emf between the splat and substrate, the calculations by assuming constant temperature of the substrate and contact heat transfer coefficient lead to high cooling rates of $10^6-5\times10^8$ K/s and contact heat transfer coefficients $10^5-2\times10^6$ W/m^2 K. Ruhl [12] numerically studied heat transfer and solidification characteristics of a splat on a substrate. Supercooling was taken into account by assuming a constant solidification temperature lower than the equilibrium melting temperature. The kinetic effect was not directly introduced. Depending on the Nusselt number, splat cooling can be controlled by either the thermal resistance of the contact surface between the splat and substrate or resistance of the solidified splat.

Shingu and Ozaki [13] studied supercooling by matching results of a heat balance calculation with those from a kinetic growth model subject to a constant undercooling. The release of latent heat, however, resulted in a heating of the undercooled melt and a decrease in supercooling. Complete suppression of recalescence is impossible because of finite external heat transfer. An account for splat cooling must include both external heat transfer and kinetic effects. A numerical heat transfer analysis combining a realistic kinetic effect of nucleation and rapid growth of the interface appears to be started from Levi and Mehrabian [9] in treating a supercooled atomized droplet. They provided a dimensionless enthalpy-temperature diagram to describe solidification following isothermal, isenthalpic, and recalescence paths. Clyne [14] proposed a parameter involving the kinetics coefficient and contact heat transfer coefficient to interpret the occurrence of recalescence. Significant recalescence was induced near the splat-substrate surface in an early stage by increasing supercooling,

---

Contributed by the Heat Transfer Division for publication in the JOURNAL OF HEAT TRANSFER. Manuscript received by the Heat Transfer Division, Sept. 7, 1999; revision received, May 8, 2000. Associate Technical Editor: F. Cheung.

thermal diffusivity, heat transfer coefficient, initial temperature of the molten layer, and reducing thickness of the molten layer, and initial temperature on the substrate surface.

Wang and Matthys [15] quantified time-dependent contact heat transfer coefficient between molten copper and a cold metallic substrate. It was found that a stepwise variation of the contact heat transfer coefficient in three main regions—liquid splat cooling, solidification, and solid splat cooling—can be used to match the calculated and measured temperature histories. In most cases, the contact heat transfer coefficient during liquid splat cooling is highest as a result of a good contact between the liquid splat and solid substrate. If a contact heat transfer coefficient in liquid splat cooling is not very large, the temperature difference across the splat is small. Significant contraction occurs perhaps only after the entire splat is solidified. On the other hand, a significant temperature gradient results in the splat if a contact heat transfer coefficient in liquid splat cooling is large. The solidified portion of the splat may contract significantly before the splat is completely solidified, and may continue to do so afterwards. This contraction results in lower contact heat transfer coefficients in solidification and solid splat cooling. If the contact heat transfer coefficient is so large that a large temperature gradient will be generated quickly in the solidified splat, the breakage of the bond and contraction may occur shortly and primarily after the melt starts solidifying, with little subsequent effect. Many other factors, as mentioned previously, may also need to explain why the contact heat transfer coefficient in solidification, in some cases, is greater than that in liquid splat cooling. Such a trend is not expected from a simple contraction model.

A substrate readily becomes molten due to high rates of sensible and latent heats released from the splat. In metals processing, such as spray deposition and microcasting, coating layers on a substrate requires a strong bonding between the layers and substrate through melting. In continuous slab or strip casting processes, substrate melting may be detrimental because of wheel or mold damage. Scott [16] measured the average and maximum cooling rate for aluminum copper alloy splats quenched on copper and glass substrates. Based on a known relationship between lamellar spacing and the freezing rate of an eutectic alloy, it was surprisingly found that the cooling rate of a splat on the glass substrate was higher than that of the same splat on a copper substrate. He suggested that the thermal contact between the splat for the glass substrate was better than the copper substrate by an evidence that the splats had melted the surface of the glass substrate slightly, thereby improving the thermal contact.

Kuijpers and Zaat [17] applied the Neumann-Schwartz formula ([18]) to predict the cooling rate of a plasma-sprayed molybdenum on an iron substrate. The assumptions were equilibrium solidification near the solidification temperature in a semi-infinite splat and substrate in a perfect contact. The results led to a melting of the substrate. Zaat [3] used the same formula to predict the minimum particle temperature needed to heat the substrate to its melting point. Steffens et al. [19] applied this formula to explain the bonding mechanism of thermally sprayed metal and ceramic composites on a metallic substrate. Tensile strength measurements of the coatings indicated that a higher contact temperature difference between a sprayed particle and the substrate usually led to a better bonding between the coating and the substrate. Amon et al. [20,21] numerically and experimentally studied the substrate melting and cooling rates for a superheated metal droplet impinging on substrates during microcasting. Neglecting interfacial resistance and kinetics of crystal growth, substrate melting, and melting front locations for different droplet and substrate temperatures were predicted. Temperature histories indicated that a highly time-dependent heat transfer coefficient at the droplet/substrate interface was required for an accurate prediction of remelting the substrate.

Wang et al. [22] numerically presented nondimensional operational maps that predict whether substrate melting will take place or not during rapid freezing of a deposited layer on a melting and then resolidification of a substrate. The model included heat transfer in both deposit and substrate, nonequilibrium kinetics at the solid-liquid interface, and time-dependent contact heat transfer coefficient. Restricted to a substrate to be melted and resolidified before the splat solidified, the results showed that a substrate can be melted by increasing the contact Biot number and superheating of the splat. The larger the solid substrate-to-liquid splat conductivity ratio, the more difficult it is to have the substrate melt. Even relatively small increases in thermal contact between the splat and substrate as the substrate melts would result in a large change in melted depth and melting rate.

Wei et al. [23] self-consistently studied rapid solidification of the splat and possible melting of the substrate. To delay freezing of the splat and melting of the substrate, increases in the Stefan number and initial temperature and a decrease in nucleation temperature of the splat were suggested. An increase in the splat-to-substrate specific heat ratio and decreases in solid conductivity of the substrate and substrate-to-splat density ratio delay freezing of the splat and accelerate melting of the substrate. To induce an early melting of the substrate while maintaining the same onset time for freezing of the splat, increases in the dimensionless kinetic coefficient and equilibrium melting temperature of the splat and a decrease in the dimensionless equilibrium melting temperature of the substrate can be chosen.

Heat transfer coefficients for an Fe-5wt percent Si melt-spun ribbon can be estimated from the measurement of temperature on the top surface ([24]). A measurement of temperature on the bottom surface of a stainless steel melt can also give the heat transfer coefficient ([25]). Using a thermocouple Bennett and Poulikskos [26] determined the temperature at the interface between the solidifying lead droplets and the substrate and obtained heat transfer coefficients. Liu et al. [27] applied the measured temperature on the top surface of the splat to predict the heat transfer coefficient. Wang and Matthys [28] measured the top surface temperature of the splat by a fast-response pyrometer and obtained the heat transfer coefficient at the contact surface between the splat and substrate.

In this work, the model proposed by Wei et al. [23] is used to study the heat transfer coefficient at the bottom surface of the splat affected by different working parameters. This work is self-consistent, since heat transport, solidification, and melting in the splat and substrate are mutually affected by each other. The kinetic condition, external heat extraction, imperfect contact, and distinct properties between phases, splat, and substrate, are taken into account. The results determine the unsteady heat transfer coefficient which is valuable for evaluating the cooling rate during rapid solidification.

System Model and Analysis

In this study, a molten splat in a thin layer of a thickness s at an initial temperature T_{10} is brought into contact suddenly with a cold substrate initially at the ambient temperature T_∞ and of a thickness d, as illustrated in Fig. 1. The x-coordinate is upward with the origin at the contact surface between the splat and substrate. Thicknesses of the solidified splat and melted substrate are, respectively, denoted by δ_1 and δ_2. Heat transport is one-dimensional under the conditions that either the thickness of the splat is much smaller than radius of curvature or the time scale for rapid solidification is shorter than 0.15 s ([21]). Otherwise, a two-dimensional model is required. Convection in molten regions of the splat and substrate is ignored, since Peclet number is less than unity for freezing a liquid splat in a typical thickness of 10^{-5} m and maximum velocity of 1 m/s near the solidification front. Physical and thermal properties are averaged within temperature ranges considered in the phases, splat, and substrate, but are allowed to be distinct. The splat freezes rapidly at a solidification velocity governed by a kinetic condition

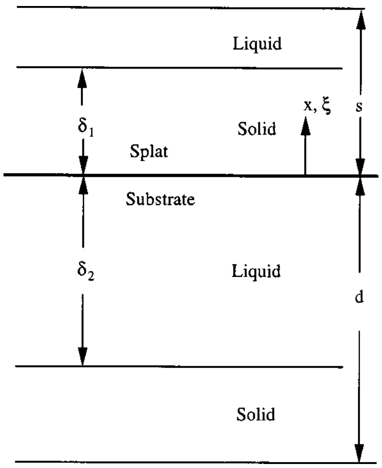

Fig. 1 Physical model and coordinate system

$$\tilde{u}_{1i}=\begin{cases}\gamma(T_{1m}-T_{1i}) & \text{for } t\geq t_N\\ 0 & \text{for } t<t_N\end{cases} \tag{1}$$

while the substrate experiences possible melting with the equilibrium temperature at the melting front. Rapid freezing proceeds only after time is greater than the time for nucleation. With the above assumptions, the heat conduction equation reduces to

$$\rho_j\frac{\partial H_j}{\partial t}=\frac{\partial}{\partial x}\left(k_j\frac{\partial T_j}{\partial x}\right) \tag{2}$$

where the subscript $j=1,2$ stand for the splat and substrate, respectively. Internal energy H_j includes sensible and latent heats $H_j=c_{pj}T_j+f_j\Delta H_j$. The heat conducted through the splat and substrate is removed at the top and bottom surfaces by convection, respectively. Stefan boundary conditions are satisfied at the solid-liquid interfaces. Conservation of the heat flux at the contact surface between the splat and substrate is

$$k_1\frac{\partial T_1}{\partial x}=k_2\frac{\partial T_2}{\partial x}. \tag{3}$$

Distinct temperatures resulting from imperfect contact of contact surfaces between the splat and substrate are governed by

$$-k_2\frac{\partial T_2}{\partial x}=h_{12}(T_2-T_1) \tag{4}$$

where h_{12} is an empirical contact heat transfer coefficient. Provided that the contact heat transfer coefficient is large, discontinuity of temperatures across the contact surface vanishes. For convenience, thermal analysis of the substrate can be avoided if a heat transfer coefficient h_{1b} is introduced and satisfied by

$$k_1\frac{\partial T_1}{\partial x}=h_{1b}(T_1-T_\infty). \tag{5}$$

This work is to predict heat transfer coefficient h_{1b} affected by different parameters.

Dimensionless Equations. Dimensionless forms of Eq. (2) applied to the splat and substrate are, respectively,

$$\mathrm{Ste}\,\frac{\partial\lambda_1}{\partial\tau}+\frac{\partial f_1}{\partial\tau}=(1+\mathrm{Ste})\,\frac{\partial}{\partial\xi}\left(K_1\frac{\partial\lambda_1}{\partial\xi}\right) \tag{6}$$

$$\frac{R}{1+\mathrm{Ste}}\left(\mathrm{Ste}\,\frac{\partial\lambda_2}{\partial\tau}+\frac{1}{H_r}\,\frac{\partial f_2}{\partial\tau}\right)=\frac{\partial}{\partial\xi}\left(K_2C_{pr}\frac{\partial\lambda_2}{\partial\xi}\right) \tag{7}$$

where dimensionless parameters are defined as

$$\mathrm{Ste}\equiv\frac{\mathrm{Ste}_1}{C_{pr}\theta_{10}}(C_{pr}\theta_{10}-1),\quad \mathrm{Ste}_1\equiv\frac{c_{p1}T_{10}}{\Delta H_1},\quad H_r\equiv\frac{\Delta H_1}{\Delta H_2},$$
$$C_{pr}\equiv\frac{c_{p1}}{c_{p2}},\quad \theta_{10}\equiv\frac{T_{10}}{T_\infty},\quad R\equiv\frac{\rho_2}{\rho_1},\quad K_1\equiv\frac{k_1}{k_{1l}},\quad K_2\equiv\frac{k_2}{k_{1l}} \tag{8}$$

and dependent and independent variables are

$$\lambda_1\equiv\frac{C_{pr}\theta_1-1}{C_{pr}\theta_{10}-1},\quad \lambda_2\equiv\frac{\theta_2-1}{C_{pr}\theta_{10}-1},$$
$$\tau\equiv\frac{k_{1l}\mathrm{Ste}\,t}{\rho_1c_{p1}s^2(1+\mathrm{Ste})},\quad \xi\equiv\frac{x}{s}. \tag{9}$$

Initial conditions are $\lambda_1=1$, $\lambda_2=0$ at $\tau=0$. Dimensionless Stefan boundary conditions of the splat and substrate, respectively, yield

$$\left.\frac{\partial\lambda_1}{\partial\xi}\right|_l+\frac{u_{1i}}{1+\mathrm{Ste}}=K_{1s}\left.\frac{\partial\lambda_1}{\partial\xi}\right|_s\quad \xi=\delta_1 \tag{10}$$

$$K_{2l}\left.\frac{\partial\lambda_2}{\partial\xi}\right|_l+\frac{\mathrm{Ru}_{2i}}{H_rC_{pr}(1+\mathrm{Ste})}=K_{2s}\left.\frac{\partial\lambda_2}{\partial\xi}\right|_s\quad \xi=\delta_2. \tag{11}$$

At the melting front ($\xi=\delta_2$), $\lambda_{2s}=\lambda_{2l}=\lambda_{2m}$. A dimensionless form of the kinetic condition from Eq. (1) is given by

$$u_{1i}=\begin{cases}\dfrac{\Gamma\theta_{10}}{\mathrm{Ste}_1}(1+\mathrm{Ste})(\lambda_{1m}-\lambda_{1i}) & \text{for } \tau\geq\tau_N\\ 0 & \text{for } \tau<\tau_N\end{cases}. \tag{12}$$

Dimensionless boundary conditions of the splat and substrate are, respectively,

$$-K_1\frac{\partial\lambda_1}{\partial\xi}=\mathrm{Bi}_{1\infty}\left(\lambda_1+\frac{1-C_{pr}}{C_{pr}\theta_{10}-1}\right)\quad \xi=1 \tag{13}$$

$$K_1\frac{\partial\lambda_1}{\partial\xi}=K_2C_{pr}\frac{\partial\lambda_2}{\partial\xi}\quad \xi=0 \tag{14}$$

$$-K_2\frac{\partial\lambda_2}{\partial\xi}=\frac{\mathrm{Bi}_{12}}{C_{pr}}\left(C_{pr}\lambda_2-\lambda_1+\frac{C_{pr}-1}{C_{pr}\theta_{10}-1}\right)\quad \xi=0 \tag{15}$$

$$K_2\frac{\partial\lambda_2}{\partial\xi}=\mathrm{Bi}_{2\infty}\lambda_2\quad \xi=-\mathrm{d/s}. \tag{16}$$

From Eq. (5) the Biot number at the bottom surface of the splat is given by

$$\mathrm{Bi}_{1b}=K_1\frac{\partial\lambda_1}{\partial\xi}\left(\lambda_1+\frac{1-C_{pr}}{C_{pr}\theta_{10}-1}\right)^{-1}. \tag{17}$$

The Biot number at the bottom surface of the splat before nucleation can be estimated from Eq. (5) by a scale analysis, or

$$\mathrm{Bi}_{1b}=c'\sqrt{\frac{\mathrm{Ste}}{(1+\mathrm{Ste})\tau}} \tag{18}$$

where the empirical constant $c'\approx0.25$ by satisfying the computed Biot number at the nucleation time, as shown later. Precisely speaking, c' is a function of $(T_{10}-T_{1b})/(T_{1b}-T_\infty)$. The Stefan number in Eq. (18) results from the chosen time scale involving the Stefan number, as can be seen in Eq. (9). On nucleation and during freezing, combining Eq. (5), the Stefan boundary condition, and kinetic condition leads to

$$\mathrm{Bi}_{1b}=c'\sqrt{\frac{\mathrm{Ste}}{(1+\mathrm{Ste})\tau}}+c''\frac{\Gamma\theta_{10}}{\mathrm{Ste}_1} \tag{19}$$

where empirical constant $c''\approx5\times10^{-4}$. During solidification, the constant c'' is actually a function of $(T_{1m}-T_{1i})/(T_{1b}-T_\infty)$.

Numerical Method. The numerical scheme accounting for distinct properties across an interface provided by Lee and Tzong

[29] has been generalized to include nonequilibrium rapid solidification in the splat and equilibrium melting in the substrate. A discretized heat conduction Eq. (6) yields

$$a_{1W}\lambda_{1j-1}+a_{1P}\lambda_{1j}+a_{1E}\lambda_{1j+1}=a_{1R} \tag{20}$$

where the coefficients are

$$a_{1W}\equiv\frac{2}{W_{1j}(\xi_{j+1}-\xi_{j-1})},\quad a_{1E}\equiv\frac{2}{E_{1j}(\xi_{j+1}-\xi_{j-1})} \tag{21}$$

$$a_{1P}=-a_{1W}-a_{1E}-\frac{\text{Ste}}{(1+\text{Ste})\Delta\tau} \tag{22}$$

$$a_{1R}\equiv\frac{1}{1+\text{Ste}}\left(\frac{f_{1j}-(f_1^0)_j}{\Delta\tau}-\frac{\text{Ste}(\lambda_1^0)_j}{\Delta\tau}\right). \tag{23}$$

The effective thermal resistances in Eq. (21) are

$$E_j=\sum_{n=1}^{M}\frac{\Delta g_n}{G(g_{n-1}^{+})},\quad W_{j+1}=\sum_{n=1}^{M}\frac{\Delta g_n}{G(g_n^{-})} \tag{24}$$

where $G(g_{n-1}^{+})$ is thermal conductivity at $g=g_{n-1}+\varepsilon$, ε is any infinitesimal value. The piecewise continuous function G has M continuous subintervals separated by $M-1$ discontinuities located at $\xi=g_n$, $n=1,2,\ldots M-1$ in the interval $[\xi_j,\xi_{j+1}]$, where $g_0=\xi_j$, $g_M=\xi_{j+1}$, and $\Delta g_n=g_n-g_{n-1}$. A discretized heat conduction equation of the substrate can be similarly obtained. The Stefan boundary condition of the splat, Eq. (10), is used to determine the enthalpy at the solid-liquid interface in the interval $[\xi_j,\xi_{j+1}]$

$$\lambda_{1i}=\left(\frac{K_{1s}}{\Delta\xi_s}+\frac{1}{\Delta\xi_l}\right)^{-1}\left(\frac{u_{1i}}{1+\text{Ste}}+\frac{K_{1s}\lambda_{1j}}{\Delta\xi_s}+\frac{\lambda_{1j+1}}{\Delta\xi_l}\right). \tag{25}$$

Interface velocity is obtained from the kinetic Eq. (12) by substituting Eq. (25). The thickness of the frozen region is then calculated from

$$\delta_1=\delta_1^0+u_{1i}\Delta\tau. \tag{26}$$

The location of the melting front in the substrate by inserting Eq. (11) yields

$$\delta_2=\delta_2^*-\frac{R(\delta_2-\xi_j)(\xi_{j+1}-\delta_2)u_{2i}}{C_{pr}H_r(1+\text{Ste})[K_{2s}(\lambda_{2i}-\lambda_{2j})+K_{2l}(\lambda_{2j+1}-\lambda_{2i})]} \tag{27}$$

where $u_{2i}=(\delta_2-\delta_2^0)/\Delta\tau$, and

$$\delta_2^*\equiv\xi_j+\frac{K_{2s}(\lambda_{2i}-\lambda_{2j})\Delta\xi_j}{K_{2s}(\lambda_{2i}-\lambda_{2j})+K_{2l}(\lambda_{2j+1}-\lambda_{2i})}. \tag{28}$$

Equation (27) does not guarantee a unique δ_2 in the interval $[\xi_j,\xi_{j+1}]$. However, the last term on the right-hand-side ([29]) can be ignored and Eq. (27) reduces to

$$\delta_2=\delta_2^* \tag{29}$$

where the truncation error $\delta_2-\delta_2^*$ would always be less than the grid size $\Delta\xi_j$, as can be seen from Eq. (27). Equation (29) is a good approximation as long as the grid size is sufficiently small. The effect of the moving liquid-solid interface on sensible heat λ_2 has been accounted through the unsteady term on the left-hand side of Eq. (7). To achieve smooth values of liquid fraction f_1 and f_2, the liquid fraction inside the jth control volume is considered to be f_{1j} or f_{2j}. Thus the differences $(f_1^0)_j-f_1$ and $f_2-(f_2^0)_j$ are, respectively, fractions of the jth control volume solidified and melted during the time interval $[\tau_0,\tau]$. The solution procedure was as follows:

1 Specify initial and working conditions, and physical and thermal properties of the splat and substrate.

2 Solve energy Eqs. (6) and (7) together with boundary conditions.

3 Calculate the location of the melting front in the substrate from Eq. (29).

4 Determine liquid fractions f_1 and f_2 in control volumes of the splat and substrate, respectively, after interface locations have been found.

5 Check convergence of enthalpy and total energy balance of the substrate and splat to relative errors less than 10^{-7}, and 10^{-3}, respectively. Otherwise, go to step 2.

6 Calculate Biot number, Bi_{1b}, from Eq. (17). Go to step 2 for the next time if time is less than nucleation time. Otherwise, after calculating interface temperature from Eq. (25), interface velocity from the kinetic Eq. (12), and thickness of the solidified splat from Eq. (26), go to step 2 for the next time.

A successive relaxation method with a relaxation factor 0.3 was used. The grid system is in uniform spaces in the splat and substrate, respectively. The predicted regions of the solidified splat and molten substrate by using different grid systems, 31×121, 101×501, and 201×1001 in the splat and substrate are shown in

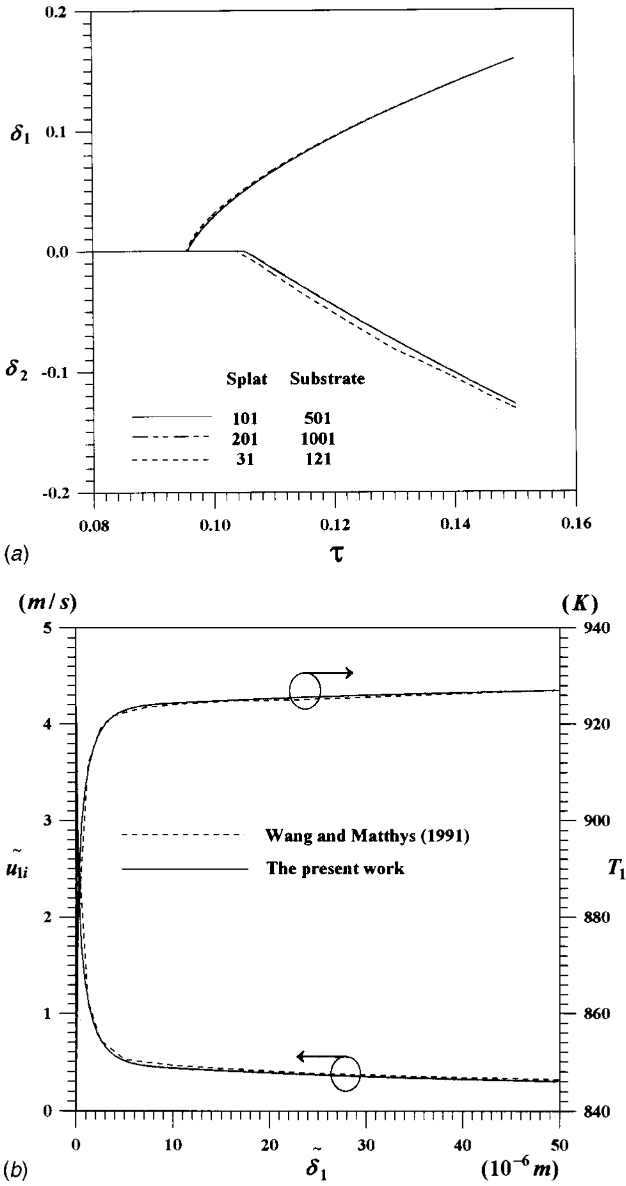

Fig. 2 Numerical clarification, (*a*) different grid systems (splat, substrate) on solutions; (*b*) predicted dimensional interface velocities and temperatures from Wang and Matthys [30] and this work.

Fig. 2(*a*). The grid system 101×501 is quite good to obtain solutions independent of the variation in meshes. The predicted velocity and temperature at the solid-liquid interface agree with those obtained from Wang and Matthys [30], as shown in Fig. 2(*b*). In this case, an aluminum splat was rapidly solidified on a copper substrate, where $T_{1m}-T_{1N}=100\,\mathrm{K}$, $\gamma=0.05\,\mathrm{m/K\,s}$, $s=50\,\mu\mathrm{m}$, and $h_{12}=10^6\,\mathrm{W/m^2\,K}$.

Results and Discussion

In this study, the primary independent dimensionless parameters to be investigated are Bi_{12}, θ_{10}, θ_{1N}, C_{pr}, R, Ste_1, K_{2s}, K_{2l}, θ_{2m}, θ_{1m}, H_r, K_{1s}, and Γ. The values of these parameters were chosen from the data provided by Wang and Matthys [30] and presented in Table 1. The effects of the contact Biot number at the splat-substrate interface on the growths of solidification and melting fronts in the splat and substrate in an earlier stage are, respectively, shown in Fig. 3. The positive and negative values of the ordinate represent locations of the solid-liquid interfaces in the splat and substrate, respectively. Referring to Eq. (4) it can be seen that the higher the contact heat transfer coefficient (or contact Biot number) is, the more perfect the contact surface is. In view of high cooling rates, an increase in the contact Biot number reduces times for phase changes and increases thicknesses of the solidified splat and melted substrate. The difference in the onset times for freezing the splat and melting the substrate reduces with increasing the contact Biot number. Since the Biot number changes from 5 to 0.8, dimensionless time for freezing delays approximately from 0.004 to 0.1. The effects of the contact Biot number on rapid solidification are therefore significant.

Unsteady variations of dimensionless enthalpies in the splat and substrate on the contact surface in an earlier stage for different contact Biot numbers are shown in Fig. 4. An increase in the contact Biot number rapidly decreases and increases enthalpies of the splat and substrate, respectively. Evidently, enthalpy in the splat decreases with increasing time until the nucleation temperature is reached. Due to nucleation and rapid solidification accompanying high evolution of latent heat, the enthalpy exhibits a jump. A further increase in time results in a gradual decrease in enthalpy. On the other hand, enthalpy in the substrate increases with time. Figure 5 shows that dimensionless enthalpy at the solidification front of the splat increases with increasing penetration depth of the interface and decreasing contact Biot number. Applying the kinetic condition, the corresponding interface velocity decreased as time increases and the contact Biot number decreases.

The use of the contact Biot number or contact heat transfer coefficient to evaluate the cooling rate requires a determination of the top surface temperature of the substrate ([15,22]) (see Eq. (4)). An often-used Biot number is Bi_{1b}, which is based on the difference in temperatures at the bottom surface of the splat and surroundings. In this work it is called the Biot number at the bottom surface of the splat. The effects of the contact Biot number on the unsteady Biot number at the bottom surface of the splat are presented in Fig. 6. It can be seen that the maximum of the Biot number at the bottom surface of the splat is identical to the contact Biot number. This is because the temperature at the top surface of the substrate is the initial or surrounding temperature as the splat contacts the substrate. The Biot number at the bottom surface of the splat and its decreasing rate reduce with increasing time and decreasing contact Biot number. The Biot number at the bottom surface of the splat exhibits a slight jump at nucleation time (see Fig. 3). The Biot number at the bottom surface of the splat thus can be considered a constant for a small contact Biot number.

The effects of dimensionless solid conductivity of the substrate on the variations of the Biot number at the bottom surface of the splat with time are presented in Fig. 7. In view of greater heat transfer dissipated to the surroundings through the substrate, an increase in dimensionless solid conductivity of the substrate increases the Biot number at the bottom surface of the splat. The nucleation time and the extent of the jump decrease with increas-

Table 1 Typical values of independent dimensionless parameters

$\mathrm{Bi}_{1\infty}$, $\mathrm{Bi}_{2\infty}$	0.01
Bi_{12}	0.8
C_{pr}	3.0
K_{1s}, K_{2l}	2.0
K_{2s}	4.0
R	3.5
Ste_1	3.6
H_r	100
Γ	20
θ_{10}	3.6
θ_{1N}	3.0
θ_{1m}	3.5
θ_{2m}	1.3

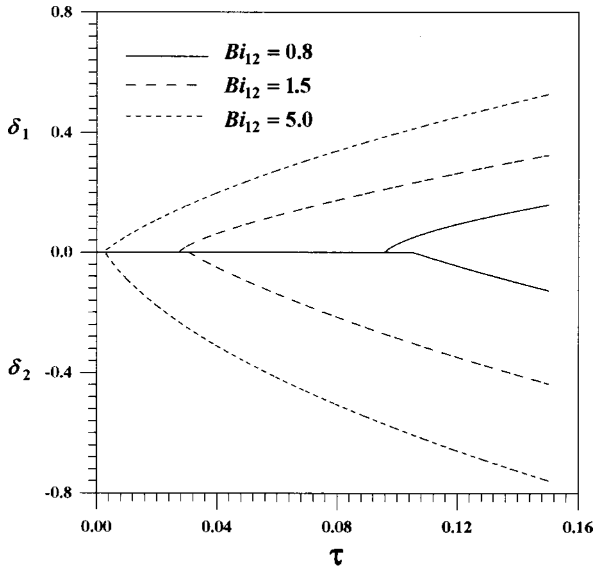

Fig. 3 Dimensionless thicknesses of the solidified splat and melted substrate versus time for different contact Biot numbers

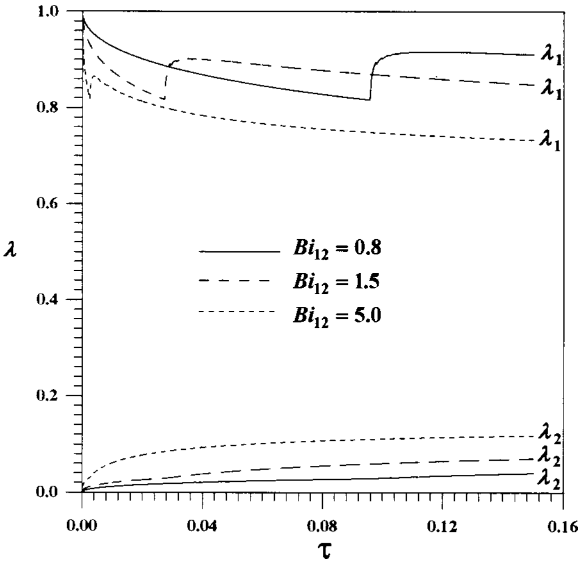

Fig. 4 Dimensionless enthalpies in the splat and substrate on the contact surface versus time for different contact Biot numbers

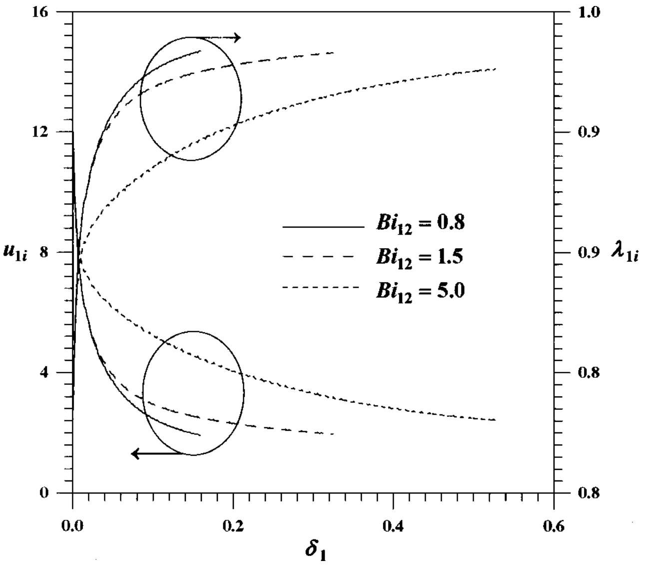

Fig. 5 Dimensionless velocity and enthalpy at the solidification front versus displacement of the interface for different contact Biot numbers.

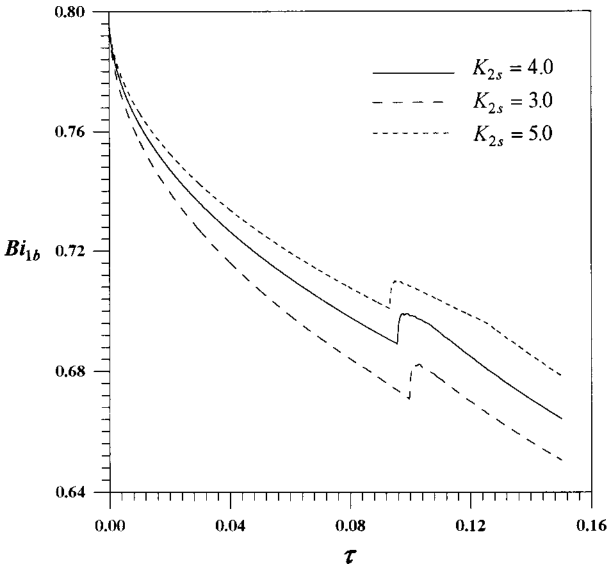

Fig. 7 Unsteady variations of Biot number at the bottom surface of the splat for different dimensionless solid conductivities of the substrate

ing solid conductivity of the substrate. Referring to Eq. (18) reveals that an increase in nucleation time reduces the Biot number at the bottom surface of the splat.

The unsteady variations of the Biot number at the bottom surface of the splat for different dimensionless liquid conductivities of the substrate are presented in Fig. 8. Evidently, as long as the substrate remains solid, liquid conductivity of the substrate has no effect on the Biot number at the bottom surface of the splat. Interestingly, the Biot number at the bottom surface of the splat splits into three curves at a dimensionless time of around 0.105. This is because the substrate becomes molten. A low liquid conductivity of the substrate reduces the Biot number at the bottom surface of the splat because heat transfer to the surroundings through the substrate decreases.

Figure 9 shows that when the substrate remains solid, the Biot number at the bottom surface of the splat is independent of equilibrium melting temperature of the substrate. Interestingly, the Biot number at the bottom surface of the splat for a dimensionless equilibrium melting temperature of 1.2 deviates from that of 1.25 and 1.3 at a dimensionless time 0.04. This is because the substrate starts to become molten. Since the thermal conductivity of a liquid is less than that of a solid, the decrease of the cooling rate reduces the Biot number at the bottom surface of the splat. Being subject to a molten substrate, freezing of the splat occurs at a dimensionless time of around 0.1. A similar result can be seen for a dimensionless equilibrium melting temperature of 1.25. The time for melting the substrate, however, increases to around 0.07. The nucleation time and the extent of the jump for the Biot number at the bottom surface of the splat slightly increases by decreasing the equilibrium melting temperature.

Figure 10 shows that an increase in the splat-to-substrate specific heat ratio decreases the Biot number at the bottom surface of the splat. This is because a high specific heat implies that chang-

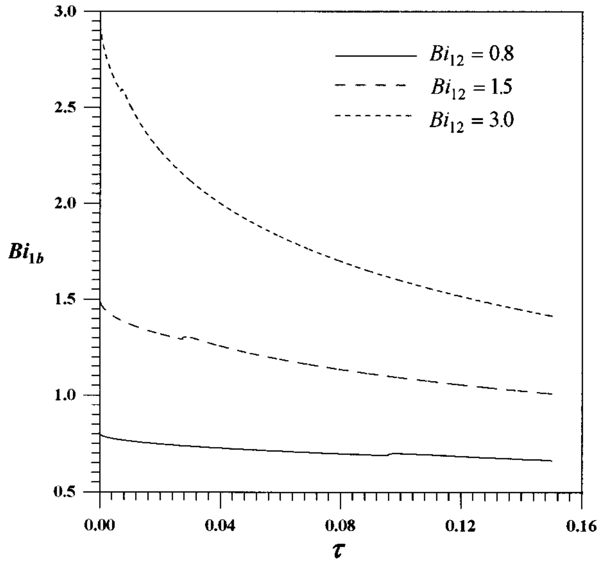

Fig. 6 Unsteady variations of Biot number at the bottom surface of the splat for different contact Biot numbers

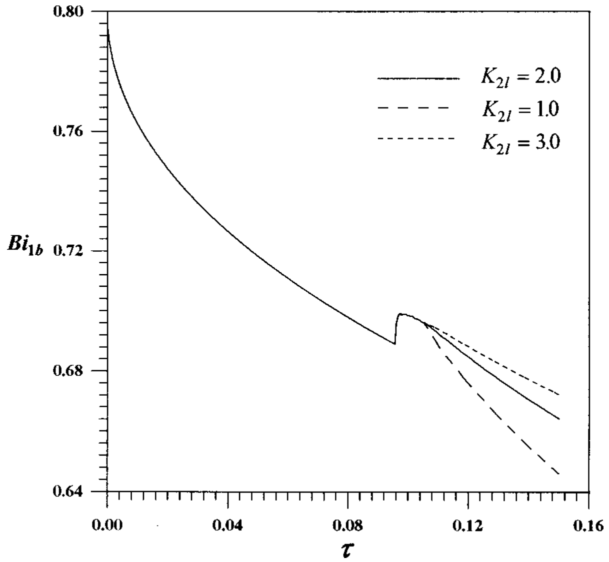

Fig. 8 Unsteady variations of Biot number at the bottom surface of the splat for different dimensionless liquid conductivities of the substrate

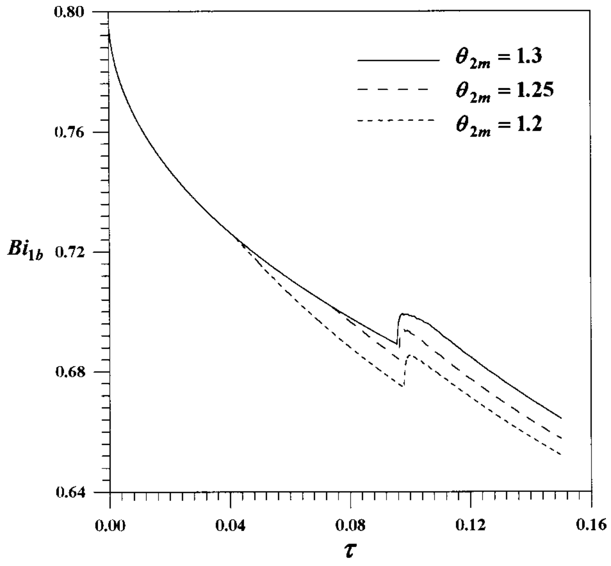

Fig. 9 Unsteady variations of Biot number at the bottom surface of the splat for different dimensionless equilibrium melting temperatures of the substrate

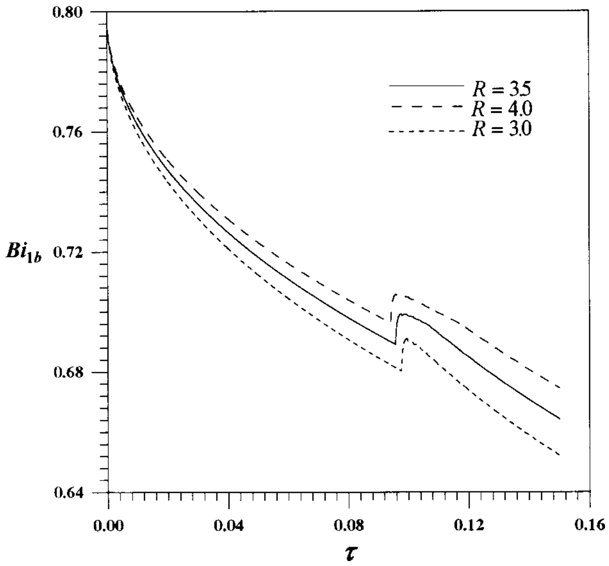

Fig. 11 Unsteady variations of Biot number at the bottom surface of the splat for different substrate-to-splat density ratios

ing a unit temperature requires a greater energy. Hence, a high specific heat ratio indicates that the temperature gradient and the resulting heat conduction in the splat at the contact surface between the splat and substrate are low. The nucleation time is also delayed by increasing the specific heat ratio. The height of the jump slightly increases with the specific heat ratio. Interestingly, the slope of the Biot number versus time exhibits a slight discontinuity at a dimensionless time around 0.12 for a specific heat ratio of 2.5. The reason for this is that the substrate becomes molten. As discussed previously, the Biot number at the bottom surface of the splat decreases. Similar results for the substrate-to-splat density ratio can be seen in Fig. 11. Since the energy required to increase a unit temperature is less for a low density, an increase in the substrate-to-splat density ratio enhances heat transfer to the substrate. This results in an increase of the Biot number at the bottom surface of the splat and decreases the nucleation time and height of the jump.

Figure 12 shows that an increase in the Stefan number of the splat increases the Biot number at the bottom surface of the splat before nucleation takes place. It should be noted that the dimensionless time is normalized by a time including the Stefan number (see Eq. (9)). On the other hand, the jump of Biot number decreases by increasing the Stefan number (see Eq. (19)). Physically speaking, a large Stefan number represents a low latent heat evolution of the splat. The Biot number at the bottom surface of the splat remains large for a high Stefan number during rapid solidification. In Fig. 13, it is interesting to find that the effect of dimensionless initial temperatures of the splat on the Biot number at the bottom surface of the splat is insignificant until nucleation takes place. Nucleation time and the extent of the jump for the Biot number at the bottom surface of the splat increase with initial temperature. Figure 14 shows that decreasing nucleation tempera-

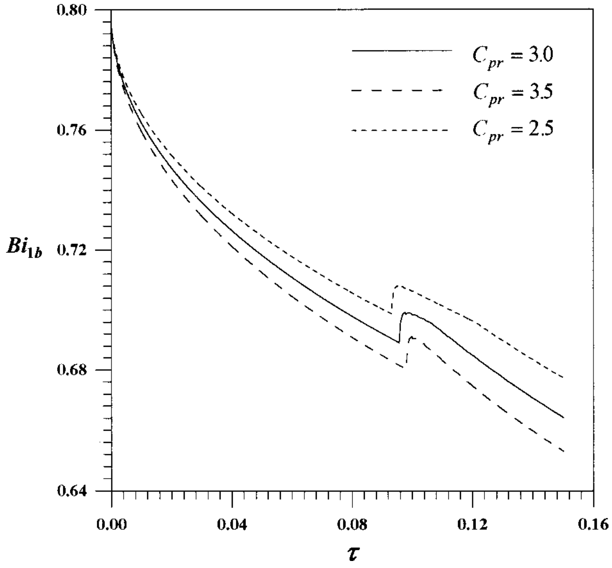

Fig. 10 Unsteady variations of Biot number at the bottom surface of the splat for different splat-to-substrate specific heat ratios

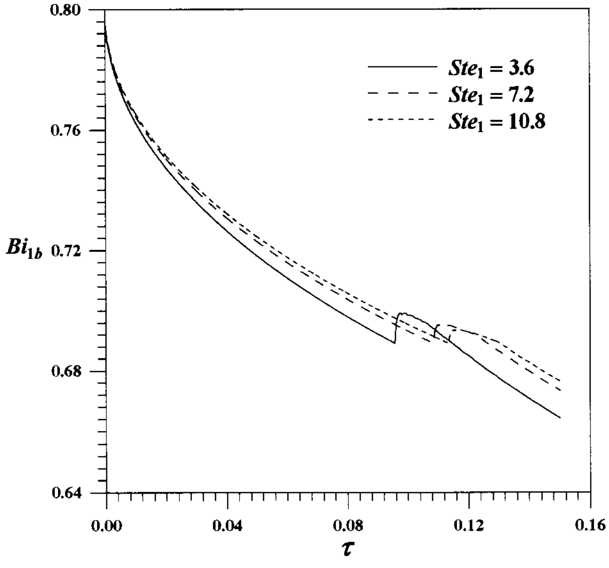

Fig. 12 Unsteady variations of Biot number at the bottom surface of the splat for different Stefan numbers of the splat

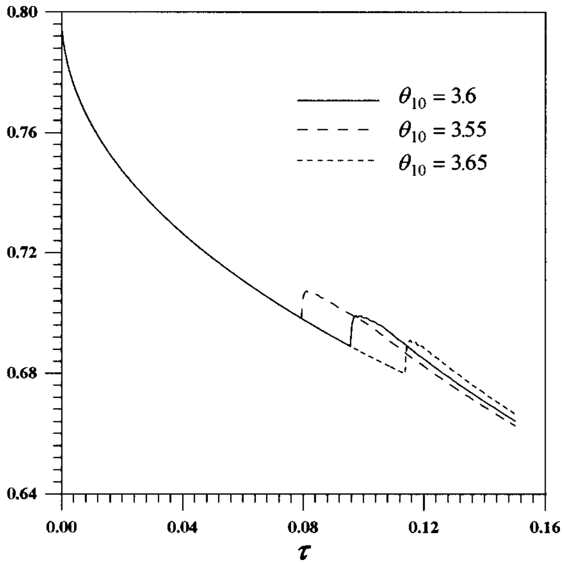

Fig. 13 Unsteady variation of Biot number at the bottom surface of the splat for different dimensionless initial temperatures of the splat

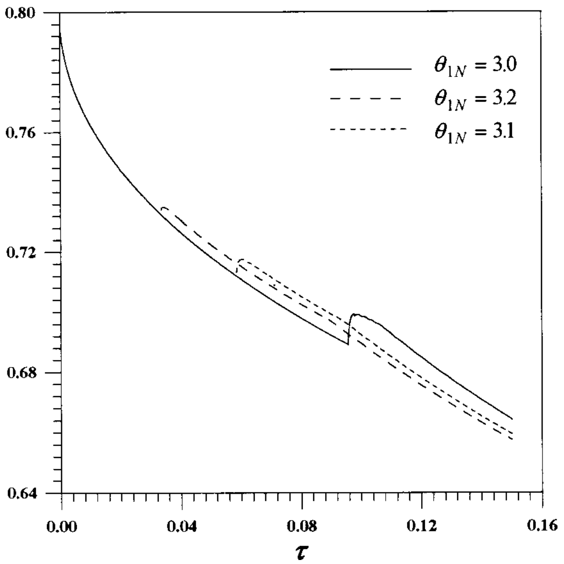

Fig. 14 Unsteady variations of Biot number at the bottom surface of the splat for different dimensionless nucleation temperatures of the splat

ture of the splat delays nucleation time and increases the Biot number at the bottom surface of the splat during rapid freezing.

This work also found that the effects of the dimensionless kinetics coefficient, equilibrium melting temperature, solid conductivity of the splat, and latent heat ratio on the Biot number at the bottom surface of the splat, dimensionless nucleation time, and the extent of the jump are slight. Increasing dimensionless kinetics coefficient, equilibrium melting temperature, solid conductivity of the splat, and decreasing latent heat ratio slightly increase the Biot number at the bottom surface of the splat.

Conclusions

The conclusions drawn are the following:

1 This work deals with heat transfer of a thin splat rapidly solidified on a cold substrate experiencing possible melting. The time-dependent heat transfer coefficient (h_{1b}) or the Biot number (Bi_{1b}) based on a temperature difference between the bottom surface of the splat and the surroundings for different dimensionless parameters, including the contact Biot number (Bi_{12}), Stefan number (Ste_1), initial and nucleation temperatures (θ_{10} and θ_{1N}), solid and liquid conductivity ratios (K_{1s}, K_{2s}, and K_{2l}), equilibrium melting temperatures (θ_{1m} and θ_{2m}), kinetics coefficient (Γ), and specific heat, density, and latent heat ratios (C_{pr}, R and H_r) is quantitatively studied.

2 The effects of the contact Biot number on rapid solidification of the splat are significant. The contact Biot number depends on the difference in temperatures across the contact surface between the splat and substrate. The unknown temperature of the substrate on the contact surface leads to a study of an often-used Biot number based on a temperature difference between the bottom surface of the splat and the surroundings.

3 The Biot number at the bottom surface of the splat cannot be considered a constant during rapid freezing. The time-dependent Biot number at the bottom surface of the splat can be divided into five regimes:

(a) The Biot number decreases with increasing time for a liquid splat in an early stage.
(b) The Biot number is further lowered if the substrate becomes molten.
(c) The Biot number jumps for the splat on nucleating.
(d) The Biot number gradually decreases in the course of rapid solidification.
(e) The Biot number further decreases if the substrate is melted.

4 Increases in the contact Biot number, density ratio, and solid conductivity of the substrate, and a decrease in specific heat ratio increase the Biot number at the bottom surface of the splat before nucleation takes place. The Biot number at the bottom surface of the splat before nucleation, however, is relatively insensitive to the variation in the initial temperature of the splat.

5 Nucleation is delayed by decreasing the contact Biot number, density ratio, solid conductivity of the substrate, and nucleation temperature, and increasing specific heat ratio and initial temperature of the splat.

6 Biot number at the bottom surface of the splat during rapid solidification increases with increasing the contact Biot number, Stefan number, density ratio, initial temperature, kinetics coefficients, melting temperatures, and solid conductivities of the splat and substrate, and decreasing nucleation temperature and specific heat ratio.

7 Decreases in melting temperature and liquid conductivity of the substrate and increase in latent heat ratio further decrease the Biot number at the bottom surface of the splat after the substrate becomes molten.

8 An increase of Biot number at the contact surface between the splat and substrate increases thicknesses of the frozen and molten regions in the splat and substrate, shortens the time for freezing and melting of the splat and substrate, respectively. The interface temperature at the solidification front of the splat is lower and the freezing rate is higher.

9 The time-dependent Biot number at the bottom surface of the splat before nucleation is scaled by Eq. (18). On nucleation and during solidification, Eq. (19) scales the Biot number at the bottom surface of the splat. An interesting study is to compare results predicted from the problem coupling between the splat and substrate and the splat (or the substrate) problem by introducing Eqs. (18) or (19). This work is currently being undertaken.

Nomenclature

Bi_{1b}, $\mathrm{Bi}_{1\infty}$, $\mathrm{Bi}_{2\infty}$, Bi_{12} = $h_{1b}s/k_{1l}$, $h_{1\infty}s/k_{1l}$, $h_{2\infty}s/k_{1l}$, $h_{12}s/k_{1l}$
C_{pr} = specific heat ratio, defined in Eq. (8)
d = substrate thickness, m
f = liquid fraction
H_r = latent heat ratio, defined in Eq. (8)

K = dimensionless thermal conductivity, defined in Eq. (8)
R = density ratio, defined in Eq. (8)
s = splat thickness, m
u_i = dimensionless solidification velocity

Greek Letters

γ = kinetics coefficient, m/s K
Γ = dimensionless kinetics coefficient $=\rho_1 s c_{p1} T_\infty \gamma / k_{1l}$
δ = dimensionless solid or liquid thickness
ξ = dimensionless coordinate, defined in Eq. (9)
ΔH = latent heat, J/kg
θ = dimensionless temperature $=T/T_\infty$
θ_{10} = dimensionless initial temperature of splat, defined in Eq. (8)
λ = dimensionless enthalpy defined in Eq. (9)
τ = dimensionless time, defined in Eq. (9)

Superscripts

0 = previous time

Subscripts

i = solid-liquid interface
m, N = melting and nucleation
0 = initial
1,2 = splat and substrate

References

[1] Anantharaman, T. R., and Suryanarayana, C., 1997, ''Review: A Decade of Quenching from the Melt,'' J. Mater. Sci., **6**, pp. 1111–1135.
[2] Jones, H., 1982, ''Rapid Solidification of Metals and Alloys,'' The Institution of Metallurgists, London, Monograph No. 8.
[3] Zaat, J. H., 1983, ''A Quarter of a Century of Plasma Spraying,'' Annu. Rev. Mater. Sci., **13**, pp. 9–42.
[4] Cahn, R. W., 1983, ''Chapter 28 Alloys Rapidly Quenched From the Melt,'' *Physical Metallurgy*, Part 2, 3rd Ed., R. W. Cahn and P. Haasen, eds., Elsevier, New York, pp. 1779–1852.
[5] Frederick, D., and Greif, R., 1985, ''A Method for the Solution of Heat Transfer Problems With a Change of Phase,'' ASME J. Heat Transfer, **107**, pp. 520–526.
[6] Viskanta, R., 1988, ''Heat Transfer During Melting and Solidification of Metals,'' ASME J. Heat Transfer, **110**, pp. 1205–1219.
[7] Turnbull, D., 1949, *Thermodynamics in Physical Metallurgy*, American Society for Metals, Cleveland, pp. 283–306.
[8] Kurz, W., and Fisher, D. J., 1989, *Fundamentals of Solidification*, Trans. Tech. Publ., Aedermannsdorf, Switzerland, pp. 220–225.
[9] Levi, C. G., and Mehrabian, R., 1982, ''Heat Flow During Rapid Solidification of Undercooled Metal Droplets,'' Metall. Trans. A, **13A**, pp. 221–234.
[10] Griffiths, W. D., 1999, ''The Heat-Transfer Coefficient During the Unidirectional Solidification of an Al-Si Alloy Casting,'' Metall. Mater. Trans. B, **30B**, pp. 473–482.
[11] Predecki, P., Mullendore, A. W., and Grant, N. J., 1965, ''A Study of the Splat Cooling Technique,'' Trans. Metall. Soc. AIME, **233**, pp. 1581–1586.
[12] Ruhl, R. C., 1967, ''Cooling Rates in Splat Cooling,'' Mater. Sci. Eng., **1**, pp. 313–320.
[13] Shingu, P. H., and Ozaki, R., 1975, ''Solidification Rate in Rapid Conduction Cooling,'' Metall. Trans. A, **6A**, pp. 33–37.
[14] Clyne, T. W., 1984, ''Numerical Treatment of Rapid Solidification,'' Metall. Trans., **15B**, pp. 369–381.
[15] Wang, G.-X., and Matthys, E. F., 1996, ''Experimental Investigation of Interfacial Thermal Conductance for Molten Metal Solidification on a Substrate,'' ASME J. Heat Transfer, **118**, pp. 157–163.
[16] Scott, M. G., 1974, ''The Effect of a Glass Substrate on Cooling Rate in Splat-Quenching,'' J. Mater. Sci., **9**, pp. 1372–1374.
[17] Kuijpers, T. W., and Zaat, J. H., 1974, ''Influence of Oxygen and Cooling Rate on the Microstructure and Microhardness of Plasma-Sprayed Molybdenum,'' Met. Technol., **1**, pp. 142–150.
[18] Carslaw, H. C., and Jaeger, J. C., 1959, *Conduction of Heat in Solids*, 2nd Ed., Clarendon Press., Oxford, pp. 87–89.
[19] Steffens, H.-D., Wielage, B., and Drozak, J., 1991, ''Interface Phenomena and Bonding Mechanism of Thermally-Sprayed Metal and Ceramic Composites,'' Surf. Coat. Technol., **45**, pp. 299–308.
[20] Amon, C. H., Merz, R., Prinz, F. B., and Schmaltz, K. S., 1994, ''Thermal Modeling and Experimental Testing of MD* Spray Shape Deposition Processes,'' *Heat Transfer 1994*; ed. G. F Hewitt, *Proceedings of Tenth International Heat Transfer Conference*, Vol. 7, IChemE Publishing, Brighton, UK, pp. 321–326.
[21] Amon, C. H., Schmaltz, K. S., Merz, R., and Prinz, F. B., 1996, ''Numerical and Experimental Investigation of Interface Bonding via Substrate Remelting of an Impinging Molten Metal Droplet,'' ASME J. Heat Transfer, **118**, pp. 164–172.
[22] Wang, S.-P., Wang, G.-X., and Matthys, E. F., 1998, ''Melting and Resolidification of a Substrate in Contact With a Molten Metal: Operational Maps,'' Int. J. Heat Mass Transf., **41**, pp. 1177–1188.
[23] Wei, P. S., Yeh, F. B., and Chiu, S. H., 2000, ''Distinct Property Effects on Rapid Solidification of a Thin Liquid Layer on a Substrate Subject to Melting Affected by Distinct Properties,'' J. Heat Trans., submitted for publication.
[24] Ludwig, A., and Frommeyer, G., 1992, ''Investigations on the Heat Transfer during PFC-Melt-Spinning by On-Line High-Speed Temperature Measurements,'' *Melt-Spinning and Strip Castings*, E. F., Matthys, ed., TMS, Warrendale, PA, pp. 163–171.
[25] Mizukami, H., Suzuki, T., and Umeda, T., 1993, ''Initial Stage of Rapid Solidification of 18-8 Stainless Steel,'' Mater. Sci. Eng., A, **A173**, pp. 361–364.
[26] Bennett, T., and Poulikakos, D., 1994, ''Heat Transfer Aspects of Splat-Quench Solidification: Modelling and Experiment,'' J. Mater. Sci., **29**, pp. 2025–2039.
[27] Liu, W., Wang, G.-X., and Matthys, E. F., 1995, ''Thermal Analysis and Measurements for a Molten Metal Drop Impacting on a Substrate: Cooling, Solidification and Heat Transfer Coefficient,'' Int. J. Heat Mass Transf., **38**, pp. 1387–1395.
[28] Wang, G.-X., and Matthys, E. F., 1994, ''Interfacial Thermal Contact during Rapid Solidification on a Substrate,'' *Heat Transfer 1994; Proceedings of the Tenth International Heat Transfer Conference*, Vol. 4, IChemE Pub., Brighton, UK, pp. 169–174.
[29] Lee, S. L., and Tzong, R. Y., 1991, ''An Enthalpy Formulation for Phase Change Problems With a Large Thermal Diffusivity Jump Across the Interface,'' Int. J. Heat Mass Transf., **34**, pp. 1491–1502.
[30] Wang, G.-X., and Matthys, E. F., 1991, ''Modelling of Heat Transfer and Solidification during Splat Cooling: Effect of Splat Thickness and Splat/Substrate Thermal Contact,'' Int. J. Rapid Solidif., **6**, pp. 141–174.

A Stagnation Flow Analysis of the Heat Transfer and Fluid Flow Phenomena in Laser Drilling

J. J. Batteh[1]
e-mail: jbatteh@engin.umich.edu

M. M. Chen
Professor of Mechanical Engineering

J. Mazumder
Professor of Mechanical Engineering

Department of Mechanical Engineering and
Applied Mechanics,
University of Michigan,
2350 Hayward Street,
2004 G. G. Brown,
Ann Arbor, MI 48109-2125

This paper presents a quasi-steady stagnation flow analysis for the material removal processes in high-intensity laser materials processing, such as laser drilling. The governing stagnation flow equations for the heat transfer and fluid flow phenomena are derived for the region near the centerline of the laser beam. The analysis accounts for conduction in the solid, conduction, and convection in the melt layer, and the latent heats of melting and vaporization. The stagnation flow governing equations and boundary conditions are appropriately normalized and solved, and the important combinations of material properties and independent laser parameters are identified. This semiquantitative analysis yields quasi-steady estimates for the penetration velocity, the thickness of the melt layer, the velocity and temperature profiles in the melt layer, and the fraction of melt that is vaporized for varying absorbed laser power and beam radius. Inviscid results from the stagnation flow analysis are shown for five different materials: aluminum, copper, low carbon steel, stainless steel, and titanium. Relatively good agreement exists between the results from the analysis and experimental data from the literature.
[S0022-1481(00)01804-1]

Keywords: *Analytical, Drilling, Heat Transfer, Melting, Vaporization*

Introduction

In high energy laser processing applications significant melting and even evaporation can occur. For processes with high enough laser intensities, this vaporization can create a keyhole that allows for welding of thick sheets and laser drilling. The initiation and maintenance of this vapor-filled keyhole cavity due to removal of molten material is a result of the complex interaction between the heat transfer, fluid flow, and phase change processes that occur in the material. In order to better understand the drilling process it is necessary to analyze in detail the fundamental physics of material removal. The basics of the laser drilling process are fairly simple; the laser beam impinges upon a stationary workpiece at room temperature. The material is heated by the beam until melting occurs; additional heating causes a melt pool to form until the melt reaches the vaporization temperature at which point liquid-vapor phase change takes place. The vaporization and subsequent recoil-pressure induced flow enable the liquid-vapor front to travel down into the workpiece; this erosion causes a hole to be drilled in the material.

Many researchers have investigated the heat transfer aspects of laser drilling and cutting. Minardi and Bishop [1] predicted temperature distributions in 2D with conduction and melting for different laser energy profiles and showed the importance of the radial laser energy distribution. Armon et al. [2] used a transient, axisymmetric heat conduction model to predict keyhole initiation times and penetration depths. Kar and Mazumder [3] developed a transient 2D model that predicted cavity shapes using the Stefan condition along the solid–liquid and liquid–vapor interfaces. Wei and Ho [4] developed a quasi-steady, axisymmetric heat conduction model to determine the shapes of the solid–liquid and liquid–vapor interfaces as a function of laser power and beam distribution parameter for a Gaussian beam. Armon et al. [5] employed a time-dependent axisymmetric heat conduction model and the enthalpy method to determine the transient cavity shapes and penetration velocities. Yilbas et al. [6] used a steady state heat transfer model to study the evaporation front in laser drilling. Modest [7,8] developed a transient 3D heat transfer model using boundary-fitted coordinates to determine cutting rates and cavity profiles in laser drilling and cutting. Yilbas and Al-Garni [9] employed a heat transfer analysis to determine steady state and transient temperature distributions, evaporation and drilling velocities, and melt layer thickness for varying laser intensities.

While the previous models ignored the details of the melt flow, experimental research has shown that liquid ejection plays an important role in laser drilling ([10,11]). Quasi-steady drilling velocities including the effects of melt expulsion were first calculated by von Allmen [12] as a function of laser intensity. Chan and Mazumder [13] developed a 1D steady state model for the temperature and viscous velocity distributions to study the materials removal rate by vaporization and liquid expulsion. Wei and Chiou [14] developed an axisymmetric, quasi-steady state model for the heat transfer and molten metal flow to determine the cavity shape, liquid layer thickness, and penetration velocity. They conclude that the cavity is formed by the upward flow of molten material due to surface tension forces. Kar et al. [15] extended their previous model ([3]) to include the effects of multiple reflections and liquid metal flow due to shear stress from the assist gas. Recently, Ganesh et al. [16–18] developed a numerical model to simulate the heat transfer and melt dynamics in laser drilling with a volume of fluid front tracking model. Semak and Matsunawa [19] studied the high velocity flow due to recoil pressure effects from the vaporization of the melt and showed from an energy balance model that convection in the melt accounts for a significant portion of the input laser energy, especially at high laser intensities. Chen et al. [20] utilized a stagnation flow analysis to study keyhole laser welding. Their analysis holds when the thickness of the molten pool is much less than the radius of the laser beam but has recently been extended to account for thicker molten pools ([21]).

In this paper a quasi-steady stagnation flow analysis has been used to determine the effect of high intensity laser power and beam size on the heat transfer, melt flow, vaporization, and the speed of penetration into the material. The equations are normal-

---

[1] To whom correspondence should be addressed.

Contributed by the Heat Transfer Division for publication in the JOURNAL OF HEAT TRANSFER. Manuscript received by the Heat Transfer Division, Apr. 12, 1999; revision received, June 9, 2000. Associate Technical Editor: D. A. Kiminski.

ized using scales derived from the governing equations. The relevant combinations of material properties and laser beam parameters are identified. These normalized equations are then solved for various metals to determine the effects of laser beam parameters and material properties on the drilling process. The analysis accounts for material removal due to both vaporization and melt expulsion and quantifies the relative importance of the two material removal mechanisms.

Analysis of the Melt Flow and Heat Transfer

As described previously, a laser beam with a specified intensity distribution can create a deep vapor-filled keyhole. Figure 1 shows a schematic of the keyhole along with an enlarged view of the stagnation flow region near the centerline of the laser beam. With sufficiently high intensities melting and vaporization are possible. After the onset of vaporization pressure gradients are established in the liquid due to the variation in the radial vaporization flux caused by the laser intensity profile. The initiation and growth of the vapor-filled keyhole region is a combination of evaporation of the melt and the recession of the melt due to flow away from the liquid–vapor boundary. Quantifying the relative importance of these two physical mechanisms of material removal is one objective of this analysis and yields insight into the fundamental physics of the drilling process.

Figure 1 shows an enlarged view of the region to be analyzed. The heat transfer and fluid flow are assumed to be axisymmetric and are represented by stagnation flow boundary layer considerations in this region near the centerline of the laser beam. The solutions are obtained using standard techniques for the solution of stagnation flow problems. The laser beam is assumed to have a Gaussian radial profile. Constant material properties are assumed for the solid and liquid, and no density change associated with melting is considered. The solid is treated as a semi-infinite domain with unidirectional heat flow. For the high laser intensities commonly used in drilling applications the melt layer thickness is typically much smaller than the radius of the laser beam. Therefore, the melt time constant is smaller than the global time constant based on the radius of the laser beam, and the melt reacts quickly to changes in the input energy. Consequently, the initial transient time for the heating and establishing of a melt layer whose surface begins to vaporize is short and usually occurs within a few microseconds for intensities around $10^{10}\,\mathrm{W/m^2}$. Thus, the process can be considered quasi-steady, especially for cw laser operation or pulsed operation with pulse lengths on the order of several hundred microseconds. Further discussion of the quasi-steady formulation is presented when comparing the results of the analysis with experimental data. Based on the previous considerations, the governing equations can be derived, simplified, and solved in the stagnation region.

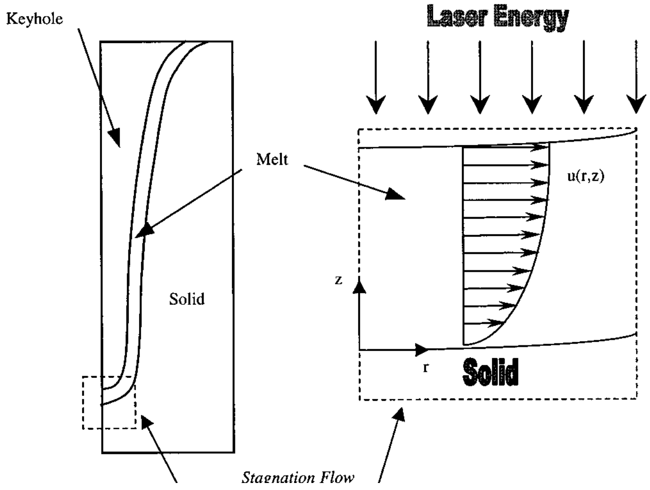

Fig. 1 Keyhole shape and enlarged view of stagnation flow region showing the coordinate system used in stagnation flow analysis

2.1 Governing Equations. The governing equations for the fluid flow and heat transfer phenomena in axisymmetric cylindrical coordinates are:

$$u\frac{\partial u}{\partial r}+v\frac{\partial u}{\partial z}=-\frac{1}{\rho}\frac{\partial p}{\partial r}+\nu\left[\frac{\partial^2 u}{\partial r^2}+\frac{\partial}{\partial r}\left(\frac{u}{r}\right)+\frac{\partial^2 u}{\partial z^2}\right] \tag{1}$$

$$u\frac{\partial v}{\partial r}+v\frac{\partial v}{\partial z}=-\frac{1}{\rho}\frac{\partial p}{\partial z}+\nu\left[\frac{\partial^2 v}{\partial r^2}+\frac{1}{r}\frac{\partial v}{\partial r}+\frac{\partial^2 v}{\partial z^2}\right] \tag{2}$$

$$\frac{1}{r}\frac{\partial(ur)}{\partial r}+\frac{\partial v}{\partial z}=0 \tag{3}$$

$$\rho c_p\left(u\frac{\partial T}{\partial r}+v\frac{\partial T}{\partial z}\right)=k\left(\frac{\partial^2 T}{\partial r^2}+\frac{1}{r}\frac{\partial T}{\partial r}+\frac{\partial^2 T}{\partial z^2}\right) \tag{4}$$

In relation to the coordinate system in Fig. 1, the temperature and flow field in the stagnation region near the centerline of the laser beam can be represented as

$$T=T(z) \tag{5}$$

$$v=v(z) \tag{6}$$

where v is the velocity in the z direction. Thus, according to continuity in Eq. (3), the velocity u in the r direction is given by

$$u(r,z)=-\frac{r}{2}v'(z) \tag{7}$$

To normalize the governing equations, appropriate scales for the cylindrical coordinates r and z and for the independent variables u, v, p, and T are needed. The scale used for the radial direction is the beam radius. Thus, the normalized radial coordinate is defined:

$$\tilde{r}=\frac{r}{R_b} \tag{8}$$

The scale for the v velocity is derived by considering the penetration speed of the melting interface and is given by the ratio of the laser heat flux to the energy required to heat and melt a unit quantity of material:

$$V=\frac{q''}{\rho[c_p(T_M-T_o)+H_m]} \tag{9}$$

The normalized velocity in the z direction is written as follows:

$$\tilde{v}=\frac{v}{V} \tag{10}$$

Using Eq. (9) a scale for the thickness of the melt can be derived by considering the effects of heat conduction and convection in the molten layer:

$$\delta=\frac{\alpha_l}{V} \tag{11}$$

Thus, the normalized z coordinate is given by the following equation:

$$\tilde{z}=\frac{z}{\delta} \tag{12}$$

A normalized u velocity can be derived from Eq. (3) along with the newly defined scales in Eqs. (8)–(9) and (11):

$$\tilde{u}=\frac{u\delta}{VR_b} \tag{13}$$

Finally, the pressure is normalized using an inertial scale:

$$\tilde{p}=\frac{p}{\rho V^2} \tag{14}$$

Normalized temperatures are defined as follows:

$$\tilde{T}=\frac{T-T_o}{T_M-T_o} \tag{15}$$

Using the normalized variables defined in Eqs. (8), (10), and (12)–(15), the normalized versions of Eqs. (1)–(4) and (7) can be written as:

$$\tilde{u}\frac{\partial\tilde{u}}{\partial\tilde{r}}+\tilde{\upsilon}\frac{\partial\tilde{u}}{\partial\tilde{z}}=-\frac{\delta^2}{R_b^2}\frac{\partial\tilde{p}}{\partial\tilde{r}}+\frac{\upsilon}{\alpha_l}\left[\frac{\delta^2}{R_b^2}\left(\frac{\partial^2\tilde{u}}{\partial\tilde{r}^2}+\frac{\partial}{\partial\tilde{r}}\left(\frac{\tilde{u}}{\tilde{r}}\right)\right)+\frac{\partial^2\tilde{u}}{\partial\tilde{z}^2}\right] \tag{16}$$

$$\tilde{u}\frac{\partial\tilde{\upsilon}}{\partial\tilde{r}}+\tilde{\upsilon}\frac{\partial\tilde{\upsilon}}{\partial\tilde{z}}=-\frac{\partial\tilde{p}}{\partial\tilde{z}}+\frac{\upsilon}{\alpha_l}\left[\frac{\delta^2}{R_b^2}\left(\frac{\partial^2\tilde{\upsilon}}{\partial\tilde{r}^2}+\frac{1}{\tilde{r}}\frac{\partial\tilde{\upsilon}}{\partial\tilde{r}}\right)+\frac{\partial^2\tilde{\upsilon}}{\partial\tilde{z}^2}\right] \tag{17}$$

$$\frac{1}{\tilde{r}}\frac{\partial(\tilde{u}\tilde{r})}{\partial\tilde{r}}+\frac{\partial\tilde{\upsilon}}{\partial\tilde{z}}=0 \tag{18}$$

$$\tilde{u}\frac{\partial\tilde{T}}{\partial\tilde{r}}+\tilde{\upsilon}\frac{\partial\tilde{T}}{\partial\tilde{z}}=\frac{\alpha}{\alpha_l}\left(\frac{\delta^2}{R_b^2}\left(\frac{\partial^2\tilde{T}}{\partial\tilde{r}^2}+\frac{1}{\tilde{r}}\frac{\partial\tilde{T}}{\partial\tilde{r}}\right)+\frac{\partial^2\tilde{T}}{\partial\tilde{z}^2}\right) \tag{19}$$

$$\tilde{\upsilon}=\tilde{\upsilon}(\tilde{z});\quad \tilde{u}(\tilde{r},\tilde{z})=-\frac{\tilde{r}}{2}\tilde{\upsilon}'(\tilde{z}) \tag{20}$$

2.2 Solution for the Solid Region. The solution for the temperature distribution in the solid in the quasi-steady formulation can be readily obtained. The quasi-steady velocity in the solid is constant and equal to the penetration velocity $\tilde{V}_{SL}$. Combined with Eq. (19) and the assumption of 1D heat transfer in the solid, the energy equation in the solid reduces to

$$\tilde{V}_{SL}\frac{\partial\tilde{T}}{\partial\tilde{z}}=\frac{k_s}{k_l}\frac{\partial^2\tilde{T}}{\partial\tilde{z}^2} \tag{21}$$

Denoting the temperature at the solid–liquid interface as the melting temperature and considering the solid to be semi-infinite with ambient temperature in the far field gives the required boundary conditions for Eq. (21):

$$\tilde{T}(0)=1;\quad \tilde{T}(-\infty)=0 \tag{22}$$

Integration of Eq. (21) with the boundary conditions in Eq. (22) yields the temperature distribution in the solid:

$$\tilde{T}(\tilde{z})=e^{k_l/k_s\tilde{V}_{SL}\tilde{z}} \tag{23}$$

where the normalized drilling speed $\tilde{V}_{SL}$ is a variable to be determined in the analysis.

2.3 Solution for the Melt Layer. Now that the temperature distribution in the solid has been determined, it is possible to derive the governing equations for the heat transfer and fluid flow in the melt region. By integrating Eqs. (16) and (17) separately, it can be shown that the pressure gradient in the r direction is a function of r only and is proportional to r ([22]). Thus, the pressure gradient takes on the following form:

$$\frac{\partial\tilde{p}}{\partial\tilde{r}}=-\tilde{a}^2\frac{R_b^2}{\delta^2}\tilde{r} \tag{24}$$

The value of the pressure gradient factor, $\tilde{a}^2$, is a variable to be determined in the analysis. When Eq. (24) is substituted into Eq. (16) along with Eq. (20), the following third order ordinary differential equation for υ results:

$$\frac{1}{2}\tilde{\upsilon}'^2-\tilde{\upsilon}\tilde{\upsilon}''+\frac{\upsilon}{\alpha_l}\tilde{\upsilon}'''-2\tilde{a}^2=0 \tag{25}$$

The boundary conditions at the solid–liquid interface are given by the following relations:

$$\tilde{\upsilon}(0)=\tilde{V}_{SL};\quad \tilde{u}(0)=-\frac{\tilde{r}}{2}\tilde{\upsilon}'(0)=0\Rightarrow\tilde{\upsilon}'(0)=0 \tag{26}$$

A free stress boundary condition is applied at the liquid–vapor interface:

$$\left.\frac{\partial\tilde{u}}{\partial\tilde{z}}\right|_{\tilde{z}=\tilde{\delta}_\upsilon}=-\frac{\tilde{r}}{2}\tilde{\upsilon}''(\tilde{\delta}_\upsilon)=0\Rightarrow\tilde{\upsilon}''(\tilde{\delta}_\upsilon)=0 \tag{27}$$

The first boundary condition in Eq. (26) represents conservation of mass at the solid–liquid boundary while the second condition yields that the newly melted fluid has no velocity in the r direction and is not a viscous boundary condition. The third boundary condition given by Eq. (27) is the viscous free shear stress boundary condition at the liquid–vapor interface. Using these three boundary conditions, the viscous velocity distribution in the melt can be obtained.

In order to derive a simple, approximate solution for Eq. (25), the ODE can be simplified by recalling that the Pr for some metals is much less than 1. In the limit Pr→0, the viscous term becomes negligible, and Eq. (25) is reduced to its inviscid form:

$$\frac{1}{2}\tilde{\upsilon}'^2-\tilde{\upsilon}\tilde{\upsilon}''-2\tilde{a}^2=0 \tag{28}$$

The viscous shear stress condition at the liquid–vapor interface must be abandoned since the ODE has been reduced to second order. Equation (28) along with Eq. (26) comprise an initial value problem for υ. Consequently, a series solution for υ can be derived by the successive differentiation of Eq. (28) and the application of Eq. (26) to yield expressions for increasing derivatives of υ. Constructing the Taylor series using the resulting derivatives yields the inviscid velocity profile:

$$\tilde{\upsilon}(\tilde{z})=\tilde{V}_{SL}-\frac{\tilde{a}^2}{\tilde{V}_{SL}}\tilde{z}^2 \tag{29}$$

Using the velocity distribution in the melt from Eq. (29), it is possible to solve the energy equation for the temperature distribution in the melt. Representing the temperature in the melt as $\tilde{\tau}(\tilde{z})$, Eq. (19) reduces to the following equation:

$$\tilde{\upsilon}\tilde{\tau}'=\tilde{\tau}'' \tag{30}$$

Requiring that the temperature at the solid–liquid interface is the melting temperature yields the first boundary condition:

$$\tilde{\tau}(0)=1 \tag{31}$$

The second boundary condition is derived from an energy balance at the solid–liquid interface. The normalized energy balance at the solid–liquid interface yields:

$$k_l\tilde{\tau}'(0)=k_s\tilde{T}'(0)+\frac{k_lH_m}{c_p(T_M-T_o)}\tilde{V}_{SL} \tag{32}$$

Substituting the previously obtained expression for the temperature distribution in the solid from Eq. (23), taking its derivative and evaluating at $\tilde{z}=0$, the second boundary condition can be rewritten in the following form:

$$\tilde{\tau}'(0)=\left[1+\frac{H_m}{c_p(T_M-T_o)}\right]\tilde{V}_{SL}\equiv\tilde{G}\tilde{V}_{SL} \tag{33}$$

where

$$\tilde{G}\equiv\left[1+\frac{H_m}{c_p(T_M-T_o)}\right] \tag{34}$$

Note that $\tilde{G}$ consists only of material properties and the initial temperature T_o. Thus, since both $\tilde{\tau}(0)$ and $\tilde{\tau}'(0)$ are now known, it is possible to develop a series solution for the temperature distribution in the melt. Once again successive differentiation of Eq. (30) and application of Eqs. (31) and (33) allows the evaluation of increasing derivatives of $\tilde{\tau}$. Substitution of these derivatives into the Taylor series expansion yields the following solution:

$$\tilde{\tau}(\tilde{z})=1+\tilde{G}\tilde{V}_{SL}\tilde{z}+\frac{1}{2}\tilde{G}\tilde{V}_{SL}^{2}\tilde{z}^{2}+\frac{1}{6}\tilde{G}\tilde{V}_{SL}^{3}\tilde{z}^{3}+\frac{1}{24}[-2\tilde{G}\tilde{a}^{2}+\tilde{G}\tilde{V}_{SL}^{4}]\tilde{z}^{4}+\frac{1}{120}[-8\tilde{G}\tilde{a}^{2}\tilde{V}_{SL}+\tilde{G}\tilde{V}_{SL}^{5}]\tilde{z}^{5}+\cdots \tag{35}$$

Note that the effect of the flow due to the $\tilde{a}^2$ parameter is not felt until the fifth term. The temperature distribution in the majority of the melt is governed by the effects of conduction and convection of the molten material while near the liquid–vapor interface vaporization and the ensuing pressure gradient affect the temperature profile. Since the temperature at the liquid–vapor interface is equal to the vaporization temperature T_v, the following equation can be obtained:

$$\frac{T_V-T_o}{T_M-T_o}=1+\tilde{G}\tilde{V}_{SL}\tilde{\delta}_v+\frac{1}{2}\tilde{G}\tilde{V}_{SL}^{2}\tilde{\delta}_v^{2}+\frac{1}{6}\tilde{G}\tilde{V}_{SL}^{3}\tilde{\delta}_v^{3}+\frac{1}{24}[-2\tilde{G}\tilde{a}^{2}+\tilde{G}\tilde{V}_{SL}^{4}]\tilde{\delta}_v^{4}+\cdots \tag{36}$$

Equation (36) is the first equation needed to solve for the three unknowns: $\tilde{\delta}_v$, $\tilde{V}_{SL}$, and $\tilde{a}^2$.

Consider now the liquid–vapor interface. Using the previously derived expressions for the velocity and temperature distributions in the melt, the energy balance at the liquid–vapor interface in dimensional form is given by the following expression:

$$k_l\tau'(\delta_v)+\rho v(\delta_v)H_v=q''_{\text{laser}} \tag{37}$$

where q''_{laser} is considered to be the fraction of the laser intensity which is absorbed at the liquid–vapor interface. Certainly not all of the emitted laser power is absorbed at the surface of the workpiece as the material absorptivity, multiple reflections, and the potential for a power-absorbing plasma can reduce the effective intensity for drilling. As the effective intensity is difficult to accurately determine, henceforth it is assumed that this value is known from experimental or other considerations, and thus the absorbed laser intensity can be considered a known input to the analysis. Replacing the dimensional variables with normalized variables, taking the derivative of Eq. (35) and evaluating it and Eq. (29) at $\tilde{z}=\tilde{\delta}_v$, Eq. (37) can be rewritten:

$$1=\frac{\dfrac{H_v}{H_m}}{1+\dfrac{c_p(T_m-T_o)}{H_m}}\left(\tilde{V}_{SL}-\frac{\tilde{a}^2\tilde{\delta}_v^2}{\tilde{V}_{SL}}\right)+\tilde{V}_{SL}+\tilde{V}_{SL}^2\tilde{\delta}_v+\frac{1}{2}\tilde{V}_{SL}^3\tilde{\delta}_v^2+\frac{1}{6}\{-2\tilde{a}^2+\tilde{V}_{SL}^4\}\tilde{\delta}_v^3+\frac{1}{24}\{-8\tilde{a}^2\tilde{V}_{SL}+\tilde{V}_{SL}^5\}\tilde{\delta}_v^4+\cdots \tag{38}$$

Equation (38) gives a relationship between $\tilde{\delta}_v$, $\tilde{V}_{SL}$, and $\tilde{a}^2$ as a function of material properties and laser parameters and is the second equation needed to solve for the three unknowns.

Previously the analysis has assumed that the heat flux from the laser is constant in the stagnation region. However, while mostly true near the centerline, the laser beam is assumed to have a Gaussian energy distribution that varies in the r direction. Thus, the laser energy decreases exponentially away from the centerline. The fraction of the emitted laser intensity that is absorbed at the liquid–vapor interface is given by the following expression:

$$q''_{\text{laser}}(r)=\frac{2P_L}{A_b}e^{-2r^2/R_b^2}=I_oe^{-2r^2/R_b^2} \tag{39}$$

It has been assumed that the recoil vapor pressure is the dominant contribution to the pressure at the interface, neglecting surface tension and other second order effects. Consequently, the liquid pressure can be approximated by the following equation from conservation of momentum at the liquid–vapor interface:

$$p\approx\rho_vV_v^2 \tag{40}$$

An expression for V_v can be calculated from conservation of mass at the vaporizing surface by using the liquid velocity and accounting for the density differences. Thus, Eq. (40) can be normalized and rewritten as:

$$\tilde{p}_o\approx\frac{\rho}{\rho_v}\left(\tilde{V}_{SL}-\tilde{a}^2\frac{\tilde{\delta}_v^2}{\tilde{V}_{SL}}\right)^2 \tag{41}$$

Near the origin it is reasonable to assume that the vaporization rate is proportional to the laser energy flux. Thus,

$$\frac{V_v}{V_{vo}}\approx\frac{q''_{\text{laser}}}{I_o}=e^{-2r^2/R_b^2}=e^{-2\tilde{r}^2} \tag{42}$$

Consequently, the expression for the pressure distribution is given by the following equation:

$$\tilde{p}\approx\tilde{p}_oe^{-4\tilde{r}^2} \tag{43}$$

In the vicinity of the centerline, a power series approximation for Eq. (43) can be derived:

$$\tilde{p}\approx\tilde{p}_o(1-4\tilde{r}^2+8\tilde{r}^4+\cdots) \tag{44}$$

Combining Eq. (41) and Eq. (44), an expression for the radial pressure gradient in terms of the stagnation flow variables results:

$$\frac{d\tilde{p}}{d\tilde{r}}\approx\tilde{p}_o(-8\tilde{r})=-8\frac{\rho}{\rho_v}\left(\tilde{V}_{SL}-\tilde{a}^2\frac{\tilde{\delta}_v^2}{\tilde{V}_{SL}}\right)^2\tilde{r} \tag{45}$$

Equating Eq. (24) and Eq. (45) and rewriting δ in terms of the laser parameters, the following expression is obtained:

$$\frac{1}{\pi^2\alpha_l^2\rho^2[c_p(T_M-T_o)+H_m]^2}\left(\frac{P_L}{R_b}\right)^2\tilde{a}^2=2\frac{\rho}{\rho_v}\left(\tilde{V}_{SL}-\tilde{a}^2\frac{\tilde{\delta}_v^2}{\tilde{V}_{SL}}\right)^2 \tag{46}$$

Equation (46) gives the third and final equation needed to solve for the inviscid stagnation flow variables: $\tilde{\delta}_v$, $\tilde{V}_{SL}$, and $\tilde{a}^2$.

Stagnation Flow Results

The inviscid stagnation flow solution was obtained numerically by the solution of the normalized set of equations: Eqs. (36), (38), and (46) for $\tilde{\delta}_v$, $\tilde{V}_{SL}$, and $\tilde{a}^2$ using the Newton–Raphson method for nonlinear root finding. Table 1 shows material properties for aluminum, copper, low carbon steel, stainless steel, and titanium taken from Chan and Mazumder [13], Mohanty et al. [23], and Patel and Brewster [24] that were used in these calculations. In addition the important dimensionless combinations of material properties that appear in the stagnation flow equations are calculated for the four materials. These dimensionless material parameters are as follows: the ratio of solid and liquid thermal conductivity, the ratio of the latent heat of melting to the sensible heat required to raise the temperature of the metal from room temperature to melting, the dimensionless vapor temperature, the ratio of the latent heats of melting and vaporization, and the ratio of liquid and vapor densities. In addition, the liquid Prandtl number for each material is given. Recall that the inviscid stagnation flow analysis is valid for small values of the Prandtl number; the values in Table 1 indicate that this assumption is reasonable for the five materials considered here.

Table 1 Material properties used in stagnation flow calculations

Property	[Units]	Aluminum	Copper	Low Carbon Steel	AISI 304 Stainless Steel	Titanium
ρ	[kg/m^3]	2700	8300	7854	7900	4500
ρ_v	[kg/m^3]	0.1173	0.257	0.218	0.218	0.163
c_{ps}	[J/kg K]	917	450	456	477	528
k_l	[W/m K]	100	190	30	14.9	20.28
k_s	[W/m K]	238	270	78.2	14.9	21.6
T_M	[°K]	933	1357	1809	1685	1940
T_V	[°K]	2793	3000	3133	3023	3558
T_o	[°K]	298	298	298	298	298
H_m	[J/kg]	3.88e5	2.05e5	2.72e5	2.73e5	3.65e5
H_v	[J/kg]	1.19e7	4.8e6	6.1e6	6.1e6	8.89e6
ν	[m^2/s]	5.45e-7	5.0e-7	7.84e-7	7.84e-7	1.26e-6
Pr_l	[-]	0.0135	0.0098	0.094	0.198	0.148
k_s/k_l	[-]	2.38	1.42	2.61	1.0	1.065
$\frac{H_m}{c_p(T_M-T_o)}$	[-]	0.67	0.43	0.39	0.41	0.42
$\frac{H_v}{H_m}$	[-]	30.7	23.4	22.4	22.3	24.4
$\frac{\rho}{\rho_v}$	[-]	2.30e4	3.23e4	3.60e4	3.62e4	2.75e4
$\frac{T_V-T_o}{T_M-T_o}$	[-]	3.93	2.55	1.88	1.96	1.99

The scaling and resulting normalization introduced here results in only one independent parameter that contains both the absorbed laser power and the beam radius. This parameter, P_L/R_b, arises from Eq. (46) and is hereafter denoted as the laser beam parameter. This parameter was varied over a range that encompasses the usual laser intensities for drilling. For a given value of the laser beam parameter, it is possible to solve for the normalized stagnation flow variables: the melt layer thickness $\tilde{\delta}_v$, the pressure gradient parameter $\tilde{a}^2$, and the drilling speed, $\tilde{V}_{SL}$. Once these values are determined, the full velocity profile in the melt and temperature distribution in the melt and solid can be obtained. The complete normalized stagnation flow results were obtained for the five different metals as functions of the independent laser beam parameter. The normalized solutions are shown for low carbon steel in Fig. 2. As outlined in the derivation of the governing equations, the variables are normalized with scales that include the independent laser parameters; therefore, the trends for the normalized variables are not necessarily indicative of the dimensional trends.

In returning to dimensional form for the penetration velocity, Eqs. (9) and (10) are used:

$$V_{SL}=\frac{1}{\rho[c_p(T_M-T_o)+H_m]}\frac{2P_L}{\pi R_b^2}f\left(\frac{P_L}{R_b}\right)\sim q'' \qquad (47)$$

where $f(P_L/R_b)$ is the material-specific, normalized penetration velocity solution. Thus, it can be seen that increasing the laser power leads to greater drilling speeds. In addition, decreasing the size of the beam leads to larger penetration speeds. The explanation is fairly simple: decreasing the beam radius for a fixed laser power results in higher laser intensities and consequently greater drilling speeds. Figure 3 shows the dimensional drilling velocity as a function of laser power for the four different metals and a fixed beam radius of 20 μm. This graph clearly shows that the drilling speed increases monotonically with laser intensity. Note that the highest penetration rates are found in aluminum while stainless steel has the lowest velocities.

From Eqs. (11) and (12), the normalized melt layer thickness $\tilde{\delta}_v$ can be rewritten in dimensional form:

$$\delta_v=\alpha_l\rho[c_p(T_M-T_o)+H_m]\frac{\pi R_b^2}{2P_L}g\left(\frac{P_L}{R_b}\right)\sim\frac{1}{q''} \qquad (48)$$

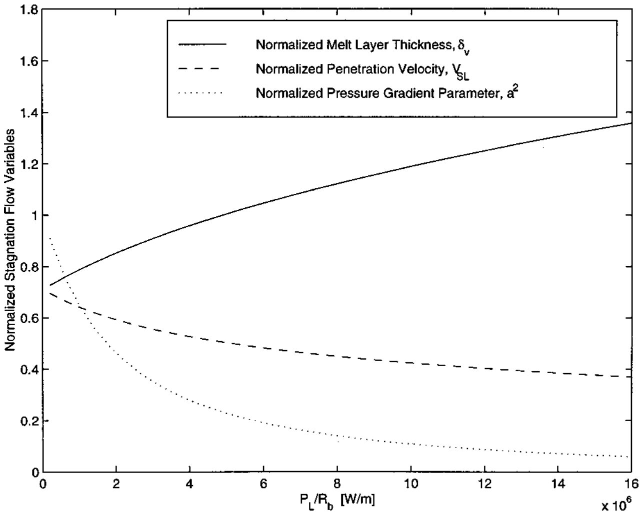

Fig. 2 Normalized stagnation flow solution for low carbon steel as a function of the laser beam parameter

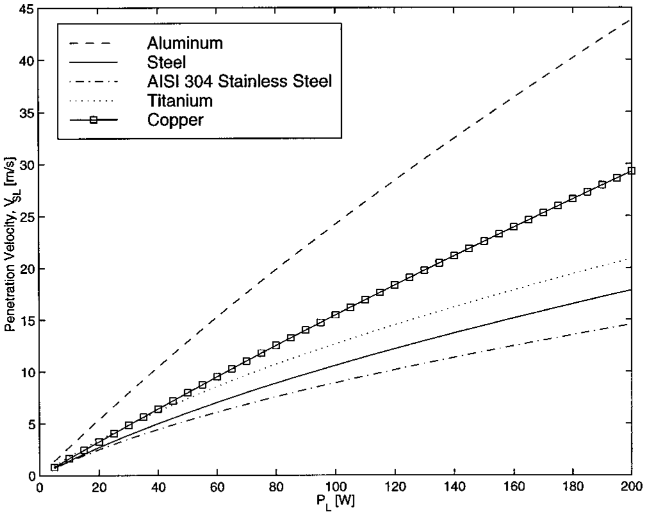

Fig. 3 Dimensional drilling speeds V_{SL} as a function of the absorbed laser power, R_b=20 μm

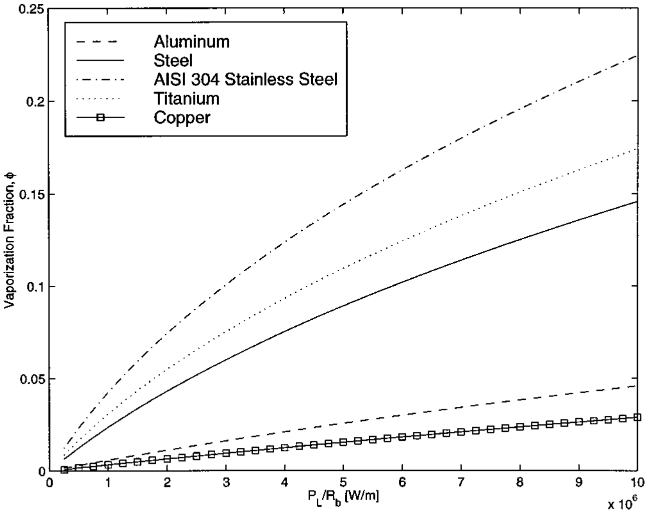

Fig. 4 Vaporization fraction ϕ as a function of the laser beam parameter

where $g(P_L/R_b)$ is the material-specific, normalized melt layer thickness solution. As the laser power increases, the melt layer decreases in size. In addition, decreasing the beam radius for a given laser power results in a smaller melt thickness. An increase in laser intensity leads to thinner melt pools. Scaling arguments show that the melt thickness is inversely proportional to the laser intensity and thus the drilling speed:

$$\delta_v \sim \frac{1}{V_{SL}} \tag{49}$$

Rewriting the pressure gradient factor $\tilde{a}^2$ in dimensional form, the following expression is obtained:

$$a^2=\frac{1}{\alpha_l^2\rho^4[c_p(T_M-T_o)+H_m]^4}\frac{16P_L^4}{\pi^4R_b^8}h\left(\frac{P_L}{R_b}\right)\sim(q'')^4 \tag{50}$$

where $h(P_L/R_b)$ is given by the material-specific, normalized pressure gradient parameter solution. It can be seen that as the laser power increases, the pressure gradient factor increases. In addition, decreasing the beam radius for a given power results in a larger value for the pressure gradient. As the laser intensity increases (either by increasing the laser power or decreasing the beam radius), the vaporization rate and thus the pressure gradient increases quadratically.

Another quantity of interest in examining the fundamental mechanics of material removal is the vaporization fraction, defined as the fraction of melted material that is evaporated rather than expelled radially from the stagnation region. Mathematically, the vaporization fraction can be defined in terms of the stagnation flow variables:

$$\phi=\frac{\tilde{v}(\tilde{\delta}_v)}{\tilde{V}_{SL}}=1-\frac{\tilde{a}^2\tilde{\delta}_v^2}{\tilde{V}_{SL}^2} \tag{51}$$

The vaporization fraction gives a quantitative estimate as to the relative importance of evaporation and melt expulsion in material removal. Figure 4 depicts the variation of the vaporization fraction as a function of the laser beam parameter. It can be seen that increasing the laser beam parameter, either by increasing the laser power or decreasing the beam radius, results in a larger vaporization fraction as the role of vaporization in the mechanics of material removal increases. For the representative values of the laser beam parameter chosen here, it can be seen that at even at very high intensities, less than 25 percent of the melted material is vaporized; the rest is expelled radially, thereby emphasizing the importance of the melt flow. Stainless steel with its low thermal conductivity shows much higher vaporization fractions than the other metals. Aluminum and copper, which are highly conductive, have the lowest vaporization fractions.

Table 2 Comparison of calculated and experimental ([25]) drilling depths, $q''=8\times10^5$ W/cm², $t_p=600$ μs

Material	Drilled Hole Depths (cm)	
	Stagnation Flow Analysis R_b = 100 μm	Experimental Values Ready (1965)
Stainless Steel	0.064	0.061
Copper	0.096	0.090
Aluminum	0.155	0.078

Table 2 shows a comparison between calculated and experimental drill depths. The experimental data are from Ready [25] for a laser beam with an intensity of 8×10^5 W/cm² and a pulse time of 600 μs. The calculated hole depths are obtained from the quasi-steady stagnation flow solution as follows:

$$d_{\text{hole}}=V_{SL}t_p \tag{52}$$

where t_p is the laser pulse time. For the analytical results, a typical beam radius of 100 μm was assumed since the experimental beam radius could not be ascertained from Ready [25]. This assumption is reasonable since variations in the drilling speed for a constant intensity of 8×10^5 W/cm² with the beam radius varied over a wide range from 50–500 μm are less than 10 percent. As mentioned previously, the stagnation flow analysis is formulated for quasi-steady drilling, a condition that is usually valid at intensities of drilling interest for cw or pulsed operation with long pulses. Scaling estimates for the transient initiation time are given by the melt time constant:

$$t_m=\frac{\alpha_l}{V^2} \tag{53}$$

For the three materials in Table 2, namely aluminum, stainless steel, and copper, the estimates for the initiation times at 8×10^5 W/cm² are 4, 3, and 25 μs, respectively. Therefore, the transient portion of the drilling process comprises only a small portion of the pulse duration, and it can be assumed within the accuracy of the analysis that the drilling is quasi-steady over the entire 600 μs pulse. The comparison between the calculated and experimental drilled hole depths is quite favorable for both copper and stainless steel. For aluminum the results are within an order of magnitude. However, it is known that aluminum, which has the lowest ionization potential of the five materials calculated here, is susceptible to the formation of a plasma plume which can act to absorb some of the incident laser power ([26]). Therefore, it is difficult to predict the power that is actually absorbed at the workpiece. While only one of several physical phenomena that occur during laser drilling that was not considered in the analysis, the formation of a plasma plume could be one explanation for the disparity between the calculated and experimental drill depths for aluminum. Reasonably good quantitative agreement exists between the calculated results and those determined experimentally.

Conclusions

The results of the quasi-steady stagnation flow analysis illustrate the importance of the melt flow in high-energy beam processes. The normalization and scaling analyses clearly show the important independent and material property parameters for laser drilling. From normalization of the governing stagnation flow equations, a single laser beam parameter, P_L/R_b, has been determined to govern the drilling physics. The size of the laser beam plays a crucial role in determining the thickness of the melt pool, the penetration rate into the material, and the mechanisms of material removal. The results show that high laser intensities (due to increased absorbed laser power or a smaller beam radius) lead to thin molten metal pools and high penetration velocities. Also, as laser intensities increase, the amount of vaporization increases, and higher pressure gradients exist within the melt pool. These high pressure gradients lead to recoil-pressure-driven flow away from the stagnation region. The analysis yields a quantitative estimate for the relative importance of material removal via vaporization and melt expulsion. Results show that only a small quantity of material is vaporized, usually less than 25 percent; the rest is expelled radially from the stagnation region. Reasonably good quantitative agreement between calculated and experimental drill depths are obtained.

Acknowledgments

This work was funded under DOD-SUB (K)-LTR DTD 10/29/96, PLM COLLABORATION AGR (Dept. of Defense) ‘‘Precision Laser Machining’’ (PLM).

Nomenclature

a^2 = pressure gradient parameter
A_b = area of the laser beam
d_{hole} = drilled hole depth
G = material property parameter
H_m = latent heat of melting
H_v = latent heat of vaporization
p_o = centerline pressure
P_L = absorbed laser power
R_b = radius of the laser beam
t_m = melt time constant
t_p = laser pulse duration
T_o = ambient temperature
T_M = melting temperature
T_v = vaporization temperature
V = melt penetration velocity scale
V_{SL} = melt penetration velocity
u, v = velocity components in r, z directions

Greek Letters

δ = melt thickness scale
δ_v = melt thickness
ϕ = vaporization fraction
τ = temperature in melt region

Subscripts

m = melt
s = solid
v = vapor

Note: Normalized variables are denoted with a tilde overscore.

References

[1] Minardi, A., and Bishop, M. J., 1988, ‘‘Two-Dimensional Temperature Distribution Within a Metal Undergoing Multiple Phase Changes Caused by Laser Irradiation at the Surface,’’ ASME J. Heat Transfer, **110**, pp. 1009–1011.

[2] Armon, E., Zvirin, Y., Laufer, G., and Solan, A., 1989, ‘‘Metal Drilling with a CO_2 Laser Beam,’’ J. Appl. Phys., **65**, No. 12, pp. 4995–5002.

[3] Kar, A., and Mazumder, J., 1990, ‘‘Two-Dimensional Model for Material Damage Due to Melting and Vaporization During Laser Irradiation,’’ J. Appl. Phys., **68**, No. 8, pp. 3884–3891.

[4] Wei, P. S., and Ho, J. Y., 1990, ‘‘Energy Considerations in High-Energy Beam Drilling,’’ Int. J. Heat Mass Transf., **33**, No. 10, pp. 2207–2217.

[5] Armon, E., Zvirin, Y., and Solan, A., 1991, ‘‘Numerical Simulation of Metal Drilling with a CO_2 Laser Beam,’’ Numer. Heat Transfer, Part B, **19**, pp. 85–104.

[6] Yilbas, B. S., Sahin, A. Z., and Davies, R., 1995, ‘‘Laser Heating Mechanism Including Evaporation Process Initiating Laser Drilling,’’ Int. J. Mach. Tools Manuf., **35**, No. 7, pp. 1047–1062.

[7] Modest, M. F., 1996, ‘‘Three-Dimensional, Transient Model for Laser Machining of Ablating/Decomposing Materials,’’ Int. J. Heat Mass Transf., **39**, No. 2, pp. 221–234.

[8] Modest, M. F., 1997, ‘‘Laser Through-Cutting and Drilling Models for Ablating/Decomposing Materials,’’ J. Laser Appl., **9**, pp. 137–145.

[9] Yilbas, B. S., and Al-Garni, A. Z., 1996, ‘‘Some Aspects of Laser Heating of Engineering Materials,’’ J. Laser Appl., **8**, pp. 197–204.

[10] Yilbas, B. S., 1995, ‘‘Study of Liquid and Vapor Ejection Processes During Laser Drilling of Metals,’’ J. Laser Appl., **7**, pp. 145–152.

[11] Yilbas, B. S., and Sami, M., 1997, ‘‘Liquid Ejection and Possible Nucleate Boiling Mechanisms in Relation to the Laser Drilling Process,’’ J. Phys. D: Appl. Phys., **30**, pp. 1996–2005.

[12] von Allmen, M., 1976, ‘‘Laser Drilling Velocity in Metals,’’ J. Appl. Phys., **47**, No. 12, pp. 5460–5463.

[13] Chan, C. L., and Mazumder, J., 1987, ‘‘One-Dimensional Steady-State Model for Damage by Vaporization and Liquid Expulsion Due to Laser-Material Interaction,’’ J. Appl. Phys., **62**, No. 11, pp. 4579–4586.

[14] Wei, P. S., and Chiou, L. R., 1988, ‘‘Molten Metal Flow Around the Base of a Cavity During a High-Energy Beam Penetrating Process,’’ ASME J. Heat Transfer, **110**, pp. 918–923.

[15] Kar, A., Rockstroh, T., and Mazumder, J., 1992, ‘‘Two-Dimensional Model for Laser-Induced Materials Damage: Effects of Assist Gas and Multiple Reflections Inside the Cavity,’’ J. Appl. Phys., **71**, No. 6, pp. 2560–2569.

[16] Ganesh, R. K., Bowley, W. W., Bellantone, R. R., and Hahn, Y., 1996, ‘‘A Model for Laser Hole Drilling in Metals,’’ J. Comput. Phys., **125**, pp. 161–176.

[17] Ganesh, R. K., Faghri, A., and Hahn, Y., 1997, ‘‘A Generalized Thermal Modeling for Laser Drilling Process—I. Mathematical Modeling and Numerical Methodolgy,’’ Int. J. Heat Mass Transf., **40**, No. 14, pp. 3351–3360.

[18] Ganesh, R. K., Faghri, A., and Hahn, Y., 1997, ‘‘A Generalized Thermal Modeling for Laser Drilling Process—II. Numerical Simulation and Results,’’ Int. J. Heat Mass Transf., **40**, No. 14, pp. 3361–3373.

[19] Semak, V. S., and Matsunawa, A., 1997, ‘‘The Role of Recoil Pressure in Energy Balance During Laser Materials Processing,’’ J. Phys. D: Appl. Phys., **30**, pp. 2541–2552.

[20] Chen, M. M, Bos, J. A., and Batteh, J. J., 1997, ‘‘Parametric Study of Keyhole Behavior Based on an Approximate Theory,’’ *Laser Institute of America, Proceedings*, **83**, No. 2, pp. G34–G43.

[21] Bos, J. A., and Chen, M. M., 1998, ‘‘An Approximate Analysis of the Melt Flow and Heat Transfer in Deep Penetration Laser Welding,’’ presented at IMECE ’98.

[22] Schlichting, H., 1968, *Boundary Layer Theory*, 6th Ed., pp. 91–92.

[23] Mohanty, P. S., Kar, A., and Mazumder, J., 1996, ‘‘A Modeling Study on the Influence of Pulse Shaping on Keyhole Laser Welding,’’ J. Laser Appl., **8**, pp. 291–297.

[24] Patel, R. S., and Brewster, M. Q., 1991, ‘‘Gas-Assisted Laser-Metal Drilling: Theoretical Model,’’ J. Thermophys. Heat Transf., **5**, No. 1, pp. 32–39.

[25] Ready, J. F., 1965, ‘‘Effects Due to Absorption of Laser Radiation,’’ J. Appl. Phys., **36**, No. 2, pp. 462–468.

[26] Charschan, S. S., 1993, *Guide to Laser Materials Processing*, Laser Institute of America, p. 147.

K. R. Cheruparambil

B. Farouk[1]
Mem. ASME
e-mail: bfarouk@coe.drexel.edu

Department of Mechanical
Engineering and Mechanics,
Drexel University,
3141 Chestnut Street,
Philadelphia, PA 19104

J. E. Yehoda
Diamonex Inc.,
Allentown, PA 18105

N. A. Macken
Department of Engineering,
Swarthmore College,
Swarthmore, PA 19081-1397

Thermal Conductivity Measurement of CVD Diamond Films Using a Modified Thermal Comparator Method

Results from an experimental study on the rapid measurement of thermal conductivity of chemical vapor deposited (CVD) diamond films are presented. The classical thermal comparator method has been used successfully in the past for the measurement of thermal conductivity of bulk materials having high values of thermal resistance. Using samples of known thermal conductivity, a calibration curve is prepared. With this calibration curve, the comparator can be used to determine thermal conductivity of unknown samples. We have significantly modified and extended this technique for the measurement of materials with very low thermal resistance, i.e., CVD diamond films with high thermal conductivity. In addition to the heated probe, the modified comparator employs a thermoelectric cooling element of increase conductive heat transfer through the film. The thermal conductivity measurements are sensitive to many other factors such as the thermal contact resistances, anisotropic material properties, surrounding air currents and temperature, and ambient humidity. A comprehensive numerical model was also developed to simulate the heat transfer process for the modified comparator. The simulations were used to develop a ''numerical'' calibration curve that agreed well with the calibration curve obtained from our measurements. The modified method has been found to successfully measure the thermal conductivity of CVD diamond films. [S0022-1481(00)00804-5]

Keywords: Condensation, Experimental, Heat Transfer, Measurement Techniques, Probes

Introduction

Measurement of thermal conductivity of synthetically produced chemical vapor deposited (CVD) diamond films is a challenging problem. Such films have very high thermal conductivities at room temperature (800 W/m.K–1800 W/m.K), are among the hardest substances known and are used in such diverse applications as cutting tools, laser diode arrays, multichip modules, integrated electronics, etc. The thermal conductivity of CVD diamond films is also known to be anisotropic, a consequence of the columnar morphology characteristic of their growth ([1]). Rapid measurement of thermal conductivity of CVD diamond films is desirable for the determination of material quality, which can enhance optimization of the process parameters.

One of the well-known methods for measurement of the thermal conductivity of any material is the guarded hot-plate device ([2]). In this method, a one-dimensional heat transfer apparatus is employed where both the heat flux and the temperature gradient across the thickness of the sample are measured. A guard heater surrounding the main heater aids in maintaining one-dimensional heat transfer throughout the material. A coolant is circulated through the device to remove heat and thermocouples are installed at appropriate places to measure temperatures. The thermal conductivity is determined by applying the one-dimensional Fourier heat-conduction equation. This method is mainly used to measure thermal conductivity of nonmetals, i.e., solids of low thermal conductivity, but can also be extended to measure the thermal conductivity of liquids and gases. Another common method to measure low conductivity, for example paper, is the ''conductivity cell'' ([3]). The principle used here is similar to that of the guarded hot-plate method. The thermal comparator method ([4]) is another technique for measuring thermal conductivity of bulk solids. In this method, a heated probe-tip makes contact with the sample for its thermal conductivity measurement. Further details and limitations of the ''classical'' thermal comparator method are given in the next section. Lambropoulos et al. [5] used the thermal comparator method to analyze the heat conduction process from the tip of the comparator to a very thin film (having low thermal conductivity) deposited on a substrate. Using axisymmetric heat conduction theory along with the measurements, they were able to measure the film thermal conductivity and the thermal resistance between the film and the substrate. Recently Mesyngier et al. [6] used the same procedure to measure the thermal conductivity of plasma deposited diamond-like carbon (DLC) films.

Natural diamond crystals (single crystal of high purity) have thermal conductivities as high as 2200–2400 W/m.K at room temperature ([7]). Measurement of the thermal conductivity of CVD diamond films has generated significant research interest in the recent past. Some of the methods to measure thermal conductivity of free-standing diamond films are the photothermal deflection method, the heated bar method, the laser flash method, and Angstrom's traveling wave method. Of these methods, only the heated bar technique actually measures the thermal conductivity. The other methods measure the thermal diffusivity (α), the ability of a material to spread heat. α is related to k via the relationship $k = \alpha\rho C$, where ρ is the density of the material and C is the specific heat. Both k and C have been measured for free-standing CVD diamond films, and found to be very close to bulk natural diamond values ([8]). The photothermal beam deflection technique ([9]), also called the thermal wave or mirage effect technique, is based on pulsed heating of the material surface by a laser beam. A second laser beam (probe beam) is either reflected off the heated spot at a small angle, or traverses the sample just above the surface. The reflected beam angle, which depends on the change in

---

[1] To whom correspondence should be addressed.

Contributed by the Heat Transfer Division for publication in the JOURNAL OF HEAT TRANSFER. Manuscript received by the Heat Transfer Division, Aug. 16, 1999; revision received, May 9, 2000. Associate Technical Editor: T. Avedesian.

the index of refraction of the air above the heated spot, is a function of the thermal conductivity of the material. In the heated bar technique ([1]), a rectangular sample is placed between a constant temperature reservoir and a heater. A series of thermocouples are attached to the sample. A second heater is used to account for radiation and convection losses to the environment. By measuring the power to the heaters and the temperature gradient, the thermal conductivity can be determined. This technique measures the parallel component of thermal conductivity. In the laser flash method ([10]) the two surfaces of the sample are coated with a 300 nm titanium layer and a laser pulse is directed to one side. This method measures the perpendicular component thermal diffusivity. The increase in temperature is monitored on the opposite side by an infrared detector. From the time response and the solution to the one-dimensional heat diffusion equation, the thermal diffusivity can be determined. The modified Angstrom's method ([11]) is based on measuring the phase lag of a heated traveling wave at a given distance from the wave origin. This method also measures the in-plane or parallel component of the thermal diffusivity. All of the above methods require expensive and/or large measurement setups. For example, the laser heating method requires very precise measurement of small angles or phase difference. The heated bar method requires elaborate preparation of samples, i.e., the deposition of thermocouples on surfaces using silver filled epoxy.

In this paper, we present a novel technique for the rapid measurement of high conductivity stand-alone diamond films. We modified the ''classical'' thermal comparator method ([4]) for successfully measuring the thermal conductivity of CVD diamond films. A numerical model was also used to aid in our experimental design and provide insights to the heat transfer process in the probe-sample assembly.

Experimental Method

The classical thermal comparator method ([4]) is discussed first in this section. We also discuss the problems associated with this methodology when applied to the measurement of thin high-conductivity diamond films. Finally, we describe a modified comparator technique that was used to produce a calibration curve, suitable for the measurement of high conductivity films.

The Classical Thermal Comparator. In the classical thermal comparator, illustrated in Fig. 1, an electrically heated probe is brought in contact with the sample. A thermocouple is attached at the probe tip and a thermal circuit is created between the probe assembly, the sample, and the base. A voltage proportional to the temperature difference between the thermocouple probe tip and a reference location within the heated probe is measured. Using samples of known thermal conductivity, a calibration curve (Fig. 2) is prepared which can then be used to determine the thermal conductivity of the unknown samples. In his paper, Powell [4] suggested that the contact pressure between the sample and the probe tip be kept at a constant value. Thus the classical approach is based on the measurement of the contact temperature—independent of load and surface finish. For soft materials (e.g., lead), this meant a large contact area between the probe tip and the sample and hence the method failed for soft samples. Powell's method was thus limited to materials having reasonably high hardness and low material conductivity (<200 W/m.K) as the measured temperature difference becomes almost independent of the sample thermal conductivity at higher values (see Fig. 2). The method was also unsuitable for thin films as the measured temperature difference was found to depend on the sample thickness for thin films. Figure 3 shows the calibration curve established using the classical thermal comparator apparatus. The comparator output obtained for diamond is much lower than the value obtained for aluminum which has a thermal conductivity of 237 W/m.K. Since the thermal conductivity of diamond (800 W/m.K) is much higher than aluminum, it is expected that the comparator reading should be higher than that of aluminum. Thus the classical method was unsuccessful in the measurements of materials which had either higher thermal conductivity or had low hardness.

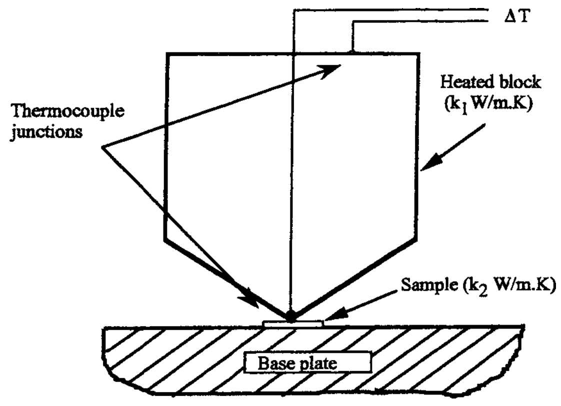

Fig. 1 Schematic of the classical thermal comparator

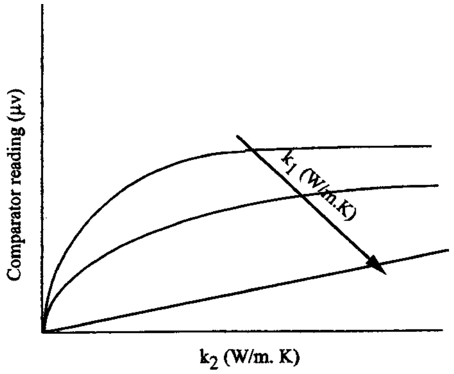

Fig. 2 Typical thermal comparator calibration curve

Limitations of the Classical Thermal Comparator. The thermal comparator works on the principle that the ''total'' heat transfer from the probe is a function of the sample thermal conductivity. There are difficulties associated with the classical thermal comparator, particularly when it is used to measure the high thermal conductivity of CVD diamond films. Below we discuss these problem areas and also indicate how they are addressed in our improved design.

Area of Contact. In the classical method, the contact pressure between the sample and the probe tip is kept constant for all samples. For softer materials, the area of contact (between probe tip and sample) is thus larger than that for harder materials. Since the ''area of contact'' is the primary conductive heat flow path from the heated probe to the sample, anomalous results are obtained by the classical method when samples having different hardnesses are used. For large contact loads, plastic deformation of the sample surface can occur, which changes the thermal resistance and the comparator output. During comparative testing, the contact area between the probe tip and the sample must be kept constant.

An elastic deformation analysis was performed in order to obtain a first-order approximation of the relative difference in area of contact between different materials. The problem of elastic contact between two spherical bodies ([12]) was considered. The radius of the area of contact ''a'' as given by elasticity theory for the two spherical bodies of radii R_1 and R_2 is

$$a=\sqrt[3]{(3\pi/4)F(m_1+m_2)R_1R_2/(R_1+R_2)} \tag{1}$$

where F is the compressive force, $m_i=(1-\nu^2)/(\pi E_i)$, where ν is the Poisson's ratio and E is the modulus of elasticity. The

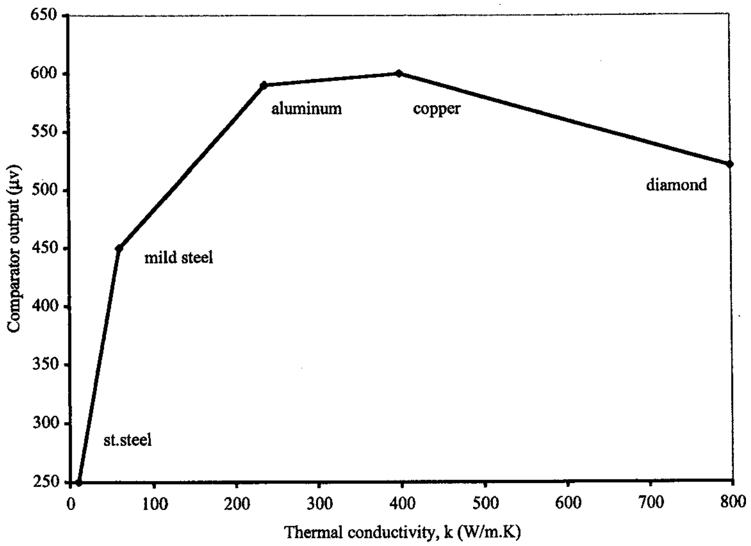

Fig. 3 Calibration curve using classical thermal comparator method

subscript *i* denotes the two spherical bodies 1 or 2. In the present case (comparator), the contact is produced between the spherical tip of the probe and a plane (sample surface). The radius of curvature of a plane can be considered to be infinite. Therefore, Eq. (1) reduces to

$$a=\sqrt[3]{(3\pi/4)F(m_1+m_2)R_1}. \tag{2}$$

For a constant contact radius ''a'' the applied load thus can be calculated as

$$F=a^3(4/3\pi)/((m_1+m_2)R_1). \tag{3}$$

The above formula can now be used to calculate the loads for different samples for maintaining a constant area of contact during measurements.

Thermal Saturation of High Conductivity Samples. In the classical comparator, the sample temperature approaches the probe temperature for samples of high thermal conductivity. Once the sample becomes thermally saturated, the heat transfer from the probe is no longer controlled by the sample thermal conductivity but by the convective heat transfer coefficient at the sample/air interface (see Fig. 1). We address this problem in our comparator by providing active cooling along the bottom of the sample. The sample is placed on a thermoelectric element that can be maintained at a temperature lower than the probe tip and the ambient temperatures. The thermoelectric element removes heat from the sample and rejects it to a heat sink that is cooled by an external fan.

Radiative Heating and Cooling. The comparator probe radiates thermal energy to the samples. Each sample is affected differently depending on its surface properties. In our comparator, a radiation shield made of aluminum encloses the heated block to reduce radiation heat transfer to the samples.

Environmental Temperature and Humidity Control. For the proper operation of the thermal comparator, heat transfer between the sample and the environment must be relatively constant (or negligibly small) for all samples. This is particularly true when the sample is actively cooled. In order to eliminate condensation on the sample, we must also ensure that the dew point of the environment remains below the surface temperature. To do this, we placed our comparator inside an enclosure to monitor the temperature and control the humidity near the exposed sample.

The Modified Thermal Comparator. A schematic of the modified thermal comparator developed is shown in Fig. 4. This comparator is home-made and is not available commercially. The modified design addresses the issues discussed above regarding the shortcomings of the classical comparator. A detailed numerical model (discussed in the next section) which simulates the heat transfer process in the probe-sample assembly aided the design of the modified comparator.

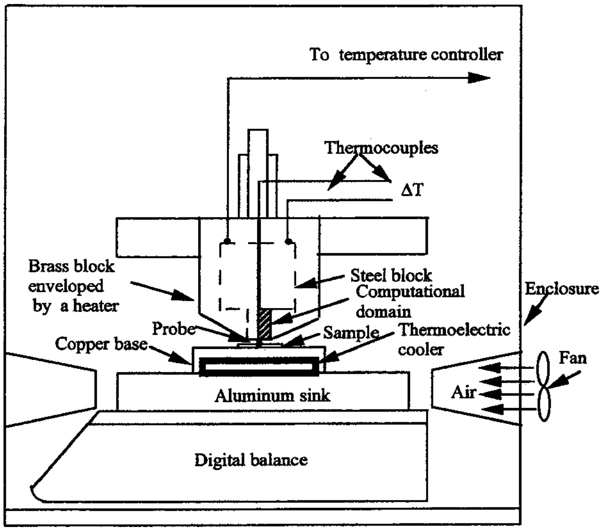

Fig. 4 Schematic of the modified thermal comparator for high conductivity samples

The thermocouple probe is held in place by a three-jaw chuck that is attached to a stainless steel block. A larger brass block that is surrounded by a heater encloses the steel block. A temperature controller maintains the steel block at 60°C. The probe also extends through an aluminum radiation shield that surrounds the jaws, stainless steel, brass, and heater. The protrusion of the probe from the shield is approximately 1.0~1.5 mm. The probe consists of a chromel-constantan (E-type) thermocouple with a stainless steel sheath of outer diameter of 254 μm. An optical microscopic characterization was done and the tip was found to be more or less spherical—not oblong. A probe with a spherical tip is preferred for two reasons. First, a probe with a flat surface at the end may have alignment problems with respect to the sample surface. Secondly, we have shown in the numerical calculations discussed later that lower contact areas yield higher sensitivity in the measurements. The use of a flat probe will result in a high contact area.

A copper-constantan thermocouple (T type) is inserted at the top of the steel block as a reference junction. The constantan terminals from the probe and the reference junction are connected to a multimeter (Fluke, model 8840A) that gives the comparator output in microvolts. The multimeter output was about 40 microvolts per 1°C of temperature difference. The probe-block assembly can be traversed in the horizontal and vertical directions by positioner arms actuated by stepper motors. The samples are placed on a copper base that covers the thermoelectric element. The thermoelectric element (Melcor, CP 1.0-254-05L) is placed on a finned aluminum heat sink which is cooled by an external fan. The load applied (F) on the samples can be read from a balance (Acculab, V-6000) on which the aluminum sink is placed. Both the load and positioner can be controlled either manually or by a computer. The entire assembly is enclosed in a clear plastic enclosure. The temperature and humidity of the enclosure are monitored. Humidity is reduced by placing desiccants in the enclosure. The dimensions of the calibration samples are 10 mm×5 mm, with a thickness of 250 μm.

Measurement Procedure. For the present measurements, the samples included stainless steel, zinc, aluminum, copper, and free-standing CVD diamond. Diamonex Inc., Allentown, PA provided two diamond samples (having thermal conductivity values of 800 and 1290 W/m.K, respectively). These samples were 250 μm thick and the top surface was polished to an average roughness of <0.1 μm, as measured by surface profilometry. The thermal conductivity of these samples was previously determined using the photothermal deflection technique.[2] The other samples were procured from Goodfellow Corp., Berwyn, PA. All samples were of known thermal conductivity. In the experiments, samples were placed side by side on the copper base with a gap between them. The brass block is then heated until a temperature of 60°C is reached and is maintained at that temperature. The thermoelectric element is controlled by using a PID controller (Wavelength Electronics, PID-1500) with the cold side maintained at a low temperature, typically 10°C. A thermistor dipped in grease is placed in between the copper base and the cold side of the thermoelectric cooling element. This gives a reading in terms of volts which can be converted to temperature in Celsius using a chart provided by Wavelength Electronics. The temperature and humidity inside the enclosure are noted using a digital thermometer and hygrometer, respectively. Air from a fan placed outside the enclosure is ducted through the aluminum heat sink for efficient heat removal. The probe is positioned approximately at the center of a sample and is traversed downward slowly until it touches the surface of the sample. The vertical motion is stopped once the designed or predicted load for that sample is reached. The temperature reading (in microvolts) shown on the multimeter is noted after steady state is achieved. The steady state is evident when there is no change in the comparator reading. The probe is then moved upwards, positioned a few steps in the horizontal direction and then moved down to contact the same sample again. Each step (for the stepper motor) in the horizontal direction is approximately 0.025 mm. The procedure is repeated until three readings are obtained at different spots on the same sample. This is done to reduce the effects or surface roughness and flatness deviations. The first reading is taken at the center of the sample and the other readings are taken at 0.5 mm on either side of the center of the sample. The time required for these readings on one sample is approximately three minutes. This is sufficient time for the system to reach steady state, as evidenced by the comparator voltage. The mean of the readings is calculated and reported in μV. Similarly, readings are taken on other samples. A calibration curve is then plotted with the thermal conductivity (of the known samples) on the x-axis and the μV reading on the y-axis. Once the calibration curve is obtained, the thermal conductivity of unknown samples (of similar dimensions to the calibration samples) can be determined.

Numerical Model

Numerical simulations of the heat transfer near the probe tip/sample contact area was performed to provide design guidelines for the modified comparator. A schematic of the computational domain considered is shown in Fig. 5. Due to axial symmetry, only one-half of the domain is shown in Fig. 5.

Steady-state axisymmetric heat conduction was considered. The domain is characterized by its complex geometry and multicomponent structure. The probe tip and the probe body consist of stainless steel. The sample material thermal conductivity was varied for the simulations. The base plate shown in the schematic was considered to be made of copper. The governing equation for the heat transfer is given by

$$\nabla.(k.\nabla T)=0 \tag{4}$$

where $k(r,z)$ is the thermal conductivity of the multicomponent domain.

For the present calculations, isotropic thermal conductivity values were considered for all samples (including diamond). Perfect contact between the probe tip and probe body and between the sample and the base plate was assumed. The contact radius ''a'' between the probe-tip and the sample can be varied for the simulations. A constant temperature boundary condition was considered along the top and right surfaces of the probe. Convective boundary conditions were considered along all other exposed surfaces of the probe, sample and the base plate. Radiative heat transfer was ignored in the calculations.

A finite volume method was used to discretize the governing equation. A multiblock body-fitted coordinate system was considered for the computational domain shown in Fig. 6. Approximately 5200 mesh points were considered for the results presented here. Grid independence studies were carried out to ensure that the above mesh size was sufficient to resolve the domain. The

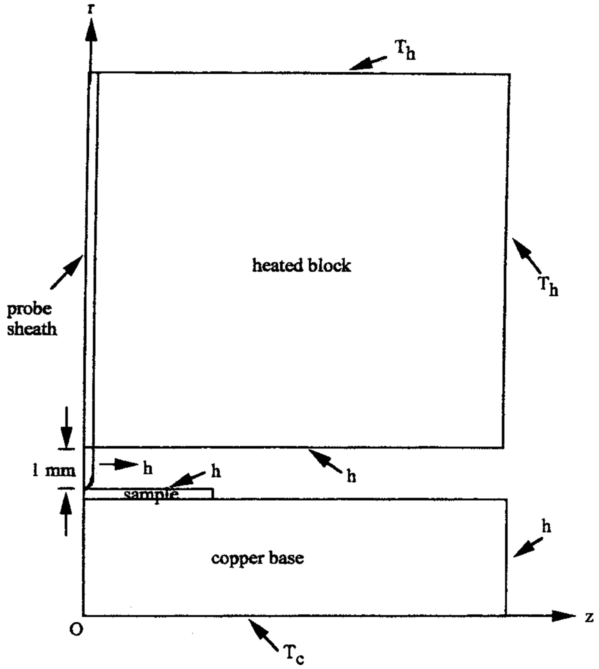

Fig. 5 Computational domain for the modified thermal comparator

---

[2] Professor P. K. Kuo carried out the measurements (with uncertainty of ±12 percent) at the Wayne State University.

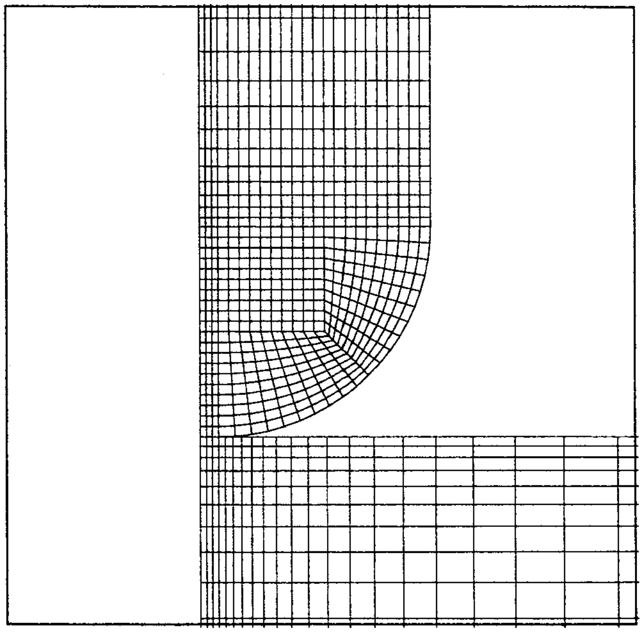

Fig. 6 Grid structure at the probe/sample interface

results are shown in Fig. 6. An iterative procedure was used to solve the system of discretized equations. The convergence criteria used is given by the formula

$$\eta=\frac{T_{i,j}^{n}-T_{i,j}^{n-1}}{T_{i,j}^{n}}. \tag{5}$$

Converged solutions were assumed when $\eta<10^{-8}$ for all mesh points. In our computations, the thermal conductivity of the samples ranged from 10 W/m.K for stainless steel AISI 304 to 1290 W/m.K for diamond. The heated block and probe material was stainless steel (AISI 410), with a thermal conductivity of 25 W/m.K. The ambient temperature was set to 25°C, and the heat transfer coefficient was considered to be 10 W/m^{2}K (for both the active cooling case and the case with no cooling). The convective heat losses from the sample occur mainly from the upper surface, which is not actively cooled. The heat transfer coefficient value was calculated from correlations for Nusselt number for convective flows ([13]). The copper base thermal conductivity was taken as 400 W/m.K for the calculations. The simulations were done using contact radii of 25.4 μm and 10 μm, respectively.

Results and Discussion

We first present the results obtained from the numerical simulations and demonstrate how the simulations provided design guidelines. Then the experimental results obtained from the modified thermal comparator are presented.

Figure 7 shows the numerically generated calibration curves with and without active cooling of the base plate. The vertical axis shows the temperature difference between the probe temperature along the top boundary (T_h in Fig. 5) and the temperature at the probe tip/sample interface. This temperature difference is, in fact, measured as the thermal comparator output. Simulations were carried out with samples of different conductivities. When the base temperature (at the bottom) is held at 25°C (same as the ambient temperature, i.e., no active cooling), the simulations show that the comparator output levels off for high conductivity samples. This situation is markedly improved when active cooling is provided at the base (10°C). Thus, in the modified comparator, we have introduced active cooling at the bottom of the base plate (see Fig. 4). From the numerical calculations, we also observed that the convection heat transfer from the probe and the sample surface is negligible, compared to the conduction heat transfer at the probe/sample and sample/base regions.

Figures 8(a) and 8(b) show computed temperature contours near the probe tip/sample interface for stainless steel and diamond samples, respectively. While the computations were done on a much larger domain (see Fig. 5), only the region near the probe tip/sample contact area is shown in Figs. 8(a) and 8(b). The overall dimensions and boundary conditions were identical for the two cases. The contact radius, *a*, was 25.4 μm. It is seen for the stainless steel sample case, that the axial temperature gradient is weak along the probe and the temperature gradients in the sample

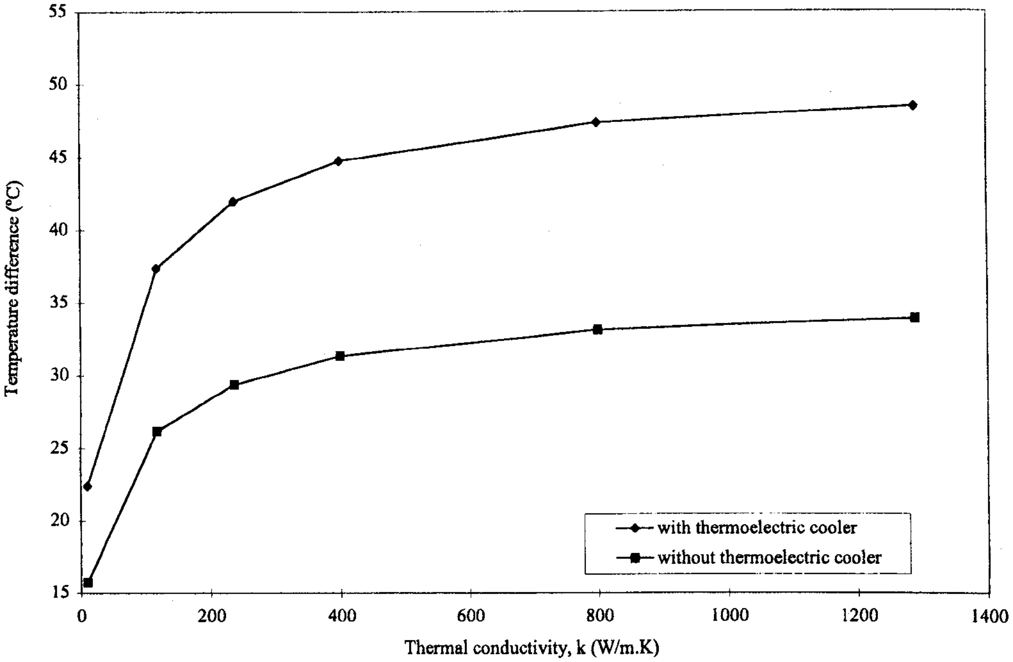

Fig. 7 Numerically generated calibration curves with and without active cooling of the base plate

are large. On the other hand, for the diamond sample case, most of the temperature drop occurs within the probe and the sample (in spite of active cooling) is nearly isothermal. Without active cooling, the diamond sample would be ''thermally saturated'' and this would result in anomalous comparator readings.

Next the effect of the contact area (and hence the loading on the probe) on the comparator output was investigated numerically. Numerically generated calibration curves for two contact radii (0.01 mm and 0.0254 mm) are shown in Fig. 9. The base temperature (bottom) was maintained at 10°C. Both calibration curves show similar trends. However, closer inspection reveals that the sensitivity of the comparator for higher thermal conductivity samples increases as the contact area decreases. A smaller contact area also requires a smaller load (which ensures that the deformations at the sample, if any, will be elastic). Figure 10 shows the variation of contact radius as a function of load as given by Eq. (3). It is seen that for the same load, different values of the contact radius are obtained for different sample materials (within elastic limits). Since Eq. (3) is only valid for elastic deformations, the predictions are limited to small loads for the softer sample materials (viz., aluminum, silver, zinc, and copper). For a given load, aluminum produces the largest contact area with the stainless steel probe and the diamond samples produces the smallest. It is clear from this figure that, to maintain a constant area of contact for all samples, the load must be carefully varied as different samples are studied. The effect of load will affect the thermal comparator output, as the heat flow from the probe to the sample is proportional to the contact area.

For the present measurements, relatively small loads were applied at the probe tip to minimize the effects of any plastic deformation. The probe radius as given by Omega Inc., is 127 μm (R_1). Table 1 lists the loads required, as given by Eq. (3), for various materials to achieve a constant contact radius of 7 μm for the probe tip. The softest material used in the present study is aluminum. It has yield strength Y of 170 MPa (Goodfellow Corporation, Berwyn, PA.). As shown in Table 1, for a contact radius 7 μm, the load F applied by the probe on the aluminum sample is 21 gms. Therefore, the mean pressure applied on aluminum is 1.36 GPa. Since the hardness of the standard samples used in the

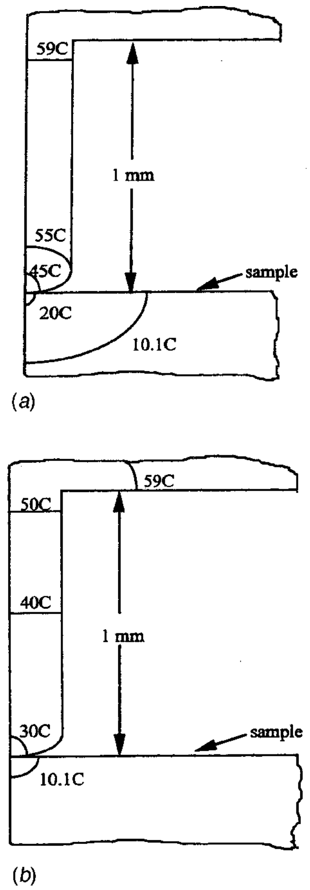

Fig. 8 Computed temperature fields in the probe/sample assembly

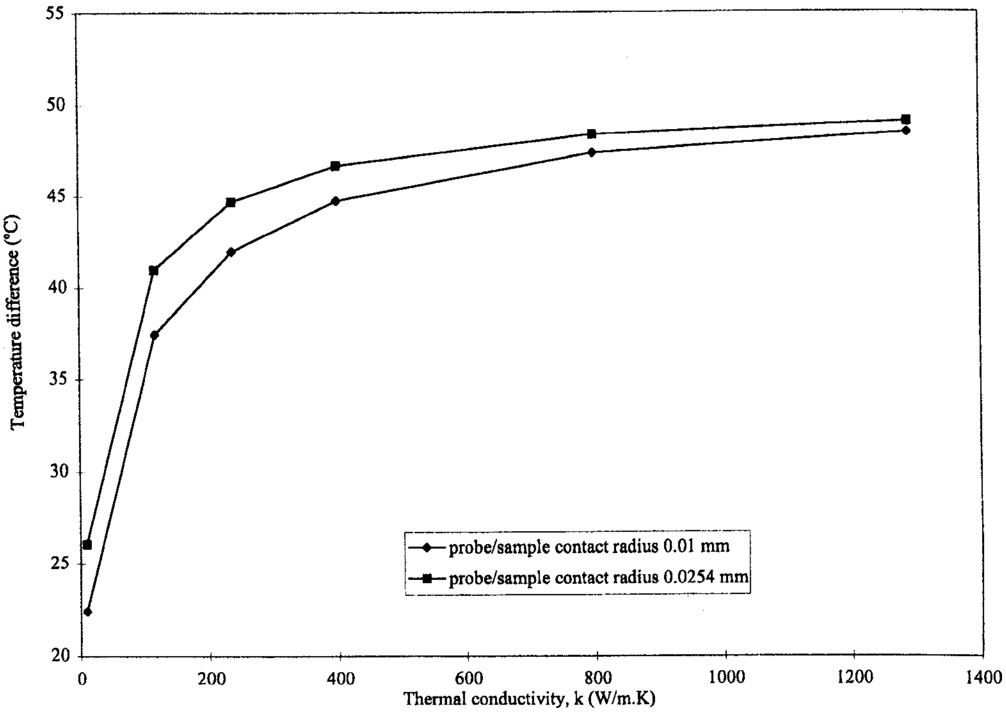

Fig. 9 Numerical calibration curve generated at two contact radii: 25.4 and 10 μm

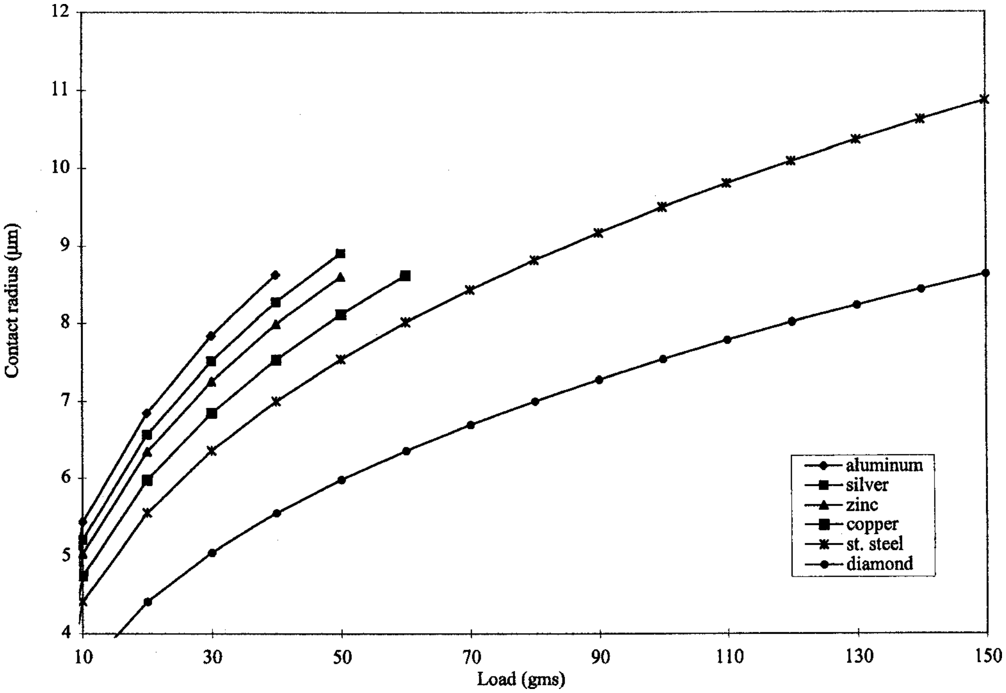

Fig. 10 Computed contact radius variation as a function of load (within elastic limit)

Table 1 Loads calculated to produce a probe/sample contact radius of 7 μm

Material	Load at Contact Radius 7 μm	Thermal Conductivity (W/m.K)
Stainless steel	40	10
Zinc	27	117
Aluminum	21	237
Copper	33	400

study (except diamond) are about 2–3 GPa, the deformations encountered can be assumed to be elastic. The same reasoning allows us to conclude that a design contact radius of 7 μm will ensure elastic deformation for all probe/sample contacts considered.

Measurements were also carried out to investigate the effect of load (within elastic limits) on thermal comparator output for selected samples. Measurements (thermal comparator outputs) were first obtained for the design loads (as given in Table 1). Then

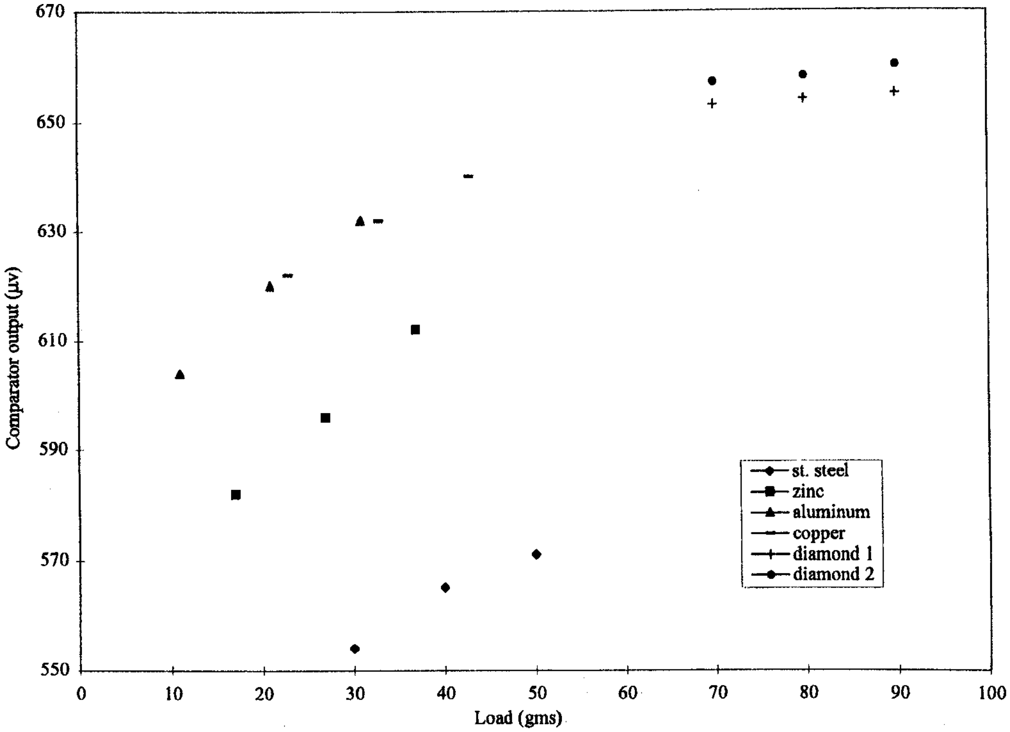

Fig. 11 Measured probe output as a function of applied load for different samples

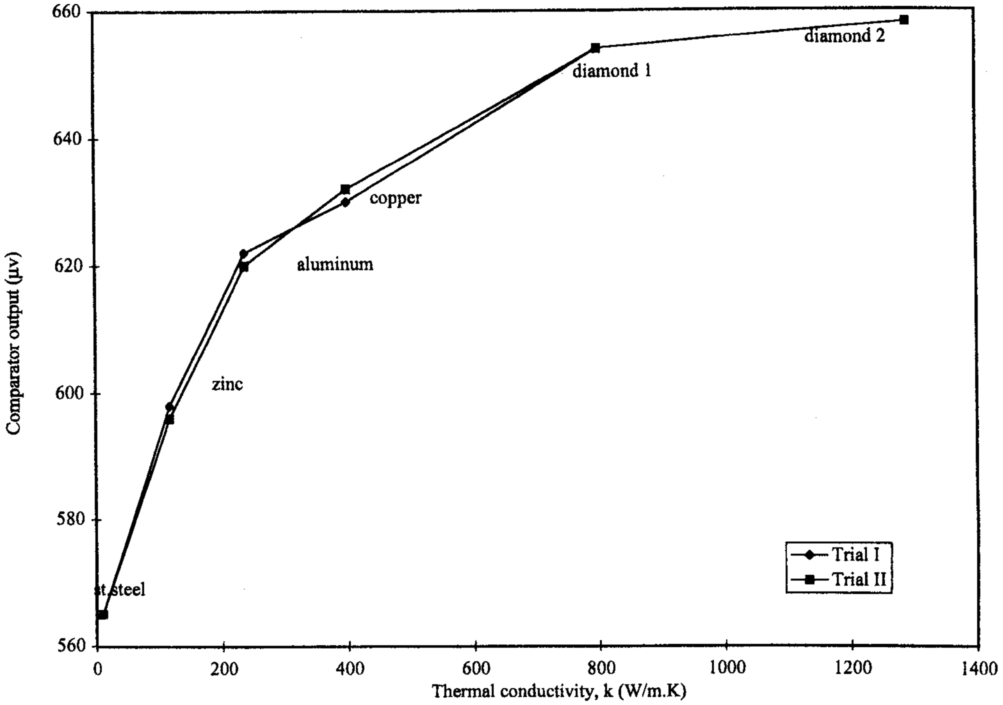

Fig. 12 Experimental calibration curve for the measurement of high thermal conductivity films

measurements were obtained for each sample by varying the design loads (±30 percent). The results are shown in Fig. 11. For these measurements, the bottom of the copper base plate (see Fig. 3) was maintained at 12.8°C. The room temperature was 21°C and the relative humidity was 35 percent. It is observed that the readings for softer materials such as aluminum and zinc showed greater variation with increase in load compared to the harder materials. Hence, if the same load is applied between the probe and samples with different mechanical properties (i.e., hardness), the thermal comparator output will no longer depend solely on the thermal conductivity of the sample. This also confirms the fact that the probe/sample contact area must be maintained approximately the same for all the samples. Our numerical simulations had earlier indicated that a smaller contact radius provides greater sensitivity to the measurements (greater relative change in thermal comparator output for change in thermal conductivities of the samples). The resolution of the balance used is 1 gm and the minimum load that is applied on the sample is 21 gms. The uncertainty in the measurement of the load is thus approximately ±4.0 percent.

Figure 12 shows a typical calibration curve obtained by our modified thermal comparator that includes high conductivity free-standing diamond samples. The measurements obtained on two different days are shown in the figure and the variation is negligible. The measurements were done with the copper base plate with its lower surface maintained at 12.8°C. Two diamond film samples (800 and 1290 W/m.K) produced thermal comparator outputs that are higher than the other samples. The resolution of the multimeter used in our experiment is 1 microvolt. From Fig. 12, the minimum comparator output is approximately 565 microvolts. The error in the comparator output would therefore be ±0.2 percent. This is not to imply that the thermal conductivity uncertainty $\Delta k/k$ is also ±0.2 percent as Fig. 12 is only a calibration curve and measurements of no samples (with unknown thermal conductivity) is reported in the figure.

Our earlier efforts to obtain the above calibration with a classical thermal comparator were unsuccessful. In fact, the thermal comparator outputs (for the classical design) for the diamond samples were even lower than those given by the aluminum samples. Presently we are making efforts in further increasing the sensitivity of the comparator reading for materials with very high thermal conductivities.

Conclusions

The classical thermal comparator method has long been used successfully for the measurement of thermal conductivity of bulk materials with high values of thermal resistance. We have significantly modified and extended these techniques for the measurement of materials with low thermal resistance, i.e., materials with high thermal conductivity. In our modified system, a thermoelectric cooling element is used to lower the base temperature and increase measurement sensitivity. This is of particular significance for the measurement of very high conductivity samples. The effect of load on contact area has been studied analytically and a load sensitivity analysis for different samples has been conducted experimentally. A comprehensive numerical model has also been developed to simulate the heat transfer process from the probe tip assembly. The model has been used to develop a ''numerical'' calibration curve that agrees well with the calibration curve obtained from our measurements. The modified method has been found to successfully generate calibration curves using high thermal conductivity diamond films. Current efforts are underway to increase the sensitivity of the device even further for high conductivity samples.

Acknowledgments

K.C. and B.F. gratefully acknowledge support from Diaomonex Inc. The authors also acknowledge the efforts of Mr. Claudio Mesyngier during the early design of the apparatus.

Nomenclature

a = contact radius (μm)
C = specific heat (kJ/kg.K)
E = modulus of elasticity (Pa)
E' = effective Young's modulus (Pa)
F = load applied (gms)
h = heat transfer coefficient (W/m^2.K)
H = hardness (GPa)
k = thermal conductivity (W/m.K)
p_m = mean pressure (GPa)
q = heat flux (W/m^2)

R_l = radius of the sample material
T = temperature (°C)
Y = material yield stress (Pa)

Greek Symbols

α = thermal diffusivity
ν = Poisson's ratio
η = convergence criterion
ρ = material density (kg/m^3)

Subscripts

i,j = location in the computational domain
1 = 1,2 materials in contact
c = cold side
h = hot side

Superscripts

n = number of iterations

References

[1] Graebner, J. E., Reiss, M. E., and Seibles, L., 1994, ''Phonon Scattering in Chemical-Vapor Deposited Diamond,'' Phys. Rev. B, **50**, pp. 3702–3713.
[2] Holman, J. P., 1984, *Experimental Methods for Engineers*, 4th Ed., McGraw-Hill, New York.
[3] Sanders, D. J., and Forsyth, R. C., 1983, ''Measurement of Thermal Conductivity and Contact Resistance of Paper and Thin-Film Materials,'' Rev. Sci. Instrum., **54**, pp. 238–244.
[4] Powell, R. W., 1969, ''Measurement Conductivity Determinations by the Thermal Comparator Methods,'' R. P. Tye, Ed., *Thermal Conductivity*, Vol. 2, Academic Press, San Diego, pp. 275–338.
[5] Lambropoulos, J. C., Jolly, M. R., Amsden, C. A., Gilman, S. E., Sinicropi, M. J., Diakomihalis, D., and Jacobs, S. D., 1989, ''Thermal Conductivity of Dielectric Thin Films,'' J. Appl. Phys., **66**, No. 9, pp. 4230–4242.
[6] Mesyngier, C., Farouk, B., Lee, Y. H., Yi, G. W., and Brown, D. W., 1998, ''Thermal Conductivity of DLC (Diamond-like Carbon) Thin Films and its Relation to Mechanical and Chemical Properties,'' *Proceedings of Thermal Conductivity 24*, Technomic, Lancaster, PA, pp. 538–548.
[7] Kittel, C., 1996, *Introduction to Solid-State Physics*, 7th Ed., John Wiley and Sons, New York.
[8] Graebner, J. E, 1996, ''Measurements of Specific Heat and Mass Density in CVD Diamond,'' Diamond and Related Materials, **5**, pp. 1366–1370.
[9] Anthony, T. R., Banholzer, W. F., Fleischer, J. F., Wei, L., Kuo, P. K., Thomas, R. L., and Pryor, R. W., 1990, ''Thermal Diffusivity of Isotropically Enriched ^{12}C Diamond,'' Phys. Rev. B, **42**, pp. 1104–1111.
[10] Graebner, J. E., Jin, S., Kammlott, G. W., Herb, J. A., and Gardinier, C. F., 1992, ''Large Anisotropic Thermal Conductivity in Synthetic Diamond Films,'' Nature (London), **359**, pp. 401–403.
[11] Feldman, A., Frederiske, P. R., and Ying, X. T., 1989, ''Thermal Wave Measurements of the Thermal Properties of CVD Diamond,'' *Diamond Optics II*, SPIE, Vol. 1146, pp. 78–84.
[12] Timoshenko, S. P., and Goodier, J. N., 1951, *Theory of Elasticity*, 2nd Ed., McGraw-Hill, New York.
[13] Incropera, P. F., and DeWitt, P. D., 1996, *Fundamentals of Heat and Mass Transfer*, 4th Ed., John Wiley and Sons, New York.

Journal of Heat Transfer

Technical Notes

This section contains shorter technical papers. These shorter papers will be subjected to the same review process as that for full papers.

Thermal Conduction and Viscous Heating in Microscale Couette Flows

Y. Sungtaek Ju
Assoc. Mem. ASME, IBM Research,
Austin, TX 78758
e-mail: just@stanfordalumni.org

The direct simulation Monte Carlo (DSMC) method is used to investigate heat conduction and viscous heating in microscale Couette flows. When augmented by the slip boundary conditions, the continuum equations are found to predict thermal conductance accurately even in the transition and ballistic flow regime for Couette flows. The viscous heat generation rate, in contrast, is significantly underpredicted by the slip flow theory. We propose an alternative approach based on kinetic theory and present a compact analytic expression for the viscous dissipation rate. [S0022-1481(00)00104-3]

Keywords: Conduction, Cooling, Heat Transfer, Microscale, Monte Carlo, Nanoscale

Microscale Couette flows occur when two parallel surfaces in relative motion are brought in close proximity to each other. One example is the air bearing of data storage devices, which enables precise control of distance between a magnetic or optical transducer and a storage media. Heat transfer across the air bearing plays an important role in the cooling of these transducers because the media serves as a primary heat sink ([1]).

Continuum description of heat generation and transfer is not valid when the mean free path of fluid molecules λ is comparable to or greater than the spacing between the two surfaces *d*. The mean free path of air molecules under the ambient condition is approximately 65 nm, which greatly exceeds the air bearing thickness in state-of-the-art magnetic disk drives. Zhang and Bogy [2] augmented the continuum governing equations with the slip boundary conditions to model heat transfer across the air bearing.

The present study employs the direct simulation Monte Carlo (DSMC) method to investigate heat transfer and viscous heating in microscale Couette flows. The DSMC method is a technique for the computer simulation of a real gas at the molecular level ([3,4]). Previous studies ([5]) applied the method to investigate fluid mechanics aspects of air bearing flows.

We consider air flows induced by the relative motion of two infinite parallel plates. The top plate is stationary while the bottom plate is moving tangentially at a constant speed. The plates are maintained at uniform temperatures.

The present DSMC computations use the following computational parameters. The cell size is either *d*/5 or λ/3, whichever is smaller. Each cell contains on average 50 simulation molecules. The size of the time step is set to be $s/3v$, where *s* is the cell size and v is the average speed of air molecules (470 m s^{-1} at 300 K). Physical quantities are averaged over 20,000 time steps. The soft sphere model ([3]) is used to compute collision rates between air molecules. The accommodation coefficients are assumed to be unity throughout the present manuscript.

Figure 1 shows the thermal conductance *h* normalized with re-

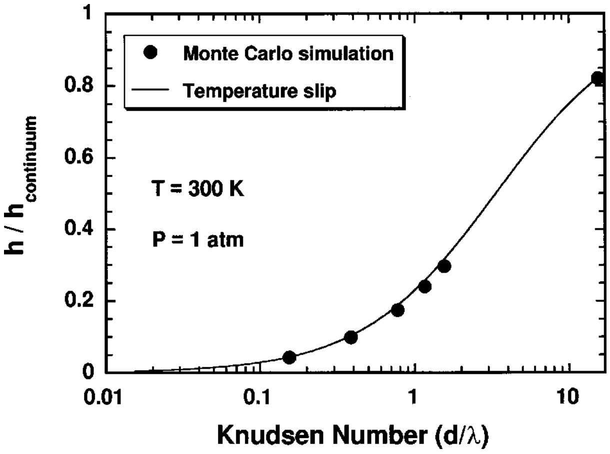

Fig. 1 Thermal conductance associated with Couette flows as a function of the Knudsen number. The conductance is normalized by the continuum value *k/d*.

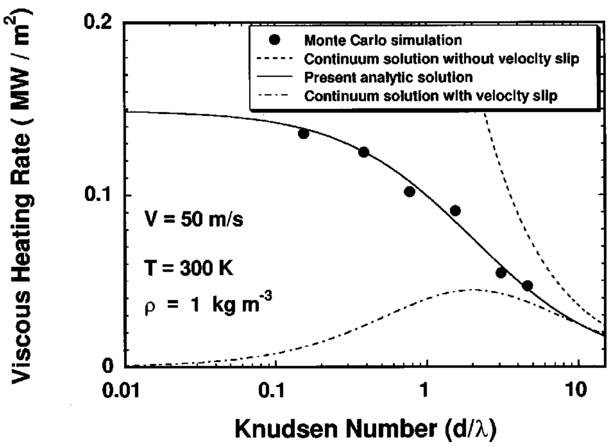

Fig. 2 Comparison between the viscous heating rates obtained from the direct simulation Monte Carlo simulation and from the analytic solutions. The continuum solutions incorporating the slip boundary conditions give $q''_{\mathrm{visc}}/2=\mu V^2 d/2(d+2\lambda)^2$, where μ is the viscosity of air.

Contributed by the Heat Transfer Division for publication in the JOURNAL OF HEAT TRANSFER. Manuscript received by the Heat Transfer Division, Feb. 18, 2000; revision received, May 17, 2000. Associate Technical Editor: H. H. Bau.

spect to the continuum value k/d. The thermal conductance is defined as $q''/\Delta T$, where q'' is the heat flux and ΔT is the temperature difference between the two plates. The thermal conductivity of air is denoted by k. The DSMC simulation results are in good agreement with the prediction obtained by solving the heat diffusion equation with the temperature slip boundary condition ([6]):

$$h=\frac{k}{d+\dfrac{4\gamma}{\gamma+1}\dfrac{1}{\mathrm{Pr}}\lambda}. \tag{1}$$

Here γ is the specific heat ratio, and Pr is the Prandtl number. The agreement indicates that the thermal conductance derived in rarefied gas dynamics can be applied for describing heat conduction in micro-lengthscale Couette flows.

Figure 2 plots the rate at which ''viscous heating'' takes place in the Couette flow. In the ballistic flow regime the DSMC simulation results deviate significantly from the prediction of the continuum equations. The discrepancy originates from the fact that intermolecular collisions occur less frequently than collisions between fluid molecules and the plates. In this regime, viscous heating is largely a manifestation of energy exchange between the plates and gas molecules in random motion. The slip flow theory ([6]) implicitly assumes that collisions between molecules with different mean velocities remain the dominant mechanism of viscous dissipation as in the continuum limit. The conventional continuum solution neglects the velocity slip and grossly overestimates the heat generation rate.

We propose an alternative approach based on an approximate solution to the Boltzmann transport equation ([7]). The rate at which gas molecules extract energy from the moving plate is equal to the number flux of molecules incident on the plate times the difference in the mean energies of incident and reflected molecules. The molecular flux is proportional to the fluid mass density ρ and the mean molecular speed c: $c\rho/4m$. The difference in the mean kinetic energy is simply equal to $mV^2/2$ in the ballistic flow regime. Here m is the mass of fluid molecules, and V is the speed of the moving plate. A more general expression can be obtained by taking appropriate moments of the two-stream Maxwellian distribution function of Lees ([7,8]) and forming the product of the wall shear stress and the plate speed. After some algebra we can write the viscous heating rate as

$$q''_{\mathrm{visc}}/2=\frac{1}{8}\rho V^2\left(\frac{8RT}{\pi}\right)^{1/2}\frac{1}{d/2\lambda+1}, \tag{2}$$

where T is the gas temperature and R is the specific gas constant. In deriving Eq. (2) it is assumed that the two plates and the air are at the same temperature. Figure 2 includes the prediction of Eq. (2), which reproduces the DSMC simulation results very well. Note that in the limit as the plate spacing goes to zero, the viscous heating rate approaches a constant value that is proportional to ρ. This dependence on the density, or equivalently on the pressure under isothermal conditions, is in stark contrast to the conventional continuum theory prediction that q''_{visc} does not vary substantially with the absolute pressure.

The net heat transfer rate between the two bounding surfaces of Couette flows can be computed by subtracting the viscous heating term from the heat conduction term:

$$q''_{\mathrm{net}}=h\Delta T-q''_{\mathrm{visc}}/2. \tag{3}$$

In applying the present results to air bearing flows, the reader is alerted to the fact that contributions from a pressure-driven flow part are not included in Eq. (2). The continuum as well as slip flow theory predicts that these contributions are small. Further study is needed for microscale flows with finite pressure gradients.

Acknowledgments

The author would like to express gratitude to Dr. Boyd and Balakrishnan at Cornell University, and to Drs. Hash and Kim at NASA Ames Research Center for their help in conducting DSMC computations.

References

[1] Tian, H., Cheung, C.-Y., and Wang, P.-K., 1997, ''Non-Contact Induced Thermal Disturbance of MR Head Signals,'' IEEE Trans. Magn., **33**, pp. 3130–3132.
[2] Zhang, S., and Bogy, D. B., 1999, ''A Heat Transfer Model for Thermal Fluctuations in a Thin Slider/Disk Air Bearing,'' Int. J. Heat Mass Transf., **42**, pp. 1791–1800.
[3] Bird, G. A., 1994, *Molecular Gas Dynamics and the Direct Simulation of Gas Flows*, Oxford University Press, Oxford.
[4] Dietrich, S., and Boyd, I. D., 1996, ''Scalar and Parallel Optimized Implementation of the Direct Simulation Monte Carlo Method,'' J. Comput. Phys., **126**, pp. 328–342.
[5] Alexander, F. J., Garcia, A. L., and Alder, B. J., 1994, ''Direct Simulation Monte Carlo for Thin-Film Bearings,'' Phys. Fluids, **6**, pp. 3854–3860.
[6] Schaaf, S. A., and Chambré, P. L., 1961, *Flow of Rarefied Gases*, Princeton University Press, Princeton, NJ.
[7] Lees, L., 1959, ''A Kinetic Theory Description of Rarefied Gas Flows,'' GALCIT Hypersonic Research Project, Memo No. 51.
[8] Vincenti, W. G., and Kruger, C. H., 1965, *Introduction to Physical Gas Dynamics*, Krieger, Melbourne, FL.

Integral Equation Solutions for Transient Radiative Transfer in Nonhomogeneous Anisotropically Scattering Media

S.-H. Wu
Graduate Student

C.-Y. Wu
Professor, Mem. ASME

Department of Mechanical Engineering, National Cheng Kung University, Tainan, Taiwan 701, R.O.C.

The integral equation formulation for transient radiative transfer in two-dimensional cylindrical nonhomogeneous absorbing and linearly anisotropically scattering media with collimated pulse irradiation is presented. The integral equations are solved by the quadrature method. The results by the present method agree quite well with those obtained by the Monte Carlo method. The effects of spatially variable properties on transient radiative transfer are investigated for various optical sizes and extinction coefficient distributions. The blocking effect on transient two-dimensional radiative transfer in nonhomogeneous media is different from that on steady-state radiative transfer. [S0022-1481(00)00204-8]

Keywords: Heat Transfer, Laser, Radiation, Scattering, Transient

Introduction

Recently transient radiative transfer in a participating medium exposed to a laser pulse has been receiving great interest due to a variety of applications, such as atmosphere remote sensing ([1]),

---

Contributed by the Heat Transfer Division for publication in the JOURNAL OF HEAT TRANSFER. Manuscript received by the Heat Transfer Division, Sept. 23, 1999; revision received, June 27, 2000. Associate Technical Editor: M. P. Menguc.

oceanographic lidar ([2,3]), optical tomography in medical imaging ([4,5]), photodynamic therapy ([6]), and estimating radiative properties of participating media ([7]). Deterministic approximations and/or the Monte Carlo method are adopted in most of the analyses on transient radiative transfer.

Transient radiative transfer in layered or nonhomogeneous media attracts increasing attention very recently. For example, most biological tissues concerned in light-based therapy or diagnosis are layers with different optical properties ([8]), and a tumor and its surrounding normal tissue, often considered in optical tomography, consist of a nonhomogeneous medium ([4]). Because of the complexity resulting from the spatially variable properties, the Monte Carlo method resorts to approximate examination ([9]). However, results obtained by the Monte Carlo method always have unavoidable random (or statistical) errors and much CPU time is usually required. Thus, in this work we aim at obtaining highly accurate solutions based on exact integral formulation to investigate deeply the influence of spatially variable properties on transient radiative transfer, and the accurate solutions can be used to further assess the accuracy of approximate methods.

The integral equation for transient radiative transfer in an isotropically scattering medium was developed by Pomraning [10]. By introducing Hunt's moments of intensity ([11]), Wu and Wu [12] have shown that the exact integral equations for transient radiative transfer in anisotropically scattering media can also be derived. Comparisons given in ([12]) indicate that the solutions of the integral formulation by a quadrature method (QM) are accurate. The QM approach is adopted here to solve transient radiative transfer in two-dimensional cylindrical, absorbing, linearly anisotropically scattering, and nonhomogeneous media with collimated pulse irradiation. To validate the integral equation solutions, the results obtained by the QM are compared with the results obtained by the reverse (or backward) Monte Carlo method (RMCM) ([13]). The RMCM provides better results at a specified point than the conventional Monte Carlo method does.

Formulation and Numerical Methods

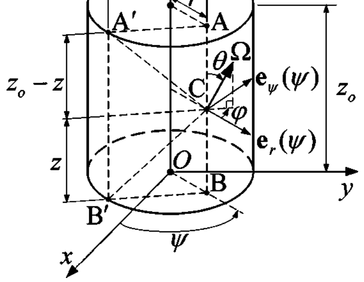

Fig. 1 The geometry and the coordinate systems (ψ is the spatial azimuthal angle, k, $\mathbf{e}_r(\psi)$ and $\mathbf{e}_\psi(\psi)$ are the unit vectors in the z, r and ψ-directions, respectively)

Transient radiative transfer under consideration happens in an absorbing, linearly anisotropically scattering, two-dimensional axisymmetric finite cylindrical medium (radius r_o and height z_o). The medium is assumed to be cold; that is, the emission of the medium is negligibly small as compared with the irradiation at the medium boundary. The radiative properties of the medium are considered to be spatially variable and time-independent, while the speed of light c keeps constant in the medium. The spatial and the directional coordinate systems are shown in Fig. 1. Both r_o and z_o are assumed to be much larger than wavelength. Then, the radiative intensity I at a position denoted by r and z along a direction Ω of the polar angle θ and the azimuthal angle φ at time t can be described by the equation of transient radiative transfer

$$\frac{1}{c}\frac{\partial I(r,z,\mu,\varphi,t)}{\partial t}+(1-\mu^2)^{1/2}\cos\varphi\,\frac{\partial I(r,z,\mu,\varphi,t)}{\partial r}-\frac{(1-\mu^2)^{1/2}\sin\varphi}{r}\frac{\partial I(r,z,\mu,\varphi,t)}{\partial\varphi}+\mu\frac{\partial I(r,z,\mu,\varphi,t)}{\partial z}+\beta(r,z)I(r,z,\mu,\varphi,t)=\beta(r,z)S(r,z,\mu,\varphi,t), \tag{1}$$

where $\mu=\cos\theta$, β is the extinction coefficient, and S is the source function expressed as

$$S(r,z,\mu,\varphi,t)=\frac{1}{4\pi}\omega(r,z)\{M_{00}(r,z,t)+a_1(r,z)[M_{10}(r,z,t)\mu+M_{11}(r,z,t)(1-\mu^2)^{1/2}\cos\varphi]\}. \tag{2}$$

Here, ω and a_1 $(-1\leqslant a_1\leqslant 1)$ denote the scattering albedo and the coefficient of the linearly anisotropically scattering phase function, respectively, and the moments of intensity are defined as

$$\begin{Bmatrix} M_{00}(r,z,t)\\ M_{10}(r,z,t)\\ M_{11}(r,z,t)\end{Bmatrix}=\int_0^{2\pi}\int_{-1}^{1} I(r,z,\mu,\varphi,t)\times\begin{Bmatrix}1\\ \mu\\ (1-\mu^2)^{1/2}\cos\varphi\end{Bmatrix}d\mu d\varphi. \tag{3}$$

Physically, M_{00} is the incident radiation, while M_{10} and M_{11} are the z and r-components of radiative flux, respectively. The ψ-component of radiative flux is zero everywhere because of the axisymmetry of the irradiation, the spatial distributions of the radiative properties, and the geometry.

The medium is exposed to a spatially uniform collimated time-dependent irradiation normal to the circular bottom surface at $z=0$, the top and lateral surfaces are free from irradiation, and the boundaries of the medium are nonparticipating. The temporal shape of the irradiation is considered to be a pulse described by a truncated Gaussian distribution. Then, the boundary conditions for Eq. (1) can be expressed as

$$I(r,0,\mu,\varphi,t)=I_oF(t)\,\delta(\mu-1)\,\delta(\varphi),\quad \text{for}\ \ 0\leqslant r\leqslant r_o,\quad \mu>0,\quad 0\leqslant\varphi<2\pi,\quad t\geqslant 0 \tag{4a}$$

$$I(r,z_o,\mu,\varphi,t)=0,\quad \text{for}\quad 0\leqslant r\leqslant r_o,\quad \mu<0,\quad 0\leqslant\varphi<2\pi,\quad t\geqslant 0 \tag{4b}$$

$$I(r_o,z,\mu,\varphi,t)=0,\quad \text{for}\quad 0\leqslant z\leqslant z_o,\quad -1\leqslant\mu\leqslant 1,\quad \pi/2<\varphi<3\pi/2,\quad t\geqslant 0 \tag{4c}$$

where δ is the delta function, and the function F is defined as

$$F(t)=\exp\left[-4(\ln 2)\left(\frac{t-t_c}{t_p}\right)^2\right], \tag{5}$$

with t_c denoting the time when the pulse reaches its maximum and t_p denoting the full width at half maximum for F. By changing the expression of F, the following integral formulation can be readily applied to the problems with other temporal shaped irradiation. We assume that there is no radiation energy within the medium initially. Thus, the initial condition is

$$I(r,z,\mu,\varphi,0)=0,\quad \text{for}\quad 0\leqslant r\leqslant r_o,\quad 0\leqslant z\leqslant z_o,\quad -1\leqslant\mu\leqslant 1,\quad 0\leqslant\varphi<2\pi. \tag{6}$$

The notation denoting the spectral dependence of the radiative properties has been omitted to simplify the mathematical formulation; the present equations are valid for monochromatic or gray radiative transfer.

Substituting the formal solution of intensity obtained from the integration of Eq. (1) into Eq. (3), we can obtain the integral equations of the moments of intensity ([14])

$$\begin{Bmatrix} M_{00}(r,z,t) \\ M_{10}(r,z,t) \\ M_{11}(r,z,t) \end{Bmatrix} = I_o F(t-z/c)\exp[-\tau(r,z,z,1,0)]\begin{Bmatrix} 1 \\ 1 \\ 0 \end{Bmatrix} H(ct-z) + \frac{1}{4\pi} H(ct-z)\int_0^{2\pi}\int_{-1}^{1}\int_0^{s_u(r,z,\mu,\varphi,t)} \beta[r'(r,s,\mu,\varphi),z'(z,s,\mu)]$$

$$\times\,\omega[r'(r,s,\mu,\varphi),z'(z,s,\mu)]\exp[-\tau(r,z,s,\mu,\varphi)]\begin{Bmatrix} 1 \\ \mu \\ (1-\mu^2)^{1/2}\cos\varphi \end{Bmatrix}\Big\langle M_{00}[r'(r,s,\mu,\varphi),z'(z,s,\mu),t-s/c]$$

$$+a_1\Big\{\mu M_{10}[r'(r,s,\mu,\varphi),z'(z,s,\mu),t-s/c] + \frac{[r(1-\mu^2)^{1/2}\cos\varphi - s(1-\mu^2)]}{r'(r,s,\mu,\varphi)}$$

$$\times M_{11}[r'(r,s,\mu,\varphi),z'(z,s,\mu),t-s/c]\Big\}\Big\rangle ds\,d\mu\,d\varphi, \tag{7}$$

where H is the Heaviside step function; s is the geometric distance from the considered point denoted by r and z to the scattering point at which radiation is scattered to contribute to the moments of intensity at the considered point,

$$\tau(r,z,s,\mu,\varphi) = \int_0^1 \beta\{[r^2 - 2r\xi s(1-\mu^2)^{1/2}\cos\varphi + \xi^2 s^2(1-\mu^2)]^{1/2}, z-\xi s\mu\} s\,d\xi, \tag{8}$$

$$r'(r,s,\mu,\varphi) = [r^2 - 2rs(1-\mu^2)^{1/2}\cos\varphi + s^2(1-\mu^2)]^{1/2}, \tag{9}$$

$$z'(z,s,\mu) = z - s\mu, \tag{10}$$

$$s_u(r,z,\mu,\varphi,t) = \min\{(ct-z)/(1-\mu), s_w(r,z,\mu,\varphi)\}, \tag{11}$$

with $\min\{x,y\}$ denoting the smaller value of x and y, and s_w denoting the distance from the considered point labeled by r and z to the nearest point on the medium boundary seen from the considered point reversely along the direction denoted by θ and φ. It is readily found that

$$s_w(r,z,\mu,\varphi) = \begin{cases} -(z_o - z)/\mu, & \text{if } -1 \leqslant \mu < \mu_1(r,z,\varphi) \\ \zeta(r,\varphi)/(1-\mu^2)^{1/2}, & \text{if } \mu_1(r,z,\varphi) \leqslant \mu \leqslant \mu_2(r,z,\varphi), \\ z/\mu, & \text{if } \mu_2(r,z,\varphi) < \mu \leqslant 1 \end{cases} \tag{12}$$

with

$$\mu_1(r,z,\varphi) = -(z_o - z)/\{(z_o - z)^2 + [\zeta(r,\varphi)]^2\}^{1/2} = -\overline{CA}/\overline{CA'}, \tag{13}$$

$$\mu_2(r,z,\varphi) = z/\{z^2 + [\zeta(r,\varphi)]^2\}^{1/2} = \overline{CB}/\overline{CB'}, \tag{14}$$

$$\zeta(r,\varphi) = r\cos\varphi + (r_o^2 - r^2\sin^2\varphi)^{1/2}. \tag{15}$$

The $\tau(r,z,s,\mu,\varphi)$ defined in Eq. (8) is the optical distance between the considered and the scattering points. As shown in Eq. (7), the s_u given by Eq. (11) represents the length determining the domain of dependence of the moments of intensity at the position (r, z). The radiative transfer at (r, z) depends only on the radiative transfer happens in the domain, because of either the finite propagation time or the finite volume of the medium. The derivation of the s_u expression is similar to that stated by Wu [15], and so it is not duplicated here.

Since the domain of dependence of the moments of intensity may vary with time, Eq. (7) is a set of integral equations of Volterra type ([14]). This feature is very different from the integral equations of time-independent radiative transfer, which are of the Fredholm type.

The method adopted to solve the integral equations of the moments of intensity is the QM. This method transforms the integral equation to a system of algebraic equations ([12,15]), and can be adapted to solve nonhomogeneous medium problems. However, it is usually hard to find an analytical expression of the optical distance between two points for an arbitrarily given variable extinction coefficient. Thus, we employ a quadrature rule to approximate the integrals over the variable ξ in Eq. (8). Besides, the trilinear interpolation (which relates the scattering parts of the moments of intensity not at any grid point to those on neighboring grid points) is employed here to simplify the computation codes.

If the medium under consideration has an abrupt change in radiative properties, for example, a layered medium, the angle-distance integrals in Eq. (7) and the integral representing the optical distance in Eq. (8) have to be split into more integrals over some subintervals to keep the integrands in the integrals continuous over each subinterval. Then, approximating each subintegral by a quadrature rule can generate accurate results.

Results and Discussion

Various distributions of the radiative properties of the media considered are given in Table 1. All of the two-dimensional cy-

Table 1 Radiative properties for cases under consideration

	βz_o	ω	a_1
A1	1.0	1.0	0.0
A2	$1.526/[1+9(z/z_o-1/2)^2]$	1.0	0.0
A3	$1.526/[1+2.25(z/z_o)^2]$	1.0	0.0
A4	$1.526/[1+2.25(z/z_o-1)^2]$	1.0	0.0
B1	5.0	1.0	0.0
B2	$7.631/[1+9(z/z_o-1/2)^2]$	1.0	0.0
B3	$7.631/[1+2.25(z/z_o)^2]$	1.0	0.0
B4	$7.631/[1+2.25(z/z_o-1)^2]$	1.0	0.0
C1	$0.5+1.5(1-r^2/r_o^2)^2[1-(2z/z_o-1)^2]^2$	$\{1+3(1-r^2/r_o^2)^2[1-(2z/z_o-1)^2]^2\}^{-1}$	1.0
C2	$0.5+2.0(1-r^2/r_o^2)^2[1-(2z/z_o-1)^2]^2$	$\{1+4(1-r^2/r_o^2)^2[1-(2z/z_o-1)^2]^2\}^{-1}$	1.0

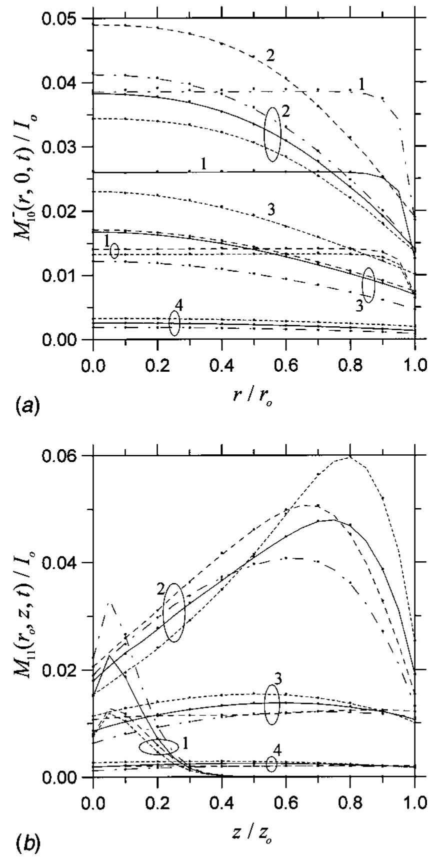

Fig. 2 The results at some instants of interest obtained by the QM and by the RMCM for cases A1–A4; (*a*) the spatial distributions of $M_{10}^{-}(r,0,t)$; (*b*) the spatial distributions of $M_{11}(r_o,z,t)$ (points: RMCM, lines: QM, 1: $ct/z_o=1.0$, 2: $ct/z_o=2.0$, 3: $ct/z_o=3.0$, 4: $ct/z_o=4.0$, ——: A1, — — —: A2, —·—: A3, - - - -: A4)

lindrical media considered are of the aspect ratio $z_o/r_o=1.0$, and are exposed to the pulse of $ct_c/z_o=1.0$ and $ct_p/z_o=0.333$. The β's of cases A1–A4 are selected such that the optical thicknesses in the *z*-direction (or the optical height) are equal to 1.0, whereas the optical thicknesses in the *z*-direction for cases B1–B4 are equal to 5.0. For a typical case with $t_p=40$ ps and $c=2.25\times10^8$ m/s, the geometric height z_o and radius r_o for $ct_p/z_o=0.333$ and $z_o/r_o=1.0$ are equal to 0.027 m. In this work, the 21×21 and the 41×41 uniformly spaced grid points are adopted for the moderate optical size cases (A1–A4, C1, and C2) and the optically thick cases (B1–B4), respectively, and the product Gaussian Legendre quadrature of $N_\varphi=N_\mu=7$ and $N_s=30$ is employed to approximate the angle-distance integrals in Eq. (7). It has been shown that the combinations of the grid sizes and the quadrature points can generate grid and quadrature-independent results ([14]). Besides, in the present computation of the two-dimensional cases with variable properties, the 40-point Gaussian Legendre quadrature is adopted to evaluate the optical distance defined in Eq. (8).

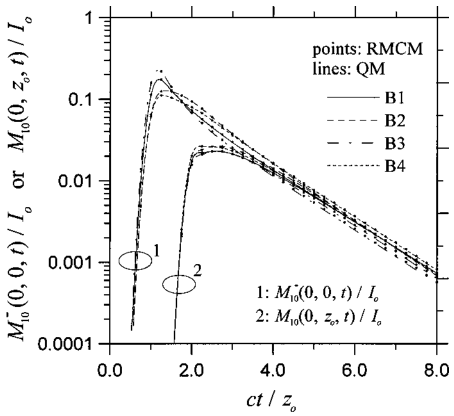

Fig. 4 The results of $M_{10}^{-}(0,0,t)$ and $M_{10}(0,z_o,t)$ obtained by the QM and by the RMCM for cases B1–B4

First, we plot the spatial distributions of $M_{10}^{-}(r,0,t)=I_oF(t)H(t)-M_{10}(r,0,t)$ and $M_{11}(r_o,z,t)$ of cases A1–A4 at the instants $ct/z_o=1.0$, 2.0, 3.0, and 4.0 in Figs. 2(*a*) and 2(*b*), respectively, and plot the temporal distributions of $M_{10}^{-}(0,0,t)=I_oF(t)H(t)-M_{10}(0,0,t)$ and $M_{10}(0,z_o,t)$ in Fig. 3. The non-smooth variations of the $M_{10}^{-}(r,0,t)$ curves near the lateral boundary and those of the $M_{11}(r_o,z,t)$ curves around the peaks, as shown in Figs. 2(*a*) and 2(*b*), are caused by the finite spatial grid points of the QM. They can be readily smoothed by using a finer mesh.

To validate the QM results, both the results obtained by the QM and those by the RMCM are shown in Figs. 2, 4, and 5. A large number of bundles, 5×10^5, are used for each RMCM result to reduce the statistical errors inherent within the RMCM results and to ensure their accuracy. The results by the two methods are in good agreement, and only very small discrepancies are found in the $M_{10}^{-}(r,0,t)$ curves for the early instants in Fig. 2(*a*) and around the peaks of the $M_{11}(r_o,z,t)$ curves in Fig. 2(*b*). The discrepan-

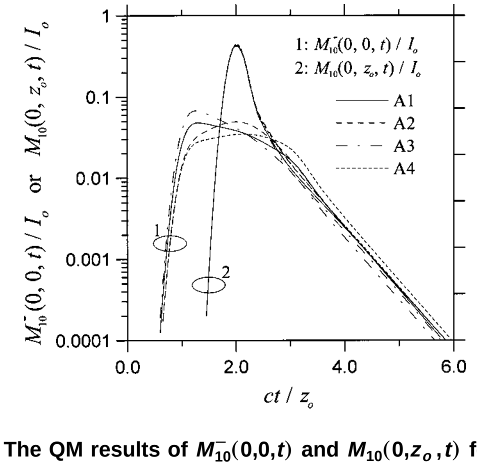

Fig. 3 The QM results of $M_{10}^{-}(0,0,t)$ and $M_{10}(0,z_o,t)$ for cases A1–A4

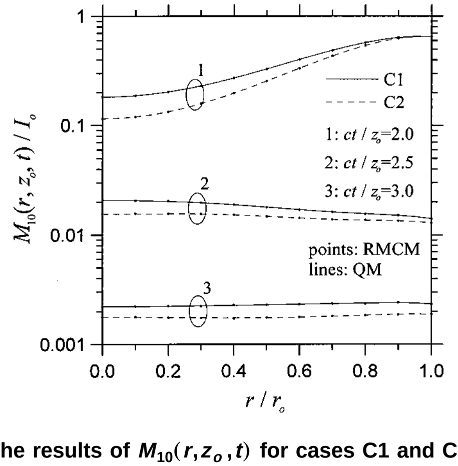

Fig. 5 The results of $M_{10}(r,z_o,t)$ for cases C1 and C2 at various instants of interest

cies are primarily due to the RMCM random errors, and they can be readily reduced by using more bundles in the RMCM computation. The estimator of the standard deviation of a RMCM result can be viewed as an indicator of the magnitude of statistical error. No estimator of the standard deviation of any RMCM result shown in Figs. 2, 4, and 5 is larger than 1.8 percent of the value of its corresponding RMCM result.

Figure 2(*a*) indicates that for cases A1–A4 the nonhomogeneity in β has a strong influence on the $M^{-}_{10}(r,0,t)$. The dependence of the $M_{10}(r,z_o,t)$ of cases A1–A4 on the distribution of β in the *z*-direction at early instants is minimal, and the discrepancy of the $M_{10}(r,z_o,t)$ among various distributions of β becomes comparable with but still smaller than that of $M^{-}_{10}(r,0,t)$ at later instants ([14]). The temporal distributions of the $M^{-}_{10}(0,0,t)$ and the $M_{10}(0,z_o,t)$ shown in Fig. 3 also reveal the same tendency. The $M^{-}_{10}(r,0,t)$ completely results from scattered radiation that strongly depends on the distribution of β, and the distribution of β near the $z=0$ surface always has a much larger influence on the $M^{-}_{10}(r,0,t)$ than that near the $z=z_o$ surface does. On the other hand, the dependence of the $M_{10}(r,z_o,t)$ on the distribution of β becomes obvious when scattered radiation is an important contributor. This always happens after the peak instant of $M_{10}(r,z_o,t)$. At those instants, the dependence of the $M_{10}(0,z_o,t)$ on the distribution of β is still smaller than that of $M^{-}_{10}(0,0,t)$, since the $M_{10}(0,z_o,t)$ depends cumulatively on the β over the entire medium, as shown in Fig. 3.

At the instants after $ct/z_o=2.5$, the $M_{10}(0,z_o,t)$ as well as the $M^{-}_{10}(0,0,t)$ of case A3 with a decreasing distribution of β has the smallest value among the A1–A4 cases. In addition to the distribution of β and the instant of the irradiation peak, the radiation loss from the lateral surface $r=r_o$ is another important factor determining the two-dimensional transient radiative transfer. The larger β near the $z=0$ surface is, the more collimated irradiation is scattered away from its incident direction and leaves the lateral surface at early time, as shown by the results of $M_{11}(r_o,z,t)$ at $ct/z_o=1.0$ in Fig. 2(*b*). Thus, the decreasing distribution of β makes less radiation energy remaining within the medium at later time than the increasing distribution of β does. This explains the results that case A3 has the smallest $M_{10}(0,z_o,t)$ and the smallest $M^{-}_{10}(0,0,t)$ among cases A1–A4 after the irradiation passes through the medium, as shown in Fig. 3.

The trends of the temporal distributions of the $M^{-}_{10}(0,0,t)$ and the $M_{10}(0,z_o,t)$ for cases B1–B4 with larger β's are similar to those for cases A1–A4 with smaller β's, as shown in Fig. 4. As shown in Fig. 4, the variable β's again have larger influence on the $M^{-}_{10}(0,0,t)$ than that on the $M_{10}(0,z_o,t)$ for the optically thick cases. Such a dependence seems to suggest that the estimation of the nonhomogeneous radiative properties from measuring M^{-}_{10} at $z=0$ is more promising than that from measuring M_{10} at $z=z_o$.

In cases C1 and C2, a particular phenomenon, the blocking effect, of multidimensional radiative transfer within nonhomogeneous media is investigated. The spatial distributions of $M_{10}(r,z_o,t)$ of cases C1 and C2 at various instants of interest are plotted in Fig. 5. Both cases have an identical constant scattering coefficient, and the β around the core for cases C1 and C2 is larger than that near the medium boundaries because of their highly absorbing cores. The optically thicker core blocks the radiative transfer from the bottom to the top across the core. Thus, as shown in Fig. 5, the $M_{10}(r,z_o,t)$ around the axis is smaller than that near the lateral boundary at the early instant $ct/z_o=2.0$. For a medium which does not have an optically thick core, the $M_{10}(r,z_o,t)$ near the lateral boundary is smaller than that around the axis because of the radiation loss from the lateral boundary ([14]). Moreover, the larger β around the core is, the more obvious the blocking phenomenon is, as shown by the curves of cases C1 and C2. However, at the later instant $ct/z_o=2.5$, the $M_{10}(r,z_o,t)$ around the center becomes larger than that near the lateral boundary. Just after the irradiation pulse passes, the radiation that is detoured by the core and is scattered very few times is the major contributor of the $M_{10}(r,z_o,t)$. Such scattered radiation arriving at the central point, $r=0$ and $z=z_o$, takes a longer path than that arriving at the point near the lateral boundary does. A longer path implies a later arriving instant. Thus, when the scattered radiation arrives at the central point, the $M_{10}(r,z_o,t)$ near the lateral boundary has declined. However, at very late instants, the $M_{10}(r,z_o,t)$ near the lateral boundary becomes larger eventually, because of the larger albedo near the boundary.

The CPU time required to solve the integral equation of M_{00} by the QM and to evaluate the M_{10}'s and the M_{11}'s on a 21×21 grid mesh with 120 time steps for one of the nonhomogeneous isotropically scattering cases, say A2, is about 7040 s on a DEC Alpha 8400 computer. For the same case, the CPU time required by the RMCM to generate the moments of intensity on a 11×11 grid mesh at six instants is about 147,000 s. The CPU time of the RMCM is almost proportional to the number of the results obtained. Thus, to generate the M_{00}'s, M_{10}'s, and M_{11}'s on a 21×21 grid mesh with 120 time steps the CPU time required by the QM is about 1/1500 of that required by the RMCM employing 5×10^5 bundles. If the medium considered in case A2 is linearly anisotropically scattering with $a_1=1.0$, we have to solve the integral equations of M_{00}, M_{10}, and M_{11}. The CPU time increases to 7180 s to solve such a case. If the number of terms of the expression of the phase function in terms of Legendre polynomials becomes more, that is, the anisotropic scattering becomes complicated, the number of the moments of intensity required to be solved increases ([12]). This implies that the required computer memory and CPU time also increase. Fortunately, a complicated phase function can be approximated by a linearly anisotropic one without loss of the accuracy of solutions for many applications ([16]).

References

[1] McCormick, N. J., 1982, ''Remote Characterization of a Thick Slab Target With a Pulsed Laser,'' J. Opt. Soc. Am., **72**, pp. 756–759.

[2] Mitra, K., and Kumar, S., 1997, ''Application of Transient Radiative Transfer Equation to Oceanographic Lidar,'' *Proceedings of the 1997 ASME International Mechanical Engineering Congress and Exposition*, HTD-Vol. 353, ASME, New York, pp. 359–365.

[3] Mitra, K., and Churnside, J. H., 1999, ''Transient Radiative Transfer Equation Applied to Oceanographic Lidar,'' Appl. Opt., **38**, pp. 889–895.

[4] Yamada, Y., 1995, ''Light-Tissue Interaction and Optical Imaging in Biomedicine,'' *Annual Review of Heat Transfer*, Vol. 6, C. L. Tien, ed., Begell House, New York, pp. 1–59.

[5] Arridge, S. R., 1999, ''Optical Tomography in Medical Imaging,'' Inverse Probl., **15**, pp. R41–R93.

[6] Wilson, B. C., and Patterson, M. S., 1986, ''The Physics of Photodynamic Therapy,'' Phys. Med. Biol., **31**, pp. 327–360.

[7] Brewster, M. Q., and Yamada, Y., 1995, ''Optical Properties of Thick, Turbid Media From Picosecond Time-Resolved Light Scattering Measurements,'' Int. J. Heat Mass Transf., **38**, pp. 2569–2581.

[8] Hielscher, A. H., Liu, H., Chance, B., Tittel, F. K., and Jacques, S. L., 1996, ''Time-Resolved Photon Emission From Layered Turbid Media,'' Appl. Opt., **35**, pp. 719–728.

[9] Yamada, Y., and Hasegawa, Y., 1996, ''Time-Dependent FEM Analysis of Photon Migration in Biological Tissues,'' JSME Int. J., Ser. B, **39**, pp. 754–761.

[10] Pomraning, G. C., 1973, *The Equations of Radiation Hydrodynamics*, Pergamon, Oxford.

[11] Hunt, G. E., 1967, ''The Transport Equation of Radiative Transfer in a Three-Dimensional Space With Anisotropic Scattering,'' J. Inst. Math. Appl., **3**, pp. 181–192.

[12] Wu, C.-Y., and Wu, S.-H., 2000, ''Integral Equation Formulation for Transient Radiative Transfer in an Anisotropically Scattering Medium,'' Int. J. Heat Mass Transf., **43**, pp. 2009–2020.

[13] Walters, D. V., and Buckius, R. O., 1994, ''Monte Carlo Methods for Radiative Heat Transfer in Scattering Media,'' *Annual Review of Heat Transfer*, Vol. 5, C. L. Tien, ed., CRC, Boca Raton, FL, pp. 131–176.

[14] Wu, S.-H, 2000, ''A Study on Transient Radiative Transfer by Solving Integral Equations and Monte Carlo Simulation,'' Ph.D. thesis, National Cheng Kung University, Tainan, Taiwan, R.O.C. (in Chinese).

[15] Wu, C.-Y., 2000, ''Propagation of Scattered Radiation in a Participating Planar Medium With Pulse Irradiation,'' J. Quant. Spectrosc. Radiat. Transf., **64**, pp. 537–548.

[16] Modest, M. F., 1993, *Radiative Heat Transfer*, McGraw-Hill, New York.

Discrete Ordinates Interpolation Method Applied to Irregular Three-Dimensional Geometries

H. Cha
Graduate Student
e-mail: hjcha@htl.kaist.ac.kr

T.-H. Song
Professor, Mem. ASME
e-mail: thsong@sorak.kaist.ac.kr

Department of Mechanical Engineering, KAIST Kusong-dong 373-1, Yusong-ku, Taejon, Korea

Introduction

Many high temperature systems such as boilers and furnaces have complicated shapes. A solution method of the radiative transfer equation (RTE) in general three-dimensional geometries has been a very important issue. Regarding fluid flow and convective heat transfer, many numerical studies have been made in irregular geometries. Recent numerical codes can employ a nonorthogonal and/or unstructured three-dimensional grid system to be compatible with the real shape. Consequently, a corresponding numerical solution method for the RTE is asked for, too.

Many numerical schemes for the RTE have been reported in the literature. To name a few, there are zonal, Monte Carlo, spherical harmonics (P_N), discrete ordinates (S_N, DOM) methods, etc. A good review of them is given by Modest [1]. Among them, the DOM is widely used because the numerical equation can be easily derived and expanded to higher order approximations, and the grid system is nearly compatible with most of the flow solvers.

Extension of the DOM has been made successfully by many researchers. Raithby and Chui [2] propose the finite volume method (FVM) applicable to nonorthogonal coordinates. Chai et al. [3] propose the FVM in a little different form. The FVM of Chai et al. is applied successfully to two-dimensional irregular geometries. Maruyama and Aihara [4] suggest REM^2 (radiation element method by ray emission model) and it is applied to complicated shapes. Charette et al. [5] extend the DOM to be applicable to a triangular element in two dimensions and a tetrahedral element in three dimensions. Cheong and Song [6] invent the DOIM (discrete ordinates interpolation method) by modifying the DOM. They carefully scrutinize the false scattering and ray effects for the DOIM. Also, the DOIM is successfully applied to two-dimensional shapes. Cha and Song [7] have further extended the DOIM to a two-dimensional unstructured grid system in complicated geometries.

Further studies have been performed in three-dimensional geometries. Chai et al. [8] have solved three-dimensional problems of a cylinder, trigonal prism, boiler, etc. using the FVM. Maruyama and Aihara [9] apply the REM^2 to arbitrary three-dimensional shapes. Sakami et al. [10] compute the radiative heat transfer in three-dimensional enclosures using a rectangular element. Seo and Kim [11] obtain reliable results in three-dimensional problems using the DOIM.

In this study, the DOIM is extended to three-dimensional, nonorthogonal, and/or unstructured grid systems. To clearly scrutinize the accuracy of the RTE solution only, the temperature of the medium is given and it is assumed to be uniform so that the exact solution is available. The dependence of solution accuracy is examined by taking different optical depths with nonscattering medium as well as various grid systems.

Discrete Ordinates Equations

The radiative transfer equation for an absorbing, emitting, and scattering medium is

$$\frac{dI(\mathbf{r},\hat{\mathbf{s}})}{ds}=-\beta(\mathbf{r})I(\mathbf{r},\hat{\mathbf{s}})+\kappa(\mathbf{r})I_b(\mathbf{r})+\frac{\sigma_s(\mathbf{r})}{4\pi}\int_{4\pi}I(\mathbf{r},\hat{\mathbf{s}}')\Phi(\hat{\mathbf{s}}',\hat{\mathbf{s}})d\Omega'. \tag{1}$$

Equation (1) is subject to the following boundary condition for diffuse walls:

$$I(\mathbf{r}_w,\hat{\mathbf{s}})=\varepsilon(\mathbf{r}_w)I_{bw}(\mathbf{r}_w)+\frac{1-\varepsilon(\mathbf{r}_w)}{\pi}\int_{\hat{\mathbf{n}}\cdot\hat{\mathbf{s}}'<0}I(\mathbf{r}_w,\hat{\mathbf{s}}')|\hat{\mathbf{n}}\cdot\hat{\mathbf{s}}|d\Omega'. \tag{2}$$

In the discrete ordinates method, Eq. (1) is written for a set of n discrete ordinates. The integral over solid angle is approximated by an appropriate numerical quadrature, i.e., for ordinate $\hat{\mathbf{s}}_i$,

$$\int_{4\pi}I(\mathbf{r},\hat{\mathbf{s}}')\Phi(\hat{\mathbf{s}}',\hat{\mathbf{s}})d\Omega'\cong\sum_{j=1}^{n}I_j\Phi(\hat{\mathbf{s}}_j,\hat{\mathbf{s}}_i)W_j \tag{3}$$

where the W_j is the quadrature weight associated with the direction $\hat{\mathbf{s}}_j$. In this manner, Eq. (1) is approximated for a set of n directional intensities (I_i),

$$\frac{dI_i}{ds}=-\beta I_i+\beta\dot{S}_i \tag{4}$$

where source term $\dot{S}_i$ is given as

$$\dot{S}_i=(1-\omega)I_b+\frac{\omega}{4\pi}\sum_{j=1}^{n}I_j\Phi(\hat{\mathbf{s}}_j,\hat{\mathbf{s}}_i)W_j. \tag{5}$$

The boundary condition for a diffuse wall is approximated as

$$I_i=\varepsilon I_{bw}+\frac{1-\varepsilon}{\pi}\sum_{\hat{\mathbf{n}}\cdot\hat{\mathbf{s}}_j<0}|\hat{\mathbf{n}}\cdot\hat{\mathbf{s}}_j|I_jW_j,\quad \hat{\mathbf{n}}\cdot\hat{\mathbf{s}}_i>0. \tag{6}$$

Equation (4) together with the boundary condition Eq. (6) constitutes a set of n simultaneous first-order linear differential equations. The ordinates $\hat{\mathbf{s}}_j$ and angular weights W_j obtained by the S_N quadrature of Kim [12] is employed in this study. The quadrature data used in the DOIM are fully symmetric around the origin of the unit sphere, i.e., rotationally symmetric. Due to the rotational symmetry, the fully symmetric quadrature data can be used in two and three-dimensional geometries in any coordinate system.

Once the intensities have been determined, the radiative heat flux can be found as

$$\mathbf{q}''(\mathbf{r})=\int_{4\pi}I(\mathbf{r},\hat{\mathbf{s}})\hat{\mathbf{s}}d\Omega. \tag{7}$$

Discrete Ordinates Interpolation Method

Consider a situation where the intensity at a grid pint P in direction $\hat{\mathbf{s}}$ must be calculated using the upstream values (see Fig. 1). The upstream point is found as *IN* on a surface of the upstream element. Note that the upstream element may be made up with any polygonal surface. The upstream element has ‘‘known’’ vertices(or grid) intensities, from which the upstream intensity at *IN* is to be found. Figure 2 shows the geometric relation between P, *IN* and the pentagonal upstream surface more in detail. In Fig. 2,

---

Contributed by the Heat Transfer Division for publication in the JOURNAL OF HEAT TRANSFER. Manuscript received by the Heat Transfer Division, Nov. 22, 1999; revision received, June 21, 2000. Associate Technical Editor: J. P. Gore.

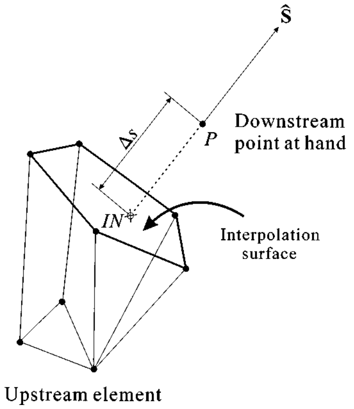

Fig. 1 Schematic of showing interpolation point between the downstream grid point and the upstream element in three-dimensional space

the intensities $(I_1, I_2, I_3, I_4, I_5)$ are the upstream values at the grid points. One can choose any type of element surface at his convenience. For example, complex shape such as a boiler can be made up using triangular surfaces at the corner sides and rectangular surfaces at the center part. In this situation, Eq. (4) is rewritten as

$$\frac{dI}{ds} = -\beta I + \beta \dot{S} \tag{8}$$

(hereafter, ordinate subscript i is omitted for brevity.)

The source term $\dot{S}$ is approximated by a Taylor series expansion about point P following Raithby and Chui [2]

$$\dot{S} = \dot{S}_P + \left.\frac{d\dot{S}}{ds}\right|_P (s - \Delta s). \tag{9}$$

Assuming we already know the intensity I_{IN}, Eq. (8) can be exactly solved for I_P, assuming constant β,

$$I_P = I_{IN} e^{-\beta \Delta s} + \int_0^{\Delta s} e^{-\beta(\Delta s - s)} \left[\dot{S}_P + \left.\frac{d\dot{S}}{ds}\right|_P (s - \Delta s) \right] \beta ds. \tag{10}$$

Performing the integration,

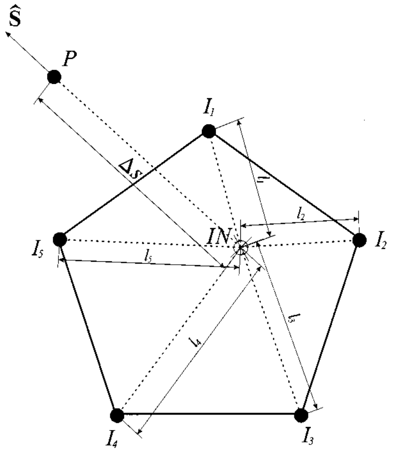

Fig. 2 Notation of grids around the interpolation point *IN* in an arbitrary interpolation surface (pentagon here)

$$I_P = I_{IN} e^{-\beta \Delta s} + \dot{S}_P (1 - e^{-\beta \Delta s}) - \frac{1}{\beta} \left.\frac{d\dot{S}}{ds}\right|_P [1 - e^{-\beta \Delta s}(1 + \beta \Delta s)]. \tag{11}$$

Indeed, I_{IN} can be interpolated as follows using first-order interpolation in the pentagon of Fig. 2:

$$I_{IN} = \frac{\frac{I_1}{l_1} + \frac{I_2}{l_2} + \frac{I_3}{l_3} + \frac{I_4}{l_4} + \frac{I_5}{l_5}}{\frac{1}{l_1} + \frac{1}{l_2} + \frac{1}{l_3} + \frac{1}{l_4} + \frac{1}{l_5}}. \tag{12}$$

The interpolation scheme could be higher order. In a complicated unstructured grid system, however, the simplest interpolation method is preferred for versatility. Equation (12) can be extended to an arbitrary polygon as

$$I_{IN} = \frac{\sum_m \frac{I_m}{l_m}}{\sum_m \frac{1}{l_m}} \tag{13}$$

where m denotes the neighboring grid points upstream of grid point P.

In the structured grid systems, the grid lines are those connecting grids along each Cartesian coordinate. However, in the unstructured grid systems, the way how the grids are interconnected to form the element surfaces should be set up in the grid-setting stage. Seo and Kim [11] have employed triangles as the interpolation surface formed by the diagonal lines of three rectangles around a vertices point of a cube. In this study, the closest element surface formed by the grid lines is taken for its simplicity. The gradient of $\dot{S}$ in Eq. (10) can be obtained from the following discretization equation:

$$\left.\frac{d\dot{S}}{ds}\right|_P = \frac{\dot{S}_P - \dot{S}_{IN}}{\Delta s} \tag{14}$$

where $\dot{S}_{IN}$ is interpolated in the same way as I_{IN}.

Emphasizing the interpolation feature of this method, Cheong and Song [6] have named this scheme ''discrete ordinates interpolation method.'' This is a pointwise nonconservative solution scheme.

Results and Discussion

Three problems are tested by using the DOIM. The medium is absorbing-emitting and nonscattering. It is maintained at a constant temperature T_g and the walls are cold black. Thus, the exact solution of the RTE at any location is given by

$$I(s) = I_{bw} e^{-\kappa s} + I_b (1 - e^{-\kappa s}). \tag{15}$$

When Eq. (15) is introduced to Eq. (7), the exact radiative wall heat flux is obtained by using the S_N quadrature integration method.

The wall heat flux is used to check the accuracy of the DOIM. The relative average error of the wall heat flux is defined as

$$\text{Error} = \sum_{\text{node}} \frac{|q''_{\text{DOIM}} - q''_{\text{exact}}| / q''_{\text{exact}}}{\text{Number of nodes}} \tag{16}$$

where q''_{DOIM} is the result of the DOIM and q''_{exact} is the exact result obtained from Eq. (15). The results are shown for various optical depths.

Nonorthogonal Hexahedral Enclosure. The first problem is to find the wall heat fluxes along the centerline of a wall ($z = 0.5$, $y = 0.0$) in a nonorthogonal hexahedral enclosure. Figure 3 shows the geometry of a hexahedral enclosure. The calculation is performed by varying the absorption coefficient ($\kappa = 0.1$, 1.0,

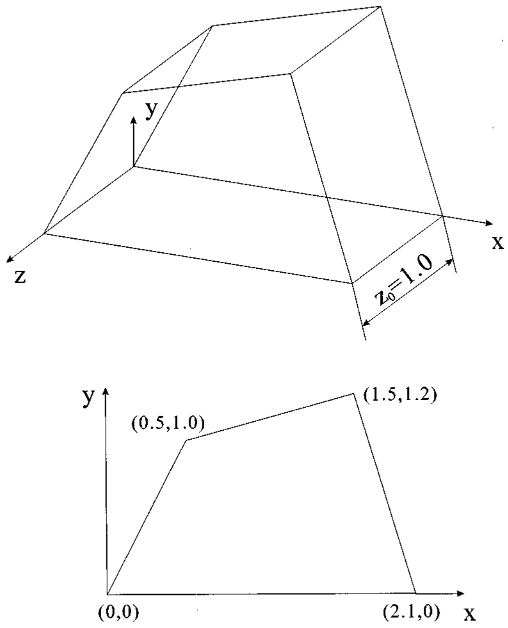

Fig. 3 Schematic of a hexahedral enclosure (unit; m)

$10\ \mathrm{m}^{-1}$) and using S_4 method. The grid system is an $11\times11\times11$ structured one. Computational results are compared with the exact solutions in Fig. 4. The heat flux is nondimensionalized by the blackbody emissive power of the gas. Examining the discrepancy, the exact solutions are smaller and the errors are larger at the corners, where the gradient of heat flux is larger. Generally, the results of the DOIM agree well with the exact solutions. It shows the applicability of the DOIM in nonorthogonal enclosures. The relative average errors are 8.53 percent at $\kappa=0.1\ \mathrm{m}^{-1}$, 7.47 percent at $\kappa=1.0\ \mathrm{m}^{-1}$, and 1.57 percent at $\kappa=10.0\ \mathrm{m}^{-1}$.

Regular Cubic Enclosure. Figure 5 shows a schematic of the structured grid system in a regular cubic enclosure. This enclosure is 1 m at each edge. Numerical results are obtained by using $11\times11\times11$ grids and S_4 method. Three optical depths $\kappa D=0.1$, 1.0, and 10 are tried.

Figure 6 shows the results of the DOIM and the exact solutions for the heat flux at a wall ($y=0.5$, $z=0.0$). Like the previous example, the error is larger near the corners. To verify the grid dependency, different grids are tested. Table 1 shows the relative average errors of the wall heat flux with varying the optical depths and the numbers of ordinates and grids. With a few exceptions, the errors are generally reduced as the numbers of ordinates and grids are increased. Improvement of accuracy by an increase of grids is not as notable as that by an increase of ordinates in this problem.

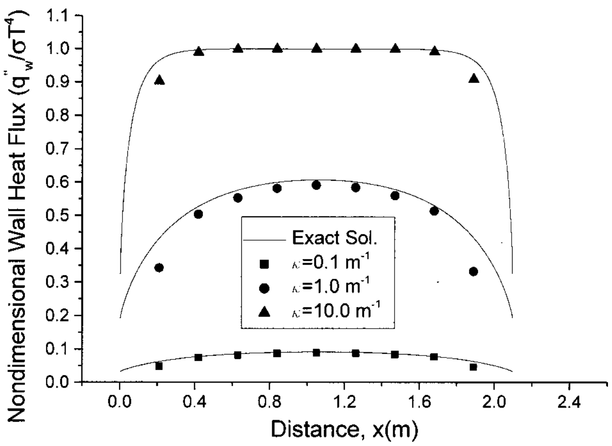

Fig. 4 Wall heat fluxes in the hexahedral enclosure of Fig. 3

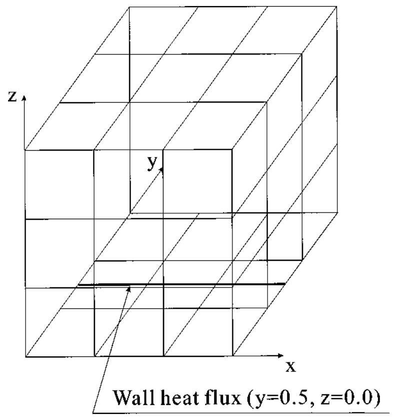

Fig. 5 Schematic of the structured grids in a cubic enclosure

Comparison of Computational Results in the Structured and Unstructured Grid Systems. The last problem is to compare the wall heat fluxes when using the structured and unstruc-

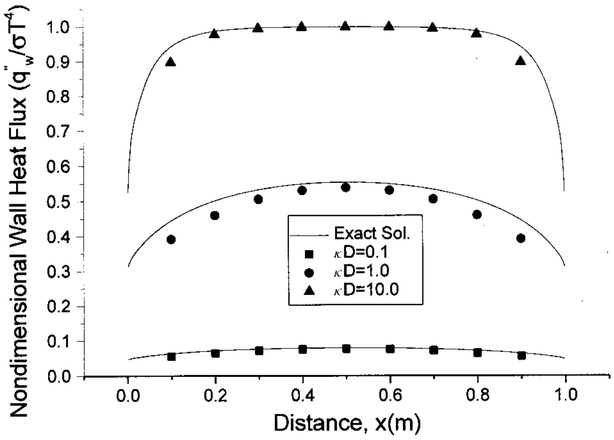

Fig. 6 Wall heat fluxes when using the 11×11×11 structured grids

Table 1 Comparison of the relative average error of the DOIM, with varying the optical depths and the numbers of grids and ordinates for the regular cubic enclosure

Optical Depth (κD)	No. of Grids	S_N	Error(%)
0.1	11×11×11	S_4	7.89
		S_6	4.73
	21×21×21	S_4	5.25
		S_6	6.50
1.0	11×11×11	S_4	6.70
		S_6	3.47
	21×21×21	S_4	4.57
		S_6	4.59
10.0	11×11×11	S_4	1.36
		S_6	0.70
	21×21×21	S_4	1.35
		S_6	0.69

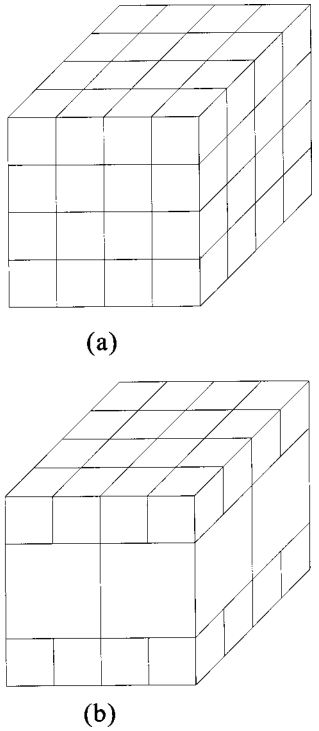

Fig. 7 Comparison of the two grid systems: (*a*) structured grids; (*b*) unstructured grids

tured grid systems for a regular cubic enclosure. Figure 7 shows a schematic of the two grid systems. The structured grid system has $11 \times 11 \times 11$ grids. The unstructured grid system has the same grids at the top and bottom surfaces, however, it is sparse between them. That is, the unstructured grid system has a top layer of $11 \times 11 \times 1$, a middle layer of $6 \times 6 \times 4$, and a bottom layer of $11 \times 11 \times 1$. In total, the structured grid system has 1331 grid points and the unstructured one has only 386 grid points. Angular quadrature is made use of by the S_4 method.

Computational results are shown in Fig. 8. Numerical results generally agree well with the exact solutions for any grid system. As in the previous results, the errors of numerical results are larger near the edges in both the two grid systems. The advantage of the unstructured grids is clear when considering the computational time. Using a personal computer with pentium 166 MHz CPU, the structured grid system consumes 126.5s while the unstructured one consumes 32.5s at $\kappa D = 1.0$. This shows that the computational time is roughly proportional to the number of grids. The relative average errors for the two grid systems are shown in Table 2. The accuracy of the unstructured grid is even slightly better. This example shows that a proper unstructured grid can yield better results both in accuracy and in computational efforts.

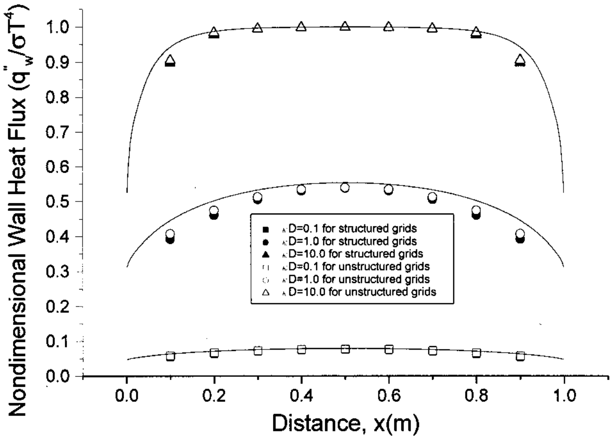

Fig. 8 Wall heat fluxes in the structured and unstructured grid systems

Table 2 The relative average errors (percent) of wall heat flux when using the structured or the unstructured grid systems

Optical Depth (κD)	Structured Grids	Unstructured Grids
0.1	7.89	5.34
1.0	6.70	4.79
10.0	1.36	1.02

Conclusions

This paper shows that the DOIM can be applied in a general grid system in three-dimensional problems. The first-order interpolation method is taken on a polygon. The DOIM shows good results in nonorthogonal coordinates for a general hexahedral enclosure as well as in orthogonal coordinates for a regular cubic enclosure. Another advantage of the DOIM is the applicability of the unstructured grids. The last application shows that shorter computational time and still accurate solution can be obtained if a proper unstructured grid system is selected. It is shown that the DOIM is a potential powerful tool for radiation analysis.

Acknowledgment

This study was supported by Korea Science and Engineering Foundation (996-1000-001-2) and National Research Laboratory Project (1999-135).

Nomenclature

I = radiative intensity, W/m^{2}sr
I_b = blackbody radiative intensity, W/m^{2}sr
l_m = length between a grid point and the interpolation point, m
n = total number of the ordinates
$\hat{\mathbf{n}}$ = inward unit normal vector at wall
$\hat{\mathbf{s}}$ = ordinate direction vector
$\dot{S}$ = source function, W/m^{2}sr
$\mathbf{q}''_w$ = radiative heat flux vector, W/m^2
$\mathbf{r}$ = position vector, m
s = coordinate along a line of sight, m
T_g = medium temperature, K
W_i = angular weights ($i = 1, \ldots, n$)
β = extinction coefficient, m^{-1}
ε = wall emissivity
κ = absorption coefficient, m^{-1}
Φ = scattering phase function
Ω = solid angle, sr
σ = Stefan-Boltzmann constant, W/m^2 K^4
σ_s = scattering coefficient, m^{-1}
ω = scattering albedo (σ_s/β)

Subscripts

i, j = indices for ordinate directions
m = upstream grid point
IN = interpolation point
P = grid point under consideration
w = wall

References

[1] Modest, M. F., 1993, *Radiative Heat Transfer*, McGraw-Hill, New York.
[2] Raithby, G. D., and Chui, E. H., 1990, ''A Finite Volume Method for Predict-

ing a Radiant Heat Transfer in Enclosures With Participating Media,'' ASME J. Heat Transfer, **112**, pp. 415–423.

[3] Chai, J. C., Lee, H. S., and Patankar, S. V., 1994, ''Finite Volume Method for Radiation Heat Transfer,'' J. Thermophys. Heat Transfer, **8**, No. 3, pp. 419–425.

[4] Maruyama, S., and Aihara, T., 1995, ''Radiative Heat Transfer of Arbitrary 3-D Participating Media with Non-participating Media by a Generalized Numerical Method REM,'' *Proc. 1st Int'l. Symposium on Radiation Transfer*, Kusadasi, pp. 153–167.

[5] Charette, A., Sakami, M., and Le Dez, V., 1997, ''Analysis of Radiative Heat Transfer in Enclosures of Complex Geometry Using the Discrete Ordinates Method,'' *Proc. 2nd Int'l. Symposium on Radiation Transfer,* Kusadasi, pp. 253–270.

[6] Cheong, K. B., and Song, T. H., 1997, ''An Alternative Discrete Ordinates Method With Interpolation and Source Differencing for Two-Dimensional Radiative Transfer Problems,'' Numer. Heat Transfer, Part B, **32**, pp. 107–125.

[7] Cha, H., and Song, T. H., 1998, ''Discrete Ordinates Interpolation Method for Solution of Radiative Transfer Equation in Arbitrary 2-D Geometry and Unstructured Grid System,'' *Proc. of 11th IHTC*, Vol. 7, pp. 267–274.

[8] Chai, J. C., Moder, J. P., and Parthasarathy, G., 1996, ''Radiation Heat Transfer in Three-Dimensional Irregular Geometries,'' *31st AIAA Thermophysics Conference*, New Orleans, pp. 1–6.

[9] Maruyama, S., and Aihara, T., 1997, ''Radiation Heat Transfer of Arbitrary Three-Dimensional Absorbing, Emitting and Scattering Media and Specular and Diffuse Surfaces,'' ASME J. Heat Transfer, **119**, pp. 129–136.

[10] Sakami, M., Charette, A., and Le Dez, V., 1998, ''Radiation Heat Transfer in Three-Dimensional Enclosures of Complex Geometry by Using the Discrete Ordinates Method,'' J. Quant. Spectrosc. Radiat. Transf., **59**, No. 1–2, pp. 117–136.

[11] Seo, S. H., and Kim, T. K., 1998, ''Study on Interpolation Schemes of the Discrete Ordinates Interpolation Method for Three-Dimensional Radiative Transfer With Nonorthogonal Grids,'' ASME J. Heat Transfer, **120**, pp. 1091–1094.

[12] Kim, T. K., 1990, ''Radiation and Combined Mode Heat Transfer Analyses in Absorbing, Emitting and Mie-Anisotropic Scattering Media Using the S-N Discrete Ordinates Method,'' Ph.D. thesis, University of Minnesota, MN.